

SEPTEMBER 2021

AJNR

VOLUME 42 • PP 1557-1740

AJNR

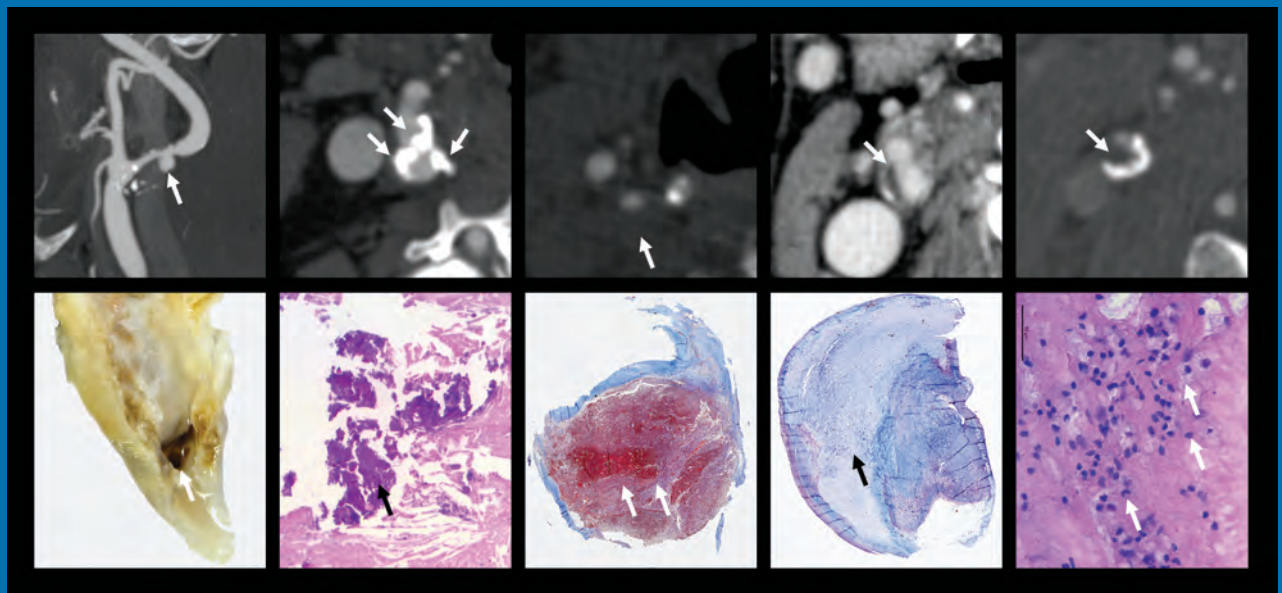
AMERICAN JOURNAL OF NEURORADIOLOGY

SEPTEMBER 2021
VOLUME 42
NUMBER 9
WWW.AJNR.ORG

THE JOURNAL OF DIAGNOSTIC AND
INTERVENTIONAL NEURORADIOLOGY

Carotid artery plaque imaging
Safety and efficacy of the Woven EndoBridge device
Second opinions in head and neck imaging

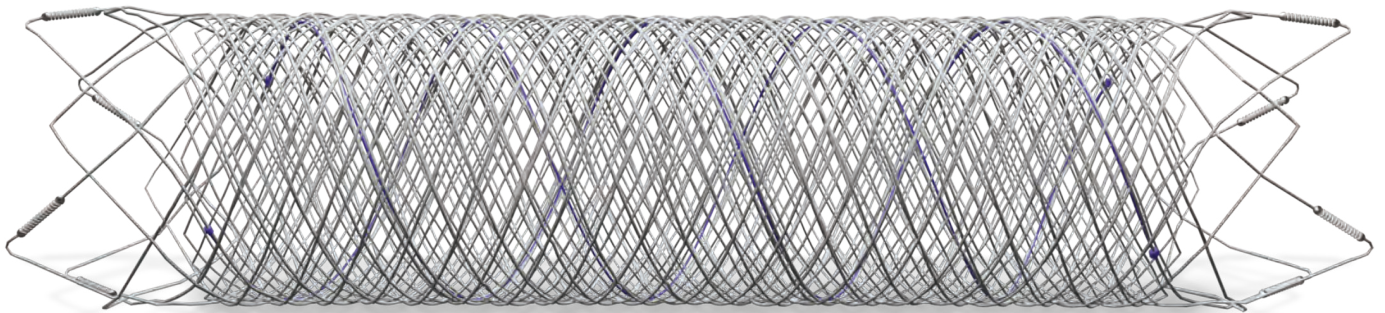
Official Journal ASNR • ASFNR • ASHNR • ASPNR • ASSR



FRED™

Flow Re-Direction
Endoluminal Device

FLOW DIVERSION.



SIMPLIFIED.



MicroVention Worldwide
Innovation Center
35 Enterprise
Aliso Viejo, CA 92656 USA
MicroVention UK Limited
MicroVention Europe S.A.R.L.
MicroVention Deutschland GmbH
Web

PH +1 714.247.8000

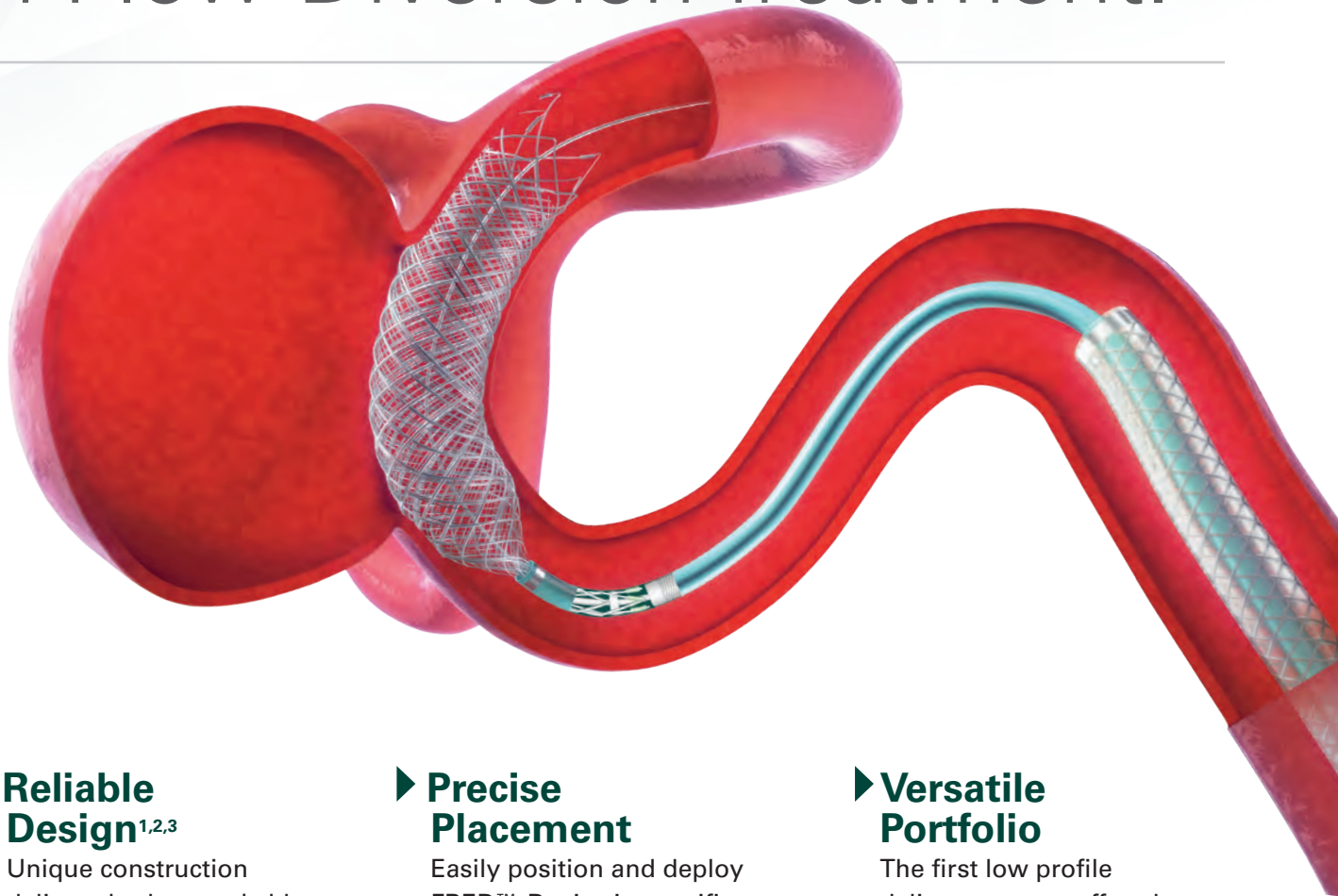
PH +1 44 (0) 191 258 6777

PH +33 (1) 39 21 77 46

PH +49 211 210 798-0

microvention.com

The New Standard of **Ease and Simplicity** in Flow Diversion Treatment.



► **Reliable Design**^{1,2,3}

Unique construction delivers both remarkable ease of use and excellent flow diversion^{1,2,3}

► **Precise Placement**

Easily position and deploy FRED™ Device in specific, targeted locations^{4,5,6}

► **Versatile Portfolio**

The first low profile delivery system offered in combination with large diameter and long length options

References:

1. TR11-211 2. TR13-171 3. TR15-055 4. TR13-192 5. TR15-072 6. TR19-145

The Flow Re-Direction Endoluminal Device (FRED™) System is indicated for use in the internal carotid artery from the petrous segment to the terminus for the endovascular treatment of adult patients (22 years of age or older) with wide-necked (neck width ≥ 4 mm or dome-to-neck ratio < 2) saccular or fusiform intracranial aneurysms arising from a parent vessel with a diameter ≥ 2.0 mm and ≤ 5.0 mm.

Use of the FRED™ System is contraindicated under these circumstances: Patients in whom anticoagulant, anti-platelet therapy, or thrombolytic drugs are contraindicated. Patients with known hypersensitivity to metal such as nickel-titanium and metal jewelry. Patients with anatomy that does not permit passage or deployment of the FRED™ System. Patients with an active bacterial infection. Patients with a pre-existing stent in place at the target aneurysm. Patients in whom the parent vessel size does not fall within the indicated range. Patients who have not received dual anti-platelet agents prior to the procedure. For complete indications, contraindications, potential complications, warnings, precautions, and instructions, see instructions for use (IFU provided in the device).

RX Only: Federal (United States) law restricts this device to sale by or on the order of a physician.

MICROVENTION™ and FRED™ are registered trademarks of MicroVention, Inc. in the United States and other jurisdictions. © 2020 MicroVention, Inc. 04/2020.



MIDRC

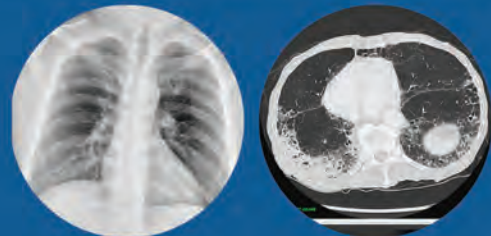
MEDICAL IMAGING AND DATA RESOURCE CENTER.

Medical Imaging in the Fight against COVID-19 Call for Contributions

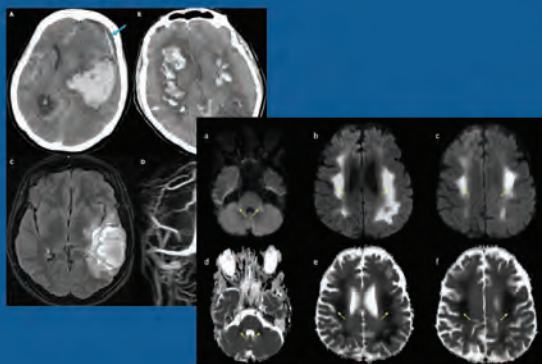
The Medical Imaging and Data Resource Center (MIDRC) is a multi-organizational initiative in the fight against the ongoing worldwide pandemic co-led by the ACR®, the RSNA, and the AAPM and is hosted at the University of Chicago.



The primary goal is to accelerate machine learning research by creating a high quality COVID-19 image commons linked to relevant clinical data made available as a public resource.



ASNR has teamed up with MIDRC to advance the understanding of the neuroimaging manifestations of COVID-19 and to enhance the MIDRC image commons.



- To ensure success, MIDRC encourages all institutions and hospitals, both small and large, to donate their COVID-19 medical images and data to the cause.
- MIDRC provides a HIPAA-compliant mechanism to securely submit medical images and clinical metadata, and is committed to helping institutions throughout the submission process.

Visit midrc.org for more information



THE UNIVERSITY OF
CHICAGO



National Institute of Biomedical Imaging and Bioengineering
Creating Biomedical Technologies to Improve Health

Explore the New ASNR Career Center



Your Premier Resource for Professional Development

- Access to jobs in the National Healthcare Career Network
- Confidential resume posting
- One-time free resume review
- Professional online profile
- Saved jobs capability

Start here: careers.asnr.org

ASNR
American Society of Neuroradiology

AJNR *go green*

***AJNR* urges American Society of Neuroradiology members to reduce their environmental footprint by voluntarily suspending their print subscription.**

The savings in paper, printing, transportation, and postage directly fund new electronic enhancements and expanded content.

The digital edition of *AJNR* presents the print version in its entirety, along with extra features including:

- Publication Preview
- Case Collection
- Podcasts
- The *AJNR* News Digest
- The *AJNR* Blog

It also reaches subscribers much faster than print. An electronic table of contents will be sent directly to your mailbox to notify you as soon as it publishes.

Readers can search, reference, and bookmark current and archived content 24 hours a day on www.ajnr.org.

ASNR members who wish to opt out of print can do so by using the *AJNR* Go Green link on the *AJNR* Website (<http://www.ajnr.org/content/subscriber-help-and-services>). Just type your name in the email form to stop print and spare our ecosystem.

ASNR 60th Annual Meeting and Symposium Neuroradiologicum XXII

CALL FOR ABSTRACTS

Join us May 13-18, 2022, to present the best scientific research in neuroradiology.

The Symposium Neuroradiologicum XXII will be held on May 13-16, followed immediately by the 60th Annual Meeting of the ASNR on May 16-18. Both meetings will be held in person and virtually.

ABSTRACT SUBMISSION DEADLINE

Monday, November 1, 2021 (11:59 PM ET)

Submit online at <https://www.aievolution.com/asn2201/>

Acceptance notifications will be sent on or before January 17, 2022, upon conclusion of peer review.

ABSTRACT SUBMISSION CATEGORIES

Scientific Oral Presentation: will be included during ASNR ONLY

Electronic Scientific Poster: will be shown during both meetings

Electronic Educational Exhibit: will be shown during both meetings

Excerpta (Oral Presentations): will be included during SNR ONLY

ABSTRACT SUBMISSION INFORMATION AND CRITERIA

1. By submitting an **Oral or Excerpta** abstract, you agree that the presenting author will register, attend and present in person. By submitting an **Electronic Poster or Educational Exhibit** abstract, you agree that the presenting author will register, attend and present virtually OR in person.
2. Presenters of accepted abstracts must register at their own expense for ASNR22 and/or SNR XXII.
3. All authors must have disclosure on file in the submission system. Remove authors with missing disclosures prior to submitting abstracts. Email education@asnr.org to add authors after the submission deadline.
4. The use of charts, tables and graphics are encouraged if relevant to the research submitted.
5. DO NOT SUBMIT DUPLICATE ABSTRACTS IN MULTIPLE CATEGORIES OR SUBMISSION TYPES.
6. Changes can be made to submitted abstracts until the deadline.
7. Available ASNR awards include the Cornelius Dyke Memorial Award, Outstanding Oral Presentation Awards and Educational Exhibit Awards.
8. The *American Journal of Neuroradiology (AJNR)* and *Neurographics* encourage presenters to submit manuscripts based on their work to *AJNR* or *Neurographics* before considering other journals.

Questions? Contact the ASNR Education Department at education@asnr.org.



ASNR22

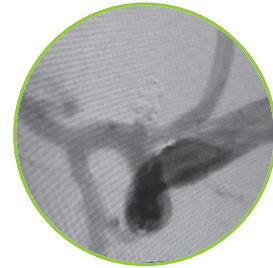
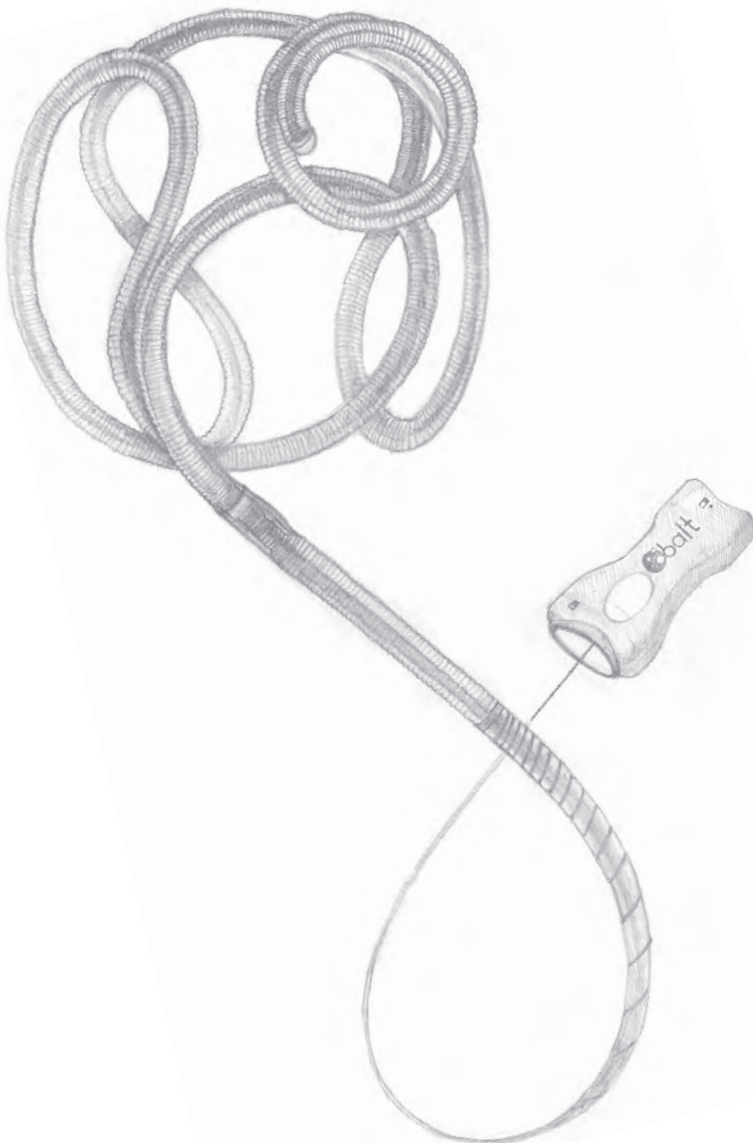


SNRXXII

May 13-18, NYC • Reconnecting The Global Neuroradiology Community

OPTIMAX

**FEEL THE DIFFERENCE:
VOLUME, SOFTNESS AND STABILITY**



Complete and Unique Offerings:

The only large volume coil
available in a **Super Soft**
configuration in 1mm to 3.5mm
diameters, including half sizes.

Visit our products page at www.Balt-USA.com to learn more.

Balt USA

29 Parker, Irvine, CA 92618
tel 949.788.1443 fax 949.788.1444

balt-usa.com

©2021 BALT USA MKTG-250 Rev. A

 **balt**
inspiring innovation

AJNR

AMERICAN JOURNAL OF NEURORADIOLOGY

SEPTEMBER 2021
VOLUME 42
NUMBER 9
WWW.AJNR.ORG

Publication Preview at www.ajnr.org features articles released in advance of print. Visit www.ajnrblog.org to comment on AJNR content and chat with colleagues and AJNR's News Digest at <http://ajnrdigest.org> to read the stories behind the latest research in neuroimaging.

1557 **PERSPECTIVES** *S.A. Greenberg*

REVIEW ARTICLE

-   1558 **Radiology-Pathology Correlations of Intracranial Clots: Current Theories, Clinical Applications, and Future Directions** *J.C. Benson, et al.* **ADULT BRAIN**

PRACTICE PERSPECTIVES

-    1566 **Roadmap Consensus on Carotid Artery Plaque Imaging and Impact on Therapy Strategies and Guidelines: An International, Multispecialty, Expert Review and Position Statement** *L. Saba, et al.* **EXTRACRANIAL VASCULAR**
-  1576 **Racial and Socioeconomic Disparities in the Use and Outcomes of Endovascular Thrombectomy for Acute Ischemic Stroke** *A.M. Mehta, et al.* **INTERVENTIONAL**

GENERAL CONTENTS

-   1584 **Evaluation of Ultrafast Wave-Controlled Aliasing in Parallel Imaging 3D-FLAIR in the Visualization and Volumetric Estimation of Cerebral White Matter Lesions** *C. Ngamsombat, et al.* **ADULT BRAIN**
-  1591 **A Volumetric Metric for Monitoring Intracranial Aneurysms: Repeatability and Growth Criteria in a Longitudinal MR Imaging Study** *X. Liu, et al.* **ADULT BRAIN**
-  1598 **Reliability and Agreement of 2D and 3D Measurements on MRAs for Growth Assessment of Unruptured Intracranial Aneurysms** *K.M. Timmins, et al.* **ADULT BRAIN**
-   1604 **Neuroimaging Findings in Retinal Vasculopathy with Cerebral Leukoencephalopathy and Systemic Manifestations** *E.S. Hoogeveen, et al.* **ADULT BRAIN**
-  1610 **Absence of Meckel Cave: A Rare Cause of Trigeminal Neuralgia** *A. Jain, et al.* **ADULT BRAIN HEAD & NECK**
-   1615 **Noninvasive Angiographic Results of Clipped or Coiled Intracranial Aneurysms: An Inter- and Intraobserver Reliability Study** *A. Benomar, et al.* **INTERVENTIONAL**
-  1621 **Safety and Efficacy of Stent-Assisted Coiling of Unruptured Intracranial Aneurysms Using Low-Profile Stents in Small Parent Arteries** *J. Kim, et al.* **INTERVENTIONAL**

AJNR (Am J Neuroradiol ISSN 0195–6108) is a journal published monthly, owned and published by the American Society of Neuroradiology (ASNR), 800 Enterprise Drive, Suite 205, Oak Brook, IL 60523. Annual dues for the ASNR include approximately 21% for a journal subscription. The journal is printed by Intellicor Communications, 330 Eden Road, Lancaster, PA 17601; Periodicals postage paid at Oak Brook, IL and additional mailing offices. Printed in the U.S.A. POSTMASTER: Please send address changes to American Journal of Neuroradiology, P.O. Box 3000, Denville, NJ 07834, U.S.A. Subscription rates: nonmember \$410 (\$480 foreign) print and online, \$320 online only; institutions \$470 (\$540 foreign) print and basic online, \$935 (\$1000 foreign) print and extended online, \$380 online only (basic), \$825 online only (extended); single copies are \$35 each (\$40 foreign). Indexed by PubMed/MEDLINE, BIOSIS Previews, Current Contents (Clinical Medicine and Life Sciences), EMBASE, Google Scholar, HighWire Press, Q-Sensei, RefSeek, Science Citation Index, SCI Expanded, Meta/CZI, ReadCube, and Semantic Scholar. Copyright © American Society of Neuroradiology.

-   1627 Safety and Efficacy of the Woven EndoBridge Device for Treatment of Ruptured Intracranial Aneurysms: A Systematic Review and Meta-analysis *M.A. Essibayi, et al.* **INTERVENTIONAL**
- 1633 The Safety of Intra-arterial Tirofiban during Endovascular Therapy after Intravenous Thrombolysis *S.H. Jang, et al.* **INTERVENTIONAL**
-  1638 Ticagrelor versus Clopidogrel in the Dual Antiplatelet Regimen for Intracranial Stenting or Flow-Diverter Treatment for Unruptured Cerebral Aneurysms: A Single-Center Cohort Study *K.Y. Park, et al.* **INTERVENTIONAL**
-  1645 Nonstenotic Carotid Plaques in Ischemic Stroke: Analysis of the STRATIS Registry *N. Singh, et al.* **EXTRACRANIAL VASCULAR**
-   1653 Altered Blood Flow in the Ophthalmic and Internal Carotid Arteries in Patients with Age-Related Macular Degeneration Measured Using Noncontrast MR Angiography at 7T *M.L. Hibert, et al.* **HEAD & NECK ADULT BRAIN**
-   1661 Time Course and Clinical Correlates of Retinal Diffusion Restrictions in Acute Central Retinal Artery Occlusion *L.A. Danyel, et al.* **HEAD & NECK ADULT BRAIN**
- 1667 Diagnostic Performance of Conebeam CT Pixel Values in Active Fenestral Otosclerosis *F. Deng, et al.* **HEAD & NECK**
- 1671 Can Assessment of the Tongue on Brain MRI Aid Differentiation of Seizure from Alternative Causes of Transient Loss of Consciousness? *J.A. Erickson, et al.* **HEAD & NECK**
-  1676 Recommendations in Second Opinion Reports of Neurologic Head and Neck Imaging: Frequency, Referring Clinicians' Compliance, and Diagnostic Yield *S.A. Heinz, et al.* **HEAD & NECK**
-   1683 Dual-Layer Spectral CT Imaging of Upper Aerodigestive Tract Cancer: Analysis of Spectral Imaging Parameters and Impact on Tumor Staging *C.C.-T. Hsu, et al.* **HEAD & NECK**
-  1690 Preoperative MRI Evaluation of Thyroid Cartilage Invasion in Patients with Laryngohypopharyngeal Cancer: Comparison of Contrast-Enhanced 2D Spin-Echo and 3D T1-Weighted Radial Gradient Recalled-Echo Techniques *C.J. Park, et al.* **HEAD & NECK**
-  1695 When Should a Brain MRI Be Performed in Children with New-Onset Seizures? Results of a Large Prospective Trial *R. Hourani, et al.* **PEDIATRICS**
-  1702 Radiomic Phenotypes Distinguish Atypical Teratoid/Rhabdoid Tumors from Medulloblastoma *M. Zhang, et al.* **PEDIATRICS FUNCTIONAL**
-  1709 Synthetic MRI in Neurofibromatosis Type 1 *G. Coban, et al.* **PEDIATRICS**
-  1716 Evaluation of Posterior Fossa Biometric Measurements on Fetal MRI in the Evaluation of Dandy-Walker Continuum *U.D. Nagaraj, et al.* **PEDIATRICS**
- 1722 Enlargement of the Optic Chiasm: A Novel Imaging Finding in Glutaric Aciduria Type 1 *A.A. Ntorkou, et al.* **PEDIATRICS**
-   1727 Atlas-Based Quantification of DTI Measures in a Typically Developing Pediatric Spinal Cord *S. Shahrampour, et al.* **PEDIATRICS FUNCTIONAL**
-  1735 Cervical Spinal Cord Degeneration in Spinocerebellar Ataxia Type 7 *C.R. Hernandez-Castillo, et al.* **SPINE**
- 1740 **35 YEARS AGO IN AJNR**

ONLINE FEATURES

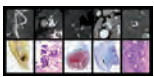
LETTERS

- E60 CT-Guided Caudal Epidural Infiltrations: A Technical Note *J. Gossner*

- E62 More on Exploiting the T1 Shinethrough and T2* Effects Using Multiecho Susceptibility-Weighted Imaging** *C.C.-T. Hsu, et al.*
- E64 Susceptibility Artifacts in the Anterior Cranial Fossa Mimicking Hemorrhage in Patients with Anosmia** *J.J. Manov, et al.*
- E66 Reply** *M.F.V.V. Aragao, et al.*
- E69 The Possible Difference of Underlying Pathophysiologies between “Ivy Sign” on Contrast-Enhanced MRI and FLAIR** *N. Mori, et al.*
- E70 Reply** *L.X. Wang, et al.*
- E71 Regarding “CTA Evaluation of Basilar Septations: An Entity Better Characterized as Aberrant Basilar Fenestrations”** *J. Hynes, et al.*

BOOK REVIEWS *R.M. Quencer, Section Editor*

Please visit www.ajnrblog.org to read and comment on Book Reviews.



Carotid plaque CT features with corresponding histology below. From Saba, et al in this issue.



Indicates Editor's Choices selection



Indicates Fellows' Journal Club selection



Indicates open access to non-subscribers at www.ajnr.org



Indicates article with supplemental online data



Indicates article with supplemental online video



Evidence-Based Medicine Level 1



Evidence-Based Medicine Level 2

EDITOR-IN-CHIEF

Jeffrey S. Ross, MD

Professor of Radiology, Department of Radiology,
Mayo Clinic College of Medicine, Phoenix, AZ

SENIOR EDITORS

Harry J. Cloft, MD, PhD

Professor of Radiology and Neurosurgery,
Department of Radiology, Mayo Clinic College of
Medicine, Rochester, MN

Christopher G. Filippi, MD

Professor and Alice Ettinger-Jack R. Dreyfuss
Chair of Radiology,
Tufts University School of Medicine,
Radiologist-in-Chief
Tufts University Medical Center, Boston, MA

Thierry A.G.M. Huisman, MD

Radiologist-in-Chief, Texas Children's Hospital,
Houston, TX

Yvonne W. Lui, MD

Associate Professor of Radiology,
Chief of Neuroradiology,
New York University School of Medicine,
New York, NY

C.D. Phillips, MD, FACR

Professor of Radiology, Weill Cornell Medical
College, Director of Head and Neck Imaging,
New York-Presbyterian Hospital, New York, NY

Lubdha M. Shah, MD, MS

Professor of Radiology and Director of Spine
Imaging, University of Utah Department of
Radiology and Imaging Sciences, Salt Lake City, UT

STATISTICAL SENIOR EDITOR

Bryan A. Comstock, MS

Senior Biostatistician,
Department of Biostatistics,
University of Washington, Seattle, WA

ARTIFICIAL INTELLIGENCE DEPUTY EDITOR

Peter D. Chang, MD

Assistant Professor-in-Residence,
Departments of Radiological Sciences,
Computer Sciences, and Pathology,
Director, Center for Artificial Intelligence in
Diagnostic Medicine (CAIDM),
University of California, Irvine, Irvine, CA

EDITORIAL BOARD

Ashley H. Aiken, Atlanta, GA

Lea M. Alhilali, Phoenix, AZ

Mohammed A. Almekhlafi, Calgary, Alberta,
Canada

Joachim Berkefeld, Frankfurt, Germany

Aashim Bhatia, Pittsburgh, PA

Waleed Brinjikji, Rochester, MN

Judah Burns, New York, NY

Danielle Byrne, Dublin, Ireland

Federico Cagnazzo, Montpellier, France

J. Levi Chazen, New York, NY

James Y. Chen, San Diego, CA

Gloria C. Chiang, New York, NY

Daniel Chow, Irvine, CA

Kars C.J. Compagne, Rotterdam, The Netherlands

Arturo Consoli, Suresnes, France

Seena Dehkharghani, New York, NY

Nilesh K. Desai, Houston, TX

Yonghong Ding, Rochester, MN

Birgit Ertl-Wagner, Toronto, Ontario, Canada

Clifford J. Eskey, Hanover, NH

Massimo Filippi, Milan, Italy

Nils D. Forkert, Calgary, Alberta, Canada

Ana M. Franceschi, New York, NY

Frank Gaillard, Melbourne, Australia

Joseph J. Gemmete, Ann Arbor, Michigan

Wende N. Gibbs, Phoenix, AZ

Philipp Gölitz, Erlangen, Germany

Brent Griffith, Detroit, MI

Joseph M. Hoxworth, Phoenix, Arizona

Raymond Y. Huang, Boston, MA

Gábor Janiga, Magdeburg, Germany

Christof Karmonik, Houston, TX

Timothy J. Kaufmann, Rochester, MN

Hillary R. Kelly, Boston, MA

Toshibumi Kinoshita, Akita, Japan

Alexander W. Korutz, Chicago, IL

Stephen F. Kralik, Houston, TX

Alexander Lerner, Los Angeles, CA

Yinsheng Li, Madison, WI

Franklin A. Marden, Chicago, IL

Markus A. Möhlenbruch, Heidelberg, Germany

Kambiz Nael, Los Angeles, CA

Renato Hoffmann Nunes, Sao Paulo, Brazil

Sasan Partovi, Cleveland, OH

Johannes A.R. Pfaff, Salzburg, Austria

Laurent Pierot, Reims, France

Alireza Radmanesh, New York, NY

Prashant Raghavan, Baltimore, MD

Eytan Raz, New York, NY

Paul M. Ruggieri, Cleveland, OH

Sebastian Schafer, Madison, WI

Maksim Shapiro, New York, NY

Timothy Shepherd, New York, NY

James Shin, New York, NY

Mark S. Shiroishi, Los Angeles, CA

Bruno P. Soares, Baltimore, MD

Jason F. Talbott, San Francisco, CA

Ruth Thiex, Everett, Washington

Vincent Thijs, Melbourne, Victoria, Australia

Anderanik Tomasian, Los Angeles, CA

Fabio Triulzi, Milan, Italy

Anja G. van der Kolk, Utrecht, the Netherlands

Arastoo Vossough, Philadelphia, PA

Elysa Widjaja, Toronto, Ontario, Canada

Leonard Yeo, Singapore

Woong Yoon, Gwangju, South Korea

David M. Yousem, Evergreen, CO

Carlos Zamora, Chapel Hill, NC

Chengcheng Zhu, Seattle, WA

EDITORIAL FELLOW

Vivek Yedavalli, Baltimore, MD

SPECIAL CONSULTANTS TO THE EDITOR

AJNR Blog Editor

Neil Lal, Denver, CO

Case of the Month Editor

Nicholas Stence, Aurora, CO

Case of the Week Editors

Matylda Machnowska, Toronto, Ontario, Canada

Anvita Pauranik, Calgary, Alberta, Canada

Vinil Shah, San Francisco, CA

Classic Case Editor

Sandy Cheng-Yu Chen, Taipei, Taiwan

Health Care and Socioeconomics Editor

Pina C. Sanelli, New York, NY

Physics Editor

Greg Zaharchuk, Stanford, CA

Podcast Editor

Courtney Tomblinson, Nashville, TN

Deputy Podcast Editor

Kevin Hiatt, Winston-Salem, NC

Twitter Editor

Roger Jordan, Houston, TX

Official Journal:

American Society of Neuroradiology

American Society of Functional Neuroradiology

American Society of Head and Neck Radiology

American Society of Pediatric Neuroradiology

American Society of Spine Radiology

Founding Editor

Juan M. Taveras

Editors Emeriti

Mauricio Castillo, Robert I. Grossman,

Michael S. Huckman, Robert M. Quencer

Managing Editor

Karen Halm

Assistant Managing Editor

Laura Wilhelm

Executive Director, ASNR

Mary Beth Hepp



Title: Brain Star (2017), Oil on Acrylic, 36 × 48 inches. In this painting, I drew a visual parallel between the undulating structures of the limbic system and the spirals of the Milky Way. The bright forms on a dark background represent a play on the appearance of immunostained neurons and that of stars in the sky. I aimed to capture the sense of wonder and humility that arise, whether one is yearning to understand the intricacies of the human brain or looking up at the night sky.

Sophie A. Greenberg, M.D., Department of Dermatology, New York Presbyterian/Columbia University Irving Medical Center, New York, NY

Radiology-Pathology Correlations of Intracranial Clots: Current Theories, Clinical Applications, and Future Directions

J.C. Benson, D.F. Kallmes, A.S. Larson, and W. Brinjikji



ABSTRACT

SUMMARY: In recent years, there has been substantial progression in the field of stroke clot/thrombus imaging. Thrombus imaging aims to deduce the histologic composition of the clot through evaluation of various imaging characteristics. If the histology of a thrombus can be reliably determined by noninvasive imaging methods, critical information may be extrapolated about its expected response to treatment and about the patient's clinical outcome. Crucially, as we move into an era of stroke therapy individualization, determination of the histologic composition of a clot may be able to guide precise and targeted therapeutic effort. Most radiologists, however, remain largely unfamiliar with the topic of clot imaging. This article will review the current literature regarding clot imaging, including its histologic backdrop, the correlation of images with cellular components and treatment responsiveness, and future expectations.

ABBREVIATIONS: MT = mechanical thrombectomy; HMCAS = hyperdense middle cerebral artery sign; NETs = neutrophil extracellular traps; RBC = red blood cell; SVS = susceptibility vessel sign; TAI = thrombus attenuation increase

The introduction of mechanical thrombectomy (MT) heralded the beginning of a new era in stroke research, in which retrieved clot tissue was available for histologic analysis. As it turned out, there was substantial heterogeneity in the histologic and physical characteristics of retrieved thrombi. This observation led to widespread exploration into the treatment implications, etiologic origins, and prognostic indicators of clot subtypes. It also accelerated the interest in the subfield of radiology-pathology correlation, in which attempts were made to use various imaging modalities to determine the histologic makeup of clots.

Two main methods have been used to characterize the histology of clot on imaging: the attenuation value of a clot on NCCT and its perviousness. MR imaging, too, has been used, but to a lesser degree. "Perviousness" refers to the degree with which blood—and, consequently, contrast—is able to flow into and through a clot. A highly pervious clot intuitively represents a porous structure that might confer increased responsiveness to thrombolysis and mechanical thrombectomy procedures. However, the still-emerging

field of clot perviousness imaging has been beset by inconclusive and, at times, contradictory data.

Nevertheless, the field of intracranial clot imaging holds promise for the future of individualization of stroke treatment. If the physical and histologic attributes of a clot can be inferred from its imaging characteristics, diagnostic imaging could allow early prognostication of various therapeutic efforts and could even be used to tailor specific pharmacologic and interventional therapies on the basis of clot subtypes. These substantial clinical implications have led to numerous scientific pursuits of perviousness imaging, particularly within the past few years. In this article, we will review the current literature on stroke clot imaging with a focus on both perviousness and radiology-pathology correlations.

Clot Histologic and Physical Characteristics

Clots are composed of 4 major components: red blood cells (RBCs), fibrin, platelets, and white blood cells. Substantial variability exists in the relative proportion of each component in various clots. The most commonly used terms to describe clot composition are RBC-rich/-poor, fibrin-rich/-poor, and platelet-rich/-poor (Fig 1). However, there is no standard definition for what makes a clot rich or poor in a given histologic component.

The histologic composition of a clot is used as a surrogate for its physical properties. RBC-rich thrombi are softer and more porous and have a lower static coefficient of friction; platelet-rich and fibrin-rich clots are harder and less porous and have a higher

Received January 11, 2021; accepted after revision April 6.

From the Department of Neuroradiology, Mayo Clinic, Rochester, Minnesota.

Funding was received by Waleed Brinjikji as part of a National Institutes of Health/National Institute of Neurological Disorders and Stroke grant: 1R01NS105853.

Please address correspondence to John C. Benson, MD, Department of Radiology, Mayo Clinic, 200 1st St SW, Rochester, MN 55905; e-mail: Benson.john3@mayo.edu

Indicates open access to non-subscribers at www.ajnr.org

Indicates article with online supplemental data.

<http://dx.doi.org/10.3174/ajnr.A7249>

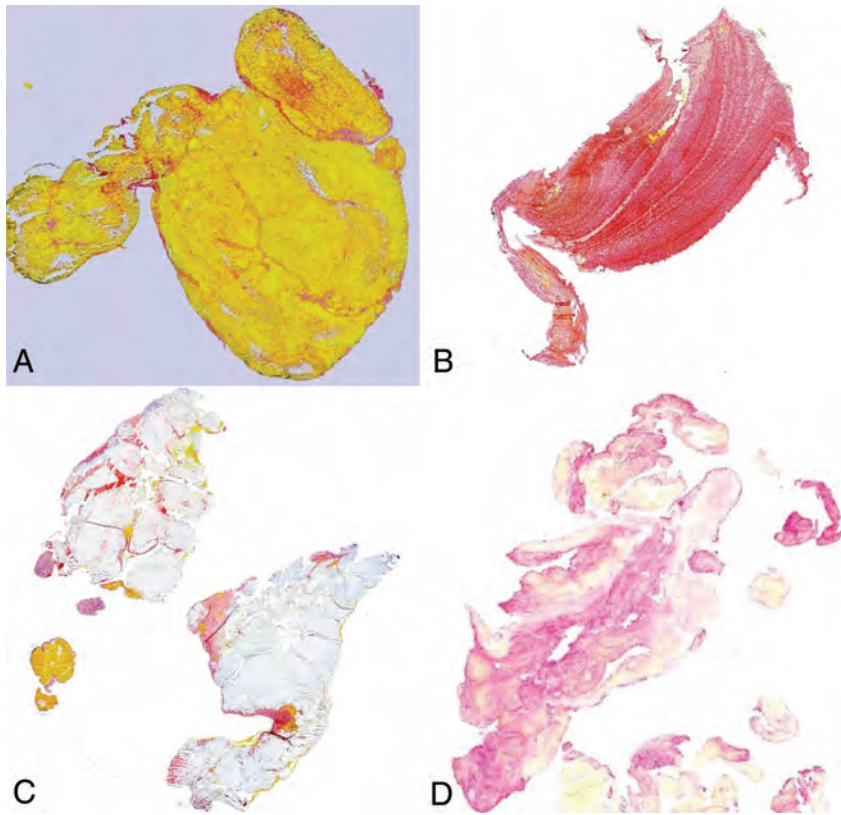


FIG 1. Histologic examples of various clot types. RBC-rich (A), fibrin-rich (B), platelet-rich (C) (all stained with Martius Scarlet Blue), and NET-rich (D) clots (immunohistochemistry using citrullinated H3 antibody) are shown, though standard definitions for these clot types have not yet been created.

static coefficient of friction.¹ However, there have not been extensive experiments into the histologic perviousness of clots.

Histologic differences among clots have direct clinical implications, particularly with regard to the ease, or difficulty, with which such clots are treated with MT or thrombolysis. RBC-rich clots are more responsive to tPA than fibrin-rich or platelet-rich clots.^{2,3} Fibrin-rich clots are also more difficult to remove during MT and require longer intervention times. Clots successfully retrieved with MT, meanwhile, exhibit higher RBC density.^{4,5}

Different pathomechanisms have been offered to explain these differences. For example, fibrin-rich clots are more likely to embolize during MT, suggesting the greater fragility of such clots.⁶ RBC-rich clots are less stiff, thus allowing better integration of stent devices into the thrombi during extraction.⁷ In addition, the greater friction exhibited by fibrin-rich clots may make them harder to remove during MT.^{1,8} However, frictional differences also make RBC clots more prone to intraprocedural migration.⁹

Perviousness Imaging

As stated above, perviousness is the extent to which blood flows through a clot. Because arterially timed contrast serves as a proxy for arterial flow, CTA represents the most conceptually straightforward technique with which to demonstrate the perviousness of a clot. The use of CTA for perviousness imaging is also an enticing

concept because it is nearly ubiquitous in stroke imaging. On CTA, perviousness is measured by comparing intraclot radiodensity units before and after the administration of arterial phase IV contrast (so-called thrombus attenuation increase [TAI]). Therefore, highly pervious clots would display substantial differences in attenuation before and after contrast infusion; impervious clots, conversely, would change minimally.

TAI is typically measured by aligning thin-section NCCT images to CTA images. ROIs are then measured along the course of the thrombus on both image sets. Subtracting the mean NCCT ROI value from the CTA ROI value yields the TAI (Fig 2).¹⁰ The method with which the TAI is determined has varied among studies. Some authors have used coregistration of NCCT and CTA to ensure measurement of the entire clot. Others, however, have simply drawn ≥ 1 circular ROI within the clot segment, thereby resulting in a less precise measurement.¹⁰ Definitions of “perviousness” have also varied (Online Supplemental Data).

For both TAI and NCCT attenuation measurements, care must be taken when dealing with highly calcified thrombi because of both the substantial impact of calcifications on attenuation values and the associated streak and partial volume artifacts. Thus, calcified thrombi are often excluded from analyses.¹¹

The use of multiphase CTA offers some potential advantages for clot perviousness imaging. Mostly, it solves the conundrum of suboptimal timing—that is, perviousness cannot be determined on CTA if the arterial phase contrast has not yet reached the thrombus in question. The additional acquisition of both venous- and delayed-phase images on multiphase CTA ensures the arrival of contrast to or through the thrombus during at least some time point. To date, however, evidence supporting the conceptual benefit of multiphase CTA in perviousness analysis remains sparse. Santos et al,¹² for example, found that venous and delayed-phase images had poorer associations with outcome than those obtained in the arterial phase. Chen et al¹³ used a more robust version of dynamic CTA, in which 26 phases were acquired as part of a CTP protocol. In doing so, the authors found that this method more successfully offset the contrast-timing issue: The maximum TAI was better associated with outcome than the standard arterial phase. Nevertheless, neither study assessed correlations between multiphase perviousness markers and the histologic composition of retrieved clots. Future studies will be needed to provide more direct evidence of the correlation between clot perviousness and findings on multiphase CTA and CTP.

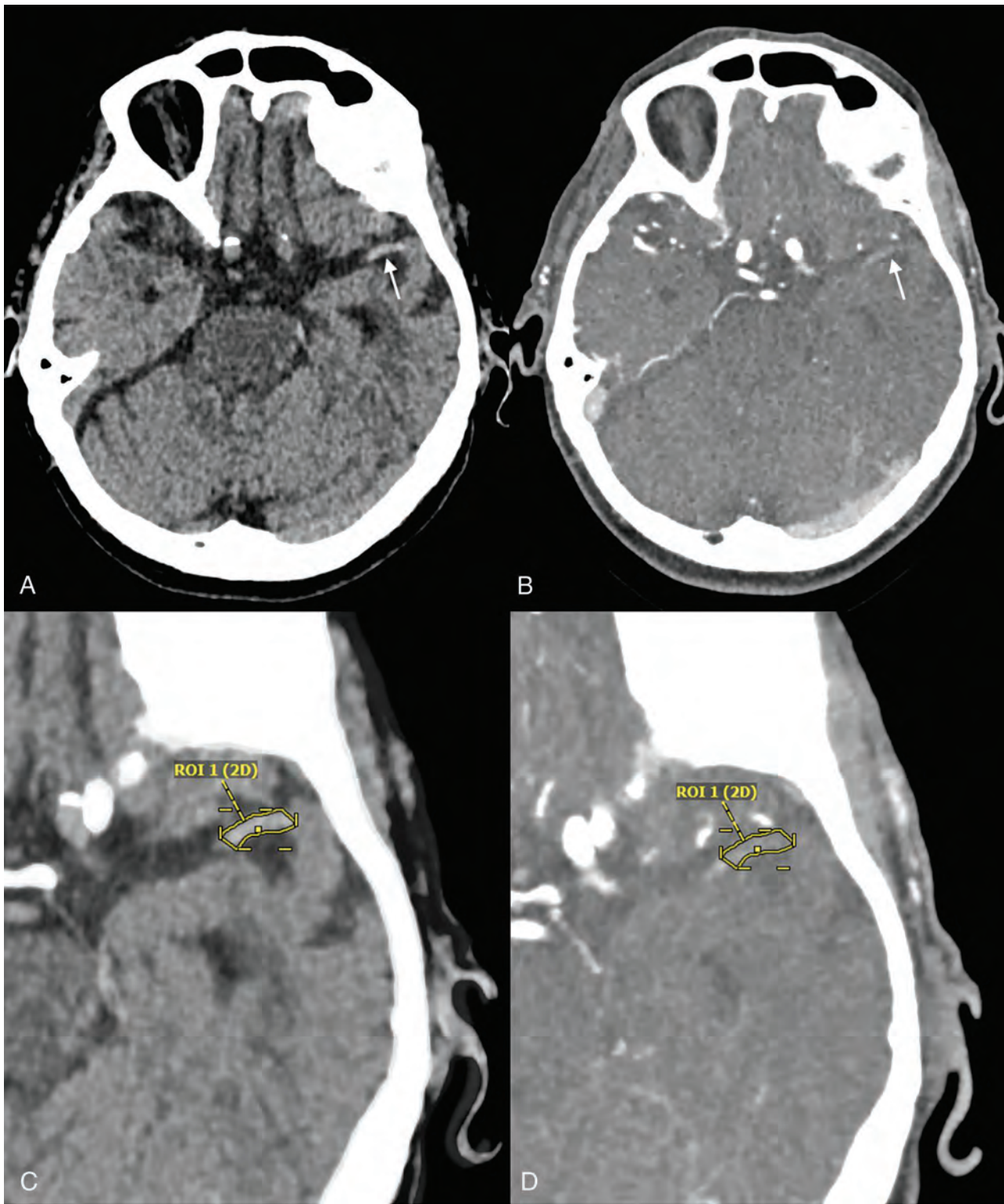


FIG 2. Measurement of clot perviousness on CT using TAI. NCCT (A) demonstrates a hyperdense vessel sign in the distal left M1 (arrow), with faint attenuation in this region also seen on CTA (arrow, B). Comparison of intraclot attenuation between the NCCT (C) and CTA (D) yields a 23% increase in Hounsfield units following contrast administration.

Histologic Correlations

On NCCT, the most common methods of clot assessment are by absolute attenuation, relative attenuation, and the presence or absence of a hyperdense middle cerebral artery sign (HMCAS).

Absolute attenuation is determined by measuring an intraclot ROI along the course of the thrombus.¹⁰ Relative attenuation is determined by comparing this calculation with similar measurements performed on the contralateral artery.¹¹ A relative measurement

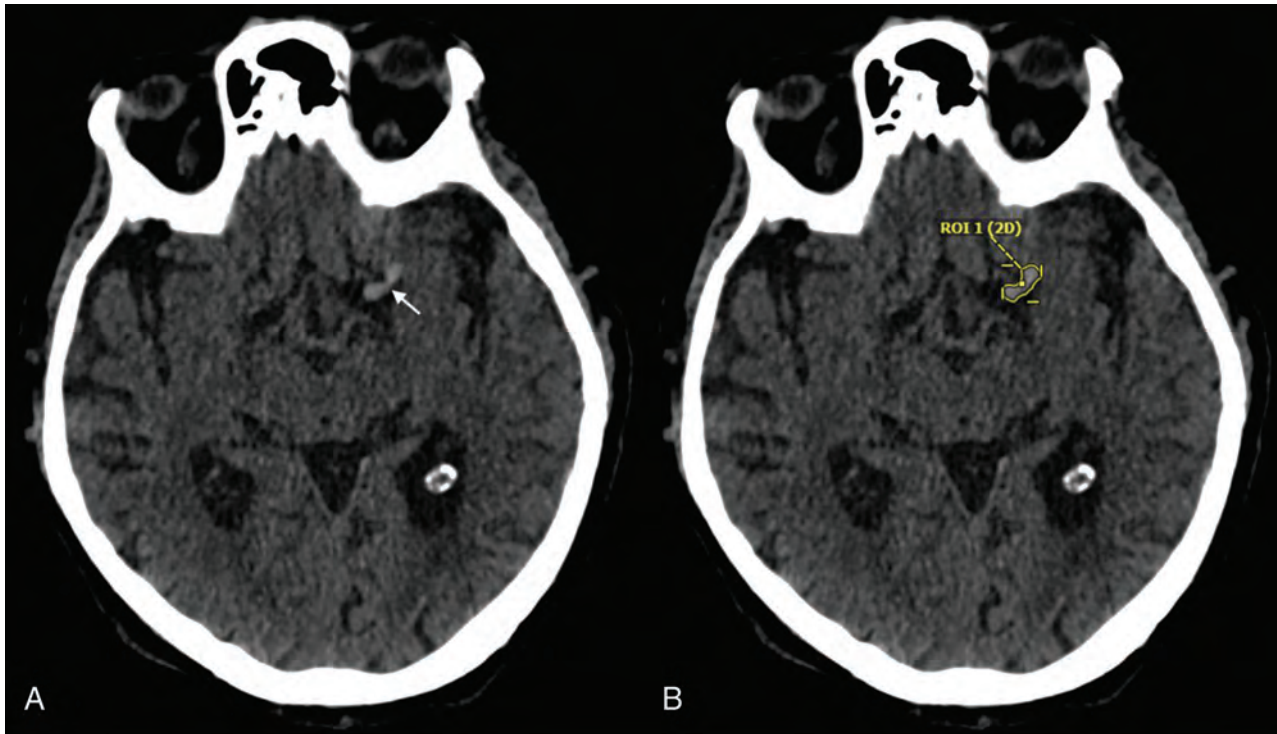


FIG 3. Intracranial clot evaluation on NCCT. Both the subjective presence of a hyperdense MCA sign (*arrow* in *A*) and objective measurement of intraclot attenuation (*B*) are predictive the histologic composition of a clot and responsiveness to treatment. Relative attenuation, in which the involved artery is compared with the contralateral side, may also be used (not shown).

may be useful because it corrects for underlying issues that might affect attenuation values, such as hematocrit or scanner differences (Fig 3).¹⁴ Generally, thin-section (≤ 2.5 mm) imaging is suggested for intraclot attenuation measurements.^{15,16} An HMCAS, conversely, is based on the subjective identification of an artery with pathologically hyperdense attenuation. MIP images are particularly useful to improve detection of HMCASs.¹⁷

Lower Hounsfield units are associated with fibrin- and/or platelet-rich clots, while higher Hounsfield units are associated with RBC-rich clots.^{2,6,7,18-20} The reported density of so-called RBC-rich clots has varied widely among reports, likely related to differences in CT scanning parameters and definitions of clot composition. Maekawa et al,²¹ for example, found the density of erythrocyte-rich clots to be 48.1 HU, compared with 32.1 HU in their fibrin-rich counterparts. Liebeskind et al,²² conversely, based their results on a subjective analysis of the presence or absence of an HMCAS, though they did report the mean density of clots having the HMCAS as 61 HU. Clot types were shown to be more accurately differentiated on dual-energy CT on an *in vitro* study, though this is yet to be validated with an *in vivo* cohort.²¹

On CTA, despite the theoretic ease with which the technique could be used to determine clot perviousness, conclusions from multiple prior attempts at histologic correlation have been frustratingly inconsistent. In the first major study to compare perviousness on CTA with histology, Berndt et al²³ found that pervious clots have greater fibrin/platelet conglomerations and less RBC fractions. Benson et al²⁴ subsequently found that pervious clots (defined as an increase in the intrathrombus Hounsfield unit of ≥ 10 on CTA compared with NCCT) were more likely to

be RBC-rich, while impervious clots were more likely to be fibrin- and white blood cell-rich. Most recently, Patel et al,⁵ using a cohort of 40 patients treated with MT, found that perviousness was associated with higher clot histologic percentages of both fibrin/platelet aggregates and was negatively correlated with the percentage of RBCs.

The reason for these contradictory results is befuddling. The superior therapeutic responses in both RBC-rich clots and pervious clots would seem to indicate that pervious clots would demonstrate erythrocyte-laden histology. However, there are several possible explanations for the observed differences. As Patel et al⁵ noted, inconsistencies in statistical methodology could have contributed to the variability in outcomes in these studies. The time between imaging and clot retrieval may also have played a role. Cines et al²⁵ found that clots undergo a natural contraction with time, and this type of histopathologic evolution could potentially have impacted the results. Next, there is some intrinsic bias in studies based solely on histologic analysis of successfully retrieved clots without any sort of postmortem analysis. Finally, the variability in results also raises the possibility that the observed differences were related to histologic markers that were not specifically assessed such as neutrophil extracellular traps (NETs) and the von Willebrand factor. Put more simply, is perviousness on imaging “seeing” markers of treatment response that we have not yet histologically determined?

On MR imaging, correlations between imaging findings and the histologic composition of clots remain relatively unknown. However, the so-called susceptibility vessel sign (SVS), a linear intravascular focus of hypointense signal on SWI, is highly

Summary of the most commonly used methods for determining clot histology and predicted treatment response on NCCT, CTA, and MR imaging^a

	Measurement Method	Histologic Correlation	Favorable Therapeutic Response
NCCT	HU	↑ HU = ↑ RBC, ↓ fibrin/platelets	↑ HU
CTA	TAI	Conflicting data	↑ TAI
MR imaging	SVS	SVS = ↑ RBC, ↓ fibrin/platelets	+ SVS

Note:—HU indicates Hounsfield unit.

^aUp and down arrows denote greater or lesser values (HU or TAI) and relative histologic composition. The plus sign denotes the presence of an imaging sign (ie, SVS).

specific for occlusive arterial thrombus.²⁶ Clots that demonstrate an SVS have been shown to be richer in RBC composition, thought to be related to the paramagnetic properties of deoxygenated hemoglobin.²⁷ Similar results have also been reported using gradient-echo sequences.^{22,28}

Treatment Response

Multiple studies have shown that treatment outcomes following IV thrombolysis are associated with thrombus density on NCCT. In general, the more dense (higher attenuating) the thrombus, the better the clot seems to respond to IV tPA.^{14,29} Puig et al,²⁹ for example, found that patients with lower relative intraclot Hounsfield units had greater resistance to IV tPA. The authors found that a relative Hounsfield unit (the Hounsfield unit of MCA on the symptomatic side/Hounsfield unit of MCA on asymptomatic side) of <.382 predicted persistent occlusion after therapy, with a sensitivity and specificity of 100% and 87%, respectively. Similarly, Kim et al¹⁴ demonstrated superior recanalization rates of patients treated with tPA in whom the clot on NCCT demonstrated higher intrathrombus attenuation values.

Similarly, hyperdense clots on NCCT are generally associated with superior outcomes during MT.^{18,30,31} Froehler et al,³² for example, reported successful recanalization in 79% of hyperdense thrombi, but in only 36% of isodense thrombi. Mofstakhar et al³³ found superior postintervention TICI grades in patients with higher thrombus density, regardless of intervention type (MT or IV or intra-arterial tPA). Likewise, on MR imaging, the presence of an SVS is predictive of higher rates of recanalization during MT and superior early clinical improvement, compatible with other results of RBC-rich clots.³⁴ Although some reports have presented data contradictory to the above findings, these represent a small minority of the current literature.³⁵

On CTA, multiple studies have demonstrated that perviousness, based on a greater TAI, predicts better recanalization in patients treated with tPA.^{10,36,37} Santos et al¹⁰ found that patients with pervious clots were more likely to have complete recanalization after tPA therapy compared with a conservatively treated cohort; there was no such significant effect of tPA treatment in patients with impervious thrombi. Mishra et al,³⁶ too, found that pervious clots were 5 times more likely to reperfuse than impervious thrombi. In theory, the superior responsiveness of pervious clots is related to the greater ability of tPA to travel through and thus act on a clot, similar to the blood in which it is administered. The tPA is, therefore, granted greater surface area on which to act; it is, thereby, hypothesized to act with greater efficiency in dissolving a clot.³⁸

Multiple studies have also explored the association between clot perviousness on imaging and the degree of success during attempts

at MT, which are also detailed in the Online Supplemental Data. Mokin et al,³⁰ for example, in examining the results from the Cardiovascular Outcomes for People Using Anticoagulation Strategies (COMPASS) trial, found that perviousness was associated with successful MT attempts. The authors reported that mean perviousness (as defined by the TAI) varied significantly between TICI subgroups: 32.6 for TICI 2c/3 and 17.7 for TICI 0-2a. Santos et al³⁹ reported data from a cohort of patients from the Multicenter Randomized Clinical Trial of Endovascular Treatment of Acute Ischemic Stroke in the Netherlands (MR CLEAN) trial. The authors found that pervious clots (defined as having a TAI of ≥10.9) were more likely to both recanalize and have a favorable outcome (mRS ≤2).

However, conflicting reports on this topic do exist. Borst et al,⁴⁰ for example, examined a number of thrombus characteristics on both NCCT and CTA: location (dichotomized as involving or not involving the ICA terminus), distance from ICA terminus to the thrombus, thrombus length and volume, density, and TAI. None of the studied clot characteristics on imaging were associated with treatment-effect modifications. Byun et al,⁴¹ similarly, found no correlation between perviousness on CTA and first-pass revascularization using stent retrievers.

Because recanalization is associated with better clinical outcomes in acute ischemic stroke, it seems implicit that pervious clots lead to more favorable outcomes. Indeed, an association between perviousness and outcome has been established.³⁹ In the study of Santos et al,¹⁰ for example, perviousness was independently associated with superior outcomes after adjusting for recanalization. The aforementioned study using dynamic CTA similarly found perviousness to predict favorable outcome on the basis of a 3-month mRS of ≤2.¹³ Multiple other studies have confirmed superior outcomes based on the 90-day mRS in patients with pervious thrombi (Table).^{15,42}

Radiomics

Radiomics, a subtype of machine learning, has recently been used to correlate clot appearance on imaging to histologic composition and clinical outcomes. Qiu et al,⁴³ for example, found that radiomic features derived from CTA and NCCT were more predictive of early recanalization following IV tPA than any single clot feature, including perviousness. Hofmeister et al⁴⁴ used radiomic features of clots on NCCT to predict both first-attempt recanalization and the overall number of passages needed to successfully recanalize a lumen. Most interesting, the radiomic features that correlated with recanalization included lower intrathrombus attenuation, in contradiction to the dogma that higher-density clots are more easily treated. The reason for the discrepancy between the study of Hofmeister et al⁴⁴ and numerous prior

studies is unknown, and reflects the need for additional investigation into this topic. An *in vitro* study using clot analogs by Velasco Gonzalez et al,⁴⁵ meanwhile, found that higher attenuation on NCCT was associated with greater composition of RBCs, while lower attenuation corresponded to greater composition of fibrin. Attempts to correlate MR imaging to clot composition with radiomics have remained sparse in comparison with CTA.⁴⁶

Other Imaging Biomarkers

Perviousness imaging and radiology-pathology correlations represent only small components of the massive field of clot imaging. Numerous other imaging biomarkers of intracranial clots exist, which hold substantial prognostic and therapeutic significance. Although this review is focused mainly on the subject of perviousness, some of these other imaging markers deserve mention, to grasp the scope of the ever-expanding field.

First, there is thrombus length, which can be measured on both CTA and NCCT.⁴⁷ On NCCT, the length of the thrombus is determined by the size of the increased intracot attenuation when an HMCAS is present. Thin-section images (≤ 2.5 mm) are required to adequately visualize clots in this manner.⁴⁸ On CTA, thrombus length is measured by the contrast gap, represented by an intra-arterial filling defect.⁴⁹ However, the distal end of the clot is essentially invisible unless pial collaterals permit opacification of the artery past the thrombus, thereby delineating the back end of the clot. Hence, CTA often leads to overestimation of thrombus length. Delayed-phase imaging, either as part of a multiphase CTA or contrast-enhanced CT, may help overcome this deficiency.⁵⁰ Shorter thrombi have more favorable metrics, including better functional outcome and reduced endovascular procedural times.¹⁵ Similar results have been reported using volumetric measurements of clots on 3D software: Smaller clots have significantly higher rates of recanalization.⁵¹

Then, there is thrombus location, which is often described on the basis of arterial segment involvement or by the “distance to thrombus” (the length between the ICA terminus and the proximal clot).⁴⁰ In general, patients with more proximal clots tend to fare worse, with poorer recanalization rates and outcomes.⁵² Bhatia et al,⁵³ for example, showed that thrombi in the distal ICA had a recanalization rate of 4.4%, while those in the M1 segment of the MCA had a recanalization rate of 32.3%. A meta-analysis by Seners et al⁵⁴ found that early recanalization was achieved in 52% of distal MCA clots, compared with 35% of clots in the proximal MCA and 13% of clots in the ICA. Such differences are at least, in part, related to the size of clots found in different locations: Larger-volume clots get lodged in the proximal arteries, while smaller clots are able to travel more distally.

The clot burden score is a semiquantitative method of measuring clot severity, which combines features of both size and location. The clot burden scoring system subtracts points on the basis of arterial segment involvement, with greater value placed on the supraclinoid ICA and MCA trunk; lower clot burden scores imply greater clot burden.⁵⁵ This feature can be assessed on both CTA or MR imaging (eg, using T2* sequences).⁵⁶ Not surprisingly, patients with increased clot burden scores (smaller clots) have better outcomes and higher rates of recanalization.^{57,58}

Future Directions

Where, then, do we currently stand in the field of clot perviousness imaging? Like the appearance of a clot on NCCT, the perviousness of a thrombus seems to predict its responsiveness to therapy. While the density of a clot on NCCT seems to also be associated with its histologic composition, a convincing correlation between perviousness and the histology of a clot remains elusive. Still, the better response of pervious clots to tPA does seem to indicate that pervious clots are more porous, allowing medications to better access and thereby act on the internal components of an occlusive thrombus. In short, what we are “seeing” with perviousness may be more related to intrinsic properties that determine therapeutic success—eg, porosity and composition that support MT—and less related to the major cellular makeup of clots.

In addition, there are complex histologic features of clots that could contribute to response or resistance to therapeutic efforts. Recently, clot components, such as NETs and von Willebrand factor, are increasingly thought to play a pivotal role in thrombus formation and stability. NETs, for example, are webs of DNA fibers that are typically used as a defensive mechanism against infectious organisms.⁵⁹ However, NETs have also been firmly implicated in the creation of thromboses: They influence the coagulation cascade, create a scaffold for RBCs, and promote platelet adhesion and aggregation.^{60,61} Not surprisingly, clots with greater composition of NETs exhibit greater resistance to endovascular therapy, with greater procedural times and number of device passes.⁶² Platelet-rich clots have higher levels of both von Willebrand factor and NETs, possibly explaining the resistance of such clots to thrombolytic effort.^{63,64}

Targeted therapies for these components are being developed. Recombinant a disintegrin and metalloprotease with thrombospondin type 1 repeats (ADAMTS13) cleaves von Willebrand factor and has been successfully used in mice to decrease infarct volume.⁶⁵ Deoxyribonuclease I has been shown to accelerate clot lysis by acting on intrathrombus NETs.⁶⁰ Eventually, novel therapeutic efforts such as these may be used as part of an increasingly complex arsenal of stroke treatment options.

More broadly, the goal of intracranial clot imaging is to individualize stroke therapy. As treatment options for stroke increase, effort will be needed to optimize recanalization on the basis of the specific imaging characteristics of intracranial thrombi. For example, if tPA were to be found to be associated with a virtually nil recanalization rate for impervious thrombi, one could use this finding as a reason to forgo fibrinolytic therapy and triage directly to endovascular therapy. Moving forward into this realm will require the rapid use of imaging features such as clot density, perviousness, and radiomics to predict the complex histologic composition of clots.

CONCLUSIONS

Today, the literature seems to support the growing consensus that perviousness is related to successful recanalization with IV tPA and MT. Effort to correlate perviousness with specific histologic compositions, meanwhile, has been relatively unrevealing. As we move into the future, it is likely that perviousness on CTA will be considered a first step in using imaging for clot characterization. Newer techniques, namely, machine learning, will likely

offer a substantial benefit for establishing etiologic mechanisms, offering prognostication on stroke outcome, and triaging patients with stroke on the basis of presumed responsiveness to various treatment strategies.

Disclosures: David F. Kallmes—UNRELATED: Grants/Grants Pending: Cerenovus, Insera Therapeutics, Comments: preclinical and clinical research*; Stock/Stock Options: Superior Medical Experts; Marblehead Medical, Comments: founder/owner. Waleed Brinjikji—RELATED: Grant: National Institutes of Health/National Institute of Neurological Disorders and Stroke, Comments: 1R01NS105853-01.* *Money paid to the institution.

REFERENCES

- Gunning GM, McArdle K, Mirza M, et al. **Clot friction variation with fibrin content: implications for resistance to thrombectomy.** *J Neurointerv Surg* 2018;10:34–38 CrossRef Medline
- Choi MH, Park GH, Lee JS, et al. **Erythrocyte fraction within retrieved thrombi contributes to thrombolytic response in acute ischemic stroke.** *Stroke* 2018;49:652–59 CrossRef Medline
- Tomkins AJ, Schleicher N, Murtha L, et al. **Platelet rich clots are resistant to lysis by thrombolytic therapy in a rat model of embolic stroke.** *Exp Transl Stroke Med* 2015;7:2 CrossRef Medline
- Shin JW, Jeong HS, Kwon H-J, et al. **High red blood cell composition in clots is associated with successful recanalization during intra-arterial thrombectomy.** *PLoS One* 2018;13:e0197492 CrossRef Medline
- Patel TR, Fricano S, Waqas M, et al. **Increased perviousness on CT for acute ischemic stroke is associated with fibrin/platelet-rich clots.** *AJNR Am J Neuroradiol* 2021;42:57–64 CrossRef Medline
- Sporns PB, Hanning U, Schwindt W, et al. **Ischemic stroke: histological thrombus composition and pre-interventional CT attenuation are associated with intervention time and rate of secondary embolism.** *Cerebrovasc Dis* 2017;44:344–50 CrossRef Medline
- Weaver FM, Duffy S, Machado I, et al. **Characterization of strut indentation during mechanical thrombectomy in acute ischemic stroke clot analogs.** *J Neurointerv Surg* 2019;11:891–97 CrossRef Medline
- Fitzgerald S, Mereuta OM, Doyle KM, et al. **Correlation of imaging and histopathology of thrombi in acute ischemic stroke with etiology and outcome.** *J Neurosurg Sci* 2019;63:292–300 CrossRef Medline
- Sporns PB, Jeibmann A, Minnerup J, et al. **Histological clot composition is associated with preinterventional clot migration in acute stroke patients.** *Stroke* 2019;50:2065–71 CrossRef Medline
- Santos EM, Dankbaar JW, Treurniet KM, et al. **Permeable thrombi are associated with higher intravenous recombinant tissue-type plasminogen activator treatment success in patients with acute ischemic stroke.** *Stroke* 2016;47:2058–65 CrossRef Medline
- Boodt N, Compagne KC, Dutra BG, et al. Coinvestigators MR CLEAN Registry. **Stroke etiology and thrombus computed tomography characteristics in patients with acute ischemic stroke: a MR CLEAN registry substudy.** *Stroke* 2020;51:1727–35 CrossRef Medline
- Santos EM, d'Esterre CD, Treurniet KM, et al. P.ROVE-IT investigators. **Added value of multiphase CTA imaging for thrombus perviousness assessment.** *Neuroradiology* 2018;60:71–79 CrossRef Medline
- Chen Z, Shi F, Gong X, et al. **Thrombus permeability on dynamic CTA predicts good outcome after reperfusion therapy.** *AJNR Am J Neuroradiol* 2018;39:1854–59 CrossRef Medline
- Kim EY, Heo JH, Lee S-K, et al. **Prediction of thrombolytic efficacy in acute ischemic stroke using thin-section noncontrast CT.** *Neurology* 2006;67:1846–48 CrossRef Medline
- Dutra BG, Tolhuisen ML, Alves HC, et al. MR CLEAN Registry Investigators. **Thrombus imaging characteristics and outcomes in acute ischemic stroke patients undergoing endovascular treatment.** *Stroke* 2019;50:2057–64 CrossRef Medline
- Santos EM, Yoo AJ, Beenen LF, et al. MR CLEAN Investigators. **Observer variability of absolute and relative thrombus density measurements in patients with acute ischemic stroke.** *Neuroradiology* 2016;58:133–39 CrossRef Medline
- Ho J, Nguyen D, Pirastefahr M, et al. **Non-enhanced CT maximum intensity projections for the detection of large vessel occlusions.** *Austin J Cerebrovasc Dis Stroke* 2017;4:1068 Medline
- Brinjikji W, Duffy S, Burrows A, et al. **Correlation of imaging and histopathology of thrombi in acute ischemic stroke with etiology and outcome: a systematic review.** *J Neurointerv Surg* 2017;9:529–34 CrossRef Medline
- Fitzgerald ST, Wang S, Dai D, et al. **Platelet-rich clots as identified by Martius Scarlet Blue staining are isodense on NCCT.** *J Neurointerv Surg* 2019;11:1145–49 CrossRef Medline
- Nielsen JM, van der Schaaf IC, van Dam L, et al. **Histopathologic composition of cerebral thrombi of acute stroke patients is correlated with stroke subtype and thrombus attenuation.** *PLoS One* 2014;9:e88882 CrossRef Medline
- Maekawa K, Shibata M, Nakajima H, et al. **Erythrocyte-rich thrombus is associated with reduced number of maneuvers and procedure time in patients with acute ischemic stroke undergoing mechanical thrombectomy.** *Cerebrovasc Dis Extra* 2018;8:39–49 CrossRef Medline
- Liebeskind DS, Sanossian N, Yong WH, et al. **CT and MRI early vessel signs reflect clot composition in acute stroke.** *Stroke* 2011;42:1237–43 CrossRef Medline
- Berndt M, Friedrich B, Maegerlein C, et al. **Thrombus permeability in admission computed tomographic imaging indicates stroke pathogenesis based on thrombus histology.** *Stroke* 2018;49:2674–82 CrossRef Medline
- Benson JC, Fitzgerald ST, Kadirvel R, et al. **Clot permeability and histopathology: is a clot's perviousness on CT imaging correlated with its histologic composition?** *J Neurointerv Surg* 2020;12:38–42 CrossRef Medline
- Cines DB, Lebedeva T, Nagaswami C, et al. **Clot contraction: compression of erythrocytes into tightly packed polyhedra and redistribution of platelets and fibrin.** *Blood* 2014;123:1596–1603 CrossRef Medline
- Payabvash S, Benson JC, Taleb S, et al. **Susceptible vessel sign: identification of arterial occlusion and clinical implications in acute ischaemic stroke.** *Clin Radiol* 2017;72:116–22 CrossRef Medline
- Kim SK, Yoon W, Kim TS, et al. **Histologic analysis of retrieved clots in acute ischemic stroke: correlation with stroke etiology and gradient-echo MRI.** *AJNR Am J Neuroradiol* 2015;36:1756–62 CrossRef Medline
- Schellinger PD, Chalela JA, Kang DW, et al. **Diagnostic and prognostic value of early MR imaging vessel signs in hyperacute stroke patients imaged <3 hours and treated with recombinant tissue plasminogen activator.** *AJNR Am J Neuroradiol* 2005;26:618–24 Medline
- Puig J, Pedraza S, Demchuk A, et al. **Quantification of thrombus Hounsfield units on noncontrast CT predicts stroke subtype and early recanalization after intravenous recombinant tissue plasminogen activator.** *AJNR Am J Neuroradiol* 2012;33:90–96 CrossRef Medline
- Mokin M, Waqas M, Fifi J, et al. **Clot perviousness is associated with first pass success of aspiration thrombectomy in the COMPASS trial.** *J Neurointerv Surg* 2021;13:509–14 CrossRef Medline
- Mokin M, Morr S, Natarajan SK, et al. **Thrombus density predicts successful recanalization with Solitaire stent retriever thrombectomy in acute ischemic stroke.** *J Neurointerv Surg* 2015;7:104–07 CrossRef Medline
- Froehler MT, Tatsumi S, Duckwiler G, et al. UCLA Stroke Investigators. **The hyperdense vessel sign on CT predicts successful recanalization with the Merci device in acute ischemic stroke.** *J Neurointerv Surg* 2013;5:289–93 CrossRef Medline
- Moftakhar P, English JD, Cooke DL, et al. **Density of thrombus on admission CT predicts revascularization efficacy in large vessel occlusion acute ischemic stroke.** *Stroke* 2013;44:243–45 CrossRef Medline

34. Darcourt J, Withayasuk P, Vukasinovic I, et al. **Predictive value of susceptibility vessel sign for arterial recanalization and clinical improvement in ischemic stroke.** *Stroke* 2019;50:512–15 CrossRef Medline
35. Topcuoglu MA, Arsava EM, Kursun O, et al. **The utility of middle cerebral artery clot density and burden assessment by noncontrast computed tomography in acute ischemic stroke patients treated with thrombolysis.** *J Stroke Cerebrovasc Dis* 2014;23:e85–91 CrossRef Medline
36. Mishra SM, Dykeman J, Sajobi TT, et al. **Early reperfusion rates with IV tPA are determined by CTA clot characteristics.** *AJNR Am J Neuroradiol* 2014;35:2265–72 CrossRef Medline
37. Labiche LA, Malkoff M, Alexandrov AV. **Residual flow signals predict complete recanalization in stroke patients treated with TPA.** *J Neuroimaging* 2003;13:28–33 Medline
38. Alexandrov AV, Demchuk AM, Felberg RA, et al. **High rate of complete recanalization and dramatic clinical recovery during tPA infusion when continuously monitored with 2-MHz transcranial Doppler monitoring.** *Stroke* 2000;31:610–14 CrossRef Medline
39. Santos EM, Marquering HA, den Blanken MD, et al. MR CLEAN Investigators. **Thrombus permeability is associated with improved functional outcome and recanalization in patients with ischemic stroke.** *Stroke* 2016;47:732–41 CrossRef Medline
40. Borst J, Berkhemer OA, Santos EM, et al. MR CLEAN Investigators. **Value of thrombus CT characteristics in patients with acute ischemic stroke.** *AJNR Am J Neuroradiol* 2017;38:1758–64 CrossRef Medline
41. Byun JS, Nicholson P, Hilditch CA, et al. **Thrombus perviousness is not associated with first-pass revascularization using stent retrievers.** *Interv Neuroradiol* 2019;25:285–90 CrossRef Medline
42. Bilgic AB, Gocmen R, Arsava EM, et al. **The effect of clot volume and permeability on response to intravenous tissue plasminogen activator in acute ischemic stroke.** *J Stroke Cerebrovasc Dis* 2020;29:104541 CrossRef Medline
43. Qiu W, Kuang H, Nair J, et al. **Radiomics-based intracranial thrombus features on CT and CTA predict recanalization with intravenous alteplase in patients with acute ischemic stroke.** *AJNR Am J Neuroradiol* 2019;40:39–44 CrossRef Medline
44. Hofmeister J, Bernava G, Rosi A, et al. **Clot-based radiomics predict a mechanical thrombectomy strategy for successful recanalization in acute ischemic stroke.** *Stroke* 2020;51:2488–94 CrossRef Medline
45. Velasco Gonzalez A, Buerke B, Görlich D, et al. **Clot analog attenuation in non-contrast CT predicts histology: an experimental study using machine learning.** *Transl Stroke Res* 2020;11:940–49 CrossRef Medline
46. Chung JW, Kim YC, Cha J, et al. **Characterization of clot composition in acute cerebral infarct using machine learning techniques.** *Ann Clin Transl Neurol* 2019;6:739–47 CrossRef Medline
47. Riedel CH, Jensen U, Rohr A, et al. **Assessment of thrombus in acute middle cerebral artery occlusion using thin-slice nonenhanced computed tomography reconstructions.** *Stroke* 2010;41:1659–64 CrossRef Medline
48. Miller TS, Brook AL, Riedel CH, et al. **Expanding the role of NCCT in acute stroke imaging: thrombus length measurement and its potential impact on current practice.** *J Neurointerv Surg* 2014;6:5–6 CrossRef Medline
49. De Meyer SF, Andersson T, Baxter B, et al. Clot Summit Group. **Analyses of thrombi in acute ischemic stroke: a consensus statement on current knowledge and future directions.** *Int J Stroke* 2017;12:606–14 CrossRef Medline
50. Mortimer AM, Little DH, Minhas KS, et al. **Thrombus length estimation in acute ischemic stroke: a potential role for delayed contrast enhanced CT.** *J Neurointerv Surg* 2014;6:244–48 CrossRef Medline
51. Yoo J, Baek JH, Park H, et al. **Thrombus volume as a predictor of nonrecanalization after intravenous thrombolysis in acute stroke.** *Stroke* 2018;49:2108–15 CrossRef Medline
52. Linfante I, Llinas RH, Selim M, et al. **Clinical and vascular outcome in internal carotid artery versus middle cerebral artery occlusions after intravenous tissue plasminogen activator.** *Stroke* 2002;33:2066–71 CrossRef Medline
53. Bhatia R, Hill MD, Shobha N, et al. **Low rates of acute recanalization with intravenous recombinant tissue plasminogen activator in ischemic stroke: real-world experience and a call for action.** *Stroke* 2010;41:2254–58 CrossRef Medline
54. Seners P, Turc G, Maier B, et al. **Incidence and predictors of early recanalization after intravenous thrombolysis: a systematic review and meta-analysis.** *Stroke* 2016;47:2409–12 CrossRef Medline
55. Tan IY, Demchuk AM, Hopyan J, et al. **CT angiography clot burden score and collateral score: correlation with clinical and radiologic outcomes in acute middle cerebral artery infarct.** *AJNR Am J Neuroradiol* 2009;30:525–31 CrossRef Medline
56. Derraz I, Bourcier R, Soudant M, et al. THRACE Investigators. **Does clot burden score on baseline T2*-MRI impact clinical outcome in acute ischemic stroke treated with mechanical thrombectomy?** *J Stroke* 2019;21:91–100 CrossRef Medline
57. Derraz I, Pou M, Labreuche J, et al. ASTER and the THRACE Trials Investigators. **Clot burden score and collateral status and their impact on functional outcome in acute ischemic stroke.** *AJNR Am J Neuroradiol* 2021;42:42–48 CrossRef Medline
58. Li G, Wu G, Qin Z, et al. **Prognostic value of clot burden score acute ischemic stroke after reperfusion therapies: a systematic review and meta-analysis.** *J Stroke Cerebrovasc Dis* 2019;28:104293 CrossRef Medline
59. Martinod K, Wagner DD. **Thrombosis: tangled up in NETs.** *Blood* 2014;123:2768–76 CrossRef Medline
60. Laridan E, Denorme F, Desender L, et al. **Neutrophil extracellular traps in ischemic stroke thrombi.** *Ann Neurol* 2017;82:223–32 CrossRef Medline
61. Fuchs TA, Brill A, Duerschmied D, et al. **Extracellular DNA traps promote thrombosis.** *Proc Natl Acad Sci U S A* 2010;107:15880–85 CrossRef Medline
62. Ducroux C, Di Meglio L, Loyau S, et al. **Thrombus neutrophil extracellular traps content impair tPA-induced thrombolysis in acute ischemic stroke.** *Stroke* 2018;49:754–57 CrossRef Medline
63. Staessens S, Denorme F, Francois O, et al. **Structural analysis of ischemic stroke thrombi: histological indications for therapy resistance.** *Haematologica* 2020;105:498–507 CrossRef Medline
64. Douglas A, Fitzgerald S, Mereuta OM, et al. **Platelet-rich emboli are associated with von Willebrand factor levels and have poorer revascularization outcomes.** *J Neurointerv Surg* 2020;12:557–62 CrossRef Medline
65. Bongers TN, de Maat MP, van Goor ML, et al. **High von Willebrand factor levels increase the risk of first ischemic stroke: influence of ADAMTS13, inflammation, and genetic variability.** *Stroke* 2006;37:2672–77 CrossRef Medline

Roadmap Consensus on Carotid Artery Plaque Imaging and Impact on Therapy Strategies and Guidelines: An International, Multispecialty, Expert Review and Position Statement

 L. Saba,  W. Brinjikji,  J.D. Spence,  M. Wintermark,  M. Castillo,  G.J. de Borst,  Q. Yang,  C. Yuan,  A. Buckler,  M. Edjlali,  T. Saam,  D. Saloner,  B.K. Lal, D. Capodanno, J. Sun, N. Balu, R. Naylor, A.v.d. Lugt, B.A. Wasserman, M.E. Kooi, J. Wardlaw, J. Gillard, G. Lanzino, U. Hedin, D. Mikulis, A. Gupta, J.K. DeMarco, C. Hess, J.V. Goethem, T. Hatsukami, P. Rothwell, M.M. Brown, and A.R. Moody



ABSTRACT

SUMMARY: Current guidelines for primary and secondary prevention of stroke in patients with carotid atherosclerosis are based on the quantification of the degree of stenosis and symptom status. Recent publications have demonstrated that plaque morphology and composition, independent of the degree of stenosis, are important in the risk stratification of carotid atherosclerotic disease. This finding raises the question as to whether current guidelines are adequate or if they should be updated with new evidence, including imaging for plaque phenotyping, risk stratification, and clinical decision-making in addition to the degree of stenosis. To further this discussion, this roadmap consensus article defines the limits of luminal imaging and highlights the current evidence supporting the role of plaque imaging. Furthermore, we identify gaps in current knowledge and suggest steps to generate high-quality evidence, to add relevant information to guidelines currently based on the quantification of stenosis.

ABBREVIATIONS: AHA = American Heart Association; IPH = intraplaque hemorrhage; LRNC = lipid-rich necrotic core

Acute ischemic stroke is a major cause of morbidity and mortality worldwide, accounting for approximately 5% of disability-adjusted life years and >10% of deaths. Approximately 20% of patients with stroke/TIA have an ipsilateral carotid stenosis of

>50%,^{1,2} and about one-third (about 10% all patients with stroke) had no warning symptoms such as transient ischemic attacks.³

Carotid artery stenosis is a well-established risk factor for ischemic stroke. Determining the best primary and secondary

Received November 18, 2020; accepted after revision January 26, 2021.

From the Department of Radiology (L.S.), University of Cagliari, Cagliari, Italy; Departments of Radiology (W.B.) and Neurosurgery (G.L.) Mayo Clinic, Rochester, Minnesota; Stroke Prevention and Atherosclerosis Research Centre (J.D.S.), Robarts Research Institute, Western University, London, Ontario, Canada; Department of Neuroradiology (M.W.), Stanford University and Healthcare System, Stanford, California; Department of Radiology (M.C.), University of North Carolina, Chapel Hill, North Carolina; Department of Vascular Surgery (G.J.d.B.), University Medical Center Utrecht, Utrecht, the Netherlands; Department of Radiology (Q.Y.), Xuanwu Hospital, Capital Medical University, Beijing, China; Departments of Radiology (C.Y., J.S., N.B.) and Surgery (T.H.), University of Washington, Seattle, Washington; Elucid Bioimaging (A.B.), Boston, Massachusetts; Department of Molecular Medicine and Surgery (U.H.), Karolinska Institutet, Stockholm, Sweden; Department of Neuroradiology (M.E.), Université Paris-Descartes-Sorbonne-Paris-Cité, IMABRAIN-INSERM-UMRI266, DHU-Neurovasc, Centre Hospitalier Sainte-Anne, Paris, France; Department of Radiology (T.S.), University Hospital, Ludwig Maximilian University of Munich, Munich, Germany; Radiologisches Zentrum (T.S.), Rosenheim, Germany; Departments of Radiology and Biomedical Imaging (D.S., C.H.), University of California San Francisco, San Francisco, California; Department of Vascular Surgery (B.K.L.), University of Maryland School of Medicine, Baltimore, Maryland; Division of Cardiology (D.C.), A.O.U. Policlinico "G. Rodolico-San Marco," University of Catania, Italy; The Leicester Vascular Institute (R.N.), Glenfield Hospital, Leicester, UK; Department of Radiology and Nuclear Medicine (A.v.d.L.), Erasmus MC, University Medical Center Rotterdam, Rotterdam, the Netherlands; The Russell H. Morgan Department of Radiology and Radiological Science (B.A.W.), Johns Hopkins Hospital, Baltimore, Maryland; Department of Radiology and Nuclear Medicine (M.E.K.), CARIM School for Cardiovascular Diseases, Maastricht University Medical Center, Maastricht, the Netherlands; Centre for Clinical Brain Sciences (J.W.), United Kingdom Dementia

Research Institute and Edinburgh Imaging, University of Edinburgh, Edinburgh, UK; Christ's College (J.G.), Cambridge, UK; Department of Vascular Surgery (U.H.), Karolinska University Hospital and Karolinska Institute, Stockholm, Sweden; Joint Department of Medical Imaging and the Functional Neuroimaging Laboratory (D.M.), University Health Network, Toronto, Ontario, Canada; Department of Radiology (A.G.), Weill Cornell Medical College, New York, New York; Walter Reed National Military Medical Center and Uniformed Services University of the Health Sciences (J.K.D.), Bethesda, Maryland; Faculty of Biomedical Sciences (J.V.G.), University of Antwerp, Antwerp, Belgium; Centre for Prevention of Stroke and Dementia (P.R.), Nuffield Department of Clinical Neurosciences, John Radcliffe Hospital, University of Oxford, UK; Stroke Research Centre (M.M.B.), Department of Brain Repair and Rehabilitation, University College of London Queen Square Institute of Neurology, University College London, UK; and Department of Medical Imaging (A.R.M.), University of Toronto, Toronto, Ontario, Canada.

The views expressed in this article are those of the authors and do not reflect the official policy of the Department of Army/Navy/Air Force, Department of Defense, or US Government. The identification of specific products or scientific instrumentation does not constitute endorsement or implied endorsement on the part of the author, Department of Defense, or any component agency.

Please address correspondence to Luca Saba, MD, University of Cagliari, Azienda Ospedaliero Universitaria di Cagliari, polo di Monserrato, Provincia di Cagliari, Italy; e-mail: lucasaba@tiscali.it; @lucasabaITA

 Indicates open access to non-subscribers at www.ajnr.org

 Indicates article with online supplemental data.

<http://dx.doi.org/10.3174/ajnr.A7223>

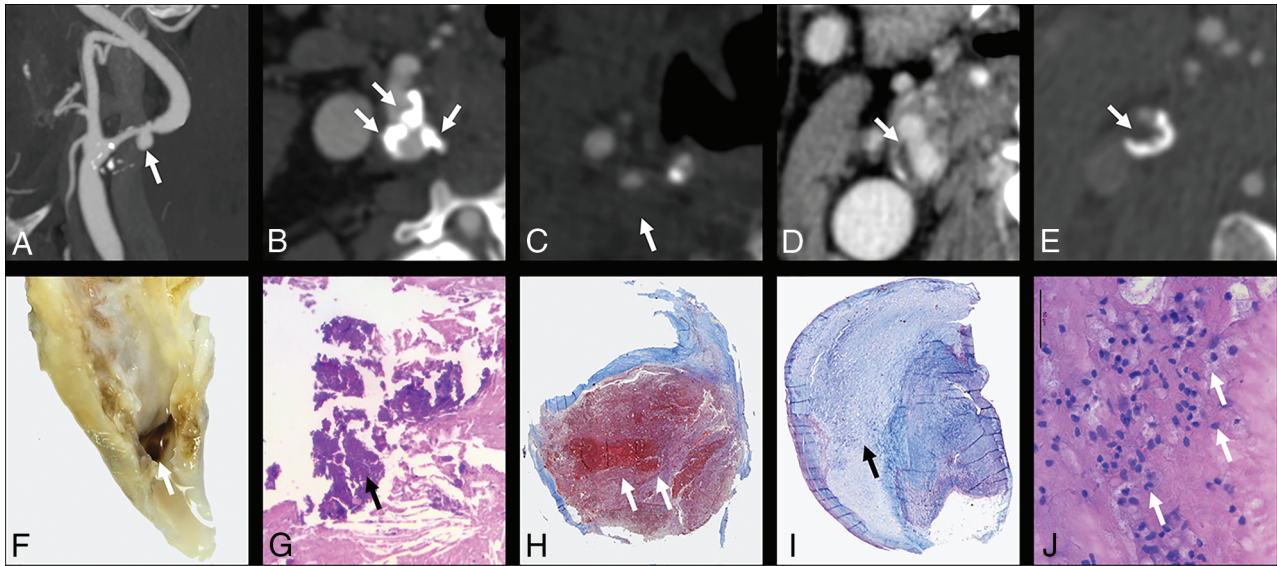


FIG 1. Different CT features. A, Plaque ulceration (arrow) is shown with the corresponding macroscopic specimen (F). B, Multiple coarse calcifications (white arrows) within the plaque are visible with the corresponding example in the H&M histologic view (G, arrow points at a calcification). The IPH is visible in H (white arrows) with the corresponding CTA that shows hypodense plaque in C (Hounsfield unit value = 18; white arrow). I, A stable plaque with a prominent fibrous cap with the major part of the plaque with collagenous connective tissue (black arrow) is shown with the corresponding CT section (D, white arrow). E, The presence of a hypodense plaque (Hounsfield unit = 37) with the corresponding histopathologic slide showing multiple inflammatory cells (J).

stroke prevention strategies for asymptomatic and symptomatic patients with carotid stenosis is a priority. The current guidelines for the management of both symptomatic and asymptomatic atherosclerosis are based on randomized trials comparing medical therapy with surgical interventions using the degree of stenosis together with symptom status without consideration of plaque morphology and composition. These were published before the advent of vessel wall imaging using MR imaging and high-resolution CT angiography (Figs 1 and 2)

From the first NASCET report that demonstrated the association between high-grade stenosis and outcome, a important evolution in both the surgical approach and medical treatment has occurred. The risk of morbidity and mortality during revascularization procedures, in particular during carotid endarterectomy, has decreased, with a reduction of mortality and severe complications.⁴⁻⁶ Moreover, several trials have provided evidence strengthening conservative medical treatment of carotid disease, including the protective effects of high-dose statin therapy and anti-inflammatory therapy such as the interleukin-1 β innate immunity pathway.⁷⁻¹⁰ Recent meta-analyses provide evidence that atherosclerosis can be reversed (“plaque regression”) with high-dose lipid-lowering therapy,¹¹ and high-dose statins may shift vulnerable plaque from a high lipid content to a more stable calcified plaque.¹¹⁻¹³ Imaging of carotid plaque morphology may, therefore, more accurately reflect the pathobiology of the plaque itself, allowing estimation of plaque risk.¹⁴ This could lead to a more cost-effective selection of expensive endovascular/surgical management options.^{9,15}

It has been >30 years since the landmark carotid surgery trials defined the degree of carotid stenosis as an important imaging biomarker for surgical management, leading to improved outcomes. However, despite this advance, carotid atherosclerotic

disease still accounts for significant morbidity and mortality suggesting the need for a variation in the management and risk stratification of subjects with carotid artery pathology based on the new diagnostic potentialities.

The purpose of this consensus document is to review the current literature, identify new imaging metrics that are associated with future cerebrovascular events and to discuss therapeutic options for specifically targeting these features. Having done so, a roadmap for multicenter diagnostic and therapeutic trials incorporating these imaging biomarkers as inclusion criteria is provided to assess patient outcome compared with management based only on the degree of stenosis.

Summary and Analysis of Existing Guidelines

In this section, we have developed a summary and analysis of existing guidelines. Currently, moderate (50%–69%) and severe (70%–99%) carotid artery stenoses are considered the key parameters together with the symptomatic/asymptomatic status of the patient in deciding management approaches. These are based primarily on NASCET results.^{16,17} A report published in *Stroke*, in 2015,¹⁸ identified 34 guidelines from 23 different regions/countries in 6 languages, in which 4 scenarios were highlighted:

1. Asymptomatic patient at average surgical risk with stenosis
2. Asymptomatic patient at high surgical risk (because of comorbidities, vascular anatomy, or undefined reasons) with stenosis
3. Symptomatic patient at average surgical risk with stenosis
4. Symptomatic patient at high surgical risk (because of comorbidities, vascular anatomy, or undefined reasons) with stenosis

In all 4 scenarios, the degree of stenosis ($\geq 50\%$) was the key point considered for treatment. In 33/34 guidelines, treatment

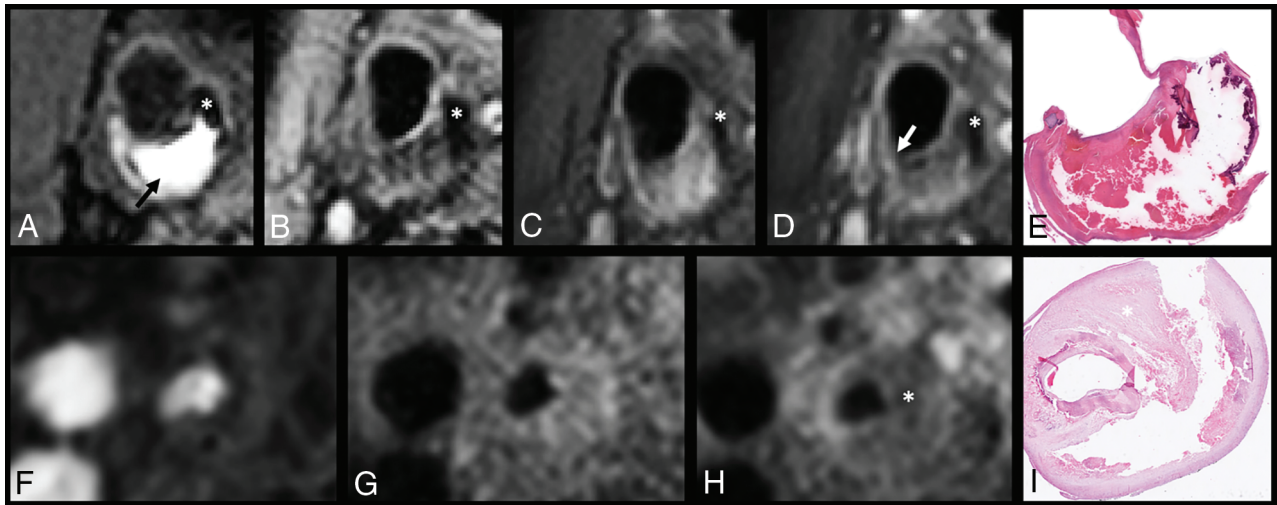


FIG 2. Upper row: Coregistered MPRAGE (A), T2-weighted TSE (B), pre- and postcontrast T1WI TSE MR images (C and D), and a corresponding histologic section (E) of a cross-section of the carotid artery with plaque. A large intraplaque hemorrhage can be recognized as a hyperintense region compared with surrounding muscle tissue in the bulk of the plaque on the MPRAGE image (arrow). Calcification can be identified as a region with hypointense signal on all 4 MR imaging weightings. On the postcontrast T1-weighted TSE image, the region with signal enhancement shows the fibrous cap (between the lumen and intraplaque hemorrhage). The disruption of this enhancement (white arrow) indicates that the fibrous cap is thin or ruptured at this location. Lower row: Coregistered TOF (F), pre- and postcontrast T1-weighted TSE MR images (G and H), and the corresponding histologic section (I) of a cross-section of the carotid artery with a plaque. An LRNC is present in the bulk of the plaque with no or slight contrast enhancement on the postcontrast T1WI (asterisk).

was considered only for symptomatic subjects. For symptomatic patients with high carotid endarterectomy risk, medical treatment alone was not endorsed in any guidelines, though the possibility was considered as an alternative option in 2.¹⁹⁻²¹ Only 1 guideline advised medical treatment alone for patients with asymptomatic carotid stenosis.

The European Society for Vascular Surgery and the European Society of Cardiology developed consensus recommendations for asymptomatic patients, recommending that plaque morphology features be considered.^{22,23} The only variation compared with the 2011 guidelines was that carotid endarterectomy is indicated in the presence of ≥ 1 imaging characteristic that may be associated with high stroke risk in asymptomatic subjects. These data indicate that the guidelines currently used worldwide do not consider the imaging-based plaque morphology/composition as a parameter for the therapeutic option and that the class of risk is based on the mere degree of stenosis and symptomatic/asymptomatic status of the patient.

However, in past years, landmark articles showing the impact of imaging-based features of carotid artery plaque vulnerability in symptomatic and asymptomatic patients with mild stenosis²⁴ and the benefit of conservative medical treatment for the plaque stabilization and reversion have been published,^{7,9,13} highlighting the need for changes in the forthcoming guidelines.

Evidence That Imaging of Plaque Composition Predicts Ischemic Stroke Risk

In the past years, evidence has accumulated in pathology and imaging fields demonstrating that plaque composition plays a key role in the vulnerability of the carotid artery plaque.

Histopathology of Unstable Plaque. Coronary atherothrombosis was described >150 years ago, and carotid stenosis was coupled

with the pathophysiology of ischemic stroke >70 years ago. The associations between histopathologic features and increased risk of stroke were described in the 1970s and 1980s, noting the association between fibrous cap rupture and thromboembolism (Fig 1)²⁵⁻²⁷ and identification of intraplaque hemorrhage (IPH) as a marker of recent symptom-producing plaques.²⁸⁻³⁰

Histopathologic studies showed that vulnerable plaques were characterized by a thin or ruptured fibrous cap, endothelial erosions, enhanced inflammation, large lipid-rich necrotic cores, immature intraplaque neovascularity, and IPH, whereas stable and asymptomatic lesions typically contain more fibrous tissue and more calcification.^{31,32}

However, the authors found that ulceration, IPH, and organizing or organized thrombi were also found in both symptomatic and asymptomatic stenotic plaques examined pathologically,^{29,33-40} suggesting a complex pathobiologic scenario for the plaque rupture. The authors found that biologic variability in plaque morphology also plays a role.

Fisher and Ojemann⁴¹ noted that “the variations in the microscopic appearance of the plaque contents seemed to be unending.” The authors found that the position of the lipid/necrotic core and thinning of the cap may be the most significant features predisposing to plaque rupture.^{27,40} Most interesting, decreasing fibrous cap thickness increases the circumferential stress on a plaque, whereas increasing stenosis severity decreases circumferential stress.⁴² This finding may help to explain why stroke risk tends to be lower in patients with critical stenosis compared with high-grade stenosis.

The American Heart Association (AHA), in 1995, published⁴³ a detailed classification scheme designed to be used as a histologic template for images obtained by a variety of invasive and noninvasive techniques in the clinical setting. In the AHA scheme

AHA classification and AHA-MR imaging–based classification

AHA Classification	Carotid MR Imaging–Based AHA Classification from Cai et al ⁴⁵
Type I: initial lesion with foam cells	Type I–II: near-normal wall thickness, no calcification
Type II: fatty streak with multiple foam cell layers	
Type III: pre-atheroma with extracellular lipid pools	Type III: diffuse intimal thickening or small eccentric plaque with no calcification
Type IV: atheroma with a confluent extracellular lipid core	Type IV–V: plaque with a lipid or necrotic core surrounded by fibrous tissue with possible calcification
Type V: fibroatheroma	
Type VI: complex plaque with possible surface defect, hemorrhage, or thrombus	Type VI: complex plaque with possible surface defect, hemorrhage, or thrombus
Type VII: calcified plaque	Type VII: calcified plaque
Type VIII: fibrotic plaque without lipid core	Type VIII: fibrotic plaque without lipid core and with possible small calcifications

(Table), revised in 2000,⁴⁴ the lesions are designated by Roman numerals, which indicate the usual sequence of lesion progression from the initial lesion, type I to type VIII, in which the fibrous tissue changes within the plaque predominate. This classification was in MR imaging and CT studies (Table).^{45,46} Virmani et al⁴⁷ built on the Stary system to more closely focus on erosion, rupture, and thinning of the fibrous cap, increasingly prevalent in the population due to widespread use of statins. The result of these developments in plaque phenotyping have converged into the most widely accepted system in use today,⁴⁸ which also suggests that further development will be possible once modalities to recognize the lesion by noninvasive means are addressed in this roadmap.

Plaque Vulnerability in Patients with Mild or No Stenosis. Conventional angiography tends to underestimate the extent of disease because the lumen can be maintained through positive remodeling of the vessel wall, further exaggerated by the anatomy of the carotid bulb. Patients with lesser degrees of stenosis represent a significant proportion of patients with stroke. In the NASCET trial, >40% of those with stroke on follow-up were from the <50% stenosis group.¹⁶ Mild stenoses, albeit associated with reduced risk of producing ischemic events, are much more common than severe stenoses and, thus, are associated with a substantial number of events: The estimated prevalence of carotid stenosis of $\geq 50\%$ in the general population ranges from 2% to 8% and the estimated prevalence of stenosis of $\geq 80\%$ ranges from 1% to 2%.⁴⁹ Detection of high-risk lesions in ever decreasing degrees of carotid stenosis will potentially require either higher resolution imaging or more conspicuous imaging biomarkers.

Features of plaque vulnerability are related to the occurrence of ischemic events independent of the degree of stenosis: Studying plaques with lower levels of luminal stenosis separates the effects of hemodynamic compromise caused by the luminal narrowing and vessel wall pathology on clinical outcomes. In a group of patients studied recently presenting with imaging-improved acute stroke with no significant stenosis (<50%), up to half were shown to have IPH in the carotid artery ipsilateral to the stroke, suggesting a possible source of cerebral^{50,51} emboli. Some morphologic features, such as ulceration, are also associated with the occurrence of ischemic events independent of the degree of stenosis.⁵² In a meta-analysis of 8 studies including 689

patients, the presence of IPH at baseline was associated with a 6-fold higher risk of cerebrovascular events, with an annualized event rate of 17.7% compared with 2.43% in patients with no IPH.⁵³ In a separate meta-analysis of 9 studies and 779 subjects, the hazard ratios for subsequent stroke/TIA were 4.59 for IPH, 3.00 for lipid-rich necrotic core (LRNC), and 5.93 for thin/ruptured fibrous cap.⁵⁴ Last, another meta-analysis recently published in 2019, including 560 patients with symptomatic and 136 patients with asymptomatic carotid stenosis, reported that the presence of IPH at baseline increased the risk of ipsilateral stroke both in symptomatic (hazard ratio = 10.2; 95% CI, 4.6–22.5) and asymptomatic (hazard ratio = 7.9; 95% CI, 1.3–47.6) patients. Among patients with symptomatic carotid stenosis, annualized event rates of ipsilateral stroke in those with IPH versus those without IPH were 9.0% versus 0.7% (<50% stenosis), 18.1% versus 2.1% (50%–69% stenosis), and 29.3% versus 1.5% (70%–99% stenosis). Multivariate analysis identified IPH (hazard ratio = 11.0; 95% CI, 4.8–25.1) and a severe degree of stenosis (hazard ratio = 3.3; 95% CI, 1.4–7.8) as independent predictors of ipsilateral stroke.⁵⁵

Plaque with Severe Stenosis and a Low Likelihood of Rupture. Several studies have demonstrated that plaque calcification is a stabilizing factor in carotid artery stenosis and is more common in asymptomatic than in symptomatic plaques.⁵⁶ Histopathologic studies demonstrated that plaques with a high burden of calcification have lower rates of inflammation, macrophage burden, neovascularization, and IPH, lending further support to the use of plaque imaging as a risk-stratification tool.¹⁴

Plaque Progression and Regression

With improvements in MR imaging, sonography, and CT, it is now possible to directly visualize the carotid wall volume and plaque composition as the vessel wall disease evolves from early/mild atherosclerosis to late-stage/severe-stage atherosclerosis.⁵⁷ Progression of plaque morphology with increasing vessel wall volume or progression of plaque components with increasing size of vulnerable plaque features or both are associated with an increased risk of future cerebrovascular and cardiovascular events.⁵⁸ Furthermore, direct visualization of the plaque response to medical therapy offers the potential for individualization of atherosclerosis treatment.⁵⁹ To use imaging for assessing the

response of carotid plaque to drug therapy, one needs to determine the reproducibility of the imaging.

Evidence of Plaque Progression and Regression. In a prospective, case-controlled study of asymptomatic patients with moderate carotid stenosis, LRNC size increased in plaques with IPH compared with plaques with no IPH.⁶⁰ The role of IPH-induced plaque progression was demonstrated in a later study of mildly stenotic asymptomatic patients in whom IPH was found to significantly increase plaque size.⁶¹ This finding suggests that IPH may occur before stenosis becomes severe and may drive the stenotic phenotype.⁵⁹ In a prospective study of asymptomatic patients with moderate stenosis, the LRNC size governed the risk of future surface disruption, suggesting that urgent lipid-lowering therapy to prevent the transition from stable to unstable atherosclerotic disease may be warranted.⁶²

Plaque progression is a major risk factor for the development of future ischemic events. Longitudinal studies have demonstrated that the presence of plaque hemorrhage⁶³ (as determined by MR imaging) or a hypoechoic plaque (on sonography) is a major risk factor for plaque progression.⁶⁴ Another mechanism for rapid significant progression of plaque volume is silent plaque rupture and healing.⁶⁵

With regard to evidence of plaque regression, lipid-lowering treatment, predominately with statin therapy, has been shown to decrease carotid plaque size and composition. Corti et al⁶⁶ were the first to show a decrease in vessel wall thickness and vessel wall area. Observational studies have all used the 1-year timeframe to study changes in vessel wall size.⁵⁹ Because wall volume showed a greater reduction in more diseased segments with statin therapy,⁶⁷ it seems that carotid MR imaging is best suited to yearly follow-up of patients with known carotid stenosis. Studies have shown that statin therapy is associated with a decrease in LRNC and an increase in fibrous tissue,⁶⁸ which precedes any reduction in plaque volume.⁶⁷ Information from natural history studies suggests that IPH may override the beneficial effects of statin therapy, but the statin type and dose were not randomized or uniform.⁶¹ No prospective trials exist testing the hypothesis that the deleterious effects of IPH can be modified with very intensive lipid-lowering therapy.

Underhill and Yuan⁵⁹ summarized the use of MR imaging monitoring of carotid plaque in clinical trials, noting the following: 1) The rate of change is slower in plaques with <50% LRNC volume, though improved image quality may allow detection of change at 6 months, 2) changes in plaque composition precede changes in plaque morphology, and 3) LRNC at baseline is needed to monitor treatment effect with MR imaging.

Sonography provides a sensitive measure of carotid plaque regression. Carotid plaques are focal and progress along the artery wall 2.4 times faster than they thicken.⁶⁹ Spence and Hackam⁷⁰ reported their experience in 4387 patients imaged with serial carotid total plaque area. In this cohort, they intensified medical therapy for patients with documented plaque progression despite guideline-based medical therapy. By “treating arteries instead of risk factors,” they significantly decreased the incidence of plaque progression and cardiovascular events, and microemboli on transcranial Doppler sonography markedly declined with intensification of medical therapy.⁷¹

Updated Drug Therapy: Evidence and Impact

It is demonstrated that a group of potentially modifiable risk factors (hypertension, regular physical activity, dyslipidemia, diet, obesity, psychosocial factors, smoking, cardiac causes, alcohol consumption, and diabetes mellitus) account for 90% of the population-attributable risks of stroke,⁷² and some classes of drugs can significantly impact these factors. In this section we will explore the latest evidence in the use of imaging and its impact on the drug therapy in the prevention of stroke.

Lipid-Lowering Therapy. Studies have shown that treatment with statins reduces the risk of stroke in patients at high risk for atherosclerosis by 21% and that this risk reduction has been associated with each 1-mmol/L (39 mg/dL) decrease in low-density lipoprotein.^{73,74} In a meta-analysis by Cannon et al,⁷⁵ published in 2006, high-intensity statin treatment reduced nonfatal cardiovascular events and led to lower stroke incidence, even in healthy individuals, with low-density lipoprotein levels of <130 mg/dL and high-sensitivity C-reactive protein levels of >2 mg/L.⁷⁶ Two randomized controlled trials have shown improved cardiovascular diseases outcomes with the addition of nonstatin lipid-lowering medications: ezetimibe⁷⁷ and evocolumab.⁷⁸ The proprotein convertase subtilisin/kexin type 9 inhibitors achieve very low nonstatin low-density lipoprotein thresholds.⁷⁹ A study published in 2016 showed that the duration of statin therapy is associated with the regression of carotid plaque neovascularization measured with dynamic contrast-enhanced MR imaging,⁸⁰ and these results were confirmed by another group in 2019,⁸¹ again with dynamic contrast-enhanced MR imaging, which demonstrated that statins rapidly and significantly decreased adventitial and plaque neovascularization at 3 months.

Antiplatelet Therapy. In a study published in 1997,⁸² the introduction of aspirin within 48 hours after ischemic stroke led to a significant reduction in recurrence within 2 weeks,⁸³ and the addition of dipyridamole and clopidogrel added significant benefit to secondary stroke prevention.⁸⁴⁻⁸⁷ Evidence suggests that while benefit occurs within 48 hours of starting aspirin for stroke prevention, there is no further benefit after 2 months.⁸⁸ The benefits of long-term treatment with dual antiplatelet therapy (aspirin plus clopidogrel) in patients with acute coronary syndrome were never replicated in patients with stroke and are associated with more bleeding complications.^{53,62,89} The impact of antiplatelet therapy on carotid artery plaque has been explored: in 2019, a sonography-based trial was published that explored the efficacy and usefulness of an antiplatelet drug (cilostazol) on the progression of carotid intima-media thickness, and the authors found that it may inhibit plaque formation.⁹⁰

Anticoagulation Therapy. In 2017, Eikelboom et al⁹¹ published the results of the Cardiovascular Outcomes for People Using Anticoagulation Strategies (COMPASS) trial. In this study, patients with coronary, peripheral, and carotid artery disease (symptomatic or asymptomatic) were included, and a combination of an anticoagulant (2.5 mg of rivaroxaban twice a day) and aspirin proved superior to aspirin alone and 5 mg of rivaroxaban twice a day. The outcome of ischemic and hemorrhagic events

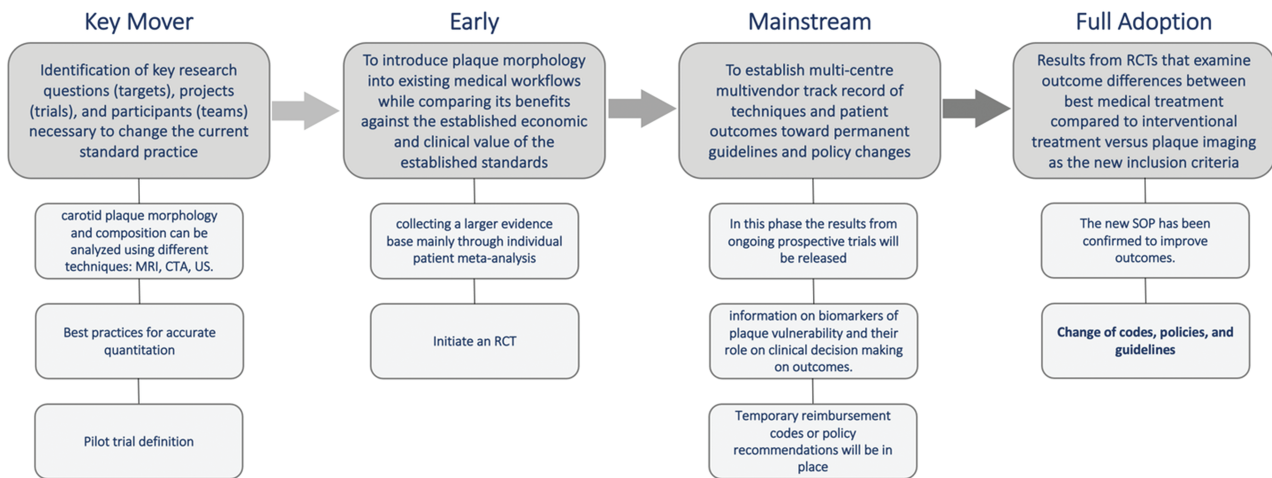


FIG 3. Roadmap graphic flow chart showing the 4 phases: key mover, early, mainstream, and full adoption. The *lighter gray boxes* represent the components of the various stages of the roadmap. RCT indicates randomized controlled trial; SOP, standard of practice; US, ultrasound.

was significantly in favor of patients in the combined treatment group, and efficacy outcomes were mainly driven by a 50% relative-risk reduction in ischemic stroke risk ($P < .001$). The recently published Rivaroxaban Versus Aspirin in Secondary Prevention of Stroke and Prevention of Systemic Embolism in Patients with Recent Embolic Stroke of Undetermined Source (NAVIGATE ESUS) trial, performed in 4723 participants with available intracranial CTA or MRA, showed that among participants with evidence of systemic atherosclerosis by either history or imaging ($n = 3820$), recurrent ischemic stroke rates were similar among those assigned to rivaroxaban (5.5%/year) versus aspirin (4.9%/year) (hazard ratio = 1.1; 95% CI, 0.84–1.5).⁹²

Anti-Inflammatory Therapy. Atherosclerosis is considered a predominantly a lipid-driven, chronic, low-grade inflammatory disease of the arterial wall.⁹³ Anti-inflammatory strategies are increasingly being considered as an attractive strategy to further reduce the residual risk of atherosclerotic cardiovascular disease.⁹⁴ The administration of canakinumab (a monoclonal antibody against interleukin-1 β) reduces the incidence of nonfatal myocardial infarction, nonfatal stroke, and cardiovascular death. Colchicine is another anti-inflammatory drug that may result in plaque stabilization,⁹⁵ reducing the incidence of noncardioembolic ischemic stroke in patients with stable coronary artery disease.⁹⁶ Promising imaging-based studies have shown the impact of anti-inflammatory therapy on plaque progression and composition in the coronary arteries,⁹⁷ suggesting similar effects and ability to assess them in the carotid arteries as addressed by this roadmap.

Suggested Roadmap

There are 2 related-but-distinct clinical tasks, phenotype classification to categorize patients to their individual disease mechanism to identify the treatments to which they would most likely respond, and risk stratification to identify how urgent interventional treatments may be, to allow patients to benefit from tailored therapeutics to ultimately lower or reverse disease progress

and ultimately shift the at-risk population to less acute manifestations of disease.

Sufficient data already exist to formally incorporate some plaque imaging in the management of atherosclerotic carotid artery disease. It is becoming increasingly important to begin the development of a common roadmap for changing the current standard of practice. We propose a 4-phase roadmap (Fig 3). This section outlines the broad overview of the roadmap, and more details are given in the Online Supplemental Data.

Key Mover (The Phase in Which the Field Has Been). Identification of key research questions (targets), projects (trials), and participants (teams) necessary to change the current standard of practice is currently confined to considering the degree of stenosis and the symptom status of the patients. This change begins by examination of existing evidence that is valuable for identifying existing knowledge gaps through systematic reviews. The results of these reviews can then be used to formulate key research priorities for guiding the development of randomized controlled trials. Outcomes from such randomized controlled trials can then be used to initiate policy discussions, including clinical implementation recommendations and the development of new reimbursement codes as required.

Early (The Phase the Field Is Entering). In this early phase, one introduces plaque morphology into existing medical workflows while comparing its benefits against the established economic and clinical values of the established standards. One must start the development of local reimbursement codes/policies in readiness for a larger body of evidence of efficacy and patient benefit. Among the most important activities of this phase is to transition beyond retrospective studies to prospective ones. The retrospective studies are inherently limited due to the fundamental confounding of the current standard of care with the incidence of events; the ability to study positive benefits of plaque morphology assessment as to the improvement in patient outcomes can only be properly studied in 2-arm studies that allow study of the hypothesized improvement without being hampered by data collection that, by definition, is not allowed to use it. The data from

these studies are expected to develop a better tool for determining the best treatment option for atherosclerosis and inform a better standard of care to reduce the incidence of adverse neurologic symptomatology and poor outcome (eg, ischemic stroke) for patients with known or suspected carotid artery disease.

Mainstream. To reach the mainstream stage, one must address the economic impact, and indications of different organizations should be taken into account to identify an optimal balance in terms of diagnostic stratification of the risk and economic impact of the process. One must establish a multicenter, multivendor track record of techniques and patient outcomes toward permanent guidelines and policy changes. A collaborative and central data base construction for rapid, large data collection and analysis would accelerate this process. Standardized imaging protocols would allow accrual from both clinical (eligible retrospective and prospective) and ongoing research imaging, with capture of standardized patient clinical data ideally with follow-up, requiring appropriate patient consent.⁹⁸

Full Adoption. Results from randomized controlled trials that examine outcome differences between the best medical treatment compared with interventional treatment (carotid endarterectomy) with treatment selection randomized to the current standards (degree of stenosis) versus plaque imaging as the new inclusion criteria will be adopted. Change in clinical practice would lead to an update of policies, guidelines, and billing codes. In parallel with the stages as they effect treatment of patients with signs and symptoms, there is an even broader application in population-based screening. Whereas the US Preventive Services Task Force has presently recommended against screening,⁹⁹ the nature of these assessments is to await the development of more powerful technologies and/or the evolution of disease prevalence until such capability is considered to have reached a crossover point. No doubt the stages that we have identified will provide additional input to this process. Regardless of whether population-based screening does or does not reach the point of being recommended, our roadmap will meet the needs of the patients with signs and symptoms regardless and, in so doing, increasingly provide screening options for patient subpopulations that would also benefit.

CONCLUSIONS

In this roadmap consensus article, we have defined the limits of luminal imaging and highlight current evidence supporting the role of plaque imaging in risk stratification and treatment of carotid artery atherosclerosis and stroke. These recommendations are supported by evidence that highlights the limits of risk stratification based on the degree of luminal stenosis alone and emphasize the predictive power of other features such as the presence of IPH. Outcome trials, which confirm image-based information and can act as a primary parameter for choosing therapeutic interventions and predicting outcomes, are fundamental for the full adoption of a plaque-imaging-based approach. This body of evidence needs to be merged with evidence from trials that show the effects of pharmaceutical agents to better understand the overall benefits of incorporating plaque imaging

metrics. This roadmap details the process for acquiring the necessary high-quality evidence to support the incorporation of plaque imaging in risk stratification and the management of carotid artery atherosclerotic disease.

ACKNOWLEDGMENTS

The authors would like to express their deepest gratitude to Riccardo Cau, Alessandra Serra, Mueez Aizaz, and Mohamed Kassem for their support and assistance with this project

Disclosures: Mauricio Castillo—UNRELATED: Employment: University of North Carolina. Peter Rothwell—UNRELATED: Board Membership: ARRIVE Trial Executive Committee; Consultancy: BMS Axiomatic Trial Data and Safety Monitoring Board; Payment for Lectures Including Service on Speakers Bureaus: Abbott for lecture on Patent Forame Ovale closure; Other: lecture on TIA for AstraZeneca. Max Wintermark—UNRELATED: Consultancy: Magnetic Insight, Subtle Medical, EMTensor, Icometrix, Nous Infosystems. Chun Yuan—UNRELATED: Grants/Grants Pending: National Institutes of Health, American Heart Association, Philips Healthcare.* Andrew Buckler—UNRELATED: Employment: Elucid Bioimaging, Davide Capodanno—UNRELATED: Board Membership: Medtronic, Comments: speaker's fee; Consultancy: BIOTRONIK, Comments: speaker's fee; Employment: Boston Scientific, Comments: speaker's fee; Expert Testimony: Daiichi Sankyo, Comments: speaker's fee; Grants/Grants Pending: Boehringer Ingelheim, Comments: speaker's fee; Payment for Lectures Including Service on Speakers Bureaus: Bayer AG, Comments: speaker's fee; Payment for Manuscript Preparation: AstraZeneca, Comments: speaker's fee. Ulf Hedin—UNRELATED: Employment: Karolinska Hospital; Grants/Grants Pending: Swedish Research Council. Waleed Brinjiki—UNRELATED: Consultancy: MicroVention, Cerenovus*; Stock/Stock Options: Marblehead Medical LLC. Thomas Hatsukami—UNRELATED: Grants/Grants Pending: investigator-initiated grant from Philips Healthcare, completed December 31, 2018.* Christopher Hess—UNRELATED: Personal Fees: GE Healthcare, Focused Ultrasound Foundation, uniQure, Comments: consultant for GE Healthcare and Data and Safety Monitoring Board member for Focused Ultrasound Foundation and uniQure; Nonfinancial Support: Siemens, Comments: research travel. Bruce A. Wasserman—UNRELATED: Grants/Grants Pending: National Institutes of Health R01.* Joanna Wardlaw—RELATED: Grant: National Institute for Health Research Health Technology Assessment Panel, Comments: funded the research.* Ajay Gupta—UNRELATED: Consultancy: ERT; Travel/Accommodations/Meeting Expenses Unrelated to Activities Listed: Siemens, GE Healthcare. Jie Sun—UNRELATED: Grants/Grants Pending: American Heart Association, Institute of Translational Health Sciences.* Niranjan Balu—UNRELATED: Patents (Planned, Pending or Issued): I hold a US patent 9,557,396 but no payment/royalties. *Money paid to the institution.

REFERENCES

1. GBD 2016 Stroke Collaborators. **Global, regional, and national burden of stroke, 1990–2016: a systematic analysis for the Global Burden of Disease Study 2016.** *Lancet Neurol* 2019;18:43–58 CrossRef Medline
2. Cheng SF, Brown MM, Simister RJ, et al. **Contemporary prevalence of carotid stenosis in patients presenting with ischaemic stroke.** *Br J Surg* 2019;106:872–78 CrossRef Medline
3. Mohr JP, Caplan LR, Melski JW, et al. **The Harvard Cooperative Stroke Registry: a prospective registry.** *Neurology* 1978;28:754–62 CrossRef Medline
4. Kumamaru H, Jalbert JJ, Nguyen LL, et al. **Surgeon case volume and 30-day mortality after carotid endarterectomy among contemporary Medicare beneficiaries: before and after national coverage determination for carotid artery stenting.** *Stroke* 2015;46:1288–94 CrossRef Medline
5. Abbott AL, Adelman MA, Alexandrov AV, et al. **Why calls for more routine carotid stenting are currently inappropriate: an international, multispecialty, expert review and position statement.** *Stroke* 2013;44:1186–90 CrossRef Medline
6. Munster AB, Franchini AJ, Qureshi MI, et al. **Temporal trends in safety of carotid endarterectomy in asymptomatic patients.** *Neurology* 2015;85:365–72 CrossRef Medline

7. Ridker PM, Everett BM, Thuren T, et al. CANTOS Trial Group. **Antiinflammatory therapy with canakinumab for atherosclerotic disease.** *N Engl J Med* 2017;377:1119–31 CrossRef Medline
8. Abbott AL. **Medical (nonsurgical) intervention alone is now best for prevention of stroke associated with asymptomatic severe carotid stenosis: results of a systematic review and analysis.** *Stroke* 2009;40:e573–83 CrossRef Medline
9. Naylor AR, Gaines PA, Rothwell PM. **Who benefits most from intervention for asymptomatic carotid stenosis: patients or professionals?** *Eur J Vasc Endovasc Surg* 2009;37:625–32 CrossRef Medline
10. Naylor AR. **Time to rethink management strategies in asymptomatic carotid artery disease.** *Nat Rev Cardiol* 2011;9:116–24 CrossRef Medline
11. Ibrahim P, Jashari F, Bajraktari G, et al. **Ultrasound assessment of carotid plaque echogenicity response to statin therapy: a systematic review and meta-analysis.** *Int J Mol Sci* 2015;16:10734–47 CrossRef Medline
12. Perisic L, Aldi S, Sun Y, et al. **Gene expression signatures, pathways and networks in carotid atherosclerosis.** *J Intern Med* 2016;279:293–308 CrossRef Medline
13. Mujaj B, Bos D, Selwaness M, et al. **Statin use is associated with carotid plaque composition: the Rotterdam Study.** *Int J Cardiol* 2018;260:213–18 CrossRef Medline
14. Karlöf E, Seime T, Dias N, et al. **Correlation of computed tomography with carotid plaque transcriptomes associates calcification with lesion-stabilization.** *Atherosclerosis* 2019;288:175–85 CrossRef Medline
15. Kapadia M, Mehri-Basha M, Madhavan R, et al. **High rate of inappropriate carotid endarterectomy in an urban medical center.** *J Stroke Cerebrovasc Dis* 2009;18:277–80 CrossRef Medline
16. Barnett HJ, Taylor DW, Eliasziw M, et al. **Benefit of carotid endarterectomy in patients with symptomatic moderate or severe stenosis.** *N Engl J Med* 1998;339:1415–25 CrossRef Medline
17. **Endarterectomy for asymptomatic carotid artery stenosis: Executive Committee for the Asymptomatic Carotid Atherosclerosis Study.** *JAMA* 1995;273:1421–28 Medline
18. Abbott AL, Paraskevas KI, Kakkos SK, et al. **Systematic review of guidelines for the management of asymptomatic and symptomatic carotid stenosis.** *Stroke* 2015;46:3288–301 CrossRef Medline
19. Ricotta JJ, Aburahma A, Ascher E, et al. **Updated Society for Vascular Surgery guidelines for management of extracranial carotid disease.** *J Vasc Surg* 2011;54:e1–31 CrossRef Medline
20. Ricotta JJ, AbuRahma A, Ascher E, et al. **Updated Society for Vascular Surgery guidelines for management of extracranial carotid disease: executive summary.** *J Vasc Surg* 2011;54:832–36 CrossRef Medline
21. Lanza G, Ricci S, Setacci C, et al. **An update on Italian Stroke Organization guidelines on carotid endarterectomy and stenting.** *Int J Stroke* 2014;9 Suppl A100:14–19 CrossRef Medline
22. Naylor AR, Ricco JB, de Borst GJ, et al. **Editor's Choice: Management of Atherosclerotic Carotid and Vertebral Artery Disease—2017 Clinical Practice Guidelines of the European Society for Vascular Surgery (ESVS).** *Eur J Vasc Endovasc Surg* 2018;55:3–81 CrossRef Medline
23. Aboyans V, Ricco JB, Bartelink ML, et al. **ESC Scientific Document Group. 2017 ESC Guidelines on the Diagnosis and Treatment of Peripheral Arterial Diseases, in collaboration with the European Society for Vascular Surgery (ESVS): document covering atherosclerotic disease of extracranial carotid and vertebral, mesenteric, renal, upper and lower extremity arteries endorsed by: the European Stroke Organization (ESO), The Task Force for the Diagnosis and Treatment of Peripheral Arterial Diseases of the European Society of Cardiology (ESC), and of the European Society for Vascular Surgery (ESVS).** *Eur Heart J* 2018;39:763–816 CrossRef Medline
24. Kopczyk A, Schindler A, Bayer-Karpinska A, et al. **Complicated carotid artery plaques as a cause of cryptogenic stroke.** *J Am Coll Cardiol* 2020;76:2212–22 CrossRef Medline
25. Estol CJ. **Dr C: Miller Fisher and the history of carotid artery disease.** *Stroke* 1996;27:559–66 CrossRef Medline
26. Ogata J, Masuda J, Yutani C, et al. **Rupture of atheromatous plaque as a cause of thrombotic occlusion of stenotic internal carotid artery.** *Stroke* 1990;21:1740–45 CrossRef Medline
27. Carr S, Farb A, Pearce WH, et al. **Atherosclerotic plaque rupture in symptomatic carotid artery stenosis.** *J Vasc Surg* 1996;23:755–65; discussion 765–66 CrossRef Medline
28. Avril G, Batt M, Guidoin R, et al. **Carotid endarterectomy plaques: correlations of clinical and anatomic findings.** *Ann Vasc Surg* 1991;5:50–54 CrossRef Medline
29. Lusby RJ, Ferrell LD, Ehrenfeld WK, et al. **Carotid plaque hemorrhage.** *Arch Surg* 1982;117:1479–88 CrossRef Medline
30. Imparato AM, Riles TS, Mintzer R, et al. **The importance of hemorrhage in the relationship between gross morphologic characteristics and cerebral symptoms in 376 carotid artery plaques.** *Ann Surg* 1983;197:195–203 CrossRef Medline
31. Kwee RM. **Systematic review on the association between calcification in carotid plaques and clinical ischemic symptoms.** *J Vasc Surg* 2010;51:1015–25 CrossRef Medline
32. Finn AV, Nakano M, Narula J, et al. **Concept of vulnerable/unstable plaque.** *Arterioscler Thromb Vasc Biol* 2010;30:1282–92 CrossRef Medline
33. Gunning AJ, Pickering GW, Robb-Smith AH, et al. **Mural thrombosis of the internal carotid artery and subsequent embolism.** *Q J Med* 1964;33:155–95 Medline
34. Eikelboom BC, Riles TR, Mintzer R, et al. **Inaccuracy of angiography in the diagnosis of carotid ulceration.** *Stroke* 1983;14:882–85 CrossRef Medline
35. Ammar AD, Wilson RL, Travers H, et al. **Intraplaque hemorrhage: its significance in cerebrovascular disease.** *Am J Surg* 1984;148:840–43 CrossRef Medline
36. Ricotta JJ, Schenk EA, Ekholm SE, et al. **Angiographic and pathologic correlates in carotid artery disease.** *Surgery* 1986;99:284–92
37. Lennihan L, Kupsky WJ, Mohr JP, et al. **Lack of association between carotid plaque hematoma and ischemic cerebral symptoms.** *Stroke* 1987;18:879–81 CrossRef Medline
38. Svindland A, Torvik A. **Atherosclerotic carotid disease in asymptomatic individuals: An histological study of 53 cases.** *Acta Neurol Scand* 1988;78:506–17 CrossRef Medline
39. Bassiouny HS, Davis H, Massawa N, et al. **Critical carotid stenoses: morphologic and chemical similarity between symptomatic and asymptomatic plaques.** *J Vasc Surg* 1989;9:202–12 Medline
40. Bassiouny HS, Sakaguchi Y, Mikucki SA, et al. **Juxtalumenal location of plaque necrosis and neof ormation in symptomatic carotid stenosis.** *J Vasc Surg* 1997;26:585–94 CrossRef Medline
41. Fisher CM, Ojemann RG. **A clinico-pathologic study of carotid endarterectomy plaques.** *Rev Neurol (Paris)* 1986;142:573–89 Medline
42. Loree HM, Kamm RD, Stringfellow RG, et al. **Effects of fibrous cap thickness on peak circumferential stress in model atherosclerotic vessels.** *Circ Res* 1992;71:850–58 CrossRef Medline
43. Sary HC, Chandler AB, Dinsmore RE, et al. **A definition of advanced types of atherosclerotic lesions and a histological classification of atherosclerosis: a report from the Committee on Vascular Lesions of the Council on Arteriosclerosis, American Heart Association.** *Arterioscler Thromb Vasc Biol* 1995;15:1512–31 CrossRef Medline
44. Sary HC. **Natural history and histological classification of atherosclerotic lesions: an update.** [Editorial]. *Arterioscler Thromb Vasc Biol* 2000;20:1177–78 CrossRef Medline
45. Cai JM, Hatsukami TS, Ferguson MS, et al. **Classification of human carotid atherosclerotic lesions with in vivo multicontrast magnetic resonance imaging.** *Circulation* 2002;106:1368–73
46. Hetterich H, Webber N, Willner M, et al. **AHA classification of coronary and carotid atherosclerotic plaques by grating-based phase-contrast computed tomography.** *Eur Radiol* 2016;26:3223–33 CrossRef Medline

47. Virmani R, Kolodgie FD, Burke AP, et al. **Lessons from sudden coronary death: a comprehensive morphological classification scheme for atherosclerotic lesions.** *Arterioscler Thromb Vasc Biol* 2000;20:1262–75 CrossRef Medline
48. Virmani R, Burke AP, Farb A, et al. **Pathology of the vulnerable plaque.** *J Am Coll Cardiol* 2006;47:(8 Suppl):C13–18 CrossRef Medline
49. Qureshi AI, Janardhan V, Bennett SE, et al. **Who should be screened for asymptomatic carotid artery stenosis? Experience from the Western New York Stroke Screening Program.** *J Neuroimaging* 2001;11:105–11 CrossRef Medline
50. Yaghi S, Elkind MV. **Cryptogenic stroke: a diagnostic challenge.** *Neurol Clin Pract* 2014;4:386–93 CrossRef Medline
51. Yaghi S, Bernstein RA, Passman R, et al. **Cryptogenic stroke: research and practice.** *Circ Res* 2017;120:527–40 CrossRef Medline
52. Ferguson GG, Eliasziw M, Barr HW, et al. **Surgical results in 1415 patients.** *Stroke* 1999;30:1751–58 CrossRef Medline
53. Saam T, Hetterich H, Hoffmann V, et al. **Meta-analysis and systematic review of the predictive value of carotid plaque hemorrhage on cerebrovascular events by magnetic resonance imaging.** *J Am Coll Cardiol* 2013;62:1081–91 CrossRef Medline
54. Gupta A, Baradaran H, Schweitzer AD, et al. **Carotid plaque MRI and stroke risk: a systematic review and meta-analysis.** *Stroke* 2013;44:3071–77 CrossRef Medline
55. Schindler A, Schinner R, Altaf N, et al. **Prediction of stroke risk by detection of hemorrhage in carotid plaques: meta-analysis of individual patient data.** *JACC Cardiovasc Imaging* 2020;13(2 Pt 1):395–406 CrossRef Medline
56. Nandalur KR, Hardie AD, Raghavan P, et al. **Composition of the stable carotid plaque: Insights from a multidetector computed tomography study of plaque volume.** *Stroke* 2007;38:935–40 CrossRef Medline
57. Saba L, Saam T, Jäger HR, et al. **Imaging biomarkers of vulnerable carotid plaques for stroke risk prediction and their potential clinical implications.** *Lancet Neurol* 2019;4422:1–14 CrossRef Medline
58. Simpson RJ, Akwei S, Hosseini AA, et al. **MR imaging-detected carotid plaque hemorrhage is stable for 2 years and a marker for stenosis progression.** *Am J Neuroradiol* 2015;36:1171–75 CrossRef Medline
59. Underhill HR, Yuan C. **Carotid MRI: a tool for monitoring individual response to cardiovascular therapy?** *Expert Rev Cardiovasc Ther* 2011;9:63–80 CrossRef Medline
60. Takaya N, Yuan C, Chu B, et al. **Presence of intraplaque hemorrhage stimulates progression of carotid atherosclerotic plaques: a high-resolution magnetic resonance imaging study.** *Circulation* 2005;111:2768–75 CrossRef Medline
61. Underhill HR, Yuan C, Yarnykh VL, et al. **Arterial remodeling in [corrected] subclinical carotid artery disease.** *JACC Cardiovasc Imaging* 2009;2:1381–89 CrossRef Medline
62. Underhill HR, Yuan C, Yarnykh VL, et al. **Predictors of surface disruption with MR imaging in asymptomatic carotid artery stenosis.** *AJNR Am J Neuroradiol* 2010;31:487–93 CrossRef Medline
63. Sun J, Underhill HR, Hippe DS, et al. **Sustained acceleration in carotid atherosclerotic plaque progression with intraplaque hemorrhage: a long-term time course study.** *JACC Cardiovasc Imaging* 2012;5:798–804 CrossRef Medline
64. Pletsch-Borba L, Selwaness M, van der Lugt A, et al. **Change in carotid plaque components: a 4-year follow-up study with serial MR imaging.** *JACC Cardiovasc Imaging* 2018;11:184–92 CrossRef Medline
65. Burke AP, Kolodgie FD, Farb A, et al. **Healed plaque ruptures and sudden coronary death: evidence that subclinical rupture has a role in plaque progression.** *Circulation* 2001;103:934–40 CrossRef Medline
66. Corti R, Fayad ZA, Fuster V, et al. **Effects of lipid-lowering by simvastatin on human atherosclerotic lesions: a longitudinal study by high-resolution, noninvasive magnetic resonance imaging.** *Circulation* 2001;104:249–52 CrossRef Medline
67. Zhao X-Q, Dong L, Hatsukami T, et al. **MR imaging of carotid plaque composition during lipid-lowering therapy a prospective assessment of effect and time course.** *JACC Cardiovasc Imaging* 2011;4:977–86 CrossRef Medline
68. Underhill HR, Yuan C, Zhao XQ, et al. **Effect of rosuvastatin therapy on carotid plaque morphology and composition in moderately hypercholesterolemic patients: a high-resolution magnetic resonance imaging trial.** *Am Heart J* 2008;155:584.e1–8 CrossRef Medline
69. DeMarco JK, Spence JD. **Plaque assessment in the management of patients with asymptomatic carotid stenosis.** *Neuroimaging Clin N Am* 2016;26:111–27 CrossRef Medline
70. Spence JD, Hackam DG. **Treating arteries instead of risk factors: a paradigm change in management of atherosclerosis.** *Stroke* 2010;41:1193–99 CrossRef Medline
71. Spence JD, Coates V, Li H, et al. **Effects of intensive medical therapy on microemboli and cardiovascular risk in asymptomatic carotid stenosis.** *Arch Neurol* 2010;67:180–86 CrossRef Medline
72. GBD 2016 Neurology Collaborators. **Global, regional, and national burden of neurological disorders, 1990–2016: a systematic analysis for the Global Burden of Disease Study 2016.** *Lancet Neurol* 2019;18:459–80 CrossRef Medline
73. Iso H, Jacobs DR, Wentworth D, et al. **Serum cholesterol levels and six-year mortality from stroke in 350,977 men screened for the multiple risk factor intervention trial.** *N Engl J Med* 1989;320:904–10 CrossRef Medline
74. Chan DK, O'Rourke F, Shen Q, et al. **Meta-analysis of the cardiovascular benefits of intensive lipid lowering with statins.** *Acta Neurol Scand* 2011;124:188–95 CrossRef Medline
75. Cannon CP, Steinberg BA, Murphy SA, et al. **Meta-analysis of cardiovascular outcomes trials comparing intensive versus moderate statin therapy.** *J Am Coll Cardiol* 2006;48:438–45 CrossRef Medline
76. Everett BM, Glynn RJ, MacFadyen JG, et al. **Rosuvastatin in the prevention of stroke among men and women with elevated levels of C-reactive protein: Justification for the Use of Statins in Prevention: an Intervention Trial Evaluating Rosuvastatin (JUPITER).** *Circulation* 2010;121:143–50 CrossRef Medline
77. Cannon CP, Blazing MA, Giugliano RP, et al. **Ezetimibe added to statin therapy after acute coronary syndromes.** *N Engl J Med* 2015;372:2387–97 CrossRef Medline
78. Sabatine MS, Giugliano RP, Keech AC, et al. **Evolocumab and clinical outcomes in patients with cardiovascular disease.** *N Engl J Med* 2017;376:1713–22 CrossRef Medline
79. Landmesser U, Chapman MJ, Stock JK, et al. **2017 Update of ESC/EAS Task Force on practical clinical guidance for proprotein convertase subtilisin/kexin type 9 inhibition in patients with atherosclerotic cardiovascular disease or in familial hypercholesterolaemia.** *Eur Heart J* 2018;39:1131–43 CrossRef Medline
80. O'Brien KD, Hippe DS, Chen H, et al. **Longer duration of statin therapy is associated with decreased carotid plaque vascularity by magnetic resonance imaging.** *Atherosclerosis* 2016;245:74–81 CrossRef
81. Du R, Cai J, Cui B, et al. **Rapid improvement in carotid adventitial angiogenesis and plaque neovascularization after rosuvastatin therapy in statin treatment-naïve subjects.** *J Clin Lipidol* 2019;13:847–53 CrossRef Medline
82. **The International Stroke Trial (IST): a randomised trial of aspirin, subcutaneous heparin, both, or neither among 19435 patients with acute ischaemic stroke—International Stroke Trial Collaborative Group.** *Lancet (London, England)* 1997;349:1569–81 CrossRef Medline
83. Russell DA, Wijayaratne SM, Gough MJ. **Relationship of carotid plaque echomorphology to presenting symptom.** *Eur J Vasc Endovasc Surg* 2010;39:134–38 CrossRef Medline
84. Halkes PH, van Gijn J, Kappelle LJ, et al. **ESPRIT Study Group. Aspirin plus dipyridamole versus aspirin alone after cerebral ischaemia of arterial origin (ESPRIT): randomised controlled trial.** *Lancet* 2006;367:1665–73 CrossRef Medline
85. Diener HC, Sacco RL, Yusuf S, et al. **Prevention Regimen for Effectively Avoiding Second Strokes (PRoFESS) study group. Effects**

- of aspirin plus extended-release dipyridamole versus clopidogrel and telmisartan on disability and cognitive function after recurrent stroke in patients with ischaemic stroke in the Prevention Regimen for Effectively Avoiding Second Strokes (PROFESS) trial: a double-blind, active and placebo-controlled study. *Lancet Neurol* 2008;7:875–84 CrossRef Medline
86. Madani A, Beletsky V, Tamayo A, et al. **High-risk asymptomatic carotid stenosis: ulceration on 3D ultrasound vs TCD microemboli.** *Neurology* 2011;77:744–50 CrossRef Medline
87. Kakkos SK, Griffin MB, Nicolaides AN, et al. **The size of juxtalumininal hypoechoic area in ultrasound images of asymptomatic carotid plaques predicts the occurrence of stroke.** *J Vasc Surg* 2013;57:609–18.e1; discussion 617–18 CrossRef Medline
88. Rothwell PM, Algra A, Chen Z, et al. **Effects of aspirin on risk and severity of early recurrent stroke after transient ischaemic attack and ischaemic stroke: time-course analysis of randomised trials.** *Lancet* 2016;388:365–75 CrossRef Medline
89. Bhatt DL, Fox KA, Hacke W, et al. CHARISMA Investigators. **Clopidogrel and aspirin versus aspirin alone for the prevention of atherothrombotic events.** *N Engl J Med* 2006;354:1706–17 CrossRef Medline
90. Hong S, Nam M, Little BB, et al. **Randomized control trial comparing the effect of cilostazol and aspirin on changes in carotid intima-medial thickness.** *Heart Vessels* 2019;34:1758–68 CrossRef Medline
91. Eikelboom JW, Connolly SJ, Bosch J, et al. **Rivaroxaban with or without aspirin in stable cardiovascular disease.** *N Engl J Med* 2017;377:1319–30 CrossRef Medline
92. Ameriso SF, Amarenco P, Pearce LA, et al. **Intracranial and systemic atherosclerosis in the NAVIGATE ESUS trial: recurrent stroke risk and response to antithrombotic therapy.** *J Stroke Cerebrovasc Dis* 2020;29:104936 CrossRef Medline
93. Seneviratne AN, Monaco C. **Role of inflammatory cells and toll-like receptors in atherosclerosis.** *Curr Vasc Pharmacol* 2015;13:146–60 CrossRef Medline
94. Bäck M, Hansson GK. **Anti-inflammatory therapies for atherosclerosis.** *Nat Rev Cardiol* 2015;12:199–211 CrossRef Medline
95. Tsvigoulis G, Katsanos AH, Giannopoulos G, et al. **The role of colchicine in the prevention of cerebrovascular ischemia.** *Curr Pharm Des* 2018;24:668–74 CrossRef Medline
96. Nidorf SM, Eikelboom JW, Budgeon CA, et al. **Low-dose colchicine for secondary prevention of cardiovascular disease.** *J Am Coll Cardiol* 2013;61:404–10 CrossRef Medline
97. Choi H, Uceda DE, Dey AK, et al. **Treatment of psoriasis with biologic therapy is associated with improvement of coronary artery plaque lipid-rich necrotic core: results from a prospective, observational study.** *Circ Cardiovasc Imaging* 2020;13:e011199 CrossRef Medline
98. Mahmoud R, Moody AR, Foster M, et al. **Sharing de-identified medical images electronically for research: a survey of patients' opinion regarding data management.** *Can Assoc Radiology J* 2019;70:212–18 CrossRef Medline
99. Paraskevas KI, Eckstein HH, Mikhailidis DP, et al. **Rationale for screening selected patients for asymptomatic carotid artery stenosis.** *Curr Med Res Opin* 2020;36:361–65 CrossRef Medline

Racial and Socioeconomic Disparities in the Use and Outcomes of Endovascular Thrombectomy for Acute Ischemic Stroke

A.M. Mehta, J.T. Fifi, H. Shoirah, T. Shigematsu, T.J. Oxley, C.P. Kellner, R.De Leacy, J. Mocco, and S. Majidi



ABSTRACT

BACKGROUND AND PURPOSE: Racial and socioeconomic disparities in the incidence, treatment, and outcomes of acute ischemic stroke exist and have been described. We aimed to characterize disparities in the use of endovascular thrombectomy in a nationally representative analysis.

MATERIALS AND METHODS: Discharge data from the Nationwide Inpatient Sample between 2006 and 2016 were queried using validated International Classification of Disease codes. Patients admitted to US hospitals with acute ischemic stroke were included and stratified on the basis of race, income, and primary payer. Trends in endovascular thrombectomy use, good outcome (discharge to home/acute rehabilitation), and poor outcome (discharge to skilled nursing facility, hospice, in-hospital mortality) were studied using univariate and multivariable analyses.

RESULTS: In this analysis of 1,322,162 patients, endovascular thrombectomy use increased from 53/111,829 (0.05%) to 3054/146,650 (2.08%) between 2006 and 2016, respectively. Less increase was observed in black patients from 4/12,733 (0.03%) to 401/23,836 (1.68%) and those in the lowest income quartile from 10/819 (0.03%) to 819/44,984 (1.49%). Greater increase was observed in the highest income quartile from 18/22,138 (0.08%) to 669/27,991 (2.39%). Black race predicted less endovascular thrombectomy use (OR = 0.79; 95% CI, 0.72–0.86). The highest income group predicted endovascular thrombectomy use (OR = 1.24; 95% CI, 1.13–1.36) as did private insurance (OR = 1.30; 95% CI, 1.23–1.38). High income predicted good outcome (OR = 1.10; 95% CI, 1.06–1.14), as did private insurance (OR = 1.36; 95% CI, 1.31–1.39). Black race predicted poor outcome (OR = 1.33; 95% CI, 1.30–1.36). All results were statistically significant ($P < .01$).

CONCLUSIONS: Despite a widespread increase in endovascular thrombectomy use, black and low-income patients may be less likely to receive endovascular thrombectomy. Future effort should attempt to better understand the causes of these disparities and develop strategies to ensure equitable access to potentially life-saving treatment.

ABBREVIATIONS: AIS = acute ischemic stroke; ECI = Elixhauser Comorbidity Index; EVT = endovascular thrombectomy; ICD = International Classification of Disease; NIS = Nationwide Inpatient Sample

Ischemic stroke is one of the leading causes of death and disability.¹ IV rtPA remains the criterion standard in acute treatment of acute ischemic stroke (AIS).² After a number of randomized controlled trials demonstrated its effectiveness, endovascular thrombectomy (EVT) has emerged as standard of care for large-

vessel occlusions of the anterior circulation within 6 hours of symptom onset and up to 24 hours for selected patients.^{2–6}

Socioeconomic and racial disparities in stroke prevalence and treatment have been studied extensively and documented in the literature. Black and Hispanic patients have a higher burden of stroke and are more likely to experience stroke earlier in life than white patients.^{1,7–9} Black patients are less likely to receive IV rtPA than white patients,¹⁰ more commonly receive inferior in-hospital stroke care including longer wait times in the emergency department,¹¹ have lower odds of receiving a door-to-CT time of <25 minutes, and have decreased likelihood of obtaining cardiac monitoring, dysphagia screening, and smoking-cessation counseling.^{10,12,13}

Also, a few studies have studied disparities in EVT. Rinaldo et al¹⁴ demonstrated that in 2016–2018, black and Hispanic patients were less likely to receive EVT than white patients. A

Received March 25, 2021; accepted after revision April 26.

From the Department of Neurosurgery (A.M.M., J.T.F., H.S., T.S., T.J.O., C.P.K., R.D.L., J.M., S.M.), Icahn School of Medicine at Mount Sinai, New York, New York; and Department of Neurology (A.M.M.), Columbia University, New York, New York.

Please address correspondence to Shahram Majidi, MD, Department of Neurosurgery, Icahn School of Medicine at Mount Sinai, 1450 Madison Avenue, Box 1136, New York, New York 10029-6574; e-mail: Shahram.majidi@mountsinai.org; @MajidiShahram; @AmolMehtaMD

Indicates article with online supplemental data.

<http://dx.doi.org/10.3174/ajnr.A7217>

recently published study using the Nationwide Inpatient Sample (NIS) also demonstrated similar findings of a racial disparity in EVT use.¹⁵ However, this study period was limited to the time before the introduction of EVT as a standard of care for AIS in 2015; thus, we have little understanding of how disparities in EVT have changed from a longitudinal perspective that includes data collected after publication of the major EVT trials.

We aimed to study the trends in both socioeconomic and racial disparities in the use of EVT during a longitudinal period of time including the years following the mainstream acceptance of EVT as standard of care for AIS in a nationally representative administrative data base. As conversations surrounding implicit bias, health care infrastructure, and the funding of culture health care evolve, it is our hope that providing further data will guide interventions designed to achieve equality.

MATERIALS AND METHODS

Data Source

The NIS is the largest publicly available all-payer health care data base. It assesses 20% of all discharges from US hospitals, including approximately 7 million discharges annually and 35 million discharges annually when weighted. A broad range of patient information includes patient-level demographics, discharge diagnoses, procedures performed during admission, and hospital-level demographics. All data in the NIS, including the specific exposures and outcomes of interest, are provided by the included hospitals and are abstracted from discharge and other administrative documentation. Patients admitted between 2006 and 2016 with the diagnosis of AIS were selected. Inclusion criteria were the diagnosis of AIS; no strict exclusion criteria were applied. EVT and AIS and other diagnoses were identified using the International Classification of Disease, Ninth Revision (ICD-9) and the International Classification of Disease, Tenth Revision (ICD-10) codes. For AIS, ICD-9 codes 433–435 and ICD-10 codes I61, I63, and I64 were used. For EVT, ICD-9 procedure code 39.74 and ICD-10 procedure codes 03CG3Z7, 03CG3ZZ, 03CG4ZZ, 03CK3Z7, 03CK3ZZ, 03CL3Z7, 03CL3ZZ, 03CM3Z7, 03CM3ZZ, 03CN3Z7, and 03CN3ZZ, were used, as per prior studies.^{16,17} No institutional review board approval was necessary because the NIS is a de-identified data base.

Outcome

The primary outcome of the analysis was EVT use, which was determined by whether a patient who had an ICD-9 or ICD-10 code for AIS also had a procedural code for EVT. Secondary outcomes included having a good outcome, which was defined by discharge to home or an acute rehabilitation hospital. Poor outcome was defined as discharge to a skilled nursing facility, hospice, or in-hospital mortality. Although mortality was included within the poor outcome category, mortality was used as its own secondary outcome as well because it was thought to be an important outcome metric in and of itself. Prior studies have demonstrated that discharge disposition is correlated with functional status in patients with stroke.¹⁸

Covariables

Information regarding median household income, primary payer, age, sex, and race is included in the NIS data base. Age was

approached as a continuous variable rather than using discrete age groups. The sex variable included male and female. The race variable provided by the NIS combines both race and ethnicity into 1 variable and includes white, black, Hispanic, Asian or Pacific Islander, Native American, or Other. Median household income was broken down into 4 categories based on national percentiles: Quartile 1 included patients whose income fell within the 0 to 25th percentiles. Quartile 2 included patients whose income fell within the 26th to 50th percentiles. Quartile 3 included patients whose income fell within the 51st to 75th percentiles. Last, quartile 4 included patients whose income fell within 76th to 100th percentiles. The NIS estimates this information on the basis of the participant's ZIP code. Primary payer information was broken down into those patients with Medicare, Medicaid, private insurance, self-pay, no charge, or other. The "Other" payment category includes Workers' Compensation, Civilian Health and Medical Program of the Uniformed Services, Civilian Health and Medical Program of the Department of Veterans Affairs, Title V, and other governmental programs. We additionally included hospital size (small, medium, large) as provided by the NIS. Last, we used ICD-9 and ICD-10 diagnosis codes to include covariates related to outcome such as tracheostomy and gastrostomy. Administration of IV rtPA was determined using ICD-9 procedural code 99.10 and ICD-10 procedural code 3E03317. The Elixhauser Comorbidity Index (ECI), a validated list of comorbidities that predict patient outcomes using ICD-9 and ICD-10 data,¹⁹ was compiled. The aggregate number of Elixhauser comorbidities for each patient was used as a surrogate for their comorbidity burden. ICD-9 codes were used for 2006 up through the third discharge quarter of 2015. ICD-10 codes were used for the fourth discharge quarter of 2015 through 2016.

Statistical Analysis

Descriptive analyses were performed by comparing the number and percentage of each variable in the group that underwent EVT with the corresponding patients who did not undergo EVT. These were presented as the total number and percentage. Univariate comparisons between these groups were performed using a χ^2 test for categorical variables and the 1-sample *t* test for continuous variables. Trend analyses were performed by determining numbers and percentages of each variable for every year in the sample. Univariate logistic regression was used to determine whether the trend was statistically significant.

Four survey-weighted multivariate logistic regression analyses were performed. Variables were included in the multivariable analysis if they emerged as statistically significant in the univariate comparisons, were not missing significant amounts of data, were of clinical interest, and were biologically/clinically feasible. The dependent variable for the first analysis was EVT use; this analysis was performed to determine which variables were independently predictive of EVT use. This analysis included the year as a continuous variable; adjusting for this allowed us to determine whether the longitudinal trends in use were significant when stratifying by individual race/ethnicity. The dependent variable for the second 2 analyses was patients having a good outcome and poor outcome after EVT, respectively. Finally, a

Demographic information stratified by EVT status

	No EVT (n = 1,309,972) No. (%)	EVT (n = 12,190) No. (%)	P Value ^a	Total (n = 1,322,162) No. (%)
Age (mean) (IQR) (yr)	72.0 (61.0–82.0)	69.0 (57.0–79.0)	<.001	72.0 (61.0–82.0)
Sex				
Female	684,329 (52.2)	6117 (50.2)	<.001	690,168 (52.2)
Race				
White	919,600 (70.2)	8596 (64.0)	<.001	928,158 (70.2)
Black	214,704 (16.4)	1564 (12.8)	<.001	216,173 (16.4)
Hispanic	98,903 (7.6)	1008 (8.3)	<.001	99,823 (7.6)
Asian	34,845 (2.7)	447 (3.7)	<.001	35,277 (2.4)
Native American	6812 (0.5)	3 (0.3)	<.001	7880 (0.6)
Other	34,825 (2.7)	448 (3.7)	<.001	35,277 (2.7)
Insurance				
Medicare	866,939 (66.2)	7037 (57.8)	<.001	873,973 (66.1)
Medicaid	102,309 (7.8)	953 (7.8)	<.001	103,420 (7.8)
Private	249,550 (19.1)	3204 (26.3)	<.001	252,829 (19.1)
Self-pay	56,290 (4.3)	519 (4.3)	.91	56,784 (4.3)
Other payer	29,736 (2.3)	280 (2.3)	.91	30,080 (2.3)
Household income				
Quartile 1	397,577 (30.4)	3233 (26.52)	<.001	400,747 (30.3)
Quartile 2	344,654 (26.3)	2938 (24.1)	<.001	347,596 (26.3)
Quartile 3	307,712 (23.5)	3088 (25.3)	<.001	310,840 (23.5)
Quartile 4	260,160 (19.9)	2930 (24.0)	<.001	263,110 (19.9)
Intravenous tPA	57,639 (4.4)	4809 (39.5)	<.001	62,935 (4.8)
Elixhauser sum	3.0 (2.0–5.0)	4.0 (3.0–6.0)	<.001	3.0 (2.0–5.0)

Note:—IQR indicates interquartile range.

^a P values reflect univariate comparison between the 2 groups represented in the columns.

multivariable logistic regression analysis was performed with the outcome of in-hospital mortality.

RESULTS

Patient Demographics

In our sample of 1,322,162 patients who had AIS between 2006 and 2016, the average age of our population was 72 years. Fifty-two percent of the patients were women; most (62%) of the patients were white, with the primary payer as Medicare (66%) (Table). There was a fairly equal distribution of income levels among our patient population, with all 4 income groups containing between approximately 19% and 30% of our patient population each. The median ECI sum for our entire patient population was 3. The average age of White patients (72.45 years) was higher than that of black (64.29 years) and Hispanic (66.02 years) patients (Online Supplemental Data). Additionally, women, on average, were older (72.68 years) than men (67.91 years).

Comorbidities

When we stratified for race (Online Supplemental Data), white patients had a lower percentage of cardiovascular risk factors such as diabetes and hypertension (diabetes, 29.73%; hypertension, 74.57%) compared with black (diabetes, 42.50%; hypertension, 82.91%) and Hispanic (diabetes, 46.24%; hypertension, 77.73%) patients. Black patients had the highest proportion of smokers (20.27%) compared with the other races. Additionally, white patients had the highest rate of cardiac arrhythmias (35.41%) compared with black (22.83%) and Hispanic (25.79%) patients.

When we stratified on the basis of income (Online Supplemental Data), the percentage of patients with diabetes and hypertension and those who were smokers was inversely

proportional to the increasing income quartiles. The percentage of patients with cardiac arrhythmias was directly proportional to the increasing income quartiles.

Income and Insurance Disparities

When we stratified by race (Online Supplemental Data), a greater proportion of black and Hispanic patients were in the lowest quartile (52.70% and 40.01%, respectively) compared with white patients (25.03%). The proportion of black and Hispanic patients was inversely proportional to increasing income quartile, with the lowest percentage of patients occupying the highest income quartile (10.39% and 13.89%, respectively). In white patients, there was no such trend in the distribution of income quartiles. A total of 22.58% of white patients were in the highest income quartile.

When we stratified by insurance, 41.80% of patients with Medicare were white, while 31.29% of patients were black and 16.35% were Hispanic. In patients with private insurance, 68.83% of patients were white, while 17.31% were black and 7.19% were Hispanic, suggesting that white patients were more likely to have private insurance than black or Hispanic patients.

When we stratified by sex, women were more likely to have Medicare (71.38%) than men (60.34%), whereas men were more likely to have private insurance (22.43%) than women (16.10%).

Trends in EVT Use

There was a notable increase in EVT use between 2006 and 2016, with 0.05% of all patients with AIS undergoing EVT in 2006, increasing linearly to 2.08% in 2016. (Fig 1). Similar trends were observed when stratifying for sex (Fig 1A) because both men and women had nearly identical rates of increase. When stratifying by race (Fig 1B), the rate of increase in EVT use in White patients

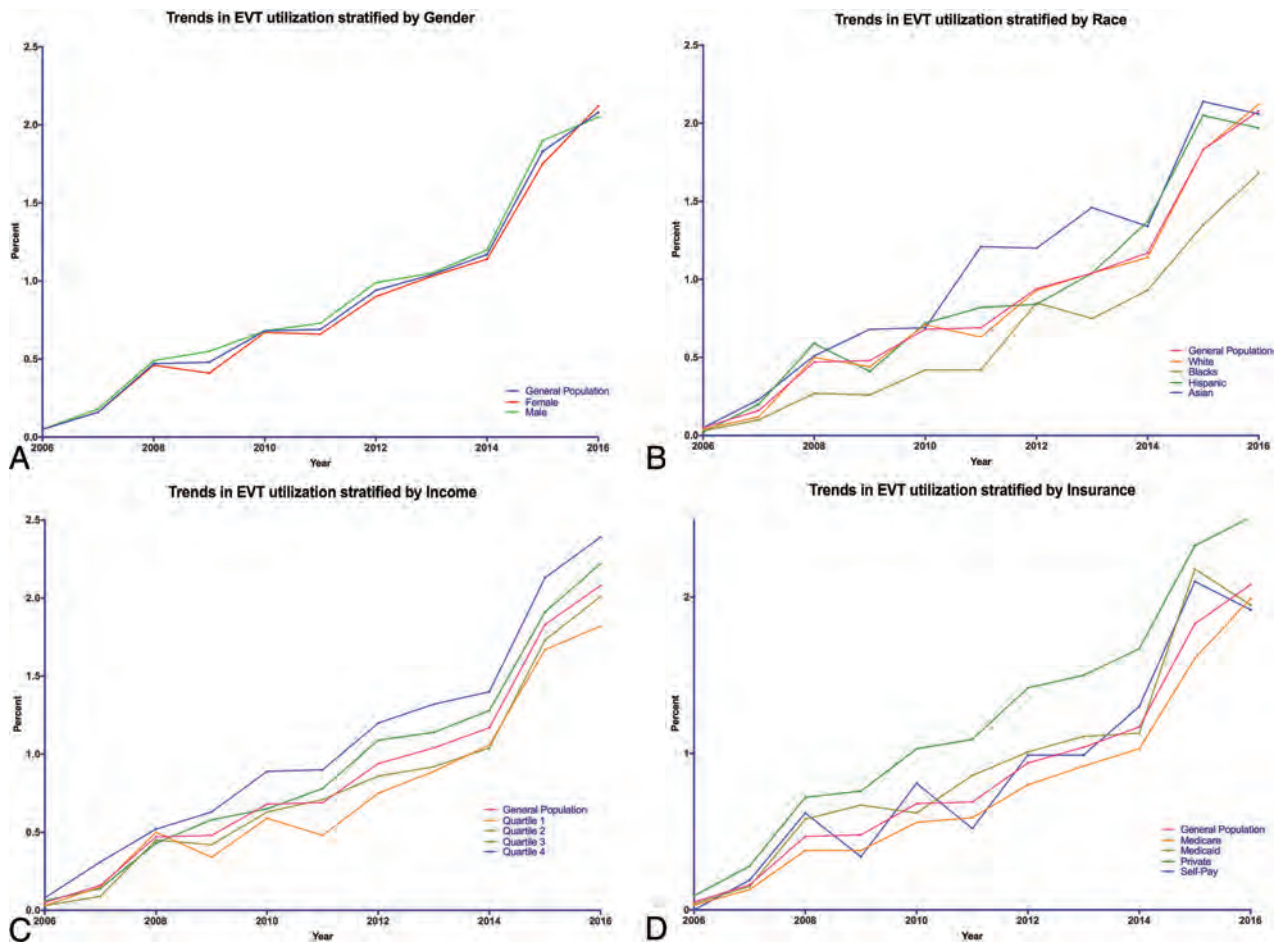


FIG 1. Trend graphs demonstrating the use of EVT in patients stratified by sex, race, insurance, and income. Higher income and private insurance demonstrate a greater increase in the rates of use of EVT than lower income groups and other types of insurance including Medicare and Medicaid. Black race has a lower increase in the rate of use of EVT than the general population as well as other races.

nearly mirrored that of the general population, increasing from 0.04% in 2006 to 2.12% in 2016, while the rate of increase in black patients was notably lower (0.03% in 2006 to 1.68% in 2016). When we stratified by income (Fig 1C), those patients in the highest income quartile had a rate of increase that was markedly higher than that of the general population, increasing from 0.08% in 2006 to 2.39% in 2016, while the use of EVT in those patients in the lowest income quartile had a rate of increase that was notably lower (0.03% in 2006 to 1.49% in 2016). Last, we stratified trends in EVT use on the basis of primary payer (Fig 1D), and a markedly increased rate in the use of EVT in patients with private insurance was observed compared with that of the general population, from 0.09% in 2006 to 2.51% in 2016. The lowest increase was observed in the Medicaid group, which increased from 0.03% in 2006 to 1.95% in 2016.

Predictors of EVT Use

We performed multivariable logistic regression (Fig 2), adjusted for race, income, primary payer, demographic variables, and other potential confounders, including age, ECI sum, congestive heart failure, diabetes mellitus, hypertension, hyperlipidemia, smoking, cardiac arrhythmias, left ventricular thrombus, valvular disease, IV rtPA, and hospital size. In this model, black race was

found to be an independent predictor of less frequent use of EVT (OR = 0.79; 95% CI, 0.72–0.86). Increasing income trended toward predicting EVT use, with the highest income quartile independently predicting EVT use (OR = 1.24; 95% CI, 1.13–1.36). Private insurance additionally independently predicted EVT use (OR 1.30; 95% CI, 1.23–1.38). As might be expected, cardiac arrhythmias and left ventricular thrombus were independent predictors of EVT use (OR = 1.85; 95% CI, 1.76–1.94; OR = 1.88; 95% CI, 1.52–2.32, respectively). Additionally, increasing hospital size independently predicted EVT use, with the large hospital size demonstrating the greatest effect (OR = 4.33; 95% CI, 3.42–5.52). All reported findings are statistically significant, with *P* value < .01, accounting for the large sample size used.

Predictors of Outcome

Multivariable logistic regression of good outcome (Fig 3), poor outcome, and in-hospital mortality was performed. Models were adjusted for race, income, primary payer, demographic variables, and other potential confounders, including age, ECI sum, congestive heart failure, diabetes mellitus, hypertension, hyperlipidemia, smoking, cardiac arrhythmias, left ventricular thrombus, valvular disease, IV rtPA, and hospital size. Predictors of good outcome included increasing income, with the median household income

Multivariable Analysis of EVT Utilization

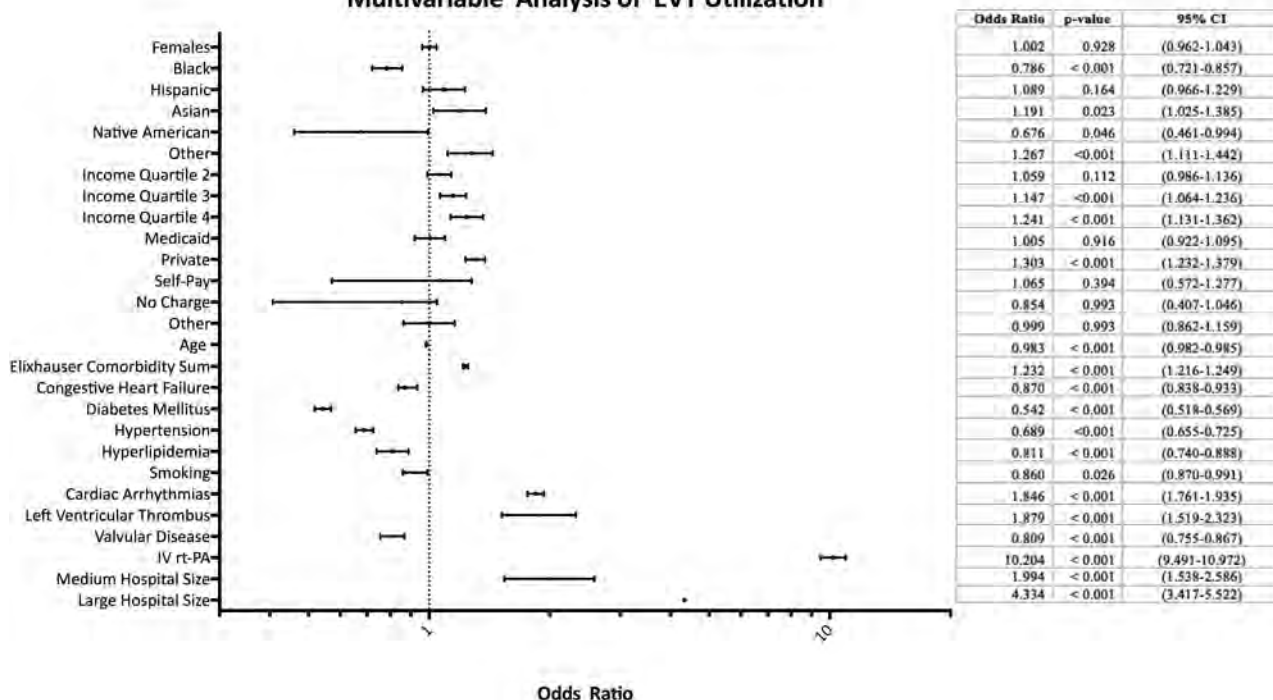


FIG 2. Multivariable regression analysis of predictors of EVT. Notably, black race has a statistically significantly lower odds ratio of EVT use. Private insurance is associated with higher odds of EVT use. Sequentially higher odds ratios of EVT are observed with each level of increasing income. Small-vessel disease risk factors such as hyperlipidemia, diabetes, and smoking are associated with decreased EVT use. Cardioembolic risk factors such as cardiac arrhythmias and left ventricular thrombus are associated with higher rates of EVT use. Increasing hospital size is also associated with increased use of EVT. For analysis of race/ethnicity, the reference category is white race. For income quartiles, the reference variable is income quartile 1. For hospital size, the reference category is small hospital size. For insurance type, the reference category is Medicare.

quartile 4 most strongly predicting good outcome (OR = 1.101; 95% CI, 1.06–1.14). Private insurance additionally independently predicted good outcome (OR = 1.36; 95% CI, 1.31–1.39).

Black race was an independent predictor of poor outcome (OR = 1.328; 95% CI, 1.298–1.358). Increasing age (OR = 1.039; 95% CI, 1.038–1.039) and increasing ECI sum (OR = 1.438; 95% CI, 1.431–1.445) additionally were independent predictors of poor outcome. Additionally, female sex appeared to be predictive of worse outcome following EVT (OR = 1.214; 95% CI, 1.203–1.225).

Hispanic ethnicity predicted in-hospital mortality with small-but-detectable odds (OR = 1.055; 95% CI, 1.021–1.090). Paradoxically, while congestive heart failure predicted in-hospital mortality (OR = 1.289; 95% CI, 1.265–1.314), diabetes mellitus (OR = 0.619; 95% CI, 0.607–0.630), hypertension (OR = 0.374; 95% CI, 0.368–0.381), and hyperlipidemia (OR = 0.511; 95% CI, 0.493–0.530) were associated with lower odds of in-hospital mortality. Similar findings were seen in the multivariable regression model for poor outcome because diabetes, hypertension, hyperlipidemia, and smoking appeared to decrease the odds of poor outcome. All reported findings are statistically significant, with P value < .01, accounting for the large sample size used.

DISCUSSION

Our study demonstrates that there may have been persistent racial and socioeconomic disparities in use of EVT in the past decade despite an overall increase of EVT in the general

population. In our large population of >1 million patients with acute ischemic stroke, we found that black and low-income patients were less likely to receive EVT compared with white patients with higher income and private insurance. These findings are consistent with prior studies. Esenwa et al¹⁵ also demonstrated, in a study of the NIS, that black patients were less likely to receive EVT compared with patients of other races. Rinaldo et al¹⁴ also demonstrated, in a large data base, that patients with commercial insurance were more likely to receive EVT and were more likely to be white rather than black or Hispanic. Multiple theories for this disparity have been postulated. One theory is that the underlying mechanism of stroke in blacks and Hispanic individuals, as well as patients in lower income populations, is more frequently from small-vessel atherosclerosis, whereas the mechanism in white and higher income patients is often cardioembolic.^{20–22} Our study does, in fact, demonstrate a greater prevalence of cardiovascular risk factors such as diabetes, hypertension, and smoking in the black, Hispanic, and low-income patients. Additionally, while the specific code for atrial fibrillation was not used, cardiac arrhythmias were present in a much higher percentage of white and higher income patients in our study than in black, Hispanic, and lower income patients. Prior studies have demonstrated that black patients are less likely to receive IV rtPA as well,¹⁰ and this disparity has been thought to be from delays in hospital arrival (distance, transportation challenges) as well delays in symptom recognition in lower income and minority

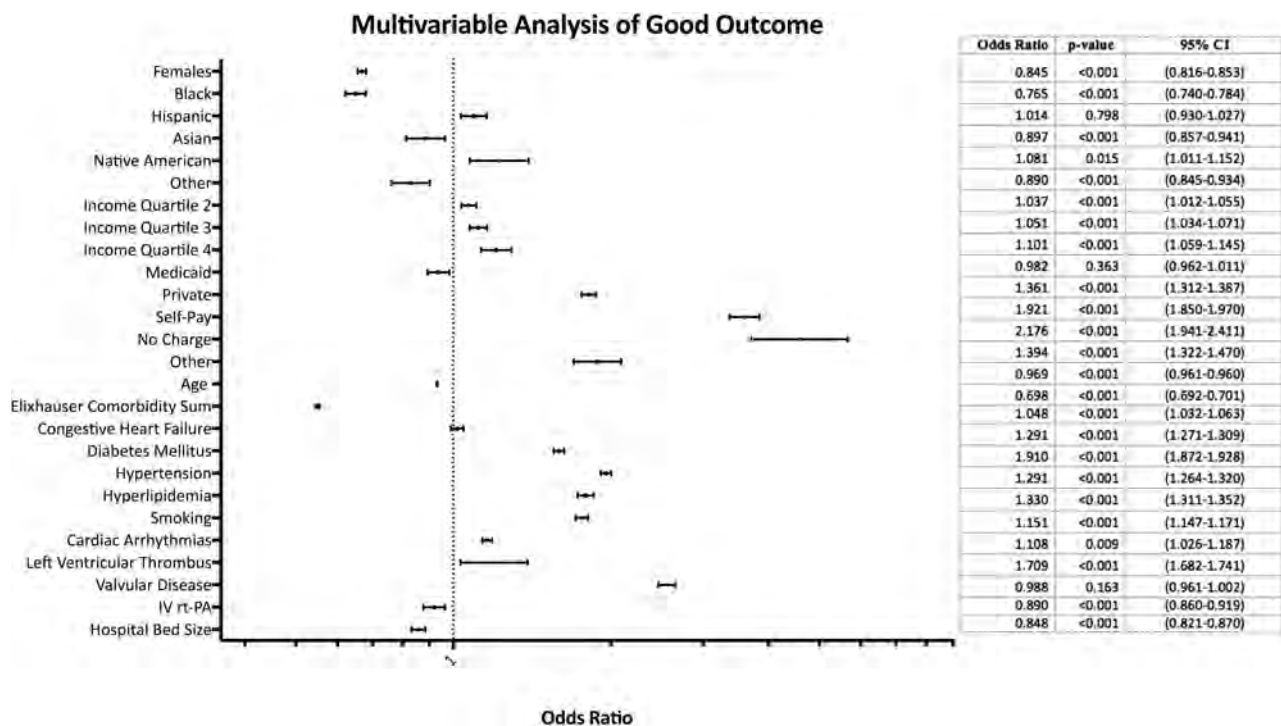


FIG 3. Multivariable regression analysis of predictors of good outcome following EVT. Female sex is associated with decreased odds of good outcome, as was black race. Increasing income quartile is associated with increased odds of good outcome. Private insurance is associated with decreased odds of good outcome. An increasing Elixhauser Comorbidity sum is associated with decreased odds of good outcome. For analysis of race/ethnicity, the reference category is white race. For income quartiles, the reference variable is income quartile 1. For hospital size, the reference category is small hospital size. For insurance type, the reference category is Medicare.

populations.²³ There is additional literature that demonstrates that black patients receive inferior hospital care, including delays in receiving treatment in the emergency department and longer door-to-CT scan times.^{11,12} Other studies suggest that other contributors include caregiver racial biases, patient mistrust, educational and cultural barriers, and the relatively small number of minority physicians,²⁴ as well as deeply rooted legacies of social and financial disenfranchisement.²⁵ Socioeconomic and racial disparity has been long recognized in stroke care. Our current 11-year analysis re-emphasizes the presence of disparity in stroke care and demonstrates that despite the widespread nationwide spike in the use of EVT as a standard of care in patients with stroke with large-vessel occlusions, the wide socioeconomic and racial disparity in provision of this service remains grossly unchanged.

Additionally, our analysis demonstrates that patients with private insurance may be more likely to have a good outcome following EVT for AIS, while black patients may be less likely to have a good outcome and are more likely to have a poor outcome. Black and Hispanic patients had approximately double the percentage of tracheostomies as well as a higher percentage of gastrostomies compared with white patients. Prior studies have also demonstrated worse poststroke outcomes in minority patients,²⁶⁻²⁸ however, there is a paucity of data regarding racial disparities in stroke outcomes following thrombectomy. Black patients in our population were slightly less likely to experience in-hospital mortality according to our multivariable analysis.

This finding is consistent with similar findings from prior studies of the NIS.¹⁵ One possible reason offered in this observation is that black patients with stroke are, on average, younger than white patients. This was the case in our study because black patients were, on average, 8 years younger than white patients. The finding that black patients with AIS are younger than white patients additionally is validated in numerous studies that demonstrate that black patients have a higher stroke burden earlier in their lives than white patients and the general population.¹⁰ It is our hope that the data presented in this study will serve as further impetus to increase resources directed toward disparity research, with the hope of ultimately understanding the causes of these disparities and developing actionable interventions to achieve equity. Specifically, defining these disparities, in addition to awareness, is an important initial step in addressing and improving the current environment.

While the rate in EVT use appeared to be similar in women and men, female sex was predictive of poor outcome following EVT. This finding is consistent with findings in prior studies demonstrating worse outcomes in women with AIS following treatment with IV rtPA and EVT.²⁹⁻³¹ The reason for worse outcome after stroke in women compared with men is not fully understood; however, higher prestroke disability, a higher admission NIHSS score, and even smaller intracranial artery diameters have been previously postulated as possible causes for this discrepancy.^{31,32}

This study has many limitations. First, the NIS does not provide many important specifics about EVT that would be relevant to outcome such as the NIHSS score, ASPECTS, last known well, TICI score following thrombectomy, or baseline functional status. Additionally, the NIS does not provide information on whether the patient had a large-vessel occlusion, which would be relevant in the discussion of EVT use. Similarly, there is no information provided in the NIS on time metrics to EVT such as the time of symptom onset to recanalization, which may directly affect the clinical outcome. Also, as with all administrative datasets, the NIS may be prone to coding errors. Finally, the NIS does not offer any readmission data; therefore, we were unable to assess long-term outcome for these patients.

CONCLUSIONS

Our nationally representative study demonstrates that despite widespread increase in use of EVT in patients with stroke, notable socioeconomic and racial disparities still exist in access to this immensely effective and life-changing treatment technique. Further studies are warranted to address this ongoing shortcoming in providing stroke treatment.

Disclosures: Johanna T. Fifi—UNRELATED: Consultancy: Stryker, Penumbra, Cerenovus; Grants/Grants Pending: Stryker, Penumbra, Viz.ai; Stock/Stock Options: Imperative Care. Christopher P. Kellner—UNRELATED: Grants/Grants Pending: Cerebrotech, Minnetronix, Siemens, Penumbra, Viz.ai, Integra LifeSciences Corporation.* J. Mocco—UNRELATED: Consultancy: Cerebrotech, Viseon, EndoStream Medical, Vastrax, RIST Neurovascular, Synchron, Viz.ai, Perflow Medical, and CVAid; Stock/Stock Options: investor in Cerebrotech, Imperative Care, EndoStream Medical, Viseon, blinktbi, Myra Medical, Serenity, Vastrax, NTL, RIST, Viz.ai, Synchron, Radical, and Truvis Medical; Other: Principal Investigator on research trials funded by Stryker Neurovascular, MicroVention, and Penumbra. Shahram Majidi—UNRELATED: Employment: The Mount Sinai Hospital. *Money paid to the institution.

REFERENCES

- Benjamin EJ, Muntner P, Alonso A, et al. American Heart Association Council on Epidemiology and Prevention Statistics Committee and Stroke Statistics Subcommittee. **Heart Disease and Stroke Statistics-2019 Update: a report from the American Heart Association.** *Circulation* 2019;139:e56–528 CrossRef Medline
- Powers WJ, Rabinstein AA, Ackerson T, et al. **Guidelines for the Early Management of Patients With Acute Ischemic Stroke: 2019 Update to the 2018 Guidelines for the Early Management of Acute Ischemic Stroke: A Guideline for Healthcare Professionals From the American Heart Association/American Stroke Association.** *Stroke* 2019;50:e344–18 CrossRef Medline
- Saver JL, Goyal M, Bonafe A, et al. **Stent-retriever thrombectomy after intravenous t-PA vs. t-PA alone in stroke.** *N Engl J Med* 2015;372:2285–95 CrossRef Medline
- Jovin TG, Chamorro A, Cobo E, et al. REVASCAT Trial Investigators. **Thrombectomy within 8 hours after symptom onset in ischemic stroke.** *N Engl J Med* 2015;372:2296–2306 CrossRef Medline
- Bracard S, Ducrocq X, Mas JL, et al. THRACE Investigators. **Mechanical thrombectomy after intravenous alteplase versus alteplase alone after stroke (THRACE): a randomised controlled trial.** *Lancet Neurol* 2016;15:1138–47 CrossRef Medline
- Goyal M, Menon BK, van Zwam WH, et al. **Endovascular thrombectomy after large-vessel ischaemic stroke: a meta-analysis of individual patient data from five randomised trials.** *Lancet* 2016;387:1723–31 CrossRef Medline
- Sacco RL, Boden-Albala B, Gan R, et al. **Stroke incidence among white, black, and Hispanic residents of an urban community: the Northern Manhattan Stroke Study.** *Am J Epidemiol* 1998;147:259–68 CrossRef Medline
- Stansbury JP, Jia H, Williams LS, et al. **Ethnic disparities in stroke: epidemiology, acute care, and postacute outcomes.** *Stroke* 2005;36:374–86 CrossRef Medline
- Morgenstern LB, Smith MA, Lisabeth LD, et al. **Excess stroke in Mexican Americans compared with non-Hispanic Whites: the Brain Attack Surveillance in Corpus Christi Project.** *Am J Epidemiol* 2004;160:376–83 CrossRef Medline
- Schwamm LH, Reeves MJ, Pan W, et al. **Race/ethnicity, quality of care, and outcomes in ischemic stroke.** *Circulation* 2010;121:1492–1501 CrossRef Medline
- Karve SJ, Balkrishnan R, Mohammad YM, et al. **Racial/ethnic disparities in emergency department waiting time for stroke patients in the United States.** *J Stroke Cerebrovasc Dis* 2011;20:30–40 CrossRef Medline
- Jacobs BS, Birbeck G, Mullard AJ, et al. **Quality of hospital care in African American and white patients with ischemic stroke and TIA.** *Neurology* 2006;66:809–14 CrossRef Medline
- Reeves MJ, Fonarow GC, Zhao X, et al. Get With The Guidelines-Stroke Steering Committee & Investigators. **Quality of care in women with ischemic stroke in the GWTG program.** *Stroke* 2009;40:1127–33 CrossRef Medline
- Rinaldo L, Rabinstein AA, Cloft H, et al. **Racial and ethnic disparities in the use of thrombectomy for acute stroke.** *Stroke* 2019;50:2428–32 CrossRef Medline
- Esenwa C, Lekoubou A, Bishu KG, et al. **Racial differences in mechanical thrombectomy use for ischemic stroke in the United States.** *Ethn Dis* 2020;30:91–96 CrossRef Medline
- Stein LK, Tuhim S, Jette N, et al. **Nationwide analysis of endovascular thrombectomy provider specialization for acute stroke.** *Stroke* 2020;51:3651–57 CrossRef Medline
- de Havenon A, Yaghi S, Mistry EA, et al. **Endovascular thrombectomy in acute ischemic stroke patients with COVID-19: prevalence, demographics, and outcomes.** *J Neurointerv Surg* 2020;12:1045–48 CrossRef Medline
- Kramer AM, Steiner JF, Schlenker RE, et al. **Outcomes and costs after hip fracture and stroke: a comparison of rehabilitation settings.** *JAMA* 1997;277:396–404 CrossRef Medline
- Li B, Evans D, Faris P, et al. **Risk adjustment performance of Charlson and Elixhauser comorbidities in ICD-9 and ICD-10 administrative databases.** *BMC Health Serv Res* 2008;8:12 CrossRef Medline
- Willey JZ, Williams O. **Letter by Willey and Williams regarding article, “Racial and Ethnic Disparities in the Utilization of Thrombectomy for Acute Stroke: Analysis of Data From 2016 to 2018.”** *Stroke* 2019;50:e339 CrossRef Medline
- White H, Boden-Albala B, Wang C, et al. **Ischemic stroke subtype incidence among whites, blacks, and Hispanics: the Northern Manhattan Study.** *Circulation* 2005;111:1327–31 CrossRef Medline
- Gutierrez J, Williams OA. **A decade of racial and ethnic stroke disparities in the United States.** *Neurology* 2014;82:1080–82 CrossRef Medline
- Tong D, Reeves MJ, Hernandez AF, et al. **Times from symptom onset to hospital arrival in the Get with the Guidelines-Stroke Program 2002 to 2009: temporal trends and implications.** *Stroke* 2012;43:1912–17 CrossRef Medline
- Johnston SC, Fung LH, Gillum LA, et al. **Utilization of intravenous tissue-type plasminogen activator for ischemic stroke at academic medical centers: the influence of ethnicity.** *Stroke* 2001;32:1061–68 CrossRef Medline
- Esenwa C, Ilunga Tshiswaka D, Gebregziabher M, et al. **Historical slavery and modern-day stroke mortality in the United States Stroke Belt.** *Stroke* 2018;49:465–69 CrossRef Medline
- Boehme AK, Siegler JE, Mullen MT, et al. **Racial and gender differences in stroke severity, outcomes, and treatment in patients with**

- acute ischemic stroke.** *J Stroke Cerebrovasc Dis* 2014;23:e255–61 CrossRef Medline
27. Burke JF, Freedman VA, Lisabeth LD, et al. **Racial differences in disability after stroke: results from a nationwide study.** *Neurology* 2014;83:390–97 CrossRef Medline
28. Kuhlemeier KV, Stiens SA. **Racial disparities in severity of cerebrovascular events.** *Stroke* 1994;25:2126–31 CrossRef Medline
29. Persky RW, Turtzo LC, McCullough LD. **Stroke in women: disparities and outcomes.** *Curr Cardiol Rep* 2010;12:6–13 CrossRef Medline
30. Petrea RE, Beiser AS, Seshadri S, et al. **Gender differences in stroke incidence and poststroke disability in the Framingham Heart Study.** *Stroke* 2009;40:1032–37 CrossRef Medline
31. Silva GS, Lima FO, Camargo EC, et al. **Gender differences in outcomes after ischemic stroke: role of ischemic lesion volume and intracranial large-artery occlusion.** *Cerebrovasc Dis* 2010;30:470–75 CrossRef Medline
32. Davison MA, Ouyang B, Keppetipola KM, et al. **Arterial diameter and the gender disparity in stroke thrombectomy outcomes.** *J Neurointerv Surg* 2018;10:949–52 CrossRef Medline

Evaluation of Ultrafast Wave–Controlled Aliasing in Parallel Imaging 3D-FLAIR in the Visualization and Volumetric Estimation of Cerebral White Matter Lesions

C. Ngamsombat, A.L.M. Gonçalves Filho, M.G.F. Longo, S.F. Cauley, K. Setsompop, J.E. Kirsch, Q. Tian, Q. Fan, D. Polak, W. Liu, W.-C. Lo, R. Gilberto González, P.W. Schaefer, O. Rapalino, J. Conklin, and S.Y. Huang



ABSTRACT

BACKGROUND AND PURPOSE: Our aim was to evaluate an ultrafast 3D-FLAIR sequence using Wave–controlled aliasing in parallel imaging encoding (Wave-FLAIR) compared with standard 3D-FLAIR in the visualization and volumetric estimation of cerebral white matter lesions in a clinical setting.

MATERIALS AND METHODS: Forty-two consecutive patients underwent 3T brain MR imaging, including standard 3D-FLAIR (acceleration factor = 2, scan time = 7 minutes 50 seconds) and resolution-matched ultrafast Wave-FLAIR sequences (acceleration factor = 6, scan time = 2 minutes 45 seconds for the 20-channel coil; acceleration factor = 9, scan time = 1 minute 50 seconds for the 32-channel coil) as part of clinical evaluation for demyelinating disease. Automated segmentation of cerebral white matter lesions was performed using the Lesion Segmentation Tool in SPM. Student *t* tests, intraclass correlation coefficients, relative lesion volume difference, and Dice similarity coefficients were used to compare volumetric measurements among sequences. Two blinded neuroradiologists evaluated the visualization of white matter lesions, artifacts, and overall diagnostic quality using a predefined 5-point scale.

RESULTS: Standard and Wave-FLAIR sequences showed excellent agreement of lesion volumes with an intraclass correlation coefficient of 0.99 and mean Dice similarity coefficient of 0.97 (SD, 0.05) (range, 0.84–0.99). Wave-FLAIR was noninferior to standard FLAIR for visualization of lesions and motion. The diagnostic quality for Wave-FLAIR was slightly greater than for standard FLAIR for infratentorial lesions ($P < .001$), and there were fewer pulsation artifacts on Wave-FLAIR compared with standard FLAIR ($P < .001$).

CONCLUSIONS: Ultrafast Wave-FLAIR provides superior visualization of infratentorial lesions while preserving overall diagnostic quality and yields white matter lesion volumes comparable with those estimated using standard FLAIR. The availability of ultrafast Wave-FLAIR may facilitate the greater use of 3D-FLAIR sequences in the evaluation of patients with suspected demyelinating disease.

ABBREVIATIONS: CAIPI = controlled aliasing in parallel imaging; DSC = Dice similarity coefficient; ICC = intraclass correlation coefficient; LVD = lesion volume difference; MS = multiple sclerosis; R = acceleration factor; TA = scan time

White matter lesions secondary to demyelination in multiple sclerosis (MS) and related disorders typically present with high T2 signal and are best evaluated with FLAIR imaging, the standard sequence for cerebral white matter lesion detection. FLAIR

is a T2-weighted sequence with nulling of the CSF signal, which increases the contrast between lesions and CSF/cerebral sulci and ventricles and improves white matter lesion detection and analysis.¹

Quantification of cerebral white matter lesion volume has become increasingly feasible for routine clinical evaluation and use in clinical trials of MS therapies due to the availability of automated segmentation tools and 3D fast spin-echo FLAIR sequences, which delineate cerebral white matter lesions at high isotropic resolution. The Lesion Segmentation Tool (LST; <https://www.applied-statistics.com>).

Please address correspondence to Susie Y. Huang, MD, PhD, Division of Neuroradiology, Department of Radiology, Massachusetts General Hospital, 55 Fruit St, GRB-273A, Boston, MA, 02114; e-mail: susie.huang@mgh.harvard.edu

Indicates open access to non-subscribers at www.ajnr.org

Indicates article with online supplemental data.

<http://dx.doi.org/10.3174/ajnr.A7191>

Received January 6, 2021; accepted after revision March 29.

From the Department of Radiology (C.N., A.L.M.G.F., M.G.F.L., S.F.C., K.S., J.E.K., Q.T., Q.F., R.G.G., P.W.S., O.R., J.C., S.Y.H.) and Athinoula A. Martinos Center for Biomedical Imaging (C.N., A.L.M.G.F., M.G.F.L., S.F.C., K.S., J.E.K., Q.T., Q.F., D.P., J.C., S.Y.H.), Massachusetts General Hospital, Boston, Massachusetts; Department of Radiology (C.N.), Faculty of Medicine, Siriraj Hospital, Mahidol University, Thailand; Harvard Medical School (A.L.M.G.F., M.G.F.L., S.F.C., K.S., J.E.K., Q.T., Q.F., R.G.G., P.W.S., O.R., J.C., S.Y.H.), Boston, Massachusetts; Harvard-MIT Division of Health Sciences and Technology (K.S., S.Y.H.), Massachusetts Institute of Technology, Cambridge, Massachusetts; Department of Physics and Astronomy (D.P.), Heidelberg University, Heidelberg, Germany; Siemens Healthcare GmbH (D.P., W.-C.L.), Erlangen, Germany; and Siemens Shenzhen Magnetic Resonance Ltd (W.L.), Shenzhen, China.

This work was supported by the National Institutes of Health, grant Nos: P41-EB030006, K23-NS096056, R01-NS118187; Siemens (research support); and Massachusetts General Hospital Claflin Distinguished Scholar Award.

de/1st.html), a promising tool for automated segmentation of T2-hyperintense lesions on FLAIR images, was developed for the quantification of MS lesion volumes and has been shown to have good agreement with manual segmentation by expert reviewers.²⁻⁷ However, the high-resolution 3D-FLAIR images required as input for this tool have long acquisition times, limiting the widespread use of automated lesion segmentation in clinical practice.

Wave-controlled aliasing in parallel imaging (CAIPI) is a recently developed fast acquisition technology that synergistically combines and extends 2 controlled aliasing approaches, 2D-CAIPI and bunch phase encoding,⁸ to achieve controlled aliasing in all 3 spatial directions (x, y, z). By taking full advantage of the 3D coil sensitivity information, Wave-CAIPI offers high acceleration factors with negligible artifacts and g-factor penalty.^{9,10} 3D-FLAIR acquired with Wave-CAIPI cuts the scan time down by more than half, possibly facilitating the broader clinical application of 3D-FLAIR in the evaluation of white matter diseases such as MS.

The goal of this study was to evaluate an ultrafast Wave-CAIPI 3D-FLAIR sequence (Wave-FLAIR)^{11,12} acquired in less than half the time of standard 3D-FLAIR for quantitative and qualitative analyses of cerebral white matter lesions.

MATERIALS AND METHODS

Subjects and Study Design

This study was approved by the institutional review board of Partners Healthcare and was Health Insurance Portability and Accountability Act-compliant. A prospective comparative study was performed at a single institution from April 2019 to March 2020. Forty-two consecutive patients undergoing brain MR imaging as part of routine clinical work-up and/or surveillance for MS and other white matter diseases were enrolled.

Data Acquisition

MR imaging was performed on 1 of 2 clinical 3T MR imaging scanners (Magnetom Prisma; Siemens) using 20- or 32-channel multichannel receiver coils, depending on the fit and comfort of the patient. Each scan included a standard 3D sampling perfection with application optimized contrasts using different flip angle evolutions (SPACE sequence; Siemens) FLAIR sequence (acceleration factor [R] = 2, scan time [TA] = 7 minutes 15 seconds), and resolution-matched ultrafast 3D Wave SPACE-FLAIR (R = 6, TA = 7 minutes 45 seconds for the 20-channel coil and R = 9, TA = 1 minute 50 seconds for the 32-channel coil) sequences. The order of the Wave and standard FLAIR sequences was reversed half-way through the study period to minimize any potential bias due to the order of acquisition. Detailed acquisition parameters for the standard and Wave SPACE-FLAIR sequences are shown in the Table.

White Matter Lesion Analysis

Quantitative Analysis. Cerebral white matter lesions were segmented using the lesion prediction algorithm implemented in the LST toolbox, Version 2.0.15 in SPM (<http://www.fil.ion.ucl.ac.uk/spm/software/spm12>).² Lesion probability maps generated by the lesion prediction algorithm from the standard and Wave-FLAIR sequences were compared using the longitudinal pipeline in LST.

Acquisition parameters for standard and wave SPACE FLAIR sequences

Parameters	Standard	Wave SPACE FLAIR
FOV read (mm)	256 × 256	256 × 256
FOV phase (%)	100	100
Matrix size	256 × 256	256 × 256
Section thickness (mm)	1	1
TR/TE/TI (ms)	5000/390/1800	5000/392/1800
Acceleration factor		
20-channel	2	6
32-channel	2	9
Bandwidth (Hz/pixel)	750	650
Scan time (sec)		
20-channel	7 minutes 15 seconds	2 minutes 45 seconds
32-channel	7 minutes 15 seconds	1 minute 50 seconds

Binarized lesion maps were created on the basis of the lesion probability maps derived from standard and Wave-FLAIR sequences using default threshold values set by the LST for all subjects. Lesions in each brain region, including periventricular, juxtacortical, infratentorial, deep white matter and subcortical white matter and deep gray matter regions, were identified and labeled by a neuroradiologist blinded to sequence type and order using the Island Tools Editor in 3D Slicer, Version 4.10.2 (<https://www.slicer.org/>) for further analyses. Lesion volume and number were compared in each brain region between the standard and Wave-FLAIR images.

Qualitative Analysis. Two neuroradiologists (J.C. and A.L.M.G.F., with 8 years of experience each), blinded to sequence type, performed a head-to-head comparison of the images. A predefined 5-point scale was used for grading white matter lesions in the locations specified in the McDonald criteria (ie, periventricular, juxtacortical, and infratentorial locations)¹³ and other locations, including subcortical white matter, deep white matter, and deep gray matter. Other variables that were evaluated included motion, pulsation artifacts, noise, and overall diagnostic quality (Online Supplemental Data). All images were evaluated in a randomized and blinded fashion. A third reader adjudicated the discrepancies (S.Y.H., with 10 years of experience).

Statistical Analysis. All statistical calculations were performed in Matlab software, Version 9.4 (MathWorks) and R statistical and computing software, Version 3.4.3 (<http://www.r-project.org/>). The Student *t* test was used to assess a statistically significant difference in lesion volumes and lesion numbers between the standard and Wave sequences. The correlations between standard and Wave-FLAIR lesion volumes and lesion numbers were assessed using Pearson correlation coefficients. The 2-way random intraclass correlation coefficient (ICC) was calculated to assess absolute agreement and consistency between standard and Wave-FLAIR lesion volumes¹⁴ as a measure of volumetric precision, with a higher ICC signifying higher intermeasurement agreement.^{5,7,14,15} Relative lesion volume difference (LVD)¹⁶ was also used to compare standard and Wave-FLAIR lesion volumes, defined as LVD = (Total Lesion Volume on Wave - Total Lesion Volume on Standard) / Total Lesion Volume on Standard. LVD

was used as a simple measure of the difference in volumes between standard- and Wave-FLAIR-segmented lesions as a fraction of the segmented lesion volume on standard FLAIR serving as the reference. To assess the overlap between segmented lesion voxels that might not be captured by LVD, we calculated the Dice similarity coefficient (DSC) as another indicator of the segmentation algorithm overlap between the 2 sequences.^{3,5,7} DSC is used in the literature to estimate regional spatial overlap, rather than just the agreement in volumetric values.¹⁷ The DSC provides information on the size and structure of an analyzed region; consequently, it is a more robust way to evaluate the similarity between 2 images. The Dice similarity coefficient of the standard and Wave images was expressed as $\text{Dice}(\text{Standard}, \text{Wave}) = 2 \times |\text{Intersection}(\text{Standard}, \text{Wave})| / (|\text{Standard}| + |\text{Wave}|)$. DSC measures have values between 0 and 1, with higher values indicating better agreement.¹⁷

In the head-to-head qualitative analysis of the standard-versus-Wave-FLAIR images, we tested for noninferiority of Wave compared with standard FLAIR¹⁸ using a noninferiority margin (Δ) of 15% as previously established.¹⁹ The null hypothesis (H_0) was that the proportion of cases in which standard FLAIR was preferred over Wave-FLAIR was $>15\%$. We used the z statistic to calculate the probability of the standard FLAIR being preferred over the Wave-FLAIR sequence in $>15\%$ of cases ($H_0 > \Delta$), with a type I error rate (α) of .05. The required sample size was estimated as described²⁰ for a single proportion (the proportion of subjects in which visualization of lesions was preferred on standard over Wave-FLAIR). For a type I error rate (α) of .05, a power ($1-\beta$) of 0.90, and noninferiority margin of 15%, a minimum of 24 cases was required.

For all statistical analyses, corrections for multiple comparison were conducted on the basis of the false discovery rate adjustment, with a false discovery rate threshold of 0.05. The raw uncorrected P values surviving false discovery rate correction are reported here.

RESULTS

Forty-two adults participated in the comparative evaluation of the standard and Wave-FLAIR sequences. Demographic information on the study subjects, including age, sex, and clinical indication for undergoing MR imaging is shown in the Online Supplemental Data. A total of 38 patients of 42 (90.5%) had white matter lesions. Thirty-six patients (85.7%) were scanned with the 20-channel coil. Twenty-two patients were scanned with standard before Wave-FLAIR, while 20 were scanned with Wave before standard FLAIR.

In this section, we first present the quantitative comparison of lesion volumes followed by the qualitative evaluation of image quality. Standard and Wave-FLAIR images were evaluated in each brain region using predefined evaluation metrics described in the Materials and Methods section.

Six patients were excluded from the LST quantitative analysis because they had no detectable lesions or severe motion artifacts resulting in failure of the automated LST processing stream. On the whole-brain level, the standard and Wave-FLAIR sequences showed no significant difference in lesion volume (167,800 versus 168,130 mm³, $P = .99$) or lesion number (520 versus 529, $P = .91$)

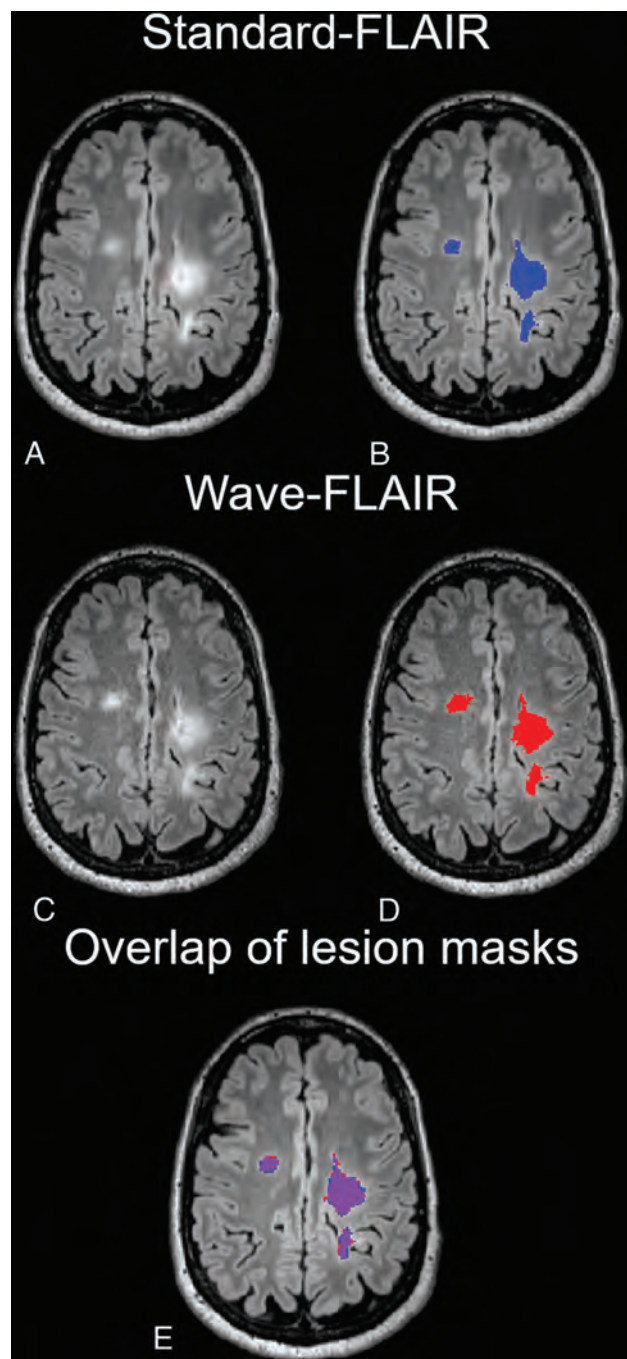


FIG 1. Comparison of standard and Wave-FLAIR images and lesion masks. A, Standard FLAIR image with the lesion mask overlaid (B, blue). Wave-FLAIR image (C) with the lesion mask (D) overlaid (red). E, Lesion masks from standard and Wave-FLAIR images overlaid on the same image (purple indicates overlap of the lesion masks).

as segmented by LST. The ICC between standard and Wave-FLAIR was 0.99. The relative LVD was 0.01 (SD, 0.05) (range, -0.012 – 0.02), and the DSC was 0.97 (SD, 0.05) (range, 0.84–0.99) (Online Supplemental Data). For lesions in each brain region (Figs 1 and 2), there was excellent correlation between standard and Wave-FLAIR images for lesion volume and lesion number (Online Supplemental Data), with no significant difference in lesion volumes ($P > .98$) (Online Supplemental Data) or

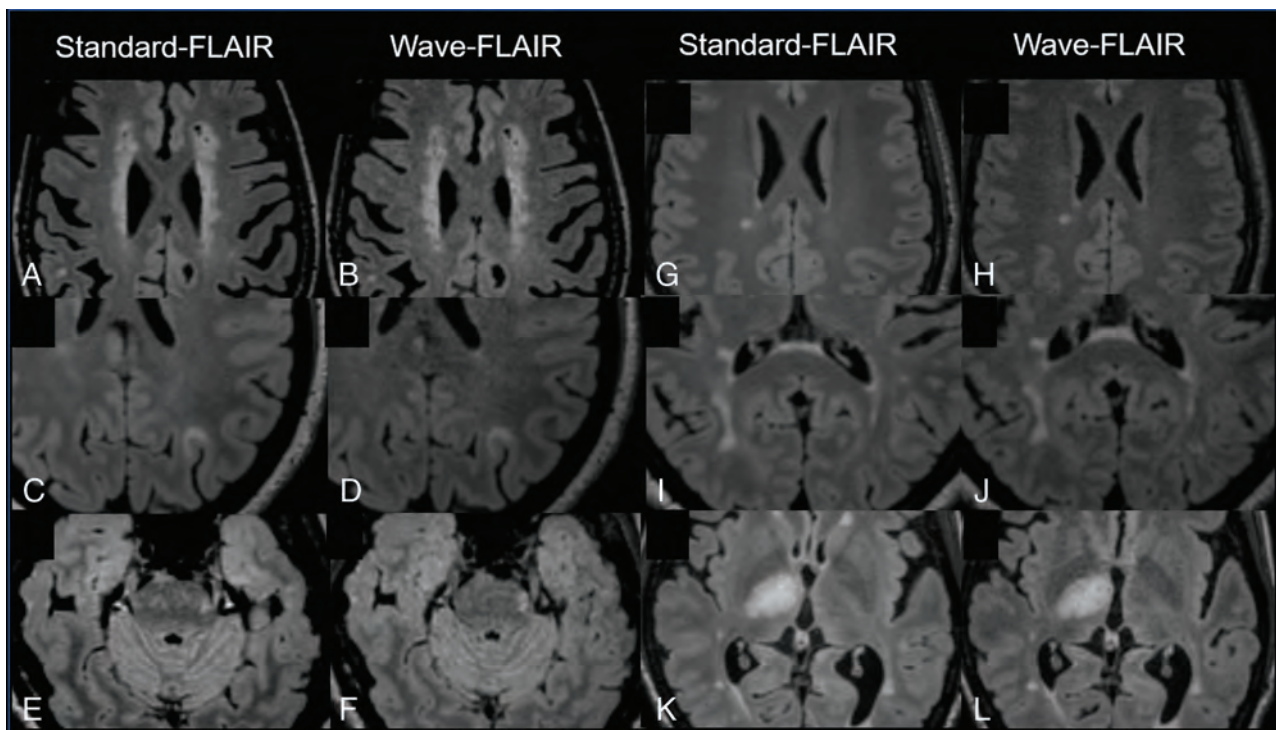


FIG 2. Comparison of MS lesions in different brain regions on standard and Wave-FLAIR images. The standard images (A, C, E, G, I, K) are on the left, and the Wave-FLAIR images (B, D, F, H, J, L) are on the right of each image pair. Lesion locations include the periventricular (A and B), juxtacortical (C and D), infratentorial (E and F), and deep white matter (G and H) and subcortical white matter (I and J) and deep gray matter (K and L).

lesion numbers ($P > .89$) (Online Supplemental Data) as segmented by LST for each sequence. The LVDs were very low for all brain regions ($< 2\%$), and the Dice coefficient was > 0.9 between the 2 sequences for all brain regions, including the periventricular, deep, and subcortical white matter and deep gray matter, with the exception of the infratentorial white matter (DSC = 0.84) (Online Supplemental Data).

Wave-FLAIR was equivalent to standard FLAIR for the visualization of lesions in the subcortical and deep white matter and deep gray matter ($P < .001$) and was noninferior to standard FLAIR in the visualization of periventricular ($P < .001$), juxtacortical ($P < .006$), and infratentorial lesions ($P < .001$) (Fig 3). There was a slightly greater preference for Wave-FLAIR in the visualization of infratentorial lesions compared with the standard FLAIR sequence.

Wave-FLAIR was noninferior to standard FLAIR in terms of motion ($P < .001$), with a slightly higher proportion of cases favoring Wave-FLAIR (7%) compared with standard FLAIR (5%) (Fig 3). Wave-FLAIR demonstrated fewer pulsation artifacts ($P < .001$) in areas such as the brain stem (Fig 2E). Wave-FLAIR demonstrated more noise overall but was ultimately noninferior in overall diagnostic quality compared with standard FLAIR ($P < .001$) (Fig 3).

DISCUSSION

In this work, we performed a systematic quantitative evaluation of cerebral white matter lesion volumes and a qualitative evaluation of lesion conspicuity, artifacts, and overall diagnostic quality of an ultrafast Wave-SPACE FLAIR sequence, which was > 2.5

times faster than the standard 3D SPACE FLAIR sequence. The results showed excellent agreement and spatial overlap between Wave- and standard FLAIR white matter lesion volumes estimated by the automated segmentation tool LST. Experienced neuroradiologists rated the accelerated Wave-FLAIR images as providing equivalent visualization of lesions in the supratentorial and infratentorial white matter compared with the standard FLAIR images, with preserved diagnostic quality. The findings support the broader application of ultrafast Wave FLAIR sequences in the evaluation of patients with white matter diseases.

White matter lesion quantification has become an increasingly important tool for characterizing the burden of disease in MS in both routine clinical evaluation and clinical trials.⁴ Manual white matter lesion segmentation is time-consuming and has the risk of rater bias. In addition, high image quality is needed for the best quantification. Automated lesion segmentation tools that require no or minimal training data are publicly available, including the LST,³ LesionTOADS (<https://github.com/sergivalverde/lesion-toads>),^{16,21} SALEM Lesion Segmentation,²² and Automated Statistical Interference for Segmentation.²³ We chose to use LST with the lesion probability algorithm (LST-lesion prediction algorithm)² because it has high accuracy in automatically segmenting MS lesions compared with manual segmentation⁷ and requires only FLAIR images as input.^{2,7} Here, we found comparable volumes and numbers of white matter lesions as segmented by LST on ultrafast Wave-FLAIR images compared with standard FLAIR, despite the slightly greater image noise observed in the Wave-FLAIR images. These findings were supported by the high ICC (0.99) and, overall, a very small LVD in all brain regions ($< 2\%$)

Head-to-Head Analysis, Standard vs. Wave-FLAIR

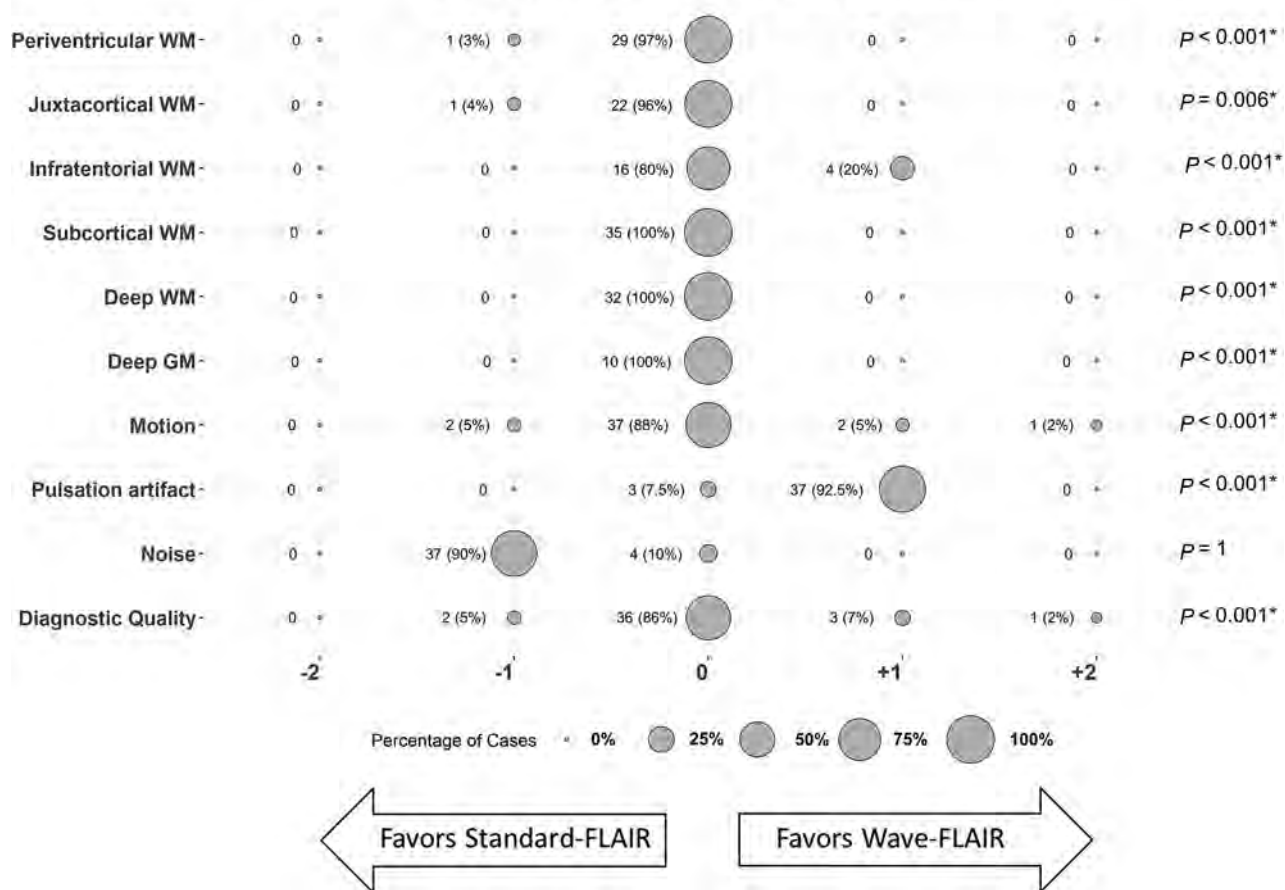


FIG 3. Balloon plot showing the head-to-head comparison of standard-versus-Wave-FLAIR images. The size of each balloon represents the relative percentage of cases with a given score; P values for noninferiority testing are specified at the end of each row. The number of cases (percentage) are also noted adjacent to each balloon. The asterisk denotes significance following correction for multiple comparisons (false discovery rate threshold of 0.05).

between the 2 sequences. The DSC was >0.9 in all supratentorial regions and slightly lower for the infratentorial region (DSC = 0.84). The lesser degree of agreement between the 2 sequences for infratentorial lesions likely reflects the known difficulty in detecting infratentorial lesions on FLAIR contrast images, which are, overall, less sensitive for posterior fossa lesions,^{24,25} resulting in a greater difference in voxels identified as part of lesions between the 2 sequences. If validated in larger studies, the overall excellent agreement in lesion quantification between Wave- and standard FLAIR suggests that Wave-FLAIR could potentially replace standard FLAIR for white matter lesion quantification in clinical and research studies using imaging in MS.

In addition to volumetric measures, we also included visual evaluation of the images by multiple neuroradiologists to assess the diagnostic performance of the Wave-FLAIR sequence, which is an important part of the patient's clinical evaluation. Wave-FLAIR provided visualization of lesions in all locations, comparable with the standard sequence. The slightly greater image noise noted in the head-to-head comparison of the accelerated Wave-FLAIR images compared with the standard FLAIR images (Fig 3)

did not compromise the overall diagnostic quality, as illustrated in Fig 1 (see Fig 1A, -C for representative standard-versus-Wave images). Furthermore, the Wave-FLAIR images showed reduced pulsatile flow artifacts in the posterior fossa, which contributed to improved visualization of infratentorial lesions, as illustrated in Fig 2E, -F. The standard FLAIR image (Fig 2) had more pulsation artifacts in the brainstem, which could lead to potential misinterpretation of a small T2-hyperintense lesion in the left lateral aspect of the pons as an artifact. This lesion clearly appeared as a distinct lesion in the Wave-FLAIR image (Fig 2F) without conspicuous artifacts in this area. The improved visualization of T2/FLAIR hyperintense lesions in the brainstem and cerebellum indicates that Wave-FLAIR may be useful in the evaluation of not only white matter disease burden but also other conditions such as stroke and tumors.

The decreased scan time of Wave-FLAIR offers synergistic benefits for the comprehensive evaluation of white matter lesions in multiple sclerosis. Highly accelerated imaging with Wave-CAIPI has been shown to reduce motion artifacts and improve the visualization of small lesions.¹⁹ In the current study, Wave-FLAIR was noninferior to standard FLAIR for motion artifacts.

One explanation for the less pronounced improvement in motion artifacts on Wave-FLAIR is that most patients (85.7%) were scanned with the 20-channel coil, for which Wave-FLAIR was still 2:45 minutes in duration. We expect that motion artifacts would be further reduced if more patients were scanned using the 32-channel coil (1:50-minute acquisition). The time-savings incurred by Wave-FLAIR may become more obvious when aggregated with other optimized fast 2D and 3D sequences.^{12,19,26,27} For example, at our institution, we have implemented the Wave-FLAIR sequence along with optimized simultaneous multislice diffusion-weighted imaging, Wave T2 SPACE, Wave-SWI, and pre- and postcontrast Wave-T1 MPRAGE sequences in the clinical MS brain MR imaging protocol, bringing the total scan time for this protocol <20 minutes. The ability to acquire multiple 3D sequences with complementary contrasts efficiently, such as Wave-FLAIR and Wave-SWI, may encourage the greater adoption of promising imaging signs such as the central vein sign and paramagnetic rim sign,²⁸⁻³⁰ which have greater specificity for demyelinating lesions in MS and, in the case of the paramagnetic rim sign, may have prognostic value in identifying lesions with chronic active inflammation associated with greater disability.³¹ We envision that the systematic incorporation of highly accelerated 3D-Wave-CAIPI sequences into clinical MR imaging protocols will provide more information per unit of time and enable the more comprehensive evaluation of a wide range of neurologic disorders, thereby advancing clinical care and clinical research along multiple fronts.

Our study had some limitations. To reduce observer bias in the qualitative evaluation, the raters were blinded to the pulse sequence, but inevitably some imaging features could help to identify the sequence and introduce observer bias. In addition, image quality also depends on the order of acquisition for each pulse sequence. In general, images acquired later in the examination would be expected to have more motion. We sought to mitigate against this bias by randomizing the acquisition order of the sequences during the study. Finally, LST underestimated total lesion numbers in patients with a high lesion load, which decreased the agreement between Wave- and standard FLAIR in certain cases, such as the assessment of confluent lesions in the periventricular area.

CONCLUSIONS

Quantitative white matter lesion volumes and qualitative evaluation of white matter lesions imaged with an ultrafast, <3-minute, Wave-FLAIR sequence showed excellent agreement, with standard FLAIR images requiring more than double the scan time in patients undergoing clinical evaluation for demyelinating disease. The findings are derived from MR imaging examinations that were performed as part of a routine clinical work-up and/or surveillance for MS and reflect the performance of these sequences in a realistic clinical setting. The availability of ultrafast 3D sequences such as Wave-FLAIR may facilitate the more comprehensive evaluation of white matter lesions in MS and other white matter diseases.

Disclosures: Augusto Lio Goncalves Filho—UNRELATED: Employment: Massachusetts General Hospital. Stephen F. Cauley—RELATED: Grant: Siemens, Comments: Siemens research grant*; UNRELATED: Grants/Grants Pending: Siemens, Comments: Siemens research grant.* Kawin Setsompop—RELATED: Grant: National Institutes of Health, Comments: R01EB020613. John E. Kirsch—UNRELATED: Grants/Grants Pending: National Institutes of Health grant. Qiyuan Tian—UNRELATED: Employment: Massachusetts General Hospital, Harvard Medical School. Daniel Polak—UNRELATED: Employment: Siemens. Wei Liu—UNRELATED: Employment: Siemens. Wei-Ching Lo—UNRELATED: Employment: Siemens. Otto Rapalino—UNRELATED: Travel/Accommodations/Meeting Expenses Unrelated to Activities Listed: GE Healthcare. John Conklin—UNRELATED: Grants/Grants Pending: Radiological Society of North America, Comments: Radiological Society of North America Research Seed Grant.* Susie Y. Huang—RELATED: Grant: Siemens, Comments: grant to support fast neuroimaging research.* *Money paid to the institution.

REFERENCES

- Filippi M, Yousry T, Baratti C, et al. **Quantitative assessment of MRI lesion load in multiple sclerosis. a comparison of conventional spin-echo with fast fluid-attenuated inversion recovery.** *Brain* 1996;119(Pt 4):1349–55 CrossRef Medline
- Schmidt P. **Bayesian inference for structured additive regression models for large-scale problems with applications to medical imaging.** *LMU München*; 2017. <https://edoc.ub.uni-muenchen.de/20373/>. Accessed July 22, 2020
- Schmidt P, Gaser C, Arsic M, et al. **An automated tool for detection of FLAIR-hyperintense white-matter lesions in multiple sclerosis.** *Neuroimage* 2012;59:3774–83 CrossRef Medline
- Schmidt P, Pongratz V, Kuster P, et al. **Automated segmentation of changes in FLAIR-hyperintense white matter lesions in multiple sclerosis on serial magnetic resonance imaging.** *Neuroimage Clin* 2019;23:101849 CrossRef Medline
- Weeda MM, Brouwer I, de Vos ML, et al. **Comparing lesion segmentation methods in multiple sclerosis: Input from one manually delineated subject is sufficient for accurate lesion segmentation.** *Neuroimage Clin* 2019;24:102074 CrossRef Medline
- Valverde S, Oliver A, Roura E, et al. **Quantifying brain tissue volume in multiple sclerosis with automated lesion segmentation and filling.** *Neuroimage Clin* 2015;9:640–47 CrossRef Medline
- Egger C, Opfer R, Wang C, et al. **MRI FLAIR lesion segmentation in multiple sclerosis: does automated segmentation hold up with manual annotation?** *Neuroimage Clin* 2017;13:264–70 CrossRef Medline
- Moriguchi H, Duerk JL. **Bunched phase encoding (BPE): a new fast data acquisition method in MRI.** *Magn Reson Med* 2006;55:633–48 CrossRef Medline
- Cauley SF, Setsompop K, Bilgic B, et al. **Autocalibrated wave-CAIPI reconstruction; Joint optimization of k-space trajectory and parallel imaging reconstruction.** *Magn Reson Med* 2017;78:1093–99 CrossRef Medline
- Bilgic B, Gagoski BA, Cauley SF, et al. **Wave-CAIPI for highly accelerated 3D imaging.** *Magn Reson Med* 2015;73:2152–62 CrossRef Medline
- Polak D, Setsompop K, Cauley SF, et al. **Wave-CAIPI for highly accelerated MP-RAGE imaging.** *Magn Reson Med* 2018;79:401–06 CrossRef Medline
- Polak D, Cauley S, Huang SY, et al. **Highly-accelerated volumetric brain examination using optimized wave-CAIPI encoding.** *J Magn Reson Imaging* 2019;50:961–74 CrossRef Medline
- Filippi M, Preziosa P, Banwell BL, et al. **Assessment of lesions on magnetic resonance imaging in multiple sclerosis: practical guidelines.** *Brain* 2019;142:1858–75 CrossRef Medline
- Reuter M, Schmansky NJ, Rosas HD, et al. **Within-subject template estimation for unbiased longitudinal image analysis.** *Neuroimage* 2012;61:1402–18 CrossRef Medline

15. Jain S, Sima DM, Ribbens A, et al. **Automatic segmentation and volumetry of multiple sclerosis brain lesions from MR images.** *Neuroimage Clin* 2015;8:367–75 CrossRef Medline
16. Le M, Tang LY, Hernandez-Torres E, et al. **FLAIR(2) improves LesionTOADS automatic segmentation of multiple sclerosis lesions in non-homogenized, multi-center, 2D clinical magnetic resonance images.** *Neuroimage Clin* 2019;23:101918 CrossRef Medline
17. Dice LR. **Measures of the amount of ecological association between species.** *Ecology* 1945;26:297–302
18. Ahn S, Park SH, Lee KH. **How to demonstrate similarity by using noninferiority and equivalence statistical testing in radiology research.** *Radiology* 2013;267:328–38 CrossRef Medline
19. Conklin J, Longo MG, Cauley SF, et al. **Validation of highly accelerated wave-CAIPI SWI compared with conventional SWI and T2*-weighted gradient recalled-echo for routine clinical brain MRI at 3T.** *AJNR Am J Neuroradiol* 2019;40:2073–80 CrossRef Medline
20. Chow SS, Shao J, Wang H. *Sample Size Calculation in Clinical Research.* Marcel Dekker; 2003
21. Shiee N, Bazin PL, Ozturk A, et al. **A topology-preserving approach to the segmentation of brain images with multiple sclerosis lesions.** *Neuroimage* 2010;49:1524–35 CrossRef Medline
22. Roura E, Oliver A, Cabezas M, et al. **A toolbox for multiple sclerosis lesion segmentation.** *Neuroradiology* 2015;57:1031–43 CrossRef Medline
23. Sweeney EM, Shinohara RT, Shiee N, et al. **OASIS is Automated Statistical Inference for Segmentation, with applications to multiple sclerosis lesion segmentation in MRI.** *Neuroimage Clin* 2013;2:402–13 CrossRef Medline
24. Lecler A, El Sanharawi I, El Methni J, et al. **Improving detection of multiple sclerosis lesions in the posterior fossa using an optimized 3D-FLAIR sequence at 3T.** *AJNR Am J Neuroradiol* 2019;40:1170–76 CrossRef Medline
25. Wang KY, Uribe TA, Lincoln CM. **Comparing lesion detection of infratentorial multiple sclerosis lesions between T2-weighted spin-echo, 2D-FLAIR, and 3D-FLAIR sequences.** *Clin imaging* 2018;51:229–34 CrossRef Medline
26. Prakkamakul S, Witzel T, Huang S, et al. **Ultrafast brain MRI: clinical deployment and comparison to conventional brain MRI at 3T.** *J Neuroimaging* 2016;26:503–10 CrossRef Medline
27. Longo MG, Conklin J, Cauley SF, et al. **Evaluation of ultrafast wave-CAIPI MPRAGE for visual grading and automated measurement of brain tissue volume.** *AJNR Am J Neuroradiol* 2020;41:1388–96 CrossRef Medline
28. Sati P, Oh J, Constable RT, et al. NAIMS Cooperative. **The central vein sign and its clinical evaluation for the diagnosis of multiple sclerosis: a consensus statement from the North American Imaging in Multiple Sclerosis Cooperative.** *Nat Rev Neurol* 2016;12:714–22 CrossRef Medline
29. Absinta M, Sati P, Fechner A, et al. **Identification of chronic active multiple sclerosis lesions on 3T MRI.** *AJNR Am J Neuroradiol* 2018;39:1233–38 CrossRef Medline
30. Clarke MA, Pareto D, Pessini-Ferreira L, et al. **Value of 3T susceptibility-weighted imaging in the diagnosis of multiple sclerosis.** *AJNR Am J Neuroradiol* 2020;41:1001–08 CrossRef Medline
31. Absinta M, Sati P, Masuzzo F, et al. **Association of chronic active multiple sclerosis lesions with disability in vivo.** *JAMA Neurol* 2019;76:1474–83 CrossRef Medline

A Volumetric Metric for Monitoring Intracranial Aneurysms: Repeatability and Growth Criteria in a Longitudinal MR Imaging Study

X. Liu, H. Haraldsson, Y. Wang, E. Kao, M. Ballweber, A.J. Martin, C.E. McCulloch, F. Faraji, and D. Saloner, for the UCSF Intracranial Aneurysm Monitoring Group



ABSTRACT

BACKGROUND AND PURPOSE: The reliability of contrast-enhanced MRA in monitoring serial volumetric changes of unruptured intracranial aneurysms has not been established. We aimed to determine the coefficient of variance of contrast-enhanced MRA in measuring aneurysm volumes, thus establishing criteria for aneurysm growth and permitting identification of variables predictive of growth.

MATERIALS AND METHODS: Aneurysm volumes were measured from serial contrast-enhanced MRA studies of patients with untreated intracranial aneurysms who underwent >2 sequential MR imaging evaluations. After coregistering all sequential studies in 3D space for each aneurysm and signal intensity normalization, aneurysm volume was determined across all time points. A linear mixed effects model was built to estimate the coefficient of variance of the measurement as well as to determine predictive variables. Growth was defined as relative growth exceeding 2 times the measurement coefficient of variance (sudden growth, as 4 times the coefficient of variance).

RESULTS: A total of 95 patients with 112 aneurysms were included (5.9 scans during 4.0 years on average, 616 scan measurements in total). The coefficient of variance was 5.5% of the aneurysm volume, and the relative growth rate was dependent on the location: anterior cerebral artery, 4.52% per year; vertebral artery, 2.46% per year; middle cerebral artery, 2.74% per year; basilar artery, 2.36% per year; internal carotid artery, 1.14% per year. Thirty-six of 112 (32%) aneurysms were characterized as growing, and 11/36 of them had an episode of sudden growth.

CONCLUSIONS: Volume measurement of unruptured intracranial aneurysms by contrast-enhanced MRA seems a reliable metric for tracking the growth trajectory of aneurysms. Furthermore, the aneurysm growth rate differs among different locations.

ABBREVIATIONS: ACA = anterior cerebral artery; CE-MRA = contrast-enhanced MRA; CV = coefficient of variance; UIA = unruptured intracranial aneurysm

It is estimated that approximately 3%–5% of the population may have unruptured intracranial aneurysms (UIAs).¹ The most acute complication of UIAs is rupture, which has a high rate of mortality and morbidity.² However, only a small percentage of aneurysms ever rupture.³ Small UIAs are often followed with repeat imaging, with the intention to treat the aneurysm after it has demonstrated growth.⁴ Although multiple studies have explored the natural history of UIAs, current clinical evaluation relies heavily on traditional factors such as UIA diameter, diameter growth on serial imaging, hemorrhagic history, and clinical

symptoms.^{5,6} UIA diameter growth is of particular clinical concern because previous studies have shown it to be a key risk factor for intracranial aneurysmal rupture.^{7–9} However, intracranial aneurysms can present with irregular and complicated geometries, and the accurate and reproducible measurement of aneurysmal diameter is challenging.¹⁰ Volume has been proposed as a more sensitive and comprehensive parameter for evaluation of aneurysm size compared with diameter measured on a 2D plane.^{11–13} While various methods have been developed for aneurysm volume calculation,¹⁴ they lack validation and little is currently known about the growth trajectory of UIAs when assessed by volumetric metrics.

The choice of imaging technique for monitoring UIAs requires careful consideration. Although providing excellent and robust

Received December 9, 2020; accepted after revision April 1, 2021.

From the Department of Interventional Neuroradiology (X.L.), Beijing Tiantan Hospital, Capital Medical University, Beijing, China; Departments of Radiology and Biomedical Imaging, and Epidemiology and Biostatistics (X.L., H.H., Y.W., E.K., M.B., A.J.M., C.E.M., F.F., D.S.), University of California San Francisco, San Francisco, California; and Department of Radiology (Y.W.), Sichuan Provincial People's Hospital, University of Electronic Science and Technology of China, Chengdu, China.

Funding was provided by research award NS059944 (D.S.) from the National Institutes of Health.

X. Liu and H. Haraldsson contributed equally to this work.

Please address correspondence to Yuting Wang, PhD, Department of Radiology and Biomedical Imaging, University of California San Francisco, San Francisco, 94121; e-mail: wangyuting_330@163.com

Indicates open access to non-subscribers at www.ajnr.org

<http://dx.doi.org/10.3174/ajnr.A7190>

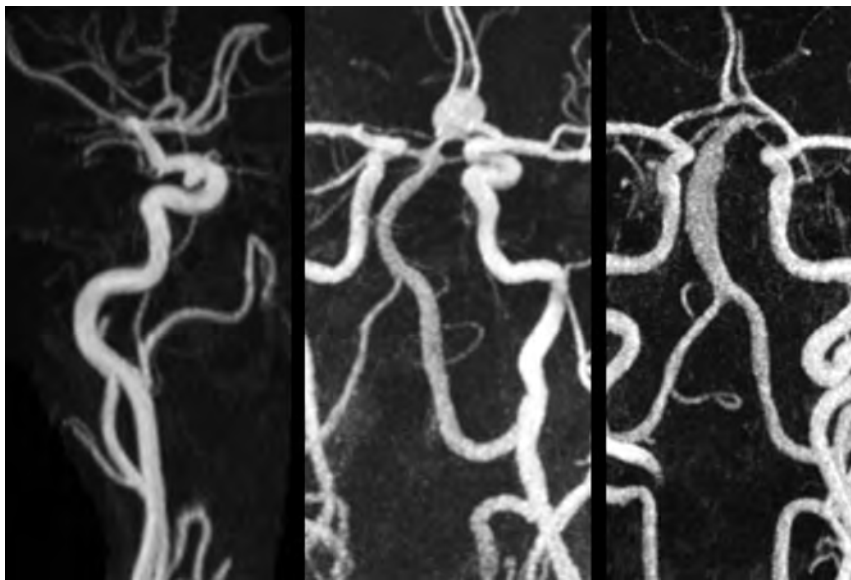


FIG 1. Maximum intensity projections of CE-MRA studies from 3 subjects. A, Subject with a saccular aneurysm of the internal carotid artery. B, Subject with a saccular aneurysm of the anterior communicating artery. C, Subject with a fusiform vertebral artery aneurysm.

results, conventional angiography and CT angiography are unsuited for serial monitoring due to invasiveness and the associated radiation dose, respectively. While contrast-enhanced MRA (CE-MRA) is minimally invasive and provides volumetric data, the reliability of CE-MRA has been verified using DSA.¹⁵ However, the repeatability of this technique has not been established for UIAs.

A reliable and well-characterized metric of change in aneurysm dimensions would help to differentiate important features of the underlying growth trajectory. For example, most previous studies have assumed a linear and continuous aneurysm growth pattern and used only the baseline and final time points to calculate the growth rate.^{3,7,16} This feature obscures cases in which aneurysms exhibit periods of intermittent rapid growth following a period of relative stability. Sudden aneurysmal growth could implicate a more acute pathologic process such as inflammation that requires more aggressive clinical management, whereas the conventional evaluation would underestimate recent rapid growth, diluting it by the overall growth rate calculation.

This study aimed to establish the coefficient of variance (CV) of volumetric measurement by CE-MRA to establish a criterion for likely aneurysm growth and, further, to identify variables predictive of growth.

MATERIALS AND METHODS

Patient Population

This prospective study was conducted under institutional review board approval of the UCSF Medical Center. All subjects gave written informed consent for study participation. Patients with UIAs were recruited between April 2001 and July 2019 for serial MR imaging monitoring studies. Although initially recruited as part of a National Institutes of Health–funded study, this study was later implemented as part of the clinical routine, and despite

the lengthy enrollment period, informed consent was always obtained for use of the image data. Inclusion criteria were the following: 18–100 years of age; diagnosed with at least 1 UIA that was not scheduled for surgical or endovascular treatment; and having undergone >2 follow-up imaging sessions. Exclusion criteria were the following: metal implants, claustrophobia, or allergy to MR contrast agents. Subjects were asked to return every 6 months for CE-MRA. Patient demographic data and cardiovascular risk factors were recorded. Study end points included operative repair, aneurysm rupture, loss to follow-up, or death.

MRA Surveillance Protocol

In the first years of the study, imaging was performed on a 1.5T scanner (Achieva; Philips, Healthcare) and in later years on a 3T scanner (Skyra; Siemens).

A weight-adjusted single dose of Gd-DTPA, diluted with saline to a 22-mL volume, was injected at 2 mL/s through an intravenous catheter placed in the antecubital vein. The delay between contrast injection and arrival at the aneurysm, T_{delay} , was determined by using a 2-mL bolus and visual inspection of the resulting dynamic series of images collected at 1-second intervals. A CE-MRA was then acquired using a 3D paracoronal slab with data acquisition initiated at a T_{delay} of 3 seconds following the start of a 20-mL injection. Representative images are shown in Fig 1.

At 1.5T, imaging was performed with either a 6-channel head coil or a 16-channel head/neck coil. Imaging included contrast-enhanced angiography (3D spoiled gradient-echo: FOV = $240 \times 180 \times 54$ mm, matrix = $400 \times 286 \times 45$, TR/TE = 5.0/1.8 ms, flip angle = 30° , sensitivity encoding factor = 2, bandwidth = 302 Hz/pixel, scanning time = 34 seconds). Elliptic-centric k -space with time to center was 6 seconds. The resultant resolution was $0.6 \times 0.6 \times 1.2$ mm.

At 3T, imaging was performed with a 20-channel head/neck coil. Imaging included contrast-enhanced angiography (3D spoiled gradient-echo: FOV = $223 \times 181 \times 84$ mm, matrix = $320 \times 260 \times 120$, TR/TE = 3.7/1.4 ms, flip angle = 20° , generalized autocalibrating partially parallel acquisition factor = 3, bandwidth = 505 Hz/pixel, scanning time = 30 seconds). Elliptic-centric k -space with time to center was 6 seconds. The resultant images had an isotropic resolution of $0.7 \times 0.7 \times 0.7$ mm.

Longitudinal Analysis of the Aneurysm Volume

Analysis of the aneurysm volume was performed with 2 thresholding iterations. The threshold for the baseline study was selected using the same windowing techniques as in clinical practice to maximize luminal volume while excluding extraluminal

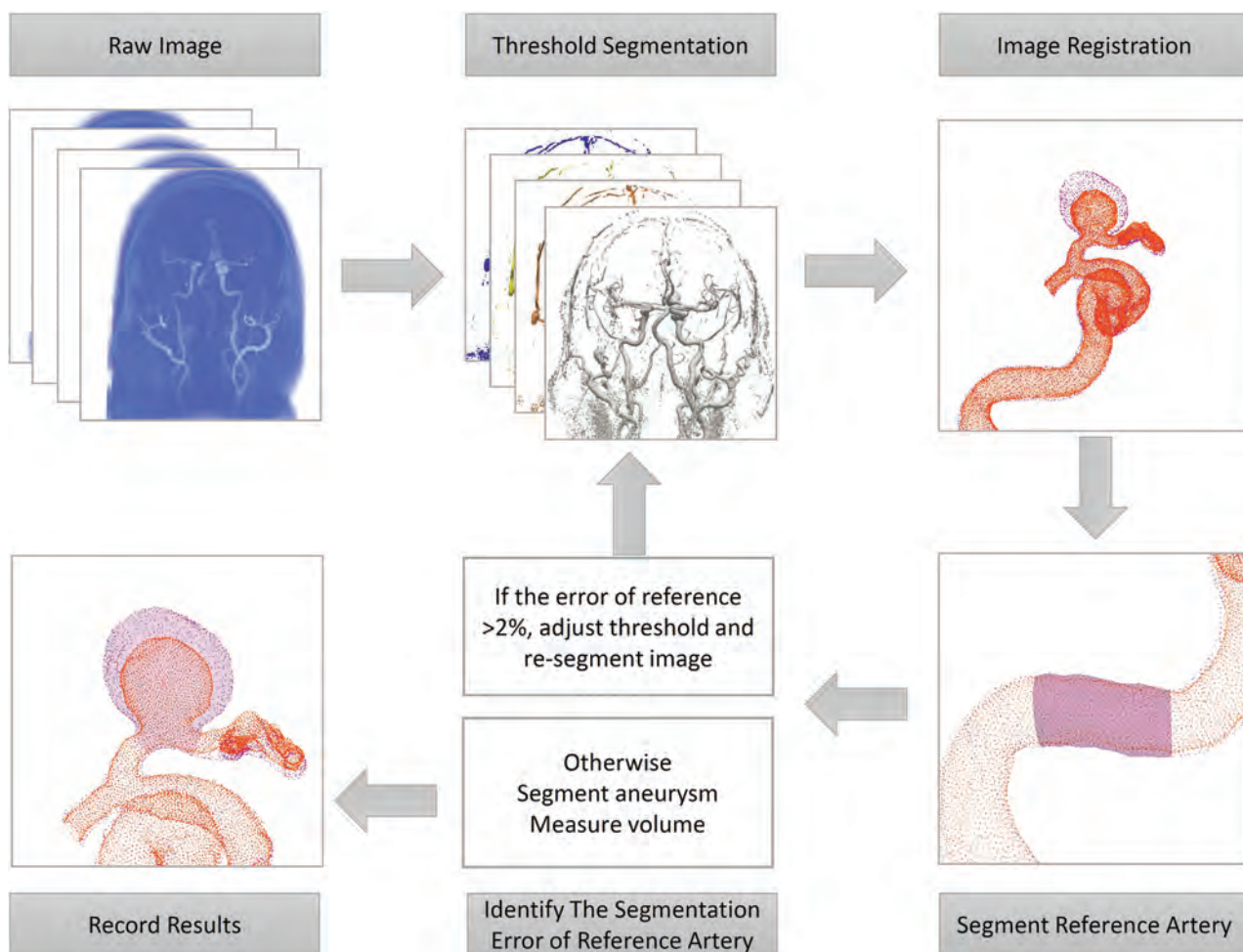


FIG 2. Diagram of the pipeline of aneurysm volume measurement.

regions. This selection was repeated on all consecutive datasets, and the 3D volumes were then placed into spatial coregistration.

The second thresholding step was performed using a reference length of vessel that was considered disease-free and presumed to have an unchanged volume during all time points. Interstudy calibration was enforced by adjusting the intensity threshold of each subsequent session to yield a measured volume of the reference artery that matched that of the baseline study to within $\pm 2\%$. Identification of the reference vessel varied with the location of the aneurysm. In general, a branch-free, relatively straight segment of the parent vessel was selected a few centimeters proximal to the aneurysm. For the most common aneurysm type, the ICA, this was typically in the petrous portion of the ICA.

The processing pipeline is illustrated in Fig 2. DICOM images were exported in the Visualization ToolKit format. Isosurfaces for baseline and follow-up studies were imported into the 3D modeling software Geomagic Design X (3D Systems) and were coregistered to the baseline study using a picked point, landmark-based registration. The volume of the reference length was measured. If it differed from that in baseline, the threshold was adjusted and a new isosurface was generated. This process was repeated iteratively until volume matching was achieved for the reference length. Cut planes were then prescribed transverse to the arteries at the proximal and

distal ends of the aneurysmal segment, and the volume contained within the isosurfaces between those planes was calculated.

Statistical Methods

The data were analyzed in R statistical and computing software (Version 3.61; <http://www.r-project.org/>) using linear mixed effects modeling (lmerTest¹⁷ for a linear mixed effect model; <https://cran.r-project.org/web/packages/lmerTest/index.html>). Homoscedasticity was obtained by log-transforming the aneurysm volumes, and time was centered for each patient. Time was included as a fixed effect, and the intercepts and slopes of the log-volume for patients and aneurysms were included as random effects. First, it was determined whether a quadratic time component was needed (Satterthwaite method, $P < .05$). Second, whether the residual differed between 1.5T and 3T (Levene test, $P < .05$) was investigated. The CV was obtained from the variance of the residuals as

$$CV = (SD \text{ of Original Scale}) / (\text{Mean of Original Scale}) = \sqrt{\exp(\text{Variance of Log-Transformed Residuals}) - 1}.$$

Predictive variables were identified using a stepwise forward selection followed by a backward elimination (Satterthwaite method, $P < .05$).

Noticeable growth was defined as relative growth > 2 times the CV (compared with the initial volume). Sudden growth

was defined as relative growth larger than 4 times the CV per year in consecutive follow-up measurements with no growth before and subsequent to that time interval.

RESULTS

A total of 101 patients who underwent >2 MR imaging scans were included in this longitudinal study. For any subject in whom there was an apparent decrease in aneurysm volume, true FISP images were examined to see whether there was any wall thickening

encroaching on the lumen, indicating thrombus layering in the aneurysm rather than simply measurement error that accounted for this volume change. Six aneurysms were noted to layer intraluminal thrombus during follow-up and were excluded from analysis. Hence the statistical analysis was performed on the basis of 95 patients with 112 aneurysms, and a total of 616 measurements (Figs 3–4).

The average maximal diameter of 112 aneurysms was 6.1 mm. The mean follow-up time for this cohort was 4.0 years, and the mean number of imaging sessions was 5.9. Detailed patient and aneurysm characteristics are presented in Table 1.

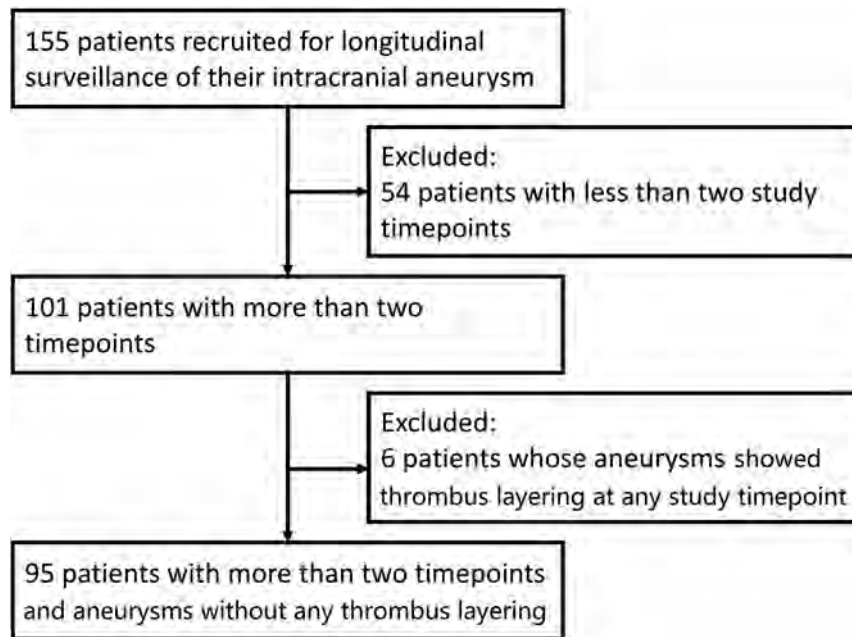


FIG 3. Patient selection flow chart.

Coefficient of Variance and Identification of Predictive Variables of Growth from Linear Mixed Effect Modeling

Including a quadratic time term did not improve the model significantly ($P = .32$). No significant difference of the residuals was found between acquisitions at 1.5T and 3T ($P = .26$). The CV was determined to be 5.5%.

Among the investigated terms (aneurysm location, saccular versus non-saccular aneurysms, sex, hypertension, hyperlipidemia, smoking, diabetes, age, and the presence of multiple aneurysms) as potential fixed effects in the best-fit linear mixed effect model, aneurysm volume growth varied by age and location, with the fastest growth in anterior cerebral artery (ACA) aneurysms, as summarized in Table 2.

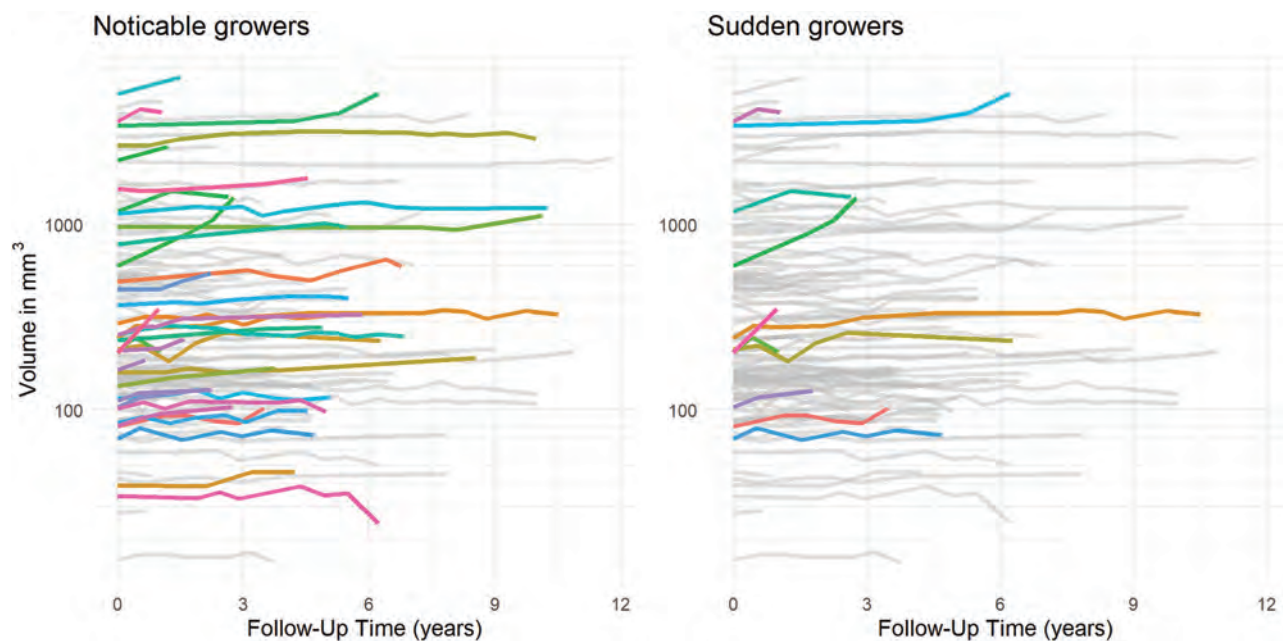


FIG 4. Plots showing evolution across time of volume for each of the 112 aneurysms. Color coding is used to highlight noticeable growers (left) and sudden growers (right).

Table 1: Demographics^a

Variable	Value
No. of patients	95
No. of aneurysms	112
Age (mean) (yr)	61.1 (SD, 17.4)
Female	62 (65.3%)
Male	33 (34.7%)
Hypertension	42 (44.2%)
Hyperlipidemia	20 (21.1%)
Smoking	32 (33.7%)
Diabetes	11 (11.6%)
Fusiform	27 (28.4%)
Nonfusiform	68 (71.6%)
ICA [mean diameter ±SD (mm)]	67 (59.8%) [6.09±4.57]
ACA [mean diameter ±SD (mm)]	10 (8.9%) [4.36±2.37]
MCA [mean diameter ±SD (mm)]	11 (9.8%) [4.74±2.36]
Vertebral artery [mean diameter ±SD (mm)]	6 (5.4%) [5.95±2.83]
Basilar artery [mean diameter ±SD (mm)]	18 (16.1%) [8.09±4.01]
Follow-up time (mean) (yr)	4.0 (SD, 2.8)
No. of imaging sessions per patient (mean)	5.9 (SD, 3.4)
Maximal diameter (mean) (mm)	6.1 (SD, 4.2)
Baseline volume (mean) (mm ³)	246.7 (139.1–663.8)

Note:—SD indicates standard deviation.

^aData are No. (%) unless otherwise indicated.

Table 2: Growth and 95% CI of the relative growth

	Relative Aneurysm Growth per Year (%)	
	Estimates	95% CI
ACA	4.07	2.28–5.87
VA	1.66	–0.44–4.03
MCA	1.41	–0.10–3.22
BA	1.32	–0.21–2.78
ICA	0.47	–0.25–1.19
Change per age (yr)	–0.044	–0.086–0.000

Note:—BA indicates basilar artery; VA, vertebral artery.

Clinical Interpretation Using the Proposed Methodology

By means of the volumetric metric suggested in this study to monitor intracranial aneurysms, noticeable growth would be defined as relative growth of >2 times the CV (11%) compared with the initial volume. Requiring change to be >2 times the CV implies that there is 95% statistical confidence that there has been a true change in aneurysm size and that the perceived change is not just measurement variability. In our study population, 8% of aneurysms had an average growth rate that would have resulted in noticeable growth in 1 year of follow-up.

Sudden growth was defined as 4 times the CV (22%) volume growth in consecutive follow-up intervals. If this methodology were applied to the patients included in this study, it would conclude that 36 of the 112 aneurysms (32%) demonstrated noticeable growth during the course of the study and that 11 of the 36 (31%) aneurysms with noticeable growth had an episode of sudden growth.

DISCUSSION

This study investigated the use of a volumetric measure to monitor UIAs across time in imaging studies with a large number of follow-

up time points. There are 3 key findings: First, the analysis demonstrates that CE-MRA, a relatively noninvasive imaging method, provides volume measurements with a CV of 5.5%. This corresponds, in most intracranial aneurysms, to an error of measurement of less than a voxel in terms of linear measurements, the conventional clinical metric. Most important, this estimate incorporates all potential contributing sources of variance, including: physiologic factors such as cardiac output, which might vary between imaging sessions; acquisition errors related to imperfect timing of contrast injection; and postprocessing errors related to user-dependent choices such as thresholding and cut plane selections. Second, the study showed that the growth rate was dependent on age and the location of the aneurysm, with UIAs of the ACA showing the fastest growth rate of 4.52% per year. Third, 11/112 (9.8%) of the UIAs presented with what appeared to be an episode of sudden growth.

Measurements of aneurysms in terms of volume is attractive because of its potential to provide a more sensitive and comprehensive assessment of change.¹⁸ Several software-based methods of volume measurement have been implemented on CTA images.¹⁴ CE-MRA has advantages in the serial monitoring of untreated UIAs because there is no radiation (as in CTA) or arterial catheterization-related risks (as in conventional angiography). CE-MRA also is not subject to flow-related artifacts, specifically saturation effects that are pronounced in slowly rotating intra-aneurysmal blood, and the benefits provided by the increased reliability of this approach are considered, in a high-risk disease condition, to outweigh the known risks of gadolinium administration. However, reliable CE-MRA measurements in longitudinal studies are challenging. They require coregistration in 3D space and also lack an absolute signal calibration for standardized thresholding—unlike CTA, which is measured in Hounsfield units.^{19,20} In this study, surface meshes of thresholded vascular territories from all time points were brought into coregistration using internal fiducials and an affine transformation. Thresholding consistency was enforced by constraining the volume of a reference length of the vessel to remain constant during all time points. Using this in-house software, we found an acceptable CV (5.5%) in the measurement of UIAs.

The existing literature on assessing aneurysm size is principally based on 2D diameter measurements. Reports on the rate of growth and risk factors for growth of UIAs are inconsistent.^{8,21–24} Furthermore, most previous studies used only 2 time points (the first and the last) to evaluate aneurysm growth, thus excluding important information on the growth trajectory in the intervening periods.^{3,7,16,25} Using such datasets, most studies assume that aneurysm growth is linear and steady, though clinical observation or even proposed growth models^{3,16} cause skepticism about this assumption. In this study, we included the often-neglected intermediate events and more sensitively identified a higher percentage of growing aneurysms (32%) than in previous studies (4%–18%).^{3,4,7,8,21,26–29} Further analysis of growth trends revealed that approximately 31% of growing aneurysms presented with a sudden/episodic growth pattern, the presentation of which is of high clinical concern. A better understanding of the growth trajectory and pattern of aneurysms will support a more judicious selection of UIAs for preventative treatment and enable the development of improved follow-up strategies for UIAs.³

Two recent meta-analyses reported aneurysm size, female sex, smoking, cavernous carotid artery location, and nonsaccular shape as independent risk factors for UIA growth. The roles of other risk factors were inconsistent.²⁹⁻³¹ Despite a partial overlap, several of these findings were not replicated in this study. Possible reasons for the discordance were the following: 1) The reported aneurysm sizes were all in terms of 2D diameters, while volumetric measures might display a different dependence; and 2) this cohort for aneurysm monitoring had generally small-sized UIAs, and the results presented here might better reflect the growth behavior of relatively small UIAs.

This study has several limitations. First, there was possible patient selection bias because the preference of patients for participating in a monitoring study could result in an over-representation of patients with relatively smaller UIAs. Also, patients with known risk factors such as a history of subarachnoid hemorrhage were not included because near-term treatment was likely. Second, it is difficult to validate the accuracy of the volume measurement method in serial studies in clinical patients against the current criterion standard of DSA, given the invasive nature of the latter. Third, because the diagnostic criteria for aneurysm sudden growth have not been explored previously, the criteria used here were based on our clinical experience. Finally, in this study, we enrolled all suitable subjects referred to us by referring clinicians. It is apparent that the clinicians were more comfortable referring aneurysms of the ICA for surveillance imaging than aneurysms in other locations where interventional treatment could have been preferred. As a result, the total number of ACA, MCA, and vertebral artery aneurysms was relatively small, and the result that the ACA location was significantly associated with greater volume growth should be interpreted with caution.

CONCLUSIONS

This proposed method of aneurysm volume measurement provides an acceptable CV for longitudinal follow-up studies compared with prior linear metrics. Approximately one-fourth of UIAs showed noticeable growth with time, and approximately one-third of these growing UIAs presented with a sudden/episodic growth pattern. Aneurysm volume measurement appears to be a sensitive and useful tool to depict and identify the growth trajectory and patterns of UIAs.

The UCSF Intracranial Aneurysm Monitoring Group

M.R. Amans, MD, D.L. Cooke, MD, C.F. Dowd, MD, V. Halbach, MD, S.W. Hetts, MD, R.T. Higashida, MD, C. Huang, MD, D. Hurwit, MD, N. Jeung, RT, S.A. Josephson, MD, A. Kim, MD, N.U. Ko, MD, M.T. Lawton, MD, W.A. Lee, MD, D. Nieuwoudt, MD, V. Rayz, PhD, S. Sohrabi, MD, W.S. Smith, MD, PhD, and C. Zhu, PhD.

Disclosures: Charles E. McCulloch—RELATED: Grant: National Institutes of Health. Alastair J. Martin—RELATED: Grant: National Institutes of Health.*
*Money paid to the institution.

REFERENCES

1. Brisman JL, Song JK, Newell DW. Cerebral aneurysms. *N Engl J Med* 2006;355:928–39 CrossRef Medline

2. Rincon F, Rossenwasser RH, Dumont A. The epidemiology of admissions of nontraumatic subarachnoid hemorrhage in the United States. *Neurosurgery* 2013;73:217–22 CrossRef Medline
3. Chien A, Callender RA, Yokota H, et al. Unruptured intracranial aneurysm growth trajectory: occurrence and rate of enlargement in 520 longitudinally followed cases. *J Neurosurg* 2019;132:1077–87 CrossRef Medline
4. Bor AS, Tiel Groenestege AT, terBrugge KG, et al. Clinical, radiological, and flow-related risk factors for growth of untreated, unruptured intracranial aneurysms. *Stroke* 2015;46:42–48 CrossRef Medline
5. Etminan N, Beseoglu K, Barrow DL, et al. Multidisciplinary consensus on assessment of unruptured intracranial aneurysms: proposal of an international research group. *Stroke* 2014;45:1523–30 CrossRef Medline
6. Greving JP, Wermer MJ, Brown RD Jr, et al. Development of the PHASES score for prediction of risk of rupture of intracranial aneurysms: a pooled analysis of six prospective cohort studies. *Lancet Neurol* 2014;13:59–66 CrossRef Medline
7. Villablanca JP, Duckwiler GR, Jahan R, et al. Natural history of asymptomatic unruptured cerebral aneurysms evaluated at CT angiography: growth and rupture incidence and correlation with epidemiologic risk factors. *Radiology* 2013;269:258–65 CrossRef Medline
8. Serrone JC, Tackla RD, Gozal YM, et al. Aneurysm growth and de novo aneurysms during aneurysm surveillance. *J Neurosurg* 2016;125:1374–82 CrossRef Medline
9. Watanabe Z, Tomura N, Akasu I, et al. Comparison of rates of growth between unruptured and ruptured aneurysms using magnetic resonance angiography. *J Stroke Cerebrovasc Dis* 2017;26:2849–54 CrossRef Medline
10. Ryu CW, Kwon OK, Koh JS, et al. Analysis of aneurysm rupture in relation to the geometric indices: Aspect ratio, volume, and volume-to-neck ratio. *Neuroradiology* 2011;53:883–89 CrossRef Medline
11. Wever JJ, Blankensteijn JD, Mali WP, et al. Maximal aneurysm diameter follow-up is inadequate after endovascular abdominal aortic aneurysm repair. *Eur J Vasc Endovas Surg* 2000;20:177–82 CrossRef Medline
12. Fillinger M; Excluder Bifurcated Endoprosthesis Clinical Investigators. Three-dimensional analysis of enlarging aneurysms after endovascular abdominal aortic aneurysm repair in the gore excluder pivotal clinical trial. *J Vasc Surg* 2006;43:888–95 CrossRef Medline
13. Lindquist Liljeqvist M, Hultgren R, Gasser TC, et al. Volume growth of abdominal aortic aneurysms correlates with baseline volume and increasing finite element analysis-derived rupture risk. *J Vasc Surg* 2016;63:1434–42 CrossRef Medline
14. Escobar-de la Garma VH, Zenteno M, Padilla-Vazquez F, et al. Comparative analysis of aneurysm volume by different methods based on angiography and computed tomography angiography. *Neurosurg Rev* 2018;41:1013–19 CrossRef Medline
15. Persson A, Dahlström N, Engellau L, et al. Volume rendering compared with maximum intensity projection for magnetic resonance angiography measurements of the abdominal aorta. *Acta Radiol* 2004;45:453–59 CrossRef Medline
16. Brady AR, Thompson SG, Fowkes FG, et al. Abdominal aortic aneurysm expansion: risk factors and time intervals for surveillance. *Circulation* 2004;110:16–21 CrossRef Medline
17. Kuznetsova A, Brockhoff PB, Christensen RH. Lmertest package: tests in linear mixed effects models. *J Stat Softw* 2017;82:1–26 CrossRef
18. Erhardt S, Marbacher S, Neuschmelting V, et al. Comparison between routine cylindrical cerebral aneurysm volume approximation and three-dimensional volume measurements in experimental aneurysms. *Neurol Res* 2014;36:739–45 CrossRef Medline
19. Pötin M, Gailloud P, Bidaut L, et al. CT angiography, MR angiography and rotational digital subtraction angiography for volumetric

- assessment of intracranial aneurysms: an experimental study. *Neuroradiology* 2003;45:404–09 CrossRef Medline
20. Hanley M, Zenzen WJ, Brown MD, et al. **Comparing the accuracy of digital subtraction angiography, CT angiography and MR angiography at estimating the volume of cerebral aneurysms.** *Interv Neuroradiol* 2008;14:173–77 CrossRef Medline
 21. Burns JD, Huston J 3rd, Layton KF, et al. **Intracranial aneurysm enlargement on serial magnetic resonance angiography: frequency and risk factors.** *Stroke* 2009;40:406–11 CrossRef Medline
 22. Chien A, Liang F, Sayre J, et al. **Enlargement of small, asymptomatic, unruptured intracranial aneurysms in patients with no history of subarachnoid hemorrhage: the different factors related to the growth of single and multiple aneurysms.** *J Neurosurg* 2013;119:190–97 CrossRef Medline
 23. Koffijberg H, Buskens E, Algra A, et al. **Growth rates of intracranial aneurysms: exploring constancy.** *J Neurosurg* 2008;109:176–85 CrossRef Medline
 24. Sonobe M, Yamazaki T, Yonekura M, et al. **Small unruptured intracranial aneurysm verification study: Suave Study, Japan.** *Stroke* 2010;41:1969–77 CrossRef Medline
 25. Leemans EL, Cornelissen BM, Said M, et al. **Intracranial aneurysm growth: consistency of morphological changes.** *Neurosurg Focus* 2019;47:E5 CrossRef Medline
 26. Huang H, O'Neill AH, Chandra RV, et al. **Asymptomatic intracranial aneurysms in the elderly: long-term clinical and radiological follow up of 193 consecutive patients.** *World Neurosurg* 2020;133:e600–08 CrossRef Medline
 27. Matsumoto K, Oshino S, Sasaki M, et al. **Incidence of growth and rupture of unruptured intracranial aneurysms followed by serial MRA.** *Acta Neurochir* 2013;155:211–16 CrossRef Medline
 28. Gondar R, Gautschi OP, Cuony J, et al. **Unruptured intracranial aneurysm follow-up and treatment after morphological change is safe: observational study and systematic review.** *J Neurol Neurosurg Psychiatry* 2016;87:1277–82 CrossRef Medline
 29. Jin D, Song C, Leng X, et al. **A systematic review and meta-analysis of risk factors for unruptured intracranial aneurysm growth.** *Int J Surg* 2019;69:68–76 CrossRef Medline
 30. Brinjikji W, Zhu YQ, Lanzino G, et al. **Risk factors for growth of intracranial aneurysms: a systematic review and meta-analysis.** *AJNR Am J Neuroradiol* 2016;37:615–20 CrossRef Medline
 31. Backes D, Rinkel GJ, Laban KG, et al. **Patient- and aneurysm-specific risk factors for intracranial aneurysm growth: a systematic review and meta-analysis.** *Stroke* 2016;47:951–57 CrossRef Medline

Reliability and Agreement of 2D and 3D Measurements on MRAs for Growth Assessment of Unruptured Intracranial Aneurysms

K.M. Timmins, H.J. Kuijff, M.D.I. Vergouwen, M.J. Otten, Y.M. Ruigrok, B.K. Velthuis, and I.C. van der Schaaf



ABSTRACT

BACKGROUND AND PURPOSE: Reliable and reproducible measurement of unruptured intracranial aneurysm growth is important for unruptured intracranial aneurysm rupture risk assessment. This study aimed to compare the reliability and reproducibility of 2D and 3D growth measurements of unruptured intracranial aneurysms.

MATERIALS AND METHODS: 2D height, width, and neck and 3D volume measurements of unruptured intracranial aneurysms on baseline and follow-up TOF-MRAs were performed by two observers. The reliability of individual 2D and 3D measurements and of change (growth) between paired scans was assessed (intraclass correlation coefficient) and stratified for aneurysm location. The smallest detectable change on 2D and 3D was determined. Proportions of growing aneurysms were compared, and Bland-Altman plots were created.

RESULTS: Seventy-two patients with 84 unruptured intracranial aneurysms were included. The interobserver reliability was good-to-excellent for individual measurements (intraclass correlation coefficient > 0.70), poor for 2D change (intraclass correlation coefficient < 0.5), and good for 3D change (intraclass correlation coefficient = 0.76). For both 2D and 3D, the reliability was location-dependent and worse for irregularly shaped aneurysms. The smallest detectable changes for 2D height, width, and neck and 3D volume measurements were 1.5, 2.0, and 1.9 mm and 0.06 mL, respectively. The proportion of growing unruptured intracranial aneurysms decreased from 10% to 2%, depending on the definition of growth (1 mm or the smallest detectable changes for 2D and 3D).

CONCLUSIONS: The interobserver reliability of the size measurements of individual 2D and 3D unruptured intracranial aneurysms was good-to-excellent but lower for 2D and 3D growth measurements. For growth assessment, 3D measurements are more reliable than 2D measurements. The smallest detectable change for 2D measurements was larger than 1 mm, the current clinical definition of unruptured intracranial aneurysm growth.

ABBREVIATIONS: ICC = intraclass correlation coefficient; SDC = smallest detectable change; UIA = unruptured intracranial aneurysm

In the adult population, the prevalence of unruptured intracranial aneurysms (UIAs) is around 3%.¹ Intracranial aneurysm rupture leads to SAH with a high case fatality rate. The PHASES (Population, Hypertension, Age, Size, Earlier subarachnoid hemorrhage and Site) study found the 5-year rupture risk of UIAs to

be, on average, 3.4% (0.5%–17.8%), depending on patient and aneurysm characteristics.² When one makes a treatment decision, the risk of aneurysm rupture is weighed against the complication risk of treatment. Aneurysm size is a key determinant in the prediction models of rupture risk.^{2,3} If a multidisciplinary team decides against preventive aneurysm treatment, the UIA is followed up with repeat TOF-MRA or CTAs to detect potential aneurysm growth. Growth is an additional rupture risk factor,⁴ and if detected, preventive treatment should be considered. TOF-MRA has been shown to systematically underestimate the size and volume of the aneurysm compared with the criterion standard DSA.⁵ However, noninvasive TOF-MRA is the first-choice imaging method for follow-up imaging in clinical practice because neither contrast agent administration nor radiation exposure is required.^{6,7}

Assessment of UIAs is performed by taking 2D size measurements of aneurysms on MRA/CTA using electronic calipers. The 3D nature of UIAs makes 2D measurements difficult and

Received December 22, 2020; accepted after revision March 29, 2021.

From the Image Sciences Institute (K.M.T., H.J.K.), Department of Neurology and Neurosurgery (M.D.I.V., Y.M.R.), UMC Utrecht Brain Center, and Department of Radiology (M.J.O., B.K.V., I.C.v.d.S.), University Medical Center Utrecht, Utrecht, the Netherlands.

We acknowledge the support from the Netherlands Cardiovascular Research Initiative: an initiative with support of the Dutch Heart Foundation, CVON2015-08 ERASE, and CVON2018-02 ANEURYSM@RISK.

Please address correspondence to Kimberley Timmins, MPhys, Image Sciences Institute, University Medical Center Utrecht, Heidelberglaan 100, Room Q.02.4.45, 3584 CX Utrecht, the Netherlands; e-mail: k.m.timmins@umcutrecht.nl

 Indicates article with online supplemental data.

<http://dx.doi.org/10.3174/ajnr.A7186>

dependent on optimal orientation in multiplanar imaging. The 2D measurements by human observers are reported to have comparable mediocre reproducibility on both CTAs and MRAs.^{8,9} These UIA measurements are relevant when comparing aneurysm size in a follow-up scan to assess aneurysm growth. Aneurysm growth is defined as an increase in either 2D height or width of at least 1 mm.¹⁰ A reliable measurement method with good agreement is important for risk assessment. In this context, the reliability depends on the variability of the aneurysm sizes among patients. The agreement describes the interobserver measurement error and is characteristic of the measurement method itself. Without knowledge of reliability and agreement, it is unclear whether a measured change in aneurysm size between baseline and follow-up scans represents real growth or is attributable to observer or scan variations.

In this study, we investigated the reliability and reproducibility of 2D size and 3D volume measurements of UIAs and change in aneurysm size and volume between baseline and follow-up MRAs. For an agreement measure, we calculated the smallest detectable change (SDC) and assessed agreement using Bland-Altman plots.

MATERIALS AND METHODS

Study Population

We included 72 patients from a series of patients with UIAs from the University Medical Center Utrecht who met the following inclusion criteria: 1) A TOF-MRA was available at both the baseline admission scan and follow-up, 2) the follow-up scan was performed at least 6 months after the baseline scan, and 3) the patient had at least 1 untreated UIA present on both baseline and follow-up MRA. Any treated aneurysm in these subjects was excluded from this study. The most recent follow-up scan in which the UIA remained untreated and unruptured was used. The scans had an in-plane resolution range of 0.175–1.04 mm and a section thickness range of 0.399–1.2 mm. All scans were obtained from 2004 to 2019. Due to the nature of the scans, protocols varied, but all scans were obtained on 1T, 1.5T, or 3T scanners with a median TR of 23 ms and a median TE of 6.4 ms across all scans. This retrospective study required no formal consent from participants. The data that support the findings of this study are available from the corresponding author on reasonable request.

Measurements

2D Measurements. Manual 2D measurements of the UIAs were performed on the IntelliSpace Portal (Phillips Healthcare). Measurements were obtained using electronic calipers on the TOF-MRAs, which could be rotated in the software. The aneurysm height, width, and neck were measured on the TOF-MRAs on a 0.1-mm scale^{11,12} as shown in parts A and C in the Figure. Aneurysm height was defined as the maximum distance from the aneurysm neck to the dome. Aneurysm width was measured perpendicular to the height along the maximum width of the UIA. The neck was measured as the maximum width of the UIA where it attached to the parent vessel. Observers determined whether the UIA shape was regular or irregular.

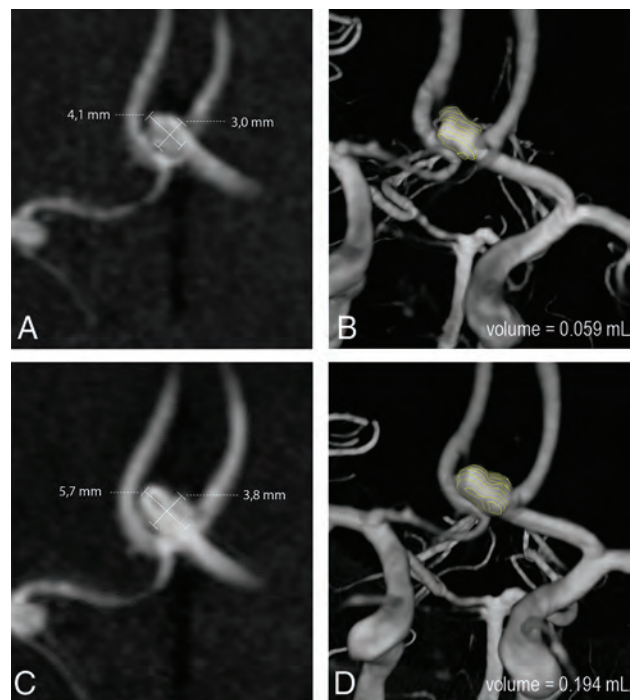


FIGURE. Baseline (A and B) and follow-up (C and D) TOF-MRA with an anterior communicating artery aneurysm that shows growth when measured in 2D (A and C) and in 3D (B and D).

All 2D measurements were performed independently by 2 observers. The observers were a neuroradiologist (I.C.v.d.S., with 15 years of experience) and a general radiologist (M.J.O., with 10 years of experience, including cerebral MRA evaluation). Individual measurements were first obtained on the baseline scan, then on the follow-up scan of the same patient. The observers were not blinded to the time order of the scans and had the baseline for comparison, as is standard in clinical practice.

3D Measurements. For 3D measurement, the UIAs were segmented from the TOF-MRAs using in-house-developed software implemented in MeVisLab (MeVis Medical Solutions). A contour was drawn around the outline of the aneurysm on axial slices, and the parent vessels were not included (Figure). The UIA volume (in milliliters) was determined on the basis of the voxels contained within the contours and the MRA voxel size. Annotations were performed independently by two observers, first on the baseline scan, followed by the follow-up scan of the same patient. The observers were the neuroradiologist (I.C.v.d.S.) and a trained medical student (D.S.).

Statistical Analysis

First, the interobserver reliability of the individual 2D measurements (height, width, neck) and 3D measurements (volume) of the aneurysms was determined. Second, on the basis of the 2D and 3D size measurements, changes in size and volume (growth) between paired baseline and follow-up scans for 2D (difference in height, width, and neck in mm) and 3D (volume difference in milliliters) were calculated. Third, the interobserver reliability of these changes in size (2D) and volume (3D) measurements was assessed by computing the intraclass correlation coefficient

Table 1: Interobserver size and volume measurements^a

Parameters	Height (mm)	Width (mm)	Neck (mm)	Volume (mL)
Observer A measurement	3.4 (2.4–4.4)	3.4 (2.2–4.5)	2.6 (2.0–3.5)	0.0278 (0.0117–0.0578)
Observer B measurement	3.4 (2.5–4.6)	3.2 (2.2–4.3)	2 (1.6–2.8)	–
Observer C measurement	–	–	–	0.0227 (0.0090–0.0470)
Absolute Diff _{obs}	0.4 (0.2–0.6)	0.45 (0.2–0.8)	0.55 (0.3–1.0)	0.0091 (0.0036–0.0206)
ICC _{agreement} (95% CI)	0.93 (0.90–0.95)	0.85 (0.80–0.89)	0.74 (0.31–0.87)	0.98 (0.97–0.98)

Note:— indicates no measurement; ICC_{agreement}, Intraclass correlation coefficient on absolute agreement between observers' measurements; Absolute Diff_{obs}, absolute difference between observers' measurements.

^a 2D and 3D measurements of the aneurysms by observers A and B for 2D and observers A and C for 3D. Total: 168 aneurysms, including both baseline and follow-up scans. Each measurement is provided as a median (quartiles 1–3). Reliability is in the bottom row as an ICC on absolute agreement (95% confidence interval).

Table 2: Interobserver change measurements^a

Parameters	Height Change (mm)	Width Change (mm)	Neck Change (mm)	Volume Change (mL)
Observer A measurement	0.2 (–0.1–0.7)	0.1 (–0.2–0.4)	0 (–0.2–0.4)	0.00001 (–0.0043–0.0011)
Observer B measurement	0.1 (–0.1–0.5)	0.1 (–0.2–0.6)	0 (–0.1–0.3)	–
Observer C measurement	–	–	–	0.0015 (–0.0054–0.0106)
Absolute Diff _{obs}	0.4 (0.2–0.7)	0.4 (0.2–0.6)	0.3 (0.1–0.7)	0.0057 (0.0024–0.0135)
ICC _{agreement} (95% CI)	0.46 (0.27–0.61)	0.45 (0.26–0.60)	0.26 (0.06–0.46)	0.76 (0.65–0.76)

Note:— indicates no measurement; ICC_{agreement}, Intraclass correlation coefficient on absolute agreement between observers' measurements; Absolute Diff_{obs}, absolute difference between observers' measurements.

^a Change between baseline and follow-up measurements of the 2D height, width, neck and 3D volume of the aneurysm by observers A and B for 2D and observers A and C for 3D. Total: 84 baseline–follow-up pairs measured by 2 observers. Substantial positive differences between baseline and follow-up may indicate growth of the aneurysm. Each measurement is provided as a median (quartiles 1–3). Reliability of the differences is provided in the bottom row as the ICC on absolute agreement (95% confidence interval).

(ICC). The ICC was calculated using a single-measurement, absolute-agreement, 2-way random-effects model.¹³ An ICC above 0.9 represents excellent reliability; between 0.75 and 0.90, good reliability; between 0.5 and 0.75, moderate reliability; and lower than 0.5, poor reliability.^{13,14} The interobserver reliability for detecting change in 2D and 3D measurements was compared in regular and irregular aneurysms.

The SDC was computed on the basis of the 2D and 3D measurements to assess the interobserver agreement. The SDC represents the minimal change that an aneurysm measurement must show to ensure that the observed change is real and not just due to measurement error. For both 2D size and 3D volume measurements, we calculated the standard error of measurement (SEM) using the ICC previously determined. The SDC was calculated from the standard error, $SEM_{agreement}$, $SDC = 1.96 \sqrt{2} SEM_{agreement}$, where $SEM_{agreement} = SD \sqrt{1 - ICC_{agreement}}$, and SD is the standard deviation of all measurements.¹⁵

Bland-Altman plots for the interobserver difference between the change in 2D and 3D measurements between baseline and follow-up scans were created to assess agreement. The difference between each observer and the overall mean of both observers was calculated and plotted. The limits of agreement from the mean (± 1.96 SD) were determined. Measurements outside the limits of agreement were considered outliers.

The number of UIAs with change in 2D height and/or width measurements larger than 1 mm, the current clinical definition of aneurysm growth,¹⁰ was determined. Next, the number of UIAs with a change in 2D height and/or width and volume larger than the determined 2D and 3D SDCs was determined. The proportion of UIAs showing growth based on the 1-mm clinical definition versus the proportion of UIAs with growth based on the SDCs was compared.

Finally, a subanalysis was performed stratifying the reliability of change measurements for aneurysm location: anterior cerebral or communicating artery, internal carotid artery, posterior communicating artery, MCA, and posterior circulation.

All data analyses were conducted using Pandas, SciPy, and Pengouin¹⁶ toolboxes with Python 3.7 (<https://www.python.org/downloads/release/python-370/>).

RESULTS

We included 72 patients with 84 UIAs. The mean age was 53 years (range, 27–73 years), and 71% were women. Most patients had 1 UIA ($n = 63$). The median time between baseline and follow-up scans was 4.7 years (range, 0.9–13.1 years). The median aneurysm height was 3.4 mm (range, 0.8–15 mm). Twenty-two percent of aneurysms were located at the anterior cerebral artery/ anterior communicating artery, 27% at the ICA or posterior communicating artery, 38% at the MCA, and 13% in the posterior circulation. The Figure shows an example of a growing aneurysm measured in 2D and 3D.

The interobserver reliability of the 2D size and 3D volume measurements is summarized in Table 1. The ICC of the individual 2D size measurements was excellent for height (0.93), good for width (0.85), and moderate for the neck (0.74). The ICC for the individual 3D volume measurement was excellent (0.98).

The ICCs for the change in measurements (growth) between the paired baseline–follow-up scans for the 2 observers are shown in Table 2. The ICC for the change in 2D measurements was poor for height (0.46), width (0.45), and neck (0.26). The ICC for the change in 3D volume measurements was good (0.76). Irregularly shaped aneurysms had a lower reliability for 2D change in height and width (ICCs = 0.23, 0.38) and 3D change in volume (ICC = 0.60) than for regular aneurysms (ICCs = 0.57, 0.47, 0.83, respectively).

On the basis of the standard error of measurement for agreement, between the 2 observers, the SDC for 2D measurements was 1.5 mm for height, 2.0 mm for width, and 1.9 mm for neck. The SDC for 3D volume measurement was 0.062 mL.

The Online Supplemental Data show Bland-Altman plots for the interobserver difference between the change in 2D and 3D

measurements between baseline and follow-up scans. The Bland-Altman plots show that there are 4–6 outliers that fall outside the limits of agreement for all change measurements between size and volume. About half of these outliers (55%) were the same for 2D and 3D and were classified as irregularly shaped by the observers. There was no relation between aneurysm size and the outliers.

The number of UIAs with a change in size measurements larger than 1 mm and a change in size and volume larger than the SDCs is shown in the Online Supplemental Data. The proportion of UIAs with growth based on the definition of 1 mm was 10%, compared with 2% when using a 1.5-mm change in height as a cutoff value (SDC for 2D height) or a 2.0-mm change in width as a cutoff value (SDC for 2D width) and a 0.062-mL change (SDC for 3D) as cut-off value.

The Online Supplemental Data indicate the reliability of the change in measurements in different locations. The reliability was found to be location-dependent for both 2D and 3D; however, 3D measurements were more reliable than 2D measurements across all locations ($ICC > 0.5$).

DISCUSSION

In this study, interobserver reliability was better for 3D than 2D measurements of UIAs, both for individual size and detection of change in size (growth). Overall, the interobserver reliability of both 2D and 3D measurements was lower for the detection of change (growth) compared with measurements on individual scans. The SDC between the baseline and follow-up scan for 2D measurements was substantially larger than the current clinical definition (1 mm), and proportions of UIAs showing growth decreased more than three-quarters depending on the growth definition.

Many studies have investigated MRAs for UIA diagnosis.¹⁷ However, few studies have investigated the interobserver reliability of 2D measurements from individual MRAs of patients, and no studies have fully investigated the reliability and agreement of growth measurements between baseline and follow-up MRAs of the same patient. The results of studies for individual 2D height and width measurements are similar to our findings, with the lowest reliability for measuring the neck. Kim et al⁸ studied intra- and interobserver individual 2D measurement variability of 33 aneurysms with a mean size of 5.1 mm, finding an ICC of 0.83–0.99 on MRAs with the lowest reliability for the neck measurement ($ICC = 0.83-0.86$). Mine et al¹⁸ compared the diagnosis and measurements of UIAs between DSAs and MRAs. Three readers assessing 56 aneurysms in MRAs determined an interobserver agreement between individual 2D maximal diameter as moderate-to-substantial ($\kappa = 0.53-0.66$) and the neck measurement as fair-to-moderate ($\kappa = 0.20-0.41$). The lower ICC for the neck is likely due to difficulty in defining an aneurysm neck, particularly if there are branching vessels emerging from the neck. This lower measurement reliability for neck measurements may have implications for treatment-planning and complication risk assessment.¹⁹ For aneurysm growth assessment, the neck measurement is less important because height and width measurements are commonly used.^{10,11}

With ever-improving image analysis techniques, 3D measurements of UIAs²⁰⁻²² are more commonly investigated, but little is

known of their reliability or reproducibility for individual size and growth measurement of UIAs in TOF-MRAs. D'Argento et al²³ found no significant difference in intra- and interobserver variability of automatic and manual 2D size measurements of UIAs on 3D DSAs and CTAs.

We determined the ICC of absolute agreement to include the systematic error of both observers and random residual errors. A substantially lower ICC for change measurements (growth) between paired baseline–follow-up scans was determined, relative to measurements from individual scans. The ratio of the systematic measurement error compared with the individual aneurysm size is smaller than the ratio of the measurement error compared with the change in aneurysm size. Thus, a small measurement error in individual measurements can have a larger influence on the subsequent change measurements in paired scans.

The interobserver agreement in 2D and 3D measurements was assessed by determining the SDC. The SDC for both 2D and 3D measurements was relatively large, compared with the median aneurysm size (3.4 mm) and median aneurysm volume (0.025 mL). For example, for 2D height, the SDC of 1.5 mm was about half of median aneurysm height. This study has a large proportion of small aneurysms, and the ratio of the SDC to aneurysm size would be better (lower) in larger aneurysms. However, because most patients who undergo follow-up MRAs have small UIAs, our population represents the clinical situation. The SDC for the 2D measurements is larger than the 1 mm used in the current definition of aneurysm growth.¹⁰ The number of UIAs showing growth according to threshold values of the SDC of 2D and 3D measurements decreased by more than three-quarters compared with this 1-mm threshold. This finding shows the influence of the thresholds for growth definition and has potential important clinical consequences for treatment decisions based on aneurysm growth.

The Bland-Altman plots (Online Supplemental Data) show that 3D interobserver differences were more similar than 2D measurements because the measurements were closer together. Most outliers for both the 2D and 3D measurements were irregularly shaped. We also found that irregular aneurysms had a lower interobserver reliability for detecting change in both 2D size and 3D volume measurements. Irregular aneurysm shape is a risk factor for rupture.^{12,24} 2D measurements and shape assessment of aneurysms are influenced by the selected viewing angle. 3D volume measurements allow a more complete shape of the UIA to be assessed with a single, rotationally-invariant measure. Furthermore, 3D segmentation may allow quantitative shape assessment of UIAs, which would be potentially beneficial in risk assessment.¹²

We found that aneurysm location affects the reliability of 2D and 3D measurements. We found that the reliability of 3D volume measurements was higher and more consistent for all locations than 2D size measurements.

There were some limitations in our study. One limitation was that the 3D measurements were determined from segmentations based on 2D annotations on axial slices, which is time-consuming and the aneurysm neck definition could be difficult, particularly when the parent vessel did not lie in-plane. Furthermore, the difference in experience of the second observers for 2D (radiologist) and 3D (student) measurements may have introduced bias. If this had influenced our results, it would be toward less agreement for

the 3D measurement between the student and the neuroradiologist. However, we found higher agreement in 3D than in 2D.

Second, most scans had small aneurysms with a median diameter of 3.4 mm (range, 0.8–15 mm). The population of patients with small UIAs is, however, representative of patients who undergo follow-up imaging. Because rupture risk increases with aneurysm size, the larger UIAs are more often treated. The protocol and quality of the MRAs between baseline and follow-up differed in some cases, possibly resulting in measurement differences, but they are realistic for clinical practice.

This study investigates TOF-MRAs only because this is the preferred imaging method for follow-up of UIAs.⁷

Our findings of a large SDC for 2D size measurements may have implications for the definition of clinical aneurysm growth¹⁰ and growth/rupture models. This subject requires further study because it would have important consequences for rupture and treatment assessment of UIAs. 2D and 3D measurements cannot be directly compared, but instead a standard growth definition should be used for both. The higher reliability of 3D measurements compared with 2D measurements implies that 3D measurements may be important for accurate assessment of aneurysm growth on TOF-MRA. Automatic or semi-automatic 3D UIA segmentation would allow faster and less operator-dependent aneurysm volume measurement for standard 3D growth assessment, alongside quantitative 3D morphologic characterization of UIAs.

CONCLUSIONS

This study found that 3D change measurements are more reliable than 2D with regard to assessing the change in size and volume measurements of UIAs. The SDC for 2D measurements was found to be larger than the current definition for clinical growth, suggesting that more studies into the reliability of 2D measurement on MRA should be performed. This study opens the door for development and incorporation into of automatic and semi-automatic segmentations and volumetric growth assessments of UIAs into clinical practice.

ACKNOWLEDGMENTS

We acknowledge Djenghiz Samlal (D. S.), University Medical Center, Utrecht, the Netherlands, for his contributions. We further acknowledge support from the focus area Applied Data Science, Utrecht University.

Disclosures: Kimberley M. Timmins—RELATED: Grant: Dutch Heart Foundation (Hartstichting), Comments: grant No. CVON2018-02 ANEURYSM@RISK.*Birgitta K. Velthuis—RELATED: Grant: Dutch Heart Foundation, CVON2015-08 ERASE, and CVON2018-02 ANEURYSM@RISK.* Mervyn D. I. Vergouwen —RELATED: Grant: Dutch Heart Foundation, 2018T076.* Ynte. M. Ruijgrok—RELATED: Grant: Dutch Heart Foundation, CVON2015-02 ERASE.* Irene. C. van der Schaaf —RELATED: Grant: Dutch Heart Foundation, CVON2018-02 ANEURYSM@RISK.* *Money paid to the institution.

REFERENCES

1. Vlak MH, Algra A, Brandenburg R, et al. **Prevalence of unruptured intracranial aneurysms, with emphasis on sex, age, comorbidity, country, and time period: a systematic review and meta-analysis.** *Lancet Neurol* 2011;10:626–36 CrossRef Medline
2. Greving JP, Wermer MJ, Brown RD, et al. **Development of the PHASES score for prediction of risk of rupture of intracranial aneurysms: a pooled analysis of six prospective cohort studies.** *Lancet Neurol* 2014;13:59–66 CrossRef Medline
3. Tominari S, Morita A, Ishibashi T, et al. **Unruptured Cerebral Aneurysm Study Japan Investigators. Prediction model for 3-year rupture risk of unruptured cerebral aneurysms in Japanese patients.** *Ann Neurol* 2015;77:1050–59 CrossRef Medline
4. Villablanca JP, Duckwiler GR, Jahan R, et al. **Natural history of asymptomatic unruptured cerebral aneurysms evaluated at CT angiography: growth and rupture incidence and correlation with epidemiologic risk factors.** *Radiology* 2013;269:258–65 CrossRef Medline
5. Takao H, Murayama Y, Ishibashi T, et al. **Comparing accuracy of cerebral aneurysm size measurements from three routine investigations: computed tomography, magnetic resonance imaging, and digital subtraction angiography.** *Neurol Med Chir (Tokyo)* 2010;50:893–99 CrossRef Medline
6. Thompson BG, Brown RD, Amin-Hanjani S, et al. **American Heart Association Stroke Council, Council on Cardiovascular and Stroke Nursing, and Council on Epidemiology and Prevention; American Heart Association; American Stroke Association. Guidelines for the Management of Patients with Unruptured Intracranial Aneurysms: A Guideline for Healthcare Professionals From the American Heart Association/American Stroke Association.** *Stroke* 2015;46:2368–2400 CrossRef Medline
7. Malhotra A, Wu X, Gandhi D, et al. **Management of small, unruptured intracranial aneurysms.** *World Neurosurg* 2020;135:379–80 CrossRef Medline
8. Kim HJ, Yoon DY, Kim ES, et al. **Intraobserver and interobserver variability in CT angiography and MR angiography measurements of the size of cerebral aneurysms.** *Neuroradiology* 2017;59:491–97 CrossRef Medline
9. Forbes G, Fox AJ, Huston J, et al. **Interobserver variability in angiographic measurement and morphologic characterization of intracranial aneurysms: a report from the International Study of Unruptured Intracranial Aneurysms.** *AJNR Am J Neuroradiol* 1996;17:1407–15 Medline
10. Hackenberg KA, Algra A, Salman RA; the Unruptured Aneurysms and SAH CDE Project Investigators, et al. **Definition and prioritization of data elements for cohort studies and clinical trials on patients with unruptured intracranial aneurysms: proposal of a multidisciplinary research group.** *Neurocrit Care* 2019;30:87–101 CrossRef Medline
11. Backes D, Vergouwen MDI, Tiel Groenestege AT, et al. **PHASES score for prediction of intracranial aneurysm growth.** *Stroke* 2015;46:1221–26 CrossRef Medline
12. Backes D, Rinkel GJ, Greving JP, et al. **ELAPSS score for prediction of risk of growth of unruptured intracranial aneurysms.** *Neurology* 2017;88:1600–06 CrossRef Medline
13. Koo TK, Li MY. **A guideline of selecting and reporting intraclass correlation coefficients for reliability research.** *J Chiropr Med* 2016;15:155–63 CrossRef Medline
14. Kottner J, Audigé L, Brorson S, et al. **Guidelines for Reporting Reliability and Agreement Studies (GRRAS) were proposed.** *J Clin Epidemiol* 2011;64:96–106 CrossRef Medline
15. de Vet HC, Terwee CB, Knol DL, et al. **When to use agreement versus reliability measures.** *J Clin Epidemiol* 2006;59:1033–39 CrossRef Medline
16. Vallat R. **Pingouin: statistics in Python.** *JOSS* 2018;3:1026 CrossRef
17. White PM, Teasdale EM, Wardlaw JM, et al. **Intracranial aneurysms: CT angiography and MR angiography for detection: prospective blinded comparison in a large patient cohort.** *Radiology* 2001;219:739–49 CrossRef Medline
18. Mine B, Pezzullo M, Roque G, et al. **Detection and characterization of unruptured intracranial aneurysms: comparison of 3T MRA and DSA.** *J Neuroradiol* 2015;42:162–68 CrossRef Medline
19. Algra AM, Lindgren A, Vergouwen MD, et al. **Procedural clinical complications, case-fatality risks, and risk factors in endovascular and neurosurgical treatment of unruptured intracranial aneurysms: a systematic review and meta-analysis.** *JAMA Neurol* 2019;76:282–93 CrossRef

20. Leemans EL, Cornelissen BM, Slump CH, et al. **Comparing morphology and hemodynamics of stable-versus-growing and grown intracranial aneurysms.** *AJNR Am J Neuroradiol* 2019;40:2102–10 CrossRef Medline
21. Chan SH, Wong KS, Woo YM, et al. **Volume measurement of the intracranial aneurysm: a discussion and comparison of the alternatives to manual segmentation.** *J Cerebrovasc Endovasc Neurosurg* 2014;16:358 CrossRef Medline
22. Piotin M, Gailloud P, Bidaut L, et al. **CT angiography, MR angiography and rotational digital subtraction angiography for volumetric assessment of intracranial aneurysms: an experimental study.** *Neuroradiology* 2003;45:404–09 CrossRef Medline
23. D'Argento F, Pedicelli A, Ciardi C, et al. **Intra- and inter-observer variability in intracranial aneurysm segmentation: comparison between CT angiography (semi-automated segmentation software stroke VCAR) and digital subtraction angiography (3D rotational angiography).** *Radiol Med* 2021;126:484–93 CrossRef Medline
24. Lindgren AE, Koivisto T, Björkman J, et al. **Irregular shape of intracranial aneurysm indicates rupture risk irrespective of size in a population-based cohort.** *Stroke* 2016;47:1219–26 CrossRef Medline

Neuroimaging Findings in Retinal Vasculopathy with Cerebral Leukoencephalopathy and Systemic Manifestations

E.S. Hoogeveen, N. Pelzer, I. de Boer, M.A. van Buchem, G.M. Terwindt, and M.C. Kruit



ABSTRACT

SUMMARY: Retinal vasculopathy with cerebral leukoencephalopathy and systemic manifestations is caused by *TREX1* mutations. High-quality systematic follow-up neuroimaging findings have not been described in presymptomatic and symptomatic mutation carriers. We present MR imaging findings of 29 *TREX1* mutation carriers (20–65 years of age) and follow-up of 17 mutation carriers (30–65 years of age). Mutation carriers younger than 40 years of age showed a notable number of punctate white matter lesions, but scan findings were generally unremarkable. From 40 years of age onward, supratentorial lesions developed with long-term contrast enhancement (median, 24 months) and diffusion restriction (median, 8 months). In these lesions, central susceptibility artifacts developed, at least partly corresponding to calcifications on available CT scans. Some lesions ($n = 2$) additionally showed surrounding edema and mass effect (pseudotumors). Cerebellar punctate enhancing lesions developed mainly in individuals older than 50 years of age. These typical neuroimaging findings should aid neuroradiologic recognition of retinal vasculopathy with cerebral leukoencephalopathy and systemic manifestations, which may enable early treatment of manifestations of the disease.

ABBREVIATIONS: Gd = gadolinium; MC = mutation carrier; RVCL-S = retinal vasculopathy with cerebral leukoencephalopathy and systemic manifestations; WML = white matter lesion

Retinal vasculopathy with cerebral leukoencephalopathy and systemic manifestations (RVCL-S) is a dominantly inherited disease caused by mutations in the *TREX1* gene.¹ RVCL-S is histologically characterized by a systemic vasculopathy of medium- and small-caliber arteries as well as veins.^{2,3} Clinically, the disease manifests from 35 to 40 years of age onward and is characterized by vascular retinopathy, Raynaud phenomenon, migraine, and dysfunction of multiple internal organs (including kidney disease, liver disease, anemia, and subclinical hypothyroidism).⁴

So far, few studies have described neuroimaging findings, mostly in symptomatic RVCL-S patients with advanced disease.^{2,5-17} A previous study described 3 types of lesions: 1) focal-to-confluent

nonenhancing white matter lesions (WMLs), 2) WMLs with punctate enhancement, and 3) rim-enhancing lesions with surrounding T2-hyperintensity (edema/gliosis) and/or diffusion restriction.⁹ These lesions with surrounding edema may become large with mass effect and are referred to as pseudotumors.

RVCL-S remains a frequently missed diagnosis, partly due to lack of recognition by radiologists. We systematically studied the neuroimaging characteristics of RVCL-S and describe the frequency and evolution of these findings in a large set of presymptomatic and symptomatic carriers.

MATERIALS AND METHODS

Participants

All family members 18 years of age and older from 3 unrelated Dutch families with RVCL-S were invited to participate in this study. Family members with unknown *TREX1* status were genetically tested. The genetic status of individuals was not disclosed to them, unless specifically requested. The study was approved by the local Medical Ethics Committee. All participants provided written informed consent before inclusion. The study was performed according to guidelines of the Declaration of Helsinki.

Study Design

The study design has been described in a previous publication in which baseline clinical data of the mutation carriers (MCs) was

Received January 18, 2021; accepted after revision April 12.

From the Departments of Radiology (E.S.H., M.A.v.B., M.C.K.) and Neurology (N.P., I.d.B., G.M.T.), Leiden University Medical Center, Leiden, the Netherlands.

G.M. Terwindt and M.C. Kruit shared last authorship.

This study was supported by the Dutch Organization for Scientific Research (GT: VIDI 917-11-31), Stichting Dioraphte (GT: 20010407), and the International Retinal Research Foundation (GT, IdB: IRR-RVCL-S 2019).

The funders had no role in the design or conduct of the study.

Please address correspondence to Mark C. Kruit, MD, PhD, Leiden University Medical Center, Department of Radiology, P.O. Box 9600, 2300 RC Leiden, the Netherlands; e-mail: m.c.kruit@lumc.nl

Indicates open access to non-subscribers at www.ajnr.org

Indicates article with online supplemental data.

<http://dx.doi.org/10.3174/ajnr.A7194>

Table 1: MR imaging markers in *TREX1* MCs at baseline^a

MR Imaging Markers	All (n = 29)	Younger than 40 Years (n = 11)	40 Years or Older (n = 18)
WMLs (mL), median (IQR)	0.97 (0.2–3.9)	0.19 (0.08–0.3)	2.66 (1.0–7.7)
Deep WMLs			
Absent	8 (28)	6 (55)	2 (11)
Punctate lesions	18 (62)	5 (45)	13 (72)
Beginning confluence	2 (7)	0	2 (11)
Large confluent areas	1 (3)	0	1 (6)
Periventricular WMLs			
Absent	19 (66)	9 (82)	10 (55)
Caps and bands	2 (7)	2 (18)	0
Smooth halo	5 (17)	0	5 (28)
Irregular extending in DWM	3 (10)	0	3 (17)
Enlarged perivascular spaces			
None	12 (41)	4 (36)	8 (44)
Mild	14 (48)	6 (55)	8 (44)
Moderate	2 (7)	0	2 (11)
Frequent	1 (3)	1 (9)	0
Central atrophy			
None	24 (83)	11 (100)	13 (72)
Moderate	5 (17)	0	5 (28)
Severe	0	0	0
Cortical atrophy			
None	27 (93)	11 (100)	16 (89)
Moderate	2 (7)	0	2 (11)
Severe	0	0	0
Lacunar infarcts	1 (3)	0	1 (6)

Note.—IQR indicates interquartile range; DWM, deep white matter.

^a Data are No. (%) unless otherwise specified.

presented.⁴ In short, all MCs underwent a baseline MR imaging for research purposes only. Follow-up imaging was acquired only in *TREX1* MCs who were aware of their genetic status for combined clinical and research purposes, using the same MR imaging scanner and scan protocol. In addition, CT scans acquired for clinical purposes during the follow-up period were included in the evaluation. The 3T MR imaging scanning protocol consisted of pre- and postgadolinium 3D-T1-weighted, 3D-FLAIR, DWI, SWI, and T2-weighted scans (Online Supplemental Data).

Measurements

The age of MCs was rounded to the nearest half-decade to protect anonymity.

General features of small-vessel disease were evaluated on baseline scans using predefined criteria (Online Supplemental Data).

As earlier described, active RVCL-S lesions were those with punctiform, linear, or rim gadolinium (Gd) enhancement and/or diffusion restriction.⁹ Number, location, and, if available, behavior across time were recorded. Colocalization of susceptibility artifacts on SWI was recorded. At follow-up, the duration of enhancement and diffusion restriction of lesions was assessed, defined as visible on at least 2 consecutive time points.

RESULTS

Baseline MR images were available in 29 MCs (17 women) with a median age of 51 years (range, 20–65 years). Follow-up MR images were available in 17 MCs (12 women) with a median age of 53 years (range, 30–65 years). The median follow-up time between baseline and the last MR imaging was 29 months (range, 20–36 months) with a median of 2 follow-up scans per MC (range, 1–7 MR images). For 2 MCs, additional CT scans were available.

Cross-Sectional Neuroimaging Characteristics

Baseline characteristics of small-vessel disease are presented in Table 1. Already, 45% of the MCs younger than

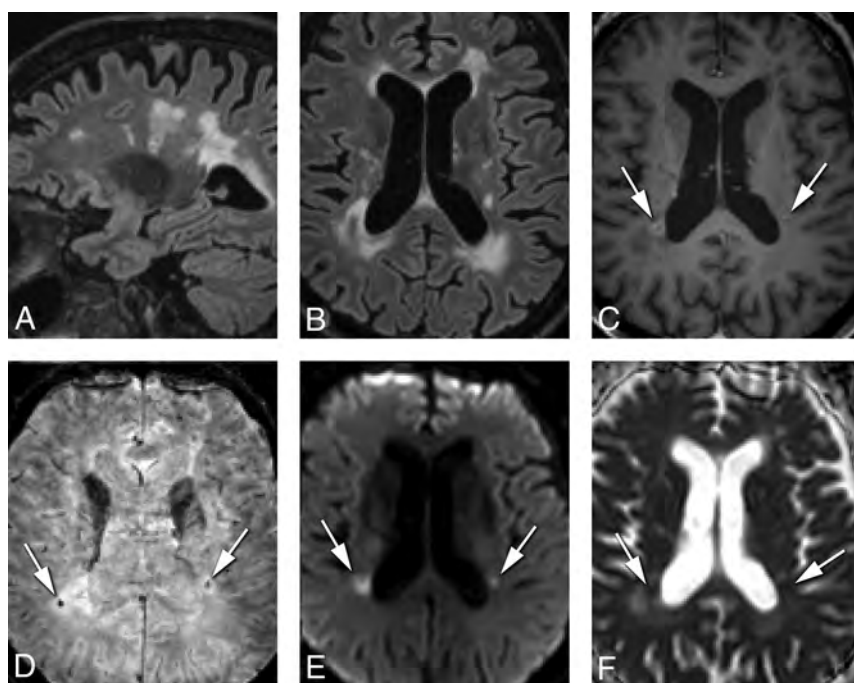


FIG 1. MR imaging characteristics of typical RVCL-S lesions in a 60-year-old man. Periventricular and deep WMLs on sagittal (A) and transverse FLAIR (B) images. On the 3D-T1-weighted Gd image (C), note a rim-enhancing lesion next to the right dorsal horn and a punctiform enhancing lesion next to the left dorsal horn (white arrows). Punctiform SWI artifacts are seen in the center of these lesions (D). High DWI (E) and low ADC signal (F) in the lesions correspond to diffusion restriction.

40 years of age showed punctate WMLs, more than expected for their age. In MCs 40 years of age or older, various degrees of white matter involvement were documented and most WMLs were located in the supratentorial periventricular and deep white matter. In contrast to earlier reports,^{3,9} the corpus callosum was also affected in a few cases with extensive WMLs. In 1 case, WMLs even seemed to have a characteristic Dawson fingers pattern (Fig 1). This MC did not have a clinical diagnosis of multiple sclerosis; however, a radiologically isolated syndrome of multiple sclerosis was not fully excluded because no CSF analyses or spinal MR images were obtained.

In total, 10 MCs showed ≥ 1 supratentorial active lesion at baseline; the youngest was 40 years of age. In these 10 MCs, a total of 44 active supratentorial RVCL-S lesions were identified. Their neuroimaging characteristics are presented in Table 2. All basal ganglia lesions showed punctiform enhancement (Fig 2). Linear or rim-enhancing lesions were mostly next to the frontal ($n = 6$) or dorsal horns ($n = 5$) of the lateral ventricles. Diffusion restriction was observed mainly in the center of lesions, except in a few larger

lesions ($n = 2$) in which restriction was at the periphery. Central punctiform or linear susceptibility artifacts were noted in 68% of lesions (Fig 1). All rim-enhancing lesions showed diffusion restriction and susceptibility artifacts. Although 1 rim-enhancing lesion had some associated edema, no pseudotumors were present at baseline. At baseline, 20 MCs were aware of their mutation status and were tested for vascular retinopathy. Nineteen MCs had signs of retinopathy (mean age, 53 [SD, 8] years). Of these, 10 (53%) had ≥ 1 supratentorial active lesion. The MC without retinopathy (50 years of age) did not have active lesions. Due to ethical concerns, MCs who did not wish to know their mutation status could not be tested for retinopathy ($n = 9$; mean age, 26 [SD, 5] years). None of them had active lesions. At baseline, 11/29 MCs (38%) had features of focal or global brain dysfunction, and 6/29 MCs (21%) had internal organ dysfunction (Online Supplemental Data).

Eight MCs (all older than 50 years of age) had cerebellar punctiform enhancing lesions at baseline (range, 1–16; 75% bilaterally; Fig 2). Eight lesions (20%) had central susceptibility artifacts; none showed diffusion restriction.

Table 2: Characteristics of active RVCL-S lesions at baseline

	All Lesions (N = 44) No. (%)
Size in mm, median (IQR)	4 (2–8)
Location	
Periventricular	12 (27)
Deep/subcortical white matter	17 (39)
Basal ganglia/thalamus	15 (34)
Characteristics of activity	
Enhancement	
Unknown ^a	2 (4)
No enhancement	2 (4)
Punctiform enhancement	24 (55)
Linear enhancement	6 (14)
Rim enhancement	10 (23)
Diffusion restriction	22 (50)
Other characteristics	
T2-hyperintensity	33 (75)
Susceptibility artifacts	30 (68)
Mass effect	0

^aIn 1 MC, no contrast was administered due to reduced kidney function. Lesions in this MC showed diffusion restriction.

Follow-up Neuroimaging Characteristics

In 5 MCs (4 women; median age, 52 years; range, 30–60 years), no active supratentorial lesions were observed at all, and 1 MC did not develop new lesions during follow-up. Of these, 4/6 MCs had signs of vascular retinopathy. In 11/17 (65%) MCs, a total of 28 new supratentorial lesions developed (Online Supplemental Data). All 11 MCs had signs of vascular retinopathy. During follow-up, 11/17 MCs (65%) had features of focal or global brain dysfunction and 8/17 MCs (47%) had internal organ dysfunction (Online Supplemental Data). We observed long-term enhancement in 46/72 (64%) lesions and long-term diffusion restriction in 26/72 (36%) lesions. In these lesions, contrast enhancement persisted for a median of 24 months (range, 2–37 months), and diffusion restriction, for 8 months (range, 3–32 months). Figure 3 illustrates long-term enhancement and diffusion restriction during 31 months of follow-up. Most lesions appeared at a certain time point, remained unchanged for a period of time, and eventually became smaller and disappeared with or without a residual lesion of gliosis and/or SWI artifacts. Six lesions were visually documented to increase in size.

Almost exclusively, lesions located in the deep and periventricular white matter became linear or rim-enhancing lesions, while the enhancement of lesions in the basal ganglia remained punctiform. Two MCs (12%) developed a rim-enhancing mass lesion with surrounding edema (pseudotumor) during follow-up (Figs 4 and 5). Both MCs received corticosteroid treatment after the first evidence of the pseudotumor, after which the pseudotumor gradually diminished in size (Fig 5). In 1 of these MCs, we noted, on consecutively acquired CT scans, the development of a punctiform calcification corresponding to SWI artifacts as long as 31 months after the first evidence of the

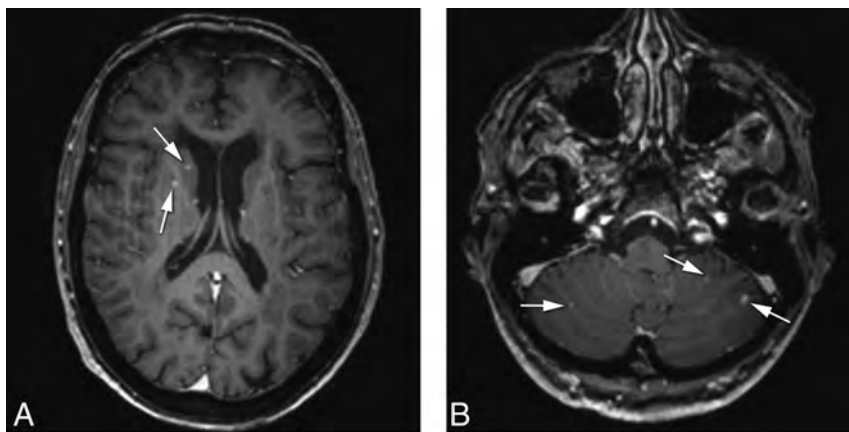


FIG 2. An example of punctiform enhancing lesions in the basal ganglia and cerebellum in a 60-year-old woman. A, Punctiform enhancing lesions (white arrows) in the putamen and caudate head on the right. B, Bilateral punctiform enhancing cerebellar lesions (white arrows).

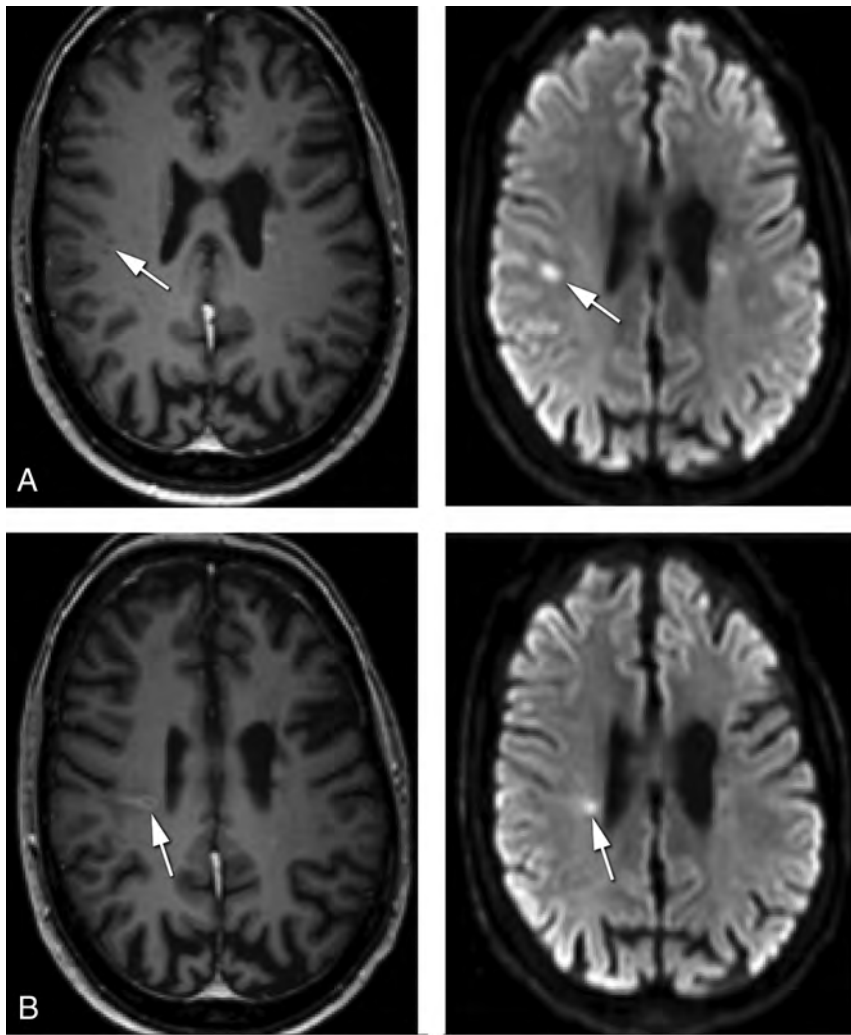


FIG 3. Long-term enhancement and diffusion restriction of a lesion during 31 months of follow-up in a 55-year-old woman. 3D-T1-weighted Gd and diffusion-weighted images acquired at baseline (A) show a punctiform enhancing lesion on the right with subtle diffusion restriction (*white arrows*), and after 31 months (B), the images show that the lesion migrates to the right ventricle (*white arrows*). The lesion is now linearly enhancing with partial rim enhancement and diffusion restriction (ADC with low values is not shown).

pseudotumor (Fig 5 and Online Supplemental Data). In 1 other MC, additional CT images were available in which multiple punctiform calcifications corresponded with part of the susceptibility artifacts on the SWI (data not shown).

Five MCs showed an increase in the number of enhancing punctiform cerebellar lesions. Two MCs developed a small rim-enhancing cerebellar lesion with associated T2 and FLAIR hyperintensity; of these, 1 also showed susceptibility artifacts. None of the cerebellar lesions showed diffusion restriction.

DISCUSSION

This study systematically reports neuroimaging findings in a group of MCs with RVCL-S in a broad age range, enabling us to describe the presentation and natural history of both subtle and more obvious MR imaging features of the disease. Recognition of these

imaging features and the evolution of lesions with time may help to diagnose RVCL-S earlier.

In MCs younger than 40 years, who were mostly clinically asymptomatic, 45% had nonspecific supratentorial punctiform WMLs, remarkable for this age. One recent study also reported WMLs in 5 patients with RVCL-S younger than 40 years of age with comparable WML volumes.¹⁷ Nonspecific WMLs become more apparent in individuals older than 40 years of age. While some MCs still have only discrete punctate WMLs, some develop more extensive confluent WMLs.

Starting from 40 years of age, supratentorial “active” lesions (with contrast enhancement and/or diffusion restriction) may develop and become more prevalent with increasing age. These active lesions were present in 50% of MCs in the 40 years and older age group. Most lesions were relatively small (± 4 mm) and were equally distributed in the periventricular white matter, deep white matter, and basal ganglia, with rim-enhancing lesions mainly found in the deep and periventricular white matter. Before, only punctiform and rim-enhancing lesions were described as characteristic of RVCL-S;⁹ however linear enhancing lesions can also be observed.

Follow-up MR imaging demonstrated that many active lesions remain stable or decrease in size and may show long-term persistence of enhancement and diffusion restriction. A general pattern is that RVCL-S lesions first show contrast enhancement as well as diffusion

restriction, and while the diffusion restriction fades away after a few months, the contrast enhancement can persist for up to 2 years. This is in accordance with a recent report in 6 symptomatic patients with RVCL-S, in which lesions showed a mean duration of diffusion restriction of 5 months and contrast enhancement of 20 months.¹⁶ Why RVCL-S lesions show such long-term enhancement and diffusion restriction is not fully understood. Histopathologic findings in RVCL-S lesions show focal areas of tissue inflammation and necrosis, which resemble findings in delayed radiation necrosis. In RVCL-S, this is assumed to result from endothelial dysfunction with blood-brain barrier dysfunction and chronic ischemia.⁹ The chronic nature of these focal areas of tissue inflammation and necrosis in RVCL-S may explain the long-term enhancement and diffusion restriction. Few lesions grew during follow-up, and in some lesions, a slow “migration” was observed, leaving earlier affected tissue behind as parenchymal loss/gliosis (Fig 3). In 2 cases, a pseudotumor

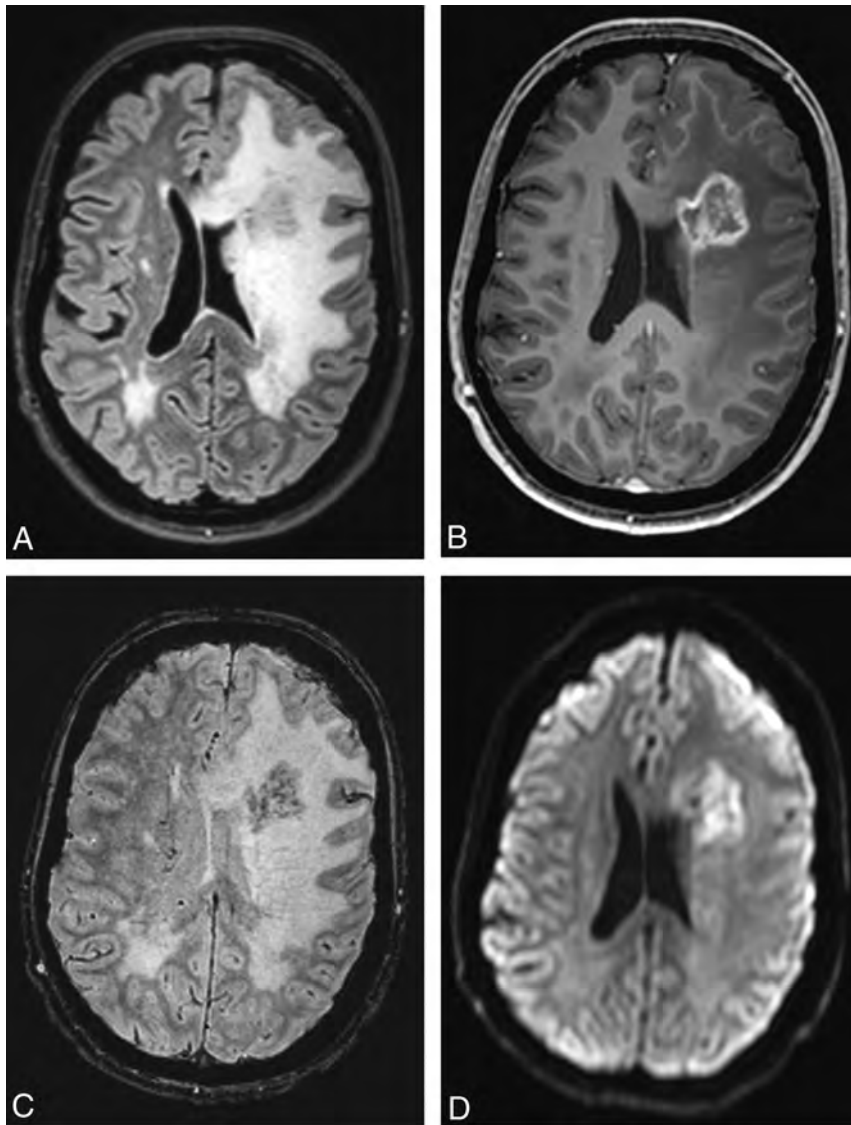


FIG 4. Imaging characteristics of a pseudotumor in a 45-year-old woman. Note a rim-enhancing lesion of 30 mm, craniolateral to the left frontal horn, with multiple dotlike susceptibility artifacts and diffusion restriction in the center of the lesion with extensive surrounding vasogenic edema with mass effect (A, FLAIR. B, 3DT1 Gd. C, SWI. D, DWI).

developed, which is much less frequent than previously reported.⁹ This difference might be related to the younger age and fewer symptomatic cases in our study compared with previous literature.

RVCL-S was associated with multiple, bilateral, mostly punctiform enhancing cerebellar lesions, some with central susceptibility artifacts. Infratentorial lesions were also reported in a previous study.¹⁶ A novel finding in this study is that these lesions start to develop with more advanced disease, around 50 years of age. Cerebellar lesions tend to progress in number, not so much in size. Only a few solitary cerebellar lesions grew in size with rim enhancement.

Up to 68% of active RVCL-S lesions were associated with susceptibility artifacts on the SWI scan, which may relate to extravasated blood products (hemosiderin), calcifications, or prominent vascular (venous) structures. Previously, RVCL-S was shown to

be associated with parenchymal calcification.^{9,15} In Fig 5, we show that focal calcifications may develop some time after the formation of an active RVCL-S lesion, in this case, as long as 31 months after the first evidence of the RVCL-S lesion. Calcifications may occur as dystrophic changes in an area of chronic parenchyma damage or as a result of vessel injury. This possibility was shown in a recent histopathologic study, in which focal calcifications associated with WMLs and granular calcifications in the walls of several vessels were described.¹⁸ In the current study, punctiform SWI artifacts were also seen in the basal ganglia and cerebellum. Proof of calcifications in the basal ganglia and cerebellar hemispheres would be a new finding in RVCL-S.⁹

In the past, neuroimaging findings of RVCL-S have been mistaken for multiple sclerosis, vasculitis, or neoplasms, and unnecessary brain biopsies have been performed in some cases.^{7,11} Diffusion restriction may be falsely interpreted as a sign of ischemia or infarction, and the features of disrupted blood-brain barrier somewhat resemble late radiotherapeutic effects and necrosis. However, the long-lasting contrast enhancement and diffusion restriction of RVCL-S lesions have not been reported in any other brain disease.

CONCLUSIONS

Although some neuroimaging characteristics in RVCL-S may be observed in other small-vessel diseases as well, the pattern and evolution of neuroimaging findings are typical for RVCL-S.

Mainly the long-term contrast enhancement with accompanying long-term diffusion restriction of RVCL-S lesions characterizes the disease. These findings, together with clinical features, should alert radiologists to consider the diagnosis of RVCL-S and enable early treatment of manifestations of the disease.

Disclosures: Irene de Boer—RELATED: Grant: Stichting Dioraphte and International Retinal Research Foundation*; UNRELATED: Royalties: UpToDate. Gisela M. Terwindt—RELATED: Grant: Stichting Dioraphte and International Retinal Research Foundation*; UNRELATED: Royalties: UpToDate. *Money paid to the institution.

REFERENCES

- Richards A, van den Maagdenberg AM, Jen JC, et al. C-terminal truncations in human 3'-5' DNA exonuclease TREX1 cause autosomal dominant retinal vasculopathy with cerebral leukodystrophy. *Nat Genet* 2007;39:1068–70 CrossRef Medline

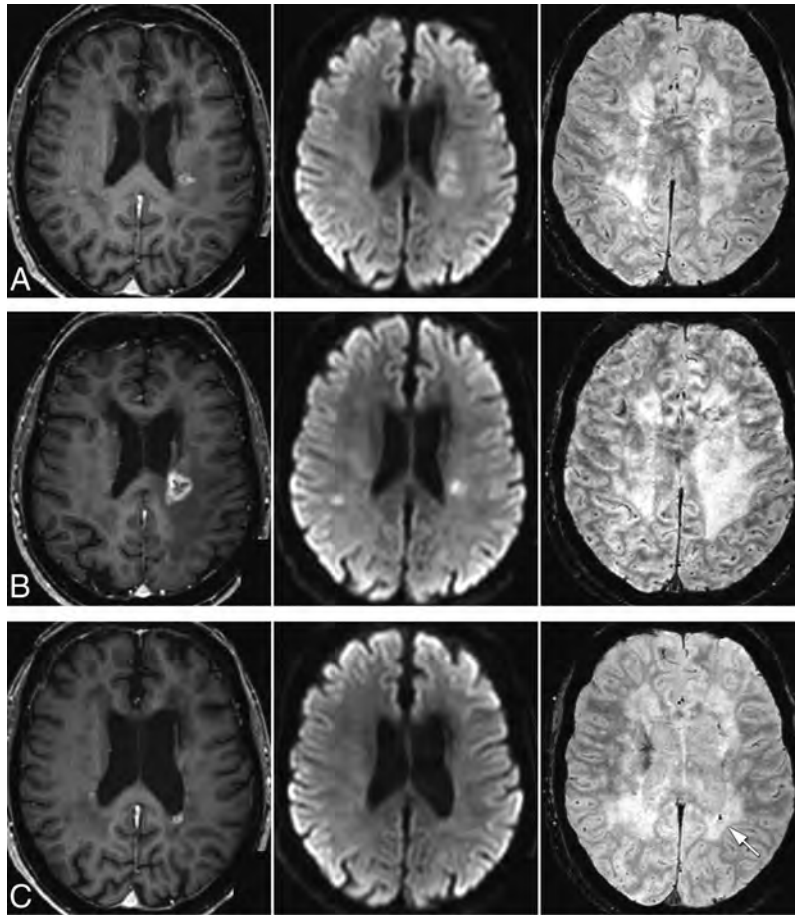


FIG 5. Imaging characteristics and evolution of a pseudotumor in a 60-year-old woman. 3D-T1-weighted Gd, diffusion-weighted, and SWI at baseline (A) show a rim-enhancing lesion with subtle diffusion restriction next to the left dorsal horn with some surrounding edema without mass effect. There were no abnormalities on the SWI. After 10 months (B), the lesion grows with new compression due to edema. Diffusion restriction is still noted, but no SWI abnormalities. After corticosteroid treatment, the enhancing lesion slowly diminished in size, and diffusion restriction disappeared at 31 months (C). A new SWI artefact in the center of the lesion is now noted (white arrow), corresponding to a focal calcification on CT acquired at 32 months, while at 15 months, no calcifications were present (Online Supplemental Data).

2. Jen J, Cohen AH, Yue Q, et al. **Hereditary endotheliopathy with retinopathy, nephropathy, and stroke (HERNS).** *Neurology* 1997;49:1322–30 CrossRef Medline
3. Kolar GR, Kothari PH, Khanlou N, et al. **Neuropathology and genetics of cerebroretinal vasculopathies.** *Brain Pathol* 2014;24:510–18 CrossRef Medline
4. Pelzer N, Hoogeveen ES, Haan J, et al. **Systemic features of retinal vasculopathy with cerebral leukoencephalopathy and systemic manifestations: a monogenic small vessel disease.** *J Intern Med* 2019;285:317–13 CrossRef Medline
5. Dhamija R, Schiff D, Lopes MB, et al. **Evolution of brain lesions in a patient with TREX1 cerebroretinal vasculopathy.** *Neurology* 2015;85:1633–34 CrossRef Medline
6. Terwindt GM, Haan J, Ophoff RA, et al. **Clinical and genetic analysis of a large Dutch family with autosomal dominant vascular**

retinopathy, migraine and Raynaud's phenomenon. *Brain* 1998;121:303–16 CrossRef Medline

7. Weil S, Reifenberger G, Dudel C, et al. **Cerebroretinal vasculopathy mimicking a brain tumor: a case of a rare hereditary syndrome.** *Neurology* 1999;53:629–31 CrossRef Medline
8. Mateen FJ, Krecke K, Younge BR, et al. **Evolution of a tumor-like lesion in cerebroretinal vasculopathy and TREX1 mutation.** *Neurology* 2010;75:1211–13 CrossRef Medline
9. Stam AH, Kothari PH, Shaikh A, et al. **Retinal vasculopathy with cerebral leukoencephalopathy and systemic manifestations.** *Brain* 2016;139:2909–22 CrossRef Medline
10. Monroy-Jaramillo N, Ceron A, Leon E, et al. **Phenotypic variability in a Mexican Mestizo family with retinal vasculopathy with cerebral leukodystrophy and TREX1 mutation p.V235Gfs*6.** *Rev Invest Clin* 2018;70:68–75 CrossRef Medline
11. Hardy TA, Young S, Sy JS, et al. **Tumefactive lesions in retinal vasculopathy with cerebral leukoencephalopathy and systemic manifestations (RVCL-S): a role for neuroinflammation?** *J Neurol Neurosurg Psychiatry* 2018;89:434–35 CrossRef
12. Carra-Dalliere C, Ayrignac X, Prieto-Morin C, et al. **TREX1 mutation in leukodystrophy with calcifications and persistent gadolinium-enhancement.** *Eur Neurol* 2017;77:113–14 CrossRef Medline
13. Gutmann DH, Fischbeck KH, Sergott RC. **Hereditary retinal vasculopathy with cerebral white matter lesions.** *Am J Med Genet* 1989;34:217–20 CrossRef Medline
14. Grand MG, Kaine J, Fulling K, et al. **Cerebroretinal vasculopathy: a new hereditary syndrome.** *Ophthalmology* 1988;95:649–59 CrossRef Medline
15. Raynowska J, Miskin DP, Pramanik B, et al. **Retinal vasculopathy with cerebral leukoencephalopathy (RVCL): a rare mimic of tumefactive MS.** *Neurology* 2018;91:e1423–28 CrossRef Medline
16. Hedderich DM, Lummel N, Deschauer M, et al. **Magnetic resonance imaging characteristics of retinal vasculopathy with cerebral leukoencephalopathy and systemic manifestations.** *Clin Neuroradiol* 2020;30:229–36 CrossRef Medline
17. Ford AL, Chin VW, Fellah S, et al. **Lesion evolution and neurodegeneration in RVCL-S: a monogenic microvasculopathy.** *Neurology* 2020;95:e1918–31 CrossRef Medline
18. Saito R, Nozaki H, Kato T, et al. **Retinal vasculopathy with cerebral leukodystrophy: clinicopathologic features of an autopsied patient with a heterozygous TREX1 mutation.** *J Neuropathol Exp Neurol* 2019;78:181–86 CrossRef

Absence of Meckel Cave: A Rare Cause of Trigeminal Neuralgia

 A. Jain,  M.S. Muneer,  L. Okromelidze,  R. McGeary,  S.K. Valluri,  A.A. Bhatt,  V. Gupta,  S.S. Grewal,  W.P. Cheshire,  E.H. Middlebrooks, and  S.J.S. Sandhu



ABSTRACT

SUMMARY: Trigeminal neuralgia is a debilitating condition with numerous etiologies. In this retrospective case series, we report a cohort of patients with a rarely described entity, absence of Meckel cave, and propose this as a rare cause of trigeminal neuralgia. A search of the electronic medical record was performed between 2000 and 2020 to identify MR imaging reports with terms including “Meckel’s cave” and “hypoplasia,” “atresia,” “collapse,” or “asymmetry.” Images were reviewed by 2 blinded, board-certified neuroradiologists. Seven cases of the absence of Meckel cave were identified. Seven patients (100%) had ipsilateral trigeminal neuralgia and ipsilateral trigeminal nerve atrophy, suggesting an association between absence of Meckel cave and trigeminal neuralgia. Absence of Meckel cave is a rare entity of unknown etiology, with few existing reports that suggest the possibility of an association with trigeminal neuralgia. Its recognition may have important implications in patient management. Future studies and longitudinal data are needed to assess treatment outcomes and added risks from surgical intervention in these patients.

ABBREVIATION: TN = trigeminal neuralgia

Trigeminal neuralgia (TN) is a debilitating condition resulting in a severely compromised quality of life in affected people.¹ It more commonly affects women and has an overall prevalence of 0.07% of the population.² Treatment of TN revolves around accurate identification of the potential etiology. Advances in neuroimaging, particularly MR imaging, have played a crucial role in assessing various structural causes of TN, such as neurovascular compression, compressive mass, or multiple sclerosis.³ Depending on the suspected etiology, various treatment options may be used, including medication, neurovascular decompression, stereotactic radiosurgery, or percutaneous balloon compression.

A rarely reported entity, absence of Meckel cave, has been described in a few patients with TN, including 2 case reports and 3 patient case series.⁴⁻⁶ Most important, there are only a few reports, to our knowledge, on the absence of Meckel cave in patients other than those with TN. This retrospective study aimed to demonstrate the potential relationship of an absent Meckel

cave with TN versus without TN, which may have important diagnostic and treatment implications.

MATERIALS AND METHODS

Study Population and Data Collection

This retrospective observational study was approved by the Mayo Clinic institutional review board. MR imaging brain radiology reports were searched from 2000 to 2020. Search terms included “Meckel’s cave” AND “collapse” OR “atresia” OR “hypoplasia” OR “atretic” or “asymmetry.” The search identified a total of 169 unique records. The search results were manually refined after reading all MR imaging brain reports thoroughly to determine whether patients had any relevant abnormality of a Meckel cave that warranted imaging review. Those with irrelevant abnormalities reported (eg, Meckel cave meningocele) were dismissed, leaving 24 patients with reports that potentially met the inclusion criteria for further imaging review. Additionally, relevant clinical data were collected, including basic demographics, medical and surgical history, and outcomes.

Imaging

All patients underwent MR imaging (3 patients on a 1.5T and 4 patients on a 3T MR imaging scanner). One patient had imaging performed only at an outside facility before any intervention at our institution. All patients had imaging with and without intravenous gadolinium contrast. Six patients had

Received January 20, 2021; accepted after revision April 20.

From the Departments of Radiology (A.J., M.S.M., L.O., R.M., S.K.V., A.A.B., V.G., E.H.M., S.J.S.S.), Neurosurgery (S.S.G., E.H.M.), and Neurology (W.P.C.), Mayo Clinic, Jacksonville, Florida.

A. Jain and M.S. Muneer contributed equally to this work.

Please address correspondence to Erik H. Middlebrooks, MD, Departments of Radiology and Neurosurgery, Mayo Clinic, 4500 San Pablo Rd, Jacksonville, FL 32224; e-mail: middlebrooks.erik@mayo.edu; @EMiddlebrooksMD

 Indicates article with online supplemental data.

<http://dx.doi.org/10.3174/ajnr.A7205>

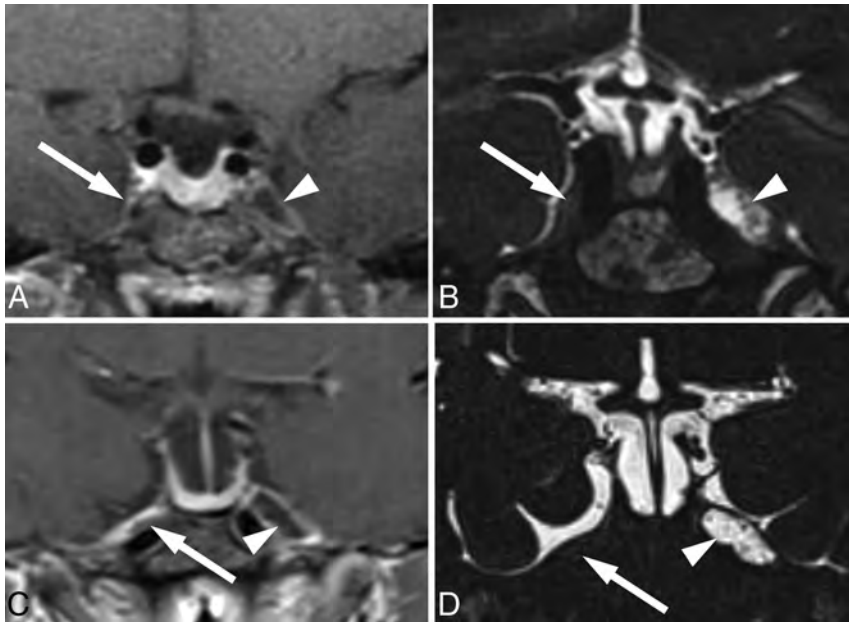


FIG 1. Postcontrast coronal T1- (A) and coronal T2-weighted SPACE images (B) in 1 patient show the absence of Meckel cave (arrow) compared with the normal side (arrowhead). In another patient, postcontrast coronal T1- (C) and coronal T2-weighted SPACE images (D) show absence of Meckel cave (arrow) compared with the normal side (arrowhead).

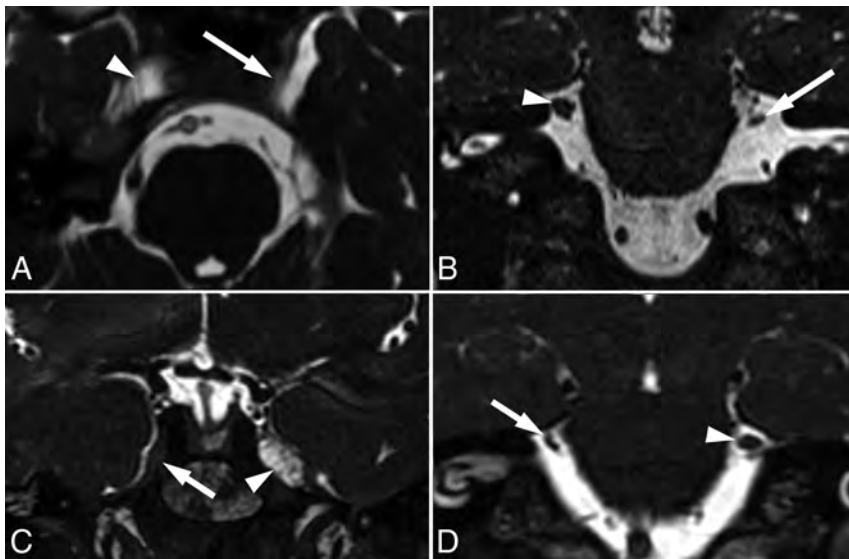


FIG 2. A, Axial CISS image shows absence of Meckel cave on the left (arrow) compared with the normal right Meckel cave (arrowhead). B, Coronal CISS image in the same patient shows atrophy of the left trigeminal nerve (arrow) compared with the normal nerve on the right (arrowhead). In another patient, coronal CISS image (C) shows absence of Meckel cave on the right (arrow) compared with the normal left Meckel cave (arrowhead). D, Coronal CISS image in the same patient shows atrophy of the right trigeminal nerve (arrow) compared with the normal nerve on the left (arrowhead).

dedicated high-resolution imaging of the posterior fossa that included a high-resolution, heavily T2-weighted sequence (eg, CISS, FIESTA, sampling perfection with application-optimized contrasts by using different flip angle evolution [SPACE sequence; Siemens]).

Image Analysis

All patients with a reported Meckel cave abnormality had their MR imaging independently re-evaluated by 2 board-certified neuroradiologists who were blinded to the clinical information for confirmation of the absence of a Meckel cave and the presence of any additional apparent cause for trigeminal neuralgia, such as neurovascular compression, mass lesion, brainstem lesion, and so forth. A third board-certified neuroradiologist was available to decide discrepancies. Absence of Meckel cave was defined by a complete absence of fluid signal on T2-weighted images. We also evaluated associated congenital or acquired abnormalities along the course of cranial nerve V and its major branches, such as skull base abnormalities, atrophy or absence of V2–V3 branches, abnormality in the superior orbital fissure along the course of V1, or atrophy of muscles of mastication. The electronic medical records of included patients were screened for demographics and clinical notes, including the presence of a trigeminal neuralgia diagnosis as well as trigeminal nerve atrophy on imaging. Cross-sectional diameter and the area of each trigeminal nerve were measured in an oblique coronal plane that was aligned perpendicular to the axis of each nerve. The nerve was measured at the midpoint of the cisternal segment of the nerve.

Statistical Analysis

Simple descriptive statistics such as measures of central tendency and dispersion were calculated using SPSS, Version 20 (IBM). When we compared the mean difference of 2 continuous variables, normality testing (eg, the Kolmogorov-Smirnov test) was run and then the appropriate nonparametric and parametric test was used (eg, paired *t* test).

RESULTS

Seven patients were identified with an absent Meckel cave (Fig 1) confirmed on MR imaging. Summary information

is de-tailed in the Online Supplemental Data. There were 7 women, with a mean age of 46.6 (SD, 14.1) years (range, 36–80 years). Of the 7 patients with an absent Meckel cave, 5 Meckel caves were absent on the right (71.4%) and 2 were absent on the left (28.6%). There was also trigeminal nerve atrophy (Fig 2 and

Online Supplemental Data) on the same side as the absent Meckel cave in all 7 patients (100%). The mean cross-sectional area of the trigeminal nerve ipsilateral to the side of the absent Meckel cave (mean, 3.9 [SD, 0.9] mm²) was less than the contralateral one (mean, 6.4 [SD, 1.5] mm²), and this difference was found to be statistically significant on a paired *t* test (*P* value < .001). Most important, no other plausible structural causes of TN, such as neurovascular compression, were found in these patients. In all cases, the main branches of the trigeminal nerve (V2–V3) were present and symmetric. Because V1 is commonly not directly visualized on standard MR imaging, evaluation was limited, but no appreciable abnormality was present in the superior orbital fissure.

TN was present in all 7 patients (100%) and was ipsilateral to the absent Meckel cave in all 7 patients (100%). One patient initially presented with facial numbness in a V1 and V2 distribution, which subsequently developed into trigeminal neuralgia in the ensuing years, with progressive nerve atrophy compared with previous scans. There were 2 patients with a reported history of idiopathic intracranial hypertension. One patient was reported to have idiopathic intracranial hypertension and Bell palsy during pregnancy 18 years before the evaluation for TN (11 years before the TN onset) but had no evidence of elevated intracranial pressure at the time of our evaluation. A second patient had a reported history of presumptive idiopathic intracranial hypertension based on clinical symptoms before her evaluation at our institution, but there was no evidence of papilledema on subsequent fundoscopic examination by ophthalmology and no evidence of elevated opening pressure.

Six of 7 (86%) patients were naïve to any interventional treatment technique for TN at the time of identification of the absent Meckel cave. One patient had undergone prior microvascular decompression at an outside institution, and preoperative imaging was unavailable. TN was initially treated medically in all patients using carbamazepine or gabapentin. In some patients, other medications such as tramadol, topiramate, or other benzodiazepines were used. Six patients (85.7%) had follow-up within the 6 months of diagnosis, with 4 having improvement (66.7%) and 2 having no improvement (33.3%) with medical therapy. Three of the 4 with initial improvement subsequently had a recurrence of symptoms and were considered medication refractory.

After the initial imaging at our institution, 1 patient was treated with microvascular decompression for suspected neurovascular compression with negative findings on imaging due to typical clinical symptoms. Additionally, 1 patient underwent rhizotomy, and 1 had stereotactic radiosurgery. Both patients who underwent surgery had no appreciable neurovascular compression found on exploration (1 before presentation at our facility and 1 at our facility). Both microvascular decompressions ultimately failed after an initial minor improvement. One patient had subsequent balloon compression, and 1 had subsequent stereotactic radiosurgery, which were safely performed. The patient with balloon compression had a positive response to therapy. The patient treated with postoperative stereotactic radiosurgery was lost to follow-up. The patient treated with stereotactic radiosurgery alone had an adequate response, while the patient treated with the rhizotomy had recurrence of TN symptoms.

DISCUSSION

Absence of a Meckel cave is an uncommon imaging finding associated with TN. A few reported cases of this entity have been shown in patients with TN, including 1 case report and a series of 3 cases.^{4–6} Our case series presents 7 patients with absence of a Meckel cave, in which all subjects had atrophy of the ipsilateral trigeminal nerve and ipsilateral TN. No patients with an absent Meckel cave were asymptomatic. Recognition of this entity as a potential cause of TN may have important diagnostic and treatment considerations.

The Meckel cave is a CSF-filled space approximately 4 × 9 mm wide at its opening and 15 mm in length, located in the middle cranial fossa, serving as a channel for the trigeminal nerve between the prepontine cistern and the cavernous sinus, housing the Gasserian ganglion.⁷ Neuroimaging of the Meckel cave is frequently performed to identify a potential cause of trigeminal neuropathy. The Meckel cave is involved in a variety of congenital, infectious, inflammatory, vascular, and neoplastic pathologies.^{7,8}

Absence of a Meckel cave is poorly understood and rarely reported. Before our series, few reported cases of an absent Meckel cave have been associated with ipsilateral TN without any prior surgical intervention on the cave.^{4–6} A hypoplastic or absent Meckel cave has been occasionally described in the setting of congenital hypoplasia or aplasia of the trigeminal nerve; however, these cases have some key differences from our patients.^{9,10} In contrast to our cohort, patients in these prior reports had symptoms that typically presented in early life and manifested as trigeminal neuropathy rather than neuralgia—commonly anesthesia in the trigeminal distribution and resulting neurotrophic keratitis.^{9,10} Additionally, 1 patient in our cohort had progressive symptoms correlated with progressive atrophy of the trigeminal nerve, which suggest a potentially acquired etiology. In our institutional records, we found no descriptions of Meckel cave absence or its descriptive equivalents—such as total collapse or aplasia—in subjects without TN or contralateral TN. The evidence thus far, however scant, points to an etiologic implication of this entity in TN. Additionally, the otherwise normal structure and function of the trigeminal nerve and lack of other associated orofacial developmental abnormalities strongly suggest that absence or marked diminution of a Meckel cave is either an acquired contraction or a primary failure of establishment of the subarachnoid space in the cave. None of our patients had a history of craniofacial herpes zoster, meningitis, or other diagnosed inflammatory process. Additionally, only 1 patient had a history of prior intracranial surgery—unfortunately, lack of available preoperative imaging makes it uncertain whether absence of Meckel cave was present before surgery. Most important, the operative note reports that there was an atrophic nerve with no evidence of neurovascular compression. Patients were all also naïve to any direct procedure on the trigeminal nerve or ganglion for TN relief. The onset of TN was also insidious, as typically seen in TN secondary to vascular impingement.

Regarding the alternative possibility of primary failure of development of the CSF space in the cave, the onset of TN late in life may be due to changes in dural compliance and thickness, leading to progressive compression of the ganglion with aging.¹¹ Experimental constriction of the peripheral nerves has been shown to result in cytokine-mediated sensitization of the dorsal

root ganglion by up-regulation of voltage-gated sodium channels. A similar mechanism has been suspected in compressive radiculopathy by herniated discs.¹² The arachnoid membrane continues from the posterior fossa into the Meckel cave, forming a CSF compartment within the cave, and extends along the nerve rootlets anteriorly to the Gasserian ganglion. The presence of surrounding CSF appears to play a critical role in the physiology and health of the sensory ganglia. Dorsal root ganglia of the spinal cord are also surrounded by a thin layer of CSF carried along the perineural sheath, and transport of intrathecal India ink particles and gene vector particles to the dorsal root ganglia is well-established.¹³

Schwann cell damage, loss of peripheral myelin, and endothelial and smooth muscle degeneration with increased collagen in the wall of the trigeminal arterioles have all been reported in patients with TN.¹⁴ Loss of surrounding CSF could lead to impairment of normal myelin and vascular repair mechanisms in the ganglia. CSF may be a normal pathway for clearance of proinflammatory cytokines such as tumor necrosis factor- α , which are known to upregulate voltage-gated sodium channels leading to the increased or ectopic firing of ganglionic neurons.¹⁵ Collapse of a Meckel cave is known to occur in spontaneous intracranial hypotension secondary to CSF hypovolemia. Facial pain and dysesthesia commonly accompany headache in spontaneous intracranial hypotension. It is entirely conceivable that the loss of CSF in a Meckel cave could play a similar role in developing trigeminal nerve hypersensitivity in spontaneous intracranial hypotension.

Our cohort had a mean age of 46.6 years, and all were women. This is in agreement with the previous reported mean ages of patients with classic TN (53 years) and secondary TN (43 years).^{16,17} Likewise, the incidence of TN is higher in women.^{18,19} The clinical presentation was similar to the more common etiologies. All patients presented with the classic electric shock-like pain along the nerve distribution and had various stimuli beyond the region of pain triggering their episodes. Most interesting, 1 patient presented with symptoms of trigeminal neuropathy with facial numbness along the V2 and V3 distributions 6 years before development of TN. On imaging, this patient had progressive trigeminal nerve atrophy across the time course of developing TN symptoms.

TN in these cases appeared to be mostly refractory to medical and procedural treatment. Microvascular decompression was not helpful in alleviating TN, and a better symptomatic response was observed after balloon compression or stereotactic radiosurgery. It is conceivable that inflation of the balloon might restore the CSF space in a Meckel cave.

Several limitations are noteworthy. The small number of patients and retrospective nature of the study limit the ability to determine causation of the absence of a Meckel cave with TN, though 100% of patients did have TN. Additionally, few surgical interventions were performed with no randomization or blinding. Thus, appropriate management of these patients cannot be completely determined, and future studies will be needed to better understand treatment outcomes. There were also limitations with imaging, such as lack of standardized protocol with 1 patient not having high-resolution CISS-like sequence or the equivalent.

CONCLUSIONS

Absence of Meckel cave is a rare entity associated with TN. Our study highlights 7 cases, adding to the previous literature of 4 cases. Despite our findings, the etiology remains unknown, and further studies and longitudinal data are needed to assess various treatment outcomes and added risks in patients. Importantly, the decision to pursue balloon compression of the ganglion versus radiation or microvascular decompression should be carefully considered, and neuroimaging plays a vital role in diagnosing this rare entity.

Disclosures: Erik H. Middlebrooks—UNRELATED: Consultancy: Varian Medical Systems Inc, Boston Scientific Corp. Sanjeet S. Grewal—UNRELATED: Consultancy: Medtronic, Boston Scientific Corp.

REFERENCES

1. Adams H, Pendleton C, Latimer K, et al. **Harvey Cushing's case series of trigeminal neuralgia at the Johns Hopkins Hospital: a surgeon's quest to advance the treatment of the 'suicide disease.'** *Acta Neurochir (Wien)* 2011;153:1043–50 CrossRef Medline
2. Cruccu G. **Trigeminal neuralgia.** *Continuum (Minneapolis)* 2017;23:396–420 CrossRef Medline
3. Cruccu G, Gronseth G, Alksne J, et al. **European Federation of Neurological Societies. AAN-EFNS guidelines on trigeminal neuralgia management.** *Eur J Neurol* 2008;15:1013–28 CrossRef Medline
4. Cleary DR, Handwerker J, Ansari H, et al. **Three cases of trigeminal neuralgia with radiographic absence of Meckel's cave.** *Stereotact Funct Neurosurg* 2019;97:249–54 CrossRef Medline
5. Sundararajan S, Loevner LA, Mohan S. **Mandibular myalgia and miniscule Meckel's caves.** *J Otorhinolaryngol Relat Spec* 2018;80:103–07 CrossRef Medline
6. Kanchan Kumar A, Rehan B, et al. **Absent Meckel's cave on MRI, in a clinically diagnosed case of trigeminal neuralgia: a very rare case report.** *Pakistan Journal of Radiology* 2020;30:293–95
7. Malhotra A, Tu L, Kalra VB, et al. **Neuroimaging of Meckel's cave in normal and disease conditions.** *Insights Imaging* 2018;9:499–510 CrossRef Medline
8. Aaron GP, Illing E, Lambertsens Z, et al. **Enlargement of Meckel's cave in patients with spontaneous cerebrospinal fluid leaks.** *Int Forum Allergy Rhinol* 2017;7:421–24 CrossRef Medline
9. Milne AD, Chui L, Mishra AV, et al. **Unilateral hypoplasia of the trigeminal ganglion.** *Can J Ophthalmol* 2005;40:772–74 CrossRef Medline
10. Kamal SM, Riccobono K, Kwok A, et al. **Unilateral pediatric neurotrophic keratitis due to congenital left trigeminal nerve aplasia with PROSE (prosthetic replacement of the ocular surface ecosystem) treatment.** *Am J Ophthalmol Case Rep* 2020;20:100854 CrossRef Medline
11. Zwirner J, Scholze M, Waddell JN, et al. **Mechanical properties of human dura mater in tension: an analysis at an age range of 2 to 94 years.** *Sci Rep* 2019;9:16655 CrossRef Medline
12. Wang C, Yu X, Yan Y, et al. **Tumor necrosis factor- α : a key contributor to intervertebral disc degeneration.** *Acta Biochim Biophys Sin (Shanghai)* 2017;49:1–13 CrossRef Medline
13. Wang X, Wang C, Zeng J, et al. **Gene transfer to dorsal root ganglia by intrathecal injection: effects on regeneration of peripheral nerves.** *Mol Ther* 2005;12:314–20 CrossRef Medline
14. Marinković S, Todorović V, Gibo H, et al. **The trigeminal vasculature pathology in patients with neuralgia.** *J Headache Pain* 2007;47:1334–39 CrossRef Medline
15. Chen X, Pang RP, Shen KF, et al. **TNF- α enhances the currents of voltage gated sodium channels in uninjured dorsal root ganglion neurons following motor nerve injury.** *Exp Neurol* 2011;227:279–86 CrossRef Medline

16. Maarbjerg S, Gozalov A, Olesen J, et al. **Trigeminal neuralgia—a prospective systematic study of clinical characteristics in 158 patients.** *Headache* 2014;54:1574–82 CrossRef Medline
17. De Simone R, Marano E, Brescia Morra V, et al. **A clinical comparison of trigeminal neuralgic pain in patients with and without underlying multiple sclerosis.** *Neurol Sci* 2005;26(Suppl 2):s150–51 CrossRef Medline
18. Katusic S, Beard CM, Bergstralh E, et al. **Incidence and clinical features of trigeminal neuralgia, Rochester, Minnesota, 1945-1984.** *Ann Neurol* 1990;27:89–95 CrossRef Medline
19. MacDonald BK, Cockerell OC, Sander JW, et al. **The incidence and lifetime prevalence of neurological disorders in a prospective community-based study in the UK.** *Brain* 2000;123:665–76 CrossRef Medline

Noninvasive Angiographic Results of Clipped or Coiled Intracranial Aneurysms: An Inter- and Intraobserver Reliability Study

A. Benomar, B. Farzin, G. Gevry, W. Boisseau, D. Roy, A. Weill, D. Iancu, F. Guilbert, L. Létourneau-Guillon, G. Jacquin, C. Chaalala, M.W. Bojanowski, M. Labidi, R. Fahed, D. Volders, T.N. Nguyen, J.-C. Gentric, E. Magro, G. Boulouis, G. Forestier, J.-F. Hak, J.S. Ghostine, Z. Kaderali, J.J. Shankar, M. Kotowski, T.E. Darsaut, and J. Raymond



ABSTRACT

BACKGROUND AND PURPOSE: Noninvasive angiography is commonly used to assess the outcome of surgical or endovascular treatment of intracranial aneurysms in clinical series or randomized trials. We sought to assess whether a standardized 3-grade classification system could be reliably used to compare the CTA and MRA results of both treatments.

MATERIALS AND METHODS: An electronic portfolio composed of CTAs of 30 clipped and MRAs of 30 coiled aneurysms was independently evaluated by 24 raters of diverse experience and training backgrounds. Twenty raters performed a second evaluation 1 month later. Raters were asked which angiographic grade and management decision (retreatment; close or long-term follow-up) would be most appropriate for each case. Agreement was analyzed using the Krippendorff α (α_K) statistic, and the relationship between angiographic grade and clinical management choice, using the Fisher exact and Cramer V tests.

RESULTS: Interrater agreement was substantial ($\alpha_K = 0.63$; 95% CI, 0.55–0.70); results were slightly better for MRA results of coiling ($\alpha_K = 0.69$; 95% CI, 0.56–0.76) than for CTA results of clipping ($\alpha_K = 0.58$; 95% CI, 0.44–0.69). Intrarater agreement was substantial to almost perfect. Interrater agreement regarding clinical management was moderate for both clipped ($\alpha_K = 0.49$; 95% CI, 0.32–0.61) and coiled subgroups ($\alpha_K = 0.47$; 95% CI, 0.34–0.54). The choice of clinical management was strongly associated with the size of the residuum (mean Cramer V = 0.77 [SD, 0.14]), but complete occlusions (grade I) were followed more closely after coiling than after clipping ($P = .01$).

CONCLUSIONS: A standardized 3-grade scale was found to be a reliable and clinically meaningful tool to compare the results of clipping and coiling of aneurysms using CTA or MRA.

ABBREVIATION: α_K = Krippendorff α

The main goal of intracranial aneurysm treatments is to prevent ruptures or rebleeding. However, because such events may be devastating, many clinicians verify angiographic results to

determine the success of therapy in each patient.^{1–3} Ruptures or rebleeding are relatively infrequent. Thus, angiographic results are often selected as outcome measures in clinical trials comparing aneurysm treatments.^{4–8} However, the repeatability of angiographic outcome measures must be verified before widespread use.

Conventional angiography, the criterion standard to diagnose aneurysms and assess the results of treatment, has been increasingly replaced by noninvasive CTA and MRA in the past decades.^{9,10} One problem is that noninvasive angiographic modalities

Received February 16, 2021; accepted after revision April 28.

From the Department of Radiology (A.B., B.F., G.G., W.B., D.R., A.W., D.J., F.G., L.L.-G., J.R.), Department of Medicine, Division of Neurology (G.J.), and Division of Neurosurgery (C.C., M.W.B., M.L.), Centre Hospitalier de l'Université de Montréal, Montreal, Quebec, Canada; Division of Neurology (R.F.), The Ottawa Hospital Ottawa, Ontario, Canada; Department of Diagnostic Radiology (D.V.), Queen Elizabeth II Health Sciences Centre, Halifax, Nova Scotia, Canada; Departments of Neurology, Neurosurgery, and Radiology (T.N.N.), Boston Medical Center, Boston, Massachusetts; Departments of Interventional Neuroradiology (J.-C.G.) and Neurosurgery (E.M.), Hôpital de la Cavale Blanche, Centre Hospitalier Régional et Universitaire de Brest, Brest, France; Department of Neuroradiology (G.B.), Centre Hospitalier Régional et Universitaire de Tours, Tours, France; Department of Neuroradiology (G.F.), University Hospital of Limoges, Limoges, France; Department of Medical Imaging (J.-F.H.), University Hospital Timone Assistance Publique - Hôpitaux de Marseille, Marseille, France; Department of Radiology (J.S.G.), Jean-Talon Hospital, Montreal, Quebec, Canada; Section of Neurosurgery (Z.K.) and Department of Radiology (J.J.S.), Health Sciences Centre, Winnipeg, Manitoba, Canada; Department of Neurosurgery (M.K.), Hôpital de la Providence, Neuchâtel, Switzerland; and Department of Surgery (T.E.D.), Division of Neurosurgery, Walter C. Mackenzie Health Sciences Centre, University of Alberta Hospital, Edmonton, Alberta, Canada.

This work was funded by a grant (No. 271994) to Anass Benomar, MD, from the Fonds de Recherche du Québec-Santé, a Canadian provincial government funding agency.

Please address correspondence to Jean Raymond, MD, Centre Hospitalier de l'Université de Montréal (CHUM), Department of Radiology, Room D03.5462b, Montreal, PQ, Canada H2X 0C1; e-mail: jean.raymond@umontreal.ca

Indicates open access to non-subscribers at www.ajnr.org

Indicates article with online supplemental data.

<http://dx.doi.org/10.3174/ajnr.A7236>

Table 1: Characteristics of patients and aneurysms included in the portfolio^a

Characteristics	Clipped (n = 30)	Coiled (n = 30)	Total (n = 60)
Women	24 (80%)	22 (73%)	46 (77%)
Age (yr)	54.5 (SD, 10.4)	51.1 (SD, 13.0)	52.8 (SD, 11.8)
Ruptured aneurysms	15 (50%)	20 (67%)	35 (58%)
Retreated aneurysms	4 (13%)	6 (20%)	10 (17%)
Anterior circulation	28 (93%)	19 (63%)	47 (78%)
Aneurysm size (mm)	11.0 (2–27)	9.7 (3–30)	10.4 (2–30)
Wide neck (>4 mm)	17 (56%)	14 (47%)	31 (52%)

^aData are (No.) (%), mean (SD), or mean (minimum–maximum).

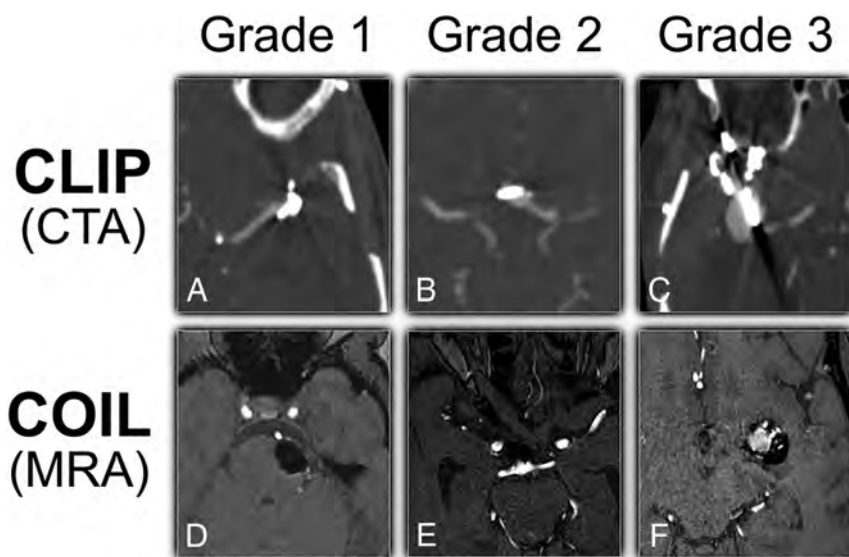


FIG 1. Illustrative cases from the portfolio of CTA clipped or MRA coiled aneurysms for each grade. The left MCA (A), anterior communicating artery (B), and right MCA (C) are CTA examples of clipped aneurysms, while the left superior cerebellar artery (D), basilar tip (E), and left MCA (F) are MRA examples of coiled aneurysms. Grade 1 (A and D): complete occlusion; grade 2 (B and E): residual neck (<2 mm using visual estimation only); grade 3 (C and F): residual aneurysm.

are used differently depending on treatments: Surgically managed patients are often followed by CTA, while patients treated with coils are more often followed by MRA.^{9,10} When one judges the comparative success of therapy in clinical reports, it would seem that comparing CTA results of clipping with MRA results of coiling would be problematic, given the different diagnostic accuracies of the 2 modalities.^{11,12} This problem is particularly relevant for clinical trials: We cannot require a catheter angiogram solely for the purposes of the study when safer, noninvasive tests clinically suffice for most patients.¹³ The problem is compounded by the proliferation of grading scales, many of which are tailored to various devices and treatment modalities.^{3,14,15} A standardized method of reporting angiographic results that would facilitate comparisons between treatments and imaging modalities is needed.

A simple, 3-grade classification for the adjudication of results of clipped and coiled aneurysms has previously been shown to be reproducible when applied to conventional angiography.¹⁵ The questions that remained unanswered after a systematic review¹⁵ and that we sought to address in this work were the following: 1) Can the same angiographic classification system be used to evaluate CTA results of clipping and MRA results of coiling? 2) Are the results repeatable when judged by various raters? 3) Does the grade

of occlusion obtained by clipping and assessed by CTA or by coiling and assessed by MRA have the same meaning in terms of clinical management?

MATERIALS AND METHODS

This article was written in accordance with the Guidelines for Reporting Reliability and Agreement Studies.¹⁶

Patient Selection

An electronic portfolio of 30 clipped and 30 coiled aneurysms was constructed. For each treatment technique, we aimed to include a wide spectrum of patients, with a balanced ratio (1:1:1) of completely occluded, residual, and gray-zone aneurysm cases to minimize the paradoxes of κ statistics.^{17,18} The number of patients per treatment group was estimated to be sufficient (>24) according to recommendations.^{19,20} For each patient, a high-definition video of the axial MRA or CTA sequences of the coiled or clipped aneurysm was provided. Patients with ruptured and unruptured aneurysms were selected from the clinical series of 1 tertiary care center (Center Hospitalier de l'Université de Montréal). Patient and aneurysm characteristics are summarized in Table 1.

Grading Scale

The grading scale is a variant of the Raymond-Roy classification.²¹ Categories of the standardized 3-grade classification system included the following: 1, complete occlusion; 2, residual neck (defined as <2 mm using visual estimation); and 3, residual aneurysm (Fig 1).¹⁵ Raters were not trained in the use of this classification system before the assessment.

Raters

Thirty-two clinicians were invited to participate: 24 (75%) raters (11 interventional neuroradiologists, 7 neurosurgeons, 4 interventional neurologists, and 2 diagnostic neuroradiologists) from 4 different countries accepted. Twenty raters agreed to perform a second evaluation of the cases in a permuted order at least 1 month later. There were 10 senior raters with >10 years of experience. Two of the interventional neuroradiologists had experience as core lab reviewers. Rater characteristics are shown in the Online Supplemental Data.

Agreement Study

An electronic survey was created and sent to the raters using the REDCap online data base manager (<https://www.project-redcap.org/>) hosted at the Center Hospitalier de l'Université de

Table 2: Interrater agreement for the grading scale^a

	CTA, Surgical (n = 30)	MRA, Endovascular (n = 30)	Total (n = 60)
Overall	0.58 (0.44–0.69)	0.69 (0.56–0.76)	0.63 (0.55–0.70)
Experience			
Junior (0–10 years; n = 14)	0.59 (0.43–0.72)	0.68 (0.56–0.76)	0.64 (0.54–0.71)
Senior (>10 years; n = 10)	0.56 (0.40–0.68)	0.69 (0.55–0.77)	0.62 (0.52–0.69)
Background			
Core lab (n = 2)	0.74 (0.54–0.87)	0.81 (0.63–0.91)	0.77 (0.64–0.86)
INR (n = 11)	0.54 (0.38–0.68)	0.65 (0.53–0.74)	0.60 (0.50–0.68)
DNR (n = 2)	0.58 (0.23–0.80)	0.87 (0.72–0.97)	0.73 (0.55–0.85)
NSX (n = 7)	0.67 (0.54–0.77)	0.71 (0.56–0.81)	0.69 (0.59–0.76)
INL (n = 4)	0.53 (0.30–0.71)	0.72 (0.57–0.82)	0.63 (0.50–0.73)

Note:—INR indicates interventional neuroradiology; DNR, diagnostic neuroradiology; NSX, neurosurgery; INL, interventional neurology.

^aData are α_K (95% CI) for the ordinal 3-grade classification. Classification grades: 1, complete occlusion; 2, residual neck (<2 mm); 3, residual aneurysm.

Montréal.^{22,23} For each of the 60 cases, raters were asked to assess the grade of occlusion and to choose the most appropriate clinical management, assuming all angiographic results concerned a ruptured aneurysm in a 65-year-old patient with a good outcome and no other medical problems. Possible options were the following: follow-up imaging in 3–5 years (or none at all); close follow-up (6–18 months); and immediate retreatment by endovascular means; or immediate retreatment by surgical means. The last 2 choices were then merged as immediate retreatment (either by surgical or endovascular means). Clinically meaningful differences were also assessed for all cases and were defined in accordance with McDonald et al²⁴ as cases for which at least one rater recommended follow-up (close or delayed) and another rater recommended retreatment (surgical or endovascular).

Statistical Analysis

All calculations were performed using R 3.5.3 statistical and computing software (<http://www.r-project.org/>).

Inter- and intrarater agreement for the grading scale and for the clinical management choices was estimated using the Krippendorff α (α_K) statistic, and the 95% confidence intervals were determined using 1000 bootstrap iterations. Interpretation of α_K values was given in accordance with Landis and Koch.²⁵ Comparisons of proportions of ratings between prespecified aneurysm and rater subgroups as well as the strength of the association between the raters' angiographic verdict and the management of the patient were evaluated using the Fisher exact test followed by a Cramer V test, with a significance threshold of .05.

RESULTS

Grading Scale

The number of aneurysms judged to be completely occluded (grade 1) by various raters varied between 10 (17%) and 36 (60%). Similarly, residual aneurysms (grade 3) were judged to be present in 11 (18%) to 36 (60%) patients. Perfect agreement among all 24 raters was found in 7/60 (12%) patients or in 22/60 (37%) after dichotomization of the scale into absence or presence of a residual

aneurysm (grades 1 + 2 versus 3). The distribution of angiographic verdicts differed between clipped and coiled aneurysms ($P = .01$): Clipped aneurysms were more often judged to be completely occluded, and coiled aneurysms were more often judged to have residual necks, while residual aneurysms were similarly allocated (Online Supplemental Data).

Overall interrater agreement of the grading scale for all raters and all patients was substantial ($\alpha_K = 0.63$; 95% CI, 0.55–0.70). When treatment and imaging modalities were considered separately, agreement was substantial for coiled aneurysms followed by MRA ($\alpha_K = 0.69$; 95% CI, 0.56–0.76) and moderate for clipped aneurysms followed by CTA ($\alpha_K = 0.58$; 95% CI, 0.44–0.69), yet with overlapping confidence intervals. Better agreement for coiled cases assessed by MRA than clipped aneurysms assessed by CTA was also a trend for all rater subgroups. Senior raters performed no better than juniors, and training background had no effect (Table 2).

Individual intrarater agreement was at least substantial for all raters and varied between 0.66 and 0.89. There were no significant differences between the mean intrarater agreement of the subgroups defined according to experience or training background. (Online Supplemental Data).

Clinical Management

After we dichotomized the clinical management into follow-up or immediate retreatment (options 1–2 versus 3), perfect agreement among all 24 raters was reached in 23/60 (38%) cases. The number of cases for which delayed follow-up imaging was chosen ranged from 0 (0%) to 36 (60%); those with close follow-up, from 12 (20%) to 53 (88%); and those with immediate retreatment, from 7 (12%) to 26 (43%) of 60 cases, depending on the rater. Sixty-five percent of cases (39/60) had a clinically meaningful difference in the choice of recommended management. Retreatment ($n = 345$ judgments of 1440) was more frequently endovascular than surgical (92%; $n = 317/345$), a preference shown by both clippers (88%) and coilers (95%).

Interrater agreement for the 3 clinical options (1, delayed follow-up; 2, close follow-up; 3, immediate retreatment) was moderate for both clipped ($\alpha_K = 0.49$; 95% CI, 0.32–0.61) and coiled aneurysm subgroups ($\alpha_K = 0.47$; 95% CI, 0.34–0.54) and was so regardless of years of experience. Raters with core lab experience ($n = 2$) were the only raters who substantially agreed for clipped ($\alpha_K = 0.75$; 95% CI, 0.55–0.88) and coiled ($\alpha_K = 0.67$; 95% CI, 0.38–0.87) subgroups (Online Supplemental Data).

Individual intrarater agreement ranged from fair ($\alpha_K = 0.31$; 95% CI, 0.06–0.51) to almost perfect ($\alpha_K = 0.88$; 95% CI, 0.78–0.96). The mean overall intrarater agreement was substantial ($\alpha_K = 0.68$ [SD, 0.14]) and did not change significantly according to rater background or experience (Online Supplemental Data).

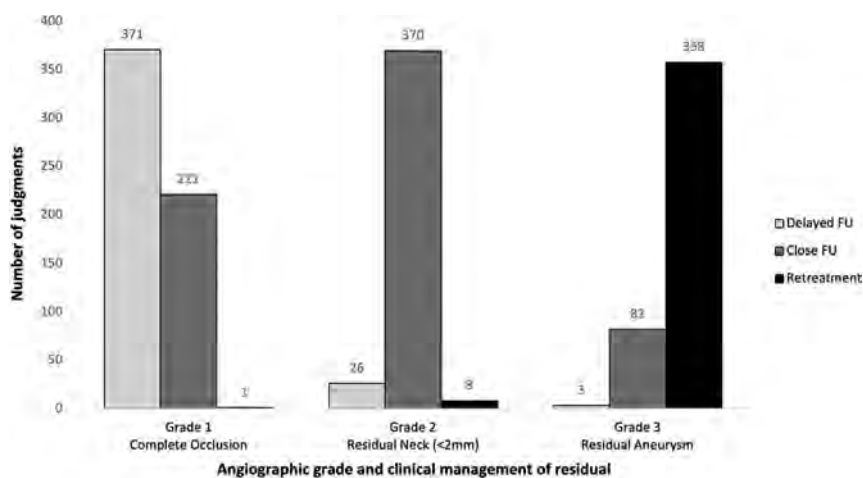


FIG 2. Total number of follow-up management choices ($n = 1440$) per chosen grade of aneurysm residuum. A choice or judgment is defined as a rater's choice of grade and clinical follow-up management for a selected treated aneurysm. FU indicates follow-up.

Relationship between Angiographic Results and Clinical Management

Raters generally selected delayed follow-up imaging for aneurysms they graded as completely occluded (63% of all grade 1 choices; $n = 371/593$), close follow-up for those graded as residual necks (92% of all grade 2 choices; $n = 370/404$) and retreatment for those graded as residual aneurysms (81% of all grade 3 choices; $n = 358/443$) ($P < .001$) (Fig 2). Clinical management differed significantly between treatment groups: Retreatments were similar, but coiled aneurysms were selected for closer follow-up than clipped aneurysms ($P < .001$) (Online Supplemental Data). Finally, for each rater, a strong association ($P < .01$) was found between angiographic results and clinical management, with a mean Cramer V of 0.77 (SD, 0.14) (Online Supplemental Data).

DISCUSSION

Many scales have been proposed to grade angiographic results of various aneurysm treatments, but a previous review has shown that few have proved to be reliable and none have previously attempted to evaluate multiple treatment or imaging modalities at the same time.¹⁵ Yet, a common language is needed to share experiences and to meaningfully compare outcomes of various treatments assessed by different noninvasive angiographic modalities. Verifying the reliability of treatment outcome measures is important if we are to learn and progress from clinical experience or using randomized trials.

In the present work, we demonstrated variability within and between raters in adjudicating angiographic results of clipping or coiling using CTA or MRA. Perhaps unsurprisingly, agreement was, for many rater and aneurysm subgroups, less concordant than when results were assessed using conventional angiography.^{15,26-28} Even if interrater agreement was suboptimal, the substantial level of agreement achieved overall among raters, regardless of treatment or imaging technique and experience or background, is somewhat reassuring. Furthermore, intrarater agreement was at least substantial for all raters.

MRA follow-up of coiled aneurysms has previously been shown to be sensitive and specific to detect aneurysm remnants and recurrences compared with DSA.^{11,29} CTA of clipped aneurysms has generally not been as accurate compared with conventional angiography, especially for small aneurysms, when multiple clips were used, on small parent vessels, or when the aneurysm was in the vicinity of bony structures.^{12,30-32} These same technical limitations may explain the trend toward lower agreement for clipped aneurysm subgroups assessed by CTA compared with coiled aneurysms assessed by MRA.

The exact same angiographic result, obtained by one or the other treatment technique, may not have the

same clinical significance in terms of clinical management. This is why we attempted to verify the clinical pertinence of the angiographic verdict of each rater for each case, assuming that the angiographic result concerned the same patient. Interrater agreement regarding the clinical management of the hypothetical case with various angiographic results was only moderate overall. This finding is not so surprising when one considers that this measure combines both disagreement in the assessment of angiographic results and disagreement in the clinical management of the same adjudicated residua. When intrarater agreement is compared, more variability is introduced at the level of clinical decisions than at the time of the angiographic verdict (Online Supplemental Data).

Divergence in clinical management may be explained by the diversity of raters from different specialties, hospitals, and countries who may apply different follow-up protocols. This feature may also explain the relatively high number of cases with clinically meaningful differences in the management decisions (65%), which are comparable with the number in previous studies.²⁴ Another important observation is the apparent different clinical meaning of a complete occlusion documented by CTA postclipping compared with a complete occlusion demonstrated by MRA postcoiling: Raters seemed more confident to opt for delayed follow-up when aneurysms were completely clipped, while being often inclined to follow completely coiled aneurysms more closely (Online Supplemental Data). This choice has also been previously observed with conventional angiography results.¹⁵ If the clinical meaning of grade 1 angiographic result differs when it is obtained by CTA on clipped aneurysms or by MRA on coiled aneurysms, by contrast, the allocation of a residual aneurysm had a more reliable clinical meaning, at least in terms of retreatment, no matter the imaging or treatment technique (Online Supplemental Data).

Given the inherent pitfalls of using a surrogate angiographic outcome measure, the impossibility of blinding assessors to the treatment received, and the variability in the clinical significance of complete occlusion (grade 1) and residual neck (grade 2) shown in the present study, we believe that the residual aneurysm

category (grade 3), as judged by core lab experts, would be a more reliable angiographic outcome measure to compare aneurysm results in clinical trials comparing various treatments.^{3,7,8} Most important, the strong correlation that was shown between the adjudication of an angiographic occlusion grade and the preferred management option for all raters, regardless of treatment or imaging technique and rater experience or background, speaks in favor of the clinical pertinence of the proposed classification.

Our study had several limitations. First, the portfolio provided only axial CTA or MRA sequences at predetermined speed and window levels that could be repeatedly reviewed, but in practice, clinicians have access to multiple sequences and can adjust windowing at will. This difference may have minimized the variability of interpretation. Second, our study did not include endovascular treatments other than coiling, such as intra-arterial or intrasaccular flow diverters. Thus, results cannot be generalized to patients treated by newer devices. The arbitrary 2-mm cutoff between the residual neck and the residual aneurysm categories was previously discussed: It was chosen as a compromise that took into account the technical limitations of noninvasive angiographic modalities.¹⁵ It was not meant to be measured with precision, and it is expected that the notion of residual neck would be differently interpreted, taking into account the initial aneurysm size.

The management question concerned a single theoretic clinical scenario, applied to all cases. Other clinical scenarios would have been more realistic. Moreover, raters were not provided with the time elapsed between initial treatment and the imaging presented for each case. Various timeframes could have led to an increase in the clinical management variability. Cases were artificially selected, as commonly done in interrater reliability studies, to cover a wide spectrum of patients despite the small size of the sample and to minimize paradoxes of κ statistics. Results may have been different had another series of patients been studied. Finally, the diagnostic accuracy of various noninvasive imaging modalities using this classification system compared with the criterion standard conventional angiography was not studied.

CONCLUSIONS

Noninvasive angiographic results of clipping or coiling of aneurysms can be reliably reported by raters of various experience and backgrounds using a standardized classification system. The proposed classification was shown to be clinically meaningful, with each grade being strongly correlated to a different management option. This classification could be used to standardize results of published randomized trials, registries, or case series.

Disclosures: Anass Benomar—RELATED: Grant: Fonds de Recherche du Québec-Santé, Comments: grant received from the Fonds de Recherche du Québec-Santé, a Canadian government funding agency. Alain Weill—UNRELATED: Employment: Centre Hospitalier de l'Université de Montréal. Laurent Létourneau-Guillon—UNRELATED: Grants/Grants Pending: fonds de soutien à l'innovation en santé et en services sociaux—MEDTEQ, Comments: cofinanced by AFX Medical Inc.* Jean Raymond—UNRELATED: Employment: Centre Hospitalier de l'Université de Montréal. Thanh Nguyen—UNRELATED: Grants/Grants Pending: Medtronic, Comments: research support*; Other: PROST study, Comments: Data and Safety Monitoring Board work. *Money paid to the institution.

REFERENCES

1. Murayama Y, Takao H, Ishibashi T, et al. Risk analysis of unruptured intracranial aneurysms: prospective 10-year cohort study. *Stroke* 2016;47:365–71 CrossRef Medline
2. Johnston SC, Dowd CF, Higashida RT, et al. Predictors of rehemorrhage after treatment of ruptured intracranial aneurysms: the Cerebral Aneurysm Rerupture After Treatment (CARAT) study. *Stroke* 2008;39:120–25 CrossRef Medline
3. Darsaut TE, Chapot R, Raymond J. Changing the rules of the game: the problem of surrogate angiographic outcomes in the evaluation of aneurysm treatments. *AJNR Am J Neuroradiol* 2020;41:2174–75 CrossRef Medline
4. White PM, Lewis SC, Nahser H, et al. HELPS Trial Collaboration. HydroCoil Endovascular Aneurysm Occlusion and Packing Study (HELPS trial): procedural safety and operator-assessed efficacy results. *AJNR Am J Neuroradiol* 2008;29:217–23 CrossRef Medline
5. Raymond J, Klink R, Chagnon M, et al. Hydrogel versus bare platinum coils in patients with large or recurrent aneurysms prone to recurrence after endovascular treatment: a randomized controlled trial. *AJNR Am J Neuroradiol* 2017;38:432–41 CrossRef
6. Darsaut TE, Desal H, Cognard C, et al. Comprehensive Aneurysm Management (CAM): an all-inclusive care trial for unruptured intracranial aneurysms. *World Neurosurg* 2020;141:e770–77 CrossRef Medline
7. Darsaut TE, Jack AS, Kerr RS, et al. International Subarachnoid Aneurysm Trial, ISAT, Part II: study protocol for a randomized controlled trial. *Trials* 2013;14:156 CrossRef Medline
8. Darsaut TE, Findlay JM, Magro E, et al. Surgical clipping or endovascular coiling for unruptured intracranial aneurysms: a pragmatic randomised trial. *J Neurol Neurosurg Psychiatry* 2017;88:663–68 CrossRef Medline
9. Wallace RC, Karis JP, Partovi S, et al. Noninvasive imaging of treated cerebral aneurysms, Part II: CT angiographic follow-up of surgically clipped aneurysms. *AJNR Am J Neuroradiol* 2007;28:1207–12 CrossRef Medline
10. Wallace RC, Karis JP, Partovi S, et al. Noninvasive imaging of treated cerebral aneurysms, Part I: MR angiographic follow-up of coiled aneurysms. *AJNR Am J Neuroradiol* 2007;28:1001–08 CrossRef Medline
11. Ahmed SU, Mocco J, Zhang X, et al. MRA versus DSA for the follow-up imaging of intracranial aneurysms treated using endovascular techniques: a meta-analysis. *J Neurointerv Surg* 2019;11:1009–14 CrossRef Medline
12. Uricchio M, Gupta S, Jakowenko N, et al. Computed tomography angiography versus digital subtraction angiography for postclipping aneurysm obliteration detection. *Stroke* 2019;50:381–88 CrossRef Medline
13. Raymond J, Darsaut TE, Altman DG. Pragmatic trials can be designed as optimal medical care: principles and methods of care trials. *J Clin Epidemiol* 2014;67:1150–56 CrossRef Medline
14. Cloft HJ, Kallmes DF. Scaling back on scales with a scale of scales. *AJNR Am J Neuroradiol* 2011;32:219–20 CrossRef Medline
15. Benomar A, Farzin B, Volders D, et al. Angiographic results of surgical or endovascular treatment of intracranial aneurysms: a systematic review and inter-observer reliability study. *Neuroradiology* 2021 Feb 24. [Epub ahead of print] CrossRef Medline
16. Kottner J, Audige L, Brorson S, et al. Guidelines for Reporting Reliability and Agreement Studies (GRRAS) were proposed. *J Clin Epidemiol* 2011;64:96–106 CrossRef Medline
17. Cicchetti DV, Feinstein AR. High agreement but low kappa, II: resolving the paradoxes. *J Clin Epidemiol* 1990;43:551–58 CrossRef Medline
18. Feinstein AR, Cicchetti DV. High agreement but low kappa, I: the problems of two paradoxes. *J Clin Epidemiol* 1990;43:543–49 CrossRef Medline
19. Donner A, Rotondi MA. Sample size requirements for interval estimation of the kappa statistic for interobserver agreement studies

- with a binary outcome and multiple raters. *Int J Biostat* 2010;6: Article 31 CrossRef Medline
20. Fahed R, Darsaut TE, Farzin B, et al. **Measuring clinical uncertainty and equipoise by applying the agreement study methodology to patient management decisions.** *BMC Med Res Methodol* 2020;20:214 CrossRef Medline
 21. Roy D, Milot G, Raymond J. **Endovascular treatment of unruptured aneurysms.** *Stroke* 2001;32:1998–2004 CrossRef Medline
 22. Harris PA, Taylor R, Minor BL, et al. REDCap Consortium. **The REDCap consortium: building an international community of software platform partners.** *J Biomed Inform* 2019;95:103208 CrossRef Medline
 23. Harris PA, Taylor R, Thielke R, et al. **Research electronic data capture (REDCap): a metadata-driven methodology and workflow process for providing translational research informatics support.** *J Biomed Inform* 2009;42:377–81 CrossRef Medline
 24. McDonald JS, Carter RE, Layton KF, et al. **Interobserver variability in retreatment decisions of recurrent and residual aneurysms.** *AJNR Am J Neuroradiol* 2013;34:1035–39 CrossRef Medline
 25. Landis JR, Koch GG. **The measurement of observer agreement for categorical data.** *Biometrics* 1977;33:159–74 CrossRef Medline
 26. Jamali S, Fahed R, Gentric JC, et al. **Inter- and intrarater agreement on the outcome of endovascular treatment of aneurysms using MRA.** *AJNR Am J Neuroradiol* 2016;37:879–84 CrossRef Medline
 27. Tollard E, Darsaut TE, Bing F, et al. **Outcomes of endovascular treatments of aneurysms: observer variability and implications for interpreting case series and planning randomized trials.** *AJNR Am J Neuroradiol* 2012;33:626–31 CrossRef Medline
 28. Kotowski M, Farzin B, Fahed R, et al. **Residual cerebral aneurysms after microsurgical clipping: a new scale, an agreement study, and a systematic review of the literature.** *World Neurosurg* 2019;121: e302–21 CrossRef Medline
 29. van Amerongen MJ, Boogaarts HD, de Vries J, et al. **MRA versus DSA for follow-up of coiled intracranial aneurysms: a meta-analysis.** *AJNR Am J Neuroradiol* 2014;35:1655–61 CrossRef Medline
 30. Pradilla G, Wicks RT, Hadelberg U, et al. **Accuracy of computed tomography angiography in the diagnosis of intracranial aneurysms.** *World Neurosurg* 2013;80:845–52 CrossRef Medline
 31. Philipp LR, McCracken DJ, McCracken CE, et al. **Comparison between CTA and digital subtraction angiography in the diagnosis of ruptured aneurysms.** *Neurosurgery* 2017;80:769–77 CrossRef Medline
 32. Wang X, Benson J, Jagadeesan B, et al. **Giant cerebral aneurysms: comparing CTA, MRA, and digital subtraction angiography assessments.** *J Neuroimaging* 2020;30:335–41 CrossRef Medline

Safety and Efficacy of Stent-Assisted Coiling of Unruptured Intracranial Aneurysms Using Low-Profile Stents in Small Parent Arteries

J. Kim, H.J. Han, W. Lee, S.K. Park, J. Chung, Y.B. Kim, and K.Y. Park



ABSTRACT

BACKGROUND AND PURPOSE: Stent-assisted coiling of intracranial aneurysms arising from small vessels (≤ 2.0 mm) is a common procedure. However, data regarding its treatment outcomes are scarce. This study evaluated the clinical and radiologic outcomes of stent-assisted coiling using low-profile stents for aneurysms of small parent arteries.

MATERIALS AND METHODS: From November 2015 to October 2020, sixty-four patients with 66 aneurysms arising from parent arteries of ≤ 2.0 mm were treated with stent-assisted coiling using a Low-Profile Visualized Intraluminal Support Junior (LVIS Jr) or the Neuroform Atlas stent in a single institution. The clinical and radiologic data were retrospectively reviewed, and the risk factors for procedure-related complications were evaluated.

RESULTS: The LVIS Jr and Neuroform Atlas stents were used in 22 (33.3%) and 44 (66.7%) cases, respectively. Technical success was achieved in 66 cases (100%). Immediate postprocedural aneurysm occlusion grades assessed by the Raymond-Roy occlusion classification were I (57.6%), II (19.7%), and III (22.7%), respectively. Procedure-related complications occurred in 10 cases (15.2%), with 8 thromboembolic complications (12.1%) and 2 hemorrhagic complications (3.0%). Procedure-related morbidity was 4.5% without mortality. On multivariate analysis, current smoking (odds ratio = 7.1, $P = .021$) had a statistically significant effect on procedure-related complications.

CONCLUSIONS: Stent-assisted coiling of intracranial aneurysms with low-profile stents in small vessels (≤ 2.0 mm) had a 100% success rate and a 15.2% overall complication rate with 4.5% morbidity. Current smoking was a significant risk factor associated with procedure-related complications.

ABBREVIATIONS: PRU = P2Y12 reaction units; RR = Raymond-Roy occlusion classification; SAC = stent-assisted coiling

In the past decade, development in neuroendovascular devices and techniques has facilitated the successful treatment of intracranial aneurysms that had been previously considered challenging or uncoilable lesions.¹ Above all, stent-assisted coiling (SAC) is widely accepted as an effective and safe treatment technique for wide-neck intracranial aneurysms^{2,3} because it can also reduce recanalization and retreatment rates.⁴

However, previously used stent placement in small vessels was technically challenging due to the difficult navigation of larger (0.021- or 0.027-inch) delivery microcatheters to these small arteries.⁵⁻⁷

Recently, low-profile stents were introduced to improve the navigability and success rate of the procedure because they can be delivered via 0.0165- or 0.017-inch microcatheters to access tortuous and smaller vessels.⁸⁻¹⁰ Although the recommended use of the low-profile stents is for a parent artery with a diameter of either ≥ 2.0 or ≥ 2.5 mm, their off-label use for the treatment of aneurysms arising from smaller parent arteries has become more common.^{11,12} However, little is known about the efficacy and safety of SAC using low-profile stents in vessels smaller than 2.0 mm.

In the present study, we aimed to investigate the clinical and radiologic outcomes of SAC using low-profile stents for the treatment of unruptured intracranial aneurysms arising from small vessels with a diameter of ≤ 2.0 mm.

Received January 15, 2021; accepted after revision April 7.

From the Department of Neurosurgery (J.K., H.J.H., J.C., Y.B.K., K.Y.P.), Severance Stroke Center, and Department of Neurosurgery (W.L., S.K.P.), Gangnam Severance Hospital, Yonsei University College of Medicine, Seoul, Republic of Korea.

This study was approved by Severance Hospital institutional review board (4-2020-0765).

Please address correspondence to Keun Young Park, MD, Department of Neurosurgery, Severance Stroke Center, Yonsei University College of Medicine, 50 Yonsei-ro, Seodaemun-gu, Seoul 03722, Korea; e-mail: kypark78.md@gmail.com

Indicates article with online supplemental data.

<http://dx.doi.org/10.3174/ajnr.A7196>

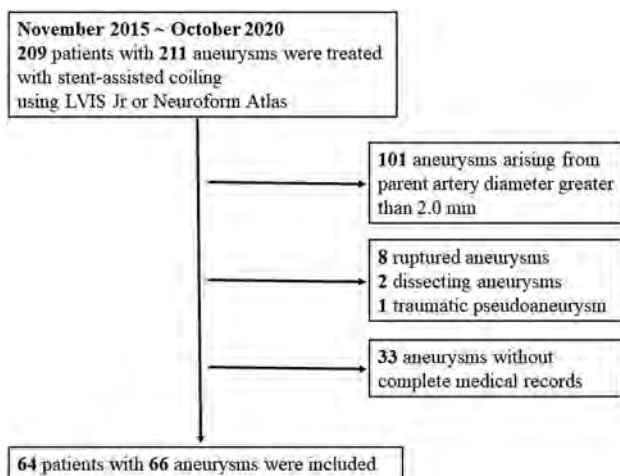


FIGURE. Inclusion and exclusion flow diagram.

MATERIALS AND METHODS

Study Design

This study was approved by our institutional review board. The need to obtain patient informed consent was waived because of the retrospective study design. The study was performed under the guidelines outlined by the Declaration of Helsinki and followed the STROBE checklist (<https://www.bmj.com/content/bmj/suppl/2021/03/10/bmj.n254.DC1/peld062092.www.pdf>).

Participants

In Korea, the Low-Profile Visualized Intraluminal Support Junior (LVIS Jr; MicroVention-Terumo) and the Neuroform Atlas (Stryker) stents are commercially available. Between November 2015 and October 2020, two hundred nine patients with 211 aneurysms were successfully treated by SAC with the LVIS Jr or Neuroform Atlas stents in a single institution. Data regarding aneurysms arising from parent arteries of ≤ 2 mm were extracted from a prospectively maintained aneurysm data base. Exclusion criteria were as follows: 1) patients with ruptured, traumatic, or vasculopathy-related aneurysms, and 2) patients with incomplete medical records or radiologic data. Finally, 64 patients with 66 aneurysms were included (Figure). The vessel-diameter measurements were made from postprocessed 3D rotational images. Patient and aneurysm characteristics, clinical outcomes, and radiologic follow-up results were obtained from electronic medical records and a prospectively registered aneurysm database. These data were retrospectively reviewed.

Endovascular Procedures and Antiplatelet Protocol

Therapeutic decisions were made by a multidisciplinary team of neurosurgeons and neurointerventionalists via consensus. Before the procedure, dual antiplatelet therapy with aspirin (100 mg once daily) plus clopidogrel (75 mg once daily) was administered to each patient for at least 5 days. Platelet function tests were conducted using the VerifyNow P2Y12 assay (Accumetrics) to measure the P2Y12 reaction units (PRU). Patients with PRU of >220 were considered clopidogrel hyporesponders¹³ and were administered supplementary cilostazol (100 mg twice daily). For patients without any antiplatelet premedication, a loading dose of

aspirin (300 mg) and clopidogrel (300 mg) was administered 1 day before or on the day of the procedure.

All procedures were performed with the patient under general anesthesia. The femoral artery was the primary target puncture site. The LVIS Jr and the Neuroform Atlas were delivered via either Headway 17 (MicroVention-Terumo) or Excelsior SL-10 (Stryker) microcatheters and were deployed using a standard procedure. Y-configuration stent placement was conducted at the operator's discretion. Coiling of the aneurysm was performed using the jailing technique ($n = 59$, 86.4%) or cell-through technique ($n = 7$, 13.6%). During the procedure, IV unfractionated heparin (3000 IU) was injected after the sheath was inserted into the femoral artery and a bolus of 1000 IU was administered every hour. When thrombus formation was noted during the procedure, intra-arterial tirofiban (0.3–1.0 mg) was injected for thrombolysis.

After the procedure, the dual antiplatelet therapy was maintained for at least 3 months unless contraindicated. Thereafter, aspirin monotherapy was continued indefinitely.

Clinical and Radiologic Follow-up

Clinical follow-up was routinely conducted at 1 and 3 months after the procedure. Routine imaging follow-ups were performed with either MRA or DSA, 1, 2, and 4 years after the procedure.

Outcome Measurements

Procedure-related complications were defined as any thromboembolic and hemorrhagic complications that occurred within 90 days, irrespective of the presence of symptoms. Thromboembolic complications included intraprocedural thromboembolism diagnosed when the contrast in a vessel stagnated, nonvisualization of the distal artery occurred, a luminal filling defect was noted during the procedure, or cerebral infarction or a transient ischemic attack occurred in a territory relevant to the procedure. Hemorrhagic complications were diagnosed when any sign of contrast leakage during the procedure was noted due to rupture of the aneurysm or vessels or when any immediate or delayed intracranial hemorrhage occurred. Clinical outcomes were assessed at the outpatient clinic using the mRS. Unfavorable outcomes were defined as a 90-day mRS score of ≥ 3 . Immediate and follow-up radiologic outcomes were assessed using the Raymond-Roy occlusion classification (RR), in which class I is defined as complete occlusion; class II, as a neck remnant; and class III, as a sac remnant.¹⁴ The procedural success rate and in-stent stenosis ($> 50\%$) were also evaluated.

Statistical Analysis

Statistical analysis was performed using SPSS Statistics 25.0 (IBM). Fisher exact tests or χ^2 tests were performed for categorical variables. Mann-Whitney tests or Student t tests were performed for continuous variables of clinical outcomes of SAC and for the univariate analysis of the risk factors for procedure-related complications. All variables with clinical importance were introduced into a multivariate analysis using the binary logistic regression method. A P value $< .05$ was considered statistically significant.

Table 1: Details of endovascular procedures

Variables	Values
Platelet function test	
PRU (SD)	187.7 (67.1)
Clopidogrel hyporesponder (No.) (%)	23 (34.8) ^a
Stent type (No.) (%)	
LVIS Jr	22 (33.3)
Neuroform Atlas	44 (66.7)
No. of stents (No.) (%)	
1	59 (89.4)
2	7 (10.6) ^b

^aModified with cilostazol (100 mg twice daily).

^bIncluding 6 Y-stent placements.

RESULTS

Patients and Aneurysms

Sixty-four patients (mean age, 60.5 years; male/female ratio = 21:43) with 66 unruptured aneurysms (61 incidental and 5 recurred) were treated. The aneurysms were located in the anterior cerebral artery ($n = 46$, 69.7%), MCA ($n = 15$, 22.7%), and vertebrobasilar artery ($n = 5$, 7.6%). The median aneurysm size was 4.59 mm (interquartile range, 3.74–6.85 mm). The median parent artery diameter was 1.78 mm (interquartile range, 1.63–1.90 mm), and the smallest diameter was 1.15 mm. These characteristics are described in the Online Supplemental Data.

Endovascular Procedures

The total number of procedures was 66 (LVIS Jr, 22; Neuroform Atlas, 44). Twenty-three (34.8%) clopidogrel hyporesponders were administered cilostazol. Among the 7 cases in which 2 stents were deployed, Y-stent placement using identical stents was performed in 6 patients. These characteristics are described in Table 1.

Immediate Postprocedural, Radiologic, and Clinical Outcomes

Stent deployment was successful in 66 cases (100.0%). Immediately after the procedure, the aneurysm occlusion grade was RR I ($n = 38$, 57.6%), RR II ($n = 13$, 19.7%), and RR III ($n = 15$, 22.7%). The procedure-related complications occurred in 9 cases (13.6%) within the first 7 days of the procedure, including 7 (10.6%) thromboembolic and 2 (3.0%) hemorrhagic complications. Among 7 thromboembolic complications, 6 cases of in-stent thrombosis were identified during the procedure and completely controlled using intra-arterial and IV tirofiban infusion, and none were symptomatic. However, 1 patient with a distal anterior cerebral artery aneurysm experienced thrombus formation during the procedure, which could not be sufficiently controlled, resulting in an acute anterior cerebral artery territory infarction (mRS 4). Hemorrhagic complications were observed in 2 patients. One patient with an anterior communicating artery aneurysm was successfully treated without any procedural events, but subarachnoid hemorrhage was diagnosed 12 hours after the procedure. It is suspected that the aneurysm was ruptured during the cell-through procedure, but the contrast leakage was not noticed during the procedure. The patient was treated with external ventricular drainage and discharged with an mRS score of 4. Another patient experienced an intraprocedural rupture of a distal anterior cerebral artery aneurysm and was discharged with an mRS score of 5 (Table 2).

Table 2: Procedure-related complications and 90-day clinical outcomes

Clinical Outcomes	Values
Procedure-related complications (No.) (%)	10 (15.2)
Thromboembolism	8 (12.1) ^a
Hemorrhage	2 (3.0)
Unfavorable outcome (mRS ≥ 3) (No.) (%)	3 (4.5)
Procedure-related mortality (No.) (%)	0

^aIncluding 7 asymptomatic cases.

Table 3: Radiologic outcomes

Aneurysm Occlusion Classification	Values
Immediate postprocedural (No.) (%)	
RR I	38 (57.6)
RR II	13 (19.7)
RR III	15 (22.7)
Follow-up occlusion (median, 12.1 mo) (No.) (%)	
RR I	51 (87.9)
RR II	4 (6.9)
RR III	3 (5.2)
Recurrence (No.) (%)	2 (3.4%) ^a
In-stent stenosis (No.) (%)	0 (0%)

^aNeither of these patients required retreatment.

Follow-up Radiologic and Clinical Outcomes

Follow-up images were available for 58 aneurysms (90.5%; DSA, 15; MRA, 43; median, 12.1 months). During the follow-up, RR I was achieved for 51 aneurysms (87.9%), RR II was achieved for 4 aneurysms (6.9%), and RR III was achieved for 3 aneurysms (5.2%). Recurrence was noted in 2 patients (3.4%), neither of whom required retreatment. No case of in-stent stenosis (>50%) occurred among the 15 patients with DSA follow-up (median, 17.1 months) (Table 3). A delayed procedure-related complication occurred in 1 patient who experienced acute embolic infarction in the left frontal lobe 2 months after undergoing stent-assisted coiling of a left MCA bifurcation aneurysm, resulting in mild dysarthria (mRS 2). Overall, 3 patients had unfavorable outcomes 90 days postprocedure, resulting in 4.5% morbidity. There was no procedure-related mortality.

Risk Factors Associated with Procedure-Related Complications

Current smoking ($P = .042$) was statistically associated with procedure-related complications on univariate analysis (Online Supplemental Data). On multivariate analysis, current smoking (OR = 7.1; 95% CI, 1.35–37.50; $P = .021$) was the only statistically significant factor. The aneurysm characteristics, parent artery diameter, stent type, and complete aneurysm occlusion were not associated with an increased risk of procedure-related complications (Table 4).

DISCUSSION

In the current study of patients who underwent SAC using low-profile stents (LVIS Jr and Neuroform Atlas) for unruptured intracranial aneurysms arising from small vessels (≤ 2.0 mm), the immediate postprocedural occlusion grades were RR I ($n = 38$, 57.6%), RR II ($n = 13$, 19.7%), and RR III ($n = 15$, 22.7%) and

Table 4: Multivariate analysis of risk factors for procedure-related complications

Variables	Odds Ratio	95% Wald CI	P Value
Age	1.08	0.99–1.19	.086
Female sex	5.38	0.61–47.72	.131
Current smoking	7.10	1.35–37.50	.021 ^a
Diabetes mellitus	3.25	0.15–72.60	.457
Cardiovascular disease	2.24	0.15–33.63	.560
Parent artery diameter	18.40	0.126–2694.60	.252
RR I	2.30	0.23–22.94	.478

^aStatistically significant.

technical success was achieved in all 66 cases. Within 90 days, procedure-related complications occurred in 10 cases (15.2%) and unfavorable outcomes were noted in 3 patients (4.5%), without mortality. The aneurysm occlusion grade was RR I or II in 55 cases (94.8%) at the last follow-up (median, 12.1 months), with a 3.4% recurrence rate.

Stent-assisted coiling is widely accepted for the treatment of wide-neck, artery-incorporated, and fusiform intracranial aneurysms. However, stent placement in small vessels using earlier stents with higher profiles remains technically challenging because these stents should be delivered via a 0.021- or 0.027-inch microcatheter, which sometimes requires an exchange technique using a 300-cm exchangeable wire.¹⁵ On the other hand, the ability of the low-profile stents to be delivered via a 0.0165- or 0.017-inch microcatheter offers an advantage when treating aneurysms arising from narrow and tortuous vessels. In the previous study of Kühn et al,¹⁶ a 93.2% (41/44) technical success rate was reported in SAC using Neuroform (Stryker) or Enterprise (Codman & Shurtleff) stents in small vessels of ≤ 2 mm. Our current study showed a higher technical success rate of 100%. Furthermore, SAC using low-profile stents for aneurysms at complex and acute-angled vasculature has also been reported. In a study of anterior communicating artery aneurysms treated with the LVIS Jr, Santillan et al¹⁷ reported a 96.0% (24/25) technical success rate. Similarly, Samaniego et al¹⁸ attempted treating PICA aneurysms with the LVIS Jr and suggested its feasibility in their case series.

Although SAC using low-profile stents seems feasible even in small vessels, the risk of procedure-related complications remains a major concern regarding stent placement because deploying stents in a small, tortuous vessel may be complicated by poor wall apposition and increased metal coverage, all of which may lead to thromboembolism. Several studies have reported treatment outcomes of SAC using earlier versions (higher profile) of Neuroform or Enterprise stents in small vessels (Online Supplemental Data). Kühn et al¹⁶ reported their experience of SAC using Enterprise and Neuroform stents in parent arteries of ≤ 2.0 mm, with 13.6% thromboembolic and 2.3% hemorrhagic complications. Chung et al¹⁹ also investigated 31 cases of SAC using Enterprise stents in parent arteries of < 2.0 mm and found thromboembolic complications without hemorrhagic complications in 9.7% of the cases. Recently, for the evaluation of low-profile stents in small vessels, Wang et al²⁰ evaluated 22 aneurysms treated using the LVIS Jr and reported 4.5% hemorrhagic and no thromboembolic complications. Another study of LVIS Jr by Santillan et al²¹ also showed 11.4% thromboembolic complications and 2.8% hemorrhagic complications in their 35 case series. However, in these 2 studies, small parent arteries

were defined as vessels smaller than 2.5 mm.^{20,21} Furthermore, they included only a small number of cases (22 and 35, respectively).

To the best of our knowledge, our study is the first and largest study including 66 aneurysms treated by SAC using low-profile stents in small vessels of ≤ 2.0 mm and showing 12.1% thromboembolic and 3.0% hemorrhagic complications (morbidity, 4.5%; mortality, 0). These complication rates were comparable with those in previous studies of low-profile stents with a larger sample size.^{11,22–24} In a study of 80 cases of SAC using Leo Baby stents (Balt Extrusion), Aydin et al²² reported an overall complication rate of 8.8% and 3.8% morbidity without mortality. Similarly, Alghamdi et al¹¹ reported 10% thromboembolic and 2.5% hemorrhagic complications, resulting in 5% morbidity and 0% mortality in 43 SAC cases using the LVIS Jr. A recent multicenter study of Neuroform Atlas demonstrated a major stroke rate of 4.4%, with a 2.2% permanent morbidity rate and a 0.5% mortality rate.²³ In a systematic review, Park et al²⁴ reported a periprocedural complication rate of 12.4% and procedure-related morbidity between 0% and 5.5% with low-profile stents (LVIS Jr and Leo Baby). Currently, low-profile stents demonstrate procedure-related complication rates comparable with those of higher-profile stents.

Several studies have investigated the risk factors associated with procedure-related complications in SAC of intracranial aneurysms.^{25,26} Complications related to stent placement have been more thoroughly evaluated in the cardiology field, in which smoking is a strong risk factor for in-stent thrombosis after percutaneous coronary intervention,²⁷ because smokers tend to be at higher thrombotic risk. In the present study, current smoking was an independent risk factor for procedure-related complications during and after SAC in small vessels (≤ 2.0 mm). This finding is contradictory to the concept of “smoker’s paradox.” Reed et al²⁸ demonstrated that smokers exhibit lower PRU than nonsmokers when treated with clopidogrel. In the present study, however, smokers showed higher PRU than nonsmokers, without statistical significance (233.6 versus 181.1, $P = .06$). Perhaps smoking does not universally reduce platelet reactivity due to the cytochrome P450 genotype-dependent effect of smoking on clopidogrel responsiveness.²⁹ Because most of the procedure-related complications were intraoperative thromboembolism, the mechanical stress exerted by the deployment of a stent on the endothelium, which was already affected by noxious stimuli such as smoking,³⁰ might contribute to immediate thrombus formation. Whether smaller vessels are more vulnerable to these risk factors remains to be elucidated.

Individual responses to clopidogrel are varied, and hyporesponse is commonly reported. Unfortunately, hyporesponse to clopidogrel increases the risk of thromboembolic events. In the present study, though statistically not significant, PRU mean value was higher in the procedure-related complication group (206.60 versus 184.24, $P = .337$). Recently, newer antiplatelet agents such as ticagrelor or prasugrel have been considered alternatives for clopidogrel hyporesponders to reduce the risk of periprocedural thromboembolic complications.^{31,32} However, in the present study, cilostazol was added to the clopidogrel hyporesponders on the basis of the initial platelet function test because ticagrelor and prasugrel were not approved by the Ministry of

Food and Drug Safety in Korea for use in neuroendovascular procedures. We did not repeat the platelet function test after administering cilostazol, so it is not clear whether the higher baseline PRU of the patients with procedure-related complications increased the risk of thromboembolic complications; however, analysis of the effects of conventional dual-antiplatelet agents plus cilostazol and the newer antiplatelet regimen would provide valuable knowledge for the management of clopidogrel hyporesponders.

In this study, all patients, identically, received 3000 IU of IV heparin initially and additional 1000 IU of IV heparin every hour during the procedure. Because the antithrombotic effect of heparin measured by activated clotting time varies among individuals, monitoring of the heparin response and patient-tailored dose selection would have lowered the thromboembolic complication rate.

Our study has several limitations. First, this was a retrospective study with a relatively small sample size of unruptured aneurysms collected from a single institution. Thus, selection bias cannot be avoided regarding the demographics and percentages observed. Furthermore, the risk-factor analysis is not supported by high statistical power due to the small sample size. Nevertheless, to the best of our knowledge, this study was performed with the largest sample gathered from a single center, and to reduce selection bias, we included 64 consecutive patients treated with low-profile stents for unruptured cerebral aneurysms arising from small vessels. Another limitation was the lack of long-term follow-up. Therefore, further studies are needed in larger populations treated with SAC using low-profile stents to assess long-term safety and durability.

CONCLUSIONS

This study demonstrates that off-label use of low-profile stents in the SAC of unruptured intracranial aneurysms arising from parent arteries of ≤ 2.0 mm is feasible and relatively safe, with a good aneurysm occlusion rate and an acceptable complication rate.

ACKNOWLEDGMENTS

We would like to thank the Biostatistics Collaboration Unit of Yonsei University College of Medicine for statistical consultation and Editage (www.editage.co.kr) for English language editing.

REFERENCES

1. Wang AS, Campos JK, Colby GP, et al. **Cerebral aneurysm treatment trends in National Inpatient Sample 2007–2016: endovascular therapies favored over surgery.** *J Neurointerv Surg* 2020;12:957–63 CrossRef Medline
2. Park KY, Kim BM, Kim DJ, et al. **Y-configuration stenting for coiling of wide-neck bifurcation aneurysms using Low-profile Visualized Intraluminal Support Junior.** *J Neurointerv Surg* 2019;11:400–04 CrossRef Medline
3. Tähtinen OI, Vanninen RL, Manninen HI, et al. **Wide-necked intracranial aneurysms: treatment with stent-assisted coil embolization during acute (<72 hours) subarachnoid hemorrhage—experience in 61 consecutive patients.** *Radiology* 2009;253:199–208 CrossRef Medline
4. Hong Y, Wang YJ, Deng Z, et al. **Stent-assisted coiling versus coiling in treatment of intracranial aneurysm: a systematic review and meta-analysis.** *PLoS One* 2014;9:e82311 CrossRef Medline
5. Huang Q, Liu J, Zhao R, et al. **The safety and efficacy of stenting in the treatment of complex posterior cerebral artery aneurysms: a seven-case report and literature review.** *Clin Neuroradiol* 2013;23:175–87 CrossRef Medline
6. Roh HG, Chun YI, Choi JW, et al. **Retrograde stent placement for coil embolization of a wide-necked posterior inferior cerebellar artery aneurysm.** *Korean J Radiol* 2012;13:510–14 CrossRef Medline
7. Zhang J, Lv X, Jiang C, et al. **Endovascular treatment of cerebral aneurysms with the use of stents in small cerebral vessels.** *Neurol Res* 2010;32:119–22 CrossRef Medline
8. Shankar JJS, Quateen A, Weill A, et al. **Canadian Registry of LVIS Jr for Treatment of Intracranial Aneurysms (CaRLA).** *J Neurointerv Surg* 2017;9:849–53 CrossRef Medline
9. Grossberg JA, Hanel RA, Dabus G, et al. **Treatment of wide-necked aneurysms with the low-profile visualized intraluminal support (LVIS Jr) device: a multicenter experience.** *J Neurointerv Surg* 2017;9:1098–102 CrossRef Medline
10. Burkhardt JK, Srinivasan V, Srivatsan A, et al. **Multicenter postmarket analysis of the Neuroform Atlas stent for stent-assisted coil embolization of intracranial aneurysms.** *AJNR Am J Neuroradiol* 2020;41:1037–42 CrossRef Medline
11. Alghamdi F, Mine B, Morais R, et al. **Stent-assisted coiling of intracranial aneurysms located on small vessels: midterm results with the LVIS Junior stent in 40 patients with 43 aneurysms.** *Neuroradiology* 2016;58:665–71 CrossRef Medline
12. ten Brinck MF, de Vries J, Bartels RHMA, et al. **NeuroForm Atlas stent-assisted coiling: preliminary results.** *Neurosurgery* 2019;84:179–89 CrossRef Medline
13. Kim CH, Hwang G, Kwon OK, et al. **P2Y12 reaction units threshold for implementing modified antiplatelet preparation in coil embolization of unruptured aneurysms: a prospective validation study.** *Radiology* 2017;282:542–51 CrossRef Medline
14. Roy D, Milot G, Raymond J. **Endovascular treatment of unruptured aneurysms.** *Stroke* 2001;32:1998–2004 CrossRef Medline
15. Akpek S, Arat A, Morsi H, et al. **Self-expandable stent-assisted coiling of wide-necked intracranial aneurysms: a single-center experience.** *AJNR Am J Neuroradiol* 2005;26:1223–31 Medline
16. Kühn AL, Hou SY, Puri AS, et al. **Stent-assisted coil embolization of aneurysms with small parent vessels: safety and efficacy analysis.** *J Neurointerv Surg* 2016;8:581–85 CrossRef Medline
17. Santillan A, Schwarz J, Boddu S, et al. **Stent-assisted coil embolization of anterior communicating artery aneurysms using the LVIS Jr stent.** *Interv Neuroradiol* 2019;25:12–20 CrossRef Medline
18. Samaniego EA, Abdo G, Hanel RA, et al. **Endovascular treatment of PICA aneurysms with a low-profile visualized intraluminal support (LVIS Jr) device.** *J Neurointerv Surg* 2016;8:1030–33 CrossRef Medline
19. Chung J, Suh SH, Hong CK, et al. **Preliminary experience with self-expanding closed-cell stent placement in small arteries less than 2 mm in diameter for the treatment of intracranial aneurysms.** *J Neurosurg* 2015;122:1503–10 CrossRef Medline
20. Wang CC, Li W, Feng ZZ, et al. **Preliminary experience with stent-assisted coiling of aneurysms arising from small (<2.5 mm) cerebral vessels using the low-profile visualized intraluminal support device.** *AJNR Am J Neuroradiol* 2017;38:1163–68 CrossRef Medline
21. Santillan A, Boddu S, Schwarz J, et al. **LVIS Jr. stent for treatment of intracranial aneurysms with parent vessel diameter of 2.5 mm or less.** *Interv Neuroradiol* 2018;24:246–53 CrossRef Medline
22. Aydin K, Arat A, Sencer S, et al. **Stent-assisted coiling of wide-neck intracranial aneurysms using low-profile Leo Baby stents: initial and midterm results.** *AJNR Am J Neuroradiol* 2015;36:1934–41 CrossRef Medline
23. Zaidat OO, Hanel RA, Sauvageau EA, et al. **Pivotal trial of the Neuroform Atlas stent for treatment of anterior circulation aneurysms: one-year outcomes.** *Stroke* 2020;51:2087–94 CrossRef

24. Park SY, Oh JS, Oh HJ, et al. **Safety and efficacy of low-profile, self-expandable stents for treatment of intracranial aneurysms: initial and midterm results—a systematic review and meta-analysis.** *Interv Neurol* 2017;6:170–82 CrossRef Medline
25. Adeeb N, Griessenauer CJ, Moore JM, et al. **Ischemic stroke after treatment of intraprocedural thrombosis during stent-assisted coiling and flow diversion.** *Stroke* 2017;48:1098–100 CrossRef Medline
26. Zuo Q, Yang P, Lv N, et al. **Safety of coiling with stent placement for the treatment of ruptured wide-necked intracranial aneurysms: a contemporary cohort study in a high-volume center after improvement of skills and strategy.** *J Neurosurg* 2019;131:435–41 CrossRef Medline
27. Faxon DP, Fuster V, Libby P, et al. **Atherosclerotic vascular disease conference: writing group III: pathophysiology.** *Circulation* 2004;109:2617–25 CrossRef Medline
28. Reed GW, Cannon CP, Waalen J, et al. **Influence of smoking on the antiplatelet effect of clopidogrel differs according to clopidogrel dose: Insights from the GRAVITAS trial.** *Catheter Cardiovasc Interv* 2017;89:190–98 CrossRef Medline
29. Park KW, Park JJ, Jeon KH, et al. **Enhanced clopidogrel responsiveness in smokers: smokers' paradox is dependent on cytochrome P450 CYP1A2 status.** *Arterioscler Thromb Vasc Biol* 2011;31:665–71 CrossRef Medline
30. Michael PR. **Cigarette smoking, endothelial injury and cardiovascular disease.** *Int J Exp Pathol* 2000;81:219–30 CrossRef Medline
31. Cho WS, Lee J, Ha EJ, et al. **Low-dose prasugrel vs clopidogrel-based tailored premedication for endovascular treatment of cerebral aneurysms.** *Neurosurgery* 2019;85:E52–59 CrossRef Medline
32. Kim KS, Fraser JF, Grupke S, et al. **Management of antiplatelet therapy in patients undergoing neuroendovascular procedures.** *J Neurosurg* 2018;129:890–05 CrossRef Medline

Safety and Efficacy of the Woven EndoBridge Device for Treatment of Ruptured Intracranial Aneurysms: A Systematic Review and Meta-analysis

M.A. Essibayi, G. Lanzino, and W. Brinjikji



ABSTRACT

BACKGROUND: The Woven EndoBridge device has been increasingly used to treat wide-neck aneurysms, particularly ruptured ones.

PURPOSE: Our aim was to investigate the safety and efficacy of the Woven EndoBridge device in the treatment of ruptured intracranial aneurysms.

DATA SOURCES: All studies evaluating the outcomes of Woven EndoBridge device use in the treatment of ruptured intracranial aneurysms from inception through 2020 were searched on Ovid Evidence-Based Medicine Reviews, EMBASE, MEDLINE, Scopus, and the Web of Science Core Collection.

STUDY SELECTION: Eighteen studies encompassing 487 patients with 496 ruptured aneurysms treated with the Woven EndoBridge device were included.

DATA ANALYSIS: We studied rates of rerupture and retreatment, angiographic outcomes at the last follow-up point, complications, and mortality rates. Data were collected on anticoagulation and antiplatelet use. Meta-analysis was performed using the random effects model.

DATA SYNTHESIS: The rate of late rebleeding was 1.1% (95% CI, 0.1%–2.1%). The treatment-related perioperative complication rate and the overall clinical complication rate were 13.2% (95% CI, 9.2%–17.2%) and 3.2% (95% CI, 1.6%–4.7%), respectively. Thirteen hemorrhagic (2%; 95% CI, 0.8%–3.3%) and 41 thromboembolic (6.8%; 95% CI, 4.6%–9%) complications occurred. Favorable clinical outcomes were achieved in 85% of patients. Procedure-related mortality and overall mortality rates were 2.1% (95% CI, 0.8%–3.3%) and 11.5% (95% CI, 7%–16%), respectively. At last follow-up, an adequate occlusion rate was 87.3% (95% CI, 82.1%–92.4%) and the retreatment rate was 5.1% (95% CI, 3%–7.3%).

LIMITATIONS: Our meta-analysis is limited by selection bias and high heterogeneity.

CONCLUSIONS: This meta-analysis demonstrated the safety and efficacy of the Woven EndoBridge device in the management of ruptured aneurysms, but further studies are needed.

ABBREVIATION: APT = antiplatelet therapy

In recent years, the Woven EndoBridge device (WEB; MicroVention) has been increasingly used for the endovascular treatment of wide-neck aneurysms, particularly ruptured ones. One of the advantages of the WEB device in the treatment of ruptured intracranial aneurysms compared with other nontraditional techniques (ie, stent-assisted coiling or flow diversion) is that

dual antiplatelet therapy is not necessary.¹ A few series have detailed the use of the WEB device in patients with ruptured aneurysms. However, these studies are relatively small and represent early experience. To assess the technical success rate, effectiveness, safety, and early follow-up of patients with aneurysmal SAH treated with the WEB device in the acute phase, we performed a systematic review and meta-analysis of published series.

Received January 11, 2021; accepted after revision March 25.

From the Departments of Neurosurgery (M.A.E., G.L., W.B.) and Radiology (G.L., W.B.), Mayo Clinic, Rochester, Minnesota.

Please address correspondence to Muhammed Amir Essibayi, MD, Department of Neurosurgery, Mayo Clinic, 200 First St SW, Rochester, MN, 55905; e-mail: m.amir.essibayi@gmail.com; @MAEssibayi

 Indicates article with online supplemental data.

<http://dx.doi.org/10.3174/ajnr.A7174>

MATERIALS AND METHODS

Search Strategy

The literature was searched by a medical librarian for “Woven EndoBridge (WEB)” or “flow diverter” combined with “aneurysm” and its variants in accordance with the Preferred

Reporting Items for Systematic Reviews and Meta-Analyses (PRISMA) guidelines² (the PRISMA checklist is provided in the Online Supplemental Data). Search strategies were created using a combination of keywords and standardized index terms. Key words included the following: “Intrasaccular flow diverter or WEB Device,” “Aneurysm, Ruptured/therapy Embolization,” “Therapeutic/instrumentation,” “Endovascular Procedures/instrumentation,” “Intracranial Aneurysm/therapy,” and “Treatment Failure Treatment Outcome.” Searches were run in September 2020 in Ovid Evidence-Based Medicine Reviews, Ovid EMBASE (1974+), Ovid MEDLINE (1946+ including Epub ahead of print, in-process, and other nonindexed citations), Scopus (1970+), and the Web of Science Core Collection (1975+). Results were limited to the English language from 2012+, with most editorials and reviews removed (full search strategy is available in the Online Supplemental Data).

Eligibility Criteria

Inclusion criteria were the following: 1) studies reporting a consecutive series of patients with ruptured intracranial aneurysms treated consecutively with the WEB device with clear reporting of the primary outcomes, and 2) series of at least 5 patients reporting clearly the complications related to the WEB device. Review articles, guidelines, technical notes, comments, and editorials were excluded.

Study Selection Process

Titles and abstracts were screened for inclusion by 1 author using EndNote (Clarivate Analytics). Full-text articles were retrieved for the included abstracts and screened by the same author and were reviewed and confirmed by the senior author. In studies that included both ruptured and unruptured aneurysms, we abstracted only data from patients with ruptured aneurysms.

Data Extraction and Outcome Measures

We extracted baseline patient characteristics from each study, including aneurysm location, aneurysm size, number of aneurysms, sex, mean age, and Hunt and Hess score at admission.

To evaluate WEB device efficacy, we identified our primary and secondary outcomes. The primary one was rebleeding (rerupture) of the aneurysm after the deployment of the WEB device. This primary outcome was chosen because the primary goal of treating a ruptured aneurysm is to prevent rerupture. Secondary outcomes included occlusion status of the aneurysm at the last follow-up point available in each study, retreatment rates, safety outcomes including WEB device-related hemorrhagic and thromboembolic complications, favorable clinical outcome represented by mRS scores between 0 and 2 at last follow-up, and procedure-related and overall mortality rates. If the patients had been followed up for >1 year, 1-year occlusion status was selected as the end point. Short-term follow-up was defined as <1-year follow-up, while ≥1-year follow-up was considered midterm follow-up. Low-quality studies included studies with a high and moderate risk of bias, and studies with a low risk of bias were identified as high-quality studies. Adequate occlusion was assessed according the occlusion scale

mentioned in each study, which generally included complete aneurysm occlusion or small neck remnant. Data were also collected concerning anticoagulation and antiplatelet use.

Study Risk of Bias Assessment

We used the Newcastle-Ottawa Quality Assessment Scale for case-control studies tool to assess the risk of bias in our included studies. Although this tool was designed for the comparative studies, we modified it, focusing on 5 questions: 1) Did the study include all patients or consecutive patients versus a selected sample; 2) was the study retrospective or prospective; 3) was angiographic and clinical follow-up satisfactory, thus allowing ascertainment of all outcomes; 4) were outcomes clearly reported; and, 5) were the operators treating the patients, the same ones who assessed angiographic and clinical outcomes?

Statistical Analysis

The cumulative incidence (event rate per patient at the end of the study) for each study was estimated, along with 95% confidence intervals. Because we anticipated marked heterogeneity in the populations and interventions across various included studies, a random effects model was used to pool incidence rates across studies. The I^2 statistic was used to express the proportion of inconsistency not attributable to chance. Analyses including subgroup meta-analysis were conducted using OpenMeta[Analyst] open-source statistical software (<http://www.cebm.brown.edu/openmeta/>).

RESULTS

Study Selection and Characteristics

After removing duplicates, we found 1701 articles. After we excluded nonrelevant articles by the screening of the title and abstract, 69 articles were included for full-text screening. Eighteen studies (19 articles)³⁻²¹ were included in our qualitative and quantitative analyses. The results of 1 included study were published in 2 separate articles that had to be included to cover the total characteristics and outcomes of the sample.^{8,9} Overall, 487 patients with 496 aneurysms were considered. The mean age was 57 years; 387 (83.6%) and 76 (16.4%) of these aneurysms were located in the anterior (commonly in anterior communicating artery, MCA, and posterior communicating artery) and posterior (commonly in the basilar artery and PICA) circulations, respectively. The mean width of the ruptured aneurysms, reported in 10 studies, was 5.6 mm. The mean height of the ruptured aneurysms (consistently reported in 5 studies) was 6.0 mm. Most aneurysms were wide-neck. Two hundred seventy-five (74.7%) patients were admitted with Hunt and Hess scores of 1–3, and 93 patients (25.3%) experienced severe SAH (Hunt and Hess score, 4–5). Forty-one additional interventions, consisting mainly of coiling or stent placement, were used for incompletely occluded ruptured aneurysms. A summary of the data of the included studies and reported baseline characteristics of the ruptured aneurysms are provided in the Online Supplemental Data. The flow diagram for study selection is provided in the Online Supplemental Data.

Primary Outcomes

The primary outcome (aneurysm rerupture after treatment with the WEB device) occurred in 1.1% of cases (95% CI, 0.1%–2.1%) (4/423 aneurysms): 0.8% (95% CI, 0.3%–2%) and 1.7% (95% CI, 0.1%–3.5%) in the studies with short- and midterm follow-ups, respectively. The rate of rerupture per month during follow-up was 0.2% (95% CI, 0.0%–0.3%).

Secondary Outcomes

A total of 285 patients from 16 studies had angiographic occlusion outcomes reported. Adequate occlusion was achieved after short-term follow-up in 193 of 216 patients (91.7%; 95% CI, 87.4%–95.9%) and after midterm follow-up in 77 of 94 patients (77%; 95% CI, 68.6%–85.4%). In total, 245 patients showed adequate occlusion (87.3%; 95% CI, 82.1%–92.4%) at last follow-up. Adequate occlusion was reported in 78.1% (95% CI, 69.4%–86.8%) among studies with high quality (low risk of bias) and 93.4% (95% CI, 90%–96.9%) among studies with low quality (high or moderate risk of bias). The mean length of follow-up ranged from 3 to 15 months, with a median of 7 months. During follow-up, 27 aneurysms required retreatment (5.1%; 95% CI, 3%–7.3%), 5.8% (95% CI, 2.8%–8.7%) at short-term and 6% (95% CI, 1.2%–10.9%) at midterm follow-up. The treatment-related perioperative complication rate was 13.2% (95% CI, 9.2%–17.1%). Only a minority of these complications (24.4%; 95% CI, 14.5%–34.3%) resulted in prolonged clinical deterioration or permanent neurologic deficits; thus, the overall clinical complication rate related to WEB device deployment was 3.2% (95% CI, 1.6%–4.7%), 13 hemorrhagic (2%; 95% CI, 0.8%–3.3%) and 41 thromboembolic (6.8%; 95% CI, 4.6%–9%) complications. At short- and midterm follow-up, 210 of 250 patients (85%; 95% CI, 78%–92.1%) and 55 of 64 patients (86.7%; 95% CI, 78.5%–95%) showed favorable clinical outcomes (mRS 0–2), respectively. Twelve patients died in the perioperative period as a result of procedure-related complications (2.1%; 95% CI, 0.8%–3.3%). The all-cause mortality rate was 11.5% (95% CI, 7%–16%).

Antiplatelet Therapy

Routine antiplatelet therapy (APT) was not used in 10 included studies, while in 8 studies, APT was routinely given before and after the procedure either as monotherapy or dual therapy for variable time intervals. Many studies reported the use of dual antiplatelet therapy for 1–2 months in cases in which a thromboembolic complication occurred or an additional device was deployed. In those who received any APT, the rate of thromboembolic and treatment-related overall complications was 7.4% (95% CI, 3.2%–11.5%) and 14.3% (95% CI, 6.1%–22.4%), respectively. In studies in which no routine APT was used, the rates of thromboembolic and treatment-related overall complications were 6.5% (95% CI, 4%–9.1%) and 13.1% (95% CI, 8.5%–17.7%), respectively. The procedure-related primary and secondary outcomes and details of the APT use are explained in the Online Supplemental Data. The forest plots of the meta-analysis of the outcomes are shown in the Figure and the Online Supplemental Data.

Risk of Bias

Of 18 studies, the risk of bias was low in 5, moderate in 10, and high in 3 studies. The smallest study had 5 patients with 5 ruptured aneurysms, and the largest study included 100 patients with 106 aneurysms (100 ruptured aneurysms).

DISCUSSION

This systematic review and meta-analysis of 18 cohort studies demonstrates that primary treatment of ruptured intracranial aneurysms with the WEB device is both safe and effective, with rerupture rates of approximately 1% and a perioperative complication rate of 13%, with most of these not resulting in additional clinical deficits. At long-term follow-up, >85% of the aneurysms showed adequate obliteration, suggesting that in general, the obliteration rate of ruptured aneurysms treated with the WEB device is high. These findings are important because they suggest that the WEB device could potentially be used routinely in the treatment of ruptured wide-neck bifurcation aneurysms.

One commonly used technique for the treatment of wide-neck bifurcation aneurysms is stent-assisted coiling. Several series have recently been published examining the efficacy of stent-assisted coiling in the treatment of ruptured aneurysms.²² In a recently published meta-analysis by Bsat et al,²² the rates of post-interventional rebleeding (2.5%) and hemorrhagic complications (8.7%) were higher than the rates of these complications in the setting of WEB device deployment according to our meta-analysis. The risk of thromboembolic complications in the meta-analysis of Bsat et al was 9.1%, and this is also higher than that found in our study (6.8%). Another meta-analysis published in 2019 compared the rate of perioperative complications for ruptured intracranial aneurysms treated with stent-assisted coiling with the rate of those treated with simple coiling and reported a 20.2% complication rate for the stent-assisted coiling group versus 13.1% for the coiling-only group.²³ Nevertheless, the rate of perioperative complications in our meta-analysis was lower (13.2%) than that in the stent-assisted coiling group and similar to the that in the coiling group. Thus, intrasaccular flow-diversion treatment with the WEB may be safer than stent-assisted coiling and as safe as primary coiling for treating wide-neck bifurcation aneurysms.

Prevention of rebleeding is the primary goal in the treatment of ruptured aneurysms. The rate of rebleeding in our meta-analysis is similar to that reported in the Analysis of Recanalization after Endovascular Treatment of Intracranial Aneurysm (ARETA) study,^{24,25} a large prospective, multicenter study conducted to assess the recanalization of ruptured intracranial aneurysms after endovascular treatment with coiling and balloon-assisted coiling. The risk of rebleeding in 753 patients with ruptured aneurysms in the ARETA study was 1% (95% CI, 0.3%–1.7%). These patients had 78 thromboembolic (10.4%) and 28 hemorrhagic (3.7%) complications, similar to the results of our study. In the International Subarachnoid Aneurysm Trial (ISAT),²⁶ 1073 patients underwent coil embolization for ruptured aneurysms. The rate of rebleeding was 1.9% in the first 30 days after the treatment and 0.8% at follow-up (30 days to 1 year); 92% of aneurysms showed adequate occlusion (66%, complete occlusion; 26%, neck remnant or subtotal occlusion), and the overall

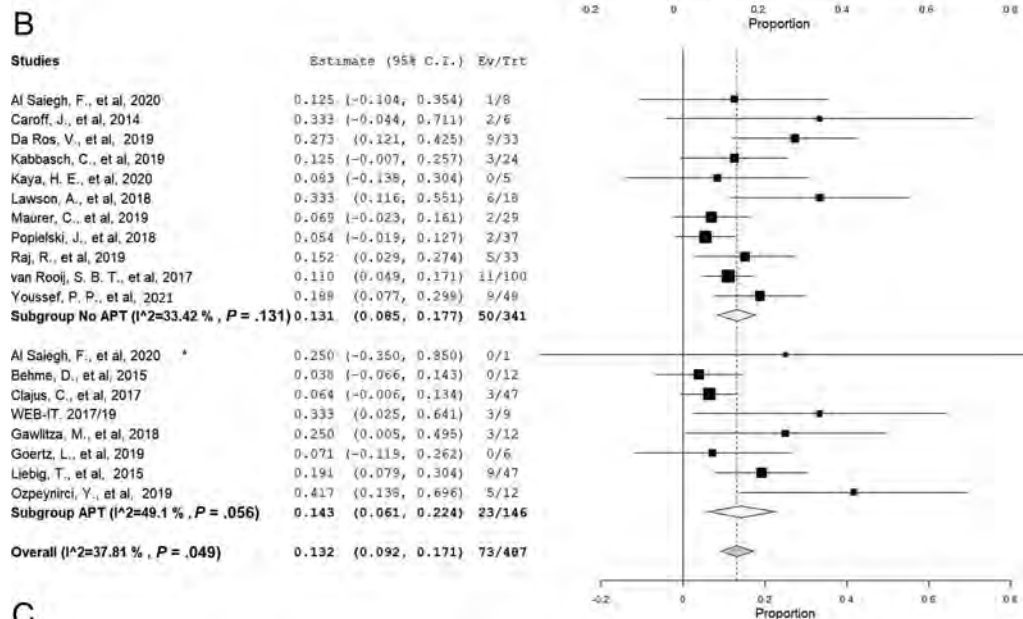
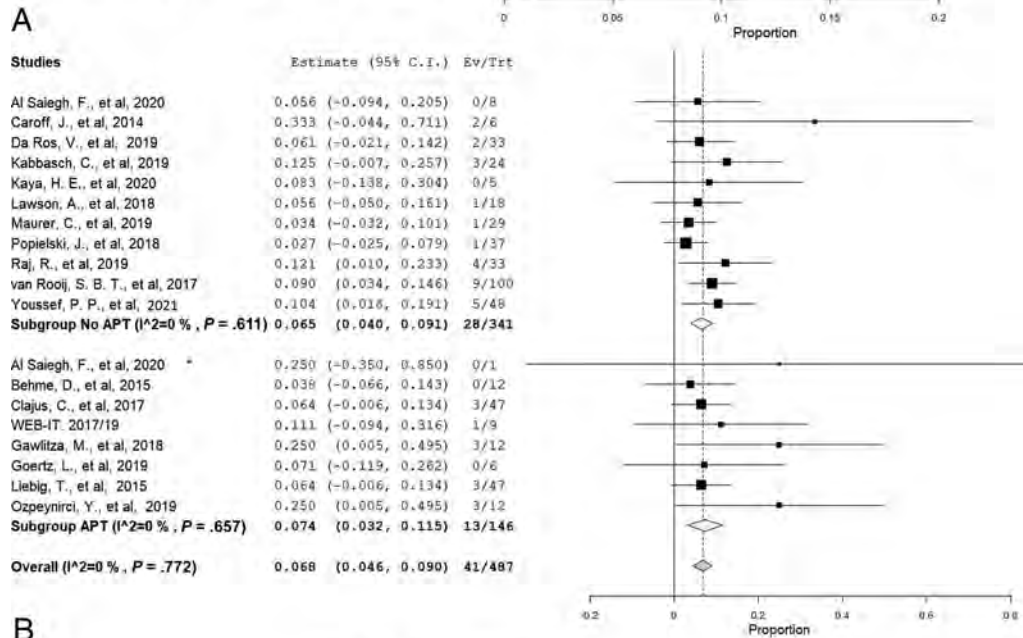
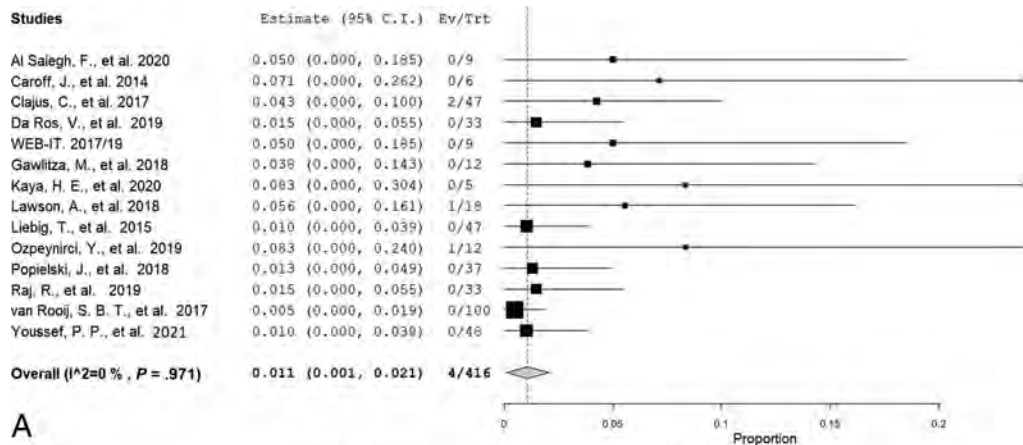


FIGURE. A, Forest plot with a random effects model shows the late rebleeding rate. B, Forest plot with a random effects model shows the rate of treatment-related perioperative complications grouped by APT use. C, Forest plot with a random effects model shows the rate of thromboembolic complications grouped by APT use. Ev/Trt indicates Event (Outcome, complication)/Treated patient.

mortality rate after 1 year was 8.1%. In comparison with ISAT, in our meta-analysis, the overall rebleeding (1%) and adequate occlusion (87%) rates were similar, an outcome especially remarkable given that the aneurysms treated with the WEB device were mostly wide-neck. The overall mortality rate (11.5%) was slightly higher. Nevertheless, 25% of our study patients were admitted with severe SAH compared with 12% in ISAT, and procedure-related mortality was around 2%. From these results, we can infer that the WEB may be as safe as simple coiling and balloon-assisted coiling to treat acutely ruptured intracranial aneurysms.

One interesting issue that has been brought up recently is whether there are differences in occlusion rates and clinical outcomes between ruptured and unruptured aneurysms treated with the WEB. In a study published by Pierot et al,²⁷ which included cumulative data from 3 clinical trials comprising >90% unruptured aneurysms (WEB Clinical Assessment of Intracranial Aneurysm Therapy [WEBCAST],²⁸ WEBCAST-2,²⁹ and the French Observatory³⁰), the rate of adequate occlusion at 1 year was found to be 79.1%, which is similar to the adequate occlusion rate (77%) of ruptured aneurysms at midterm follow-up in our meta-analysis. In the WEBCAST study, 85.4% of the treated unruptured aneurysms had adequate occlusion at short-term follow-up (6 months), which is only slightly less than that in our study of ruptured aneurysms (91.7%). This can be referred to prothrombotic milieu in the setting of SAH that may accelerate aneurysm thrombosis.³¹ The rate of retreatment in unruptured aneurysms at 1-year follow-up was 6.9%,²⁷ which is also similar to that in our study (6%). Thromboembolic adverse events occurred in 14.4% of the patients in the cumulative data of Pierot et al, which is twice as high as that in our results (6.8%). However, the symptomatic thromboembolic events with clinical sequelae were reported as 3%, which is similar to the rate (3.2%) of overall clinical complications in our meta-analysis. Furthermore, the rate (2%) of hemorrhagic complications in this study is also similar to that in the previous study with unruptured aneurysms (1.8%). These results demonstrate that the WEB device has a high efficacy and feasibility in the management of ruptured wide-neck cerebral aneurysms, similar to what was confirmed in the past for unruptured wide-neck aneurysms.

The main advantage of using the WEB device over stent or flow-diversion techniques is the absence of the requirement for periprocedural dual antiplatelet treatment. This is especially important in the acute phase of aneurysmal SAH when patients often require invasive procedures such as placement of external ventricular drains or lumbar drains and ventriculoperitoneal shunts, procedures that can be complicated by hemorrhage in the setting of dual antiplatelet therapy. While there was no notable difference in thromboembolic (non-APT, 6.5%; APT, 7.4%) and overall complication (non-APT, 13.1%; APT, 14.3%) rates between patients with and without routine nonuse of antiplatelet therapy in our meta-analysis, at our center, we continue to place these patients on antiplatelet therapy with high-dose aspirin and clopidogrel (Plavix) because we believe that this prevents severe acute thrombosis after WEB device placement in ruptured aneurysms.

Limitations

All the included studies in this meta-analysis were uncontrolled, and many of them were retrospective and single-center. Thus,

our meta-analysis is limited by selection bias and the heterogeneity that arises from the variability in aneurysm morphologies, patient scenarios, operator experience, and practice protocols (eg, pre- and postoperative antiplatelet therapy application methods). Despite our effort to exclude overlapping patient populations, the possibility of overlap in patients among the studies remains. The mean follow-up periods among the included studies were variable and modest in terms of length. However, we tried to reduce this variety by selecting the last follow-up point or 1-year follow-up results. Most of the studies in the literature lack the stratification of outcomes based on aneurysm rupture status. Among those that investigated outcomes on the basis of the rupture status, many did not report the impact of important variables such as the type and size of the WEB device and baseline patient morbidity in the treatment outcomes. The rate of adequate occlusion in studies with low quality, mostly due to self-assessment of the angiographic and clinical outcomes, was higher (93.4%) than that of high-quality-studies (78.1%). This finding raises the question of bias that results from including such low-quality studies. Furthermore, the relatively small sample of patients with reported angiographic outcomes, absence of a single and common standard method for assessment of aneurysm occlusion, lack of a control group, and the short duration of follow-up may affect the reliability of the results concerning the safety and durability of aneurysm occlusion. Therefore, the overall certainty in the evidence at present is rated as low.³² Finally, this meta-analysis has concentrated on only ruptured aneurysms, which can be a limitation. However, the main advantage of this meta-analysis was the thorough assessment of WEB device efficacy and safety in acute subarachnoid hemorrhage situations.

CONCLUSIONS

Our meta-analysis of 18 studies including around 500 ruptured aneurysms treated with the WEB device demonstrated the safety and efficacy of the WEB device in the management of wide-neck ruptured aneurysms. Further studies and randomized clinical trials with longitudinal follow-up directly comparing the WEB with other established techniques (ie, coiling, clipping, stent-assisted coiling, and so forth) are needed.

Disclosures: Giuseppe Lanzino—UNRELATED: Consultancy: Superior Medical Experts, Nested Knowledge. Waleed Brinjikji—RELATED: Consulting Fee or Honorarium: MicroVention, Comments: consultant and proctor for MicroVention*; UNRELATED: Board Membership: Marblehead Medical LLC, Comments: owner; Consultancy: Cerenovus.* *Money paid to the institution.

REFERENCES

1. Mine B, Pierot L, Lubicz B. **Intrasaccular flow-diversion for treatment of intracranial aneurysms: the Woven EndoBridge.** *Expert Rev Med Devices* 2014;11:315–25 CrossRef Medline
2. Moher D, Liberati A, Tetzlaff J, et al. **Preferred Reporting Items for Systematic Reviews and Meta-Analyses: the PRISMA Statement.** *PLoS Med* 2009;6:e1000097 CrossRef Medline
3. Al Saiegh F, Hasan D, Mouchtouris N, et al. **Treatment of acutely ruptured cerebral aneurysms with the Woven EndoBridge device: experience post-FDA approval.** *Neurosurgery* 2020;87:E16–22 CrossRef Medline
4. Behme D, Berlis A, Weber W. **Woven EndoBridge intrasaccular flow disrupter for the treatment of ruptured and unruptured**

- wide-neck cerebral aneurysms: report of 55 cases. *AJNR Am J Neuroradiol* 2015;36:1501–06 CrossRef Medline
5. Caroff J, Mihalea C, Dargento F, et al. **Woven EndoBridge (WEB) device for endovascular treatment of ruptured intracranial wide-neck aneurysms: a single-center experience.** *Neuroradiology* 2014;56:755–61 CrossRef Medline
 6. Clajus C, Strasilla C, Fiebig T, et al. **Initial and mid-term results from 108 consecutive patients with cerebral aneurysms treated with the WEB device.** *J Neurointerv Surg* 2017;9:411–17 CrossRef Medline
 7. Da Ros V, Bozzi A, Comelli C, et al. **Ruptured intracranial aneurysms treated with Woven EndoBridge intrasaccular flow disruptor: a multicenter experience.** *World Neurosurg* 2019;122:e498–505 CrossRef Medline
 8. Fiorella D, Boulos A, Turk AS, et al. **The safety and effectiveness of the LVIS stent system for the treatment of wide-necked cerebral aneurysms: final results of the pivotal US LVIS trial.** *J Neurointerv Surg* 2019;11:357–61 CrossRef Medline
 9. Arthur AS, Molyneux A, Coon AL, et al. **The safety and effectiveness of the Woven EndoBridge (WEB) system for the treatment of wide-necked bifurcation aneurysms: final 12-month results of the pivotal WEB Intrasaccular Therapy (WEB-IT) study.** *J Neurointerv Surg* 2019;11:924–30 CrossRef Medline
 10. Gawlitz M, Soize S, Januel A-C, et al. **Treatment of recurrent aneurysms using the Woven EndoBridge (WEB): anatomical and clinical results.** *J Neurointerv Surg* 2018;10:629–33 CrossRef Medline
 11. Goertz L, Liebig T, Siebert E, et al. **Extending the indication of Woven EndoBridge (WEB) embolization to internal carotid artery aneurysms: a multicenter safety and feasibility study.** *World Neurosurg* 2019;126:e965–74 CrossRef Medline
 12. Kabbasch C, Goertz L, Siebert E, et al. **WEB embolization versus stent-assisted coiling: comparison of complication rates and angiographic outcomes.** *J Neurointerv Surg* 2019;11:812–16 CrossRef Medline
 13. Kaya HE, Bakdik S, Keskin F, et al. **Endovascular treatment of intracranial aneurysms using the Woven EndoBridge (WEB) device: retrospective analysis of a single center experience.** *Clin Imaging* 2020;59:25–29 CrossRef Medline
 14. Lawson A, Molyneux A, Sellar R, et al. **Safety results from the treatment of 109 cerebral aneurysms using the Woven EndoBridge technique: preliminary results in the United Kingdom.** *J Neurosurg* 2018;128:144–53 CrossRef Medline
 15. Liebig T, Kabbasch C, Strasilla C, et al. **Intrasaccular flow disruption in acutely ruptured aneurysms: a multicenter retrospective review of the use of the WEB.** *AJNR Am J Neuroradiol* 2015;36:1721–27 CrossRef Medline
 16. Maurer C, König I, Berlis A, et al. **Two-center experience in the endovascular treatment of intracranial aneurysms using the Woven EndoBridge 17 device including midterm follow-up results: a retrospective analysis.** *AJNR Am J Neuroradiol* 2019;40:1517–22 CrossRef Medline
 17. Ozpeynirci Y, Braun M, Pala A, et al. **WEB-only treatment of ruptured and unruptured intracranial aneurysms: a retrospective analysis of 47 aneurysms.** *Acta Neurochir (Wien)* 2019;161:1507–13 CrossRef Medline
 18. Popielski J, Berlis A, Weber W, et al. **Two-center experience in the endovascular treatment of ruptured and unruptured intracranial aneurysms using the WEB device: a retrospective analysis.** *AJNR Am J Neuroradiol* 2018;39:111–17 CrossRef Medline
 19. Raj R, Rautio R, Pekkola J, et al. **Treatment of ruptured intracranial aneurysms using the Woven EndoBridge device: a two-center experience.** *World Neurosurg* 2019;123:e709–16 CrossRef Medline
 20. van Rooij SB, van Rooij WJ, Peluso JP, et al. **WEB treatment of ruptured intracranial aneurysms: a single-center cohort of 100 patients.** *AJNR Am J Neuroradiol* 2017;38:2282–87 CrossRef Medline
 21. Youssef PP, Dornbos D, III, Peterson J, et al. **Woven EndoBridge (WEB) device in the treatment of ruptured aneurysms.** *J Neurointerv Surg* 2021;13:443–46 CrossRef Medline
 22. Bsat S, Bsat A, Tamim H, et al. **Safety of stent-assisted coiling for the treatment of wide-necked ruptured aneurysm: a systematic literature review and meta-analysis of prevalence.** *Interv Neuroradiol* 2020;26:547–56 CrossRef Medline
 23. Zhang X, Zuo Q, Tang H, et al. **Stent assisted coiling versus non-stent assisted coiling for the management of ruptured intracranial aneurysms: a meta-analysis and systematic review.** *J Neurointerv Surg* 2019;11:489–96 CrossRef Medline
 24. Pierot L, Barbe C, Nguyen HA, et al. **Intraoperative complications of endovascular treatment of intracranial aneurysms with coiling or balloon-assisted coiling in a prospective multicenter cohort of 1088 participants: Analysis of Recanalization after Endovascular Treatment of Intracranial Aneurysm (ARETA) study.** *Radiology* 2020;295:381–89 CrossRef Medline
 25. Pierot L, Barbe C, Herbreteau D, et al. **Rebleeding and bleeding in the year following intracranial aneurysm coiling: analysis of a large prospective multicenter cohort of 1140 patients: Analysis of Recanalization after Endovascular Treatment of Intracranial Aneurysm (ARETA) study.** *J NeuroInterv Surg* 2020;12:1219–25 CrossRef Medline
 26. Molyneux AJ, Kerr RS, Yu L-M, et al. International Subarachnoid Aneurysm Trial (ISAT) Collaborative Group. **International subarachnoid aneurysm trial (ISAT) of neurosurgical clipping versus endovascular coiling in 2143 patients with ruptured intracranial aneurysms: a randomised comparison of effects on survival, dependency, seizures, rebleeding, subgroups, and aneurysm occlusion.** *Lancet* 2005;366:809–17 CrossRef Medline
 27. Pierot L, Moret J, Barreau X, et al. **Safety and efficacy of aneurysm treatment with WEB in the cumulative population of three prospective, multicenter series.** *J Neurointerv Surg* 2018;10:553–59 CrossRef Medline
 28. Pierot L, Costalat V, Moret J, et al. **Safety and efficacy of aneurysm treatment with WEB: results of the WEBCAST study.** *J Neurosurg* 2016;124:1250–56 CrossRef Medline
 29. Pierot L, Gubucz I, Buhk JH, et al. **Safety and efficacy of aneurysm treatment with the WEB: results of the WEBCAST 2 study.** *AJNR Am J Neuroradiol* 2017;38:1151–55 CrossRef Medline
 30. Pierot L, Moret J, Turjman F, et al. **WEB treatment of intracranial aneurysms: clinical and anatomic results in the French Observatory.** *AJNR Am J Neuroradiol* 2016;37:655–59 CrossRef Medline
 31. Hamilton MG, Dold ON. **Spontaneous disappearance of an intracranial aneurysm after subarachnoid hemorrhage.** *Can J Neurol Sci* 1992;19:389–91 Medline
 32. Murad MH, Montori VM, Ioannidis JPA, et al. **How to read a systematic review and meta-analysis and apply the results to patient care: users' guides to the medical literature.** *JAMA* 2014;312:171–79 CrossRef Medline

The Safety of Intra-arterial Tirofiban during Endovascular Therapy after Intravenous Thrombolysis

S.H. Jang, S.-I. Sohn, H. Park, S.-J. Lee, Y.-W. Kim, J.M. Hong, C.-H. Kim, J.W. Choi, D.-H. Kang, Y.-S. Kim, Y.-H. Hwang, J.S. Lee, and J.-H. Hong

ABSTRACT

BACKGROUND AND PURPOSE: The safety and efficacy of tirofiban during endovascular therapy in patients undergoing intravenous thrombolysis with recombinant IV tPA remain unclear. This study aimed to investigate the safety and efficacy of intra-arterial tirofiban use during endovascular therapy in patients treated with IV tPA.

MATERIALS AND METHODS: Using a multicenter registry, we enrolled patients with acute ischemic stroke who underwent endovascular therapy. Safety outcomes included postprocedural parenchymal hematoma type 2 and/or thick subarachnoid hemorrhage, intraventricular hemorrhage, and 3-month mortality. Efficacy outcomes included the successful reperfusion rate, postprocedural reocclusion, and good outcomes at 3 months (mRS scores of 0–2). The tirofiban effect on the outcomes was evaluated using a multivariable analysis while adjusting for potential confounders.

RESULTS: Among enrolled patients, we identified 314 patients with stroke (279 and 35 patients in the no tirofiban and tirofiban groups, respectively) due to an intracranial artery occlusion who underwent endovascular therapy with intravenous thrombolysis. A multivariable analysis revealed no association of intra-arterial tirofiban with postprocedural parenchymal hematoma type and/or thick subarachnoid hemorrhage (adjusted OR, 1.07; 95% CI, 0.20–4.10; $P = .918$), intraventricular hemorrhage (adjusted OR, 0.43; 95% CI, 0.02–2.85; $P = .467$), and 3-month mortality (adjusted OR, 0.38; 95% CI, 0.04–1.87; $P = .299$). Intra-arterial tirofiban was not associated with good outcome (adjusted OR, 2.22; 95% CI, 0.89–6.12; $P = .099$).

CONCLUSIONS: Using intra-arterial tirofiban during endovascular therapy after IV tPA could be safe.

ABBREVIATIONS: aOR = adjusted OR; EVT = endovascular therapy; IA = intra-arterial; ICAS-O = intracranial atherosclerotic stenosis–related occlusion; IVT = intravenous thrombolysis; LVO = large-vessel occlusion; mTICI = modified TICI

Given the positive findings of randomized controlled trials of endovascular therapy (EVT) with newer devices,^{1–5} EVT has become a standard therapy for anterior circulation ischemic stroke.^{2,4} Although it remains unclear whether EVT combined with intravenous thrombolysis (IVT) with tPA is better than EVT alone, the American Stroke Association/American Heart Association guidelines recommends IVT for eligible patients with large-vessel occlusion (LVO).⁶

IV tPA improves outcomes in patients with acute ischemic stroke.⁷ However, given that IV tPA increases the risk of intracranial hemorrhage, it limits additional procedural techniques

during EVT. A large pivotal study on EVT reported that 29% of patients lacked successful reperfusion (modified TICI [mTICI] $\geq 2b$).⁸ Additionally, during EVT, endothelial damage can occur with resulting platelet activation, which causes reocclusion.⁹ This often requires rescue treatment, including balloon angioplasty, stent placement, or adjuvant thrombolytic infusion. Although antiplatelet agents or thrombolytic infusion has benefits in cases involving stent deployment or ongoing thrombus formation, these treatments may increase the risk of bleeding complications.

Tirofiban is the most commonly used rescue thrombolytic.¹⁰ However, its safety and efficacy in EVT among patients with acute ischemic stroke remain unclear.^{11–17} Additionally, although studies of EVT have reported that 83% of patients were treated with IV tPA before EVT,⁸ there is no evidence regarding the use of tirofiban during EVT in patients treated with IV tPA.

Therefore, this study aimed to investigate the safety and efficacy of intra-arterial (IA) tirofiban during EVT in patients treated with IV tPA.

Received December 31, 2020; accepted after revision April 7, 2021.

From the Departments of Neurology (S.H.J., S.-I.S., H.P., J.-H.H.) and Neurosurgery (C.-H.K.), School of Medicine, Keimyung University School of Medicine, Daegu, South Korea; Departments of Neurology (S.-J.L., J.M.H., J.S.L.) and Radiology (J.W.C.), School of Medicine, Ajou University, Suwon, South Korea; Departments of Neurology (Y.-W.K., Y.-H.H.), Neurosurgery (D.-H.K.), and Radiology (Y.-S.K.), School of Medicine, Kyungpook National University, Daegu, South Korea.

Please address correspondence to Jeong-Ho Hong, MD, Department of Neurology, Keimyung University School of Medicine, 1095 Dalgubeol-daero, Dalseo-gu Daegu, South Korea, 42601; e-mail: neurohong79@gmail.com
<http://dx.doi.org/10.3174/ajnr.A7203>

MATERIALS AND METHODS

Patients

This study used the Intracranial Atherosclerotic Occlusion and Neurointervention-Korean Retrospective registry. Briefly, this study collected data from patients with acute ischemic stroke who underwent EVT between 2011 and 2016 in 3 comprehensive centers in Korea. The inclusion criteria of the present study were the following: 1) treated with IV tPA for acute ischemic stroke within 4.5 hours of symptom onset, and 2) having LVO in the ICA, MCA M1, and MCA M2. The exclusion criteria were the following: 1) missing 3-month mRS scores; 2) extracranial and/or tandem intracranial large-artery occlusions; 3) known thrombocytopenia at presentation or a thrombocyte count of $\leq 100 \times 10^9/L$; and 4) having other stroke etiologies, including vasculitis, arterial dissection, or Moyamoya disease. This study was approved by the local institutional review board (Keimyung University Dongsan Hospital IRB: 2016-01-038-009; Ajou University Hospital IRB: AJIRB-MED-OBS-15-483, AJIRB-MED-OBS-17-094; Kyungpook National University Hospital IRB: 2016-01-020-006), which waived the requirement for written informed consent given the retrospective and registry-based design. The data sets used and/or analyzed during the present study are available from the corresponding author on reasonable request.

IVT and EVT Procedures

On the basis of the international guidelines, IV tPA, 0.9 mg/kg, was administered within 4.5 hours of symptom onset in all centers.⁶ Angiography was usually performed with the patient under local anesthesia. The EVT procedure was chosen at the discretion of neurointerventionalists. Stent retrieval and contact aspiration methods were routinely selected. In case of failed EVT for LVO, rescue treatments, including emergency stent placement, balloon angioplasty, or tirofiban infusion, were administered.

IA Tirofiban Treatment

The choice of using tirofiban was similarly at the discretion of the interventionalists in the following situations: 1) when the interventionalist detected thrombus embolization causing distal arterial occlusion and thrombus was likely to be distally embolized and risky; 2) when reocclusion reoccurred due to intracranial atherosclerosis; 3) when the target artery remained occluded or rescue treatment with emergency stent placement or balloon angioplasty due to postthrombectomy residual stenosis was required; and 4) when patients had a high possibility of reocclusion (high-grade intracranial stenosis or progression of stenosis, and so forth) after occluded arteries were recanalized during EVT. Treatment involved 0.5 mg (2 mL) of tirofiban diluted with 8 mL of normal saline injected with an infusion rate of 1 mL/min. Alternately, if 1 mg (4 mL) of tirofiban was required at first, treatment involved 1 mg (4 mL) of tirofiban diluted with 6 mL of normal saline injected at a rate of 1 mL/min. On follow-up angiography immediately and 10 minutes after infusion of IA, if additional tirofiban was needed, the same protocol was used. Total IA tirofiban infusion ranged from 0.5 to 2.0 mg.

Data Acquisition and Outcomes

We analyzed clinical characteristics, including age, sex, NIHSS score on admission, and baseline mRS scores. The LVO etiology was determined using angiographic diagnosis as previously reported.¹⁹ Brain CT was performed to evaluate hemorrhagic complications immediately and 12–24 hours after EVT. The safety outcomes included adverse hemorrhagic complications, intraventricular hemorrhage, and mortality. Intracranial hemorrhages were classified on the basis of the European Cooperative Acute Stroke Study.²⁰ Serious hemorrhagic complications were defined as parenchymal hematoma type 2 and/or thick SAH with or without intraventricular hemorrhage (modified Fisher grade 3 or 4 of SAH). The efficacy outcomes included successful reperfusion, postprocedural reocclusion, and 3-month mRS scores. On the basis of the final angiography, successful reperfusion was defined as an mTICI grade of 2b or 3. Postprocedural reocclusion was evaluated using angiography performed until discharge by comparing it final angiography performed during EVT. Good outcomes at 3 months were defined as mRS scores of 0–2.

Statistical Analyses

Descriptive statistics were used for between-group comparisons of patient characteristics and outcomes. Categorical variables were analyzed using χ^2 tests or Fisher exact tests and were presented as percentages. Continuous variables were analyzed using the Student *t* test or Mann-Whitney *U* test and were presented as median and interquartile range.

Multivariable logistic regression analysis was performed to evaluate the efficacy and safety outcomes. Variables with $P < .15$ in the bivariate analysis were included in the multivariable logistic regression analysis. All statistical analyses were performed using R statistical and computing software (<http://www.r-project.org/>). For all analysis, $P < .05$ was considered statistically significant.

RESULTS

Patients

We analyzed a total of 314 patients who underwent EVT combined with IV tPA. Among them, 35 patients were treated with IA tirofiban (tirofiban group), while 279 patients were not (no tirofiban group) (Fig 1). Table 1 shows the baseline characteristics of the recruited participants. Compared with the no tirofiban group, the tirofiban group had significantly more cases of intracranial atherosclerotic stenosis-related occlusion (ICAS-O) (10.0% versus 51.4%, $P < .001$), higher rates of intracranial stent placement (3.2% versus 17.1%, $P = .001$), and higher rates of intraprocedural reocclusion (3.6% versus 31.4%, $P < .001$). There was no significant between-group difference in the age, baseline NIHSS scores, and ASPECTS.

Patient Outcomes: Safety and Efficacy

The Table 2 present the safety and efficacy outcomes. Serious hemorrhage was observed in 11.1% and 8.6% of patients in the no tirofiban and tirofiban groups, respectively ($P = .867$). Intraventricular hemorrhage was observed in 6.8% and 2.9% of the patients in the no tirofiban and tirofiban groups, respectively ($P = .592$). The 3-month mortality rate was 12.5% and 5.7% in the no tirofiban and tirofiban groups, respectively ($P = .366$). Multivariable analysis revealed no association of IA tirofiban

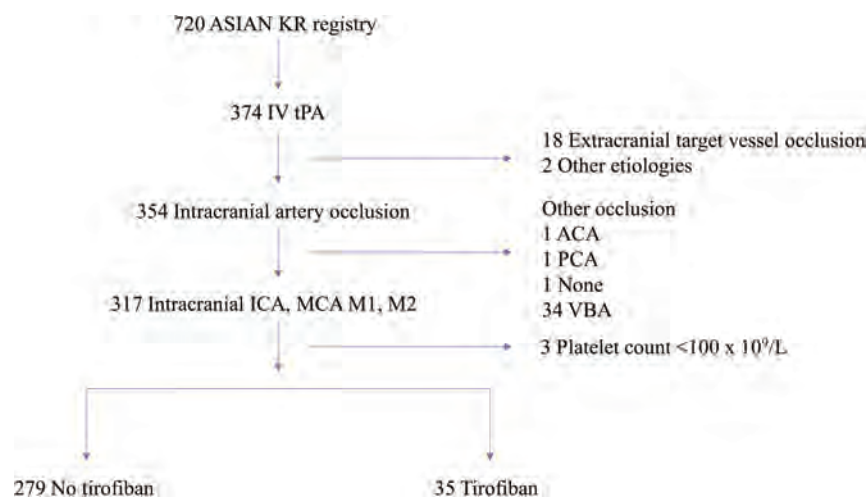


FIG 1. Study flow chart. The Acute Stroke due to Intracranial Atherosclerotic occlusion and Neurointervention-Korean Retrospective (ASIAN KR) registry. ACA indicates anterior cerebral artery; PCA, posterior cerebral artery; VBA, vertebrobasilar artery.

Table 1: Baseline characteristics of patients

	No Tirofiban (n = 279)	Tirofiban (n = 35)	P Value
Age (median) (IQR) (yr)	69.0 (60.0–76.0)	66.0 (55.5–73.0)	.163
Sex (male)	144 (51.6%)	24 (68.6%)	.086
Hypertension	174 (62.4%)	18 (51.4%)	.286
DM	60 (21.5%)	9 (25.7%)	.726
Hyperlipidemia	75 (26.9%)	12 (34.3%)	.470
Prior antiplatelet	89 (31.9%)	7 (20.0%)	.213
Prior anticoagulant	29 (10.4%)	1 (2.9%)	.261
NIHSS on admission (median) (IQR)	17.0 (13.0–20.0)	16.0 (12.0–20.0)	.448
Onset-to-puncture time (min, median) (IQR)	204.0 (153.0–257.5)	184.0 (150.0–281.5)	.622
Onset-to-final angiography time (min, median) (IQR)	273.0 (214.5–349.0)	303.0 (241.0–348.5)	.230
Etiology of LVO			<.001
Embollic occlusion	231 (82.8%)	16 (45.7%)	
ICAS occlusion	28 (10.0%)	18 (51.4%)	
Intractable (failed thrombectomy)	20 (7.2%)	1 (2.9%)	
Target artery occlusion			.725
Terminal ICA	113 (40.5%)	11 (31.4%)	
MCA M1	139 (49.8%)	20 (57.1%)	
MCA M2	27 (9.7%)	4 (11.4%)	
Intraprocedural reocclusion	10 (3.6%)	11 (31.4%)	<.001
Intracranial stent placement	9 (3.2%)	6 (17.1%)	.001
Intracranial ballooning	8 (2.9%)	0 (0.0%)	.656
ASPECTS (median) (IQR)	7.0 (4.0–9.0)	8.0 (4.5–9.5)	.899

Note:—IQR indicates interquartile range; DM, diabetes mellitus; ICAS, intracranial atherosclerotic stenosis.

with serious hemorrhage (adjusted OR [aOR], 1.07; 95% CI, 0.20–4.10; $P = .918$), intraventricular hemorrhage (aOR, 0.43; 95% CI, 0.02–2.85; $P = .467$), and death at 3 months (aOR, 0.38; 95% CI, 0.04–1.87; $P = .299$). There was successful reperfusion in 75.3% and 80.0% of patients in the no tirofiban and tirofiban groups, respectively ($P = .684$). After adjustment, IA tirofiban was not associated with successful reperfusion (aOR, 1.56; 95% CI, 0.5–5.34; $P = .440$).

At 3 months, 53.8% and 57.1% of patients in the no tirofiban and tirofiban groups, respectively, showed good outcome ($P = .843$). Postprocedural reocclusion until discharge was observed

in 4.4% and 2.9% of the patients in the no tirofiban and tirofiban groups, respectively ($P = .688$). We analyzed 255 patients in whom postprocedural reocclusion until discharge in patients with mTICI $\geq 2a$ was assessed for subgroup analysis. Four (17.4%) patients in the no tirofiban group and none (0%) in the tirofiban group had postprocedural reocclusion until discharge in ICAS-O, but the difference was not statistically significant (4/23, 17.4% versus 0/16, 0%, $P = .221$). In embolic occlusion, postprocedural reocclusion was not found to be different between the no tirofiban and the tirofiban groups (4/203, 2.0% versus 1/13, 7.7%, $P = .705$) (Fig 2).

DISCUSSION

In clinical practice, the efficacy of antiplatelet administration when performing EVT in patients treated with IV tPA remains unclear. There is limited available evidence regarding optimal antiplatelet administration during EVT, with antiplatelets being recommended during stent deployment for EVT;²¹ however, the 2018 American Heart Association/American Stroke Association guidelines indicate that aspirin administration should generally be delayed until after 24 hours for those treated with IV tPA.⁶ Tirofiban may be an alternative rescue treatment for neurointerventionalists. Related literature is limited to case series and retrospective reviews of a single-center data base,^{22,23} moreover, these studies were performed without considering the use of IV tPA. Therefore, the safety and efficacy of tirofiban

during EVT after IV tPA remain unclear. In this study, IA injection of tirofiban during EVT in patients treated with IV tPA did not increase the risk of adverse intracranial hemorrhage and mortality compared with patients without tirofiban injections.

Tirofiban is a reversible fibrinogen antagonist that binds to the glycoprotein IIb/IIIa receptor on platelets.²⁴ Tirofiban inhibits platelet aggregation in a dose-dependent manner, which exerts an antiplatelet effect after a 30-minute loading dose. It has a short half-life, with platelet function being normalized after 4 hours.^{25,26} Given these pharmacokinetics, tirofiban may be beneficial when hemorrhagic complications occur. The inconsistent results of tirofiban as

Table 2: Patient safety and efficacy outcomes

	No tirofiban (n = 279)	Tirofiban (n = 35)	Unadjusted OR (95% CI)	Adjusted ^a OR (95% CI)	P value Unadjusted/Adjusted ^a
Successful reperfusion	210 (75.3%)	28 (80.0%)	1.31 (0.57–3.38)	1.56 (0.53 to 5.34)	.684/.440
Postprocedural reocclusion ^b	11 (4.4%)	1 (2.9%)	0.65 (0.03–3.52)	0.19 (0.01–1.30)	.688/.151
3-month good outcome	150 (53.8%)	20 (57.1%)	1.14 (0.56–2.36)	2.22 (0.89–6.12)	.843/.099
3-month death	35 (12.5%)	2 (5.7%)	0.42 (0.06–1.47)	0.38 (0.04–1.87)	.366/.299
Serious hemorrhage	31 (11.1%)	3 (8.6%)	0.75 (0.17–2.25)	1.07 (0.20–4.10)	.867/.918
IVH	19 (6.8%)	1 (2.9%)	0.04 (0.02–2.03)	0.43 (0.02–2.85)	.592/.467

Note:—IVH indicates intraventricular hemorrhage; OR, Odds ratio.

^aAdjusted for sex, intraprocedural reocclusion, intracranial stenting, etiology of large vessel occlusion.

^bPostprocedural reocclusion was assessed in 248 patients (no tirofiban group) and in 34 patients (tirofiban group).

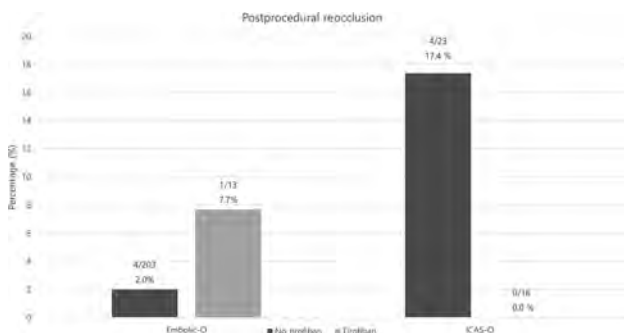


FIG 2. Subgroup analysis for postprocedural reocclusion in patients with mTICI $\geq 2a$. In Embolic-O, postprocedural reocclusion is 2.0% in patients without IA tirofiban and 7.7% in those with IA tirofiban. Patients with ICAS-O with IA tirofiban tend to have less postprocedural reocclusion than those without IA tirofiban (no tirofiban, 17.4%, versus tirofiban, 0.0%). Embolic-O indicates embolic occlusion.

an adjunct therapy during EVT may be attributed to differences in the administration method. Kellert et al¹² suggested that IV tirofiban increased fatal intracranial hemorrhage and poor functional outcomes in patients treated with EVT. In contrast to IV tirofiban, previous small-scale studies have shown that IA tirofiban during EVT could be safe.^{18,27,28} We revealed that IA tirofiban did not increase the bleeding risk in patients who underwent EVT with IV tPA. These results are consistent with previous studies on tirofiban that did not consider using IV tPA.^{16,29} The safety of tirofiban may be attributed to several advantages when administering tirofiban via IA. IA tirofiban can be administered at a lower dose than IV tirofiban. In the study by Kellert et al, tirofiban was administered IV, infused at 0.4 $\mu\text{g}/\text{kg}/\text{min}$ during 30 minutes, followed by a continuous infusion of 0.1 $\mu\text{g}/\text{kg}/\text{min}$ for 48 hours. The total tirofiban dose is 18 mg for a 60-kg adult. Our dose (ranging from 0.5 to 2.0 mg) is smaller than the IV tirofiban dose; moreover, tirofiban can be administered in a target artery. We speculated that the dose was an important factor and that low-dose tirofiban was feasible during EVT in patients treated with IV tPA.

Reocclusion could require additional rescue treatment and eventually delay the final reperfusion time, which results in a poor outcome.^{30–33} A recent observational study reported more frequent reocclusion in ICAS-O than in embolic occlusion. Additionally, inflammatory reactions and platelet aggregation can result in more ischemic events in patients with ICAS-O. In this study, the tirofiban group showed a high frequency of the ICAS-O subtype. However, our study showed similar good outcomes at 3 months between the 2 groups, even though there was more intraprocedural

reocclusion in the tirofiban group. A previous study suggested that ICAS-O had good collaterals.³⁴ Good collaterals are related to hemodynamic factors, including increased distribution of thrombolytics to the clot surface, potentially making the clot more susceptible to thrombolysis. This feature may affect clinical outcomes in patients treated with IA tirofiban. Additionally, we analyzed this subgroup to investigate the effect of IA tirofiban on vessel patency in the group with ICAS-O. Patients with ICAS-O with IA tirofiban tend to have less postprocedural reocclusion than those without IA tirofiban. While we did not investigate long-term vessel patency after IA tirofiban, these findings suggested that IA tirofiban may help maintain vessel patency in ICAS-O. Further studies of long-term vessel patency will be needed to prove this possibility.

Rescue treatment, including tirofiban, is often required during EVT. However, numerous neurointerventionalists have expressed concerns regarding the use of tirofiban after IV tPA due to the hemorrhage risk. Among patients without EVT, tirofiban after IV tPA has been reported as safe in previous study comparing the safety and preliminary efficacy between patients undergoing IV tPA with tirofiban and those undergoing IV tPA without it;³⁵ this finding is consistent with ours. Our findings regarding safety might inform neurointerventionalists when making decisions regarding the use of tirofiban when rescue treatment is needed during EVT with IV tPA. However, we did not determine the patients eligible for tirofiban administration. Previous studies have demonstrated that tirofiban should be administered to patients with a small core volume.³⁶ Further studies are required to elucidate specific patients eligible for safe tirofiban administration.

This study has several limitations. First, the study is limited in its sample size. Specifically, only 35 patients received IA tirofiban in addition to IV tPA. Second, this was a retrospective study without a prespecified infusion speed and dose of IA tirofiban. However, there were no extensive variances in the dose and infusion speed. All participating centers had a protocol, with the total dose and infusion speed of tirofiban being 0.5–2.0 mg and 0.05–0.1 mg/min, respectively. Third, given that the use of IA tirofiban was at the discretion of the neurointerventionalist, there might be a selection bias. Specifically, the neurointerventionalists might have decided to use IA tirofiban only when they considered it safe.

CONCLUSIONS

Using IA tirofiban during EVT after IV tPA could be safe.

Disclosures: Sung-Il Sohn—UNRELATED: Employment: Keimyung University.

REFERENCES

1. Berkhemer OA, Fransen PS, Beumer D, et al. **A randomized trial of intraarterial treatment for acute ischemic stroke.** *N Engl J Med* 2015;372:11–20 CrossRef Medline
2. Campbell BC, Mitchell PJ, Kleinig TJ, et al. **Endovascular therapy for ischemic stroke with perfusion-imaging selection.** *N Engl J Med* 2015;372:1009–18 CrossRef Medline
3. Goyal M, Demchuk AM, Menon BK, et al. **Randomized assessment of rapid endovascular treatment of ischemic stroke.** *N Engl J Med* 2015;372:1019–30 CrossRef Medline
4. Saver JL, Goyal M, Bonafe A, et al. **Stent-retriever thrombectomy after intravenous t-PA vs. t-PA alone in stroke.** *N Engl J Med* 2015;372:2285–95 CrossRef Medline
5. Jovin TG, Chamorro A, Cobo E, et al. **Thrombectomy within 8 hours after symptom onset in ischemic stroke.** *N Engl J Med* 2015;372:2296–2306 CrossRef Medline
6. Powers WJ, Rabinstein AA, Ackerson T, et al. **Guidelines for the early management of patients with acute ischemic stroke: 2019 update to the 2018 guidelines for the early management of acute ischemic stroke: a guideline for healthcare professionals from the American Heart Association/American Stroke Association.** *Stroke* 2019;50:e344–418 CrossRef Medline
7. Emberson J, Lees KR, Lyden P, et al. **Effect of treatment delay, age, and stroke severity on the effects of intravenous thrombolysis with alteplase for acute ischaemic stroke: a meta-analysis of individual patient data from randomised trials.** *Lancet* 2014;384:1929–35 CrossRef Medline
8. Goyal M, Menon BK, van Zwam WH, et al. **Endovascular thrombectomy after large-vessel ischaemic stroke: a meta-analysis of individual patient data from five randomised trials.** *Lancet* 2016;387:1723–31 CrossRef Medline
9. Teng D, Pannell JS, Rennert RC, et al. **Endothelial trauma from mechanical thrombectomy in acute stroke: In vitro live-cell platform with animal validation.** *Stroke* 2015;46:1099–1106 CrossRef Medline
10. Yang M, Huo X, Miao Z, et al. **Platelet glycoprotein IIb/IIIa receptor inhibitor tirofiban in acute ischemic stroke.** *Drugs* 2019;79:515–29 CrossRef Medline
11. Luo Y, Yang Y, Xie Y, et al. **Therapeutic effect of pre-operative tirofiban on patients with acute ischemic stroke with mechanical thrombectomy within 6-24 hours.** *Interv Neuroradiol* 2019;25:705–09 CrossRef Medline
12. Kellert L, Hametner C, Rohde S, et al. **Endovascular stroke therapy: tirofiban is associated with risk of fatal intracerebral hemorrhage and poor outcome.** *Stroke* 2013;44:1453–55 CrossRef Medline
13. Zhao W, Che R, Shang S, et al. **Low-dose tirofiban improves functional outcome in acute ischemic stroke patients treated with endovascular thrombectomy.** *Stroke* 2017;48:3289–94 CrossRef Medline
14. Pan X, Zheng D, Zheng Y, et al. **Safety and efficacy of tirofiban combined with endovascular treatment in acute ischaemic stroke.** *Eur J Neurol* 2019;26:1105–10 CrossRef Medline
15. Lee JI, Gliem M, Gerdes G, et al. **Safety of bridging antiplatelet therapy with the GPIIb-IIIa inhibitor tirofiban after emergency stenting in stroke.** *PLoS One* 2017;12:e0190218 CrossRef Medline
16. Zhang S, Hao Y, Tian X, et al. **Safety of intra-arterial tirofiban administration in ischemic stroke patients after unsuccessful mechanical thrombectomy.** *J Vasc Interv Radiol* 2019;30:141 CrossRef Medline
17. Kang DH, Yoon W, Kim SK, et al. **Endovascular treatment for emergent large vessel occlusion due to severe intracranial atherosclerotic stenosis.** *J Neurosurg* 2018 June 1:1–8 [Epub ahead of print] CrossRef Medline
18. Kang DH, Kim YW, Hwang YH, et al. **Instant reocclusion following mechanical thrombectomy of in situ thromboocclusion and the role of low-dose intra-arterial tirofiban.** *Cerebrovasc Dis* 2014;37:350–55 CrossRef Medline
19. Lee JS, Lee SJ, Yoo JS, et al. **Prognosis of acute intracranial atherosclerosis-related occlusion after endovascular treatment.** *J Stroke* 2018;20:394–403 CrossRef Medline
20. Fiorelli M, Bastianello S, von Kummer R, et al. **Hemorrhagic transformation within 36 hours of a cerebral infarct: relationships with early clinical deterioration and 3-month outcome in the European Cooperative Acute Stroke Study I (Ecass I) cohort.** *Stroke* 1999;30:2280–84 CrossRef Medline
21. Evans MR, White P, Cowley P, et al. **Revolution in acute ischaemic stroke care: a practical guide to mechanical thrombectomy.** *Pract Stroke* 2017;17:252–65 CrossRef Medline
22. Heck DV, Brown MD. **Carotid stenting and intracranial thrombectomy for treatment of acute stroke due to tandem occlusions with aggressive antiplatelet therapy may be associated with a high incidence of intracranial hemorrhage.** *J Neurointerv Surg* 2015;7:170–75 CrossRef Medline
23. Ernst M, Butscheid F, Fiehler J, et al. **Glycoprotein IIb/IIIa inhibitor bridging and subsequent endovascular therapy in vertebrbasilar occlusion in 120 patients.** *Clin Neuroradiol* 2016;26:169–75 CrossRef Medline
24. Kim KS, Fraser JF, Grupke S, et al. **Management of antiplatelet therapy in patients undergoing neuroendovascular procedures.** *J Neurosurg* 2018;129:890–905 CrossRef Medline
25. Harder S, Klinkhardt U, Alvarez JM. **Avoidance of bleeding during surgery in patients receiving anticoagulant and/or antiplatelet therapy: pharmacokinetic and pharmacodynamic considerations.** *Clin Pharmacokinet* 2004;43:963–81 CrossRef Medline
26. McClellan KJ, Goa KL. **Tirofiban: a review of its use in acute coronary syndromes.** *Drugs* 1998;56:1067–80 CrossRef Medline
27. Kwon JH, Shin SH, Weon YC, et al. **Intra-arterial adjuvant tirofiban after unsuccessful intra-arterial thrombolysis of acute ischemic stroke: preliminary experience in 16 patients.** *Neuroradiology* 2011;53:779–85 CrossRef Medline
28. Goh DH, Jin SC, Jeong HW, et al. **Mechanical Solitaire thrombectomy with low-dose booster tirofiban injection.** *Neurointervention* 2016;11:114–19 CrossRef Medline
29. Kim YW, Sohn SI, Yoo J, et al. **Local tirofiban infusion for remnant stenosis in large vessel occlusion: tirofiban assist study.** *BMC Neurol* 2020;20:284 CrossRef Medline
30. Baek JH, Kim BM, Kim DJ, et al. **Importance of truncal-type occlusion in stentriever-based thrombectomy for acute stroke.** *Neurology* 2016;87:1542–50 CrossRef Medline
31. Chang Y, Kim BM, Bang OY, et al. **Rescue stenting for failed mechanical thrombectomy in acute ischemic stroke: a multicenter experience.** *Stroke* 2018;49:958–64 CrossRef Medline
32. Lee JS, Hong JM, Lee KS, et al. **Primary stent retrieval for acute intracranial large artery occlusion due to atherosclerotic disease.** *J Stroke* 2016;18:96–101 CrossRef Medline
33. Yoon W, Kim SK, Park MS, et al. **Endovascular treatment and the outcomes of atherosclerotic intracranial stenosis in patients with hyperacute stroke.** *Neurosurgery* 2015;76:680–86; Discussion 686 CrossRef Medline
34. Liebeskind DS, Cotsonis GA, Saver JL, et al. for the Warfarin-Aspirin Symptomatic Intracranial Disease (WASID) Investigators. **Collaterals dramatically alter stroke risk in intracranial atherosclerosis.** *Ann Neurol* 2011;69:963–74 CrossRef Medline
35. Li W, Lin L, Zhang M, et al. **Safety and preliminary efficacy of early tirofiban treatment after alteplase in acute ischemic stroke patients.** *Stroke* 2016;47:2649–51 CrossRef Medline
36. Yang J, Wu Y, Gao X, et al. **Intraarterial versus intravenous tirofiban as an adjunct to endovascular thrombectomy for acute ischemic stroke.** *Stroke* 2020;51:2925–33 CrossRef

Ticagrelor versus Clopidogrel in the Dual Antiplatelet Regimen for Intracranial Stenting or Flow-Diverter Treatment for Unruptured Cerebral Aneurysms: A Single-Center Cohort Study

 K.Y. Park,  T. Ozaki,  A. Kostynsky,  H. Kortman,  A. Hilario,  P. Nicholson,  R. Agid,  T. Krings, and  V.M. Pereira



ABSTRACT

BACKGROUND AND PURPOSE: Ticagrelor is a novel P2Y₁₂ antagonist, and little is known about its efficacy and safety in the endovascular treatment of aneurysms. This study evaluated the efficacy and safety of ticagrelor versus clopidogrel for stent-assisted coiling or flow-diversion treatment in patients with unruptured cerebral aneurysms.

MATERIALS AND METHODS: From November 2003 to February 2019, two hundred one patients (mean age, 57.5 years; 156 women) with 233 unruptured aneurysms underwent stent-assisted coiling or flow-diversion treatment. All patients received antiplatelet therapy of aspirin plus clopidogrel (clopidogrel group, 121 patients with 140 aneurysms) or aspirin plus ticagrelor (ticagrelor group, 80 patients with 93 aneurysms). The clinical and radiologic data in each group were retrospectively reviewed and compared.

RESULTS: Two hundred thirty-six procedures were performed, including stent-assisted coiling ($n = 101$) and flow diversion ($n = 135$). At 90 days, the primary outcome—a composite of any stroke and death—occurred in 9.9% of the clopidogrel group and 8.6% of the ticagrelor group ($P = .822$). Ischemic stroke occurred in 10 (7.0%) of the clopidogrel group and 7 (7.5%) of the ticagrelor group ($P > .999$). Disabling stroke occurred in 4 (2.8%) in the clopidogrel group and in 4 (4.3%) in the ticagrelor group ($P = .716$). Ninety-day death occurred in 3 (2.1%) in the clopidogrel group and 1 (1.1%) in the ticagrelor group ($P > .999$). Any bleeding at 90 days occurred in 13 (9.2%) in the clopidogrel group and 6 (6.5%) in the ticagrelor group ($P = .479$).

CONCLUSIONS: Ticagrelor appears to be as effective and safe as clopidogrel in stent-assisted coiling or flow-diversion treatment for unruptured cerebral aneurysms.

ABBREVIATION: DAPT = dual antiplatelet therapy

Endovascular coiling is an established treatment for ruptured or unruptured cerebral aneurysms.^{1,2} However, some aneurysms, such as wide-neck, large, or giant and dissecting fusiform aneurysms, are still challenging. Currently, stent-assisted coiling and flow diversion have been widely accepted as potential treatment modalities for challenging or uncoilable lesions. However,

thromboembolic complications are still a risk in stent-assisted coiling and flow-diversion procedures.

Dual antiplatelet therapy (DAPT) with aspirin plus clopidogrel is a first-line regimen for neuroendovascular procedures.^{3,4} However, individual responses to clopidogrel are varied,⁵ and hyporesponse is commonly reported.⁶ Unfortunately, hyporesponse to clopidogrel increases the risk of thromboembolic events.⁷⁻⁹ Thus, to minimize any complications related to procedures or DAPT, novel antiplatelet medication may be of benefit for patients undergoing neuroendovascular procedures.^{10,11}

Ticagrelor is an oral and reversible P2Y₁₂ antagonist approved by the FDA in 2011.¹² Large trials have proved the efficacy and safety of ticagrelor for coronary disease.^{13,14} Because of its success with coronary disease, ticagrelor treatment has also been attempted for cerebrovascular disease^{15,16} and was shown to be superior to aspirin in the secondary prevention of stroke under specific circumstances.^{17,18} Thus, ticagrelor is emerging as a novel medication for neuroendovascular procedures. However, little is

Received January 12, 2021; accepted after revision April 25.

From the Division of Neuroradiology (K.Y.P., T.O., A.K., H.K., A.H., P.N., R.A., T.K., V.M.P.), Joint Department of Medical Imaging, Toronto Western Hospital, University Health Network, Toronto, Ontario, Canada; Department of Neurosurgery (K.Y.P.), Severance Stroke Center, Severance Hospital, Yonsei University College of Medicine, Seoul, Republic of Korea; and Department of Radiology (H.K.), ETZ Elisabeth Hospital, Tilburg, the Netherlands.

Paper previously presented, in part, at: Annual Meeting of the Korean Neurosurgical Society, Virtual; October 24, 2020; Seoul, Republic of Korea.

Please address correspondence to Keun Young Park, MD, PhD, Department of Neurosurgery, Severance Stroke Center, Severance Hospital, Yonsei University College of Medicine, 50 Yonsei-ro, Seodaemun-gu, Seoul 03722, Korea; e-mail: kypark78.md@gmail.com

 Indicates article with online supplemental data.

<http://dx.doi.org/10.3174/ajnr.A7216>

known about the efficacy and safety of ticagrelor for the endovascular treatment of aneurysms.

In the present study, the efficacy and safety of ticagrelor treatment in conjunction with stent-assisted coiling or flow-diversion treatment in patients with unruptured cerebral aneurysms were evaluated and compared with those of clopidogrel.

MATERIALS AND METHODS

Study Design

University Health Network, Toronto Western Hospital institutional review board approved this study and waived the need to obtain patient informed consent because of the retrospective study design. The study was performed under the guidelines outlined by the Declaration of Helsinki and followed the Strengthening The Reporting of OBservational Studies in Epidemiology (STROBE) checklist (https://www.elsevier.com/___data/promis_misc/ISSM_STROBE_Checklist.pdf).

Participants

From November 2003 to February 2019, two hundred seventy-four consecutive patients underwent stent-assisted coiling or flow diversion for cerebral aneurysms at our institution. Patients treated with DAPT of aspirin plus clopidogrel or ticagrelor were included. Patients treated for ruptured aneurysms, intracranial atherosclerotic stenosis, iatrogenic dissection, or carotid cavernous fistula were excluded. A total of 201 patients with 233 unruptured aneurysms were included and divided into the clopidogrel or ticagrelor group.

Using the electronic patient records and imaging data base, we retrospectively evaluated the characteristics of patients and target aneurysms, procedural details, and clinical and angiographic follow-up results.

DAPT Protocol

Before the procedure, DAPT was administered to patients for at least 3 days according to the institution's protocol.¹⁹ For the clopidogrel group, aspirin (81 mg once daily) and clopidogrel (75 mg once daily) were administered. For the ticagrelor group (due to the change of the operator's preference since 2016), aspirin (81 mg once daily) and ticagrelor (90 mg twice daily) were administered. For patients without any DAPT premedication, a loading dose of aspirin (325 mg) plus clopidogrel (300 mg) or ticagrelor (180 mg) was also administered on the day of the procedure. Neither a platelet function test nor a modification of DAPT was performed.

Under general anesthesia and systemic heparinization, patients underwent stent-assisted coiling or a flow-diversion procedure in the usual manner. Systematic heparinization was performed according to institutional protocol (500-1000 IU/10 kg of body weight of heparin IV following placement of the femoral/radial sheath, followed by a 1000 IU hourly during the procedure). After the procedure, DAPT was maintained for 3-6 months, followed by discontinuation of clopidogrel or ticagrelor treatment. Aspirin monotherapy was maintained indefinitely.

Outcome Measurements

The primary outcome was a composite occurrence of stroke and death within 90 days after the procedure. Stroke was defined as

neurologic functional loss by an ischemic or hemorrhagic event, with residual symptoms lasting at least 24 hours or leading to death.¹³ The first secondary outcome was a 90-day occurrence of ischemic stroke restricted to the treated vascular territory, identified on CT or MR images. Other secondary outcomes included the following: 1) 90-day occurrence of disabling stroke, which was defined as any ischemic or hemorrhagic stroke with a change of the mRS score of >1 ,¹⁵ and 2) any death. Additionally, the safety outcome was evaluated, which was defined as a 90-day occurrence of any bleeding event (neurologic or non-neurologic) requiring a medical intervention. The incidence of medication change due to adverse events was also assessed.

Imaging Follow-up

Contrast-enhanced MR angiography was routinely performed for the evaluation of the posttreatment occlusion grade of aneurysms.^{20,21} All MR imaging examinations were performed using a 1.5T or 3T MR imaging scanner using gadolinium contrast injected at a rate of 1.5 mL per second to a total of 15 mL followed immediately by a flush of 30 mL of saline. Further details were described in previous studies.^{20,21} In some cases, CT angiography was alternatively performed for the evaluation of aneurysms treated using flow diversion only. The final follow-up angiographic imaging was retrospectively reviewed by 2 independent investigators (a neuroradiologist and a neurointerventionalist). In the event of different diagnoses between the 2 investigators, another neurointerventionalist reviewed the data, and all 3 investigators came to a consensus regarding the results. The aneurysm occlusion grade was assessed by the Raymond-Roy occlusion classification, in which class I is defined as complete occlusion; class II, as neck remnant; and class III, as sac remnant.²² In-stent stenosis was divided into 2 grades: 1) none, or $<50\%$ and 2) $\geq 50\%$. If a stented vessel could not be evaluated due to a "marker band effect,"²¹ the results were marked as "unknown."

Statistical Analysis

Univariate analysis to compare baseline characteristics and outcomes between the 2 groups was performed using the χ^2 test, Fisher exact test, Mann-Whitney *U* test, and standard *t* tests. For the evaluation of risk factors associated with thromboembolic or hemorrhagic complications after the procedure, all variables with clinical importance were introduced into a multivariate analysis using the binary logistic regression method. Significance was defined as $P < .05$. Statistical analyses were performed using SPSS Statistics 25.0 for Windows (IBM).

RESULTS

Patients and Aneurysms

A total of 201 patients (mean age, 57.5 years; male/female ratio = 45:156) with 233 unruptured aneurysms (saccular, 222; fusiform, 11) were successfully treated. The clopidogrel group consisted of 121 patients with 140 aneurysms, and the ticagrelor group consisted of 80 patients with 93 aneurysms. Baseline characteristics of the patients were not different between the 2 groups (Online Supplemental Data).

Among 233 aneurysms, the presentation, location, and type of aneurysms were not different between the 2 groups. However,

Table 1: Procedural details

	Overall	Aspirin+Clopidogrel Group	Aspirin+Ticagrelor Group	P Value
Procedures	236	143 ^a	93 ^b	.283
Stent-assisted coiling (%)	101	57 (39.9)	44 ^b (47.3)	
Neuroform (Stryker)	6	5	1	
Enterprise (Cordis)	13	13	0	
Solitaire (Medtronic)	1	1	0	
LVIS (MicroVention)	46	27	19	
LEO (Balt)	17	5	12	
Atlas (Stryker)	15	5	10	
Combined	3	1	2	
Flow diverter (%)	135	86 ^a (60.1)	49 (52.7)	
Pipeline (Medtronic)	104	69	35	
Silk (Balt)	19	15	4	
Surpass (Stryker)	12	2	10	

^aIncluding 1 salvage therapy for poor wall apposition of Surpass.

^bIncluding 2 salvage therapies for coil protrusion and Pipeline flow-diverter migration.

Table 2: Treatment outcomes

	Overall	Aspirin + Clopidogrel Group	Aspirin + Ticagrelor Group	P Value
Nonavailable data	1	1	0	
Primary outcome (%)	22 (9.4)	14 (9.9)	8 (8.6)	.822
Secondary outcomes (%)				
Ischemic stroke	17 (7.2)	10 (7.0)	7 (7.5)	>.999
Disabling stroke	8 (3.4)	4 (2.8)	4 (4.3)	.716
Any death	4 (1.7)	3 (2.1) ^a	1 (1.1) ^b	>.999
Safety outcome (%)	19 (8.1)	13 (9.2)	6 (6.5)	.479
mRS (%)				.484
0–2	227 (96.6)	136 (95.8)	91 (97.8)	
3–6	8 (3.4)	6 (4.2)	2 (2.2)	
Medication change (%)	12 (5.1)	6 (4.2)	6 (6.5)	.547

^aMajor infarction due to infectious vasculopathy, retroperitoneal bleeding, and liver failure.

^bBasilar occlusion.

the median aneurysm size was slightly larger in the clopidogrel group than in the ticagrelor group (8.6 versus 7.0 mm, $P = .006$) (Online Supplemental Data).

Endovascular Procedures

The total number of procedures was 236 (stent-assisted coiling, 101; flow diversion, 135). In the clopidogrel group, stent-assisted coiling procedures totaled 57 (39.9%) and flow diversion totaled 86 (60.1%), including 1 salvage treatment for poor wall apposition of a flow-diversion device. In the ticagrelor group, stent-assisted coiling totaled 44 (47.3%), including 2 salvage treatments: 1 for coil protrusion and 1 for flow-diverter migration, and flow diversion totaled 49 (52.7%). Procedure types were similarly distributed between the 2 groups ($P = .283$) (Table 1).

Outcomes

All cases were assessed except 1 (nonavailable medical records after discharge) from the clopidogrel group. The primary outcome occurred in 22 cases (9.4%), which was not significantly different

between the 2 groups (clopidogrel group, $n = 14$ [9.9%]; ticagrelor group, $n = 8$ [8.6%]; $P = .822$); 90-day ischemic stroke in the treated vascular territory occurred in 10 (7.0%) in the clopidogrel group and 7 (7.5%) in the ticagrelor group ($P > .999$), and 90-day disabling stroke occurred in 4 (2.8%) in the clopidogrel group and 4 (4.3%) in the ticagrelor group ($P = .716$). Ninety-day death occurred in 3 (2.1%) in the clopidogrel group and 1 (1.1%) in the ticagrelor group ($P > .999$). Each cause of death is explained in Table 2.

Ninety-day bleeding events occurred in 19 cases (8.1%, 4 neurologic and 15 non-neurologic), 13 in the clopidogrel group (9.2%) and 6 in the ticagrelor group (6.5%) ($P = .479$). Of the 4 neurologic complications, 2 were due to intraprocedural rupture, 1 was due to nonaneurysmal subarachnoid hemorrhage (clopidogrel group), and 1 was due to hypertensive intracerebral hemorrhage of the basal ganglia (ticagrelor group). All bleeding events were conservatively treated without any disability. Among the 15 non-neurologic complications, 12 were due to puncture site problems (clopidogrel group, $n = 9$; ticagrelor group, $n = 3$), 2 were due to gastrointestinal hemorrhages (1 in each group), and 1 was due to vaginal hemorrhage (ticagrelor group).

Overall, medication was changed in 12 cases (5.1%), slightly more frequently ($n = 6$, 6.5%) in the ticagrelor group than in the clopidogrel group ($n = 6$, 4.2%) because dyspnea ($n = 3$) was more common in the ticagrelor group. However, this result was not statistically different ($P = .547$) (Table 2). After a medication change, all dyspnea was resolved.

Follow-up Imaging

Follow-up imaging data were available for 211 aneurysms (median, 25.1 months; clopidogrel, $n = 126$; ticagrelor, $n = 85$). The median follow-up period was 37.0 months (range, 25.0–48.75 months) in the clopidogrel group and 13.8 months (range, 7.5–23.1 months) in the ticagrelor group ($P < .001$).

Regarding aneurysm occlusion, class I was noted in 154 cases (73.0%), which was the same between the 2 groups (clopidogrel, $n = 92$, 73.0%; ticagrelor, $n = 62$, 72.9%; $P = .552$). In-stent stenosis could not be assessed in 17 cases (8.1%). None or mild in-stent stenosis (<50%) was identified in 114 (90.5%) in the clopidogrel group and 74 (87.1%) in the ticagrelor group ($P = .603$). Follow-up imaging results are shown in Table 3.

Table 3: Radiologic follow-up results

	Overall	Aspirin + Clopidogrel Group	Aspirin + Ticagrelor Group	P Value
Follow-up (%)	211/233 (90.6)	126/140 (90.0)	85/93 (91.4)	
Period (median) (IQR) (mo)	25.1	37.0 (25.0–48.75)	13.8 (7.5–23.1)	<.001
Aneurysm occlusion ^a (%)				.552
I	154 (73.0)	92 (73.0)	62 (72.9)	
II	27 (12.8)	14 (11.1)	13 (15.3)	
III	30 (14.2)	20 (15.9)	10 (11.8)	
In-stent stenosis				.603
<50%	188 (89.1)	114 (90.5)	74 (87.1)	
>50%	6 (2.8)	2 (1.6)	4 (4.7)	
Unknown ^b	17 (8.1)	10 (7.9)	7 (8.2)	
Retreatment	16 (6.8)	10 (7.0)	6 (6.5)	>.999

^aRaymond-Roy Occlusion Classification.

^bStented vessel could not be evaluated due to a marker band effect.

Table 4: Risk factors associated with thromboembolic complications

	Odds Ratio	95% Wald CI	P Value
Sex	0.736	0.220–2.467	.620
Age	0.999	0.945–1.056	.972
Hypertension	1.652	0.479–5.703	.427
Smoking	0.881	0.265–2.926	.836
Previous stroke/TIA	2.039	0.493–8.427	.325
Dyslipidemia	1.350	0.409–4.458	.622
Prior antithrombotic usage	0.344	0.108–1.098	.072
Aneurysm presentation			
Unruptured, symptomatic	0.914	0.159–5.265	.920
Recurrent or residual	0.659	0.168–2.581	.550
Aneurysm location (posterior circulation)	0.807	0.168–2.581	.774
Aneurysm morphology (fusiform)	4.878	0.885–26.887	.069
Aneurysm size	1.037	0.955–1.127	.386
Antiplatelet medication (ticagrelor)	1.035	0.348–3.083	.950
Treatment technique (flow-diverter)	1.218	0.317–4.676	.774

Table 5: Risk factors associated with hemorrhagic complications

	Odds Ratio	95% Wald CI	P Value
Sex	0.640	0.205–1.994	.441
Age	1.013	0.965–1.063	.613
Hypertension	0.549	0.179–1.679	.293
Smoking	1.138	0.385–3.363	.814
Previous stroke/TIA	0.600	0.129–2.796	.516
Dyslipidemia	0.800	0.233–2.744	.722
Prior antithrombotic usage	0.978	0.244–3.928	.975
Aneurysm presentation			
Unruptured, symptomatic	0.380	0.039–3.726	.406
Recurrent or residual	1.187	0.345–4.081	.786
Aneurysm location (posterior circulation)	1.755	0.525–5.864	.361
Aneurysm morphology (fusiform)	0.592	0.060–5.840	.654
Aneurysm size	0.989	0.904–1.083	.812
Antiplatelet medication (ticagrelor)	0.669	0.230–1.946	.461
Treatment technique (flow-diverter)	0.948	0.297–3.025	.929

Risk Factors Associated with Thromboembolic or Hemorrhagic Complications

On multivariate analysis, prior antithrombotic usage (OR = 0.344; 95% CI, 0.108–1.098; $P = .072$) and fusiform morphology (OR =

4.878; 95% CI, 0.885–26.887; $P = .069$) could be associated with the risk of thromboembolic complications within 90 days but were not statistically significant (Table 4). Any risk factors including ticagrelor medication were not associated with hemorrhagic complications within 90 days (Table 5).

Subgroup Analysis by Treatment Technique

When we compared the difference in outcomes according to each treatment technique, there was no difference in outcomes between the clopidogrel and the ticagrelor groups in the stent-assisted coiling subgroup ($n = 100$, non-available data = 1). This finding was the same for the flow-diversion subgroup ($n = 135$) (Table 6).

DISCUSSION

In the present study of patients who underwent stent-assisted coiling or flow diversion for unruptured cerebral aneurysms, the primary outcome (90-day composite of any stroke and death) and secondary outcomes (90-day ischemic stroke, disabling stroke, or any death) were the same in the ticagrelor and the clopidogrel groups. Moreover, 90-day bleeding events did not differ between the 2 groups.

The combination of aspirin plus clopidogrel has been a standard DAPT for neuroendovascular procedures. Clopidogrel is a prodrug whose active form requires a metabolic pathway and irreversibly inhibits a P2Y₁₂ receptor. This process is complex and influenced by several factors. As a result, hyporesponse to clopidogrel is common with a 5%–44% frequency⁶ and is known to be associated with a higher risk of thromboembolic events during neuroendovascular procedures.^{7–9} The VerifyNow P2Y₁₂ assay (Accumetrics) is widely used for the evaluation of a platelet response in clinical practice.²³ However, there is no standardized definition or cutoff value regarding clopidogrel responsiveness on the VerifyNow assay.^{24–26}

As a result, regular evaluation of clopidogrel responsiveness and modification of antiplatelet regimens are still controversial.²⁷

Unlike clopidogrel, ticagrelor does not require hepatic metabolism for activation, and it reversibly and directly inhibits the

Table 6: Subgroup analysis by treatment technique

	Overall	Aspirin+Clopidogrel Group	Aspirin+Ticagrelor Group	P Value
Nonavailable data	1	1	0	
Stent-assisted coiling (%)	100	56 (56.0)	44 ^a (44.0)	
Primary outcome (%)	10 (10.0)	6 (10.7)	4 (9.1)	>.999
Secondary outcomes (%)				
Ischemic stroke	6 (6.0)	3 (5.4)	3 (6.8)	>.999
Disabling stroke	2 (2.0)	1 (1.8)	1 (2.3)	>.999
Any death	2 (2.0)	2 (3.6)	0	.502
Safety outcome (%)	9 (9.0)	7 (12.5)	2 (4.5)	.292
Flow-diverter (%)	135	86 ^b (60.6)	49 (52.7)	
Primary outcome (%)	12 (8.9)	8 (9.3)	4 (8.2)	>.999
Secondary outcomes (%)				
Ischemic stroke	11 (8.1)	7 (8.1)	4 (8.2)	>.999
Disabling stroke	6 (4.4)	3 (3.5)	3 (6.1)	.668
Any death	2 (1.5)	1 (1.2)	1 (2.0)	>.999
Safety outcome (%)	10 (7.4)	6 (7.0)	4 (8.2)	>.999

^aIncluding 2 salvage therapies for coil protrusion and Pipeline flow-diverter migration.

^bIncluding 1 salvage therapy for poor wall apposition of Surpass.

P2Y12 receptor with more rapid and greater platelet inhibition.²⁸ Furthermore, low platelet response is less common in patients using ticagrelor than in those using clopidogrel.²⁹ On the basis of these results, recent studies have tried to evaluate the safety and efficacy of ticagrelor as an alternative regimen to clopidogrel for neuroendovascular procedures.

Ticagrelor treatment has been attempted for clopidogrel hyporesponders.³⁰ In a pilot study by Hanel et al,³¹ 18 cases of clopidogrel hyporesponders were treated with ticagrelor, ultimately suggesting the potential of ticagrelor as an alternative antiplatelet regimen. In a multicenter cohort study by Moore et al,³² ticagrelor was administered for clopidogrel hyporesponders ($n = 50$), and outcomes were retrospectively compared with those of clopidogrel responders ($n = 53$). Consequently, thromboembolic and hemorrhagic complications did not substantially differ between clopidogrel (7.9%) and ticagrelor (4.2%) groups in that study.

To directly compare clopidogrel with ticagrelor, Soize et al³³ conducted a 1:1 matched cohort study with 80 patients undergoing flow-diversion or flow-disrupter procedures. In that study, each procedure was performed without either a platelet function test or a modification of antiplatelet therapy, and treatment outcomes between the clopidogrel and ticagrelor groups were directly compared. Among patients in the clopidogrel group, there could be hyporesponders to clopidogrel that affect the unfavorable results. On the other hand, a larger benefit from ticagrelor was anticipated in the ticagrelor group. Nevertheless, that study showed that both treatments were equally safe, and the number of thromboembolic and hemorrhagic complications did not differ between the 2 groups.³³ Similarly, the present study showed that 90-day ischemic stroke occurrence was not statistically different between the 2 groups (clopidogrel group, 7.0%; ticagrelor group, 7.5%; $P > .999$). However, these results should be interpreted with caution due to the relatively small sample size.

In the present study, the rate of ischemic complications in the ticagrelor group appeared to be higher than the values reported by recent studies (4.2%³² and 2.5%,³³ respectively). For the precise evaluation of complication rates related to DAPT with aspirin plus ticagrelor, Narata et al³⁴ conducted a retrospective

cohort study with 154 consecutive patients who underwent stent-assisted coiling ($n = 41$) or flow-diversion ($n = 113$) treatment. That study included the largest cohort of ticagrelor use in the neuroendovascular field and showed a 1.9% rate of symptomatic ischemic complications after the procedures. In our opinion, this difference was due to 2 disparities: 1) patients with stroke/TIA, and 2) aneurysm size. The present study included 20.9% of patients with stroke/TIA, which was approximately 8-fold higher than in the general population (2.7%).³⁵ This may have affected the observed rate of ischemic complications. Furthermore, the aneurysm size (median, 7.95 mm) that was included in the present study was demonstrably larger than that in the studies by Moore et al³² (median, 6 mm) and Soize et al³³ (mean, 6.5 mm). Aneurysm size is a well-known risk factor of complications.³⁶ Thus, this size disparity may be related to the difference in the observed rate of ischemic complications in the present study. Nevertheless, in the present study, the overall ischemic stroke rate (7.2%) was similar to that found in meta-analyses of stent-assisted coiling³⁷ and flow-diversion^{38,39} treatment. Overall morbidity (3.4%) and mortality (1.7%) were slightly lower than those reported in previous studies.³²⁻³⁴

The major concern regarding ticagrelor treatment is the increased rate of fatal intracranial bleeding.¹³ However, Narata et al³⁴ reported a 3.9% rate of intracranial bleeding after ticagrelor treatment, a rate similar to or lower than that found in recent studies of clopidogrel used in stent-assisted coiling (3.0%)⁴⁰ and flow-diversion (10.4%)⁴¹ procedures. In the present study, overall intracranial bleeding was 1.7%, with the clopidogrel group (2.1%) showing more bleeding than the ticagrelor group (1.1%) but without any statistical significance. This result was also similar to that found in recent studies of prasugrel used in stent-assisted coiling (2.0%)¹⁰ or in any neuroendovascular procedures (0.7%).¹¹ Another concern with ticagrelor treatment is dyspnea. In the Platelet Inhibition and Patient Outcome (PLATO) trial, dyspnea occurred more commonly in the ticagrelor group (0.9%).¹³ Narata et al³⁴ also reported 1 case of dyspnea. Similarly, the present study also included 3 cases of dyspnea (3.2%) in the ticagrelor group, which were resolved after a medication change.

In terms of efficacy, the present study also suggested comparable angiographic results regarding the aneurysm occlusion grade, in-stent stenosis, and retreatment between the 2 groups. However, the follow-up period was significantly shorter in the ticagrelor group than in the clopidogrel group (median, 13.8 versus 37.0 months; $P < .001$). Further long-term follow-up is mandatory.

Our study has several limitations. First, because of the limitations inherent in the retrospective design, a selection bias was inevitable regarding the demographics and percentages observed. To lessen selection bias, we included 201 consecutive patients treated with stent-assisted coiling or flow diversion for unruptured cerebral aneurysms. To the best of our knowledge, this study was performed with the largest sample gathered from a single center. The second limitation is a lack of a platelet function test. As mentioned above, we did not use a platelet function test due to its unestablished role in the clinical field. As a result, we could not obtain any laboratory data about the inhibitory effect of each medication on platelets, and we did not modify any antiplatelet regimen. Nevertheless, this is the largest study to directly compare the efficacy and safety of clopidogrel and ticagrelor in neuroendovascular procedures.

CONCLUSIONS

Ticagrelor appears to be as effective and safe as clopidogrel in stent-assisted coiling or flow-diversion treatment for unruptured cerebral aneurysms. A future randomized controlled trial would be ethically feasible and expected.

ACKNOWLEDGMENTS

We would like to thank Hye Jung Shin, MS, for statistical consultation and Editage (www.editage.com) for English language editing.

Disclosures: Timo Krings—UNRELATED: Consultancy: Stryker, Penumbra, Medtronic, Cerenovus; Royalties: Thieme; Stock/Stock Options: Marblehead Medical. Vitor Mendes Pereira—RELATED: Consulting Fee or Honorarium: Medtronic, Balt, Stryker, Comments: proctorship Principal Investigator of the EVOLVE study.

REFERENCES

- Lin N, Cahill KS, Frerichs KU, et al. **Treatment of ruptured and unruptured cerebral aneurysms in the USA: a paradigm shift.** *J Neurointerv Surg* 2018;10:i69–76 CrossRef Medline
- Luther E, McCarthy DJ, Brunet MC, et al. **Treatment and diagnosis of cerebral aneurysms in the post-International Subarachnoid Aneurysm Trial (ISAT) era: trends and outcomes.** *J Neurointerv Surg* 2020;12:682–87 CrossRef Medline
- Faught RW, Satti SR, Hurst RW, et al. **Heterogeneous practice patterns regarding antiplatelet medications for neuroendovascular stenting in the USA: a multicenter survey.** *J Neurointerv Surg* 2014;6:774–79 CrossRef Medline
- Gupta R, Moore JM, Griessenauer CJ, et al. **Assessment of dual-antiplatelet regimen for Pipeline embolization device placement: a survey of major academic neurovascular centers in the United States.** *World Neurosurg* 2016;96:285–92 CrossRef Medline
- Gurbel PA, Bliden KP, Hiatt BL, et al. **Clopidogrel for coronary stenting: response variability, drug resistance, and the effect of pretreatment platelet reactivity.** *Circulation* 2003;107:2908–13 CrossRef

- Kulickowski W, Witkowski A, Polonski L, et al. **Interindividual variability in the response to oral antiplatelet drugs: a position paper of the Working Group on antiplatelet drugs resistance appointed by the Section of Cardiovascular Interventions of the Polish Cardiac Society, endorsed by the Working Group on Thrombosis of the European Society of Cardiology.** *Eur Heart J* 2009;30:426–35 CrossRef Medline
- Fifi JT, Brockington C, Narang J, et al. **Clopidogrel resistance is associated with thromboembolic complications in patients undergoing neurovascular stenting.** *AJNR Am J Neuroradiol* 2013;34:716–20 CrossRef Medline
- Yang H, Li Y, Jiang Y. **Insufficient platelet inhibition and thromboembolic complications in patients with intracranial aneurysms after stent placement.** *J Neurosurg* 2016;125:247–53 CrossRef Medline
- Asai T, Miyachi S, Izumi T, et al. **Relationship between low response to clopidogrel and periprocedural ischemic events with coil embolization for intracranial aneurysms.** *J Neurointerv Surg* 2016;8:752–55 CrossRef Medline
- Sadat J, Chau Y, Gaudart J, et al. **Prasugrel versus clopidogrel in stent-assisted coil embolization of unruptured intracranial aneurysms.** *Interv Neuroradiol* 2017;23:52–59 CrossRef Medline
- Cho WS, Lee J, Ha EJ, et al. **Low-dose prasugrel vs clopidogrel-based tailored premedication for endovascular treatment of cerebral aneurysms.** *Neurosurgery* 2019;85:E52–59 CrossRef Medline
- FDA approves blood-thinning drug Brilinta to treat acute coronary syndromes. <https://wayback.archive-it.org/7993/20170112024017/http://www.fda.gov/NewsEvents/Newsroom/PressAnnouncements/ucm263964.htm>. Accessed July 20, 2011
- Wallentin L, Becker RC, Budaj A, et al. **Ticagrelor versus clopidogrel in patients with acute coronary syndromes.** *N Engl J Med* 2009;361:1045–57 CrossRef Medline
- Bonaca MP, Bhatt DL, Cohen M, et al. **Long-term use of ticagrelor in patients with prior myocardial infarction.** *N Engl J Med* 2015;372:1791–800 CrossRef Medline
- Johnston SC, Amarenco P, Albers GW, et al. **Ticagrelor versus aspirin in acute stroke or transient ischemic attack.** *N Engl J Med* 2016;375:35–43 CrossRef Medline
- Easton JD, Aunes M, Albers GW, et al. **SOCRATES Steering Committee and Investigators. Risk for major bleeding in patients receiving ticagrelor compared with aspirin after transient ischemic attack or acute ischemic stroke in the SOCRATES study (Acute Stroke or Transient Ischemic Attack Treated With Aspirin or Ticagrelor and Patient Outcomes).** *Circulation* 2017;136:907–16 CrossRef Medline
- Wang Y, Minematsu K, Wong KS, et al. **Ticagrelor in acute stroke or transient ischemic attack in Asian patients: from the SOCRATES Trial (Acute Stroke or Transient Ischemic Attack Treated With Aspirin or Ticagrelor and Patient Outcomes).** *Stroke* 2017;48:167–73 CrossRef
- Amarenco P, Albers GW, Denison H, et al. **Efficacy and safety of ticagrelor versus aspirin in acute stroke or transient ischaemic attack of atherosclerotic origin: a subgroup analysis of SOCRATES, a randomised, double-blind, controlled trial.** *Lancet Neurol* 2017;16:301–10 CrossRef Medline
- Orru E, Rice H, De Villiers L, et al. **First clinical experience with the new Surpass Evolve flow diverter: technical and clinical considerations.** *J Neurointerv Surg* 2020;12:974–80 CrossRef Medline
- Agid R, Willinsky RA, Lee SK, et al. **Characterization of aneurysm remnants after endovascular treatment: contrast-enhanced MR angiography versus catheter digital subtraction angiography.** *AJNR Am J Neuroradiol* 2008;29:1570–74 CrossRef Medline
- Agid R, Schaaf M, Farb R. **CE-MRA for follow-up of aneurysms post stent-assisted coiling.** *Interv Neuroradiol* 2012;18:275–83 CrossRef Medline
- Roy D, Milot G, Raymond J. **Endovascular treatment of unruptured aneurysms.** *Stroke* 2001;32:1998–2004 CrossRef Medline

23. Taylor LI, Dickerson JC, Dambrino RJ, et al. **Platelet testing in flow diversion: a review of the evidence.** *Neurosurg Focus* 2017;42:E5 CrossRef Medline
24. Kim KS, Fraser JF, Grupke S, et al. **Management of antiplatelet therapy in patients undergoing neuroendovascular procedures.** *J Neurosurg* 2018;129:890–905 CrossRef Medline
25. Kim CH, Hwang G, Kwon OK, et al. **P2Y12 reaction units threshold for implementing modified antiplatelet preparation in coil embolization of unruptured aneurysms: a prospective validation study.** *Radiology* 2017;282:542–51 CrossRef Medline
26. Delgado Almandoz JE, Crandall BM, Scholz JM, et al. **Last-recorded P2Y12 reaction units value is strongly associated with thromboembolic and hemorrhagic complications occurring up to 6 months after treatment in patients with cerebral aneurysms treated with the Pipeline Embolization Device.** *AJNR Am J Neuroradiol* 2014;35:128–35 CrossRef Medline
27. Price MJ, Berger PB, Teirstein PS, et al. **Standard- vs high-dose clopidogrel based on platelet function testing after percutaneous coronary intervention: the GRAVITAS randomized trial.** *JAMA* 2011;305:1097–105 CrossRef
28. Gurbel PA, Bliden KP, Butler K, et al. **Randomized double-blind assessment of the ONSET and OFFSET of the antiplatelet effects of ticagrelor versus clopidogrel in patients with stable coronary artery disease: the ONSET/OFFSET study.** *Circulation* 2009;120:2577–85 CrossRef
29. Orme RC, Parker WA, Thomas MR, et al. **Study of two dose regimens of ticagrelor compared with clopidogrel in patients undergoing percutaneous coronary intervention for stable coronary artery disease (STEEL-PCI).** *Circulation* 2018;138:1290–1300 CrossRef Medline
30. Gurbel PA, Bliden KP, Butler K, et al. **Response to ticagrelor in clopidogrel nonresponders and responders and effect of switching therapies: the RESPOND study.** *Circulation* 2010;121:1188–99 CrossRef
31. Hanel RA, Taussky P, Dixon T, et al. **Safety and efficacy of ticagrelor for neuroendovascular procedures: a single center initial experience.** *J Neurointerv Surg* 2014;6:320–02 CrossRef Medline
32. Moore JM, Adeb N, Shallwani H, et al. **A multicenter cohort comparison study of the safety, efficacy, and cost of ticagrelor compared to clopidogrel in aneurysm flow diverter procedures.** *Neurosurgery* 2017;81:665–71 CrossRef Medline
33. Soize S, Foussier C, Manceau PF, et al. **Comparison of two preventive dual antiplatelet regimens for unruptured intracranial aneurysm embolization with flow diverter/disrupter: a matched-cohort study comparing clopidogrel with ticagrelor.** *J Neuroradiol* 2019;46:378–83 CrossRef Medline
34. Narata AP, Amelot A, Bibi R, et al. **Dual antiplatelet therapy combining aspirin and ticagrelor for intracranial stenting procedures: a retrospective single center study of 154 consecutive patients with unruptured aneurysms.** *Neurosurgery* 2019;84:77–83 CrossRef Medline
35. Benjamin EJ, Blaha MJ, Chiuve SE, et al. **American Heart Association Statistics Committee and Stroke Statistics Subcommittee. Heart disease and stroke statistics-2017 update: a report from the American Heart Association.** *Circulation* 2017;135:e146–603 CrossRef Medline
36. Bhatia KD, Kortman H, Orru E, et al. **Periprocedural complications of second-generation flow diverter treatment using Pipeline Flex for unruptured intracranial aneurysms: a systematic review and meta-analysis.** *J Neurointerv Surg* 2019;11:817–24 CrossRef Medline
37. Phan K, Huo YR, Jia F, et al. **Meta-analysis of stent-assisted coiling versus coiling-only for the treatment of intracranial aneurysms.** *J Clin Neurosci* 2016;31:15–22 CrossRef Medline
38. Brinjikji W, Murad MH, Lanzino G, et al. **Endovascular treatment of intracranial aneurysms with flow diverters: a meta-analysis.** *Stroke* 2013;44:442–47 CrossRef
39. Podlasek A, Al Sultan AA, Assis Z, et al. **Outcome of intracranial flow diversion according to the antiplatelet regimen used: a systematic review and meta-analysis.** *J Neurointerv Surg* 2020;12:148–55 CrossRef Medline
40. Kabbasch C, Goertz L, Siebert E, et al. **WEB embolization versus stent-assisted coiling: comparison of complication rates and angiographic outcomes.** *J Neurointerv Surg* 2019;11:812–16 CrossRef Medline
41. Skukalek SL, Winkler AM, Kang J, et al. **Effect of antiplatelet therapy and platelet function testing on hemorrhagic and thrombotic complications in patients with cerebral aneurysms treated with the Pipeline Embolization Device: a review and meta-analysis.** *J Neurointerv Surg* 2016;8:58–65 CrossRef Medline

Nonstenotic Carotid Plaques in Ischemic Stroke: Analysis of the STRATIS Registry

 N. Singh,  J. Ospel, A. Mayank,  M. Marko,  O.O. Zaidat,  N.H. Mueller-Kronast,  D.S. Liebeskind, and  M. Goyal, on behalf of the STRATIS Investigators



ABSTRACT

BACKGROUND AND PURPOSE: Few studies assess nonstenotic carotid plaques on CTA, and the causative role of these plaques in stroke is not entirely clear. We used CTA to determine the prevalence of nonstenotic carotid plaques (<50%), plaque features, and their association with ipsilateral strokes in patients with cardioembolic and cryptogenic strokes.

MATERIALS AND METHODS: Data were from the Systematic Evaluation of Patients Treated With Neurothrombectomy Devices for Acute Ischemic Stroke (STRATIS) registry, a prospective, nonrandomized registry of patients undergoing thrombectomy with the Solitaire device. The prevalence of nonstenotic carotid plaques ipsilateral and contralateral to the stroke was compared in patients with cryptogenic and cardioembolic strokes. Plaque features were further compared within both subgroups between patients with and without ipsilateral stroke. Adjusted associations among nonstenotic carotid plaque, plaque characteristics, and ipsilateral stroke in both subgroups were determined with logistic regression.

RESULTS: Of the 946 patients in the data base, 226 patients with cardioembolic stroke (median age, 72 years) and 141 patients with cryptogenic stroke (median age, 69 years) were included in the analysis. The prevalence of nonstenotic carotid plaque in the cardioembolic and cryptogenic subgroups was 33/226 (14.6%) and 32/141 (22.7%), respectively. Bilateral nonstenotic carotid plaques were seen in 10/226 (4.4%) patients with cardioembolic and 13/141 (9.2%) with cryptogenic strokes. Nonstenotic carotid plaques were significantly associated with ipsilateral strokes in the cardioembolic stroke (adjusted OR = 1.91; 95% CI, 1.15–3.18) and the cryptogenic stroke (adjusted OR = 1.69; 95% CI, 1.05–2.73) groups. Plaque irregularity, hypodensity, and per-millimeter increase in plaque thickness were significantly associated with ipsilateral stroke in the cryptogenic subgroup.

CONCLUSIONS: Nonstenotic carotid plaques were significantly associated with ipsilateral stroke in cardioembolic and cryptogenic stroke groups, and there was an association of plaque irregularity and hypodense plaque with ipsilateral stroke in the cryptogenic group, suggesting these plaques could be a potential cause of stroke in these patient subgroups.

ABBREVIATIONS: aOR = adjusted OR; ESUS = embolic stroke of undetermined source; IQR = interquartile range; SyNC = symptomatic nonstenotic carotid plaques

Secondary prevention of ischemic stroke relies on accurate determination of underlying stroke etiology. According to the

Trial of Org 10172 in Acute Stroke Treatment (TOAST) criteria, which is the most commonly used classification system,¹ large-artery disease is considered to be the stroke etiology in patients with carotid stenosis of >50%. The cutoff for TOAST–large artery disease was an arbitrary one, and later on, the 50% cutoff emerged from the NASCET trial, in which the maximal benefit of carotid endarterectomy was seen among patients with >50% carotid stenosis based on DSA measurements.^{2,3} Other common stroke etiologies according to TOAST are cardioembolic stroke and stroke with an undetermined source. However, the “undetermined source” category has some error because it includes patients with no source as well multiple sources. For this very reason, the term “embolic stroke of undetermined source” (ESUS) was coined in 2014, and it includes patients with “no source” only. ESUS accounts for up to one-third of ischemic strokes, and

Received January 4, 2021; accepted after revision April 27.

From the Departments of Clinical Neurosciences (N.S., A.M., M.G.) and Diagnostic Imaging (M.G.), Foothills Medical Center, University of Calgary, Calgary, Alberta, Canada; Department of Radiology (J.O.), University Hospital of Basel, Basel, Switzerland; Department of Neurology (M.M.), Medical University of Vienna, Vienna, Austria; Neuroscience Institute (O.O.Z.), Mercy Health St. Vincent Medical Center, Toledo, Ohio; Department of Neurology (N.H.M.-K.), Delray Medical Center, Delray Beach, Florida; and UCLA Comprehensive Stroke Center (D.S.L.), Los Angeles, California.

Please address correspondence to Mayank Goyal, MD, PhD, Departments of Radiology and Clinical Neurosciences, University of Calgary, Foothills Medical Centre, 1403 29th St NW, Calgary, AB T2N 2T9, Canada; e-mail: mgoyal@ucalgary.ca; @mayankGO; @nishita_singh3; @johanna_ospel



Indicates article with online supplemental data.

<http://dx.doi.org/10.3174/ajnr.A7218>

recent studies have shown that ESUS embodies various causes like a patent foramen ovale and atrial cardiomyopathy, in addition to nonstenotic carotid plaques.⁴

In a recent meta-analysis, the risk of recurrent stroke/TIA in patients with nonstenotic carotid plaques was 2.6/100 person-years and increased to 4.9/100 person-years if intraplaque hemorrhage was present.⁵ Furthermore, even in cardioembolic strokes, it has been shown that nonstenotic carotid disease (<50%) as a competing source of stroke is present in 9%–12%. Acknowledging these plaques as a competing cause of stroke may lead to reclassification of diagnoses in up to 22% of patients with cardioembolic stroke.⁶ Thus, it may be incorrect to conclude that the presence of a cardiac source, such as atrial fibrillation, is sufficient to establish stroke causality. In addition, the NAVIGATE ESUS trial, which evaluated the efficacy of oral anticoagulation with rivaroxaban in patients with ESUS compared with aspirin, failed to show any benefit with rivaroxaban. The trialists attributed this outcome to the high enrollment of patients with nonstenotic carotid disease, in whom antiplatelets may be more effective than anticoagulation.⁷

Recently, a classification suggested stratification of these nonstenotic carotid plaques on the basis of clinical and imaging features into possible, probable, and definite sources of stroke (symptomatic nonstenotic carotid plaques [SyNC]).⁸ This classification defines definite SyNC as patients with nonstenotic plaque with changing morphology on at least 2 different examinations with imaging findings consistent with stroke in the corresponding ICA territory in the absence of another cause. Probable SyNC was further stratified into the presence or absence of a cardiac cause with more strict criteria in presence of a competing cardiac cause.

We hypothesized that nonstenotic carotid plaques are a possible underlying stroke etiology in patients with cryptogenic and cardioembolic stroke, and we investigated the association of nonstenotic carotid plaques on CTA with ipsilateral strokes in patients with cryptogenic and cardioembolic stroke and aimed to identify plaque features that are independently associated with ipsilateral strokes within this patient sample.

MATERIALS AND METHODS

Study Population and Inclusion Criteria

The Systematic Evaluation of Patients Treated With Neurothrombectomy Devices for Acute Ischemic Stroke (STRATIS) registry (<https://clinicaltrials.gov/ct2/show/NCT02239640>) is a prospective, multicenter registry evaluating the use of the Solitaire Revascularization Device (Covidien) and the Capture low-profile revascularization device (MindFrame) in patients presenting with an acute ischemic stroke in the setting of a large intracranial vessel occlusion (clinicaltrials.gov unique identifier: NCT02239640). Details of the registry have been previously reported.⁹ Ethics approval was received from the local institutional review board. Stroke etiology was classified according to the TOAST criteria¹ as either large-artery atherosclerosis (the presence of >50% stenosis of the carotid or a major intracranial branch artery), cardioembolic (the presence of a cardiac embolic source such as atrial fibrillation detected on an electrocardiogram or a left atrial appendage thrombus detected on transthoracic or transesophageal sonography), small-vessel disease (the presence of lacunar infarction), other rare etiologies (eg, hypercoagulopathies), or undetermined source/

cryptogenic (all other categories have been ruled out and the etiology cannot be determined, or multiple competing causes are present). In this study, only patients with cardioembolic and cryptogenic strokes (as classified by the investigator) were included, ie, those with large-artery atherosclerosis (>50% carotid or major intracranial branch stenosis) and small-vessel disease were excluded. Furthermore, assessment of both extracranial carotid arteries was mandatory for inclusion, ie, patients with extracranial carotid artery occlusion and those for whom neck CTA imaging was not available were excluded. We also excluded patients for whom no clinical data were available. Informed consent was obtained before the study from all individuals.

Image Analysis

Head and neck CTA collected from patients within 7 days of symptom onset was used to review carotid morphology. All CTAs were assessed before endovascular treatment. A radiologist and neurologist read all images by consensus using OsiriX 9.5.2 imaging software (<http://www.osirix-viewer.com>). Conflicts were resolved by a senior neuroradiologist. The readers were blinded to clinical information and follow-up imaging at all times. The interobserver agreement (unweighted κ) between the 2 observers was 0.7 (Online Supplemental Data).

The following plaque features were reported for both carotid arteries in each patient: degree of stenosis ($\leq 30\%$ versus 31%–50%), maximum plaque thickness (in millimeters), the presence of plaque irregularity, ulceration (defined as contrast in a plaque extending >1 mm beyond the opacified lumen with indentation, fissure, or erosion on the luminal surface of a plaque), focal hypodensity, and the presence of a carotid web and plaque calcification (predominantly calcified plaque [$\geq 50\%$ calcified plaque components] versus predominantly noncalcified [$< 50\%$ calcified plaque components]). The degree of stenosis was measured as per the NASCET criteria² ($\leq 30\%$ versus 31%–50%). Carotid stenosis was measured on axial source images at the narrowest portion of the carotid bulb/proximal internal carotid artery after a straight course of the artery perpendicular to the axial plane had been confirmed on sagittal images. In vessels with substantial tortuosity, the degree of stenosis was measured on either sagittal or coronal images, depending on the orientation of the course of the artery. The distal internal carotid artery diameter was measured 1- to 2-cm distal to the bulb, where the vessel walls are parallel and no longer tapering.¹⁰ Plaque features were identified for both carotid arteries in each patient. These were the following: degree of stenosis ($\leq 30\%$ versus 31%–50%), plaque thickness (in millimeters, in which the abluminal marker was set at the interface between vessel wall and surrounding tissue and the inner marker was set at the interface between plaque and vessel lumen), the presence of plaque irregularity (qualitative assessment of the surface of the plaque that is not smooth but without a crater),^{11,12} ulceration¹¹ (qualitative assessment of crater/ulcer presence at the plaque surface), focal areas of hypodensity within the plaque (yes/no) (plaque hypodensity was defined as plaque density values that are unequivocally hypodense compared with the adjacent vessel wall on visual inspection),¹¹ and the presence of carotid web (yes/no)^{13,14} and plaque calcification (yes/no).¹⁵

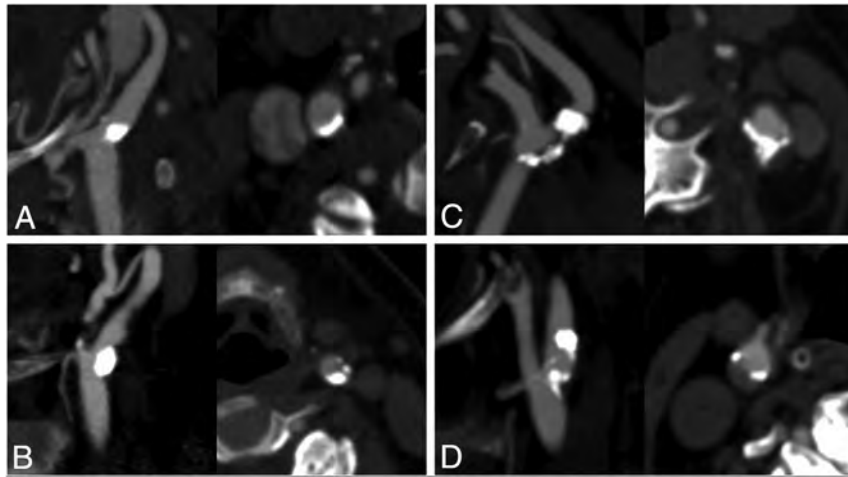


FIG 1. Sagittal oblique reformat and axial CT angiographic images of exemplary cases of nonstenotic carotid plaques with varying morphology in patients with ipsilateral ischemic stroke. All plaques were classified as predominantly calcified. A, Predominantly calcified plaque. B, C, and D, Predominantly calcified plaque with hypodense plaque features.

Donut sign for intraluminal carotid thrombus was defined as a filling defect within the lumen completely surrounded by contrast on at least 2 contiguous axial source images.¹⁶ Plaques were classified as either predominantly calcified (calcified plaque component on visual assessment $\geq 50\%$) or predominantly noncalcified. A carotid web was identified when there was a thin, smooth, membrane-like intraluminal filling defect along the posterior wall of the carotid bulb on oblique sagittal images and a corresponding thin septum on axial images.¹⁷ An unremarkable carotid artery was defined by the absence of any carotid plaque, web, or intraluminal thrombus. In keeping with a previous publication of our group, nonstenotic carotid plaque was defined as the presence of ≥ 1 plaque in the cervical ICA with $< 50\%$ luminal narrowing. Isolated, small (< 2 mm), abluminal calcifications without any luminal narrowing were not considered nonstenotic plaque.¹³ We deliberately excluded predominantly calcified plaques from this definition because they have been shown to be less likely to be symptomatic.¹⁴ Thus, carotid arteries with isolated abluminal calcifications were included in plaque feature analysis but were excluded from the definition of SyNC. An unremarkable carotid artery was defined by the absence of any carotid plaque, web, or intraluminal thrombus.

The outcome of interest was ipsilateral/“concordant,” defined as strokes due to occlusion of an intracranial vessel in the territory of the ipsilateral ICA vascular territory. Bilateral and posterior circulation strokes were, therefore, not classified as ipsilateral/concordant strokes because these strokes are in a vascular territory that is not supplied by the ipsilateral carotid artery; hence, they cannot be caused by a nonstenotic carotid plaque in the carotid artery. Figures 1–3 show some examples of predominantly calcified and noncalcified nonstenotic carotid plaques, respectively, in patients with ipsilateral ischemic stroke. All imaging was also assessed for the presence of intracranial atherosclerotic disease ($> 50\%$ stenosis).

Statistical Analysis

Baseline characteristics and imaging features for the overall patient sample and for the cryptogenic and cardioembolic subgroups, respectively, were reported using descriptive statistics. The prevalence of any nonstenotic carotid plaque and differences in baseline characteristics of patients with cryptogenic and cardioembolic strokes with-versus-without nonstenotic carotid plaques were assessed with the Fisher exact test (categorical variables) and the Wilcoxon rank sum test (continuous variables). We then conducted additional analyses on a carotid level to determine the prevalence of nonstenotic carotid plaques on ipsilateral-versus-contralateral strokes in cryptogenic and cardioembolic strokes. Differences were assessed using the

Fisher exact test. In a next step, univariable logistic regression analysis was performed to assess whether any of the assessed plaque features were significantly associated with ipsilateral stroke in both subgroups (on a carotid level). In case of a statistically significant association in univariable analysis, multivariable analysis was performed with adjustment for patient age and sex as forced variables. Because the unit of analysis was the carotid artery, the patient was included as a cluster variable in the model.^{15,18} Adjusted and unadjusted odds ratios were reported for these models with their corresponding 95% CIs. Two-sided $P < .05$ was considered statistically significant. Statistical analysis was performed with STATA/MP 15.1 (StataCorp).

RESULTS

Of 946 patients included in the registry, 381 (36%) were excluded due to lack of imaging data. Of the remaining 565 patients, 130 (23%) were classified as having stroke due to large-artery atherosclerosis and were excluded. Of the remaining 435 patients, 174 (40%) patients were classified as having cryptogenic stroke and 261 patients (60%) were classified as having cardioembolic stroke. Of those, ICAs could be assessed bilaterally in 141 patients with cryptogenic stroke and 226 with cardioembolic stroke who were included in the following analysis (Online Supplemental Data). None of the patients had evidence of intracranial stenosis. In patients who received alteplase, the mean onset-to-alteplase time was 113.4 (SD, 50.5) minutes. Baseline clinical and imaging characteristics of the overall cohort and patients with cryptogenic and cardioembolic strokes can be found in Table 1.

Prevalence of Nonstenotic Carotid Plaques in Cryptogenic and Cardioembolic Subgroups

The prevalence of nonstenotic carotid plaque on any side was 65/367 (17.7%), of which 23 patients (6.3%) had bilateral nonstenotic carotid plaques. The prevalence of nonstenotic carotid plaque in the cardioembolic and cryptogenic subgroups was 33/226 (14.6%) and 32/141 (22.7%), respectively, whereas 10/226 (4.4%)

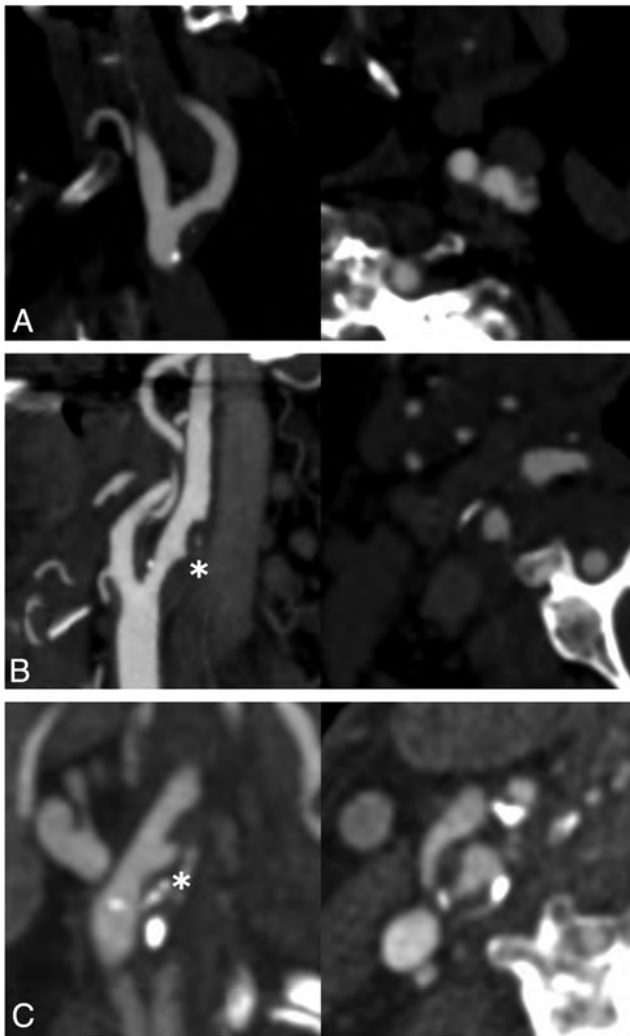


FIG 2. Sagittal oblique reformatted and axial CT angiographic images of exemplary cases of nonstenotic carotid plaques with varying morphology in patients with ipsilateral ischemic stroke. All plaques were classified as predominantly noncalcified. A, Predominantly noncalcified and hypodense plaque. B, Predominantly noncalcified, hypodense, and irregular plaque. C, Predominantly noncalcified, hypodense, and ulcerated plaque.

patients with cardioembolic stroke and 13/141 (9.2%) with cryptogenic stroke had bilateral nonstenotic carotid plaques. Baseline characteristics for patients with-versus-without nonstenotic carotid plaques for both subgroups are shown in the Online Supplemental Data. Patients with cryptogenic stroke with nonstenotic carotid plaques were younger than those with cryptogenic stroke without nonstenotic carotid plaques (median, 71; interquartile range [IQR], 60–79; and median, 61 years; IQR, 51–71), respectively, p value 0.20). No significant differences in baseline characteristics were seen in patients with cardioembolic stroke.

Prevalence of Ipsilateral/Nonstenotic Carotid Plaques (Carotid-Level Analysis). In patients with cardioembolic stroke, nonstenotic carotid plaques were significantly more common ipsilateral to the side of the stroke than contralateral to it (35/210 [16.7%] ipsilateral versus 23/242 [9.5%] contralateral, $P=.025$). In patients with cryptogenic stroke, nonstenotic carotid plaques were

nominally also more frequent ipsilateral to the side of the stroke (31/130 [23.9%] ipsilateral versus 24/152 [15.8%] contralateral), though the difference did not reach statistical significance ($P=.099$; Table 2).

In univariable analysis, nonstenotic carotid plaques were significantly associated with ipsilateral/concordant strokes in cryptogenic stroke (unadjusted OR = 1.67; 95% CI, 1.04–2.69) and cardioembolic strokes (unadjusted OR = 1.90; 95% CI, 1.15–3.16). After we adjusted for patient age and sex with patient as a cluster variable, this relationship remained significant (cryptogenic stroke: adjusted OR [aOR] = 1.69; 95% CI, 1.05–2.73; cardioembolic stroke: aOR = 1.91; 95% CI, 1.15–3.18).

Carotid Plaque Features Associated with Ipsilateral Ischemic Stroke (Carotid-Level Analysis). In univariable analysis, none of the plaque features were significantly associated with ipsilateral stroke in the cardioembolic subgroup. Thus, multivariable analysis was not performed. In the cryptogenic subgroup, plaque irregularity (aOR = 2.50; 95% CI, 1.22–5.14), plaque hypodensity (aOR = 1.89; 95% CI, 1.14–3.14), and maximum plaque thickness (aOR = 1.29; 95% CI, 1.05–1.57) were significantly associated with ipsilateral stroke, with nearly twice the odds of ipsilateral stroke. These associations were not confounded after adjusting for patient age, sex, and clustering by patients (Table 3).

Thus, we found an absolute risk of ipsilateral stroke with nonstenotic carotid plaques to be twice as high in the cardioembolic group and 1.5 times higher in cryptogenic group compared with the contralateral side (Table 2).

DISCUSSION

In this population of patients with acute ischemic stroke with proven intra-arterial occlusion, we found a significant association of nonstenotic carotid plaques with ipsilateral stroke in the cardioembolic group and a numeric increase in nonstenotic carotid plaques on the ipsilateral side in the cryptogenic group compared with the contralateral side. Nonstenotic plaques were more common on the ipsilateral side in the cryptogenic (23.9%) group versus the cardioembolic group (16.7%). These findings are in line with growing evidence suggesting nonstenotic carotid plaques as a potential etiology in ischemic stroke. Another recent substudy from the INTERRSeCT dataset of 138 patients with ESUS also showed that nonstenotic carotid plaques were significantly more common on the side of the stroke, suggesting a possible causal role.¹³ This study differs from the INTERRSeCT substudy because it includes only patients with large-vessel occlusion. In addition, it tries to assess the association of ipsilateral stroke in patients with a presumed cardioembolic etiology. Another study by Kopczak et al¹⁹ analyzed carotid artery plaques (CAPs) using MR imaging in patients with cryptogenic stroke compared with patients with stroke with small-vessel disease or cardioembolic stroke. They found a significantly higher prevalence of ipsilateral complicated carotid artery plaques in patients with cryptogenic stroke than in the reference group (31% versus 15%). Yet another study used a CTA-based assessment of plaque thickness and showed that plaque thickness was greater on the side of the ipsilateral stroke in the ESUS subgroup.²⁰ These findings highlight

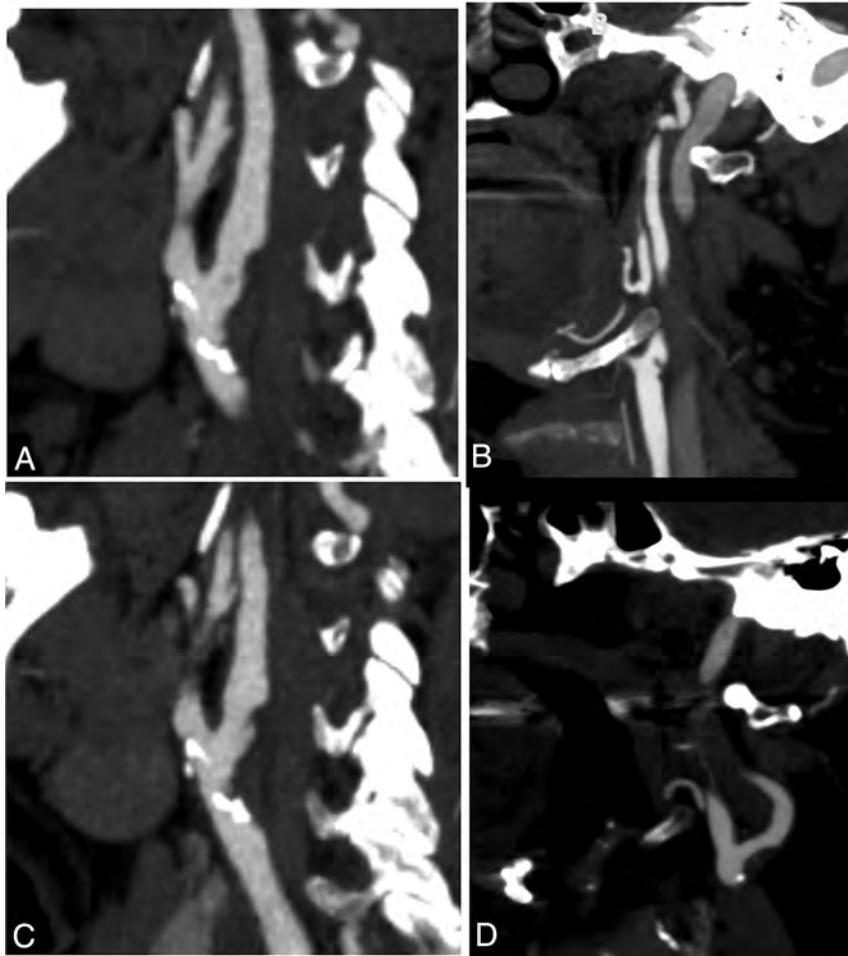


FIG 3. Sagittal oblique reformat and axial CT angiographic images of exemplary cases of nonstenotic carotid disease with varying morphology in patients with ipsilateral ischemic stroke. *A*, Predominantly noncalcified plaque with an irregular surface. *B*, Carotid web. *C*, Predominantly noncalcified plaque with ulceration. *D*, Predominantly noncalcified plaque with hypodense plaque features.

the potential role of SyNC contributing to stroke mechanisms on the basis of morphologic features beyond the degree of stenosis.

We could not identify significant association between specific plaque features and ipsilateral stroke in the cardioembolic group. However, in the cryptogenic group, we could identify plaque features (plaque hypodensity, irregularity, and maximum plaque thickness) that were significantly more common on the ipsilateral side, even after adjusted analysis. These findings are hypothesis-generating and contribute to the identification of vulnerable plaques.^{14,21} They also suggest that a subset of cryptogenic strokes may be caused by these vulnerable plaques with significant plaque burden, despite low-grade luminal stenosis. Even though the strength of association of nonstenotic carotid plaques and ipsilateral stroke was higher with cardioembolic stroke than in the cryptogenic group, we found more high-risk plaque features in the cryptogenic stroke population.

Another recent study concluded that high-risk plaques were more prevalent ipsilateral to the ischemic hemisphere across

several stroke subtypes (especially ESUS and cardioembolic categories), and accounting for them could have led to reclassification of the stroke etiology in up to 15% of cases in their sample.⁷ These observations support the possible causal association between nonstenotic carotid plaques and stroke, especially in patients presumed to have a cardioembolic etiology. Nevertheless, in the presence of a competing etiology, it would be prudent to see the distribution of DWI findings on MR imaging. The presence of DWI findings beyond a vascular territory or involving multiple vascular territories would support a cardioembolic etiology. In this study, we considered a stroke to be ipsilateral only in the absence of evidence of stroke in other arterial territories, further substantiating our findings. However, 64% of patients did not have follow-up MR imaging, and CT scans were used for assessment of stroke, which are not sensitive for detecting smaller embolic strokes. In addition, patients underwent endovascular thrombectomy, and small diffusion lesions outside the expected territory could be related to the procedure.

Results from these studies and several others are similar to ours and support our belief of moving beyond conventional stenosis measures to categorize carotid disease and broaden our horizon to identify stroke etiology, especially in the cryptogenic subpopulation.^{8,16,22–26}

Limitations

This study has several limitations. We used nonrandomized data that were analyzed in a retrospective fashion, and patients with missing imaging data were excluded, possibly having led to some selection bias. We do not have a detailed reasoning for lack of imaging data, but we suspect that this could be due to problems with the transfer of images. In addition, the registry included only patients with large-vessel occlusion, forming only a piece of the total population of ischemic stroke. It may be that these patients had a nonstenotic plaque on the ipsilateral side to begin with, which may have dislodged into the anterior circulation, leading to large-vessel occlusion. It may be insightful to assess the prevalence of these nonstenotic carotid plaques in patients with minor stroke and/or the non-large-vessel occlusion population.

There are no validated criteria for carotid plaque assessment on CTA. The degree of stenosis and plaque measurements were

Table 1: Patient baseline characteristics for the entire patient sample (n = 367), patients with cardioembolic stroke (n = 226), and patients with cryptogenic stroke (n = 141)

Variable	Entire Patient Sample (n = 367)	Cardioembolic Stroke (n = 226)	Cryptogenic Stroke (n = 141)	P Value ^a
Age (median) (IQR) (yr)	71 (60–81)	72 (62–82)	69 (59–78)	.23
Female sex (No.) (%)	189/367 (51.5)	116/226 (51.3)	73/141 (51.8)	.51
Baseline NIHSS (median) (IQR)	16 (12–20)	16 (12–20)	17 (13–22)	.09
Comorbidities (No.) (%)				
CAD	107 (29.2)	68 (30.1)	39 (27.7)	.63
Previous stroke	46 (12.5)	32 (14.2)	14 (9.9)	.26
Previous ICH	7 (1.9)	3 (1.3)	4 (2.8)	.43
Previous TIA	24 (6.5)	14 (6.2)	10 (7.1)	.82
Diabetes	94 (25.6)	54 (23.9)	40 (28.4)	.39
Hypertension	267 (72.8)	169 (74.8)	98 (69.5)	.28
Smoking (No.) (%)				
Current smoker	69/333 (20.7)	35/204 (17.2)	34/129 (26.4)	.001
Former smoker	106/333 (31.8)	80/204 (39.2)	26/129 (24.5)	.001
ASPECTS (median) (IQR)	9 (8–9)	9 (8–9)	9 (8–9)	.88
Occlusion site (No.) (%)	(n = 330)	(n = 210)	(n = 120)	.43
ICA (intracranial)	47 (12.8)	28 (12.4)	19 (13.5)	
M1	235 (64.0)	147 (65.0)	88 (62.4)	
M2	65 (17.7)	42 (18.6)	23 (16.3)	
Other	20 (5.5)	9 (4.0)	11 (7.8)	

Note:—CAD indicates coronary artery disease; ICH, intracerebral hemorrhage

^aDerived from the Wilcoxon rank sum test (continuous variables) or Fisher exact test (categorical variables).

Table 2: Ipsilateral and contralateral nonstenotic carotid plaque in patients with cryptogenic and cardioembolic stroke

Overall Ischemic Strokes (n = 367 Patients/734 Carotid Arteries)		
Cardioembolic stroke ^b (n = 226 patients/452 carotid arteries)		
Ipsilateral stroke	Yes	No (contralateral/unaffected side)
Nonstenotic carotid plaque (No.) (%)	35 (16.7)	23 (9.5)
No nonstenotic carotid plaque (No.) (%)	175 (83.3)	219 (90.5)
Total (No.) (%) ^a	210 (100)	242 (100)
Cryptogenic stroke ^b (n = 141 patients/282 carotid arteries)		
Ipsilateral stroke	Yes	No (contralateral/unaffected side)
Nonstenotic carotid plaque (No.) (%)	31 (23.9)	24 (15.8)
No nonstenotic carotid plaque (No.) (%)	99 (76.2)	128 (84.2)
Total (No.) (%) ^a	130 (100)	152 (100)

^aNote that 16 patients in the cardioembolic group and 11 patients in the cryptogenic group had bilateral and/or posterior circulation strokes that were not confined to the ipsilateral ICA vascular territory. These strokes were, therefore, classified neither as right-sided nor left-sided strokes.

^bTwo-sided P value (derived from the Fisher exact test) = .025 for cardioembolic strokes and .099 for cryptogenic stroke.

obtained on axial CTA source images, but it is not uncommon to see the carotid artery following a curved course that is not perpendicular to the axial plane. This may have limited the accuracy of our measurements in comparison with more complex planimetric and volumetric measurements.¹² We did not use high-resolution MR imaging to identify plaque features, which may have led to underreporting of plaque features such as ulceration. However, we aimed to assess plaque features in a manner that could be easily used in the acute stroke setting. Owing to one-time cross-sectional assessment, we were unable to comment on nonstenotic plaques ipsilateral to the asymptomatic hemisphere as they may have caused events in the past or may become symptomatic in future. The registry did not capture the side of previous strokes/TIAs, and it was, therefore, not possible to correlate previous stroke location to carotid vascular territories. In addition, we did not have sufficient data on cardiovascular risk factors and workflow times for a detailed analysis. From an etiologic classification standpoint, a detailed cardiology work-up, including 24-hour electrocardiograms and echo-

cardiograms, was not available for most patients in this dataset, and a cryptogenic etiology was investigator-determined. Thus, some patients with >1 cause may have been classified into this category. Last, these findings prove only an association and not causation. Larger longitudinal prospective studies are needed to establish a causal link between nonstenotic carotid plaques and ipsilateral ischemic stroke.

CONCLUSIONS

We found a significant association between the presence of nonstenotic carotid plaques with ipsilateral strokes in patients with both cryptogenic and cardioembolic strokes. Plaque hypodensity, irregularity, and maximum plaque thickness were significantly associated with ipsilateral strokes in the cryptogenic group. This finding suggests that nonstenotic carotid plaques could be a potential stroke etiology in patients with ischemic stroke who are classified into causes other than large artery disease. Further research to confirm a causative role of nonstenotic carotid

Table 3: Plaque features with significant association with ipsilateral strokes in patients with cryptogenic and cardioembolic strokes

Plaque Feature	uOR (95%CI)	aOR (95%CI) ^a
Cardioembolic stroke (n = 226 patients/452 carotid arteries)		
Predominantly calcified plaque	0.75 (0.52–1.09)	
Irregularity	1.50 (0.81–2.79)	
Ulceration	1.94 (0.46–8.23)	
Hypodense plaque	1.17 (0.77–1.76)	
Maximum plaque thickness	1.11 (0.95–1.30)	
Donut sign	— ^b	
Stenosis degree (31%–50% vs 0%–30%)	1.05 (0.77–1.43)	
Web ^c	3.49 (0.36–33.83)	
Unremarkable carotid artery (absence of any of the above-mentioned features)	0.96 (0.66–1.40)	
Cryptogenic stroke (n = 141 patients/282 carotid arteries)		
Predominantly calcified plaque	0.94 (0.58–1.51)	
Irregularity	2.32 (1.15–4.70)	2.50 (1.22–5.14)
Ulceration	1.47 (0.39–5.59)	
Hypodense plaque	1.78 (1.09–2.92)	1.89 (1.14–3.14)
Maximum plaque thickness	1.24 (1.03–1.50)	1.29 (1.05–1.57)
Donut sign ^c	1.17 (0.07–18.90)	
Stenosis degree (31%–50% vs. 0%–30%)	1.31 (0.89–1.96)	
Web ^c	1.77 (0.29–10.77)	
Unremarkable carotid artery (absence of any of the above-mentioned features)	0.75 (0.46–1.21)	

Note:—uOR indicates unadjusted OR.

^a With adjustment for age and sex and patient as a cluster variable. Multivariable analysis was performed for variables only when a significant association was found in univariable analysis.

^b Omitted because of collinearity (all patients with a donut sign had ipsilateral strokes).

^c Not a plaque feature but included in the definition of nonstenotic carotid disease.

plaques and to identify potential high-risk plaque features on CTA and other imaging modalities is needed.

Disclosures: Osama O. Zaidat—UNRELATED: Consultancy: Consultant/advisory board member at the National Institutes of Health (NIH) StrokeNet, Penumbra, Medtronic Neurovascular, Codman, and Stryker; Grants/Grants Pending: grant for the multicenter TESLA study; Patents (Planned, Pending or Issued): Galaxy Therapeutics and O.O. Z., Comments: grants under Galaxy Therapeutics and to O.O.Z. Nils H. Mueller-Kronast—RELATED: Fees for Participation in Review Activities such as Data Monitoring Boards, Statistical Analysis, Endpoint Committees, and the Like: Medtronic, Comments: Steering Committee of the STRATIS registry. David S. Liebeskind—RELATED: Consulting Fee or Honorarium: Medtronic, Comments: imaging core lab; UNRELATED: Consultancy: Cerenovus, Genentech, Medtronic, Stryker, Vesalio, Comments: imaging core lab. Mayank Goyal—RELATED: Consulting Fee or Honorarium: Medtronic, Comments: advice on acute stroke intervention; UNRELATED: Consultancy: Stryker, MicroVention, Mentice; Grants/Grants Pending: Stryker, Cerenovus, NoNO*; Patents (Planned, Pending or Issued): GE Healthcare, MicroVention; Royalties: GE Healthcare, MicroVention. *Money paid to the institution.

REFERENCES

- Adams HP, Bendixen BH, Kappelle LJ, et al. Classification of subtype of acute ischemic stroke: definitions for use in a multicenter clinical trial—TOAST. *Trial of Org 10172 in Acute Stroke Treatment*. *Stroke* 1993;24:35–41 CrossRef Medline
- Ferguson GG, Eliasziw M, Barr HW, et al. The North American Symptomatic Carotid Endarterectomy Trial. *Stroke* 1999;30:1751–58 CrossRef Medline
- Randomised trial of endarterectomy for recently symptomatic carotid stenosis: final results of the MRC European Carotid Surgery Trial (ECST). *Lancet* 1998;351:1379–87 CrossRef Medline
- Hart RG, Connolly SJ, Mundt H. Rivaroxaban for stroke prevention after embolic stroke of undetermined source. *N Engl J Med* 2018;379:987 CrossRef Medline
- Singh N, Marko M, Ospel JM, et al. The risk of stroke and TIA in nonstenotic carotid plaques: a systematic review and meta-analysis. *AJNR Am J Neuroradiol* 2020;41:1453–59 CrossRef Medline
- Kamel H, Navi BB, Merkler AE, et al. Reclassification of ischemic stroke etiological subtypes on the basis of high-risk nonstenosing carotid plaque. *Stroke* 2020;51:504–10 CrossRef Medline
- Hart RG, Diener HC, Coutts SB, et al. Cryptogenic Stroke/ESUS International Working Group. Embolic strokes of undetermined source: the case for a new clinical construct. *Lancet Neurol* 2014;13:429–38 CrossRef Medline
- Goyal M, Singh N, Marko M, et al. Embolic stroke of undetermined source and symptomatic nonstenotic carotid disease. *Stroke* 2020;51:1321–25 CrossRef Medline
- Mueller-Kronast NH, Zaidat OO, Froehler MT, et al. STRATIS Investigators. Systematic evaluation of patients treated with neurothrombectomy devices for acute ischemic stroke: primary results of the STRATIS Registry. *Stroke* 2017;48:2760–68 CrossRef Medline
- Fox EJ. Management of worsening multiple sclerosis with mitoxantrone: a review. *Clin Ther* 2006;28:461–74 CrossRef Medline
- de Weert TT, Cretier S, Groen HC, et al. Atherosclerotic plaque surface morphology in the carotid bifurcation assessed with multidetector computed tomography angiography. *Stroke* 2009;40:1334–40 CrossRef Medline
- Saba L, Yuan C, Hatsukami TS, et al. Vessel Wall Imaging Study Group of the American Society of Neuroradiology. Carotid Artery Wall Imaging: Perspective and Guidelines from the ASNR Vessel Wall Imaging Study Group and Expert Consensus Recommendations of the American Society of Neuroradiology. *AJNR Am J Neuroradiol* 2018;39:E9–31 CrossRef Medline
- Compagne KC, van Es AC, Berkhemer OA, et al. MR CLEAN Trial Investigators. Prevalence of carotid web in patients with acute intracranial stroke due to intracranial large vessel occlusion. *Radiology* 2018;286:1000–07 CrossRef Medline
- Zhang AJ, Dhruv P, Choi P, et al. A systematic literature review of patients with carotid web and acute ischemic stroke. *Stroke* 2018;49:2872–76 CrossRef Medline
- Eesa M, Hill MD, Al-Khathaami A, et al. Role of CT angiographic plaque morphologic characteristics in addition to stenosis in predicting the symptomatic side in carotid artery disease. *AJNR Am J Neuroradiol* 2010;31:1254–60 CrossRef Medline
- Menon BK, Singh J, Al-Khathaami A, et al. Calgary CTA Study Group. The donut sign on CT angiography: an indicator of reversible intraluminal carotid thrombus? *Neuroradiology* 2010;52:1055–56 CrossRef Medline

17. Hu H, Zhang X, Zhao J, et al. **Transient ischemic attack and carotid web.** *AJNR Am J Neuroradiol* 2019;40:313–18 CrossRef Medline
18. UCLA Institute for Digital Research and Education. Statistical Consulting. **What are the some of the methods for analyzing clustered data in Stata?** <https://stats.idre.ucla.edu/stata/faq/what-are-the-some-of-the-methods-for-analyzing-clustered-data-in-stata/>. Accessed November 30, 2020
19. Kopcak A, Schindler A, Bayer-Karpinska A, et al. **Complicated carotid artery plaques as a cause of cryptogenic stroke.** *J Am Coll Cardiol* 2020;76:2212–22 CrossRef Medline
20. Knight Greenfield A, Quitlong Nario JJ, Vora A, et al. **Associations between features of nonstenosing carotid plaque on computed tomographic angiography and ischemic stroke subtypes.** *J Am Heart Assoc* 2019;8:e014818 CrossRef Medline
21. Nighoghossian N, Derex L, Douek P. **The vulnerable carotid artery plaque.** *Stroke* 2005;36:2764–72 CrossRef Medline
22. Ospel JM, Singh N, Marko M, et al. **Prevalence of ipsilateral nonstenotic carotid plaques on computed tomography angiography in embolic stroke of undetermined source.** *Stroke* 2020;51:1743–49 CrossRef Medline
23. Coutinho JM, Derkatch S, Potvin AR, et al. **Nonstenotic carotid plaque on CT angiography in patients with cryptogenic stroke.** *Neurology* 2016;87:665–72 CrossRef Medline
24. Kanter MC, Tegeler CH, Pearce LA, et al. **Carotid stenosis in patients with atrial fibrillation: prevalence, risk factors, and relationship to stroke in the Stroke Prevention in Atrial Fibrillation study.** *Arch Intern Med* 1994;154:1372–77 Medline
25. Gupta A, Baradaran H, Schweitzer AD, et al. **Carotid plaque MRI and stroke risk.** *Stroke* 2013;44:3071–77 CrossRef Medline
26. Singh N, Moody AR, Panzov V, et al. **Carotid intraplaque hemorrhage in patients with embolic stroke of undetermined source.** *J Stroke Cerebrovasc Dis* 2018;27:1956–59 CrossRef Medline

Altered Blood Flow in the Ophthalmic and Internal Carotid Arteries in Patients with Age-Related Macular Degeneration Measured Using Noncontrast MR Angiography at 7T

M.L. Hibert, Y.I. Chen, N. Ohringer, W.J. Feuer, N.K. Waheed, J.S. Heier, M.W. Calhoun, P.J. Rosenfeld, and J.R. Polimeni



ABSTRACT

BACKGROUND AND PURPOSE: Age-related macular degeneration is associated with reduced perfusion of the eye; however, the role of altered blood flow in the upstream ophthalmic or internal carotid arteries is unclear. We used ultra-high-field MR imaging to investigate whether the diameter of and blood flow in the ophthalmic artery and/or the ICA are altered in age-related macular degeneration and whether any blood flow changes are associated with disease progression.

MATERIALS AND METHODS: Twenty-four patients with age-related macular degeneration and 13 similarly-aged healthy controls participated. TOF and high-resolution dynamic 2D phase-contrast MRA ($0.26 \times 0.26 \times 2\text{mm}^3$, 100-ms effective sampling rate) was acquired at 7T. Vessel diameters were calculated from cross-sectional areas in phase-contrast acquisitions. Blood flow time-series were measured across the cardiac cycle.

RESULTS: The ophthalmic artery vessel diameter was found to be significantly smaller in patients with age-related macular degeneration than in controls. Volumetric flow through the ophthalmic artery was significantly lower in patients with late age-related macular degeneration, with a significant trend of decreasing volumetric ophthalmic artery flow rates with increasing disease severity. The resistance index was significantly greater in patients with age-related macular degeneration than in controls in the ophthalmic artery. Flow velocity through the ophthalmic artery and ICA was significantly higher in patients with age-related macular degeneration. Ophthalmic artery blood flow as a percentage of ipsilateral ICA blood flow was nearly double in controls than in patients with age-related macular degeneration.

CONCLUSIONS: These findings support the hypothesis that vascular changes upstream to the eye are associated with the severity of age-related macular degeneration. Additional investigation into the potential causality of this relationship and whether treatments that improve ocular circulation slow disease progression is warranted.

ABBREVIATIONS: AMD = age-related macular degeneration; EC = eddy current; GEE = generalized estimating equation; OA = ophthalmic artery; PC = phase-contrast; VENC = encoding velocity

Age-related macular degeneration (AMD) is a late-onset complex genetic disease—and the leading cause of blindness

Received December 21, 2020; accepted after revision April 4, 2021.

From the Athinoula A. Martinos Center for Biomedical Imaging (M.L.H., Y.I.C., N.O., J.R.P.), Massachusetts General Hospital, Charlestown, Massachusetts; Department of Radiology (Y.I.C., J.R.P.), Harvard Medical School, Boston, Massachusetts; Department of Ophthalmology (W.J.F., P.J.R.), Bascom Palmer Eye Institute, University of Miami Miller School of Medicine, Miami, Florida; New England Eye Center (N.K.W.), Tufts Medical Center, Boston, Massachusetts; Ophthalmic Consultants of Boston (J.S.H.), Boston, Massachusetts; OcuDyne Inc (M.W.C.), Roseville, Minnesota; and Harvard-Massachusetts Institute of Technology Division of Health Sciences and Technology (J.R.P.), Massachusetts Institute of Technology, Cambridge, Massachusetts.

This work was supported, in part, by the National Institutes of Health (National Institute of Biomedical Imaging and Bioengineering grants P41-EB015896 and R01-EB019437), the BRAIN Initiative (National Institute of Mental Health grant R01-MH111419), and the Massachusetts General Hospital/Harvard-Massachusetts Institute of Technology Division of Health Sciences and Technology Athinoula A. Martinos Center for Biomedical Imaging and was made possible by the resources provided by National Institutes of Health Shared Instrumentation Grants S10-RR023401, S10-RR019307, S10-RR023043, S10-RR019371, and S10-RR020948. It was also supported by OcuDyne Inc.

among the elderly worldwide—caused by irreversible damage to the macula, resulting in central vision loss.^{1,2} AMD is divided into 3 stages known as early, intermediate, and late.³ Early and intermediate AMD are characterized by drusen—lipoprotein deposits under the retinal pigment epithelium—which increase in size along with pigment deposition, while late AMD is characterized by either the presence of exudation caused by macular neovascularization or the formation of macular atrophy known as geographic atrophy. Due to their clinical features, nonexudative

Please address correspondence to Jonathan R. Polimeni, PhD, Athinoula A. Martinos Center for Biomedical Imaging, Massachusetts General Hospital, 149 Thirteenth St, Suite 2301, Charlestown, MA, 02129; e-mail: jonp@nmr.mgh.harvard.edu

Indicates open access to non-subscribers at www.ajnr.org

Indicates article with online supplemental data.

<http://dx.doi.org/10.3174/ajnr.A7187>

AMD is also referred to as dry AMD, while exudative or neovascular AMD is referred to as wet AMD. Approximately 15% of AMD progresses to the exudative form of the disease, which can be treated with intravitreal injections of vascular endothelial growth factor inhibitors, but there are no effective treatment options for dry AMD regardless of stage.⁴

The choroid is the vascular layer that provides most of the nutritional support to the outer retina and retinal pigment epithelium, which are the layers primarily affected in the macula in AMD. Prior studies have demonstrated reduced choroidal perfusion in patients with AMD, measured with Doppler imaging^{5,6} and more recently with MR imaging-based perfusion measures.⁷ Reduced choroidal perfusion was found to correlate to AMD severity⁶ and also the risk of developing wet AMD.⁸ In addition, risk factors for developing AMD include cardiovascular disease and a history of smoking.⁹ These studies indicate an important link between blood flow and development and progression of AMD. It is unclear whether the vasculature upstream to the choroid is altered in patients with AMD.

In this report, we investigated whether vessel diameters and blood flow in the ophthalmic artery (OA) or the internal carotid artery (ICA), the first two arteries upstream of the choroid, are altered in AMD. We used 7T MRA to obtain high-resolution measures of OA and ICA blood flow and morphometry without the use of intravascular contrast agents. Here 7T MRA was chosen over lower magnetic field strengths due to its higher SNR, which enables imaging at the higher spatial resolution with sufficient SNR to reliably assess vessels with small cross-sectional diameters such as the OA.^{10,11} This imaging protocol has the potential to detect abnormalities in the relevant vascular anatomy and associated blood flow in individual patients. This work will lead to a better understanding of the vascular changes beyond the choroid and may aid in the development of new treatment strategies for both wet and dry AMD.

MATERIALS AND METHODS

Study Participants

Subjects with different stages of AMD and similarly aged controls participated in this study, approved by the Partners Human Research Committee, after providing written informed consent. Patients were referred from two Boston-area ophthalmologists who provided patients' diagnostic information, and the stages of AMD were confirmed by two retina specialists (N.K.W. and P.J.R.). Healthy controls were identified using advertisements in the greater Boston area and also included spouses of patients enrolled in the study. Exclusion criteria for both patients and controls included contraindications for MR imaging, color vision deficiency/color blindness, and a history of neurologic or psychiatric illnesses. Some patients had a different stage of AMD in each eye. In all cases, left and right OAs and ICAs were scanned and analyzed separately. Images with head motion artifacts were excluded.

MR Imaging Data Acquisition

All subjects were scanned on a whole-body 7T Magnetom MR imaging scanner (Siemens) using a 32-channel head receive array coil with a birdcage transmit coil built in-house.¹² We performed local B_0 shimming in the region around the OAs using a high-resolution local B_0 field map (WIP 452B; Siemens). A 0.5-mm

isotropic 3D-TOF-MRA scan covering the OAs and carotid siphon was acquired for each subject with the following parameters: TR/TE = 21/1.83 ms, flip angle = 45°, slab thickness = 24 mm, bandwidth = 766 Hz/pixel, acceleration factor = 2, acquisition time = 8 minutes 44 seconds. To minimize the TE value, we disabled flow compensation; with a sufficiently low TE value, streaking or displacement artifacts due to pulsatile or steady flow, respectively, are minimized, reducing the need for flow compensation. During protocol development, it was found that the ultrashort TE of 1.83 ms and an asymmetric echo factor of 36% were critical to obtaining sufficient SNR to visualize the entire path of the OA.

Blood flow estimation for each OA was performed with a single-slice high-resolution 2D dynamic quantitative phase-contrast (PC) MRA acquisition. The 3D-TOF images were used to carefully position the PC acquisitions orthogonal to the trajectory of each OA and approximately 1.5 cm distal to the ostium and before any branches of the OA (Fig 1), along the distal segment of the OA past "angle b,"¹³ the second bend in the OA. The PC-MRA acquisitions used a single velocity encoding direction and multiple encoding velocities (VENCs) with the following parameters: $0.26 \times 0.26 \times 2 \text{ mm}^3$ voxels and TR/TE/flip angle = 34.2/5.39 ms/15°. Acquisition times varied on the basis of subjects' heart rates but typically lasted approximately 8–10 minutes. To enable straightforward identification of the OA without image registration, we centered the FOV of each PC-MRA acquisition on the OA.

Blood flow estimation in each ICA followed a similar protocol, positioning each 2D-PC-MRA acquisition below the carotid siphon. Due to the larger vessel size, we opted for a lower in-plane resolution ($0.5 \times 0.5 \times 2 \text{ mm}^3$) with TR/TE/flip angle = 27.2/3.9 ms/15°. Acquisition times varied on the basis of the subjects' heart rates but typically lasted approximately 4–5 minutes.

PC-MRA acquisitions were cardiac-gated prospectively, using the MR imaging system vendor's built-in pulse oximeter trigger, and had 3 VENCs, which were typically 25, 45, and 70 cm/s for OA acquisitions and 45, 70, and 110 cm/s for ICA acquisitions. Pilot scans indicated that these values would be appropriate for these two vessels of interest in most subjects and that the optimal VENC for dynamic analysis varied among subjects. Additional PC-MRA acquisitions with adjusted VENCs were included when an individual subject's peak flow rates were observed to be outside the default VENC range. Due to cardiac rate variations across participants, there was minor variability in the temporal resolution of the blood flow acquisition; on average, 29.7 (SD, 5.2) samples were acquired during the cardiac cycle, and the average cycle duration was 981 (SD, 164) ms, yielding an average sampling rate of 33 (SD, 6) ms. All analyses were performed on image data reconstructed online using the vendor-supplied software.

Eddy Current Correction

Due to the relatively large gradient strengths used for velocity encoding, VENC-specific spatially varying phase changes could be induced by eddy currents (ECs) during the acquisition. These unwanted phase effects could cause artifactual differences in the estimated phase, increasing or decreasing the calculated flow velocities from the true velocity.¹⁴ Thus, these EC biases were

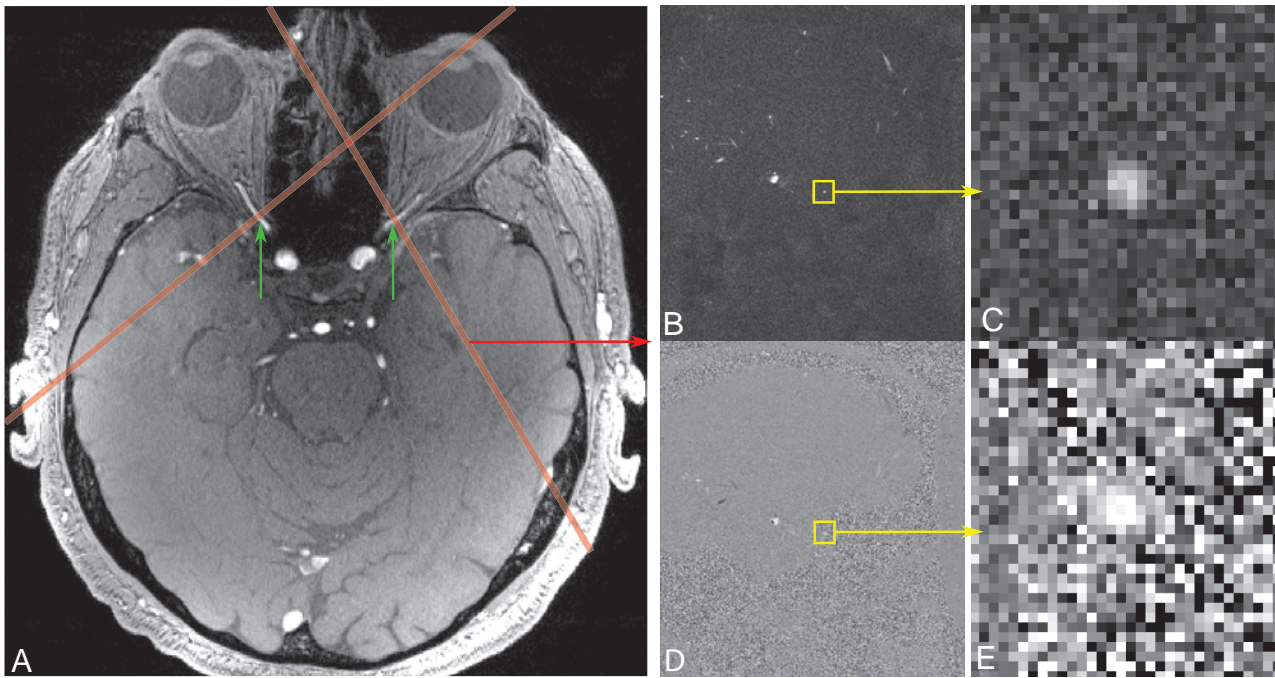


FIG 1. Positioning of PC-MRA slices using the 3D-TOF-MRA data as an anatomic guide. *A*, Red lines depict cross-sections of the triple-oblique positioning and location of PC-MRA slices centered on and perpendicular to each OA (green arrows), identified from the reference 3D-TOF image. The OA cross-section can be visualized in the center of the magnitude (*B* and *C*) and phase (*D* and *E*) images from a PC-MRA scan (yellow box represents an enlarged region from *B* and *D* in *C* and *E*, respectively).

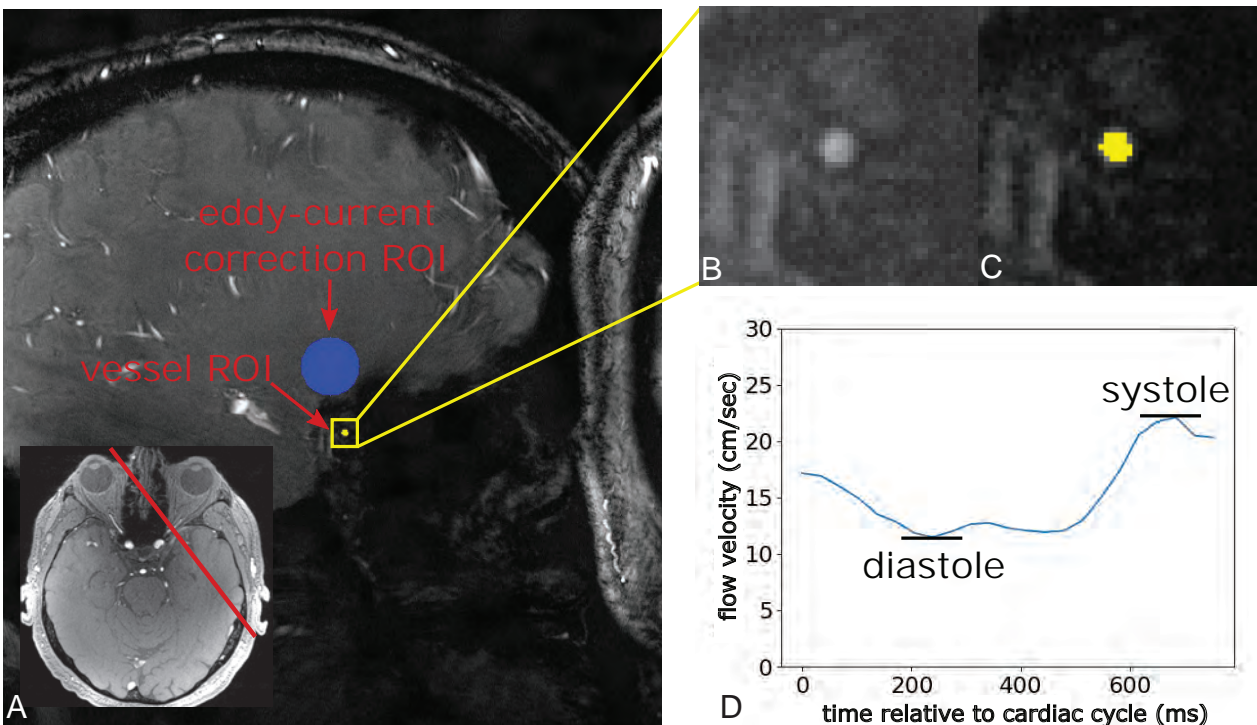


FIG 2. Analysis procedure for correcting EC bias and defining the vessel ROI. *A*, A PC-MRA magnitude image is used to place a 12-mm-diameter ROI for EC correction in vessel-free tissue adjacent to the vessel ROI (blue). The red line in the inset TOF image indicates the PC-MRA slice position. The vessel ROI (yellow) is shown within the yellow box, which depicts the region enlarged in *B* and *C*. Enlarged PC-MRA magnitude images show the vessel cross-section alone (*B*) and with the vessel ROI superimposed (*C*). *D*, Time-series of EC-corrected flow data in units of centimeters/second from 1 example PC-MRA acquisition with a single VENC value in 1 subject.

Summary of vessel diameter and blood flow measures stratified by disease stage^a

	Control (Mean) (SD) (n = 20 OA, 24 ICA)	Early AMD (Mean) (SD) (n = 9 OA, 15 ICA)	Interm. AMD (Mean) (SD) (n = 7 OA, 8 ICA)	Late AMD (Mean) (SD) (n = 12 OA, 17 ICA)	All AMD (Mean) (SD) (n = 28 OA, 40 ICA)
OA diameter (mm)	1.1 (0.19)	0.9 (0.25) P = .11	1.0 (0.26) P = .42	0.8 (0.25) P < .01 ^b	0.9 (0.26) P < .01 ^b
OA volume flow (mL/min)	7.0 (3.0)	6.5 (4.2) P = .74	5.6 (3.1) P = .37	3.8 (1.8) P < .01 ^b	5.1 (3.2) P = .07
OA flow velocity (cm/s) ^c	13.1 (4.0)	16.0 (4.5) P < .01 ^b	11.9 (4.3) P = .91	15.0 (5.7) P = .03 ^b	14.6 (5.1) P = .02 ^b
OA RI	0.70 (0.10)	0.82 (0.10) P < .01 ^b	0.81 (0.06) P < .01 ^b	0.80 (0.07) P < .01 ^b	0.81 (0.08) P < .01 ^b
ICA diameter (mm)	4.3 (0.51)	4.2 (0.52) P = .38	4.6 (0.63) P = .47	4.2 (0.44) P = .55	4.3 (0.52) P = .67
ICA volume flow (mL/min) ^c	163.1 (44.8)	154.3 (44.2) P = .98	167.0 (23.4) P = .49	166.6 (27.7) P = .19	162.2 (33.8) P = .46
ICA flow velocity (cm/s) ^c	18.3 (3.5)	18.7 (3.7) P = .07	17.8 (4.5) P = .58	20.6 (5.2) P < .01 ^b	19.4 (4.6) P < .01 ^b
ICA RI	0.61 (0.09)	0.66 (0.09) P = .18	0.70 (0.04) P < .01 ^b	0.65 (0.11) P = .29	0.67 (0.09) P = .07

Note:—RI indicates resistance index; Interm., intermediate.

^a Values represent group mean and group SD, and reported *P* values indicate significance relative to controls based on a GEE analysis followed by post hoc least significant difference comparisons between disease groups and controls. The sample size for ophthalmic artery measurements was 48 hemisphere measurements from 30 subjects. The sample size for the ICA measurements was 64 hemispheres of 33 subjects.

^b Tests that were significant at the *P* < .05 level (uncorrected).

^c Adjusted for age, which was statistically significant (*P* < .05) in the GEE model.

estimated and corrected on a per-scan basis by placing a 12-mm-diameter circular ROI in tissue devoid of visible vessels adjacent to each vessel ROI (Fig 2), similar to a previously described correction method.¹⁴⁻¹⁶ The average phase within this ROI was subtracted from the phase image before further analysis. The average phase offset in the adjacent tissue ROIs corresponding to the OA was -0.01 radians for patients with AMD and -0.04 radians for controls (*P* > .05), and in the ROIs corresponding to the ICA, it was 0.25 radians for patients with AMD and 0.21 radians for controls (*P* > .05).

Flow Phantom Measurements

A custom-built flow phantom was used to validate PC-MRA measurements and the data-analysis procedure. Briefly, the tubing of the flow phantom was wrapped twice around a spherical agar gel phantom and placed in the receive coil. The flow phantom consisted of a continuous circuit of water driven by a constant-flow-rate pump with a controllable flow rate attached to a flowmeter rated at ±4% accuracy (McMaster-Carr part number 5079k54). The MR imaging acquisition procedure described above was followed. Phantom data were analyzed with and without correction of EC biases. Flow phantom measurements with the phantom set to a flow rate of 20 cm/s, similar to the mean flow rate through the ICAs, indicated that the quantitative accuracy of the flow measurement was improved with the EC correction and was, on average, better than 0.8 cm/s after correction (Online Supplemental Data).

MR Imaging Data Analysis: Morphometry and Flow Quantification

PC-MRA data were analyzed using the data from the lowest VENC available, which either did not result in phase aliasing or were able to be unaliased. Vessel ROIs were defined manually in

a 2-step process using both magnitude-valued intensities and velocity-weighted phase-valued data from each VENC. First, candidate voxels were identified from the magnitude-valued image; then, this grouping of voxels was refined using the dynamic velocity-weighted data to select those candidate voxels exhibiting a clear change in velocity between the systolic and diastolic phases (Fig 2). Portions of voxel-specific time-series with aliased phase data were identified by comparing the sign of the phase value with that in the time-series of a larger VENC, which was manually confirmed to not contain aliased phase data. These aliased portions of phase data were then unwrapped before further analyses.

The area of all voxels in the vessel ROI was calculated and used to convert between linear flow velocity (*U*) and volumetric flow rate (*Q*) according to the formula: $Q = U \times \text{Vessel Area}$. Flow measurements from all voxels within the vessel ROI at each time point were averaged to obtain a mean vessel flow time-series, which was then temporally filtered using a 3-point mean kernel, yielding an effective temporal resolution of approximately 100 ms. These filtered data were used in all further analyses.

OA and ICA flow properties were quantified using four parameters:

- 1) Mean flow rates were calculated across the filtered time-series covering a complete cardiac cycle.
- 2) The maximum systolic velocity (U_{syst}) and volumetric flow (Q_{syst}) and minimum diastolic velocity (U_{dias}) and volumetric flow (Q_{dias}) were obtained from the filtered time-series. The resistance index (RI) was calculated as the ratio of the difference between U_{syst} and U_{dias} to U_{syst} :

$$RI = \frac{U_{\text{syst}} - U_{\text{dias}}}{U_{\text{syst}}}$$

- 3) OA flow rates were normalized to ipsilateral ICA flow rates.

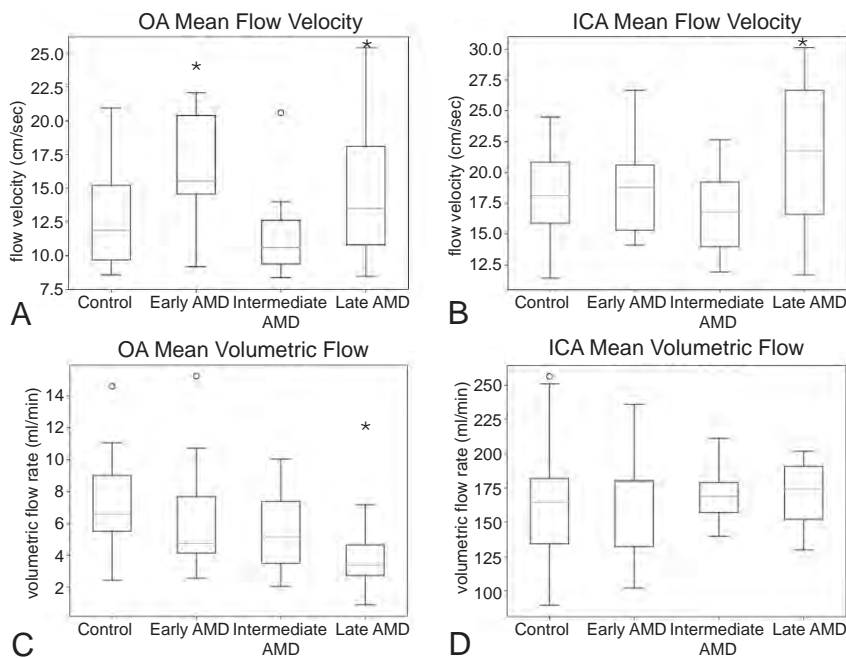


FIG 3. Boxplots of unnormalized flow velocities (A and B) and volumetric flow rates (C and D) in the OAs (A and C) and ICAs (B and D). Vessels were divided into 4 groups: healthy controls, early AMD, intermediate AMD, and late AMD. The asterisk signifies $P < .05$ compared with controls.

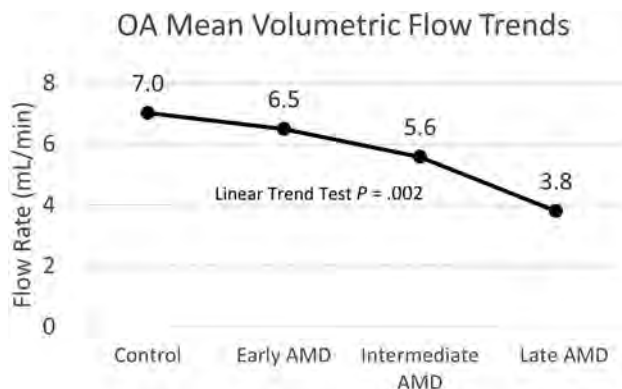


FIG 4. Linear trend test plot, which demonstrates that the rate of decline in OA volumetric flow with disease progression is statistically significant.

4) OA and ICA inner diameters were estimated by assuming that the vessel cross-section is a circular disc, calculating the cross-sectional area of the vessel ROI, and then estimating the diameter of the circle on the basis of this area.

Statistical Analysis

Because measurements from both hemispheres of some patients and controls were included in the statistical analysis, we used the generalized estimating equation (GEE) method with a linear link function to account for correlated data.¹⁷ Patient group means were compared with those of controls with post hoc least significant difference tests. Trends in group means were assessed by assigning an ordinal code from 0 through 3 to the healthy controls, early AMD, intermediate AMD, and late AMD

measurements, respectively, and fitting this code in the GEE model as a covariate. Age was included in the GEE model as well as calculation of post hoc comparisons if statistically significant. The GEE approach also has the advantage of leaving the estimates of the group means unchanged for those variables for which age did not significantly influence the measurements, simplifying interpretation. A P value $< .05$ was considered statistically significant, and P values were not adjusted for multiple comparisons. Reported values are expressed as mean (SD).

RESULTS

Thirty-seven subjects (24 patients with AMD; 14 women and 10 men; mean age, 77.8 [SD, 8.2] years; and 13 controls; 8 women and 5 men; mean age, 69.3 [SD, 7.4] years) were enrolled in the study. Data from 16 patient OAs, 6 patient ICAs, 6 control OAs, and 2 control ICAs were discarded before quantifying flow rates due to subject motion. In addition, data from 1 patient with atrial fibrillation were not usable, and 2 patients had AMD diagnosed in only 1 eye, and for these, only the OA corresponding to the eye with AMD was included in our analyses. In total, data from 28 OAs and 40 ICAs from 21 patients with AMD and 20 OAs and 24 ICAs from 12 healthy similarly-aged controls were included in the analyses. In analyses of OA flow rates normalized to upstream ICA flow rates, only OA-ICA pairs in which data from both vessels were usable were included, resulting in 28 pairs from patients with AMD (9 early AMD, 7 intermediate AMD, and 12 late AMD) and 20 pairs from healthy similarly-aged controls. The late AMD group included both late dry AMD and wet AMD.

Mean flow velocities differed between controls and patients in both the OA and the ICA. Mean volumetric flow rates through the OA were only significantly lower in patients with late AMD relative to controls, while volumetric flow rates through the ICA were similar between groups (Table and Fig 3). Furthermore, there was a statistically significant trend of decreasing volumetric flow rates through the OA as disease severity increased from the early to late stage ($P = .002$, GEE test of trend in means, Fig 4). In 3 subjects with intermediate stage dry AMD in one eye and wet AMD in the other eye, this pattern was maintained; the OA on the side with wet AMD had a volumetric flow rate at least 1.6 mL/min lower than that on the side with intermediate dry AMD. This difference in volumetric flow rates was mainly driven by reduction in the OA diameter in patients with AMD ($P < .05$, Table). The right OA was scanned twice in 1 subject using identical acquisition parameters and analyzed independently; the mean volumetric flow rates agreed within 10%, while the vessel ROI (and hence the diameter) was identical across the two scans. This low discrepancy of 10%

between scans (albeit based on 1 repeat scan in 1 subject) was substantially less than the difference observed between the controls and the patients with AMD overall (27%) and the

late AMD group (46%), suggesting that our measurement precision is sufficient to detect these group-level differences.

The difference in flow rates is further elucidated by normalizing the OA flow to the upstream ICA flow on a per-vessel basis; normalized volumetric OA flow in controls is nearly double that of patients on average ($P < .01$, GEE test of trend in means, Fig 5A). The resistance index was calculated to capture blood flow dynamics over the cardiac cycle and was significantly higher compared with controls in the OA in the overall group of patients with AMD, but only in the patient group with intermediate stage AMD in the ICA ($P < .05$, Table and Fig 6).

DISCUSSION

While previous research has found that flow velocities in the choroïd⁵ and retina¹⁸ do not differ between controls and patients but volumetric flow rates do, our study found both significantly higher flow velocities in the OA and ICA in patients compared with controls, as well as significantly lower volumetric flow in the OA in patients compared with controls. These results suggest that vascular changes may potentially begin upstream of the choroïd. Our data report only an association and cannot establish causality. It is possible that the reduced upstream blood flow may be caused instead by reduced metabolic demand from retinal degradation. Future studies may seek to clarify the causal relation between reduced upstream blood flow and AMD. Our results do, however, suggest a mechanism for the reduced choroïdal perfusion, which is thought to be a contributing factor to the development of late AMD.⁶

To our knowledge, the finding that OA diameters are decreased in patients with AMD has not previously been reported. The underlying cause of this decrease bears further investigation. Our use of PC-MRA images to measure the inner vessel diameters could introduce error because the diameter measurement could be impacted by flow velocities. If flow velocities were lower, the diameter measurement could be underestimated. However, we found a statistically significant trend in which flow velocities increase slightly as vessel diameter decreases, suggesting that our estimates of smaller vessel diameters are not due to this potential bias. In addition, the true spatial resolution of the PC scan could affect the accuracy of our vessel diameter measurements. However, we found that the true spatial resolution is negligibly different from the voxel

size; the expected blurring due to T_2^* decay during each gradient-echo line readout of duration, 5 ms, was $<4\%$.

For our flow measurements, we used a single velocity encoding direction, and care was taken to angle the PC-MRA slice perpendicular to the OA. If, however, a slice were imperfectly positioned, this would result in a biased blood velocity estimate that was lower than the true velocity. For a large obliquity of 25° , this would result in an underestimate of about 10% in absolute velocity.¹⁶ Perhaps if the OA were more curved in patients with AMD, there might be more obliquity leading to an underestimation of

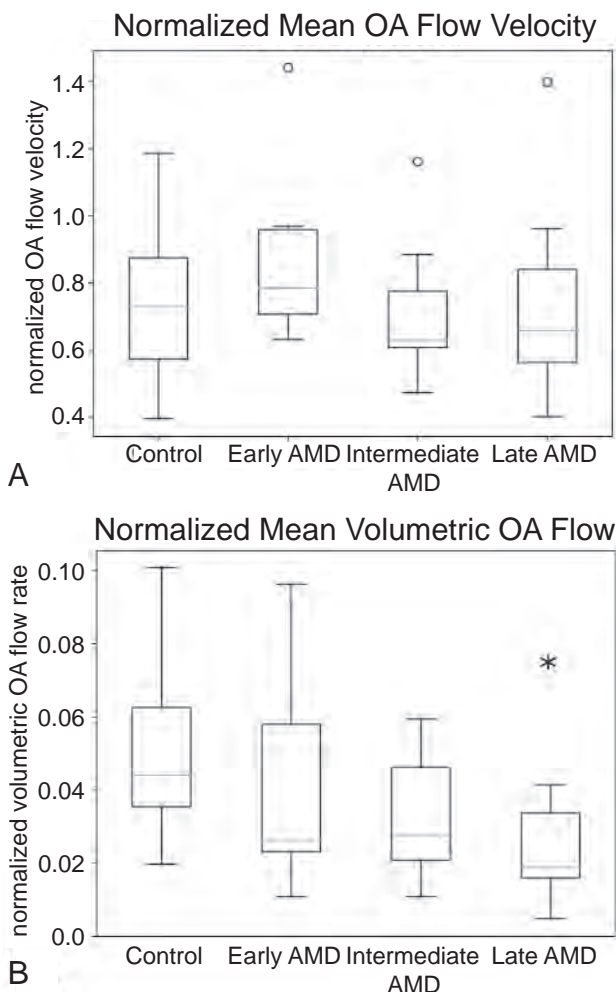


FIG 5. Boxplots of flow velocity (A) and volumetric flow (B) in the OA normalized to upstream ICA flow rates. Normalized flow values represent the OA flow as a ratio of ICA flow. Vessels are divided into 4 groups: healthy controls, early AMD, intermediate AMD, and late AMD. The asterisk signifies $P < .05$ compared with controls.

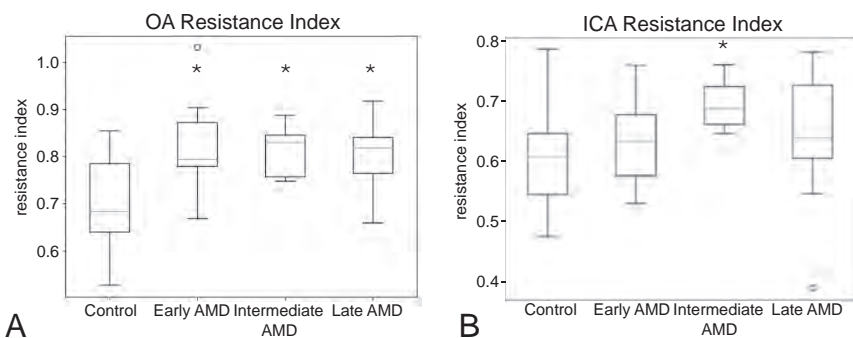


FIG 6. Resistance indices for the OA (A) and ICA (B). Vessels are divided into 4 groups: healthy controls, early AMD, intermediate AMD, and late AMD. The asterisk signifies $P < .05$ compared with controls.

flow velocity in these patients, but we found the opposite: Flow velocity was found to be higher in patients with AMD. In addition, any systematic obliquity in patients with AMD would have led to an increase in the OA diameter in these patients, but we found decreased OA diameters. Nevertheless, it seems most likely that any obliquity, if it is present, is small and is unlikely to be systematically different between groups. Therefore, this effect likely contributes to the variance across subjects but not to bias across groups.

Further limitations of this study include the overall small sample size and the younger average age of the control population. AMD is a complex genetic disease associated with a wide range of systemic comorbidities such as cardiovascular disease, hypertension, obesity, and nutritional deficiencies. While larger future studies are needed to investigate the effects of these comorbidities on OA and ICA blood flow, this limitation does not diminish the importance of our imaging strategy and findings of abnormalities in blood flow. Additionally, our data are in close agreement with flow measures through the OA reported recently in healthy elderly subjects ($n = 84$ eyes) based on lower-resolution data at 3T;¹⁵ this previous study reported similar flow velocities and volumetric flow rates and a resistance index of 0.68 (SD, 0.08) compared with our value of 0.70 (SD, 0.10) in similarly-aged control subjects.

While quantifying flow through the OA was the primary goal of this study, flow through the ICA was also investigated to differentiate OA flow changes from any systemic flow alterations. The increase in the resistance index in both the ICA and OA combined with the decreased OA volumetric flow as a percentage of ICA volumetric flow suggests that there may be both systemic and local vascular changes associated with AMD. These metrics could not be evaluated using only a vessel-diameter measurement; dynamic flow measurements were necessary to detect these differences between patients with AMD and controls.

CONCLUSIONS

Our findings of structural and flow differences in the vasculature of patients with AMD compared with healthy controls indicate that changes in vasculature upstream of the eye are associated with AMD. If, motivated by our finding, future studies can establish a causal link between these upstream changes and AMD, it may raise the possibility of treatment strategies targeting the OA to restore blood flow to the retina in patients with AMD.

ACKNOWLEDGMENTS

The authors would like to thank Dr Bastien Guérin for providing the flow phantom used to validate the PC-MRA measurements, Siemens for providing WIP 452B, and Dr Himanshu Bhat for technical assistance with the quantitative PC-MRA pulse sequence.

Disclosures: Matthew L. Hibert—RELATED: Grant: OcuDyne Inc.* Yinchong Iris Chen—RELATED: Grant: OcuDyne, Comments: study sponsor.* Nadia K. Waheed—RELATED: Grant: OcuDyne, Comments: My institution was a clinical trial site for the study and, as such, received reimbursement for services provided to subjects in the process of screening for eligibility*. UNRELATED: Employment: Gyroscope Therapeutics,

Comments: employee at Gyroscope, a clinical stage gene therapy company; Stock/Stock Options: OcuDyne. Jeffrey S. Heier—UNRELATED: Board Membership: Ocular Therapeutix, Comments: member of the Board of Directors; Consultancy: 4D Molecular Therapeutics, Adverum Biotechnologies, Aerie, Aerpio Pharmaceuticals, Aldeyra Therapeutics, Allegro, Alzheon, Annxon Biosciences, Apellis Biosciences, Aprea, AsclepiX Therapeutics, Aviceda Therapeutics, Bionic Vision Technologies, Dark Horse, DTx Pharma, Eloxx Pharmaceuticals, Galimedix Therapeutics, Genentech, Graybug Vision, Gyroscope, Iveric Bio, jCyte, Chengdu Kanghong Pharmaceutical Group, LensGen, NM Novartis, Ocular Therapeutix, OcuTerra, Oxurion, Palatetechnologies, Regeneron Pharmaceuticals, Regenxbio, Stealth, Thea, Verseon, Vinci, Voyant, Comments: I serve as scientific consultant for these companies; Grants/Grants Pending: Apellis Pharmaceuticals, AsclepiX, Bayer, Genentech, Gyroscope, Hamera, Iveric, Chengdu Kanghong Pharmaceutical Group, Kodiak Sciences, Notal Vision, Novartis, Regeneron, Regenxbio, Stealth, Comments: I serve as Principal Investigator for clinical trials with these sponsors*; Stock/Stock Options: Adverum, Aldeyra, Allegro, Aviceda, Digital Surgery Solution, DTx Pharma, jCyte, Ocular Therapeutix, Vinci, Comments: stock or stock options for scientific consulting services. Michael W. Calhoun—UNRELATED: Employment: OcuDyne Inc, Comments: I currently serve as Vice President of Research for OcuDyne Inc. Philip R. Rosenfeld—UNRELATED: Consultancy: OcuDyne, Comments: consulting relationship with OcuDyne; Stock/Stock Options: OcuDyne, Comments: stock options that have not been exercised. Jonathan R. Polimeni—RELATED: Grant: OcuDyne, Comments: grant contract managed by Massachusetts General Hospital (as indicated in the article)*; Payment for Writing or Reviewing the Manuscript: OcuDyne, Comments: payment for finalizing manuscript after the end of the grant period. William J. Feuer—RELATED: Personal Fees: OcuDyne, Comments: fee for statistical consulting/analysis. *Money paid to the institution.

REFERENCES

- Ling Wong W, Su X, Li X, et al. **Global prevalence of age-related macular degeneration and disease burden projection for 2020 and 2040: a systematic review and meta-analysis.** *Lancet Glob Heal* 2014;2:e106–16 CrossRef Medline
- Ratnapriya R, Chew EY. **Age-related macular degeneration-clinical review and genetics update.** *Clin Genet* 2013;84:160–16 CrossRef Medline
- Ferris FL, Wilkinson CP, Bird A, et al. **Clinical classification of age-related macular degeneration.** *Ophthalmology* 2013;120:844–51 CrossRef Medline
- Dry vs Wet Age-Related Macular Degeneration.** AMDF. <https://www.macular.org/dry-vs-wet-macular-degeneration>. Accessed November 2, 2019
- Boltz A, Luksch A, Wimpissinger B, et al. **Choroidal blood flow and progression of age-related macular degeneration in the fellow eye in patients with unilateral choroidal neovascularization.** *Invest Ophthalmol Vis Sci* 2010;51:4220–25 CrossRef Medline
- Metelitsina TI, Grunwald JE, DuPont JC, et al. **Foveolar choroidal circulation and choroidal neovascularization in age-related macular degeneration.** *Invest Ophthalmol Vis Sci* 2008;49:358–63 CrossRef Medline
- Dai W, O'Loughlin L, Yu G, et al. **Arterial spin labeling measured choroidal blood flow is reduced in age-related macular degeneration and correlates with severity level.** *Proc Intl Soc Mag Reson Med* 2016;24:1416
- Grunwald JE, Metelitsina TI, DuPont JC, et al. **Reduced foveolar choroidal blood flow in eyes with increasing AMD severity.** *Invest Ophthalmol Vis Sci* 2005;46:1033–38 CrossRef Medline
- Chaine G, Hullo A, Sahel J, et al. **Case-control study of the risk factors for age related macular degeneration.** *Br J Ophthalmol* 1998;82:996–1002 CrossRef Medline
- Stamm AC, Wright CL, Knopp M, V, et al. **Phase contrast and time-of-flight magnetic resonance angiography of the intracerebral arteries at 1.5, 3 and 7 T.** *Magn Reson Imaging* 2013;31:545–49 CrossRef Medline
- Kang CK, Park CA, Lee DS, et al. **Velocity measurement of microvessels using phase-contrast magnetic resonance angiography at 7 Tesla MRI.** *Magn Reson Med* 2016;75:1640–46 CrossRef Medline
- Keil B, Triantafyllou C, Hamm M, et al. **Design optimization of a 32-channel head coil at 7T.** In: *Proceedings of the International Society of Magnetic Resonance in Medicine*, Stockholm, Sweden. May 1–7, 2010

13. Hayreh SS, Dass R. **The ophthalmic artery, I: origin and intra-cranial and intra-canalicular course.** *Br J Ophthalmol* 1962;46:65–98 CrossRef Medline
14. Pelc NJ, Sommer FG, Li KC, et al. **Quantitative magnetic resonance flow imaging.** *Magn Reson Q* 1994;10:125–17 Medline
15. Ambarki K, Hallberg P, Jóhannesson G, et al. **Blood flow of ophthalmic artery in healthy individuals determined by phase-contrast magnetic resonance imaging.** *Invest Ophthalmol Vis Sci* 2013;54:2738–45 CrossRef Medline
16. Bernstein MA, King KF, Zhou XJ. *Handbook of MRI Pulse Sequences.* Academic Press; 2004
17. Ying G-S, Maguire MG, Glynn R, et al. **Tutorial on biostatistics: linear regression analysis of continuous correlated eye data.** *Ophthalmic Epidemiol* 2017;24:130–40 CrossRef Medline
18. Ciulla TA, Harris A, Chung HS, et al. **Color Doppler imaging discloses reduced ocular blood flow velocities in nonexudative age-related macular degeneration.** *Am J Ophthalmol* 1999;128:75–80 CrossRef Medline

Time Course and Clinical Correlates of Retinal Diffusion Restrictions in Acute Central Retinal Artery Occlusion

L.A. Danyel, M. Miszczuk, F. Connolly, K. Villringer, G. Bohner, M. Rossel-Zemkougou, and E. Siebert



ABSTRACT

BACKGROUND AND PURPOSE: Retinal diffusion restrictions were recently identified as a regular finding in acute central retinal artery occlusion. We sought to investigate the influence of technical MR imaging and clinical parameters on the detection rate of retinal diffusion restrictions on standard brain DWI.

MATERIALS AND METHODS: In this retrospective cohort study, MR imaging scans of patients with central retinal artery occlusion were assessed by 2 readers for retinal diffusion restrictions on DWI performed within 2 weeks after vision loss. The influence of clinical and technical MR imaging parameters and the time interval between symptom onset and DWI on the presence of retinal diffusion restrictions were evaluated.

RESULTS: One hundred twenty-seven patients (mean age, 69.6 [SD 13.9] years; 59 women) and 131 DWI scans were included. Overall, the MR imaging sensitivity of retinal diffusion restrictions in acute central retinal artery occlusion was 62.6%–67.2%. Interrater and intrarater agreement for retinal diffusion restrictions was “substantial” with $\kappa_{\text{inter}} = 0.70$ (95% CI, 0.57–0.83) and $\kappa_{\text{intra}} = 0.75$ (95% CI, 0.63–0.88). Detection of retinal diffusion restrictions did not differ with differences in field strengths (1.5 versus 3T, $P = .35$) or sequence type ($P = .22$). Retinal diffusion restrictions were consistently identified within the first week with a peak sensitivity of 79% in DWI performed within 24 hours after symptom onset. Sensitivity of retinal diffusion restrictions declined in the second week (10.0%, $P < .001$). Absence of retinal diffusion restrictions was more prevalent in patients without fundoscopic retinal edema (60% versus 27.1%, $P = .004$) and with restitution of visual acuity at discharge (75% versus 28.4%, $P = .006$).

CONCLUSIONS: Retinal diffusion restrictions in acute central retinal artery occlusion can be reliably identified on DWI performed within 24 hours and 1 week after onset of visual impairment. Detectability of retinal diffusion restrictions is dependent on the clinical course of the disease.

ABBREVIATIONS: CRAO = central retinal artery occlusion; logMAR = Logarithm of the Minimum Angle of Resolution; RDR = retinal diffusion restrictions; VA = visual acuity

Sudden and painless monocular visual impairment is the characteristic clinical feature of nonarteritic acute central retinal artery occlusion (CRAO), which is mainly caused by proximal embolism originating from the heart or atherosclerotic lesions of the aortic arch and carotid arteries.¹ Patients with CRAO develop persistent and debilitating central scotoma if the blood supply to

the eye is not re-established in time. While there is disagreement on the choice of treatment to achieve retinal reperfusion,² there is consensus to treat as early as possible because the chance for visual improvement dwindles with the duration of retinal ischemia.³

Because macular edema or alteration of retinal arteries may not always be apparent at the first fundoscopic evaluation,⁴ supplementary diagnostics such as fluorescein angiography and optical coherence tomography are necessary.^{5,6} Patients with CRAO have an elevated risk of consecutive stroke, which underlines the importance of timely and accurate diagnosis.^{7,8} One-quarter of patients with acute CRAO show concurrent cerebral infarction on DWI.^{9–11}

We recently identified retinal diffusion restrictions (RDR) as a frequent finding in patients with CRAO on standard 1.5T and 3T brain stroke DWI,¹² which contribute to diagnosis of retinal ischemia. While these RDR were accurate in discerning patients with CRAO from those with ischemic stroke and transient ischemic

Received October 27, 2020; accepted after revision April 4, 2021.

From the Department of Neurology (L.A.D., F.C.), Institute for Neuroradiology (M.M., G.B., E.S.), Center for Stroke Research Berlin (K.V.), and Department of Ophthalmology (M.R.-Z.), Charité-Universitätsmedizin, Berlin, Germany.

L.A. Danyel is participant in the BIH-Charité Clinician Scientist Program funded by the Charité-Universitätsmedizin Berlin and the Berlin Institute of Health.

Please address correspondence to Leon Alexander Danyel, MD, Department of Neurology, Charité, Universitätsmedizin Berlin, Germany, Augustenburger Platz 1, 13353 Berlin, Germany; e-mail: leon.danyel@charite.de

Indicates article with online supplemental data.

<http://dx.doi.org/10.3174/ajnr.A7201>

attack, sensitivity for RDR in CRAO was only moderate (up to 0.75).¹² To the best of our knowledge, apart from incidental descriptions in case reports or small case series,¹³⁻¹⁵ no further studies of RDR in CRAO exist as of today. Because available literature is scarce, no information exists on how clinical and ophthalmologic features of CRAO or technical MR imaging parameters contribute to the detection rate of RDR in retinal ischemia. Moreover, the time course of RDR in CRAO is unknown. Therefore, we performed a large retrospective cohort study to further investigate these questions.

MATERIALS AND METHODS

Patients

All consecutive patients with CRAO treated in our institution between January 2010 and December 2019 with available brain MR imaging including diffusion-weighted imaging performed within 2 weeks after clinical onset were included into this single-center retrospective cohort study. Potential candidates were identified through a medical data base inquiry based on the respective codes of the International Classification of Diseases (H34.0-H34.2; H34.8; and H34.9) and the German Operation and Procedure Classification System (3-800 and 3-820).

Patients were included in the study if they met the CRAO diagnostic criteria of sudden, painless, and persistent monocular vision loss accompanied by characteristic fundoscopic features, including retinal opacity, a cherry-red spot, the presence of emboli, attenuation of arteries, and/or optic disc pallor/edema. Patients missing typical ophthalmoscopic findings of CRAO were included if the diagnosis could be based on optical coherence tomography and/or fluorescein angiography. Patients with sole retinal branch occlusion and amaurosis fugax were not included in this study. Furthermore, we did not include patients with a possible diagnosis of giant cell arteritis according to the American College of Rheumatology 1990 criteria.

We systematically recorded relevant patient data, including visual acuities (VA), fundoscopic features, medical histories (including hypertension, hypercholesterolemia, diabetes mellitus, atrial fibrillation, and smoking habits), laboratory findings (including glycated hemoglobin and lipid profiles), evidence of VA restoration at discharge, and intravenous thrombolytic therapy if received. Patients were eligible for rtPA treatment until 4.5 hours after symptom onset. Contraindications for intravenous thrombolysis with rtPA were congruent with those established for the treatment of acute ischemic stroke.¹⁶ Categorization of visual impairment at initial presentation was adapted from the World Health Organization International Statistical Classification of Diseases and Related Health Problems (10th revision, 2016):

Category 0: mild or no visual impairment: $VA \geq 0.3$ (≤ 0.52 Logarithm of the Minimum Angle of Resolution [logMAR]).

Category 1: moderate visual impairment: $VA < 0.3/\geq 0.1$ ($>0.52/\leq 1.0$ logMAR).

Category 2: severe visual impairment: $VA < 0.1/\geq 0.05$ ($>1.0/\leq 1.3$ logMAR).

Category 3: blindness: $VA < 0.05$ (>1.3 logMAR).

DWI Analysis

MR imaging was performed as part of the routine clinical work-up of patients with CRAO to identify concurrent ischemic stroke

on two 1.5T scanners (Magnetom Aera; Siemens) each with 20-channel head coils and a 3T scanner (Magnetom Skyra; Siemens) with a 20-channel head coil. The DTI sequence used for DWI calculation was acquired on a 3T scanner (Magnetom Trio; Siemens) with a 32-channel head coil. TRACE DWI ($b = 1000$ s/mm²) images from EPI-DWI sequences or calculated from EPI-DTI sequences were evaluated. Section thicknesses were 2.5 mm (DTI), and 3, 5, and 7 mm (DWI). Further sequence details are given in the Online Supplemental Data. DWI was evaluated for RDR by a board-certified neuroradiologist (reader 1, with >15 years of experience in MR stroke imaging), and a radiology resident-in-training for neuroradiology (reader 2, with 2 years of neuroradiologic experience) who were blinded to the CRAO side and clinical data. DWI was considered positive for RDR if a clearly discernable abnormal signal increase was present in the inner wall of the affected globe on at least 2 adjacent slices compared with the contralateral eye. In cases of RDR, reader 1 additionally evaluated the presence of visually correlating low signal on the ADC map as well as concurrent restricted diffusion of the optic nerve. Furthermore, reader 1 performed a second complete DWI review for the presence of RDR 12 months after the first evaluation. The time span between symptom onset and DWI was recorded and categorized into 5 subgroups: ≤ 24 hours, $>24-72$ hours, >72 hours to 7 days, $>7-14$ days, and "unclear" in cases in which definite classification was not possible.

Statistical Analysis

SPSS Statistics for Windows, software (Version 25.0; IBM) was used for statistical analysis. Interrater and intrarater agreement were analyzed using Cohen's kappa statistics. For this purpose, the observed percentage of agreement Pr(a) and expected Pr(e) were used to calculate the unweighted κ using the formula:

$$\kappa = \frac{\text{Pr}(a) - \text{Pr}(e)}{[1 - \text{Pr}(e)]}$$

The interpretation of agreement for κ was categorized as poor ($\kappa < 0.00$), slight ($0.00 \leq \kappa \leq 0.20$), fair ($0.21 \leq \kappa \leq 0.40$), moderate ($0.41 \leq \kappa \leq 0.60$), substantial ($0.61 \leq \kappa \leq 0.80$), or almost perfect ($0.81 \leq \kappa \leq 1.00$), respectively.

We evaluated the impact of different clinical and technical MR imaging parameters for the presence/absence of RDR in CRAO using χ^2 statistics and Bonferroni post hoc analysis if applicable. A P value $< .05$ was considered statistically significant. Descriptive statistics are presented as mean (SD). The aforementioned clinical parameters included the following: visual acuity at presentation, fundoscopic presence of retinal edema, time span between symptom onset and DWI, thrombolytic therapy, and evidence of VA restitution at discharge. Technical MR imaging parameters included electromagnetic field strength and image section thickness.

Study approval was obtained from the local ethics committee (Charité, Universitätsmedizin Berlin, EA1/177/19).

RESULTS

Of 355 candidates identified through our medical data base inquiry, 131 patients matched CRAO diagnostic criteria and had diffusion-weighted imaging performed within 2 weeks after

clinical onset. In 4 subjects, artifacts rendered the assessment of the retina on DWI impossible. Consequently, 127 patients (mean age, 69.6 [SD, 13.9] years; 59 women) were included in this study. Table 1 details clinical, fundoscopic, and radiologic characteristics of patients with CRAO.

Prevalence of Retinal Diffusion Restrictions

In total, 131 MR images were analyzed (in 127 patients). RDR was present in 88 (reader 1, 67.2%) and 82 (reader 2, 62.6%) of

Table 1: Clinical, fundoscopic, and radiologic characteristics of patients with CRAO

Patient Characteristics	No. (N = 127)	%
Medical history		
Hypertension	94	74.0%
Dyslipidemia	87	68.5%
Diabetes mellitus type 2	34	26.8%
Smoking	34	26.8%
rtPA treatment	22	17.3%
Atrial fibrillation	13	10.2%
Fundoscopic findings		
Retinal opacity/CRS	107	84.3%
Attenuated arteries	77	60.6%
Optic disc pallor/edema	53	41.7%
Visible emboli	34	26.8%
Radiologic features		
ON restricted diffusion	17	13.0%
Acute brain infarction	36	28.4%
Carotid artery stenosis	34 (125)	26.8%
Carotid artery occlusion	3 (125)	2.4%

Note:—CRS indicates cherry-red spot; ON, optic nerve.

131 scans, respectively, with 57 cases (reader 2, 64.8%) showing visually correlating low signal on the ADC map. Both interrater and intrarater agreement for RDR were “substantial” with unweighted $\kappa_{\text{inter}} = 0.70$ (95% CI, 0.57–0.83) and $\kappa_{\text{intra}} = 0.75$ (95% CI, 0.63–0.88). Concurrent restricted diffusion of the optic nerve was noted in 17 cases (reader 1, 13.0%). Figures 1 and 2 illustrate characteristic examples of RDR on 1.5T and 3T DWI.

The overall side of distribution of CRAO was balanced with 64 (50.4%) left- and 63 (49.6%) right-sided occlusions. In 1 (reader 1, 0.8%) and 2 cases (reader 2, 1.5%), RDR were falsely attributed to the healthy eye (DWI restriction rated as “absent” for the affected eye).

Association between Retinal Diffusion Restrictions and Clinical Features

Visual acuity on initial presentation was <0.05 (>1.3 logMAR, legal blindness) for most patients (104, 81.9%). Visual impairment of the remaining patients was severe in 10 (7.9%), moderate in 9 (7.1%), and mild in 4 cases (3.2%). There were no statistically relevant differences in the frequency of RDR among the visual impairment groups ($P = .07$), though RDR were more frequent in patients with VA <0.05 (“blindness”: 75/104 or 72.1%; compared with severe visual impairment: 4/10 or 40%; moderate visual impairment: 5/9 or 55.6%; and mild visual impairment: 2/4 or 50%). Most interesting, the absence of RDR was significantly more frequent in patients with complete restitution of visual acuity at discharge (6/8 or 75%) compared with patients without reported remission (33/116 or 28.4%, $P = .006$).

Fundoscopic findings are detailed in Table 1. Patients showing neither retinal opacity nor a cherry-red spot during ophthalmoscopic evaluation were significantly more likely to show no RDR (12/20 or 60%) compared with patients with visible retinal opacity and/or cherry-red spot (29/107 or 27.1%, $P = .004$). No statistical relationship was observed between the presence of attenuated arteries, optic disc pallor/edema, or visible emboli and the presence of RDR on DWI, respectively (data not shown).

Intravenous rtPA was administered in a total of 22 patients with CRAO (17.32%). χ^2 testing, however, revealed no differences in the presence of RDR between rtPA-treated and untreated patients with CRAO ($P = .58$). Likewise, the frequency of RDR did not differ between patients with and without acute cerebral ischemia on DWI (26/36 or 72.2% versus 59/91 or 64.8%, $P = .43$).

Impact of MR Imaging Parameters on the Detection of Retinal Diffusion Restrictions

Table 2 details the distribution of RDR according to technical MR imaging parameters. MR imaging sensitivity for

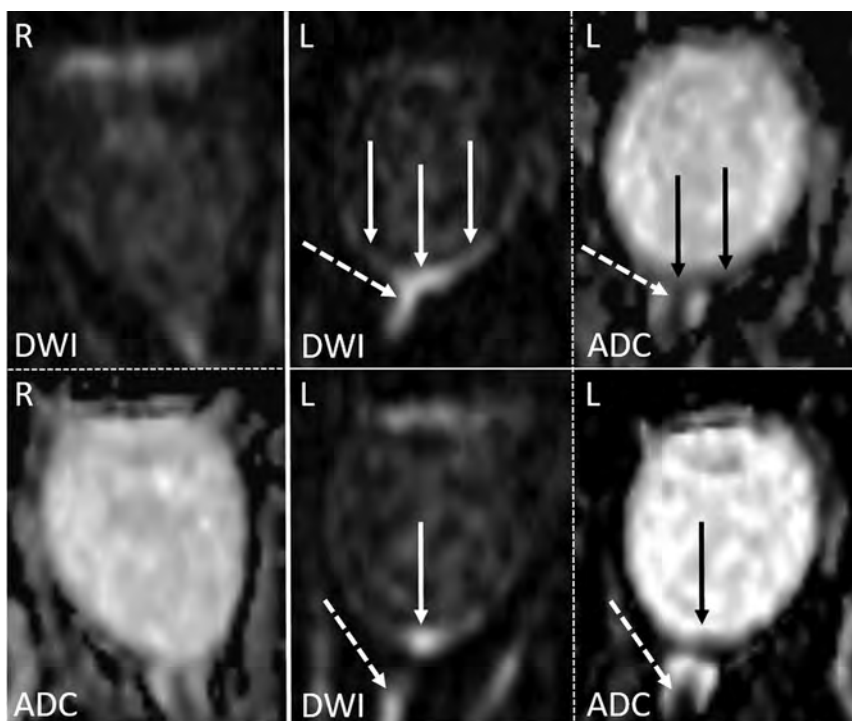


FIG 1. An example of RDR on 1.5T DWI in acute left-sided CRAO (solid arrows) visible on 2 adjacent slices, as well as diffusion restriction of the anterior optic nerve (dotted arrows), all with qualitative ADC reduction. The normal right eye is shown for comparison.

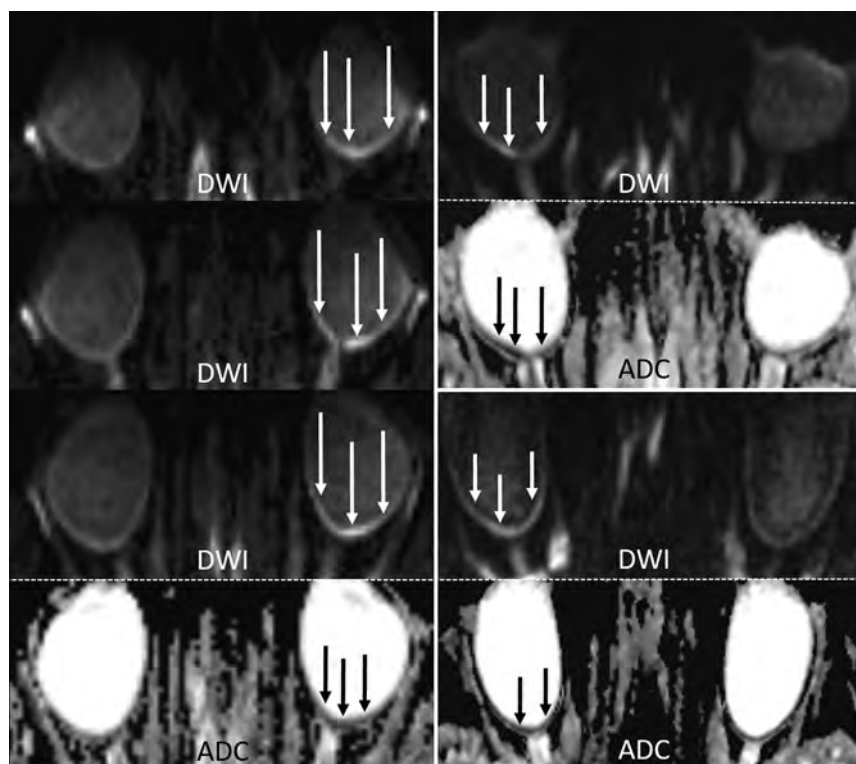


FIG 2. Examples of RDR on 3T diffusion-weighted MR imaging in acute CRAO (DWI, $b=1000s/mm^2$, and ADC images). *Left column:* In this patient with left-sided CRAO, clear RDR with subtle retinal thickening is shown (white arrows), more pronounced temporally, on 3 consecutive slices (TRACE DWI calculated from the DTI-EPI sequence) and with corresponding qualitative ADC reduction (black arrows). *Right column:* Two cases of right-sided CRAO are shown with RDR (DWI hypersignal and corresponding visually qualitative ADC reduction). While the upper case is more temporally pronounced, the lower case is more uniformly affecting both the temporal and nasal parts of the retina.

Table 2: Distribution of retinal DWI restrictions according to MR imaging parameters

MR Imaging Parameter	Scans ($n = 131$)	RDR	P Value
Field strength			
1.5T	52 (39.69%)	31/52 (59.6%)	.14
3T	79 (60.31%)	57/79 (72.2%)	
Sequence/section thickness			
Calc. DWI-TRACE 2.5 mm	60 (45.80%)	44/60 (73.3%)	.22
DWI-EPI TRACE (3 mm)	68 (51.91%)	43/68 (63.2%)	
DWI-EPI TRACE (5 mm)	1 (0.73%)	0/1	
DWI-EPI TRACE (7 mm)	2 (1.53%)	1/2 (50%)	

Note:—Calc. indicates calculated.

CRAO detection did not differ significantly regarding differences in field strengths (1.5T versus 3T, $P = .14$) or sequence types used (3-mm DWI-EPI TRACE versus 2.5-mm calculated DWI-TRACE from DTI-EPI; $P = .22$). Five- and 7-mm DWI-EPI TRACE was not included in the analysis because of the low absolute number of scans performed ($n = 3$).

Time Course of Retinal DWI Restrictions

Time intervals between clinical onset of visual impairment and DWI were as follows: ≤ 24 hours in 28 (21.4%), >24 –72 hours in 63 (48.1%), >72 hours to 7 days in 23 (17.6%), and >7 –14 days in 10 (7.6%) cases. For 7 scans (5.3%), an unambiguous assignment to a time group was not possible. Overall detection rates of

RDR were comparable for both readers among time interval groups up to 1 week between clinical onset and DWI. A multiple-comparison χ^2 test with post hoc Bonferroni correction identified RDR to be significantly less frequent in DWI performed 1 week after onset of vision loss (>7 –14 days, 1/10 or 10.0%; reader 1: $P < .001$, reader 2: $P = .005$). Notably, sensitivity for RDR was the highest in DWI performed within 24 hours after CRAO onset (0.79, reader 1), though this difference did not reach statistical relevance. Figure 3 details the distribution and sensitivity of DWI stratified into predefined time intervals between the onset of visual impairment and MR imaging.

DISCUSSION

Since our first description of RDR on standard stroke DWI, it remained unclear to what extent clinical features and technical MR imaging parameters contributed to the limited sensitivity (0.7–0.75) observed in our small retrospective cohort of 20 patients with CRAO,⁹ especially, because further scientific literature on RDR in CRAO up until now has been limited to incidental reports.^{10–12}

In this study, we retrospectively investigated 127 patients, which, as of today, constitute the largest cohort of retinal DWI in CRAO. Although we found slightly lower overall sensitivity (reader 1: 0.67, reader 2: 0.63) for RDR in CRAO than previously reported,¹² sensitivity increased up to 0.79 (reader 1) in DWI performed within 24 hours after onset of vision loss.

It is conceivable that the presence of RDR in CRAO, similar to cerebral ischemia, indicates cytotoxic edema developing on disruption of cellular ion homeostasis through failure of adenosine triphosphate-dependent membrane pumps with consecutive intracellular shifts of water.^{17,18} We found a direct association of RDR and retinal edema because patients with fundoscopic absence of retinal edema (identified through retinal opacity and/or cherry-red spot) on admission were more likely to lack RDR on DWI.

We observed a tendency of RDR to be more frequent in patients with severe visual impairment, though differences did not reach statistical relevance. This seems conceivable because the severity of visual impairment does not necessarily depend on the extent of retinal ischemia alone but on whether the foveal region is affected or spared, eg, in a patent cilioretinal artery. A

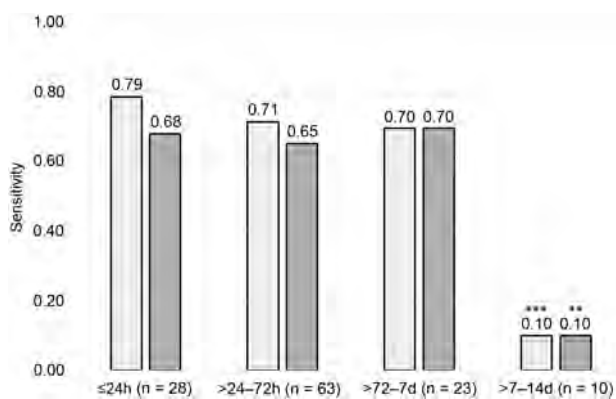


FIG 3. Distribution of DWI and sensitivity of retinal diffusion restrictions in patients with central retinal artery occlusion according to the onset-to-MR imaging time intervals (reader 1: white columns; reader 2: gray columns). Double asterisks indicate $P < .01$; triple asterisks, $P < .001$.

focal macular ischemia may, therefore, lead to extensive visual impairment, while the total area of retinal ischemia remains small, which, in turn, may affect the visibility of RDR in CRAO. Most interesting, the absence of RDR was more frequent in patients with complete restitution of VA on discharge, linking RDR to clinical severity in CRAO.

Our study is the first to investigate the time-dependency of RDR in CRAO, which we identified in most patients with CRAO with DWI performed within 24 hours up to 1 week after the onset of vision loss. On the contrary, our data suggest that the sensitivity of RDR declines 1 week after the onset of CRAO. Thus, diffusion restrictions in CRAO seem to occur early and do not show a delay as observed in small brain stem and cerebellar infarctions.¹⁹⁻²¹ Most interesting, 3 patients had DWI performed within the hyperacute phase of CRAO (1 hour, 2 hours, and within 2–5 hours after the onset of visual impairment), 2 of whom already showed RDR. This finding indicates that by principle, RDR may be identified in patients with CRAO presenting within the suggested time window for thrombolytic therapy.²² The cross-sectional design of our analysis necessitates further research on the time-dependency of RDR, eg, within the scope of a longitudinal investigation.

A substantial proportion of our cohort of patients with CRAO had concurrent cerebral infarction on DWI (28%), irrespective of RDR. This observation is in accordance with previous studies, which found acute ischemic stroke in 19%–28% of patients and indicates the causative role of proximal embolism in nonarteritic CRAO.^{9-11,23}

This study is limited by its retrospective design and the absence of a control cohort, which increase the risk of observer bias for our diagnostic accuracy assessment of RDR. However, in our previous study, we investigated standard test quality criteria and interrater agreement for RDR using a control cohort of patients with stroke and 2 blinded readers.¹² Assessment of RDR by standard DWI was possible with high specificity (0.80–1.00) and negative predictive value (0.76–0.80), with only very few cases of DWI changes falsely attributed to controls or the wrong eye of patients with CRAO. The overall sensitivity and interrater

reliability for RDR in CRAO reported here are in accordance with the results from our previous study. Additionally, we did not perform ADC value measurements due to technical limitations, foremost the subvoxel dimension of the retinal thickness (between 200–400 μm), which results in considerable partial volume averaging effects, which we specified previously.¹² As a consequence, the magnitude of diffusion restriction (ADC reduction) secondary to cytotoxic edema on one hand and a potential T2 shinnethrough component (ADC elevation) secondary to vasogenic edema cannot be determined precisely with our methodology. However, we performed a visual qualitative evaluation of the ADC maps and were able to confirm true diffusion restriction in a substantial proportion (64.8%) of cases with positive findings on DWI by corresponding low signal.

Our data did not allow a reliable assessment of visual outcome through visual acuity and/or perimetric visual field testing because ophthalmologic follow-up examinations were not reliably documented in our data base. However, cases of complete restitution of visual acuity at the time of discharge from the hospital were specified in our medical documentation and, hence, used for analysis.

All patients underwent routine brain MR imaging not optimized for the visualization of the retina and surrounding structures. Furthermore, DWI was acquired using different scanners, receive coils, and sequences. We acknowledge that the heterogeneous technical realization of image acquisition is a limitation of our study. Yet, it documents that RDR in CRAO are visible in a variety of routine MR imaging setups. Future investigations should focus on the technical improvement of MR imaging protocols in CRAO. In this regard, more recent developments in DWI sequence techniques such as readout-segmented DWI, small-FOV DWI, and fast spin-echo radial acquisition DWI sequences have already been proved valuable for imaging of various orbital and skull base pathologies, including intraocular masses, optic neuritis, and cholesteatoma.²⁴⁻²⁶ By achieving either higher signal-to-noise ratios or reduced distortion, movement, and susceptibility artifacts, these techniques may improve the diagnostic potential of MR imaging for acute CRAO compared with conventional EPI sequences by better exploiting and visualizing the rather small amount of signal provided by the delicate retinal cell layers.

A number of case reports have described the occurrence of RDR in other retinal pathologies, such as retinal necrosis in herpes simplex virus type 1 infection,¹³ subretinal abscess,²⁷ and ophthalmic vein thrombosis due to cavernous sinus thrombophlebitis.²⁸ Hence, further studies are warranted to investigate the specificity of RDR to identify CRAO in patients presenting with sudden, painless, monocular visual impairment.

CONCLUSIONS

Our retrospective analysis of 127 patients confirms RDR as a regular finding in acute CRAO and, for the first time, reveals the time course of RDR with good detectability in DWI performed within 24 hours up to 1 week after onset of visual impairment. Visibility of RDR on DWI may indicate irreversible retinal

damage due to cytotoxic edema and is dependent on the clinical course of the disease.

REFERENCES

1. Hayreh SS, Podhajsky PA, Zimmerman MB. **Retinal artery occlusion: associated systemic and ophthalmic abnormalities.** *Ophthalmology* 2009;116:1928–36 CrossRef Medline
2. Youn TS, Lavin P, Patrylo M, et al. **Current treatment of central retinal artery occlusion: a national survey.** *J Neurol* 2018;265:330–35 CrossRef Medline
3. Hayreh SS, Zimmerman MB, Kimura A, et al. **Central retinal artery occlusion: retinal survival time.** *Exp Eye Res* 2004;78:723–36 CrossRef Medline
4. Hayreh SS, Zimmerman MB. **Fundus changes in central retinal artery occlusion.** *Retina* 2007;27:276–89 CrossRef Medline
5. Ahn SJ, Woo SJ, Park KH, et al. **Retinal and choroidal changes and visual outcome in central retinal artery occlusion: an optical coherence tomography study.** *Am J Ophthalmol* 2015;159:667–76 CrossRef Medline
6. Hayreh SS. **Acute retinal arterial occlusive disorders.** *Prog Retin Eye Res* 2011;30:359–94 CrossRef Medline
7. Chang YS, Jan RL, Weng SF, et al. **Retinal artery occlusion and the 3-year risk of stroke in Taiwan: a nationwide population-based study.** *Am J Ophthalmol* 2012;154:645–52 CrossRef Medline
8. Park SJ, Choi NK, Yang BR, et al. **Risk and risk periods for stroke and acute myocardial infarction in patients with central retinal artery occlusion.** *Ophthalmology* 2015;122:2336–43 CrossRef Medline
9. Golsari A, Bittersohl D, Cheng B, et al. **Silent brain infarctions and leukoaraiosis in patients with retinal ischemia: a prospective single-center observational study.** *Stroke* 2017;48:1392–96 CrossRef Medline
10. Lauda F, Neugebauer H, Reiber L, et al. **Acute silent brain infarction in monocular visual loss of ischemic origin.** *Cerebrovasc Dis* 2015;40:151–56 CrossRef Medline
11. Lee J, Kim SW, Lee SC, et al. **Co-occurrence of acute retinal artery occlusion and acute ischemic stroke: diffusion-weighted magnetic resonance imaging study.** *Am J Ophthalmol* 2014;157:1231–38 CrossRef Medline
12. Danyel LA, Bohner G, Connolly F, et al. **Standard diffusion-weighted MRI for the diagnosis of central retinal artery occlusion: a case-control study.** *Clin Neuroradiol* 2020 Sept 16 [Epub ahead of print] CrossRef Medline
13. Alsinaidi O, Shaikh AG. **Diffusion-weighted magnetic resonance imaging in acute retinal pathology.** *Neuroophthalmology* 2018;42:191–93 CrossRef Medline
14. Pottabattula B, Smith G, Nagaraja N, et al. **Demonstration of acute retinal ischemia on diffusion weighted magnetic resonance imaging.** *Clin Imaging* 2020;59:126–28 CrossRef Medline
15. Vicente M, Serrano AR, Falgas N, et al. **Diffusion restriction in the optic nerve and retina in patients with carotid occlusion.** *Neurologist* 2017;22:77–79 CrossRef Medline
16. Hasan TF, Rabinstein AA, Middlebrooks EH, et al. **Diagnosis and management of acute ischemic stroke.** *Mayo Clin Proc* 2018;93:523–38 CrossRef Medline
17. Huisman TA. **Diffusion-weighted imaging: basic concepts and application in cerebral stroke and head trauma.** *Eur Radiol* 2003;13:2283–97 CrossRef Medline
18. Schaefer PW, Grant PE, Gonzalez RG. **Diffusion-weighted MR imaging of the brain.** *Radiology* 2000;217:331–45 CrossRef Medline
19. Kattah JC, Talkad AV, Wang DZ, et al. **HINTS to diagnose stroke in the acute vestibular syndrome: three-step bedside oculomotor examination more sensitive than early MRI diffusion-weighted imaging.** *Stroke* 2009;40:3504–10 CrossRef Medline
20. Oppenheim C, Stanescu R, Dormont D, et al. **False-negative diffusion-weighted MR findings in acute ischemic stroke.** *AJNR Am J Neuroradiol* 2000;21:1434–40 Medline
21. Saber Tehrani AS, Kattah JC, Mantokoudis G, et al. **Small strokes causing severe vertigo: frequency of false-negative MRIs and non-lacunar mechanisms.** *Neurology* 2014;83:169–73 CrossRef Medline
22. Mac Grory B, Lavin P, Kirshner H, et al. **Thrombolytic therapy for acute central retinal artery occlusion.** *Stroke* 2020;51:687–95 CrossRef Medline
23. Helenius J, Arsava EM, Goldstein JN, et al. **Concurrent acute brain infarcts in patients with monocular visual loss.** *Ann Neurol* 2012;72:286–93 CrossRef Medline
24. Xu X, Wang Y, Hu H, et al. **Readout-segmented echo-planar diffusion-weighted imaging in the assessment of orbital tumors: comparison with conventional single-shot echo-planar imaging in image quality and diagnostic performance.** *Acta Radiol* 2017;58:1457–67 CrossRef Medline
25. Tian Y, Wang J, Li M, et al. **Comparison of field-of-view optimized and constrained undistorted single-shot diffusion-weighted imaging and conventional diffusion-weighted imaging of optic nerve and chiasma at 3T.** *Neuroradiology* 2018;60:903–12 CrossRef Medline
26. Sheng Y, Hong R, Sha Y, et al. **Performance of TGSE BLADE DWI compared with RESOLVE DWI in the diagnosis of cholesteatoma.** *BMC Med Imaging* 2020;20:40 CrossRef Medline
27. Peeler C, Parmar H, Trobe JD. **Subretinal abscess causing restricted diffusion on magnetic resonance imaging.** *J Neuroophthalmol* 2013;33:354–58 CrossRef Medline
28. Chen JS, Mukherjee P, Dillon WP, et al. **Restricted diffusion in bilateral optic nerves and retinas as an indicator of venous ischemia caused by cavernous sinus thrombophlebitis.** *AJNR Am J Neuroradiol* 2006;27:1815–16 Medline

Diagnostic Performance of Conebeam CT Pixel Values in Active Fenestral Otosclerosis

F. Deng, P. Touska, K.L. Reinshagen, H.D. Curtin, and A.F. Juliano

ABSTRACT

BACKGROUND AND PURPOSE: Quantitative bone densitometry on multidetector CT of the temporal bone is a diagnostic adjunct for otosclerosis in its active (spongiotic) phase, but translating this technique to conebeam CT is limited by the technical variability of conebeam CT pixel values. The purpose of this study was to evaluate the performance of internally calibrated conebeam CT pixel value measurements that can enable the determination of active fenestral otosclerosis (otospongiosis).

MATERIALS AND METHODS: This study included 37 ears in 22 patients with a clinical diagnosis of otospongiosis in those ears and 35 ears in 22 control patients without the diagnosis. Temporal bone conebeam CT was performed. ROIs were set anterior to the oval window, in the lateral semicircular canal bone island, and in a nearby aerated space. Mean conebeam CT pixel values in these regions determined the relative attenuation ratio of the area anterior to the oval window normalized to normal otic capsule bone and air.

RESULTS: The relative attenuation ratio for cases of otospongiosis was significantly lower than that for controls ($P < .001$). Based on receiver operating characteristic analysis, the optimal cutoff relative attenuation ratio was 0.876, which had an accuracy of 97.2% for the diagnosis of otospongiosis.

CONCLUSIONS: Internally calibrated pixel value ratios in temporal bone conebeam CT can feasibly help diagnose active/spongiotic-phase fenestral otosclerosis in an objective manner.

ABBREVIATIONS: CBCT = conebeam CT; MDCT = multidetector CT; RAR = relative attenuation ratio

Imaging diagnosis of the active or spongiotic/lucent phase of otosclerosis (otospongiosis) relies primarily on the detection of abnormal hypodensity involving the otic capsule on multidetector CT (MDCT). The preferential site of involvement for fenestral otospongiosis is the region anterior to the oval window. Prior studies support quantitative bone densitometry on MDCT as a diagnostic aid for fenestral otospongiosis.¹⁻⁵

Conebeam CT (CBCT) has gained interest in temporal bone imaging for its ability to produce high-spatial-resolution images, but a barrier to assessing bone density on CBCT is the technical variability of CBCT pixel values. Compared with MDCT, CBCT is more susceptible to regional artifacts due to off-axis x-ray beam

projections, beam hardening, and scatter radiation, particularly involving high-density material within the beam path but outside the reconstructed FOV (exomass).⁶ These artifacts can vary among patients, acquisition parameters, and reconstruction methods. Recognizing these limitations, current CBCT manufacturers often do not scale pixel (gray) values to Hounsfield units, as that would misleadingly imply accurate and standardized density representations. However, some authors have suggested correcting for some of these effects by calibrating CBCT pixel values using internal references.^{6,7}

The purpose of this study was to evaluate the performance of internally calibrated CBCT pixel value measurements/ratios that can enable objective determination of fenestral otospongiosis.

MATERIALS AND METHODS

Patients

A retrospective case-control study was approved by the institutional review board of Massachusetts Eye and Ear. The cases were 22 consecutive patients with a clinical diagnosis of otospongiosis who underwent CBCT of the temporal bones between January

Received January 15, 2021; accepted after revision April 16.

From the Department of Radiology (F.D.), Massachusetts General Hospital, Harvard Medical School, Boston, Massachusetts; Department of Radiology (P.T.), Guy's Hospital, Guy's and St. Thomas' Hospitals National Health Service Foundation Trust, London, UK; and Department of Radiology (K.L.R., H.D.C., A.F.J.), Massachusetts Eye and Ear, Harvard Medical School, Boston, Massachusetts.

Paper previously presented, in part, at: Annual Meeting of the American Society of Neuroradiology, May 30 to June 4, 2020; Virtual.

Please address correspondence to Amy F. Juliano, MD, Department of Radiology, MA Eye and Ear, 243 Charles St, Boston, MA 02114; e-mail: amy_juliano@meei.harvard.edu; @amyfjuliano

<http://dx.doi.org/10.3174/ajnr.A7192>

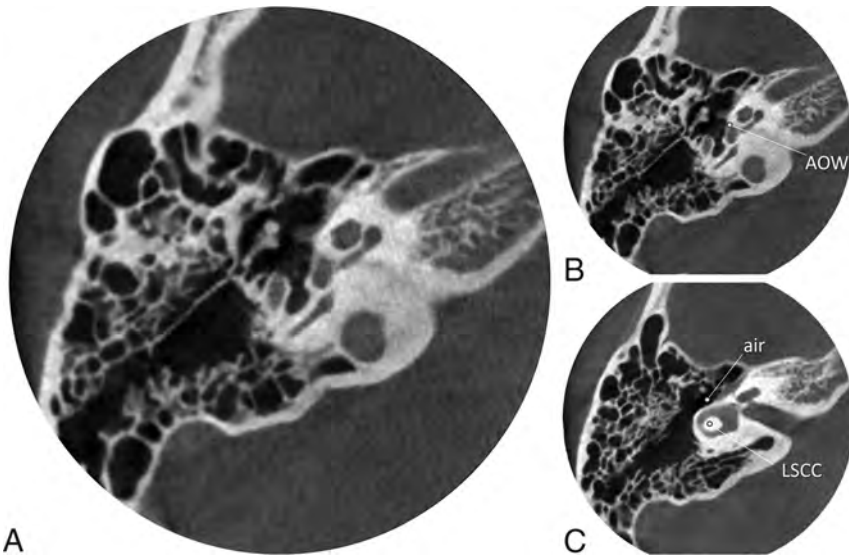


FIG 1. Temporal bone conebeam CT in a representative patient with otospongiosis. An image at the level of the oval window is shown without (A) and with (B) ROIs drawn anterior to the oval window (AOW). Additional ROIs at a separate level (C) are shown off-center within the lateral semicircular canal bone island (LSCC) and adjacent aerated cavity (air). The RAR in this patient was 0.756.

2016 and June 2017. The clinical diagnosis was established on the basis of history, otologic examination, and audiogram findings. Of the 44 ears in 22 patients, 7 ears were not included in the study because they either did not have clinical evidence of otosclerosis (the patients had unilateral signs and symptoms) or the scan showed postoperative findings (eg, stapes implant) that could suggest the diagnosis of otospongiosis and thereby unblind the reviewer. The controls were an equal number of patients without clinical evidence of otospongiosis, including normal audiogram findings, who were matched within a decade of age and scanned on the same CBCT unit between May 2018 and July 2018 for other indications (eg, dizziness, vertigo, facial palsy). Of the 44 ears in 22 controls, 35 ears were imaged (9 patients underwent unilateral CBCT).

Image Acquisition

All patients underwent dedicated temporal bone CBCT without intravenous contrast. Patients were imaged on a sitting CBCT unit, 3D Accuitomo (Morita), with a small FOV of 6×6 cm, tube potential = 90 kV(peak), tube current = 8 mA, high-resolution mode with rotation time = 30.8 seconds, pixel size = $125 \times 125 \mu\text{m}$, and section thickness = 0.5 mm. Patients had one or both temporal bones imaged separately in 1 session. Axial reformats of the temporal bones were created in a plane parallel to the that of the lateral semicircular canal. Images were exported to a PACS for viewing and analysis.

Image Analysis

Blinded to the clinical diagnoses, 2 radiologists (A.F.J. with 10 years of head and neck radiology experience; and either P.T. or K.L.R. with 4 years and 2 years of head and neck radiology

experience, respectively) independently measured CBCT pixel values on axial reformatted images for each CBCT examination. Round or oval ROIs of 0.5 mm^2 were placed in 3 areas in each case (Fig 1), anterior to the oval window, in the lateral semicircular canal bone island, and in an aerated space within the middle ear cleft nearest the lateral otic capsule (air). The area anterior to the oval window was selected as the area of interest for assessment of otospongiosis because that is most often involved initially by otospongiosis.⁸⁻¹⁰ The lateral semicircular canal bone island was chosen as an internal reference, as others have done,¹¹ because it is not an area described as involved by otospongiosis¹² and has a predictably large enough area for placing a 0.5-mm^2 ROI. Occasionally, a central hypodensity has been noted in the lateral semicircular canal bone island as an anatomic variant,¹³ so we deliberately placed the ROI off-center to avoid such variants.

The mean CBCT pixel value for each of the 3 ROIs was calculated using values obtained from the 2 readers for each temporal bone. A relative attenuation ratio (RAR) was then calculated for each CBCT examination: (anterior to the oval window – air) / (lateral semicircular canal bone island – air).

Statistical Analysis

The interrater correlation for the RAR was determined; then, the RAR was averaged between raters. Differences among groups were evaluated using the unpaired, 2-tailed Student *t* test. Diagnostic performance in predicting otospongiosis was evaluated using receiver operating characteristic analysis. An optimal operating point was identified by maximizing the Youden J statistic (sensitivity + specificity – 1). These statistics were computed using XLSTAT (Version 2016.2; Addinsoft) on Excel (Version 2011; Microsoft 365) and depicted using GraphPad Prism software (Version 9.0; GraphPad Software).

RESULTS

Patient Characteristics

Twenty-two individuals (4 men and 18 women; age range, 24–65 years; mean age, 46 [SD, 11] years) for a total of 37 ears were included in the otospongiosis group. Twenty-two individuals (14 men and 8 women; age range, 17–67 years; mean age 47 [SD, 14] years) for a total of 35 ears were included in the control group.

Relative Attenuation Ratio

The interrater reliability for the RAR was high (Pearson $r = 0.93$). The mean RAR for cases of otospongiosis was 0.701 (SD, 0.095), compared with 0.997 (SD, 0.058) for controls, a statistically significant difference ($P < .001$; Fig 2).

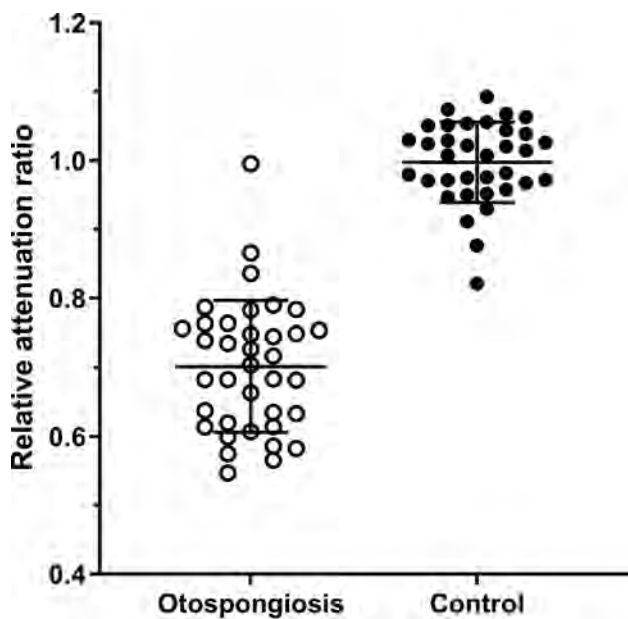


FIG 2. RAR. Individual ears with otopospongiosis (open circle; $n = 37$) and controls (solid circle; $n = 35$) are shown with group means and SDs (bars). The RAR in otopospongiotic ears was significantly less than that in control ears ($P < .001$).

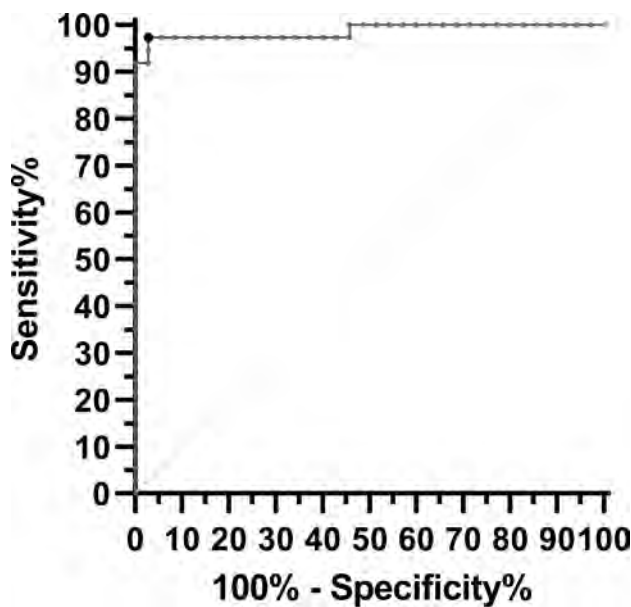


FIG 3. Receiver operating characteristic curve. The area under the curve (solid line) was 0.986, which was significantly different from the area under the line of identity (dashed line; $P < .001$). The operating point at which the Youden J statistic is maximized is shown as a larger black dot (RAR threshold = 0.876, sensitivity = 97.3%, specificity = 97.1%).

Performance

The area under the receiver operating characteristic curve was 0.986 (95% CI, 0.981–1.000; $P < .001$ for difference from 0.5; Fig 3). The optimal RAR cutoff was 0.876. Below this cutoff, otopospongiosis was correctly predicted with a sensitivity of 97.3% (95% CI, 86.2%–99.5%), specificity of 97.1% (95% CI, 85.5%–99.5%), and accuracy of 97.2%.

DISCUSSION

Otosclerosis is a primary osteodystrophy involving the otic capsule in adults. The earlier, histologically active phase of otosclerosis is also referred to as otopospongiosis in reference to the appearance of spongy bone that has abundant vascular spaces within it.¹⁴ In combination with clinical and audiologic evaluations, imaging plays a role in the diagnosis of otopospongiosis. Specifically, MDCT demonstrates hypodensity in the otic capsule, most commonly located in the region anterior to the oval window in so-called fenestral otopospongiosis. In the later inactive/sclerotic phase, the bone becomes denser and can appear thickened.¹⁵

The CT appearance of early-phase active fenestral otopospongiosis can be subtle. Prior studies support quantitative bone densitometry on MDCT as a diagnostic aid.^{1–5} These studies measured the Hounsfield units within regions anterior to the oval window in patients with and without otopospongiosis. Depending on the study, the mean bone density in otopospongiosis fell in the range of 1008–1649 HU, whereas the means in control ears were significantly higher in the range of 1396–2416 HU.^{1–5}

While MDCT has been the reference standard for otopospongiosis imaging, CBCT has gained interest in temporal bone imaging for its ability to produce high-spatial-resolution images potentially by using less radiation than MDCT.^{16,17} However, a barrier to assessing bone density on CBCT is the variability of CBCT pixel values (gray levels).¹⁸ CBCT output is not expressed in Hounsfield units and may differ across units, protocols, and patients due to technical factors arising from the conebeam geometry and limited FOVs. Assessment of material density on CBCT images relies on relative values, rather than absolute values as is the case with Hounsfield units in MDCT. However, many groups have found strong linear correlations between actual Hounsfield units on MDCT and CBCT pixel values in most devices.^{18–27}

In this study, we calibrated CBCT pixel values using 3 internal references to obtain an RAR that allows quantitative assessment of bone density.⁷ We selected the lateral semicircular canal bone island away from the edges bordering on the canal lumen as a reference standard because that area is rarely if ever described as a region affected by otopospongiosis/otosclerosis.¹² Uncommonly, the bone island may contain anatomic variant radiolucencies that would need to be excluded from measurement, but these variants did not occur in our study cohort. We further normalized the pixel values for bone by subtracting the pixel values of nearby air from them. Using this method, we found that the mean RAR for cases of fenestral otopospongiosis was about 0.7 (ie, the mean normalized pixel value in diseased bone anterior to the oval window was 70% that of unaffected bone), compared with 1.0 for controls. We suggest an RAR cutoff value of 0.876, below which fenestral otopospongiosis can be predicted with high sensitivity and specificity.

Our study has limitations. We used a single CBCT unit and imaging protocol, and measurements may differ under other technical parameters. There was no histologic confirmation of disease, but all cases fulfilled clinical criteria that were confirmatory of fenestral otopospongiosis. The study cohort did not include children or older adults. Otopospongiosis is primarily an entity seen in young and middle-aged adults, and otic capsule density should not be age-dependent, especially once past the neonatal or infancy period when the cochlear cleft may be prominent. The

density of diseased bone changes with time, so densitometry would not be expected to help diagnose cases presenting in the later, inactive/sclerotic phase, when alternative features at CT like otic capsule contour and thickness may be informative.¹⁵ Our study did not evaluate less common diseases that can decrease otic capsule density such as osteogenesis imperfecta and Paget disease of the temporal bone, which may mimic the densitometric findings in otospongiosis.

Several areas of future research are suggested. First, replication is required with different CBCT scanners and settings to ensure generalizability of our quantitative findings. Second, future studies may corroborate the relative attenuation evaluation on CBCT with audiometry, as has been shown with MDCT densitometry in fenestral otospongiosis.³ Finally, a CT grading system of otospongiosis based on location (fenestral, localized cochlear, and diffuse cochlear disease) was proposed in 2005;²⁸ the use of relative attenuation analysis on CBCT can, therefore, also be investigated in retrofenestral locations.

CONCLUSIONS

Change in bone density is an imaging feature of fenestral otospongiosis. Internally calibrated pixel value ratios in temporal bone CBCT can feasibly help diagnose active/spongiotic-phase fenestral otosclerosis in an objective manner.

REFERENCES

1. Kawase S, Naganawa S, Sone M, et al. **Relationship between CT densitometry with a slice thickness of 0.5 mm and audiometry in otosclerosis.** *Eur Radiol* 2006;16:1367–73 CrossRef Medline
2. Grayeli AB, Yrieix CS, Imauchi Y, et al. **Temporal bone density measurements using CT in otosclerosis.** *Acta Otolaryngol* 2004;124:1136–40 CrossRef Medline
3. Zhu M, Sha Y, Zhuang P, et al. **Relationship between high-resolution computed tomography densitometry and audiometry in otosclerosis.** *Auris Nasus Larynx* 2010;37:669–75 CrossRef Medline
4. Kutlar G, Koyuncu M, Elmali M, et al. **Are computed tomography and densitometric measurements useful in otosclerosis with mixed hearing loss? A retrospective clinical study.** *Eur Arch Otorhinolaryngol* 2014;271:2421–25 CrossRef Medline
5. Viza Puiggrós I, Granell Moreno E, Calvo Navarro C, et al. **Diagnostic utility of labyrinth capsule bone density in the diagnosis of otosclerosis with high resolution tomography.** *Acta Otorrinolaringol Esp* 2020;71:242–48 CrossRef Medline
6. Molteni R. **Prospects and challenges of rendering tissue density in Hounsfield units for cone beam computed tomography.** *Oral Surg Oral Med Oral Pathol Oral Radiol* 2013;116:105–19 CrossRef Medline
7. Liu Y, Bäuerle T, Pan L, et al. **Calibration of cone beam CT using relative attenuation ratio for quantitative assessment of bone density: a small animal study.** *Int J Comput Assist Radiol Surg* 2013;8:733–39 CrossRef Medline
8. Juliano AF, Ginat DT, Moonis G. **Imaging review of the temporal bone, Part II: traumatic, postoperative, and noninflammatory non-neoplastic conditions.** *Radiology* 2015;276:655–72 CrossRef Medline
9. Puac P, Rodríguez A, Lin HC, et al. **Cavitary plaques in otospongiosis: CT findings and clinical implications.** *AJNR Am J Neuroradiol* 2018;39:1135–39 CrossRef Medline
10. Yagi C, Morita Y, Takahashi K, et al. **Otosclerosis: anatomical distribution of otosclerotic loci analyzed by high-resolution computed**

- tomography.** *Eur Arch Otorhinolaryngol* 2019;276:1335–40 CrossRef Medline
11. Min JY, Chung WH, Lee WY, et al. **Otosclerosis: incidence of positive findings on temporal bone computed tomography (TBCT) and audiometric correlation in Korean patients.** *Auris Nasus Larynx* 2010;37:23–28 CrossRef Medline
12. McKenna M, Merchant S. **Disorders of bone.** In: Merchant S, Nadol J, Jr, eds. *Schuknecht's Pathology of the Ear.* 3rd ed. People's Medical; 2010:720–24
13. Lan MY, Shiao JY, Ho CY, et al. **Measurements of normal inner ear on computed tomography in children with congenital sensorineural hearing loss.** *Eur Arch Otorhinolaryngol* 2009;266:1361–64 CrossRef Medline
14. Quesnel AM, Ishai R, McKenna MJ. **Otosclerosis: temporal bone pathology.** *Otolaryngol Clin North Am* 2018;51:291–303 CrossRef Medline
15. Sanghan N, Chansakul T, Kozin ED, et al. **Retrospective review of otic capsule contour and thickness in patients with otosclerosis and individuals with normal hearing on CT.** *AJNR Am J Neuroradiol* 2018;39:2350–55 CrossRef Medline
16. Miracle AC, Mukherji SK. **Conebeam CT of the head and neck, Part 1: physical principles.** *AJNR Am J Neuroradiol* 2009;30:1088–95 CrossRef Medline
17. Miracle AC, Mukherji SK. **Conebeam CT of the head and neck, Part 2: clinical applications.** *AJNR Am J Neuroradiol* 2009;30:1285–92 CrossRef Medline
18. Pauwels R, Nackaerts O, Bellaiche N, et al. **SEDENTEXCT Project Consortium. Variability of dental cone beam CT grey values for density estimations.** *Br J Radiol* 2013;86:20120135 CrossRef Medline
19. Lagravère MO, Carey J, Ben-Zvi M, et al. **Effect of object location on the density measurement and Hounsfield conversion in a NewTom 3G cone beam computed tomography unit.** *Dentomaxillofac Radiol* 2008;37:305–08 CrossRef Medline
20. Naitoh M, Hirukawa A, Katsumata A, et al. **Evaluation of voxel values in mandibular cancellous bone: relationship between cone-beam computed tomography and multislice helical computed tomography.** *Clin Oral Implants Res* 2009;20:503–06 CrossRef Medline
21. Mah P, Reeves TE, McDavid WD. **Deriving Hounsfield units using grey levels in cone beam computed tomography.** *Dentomaxillofac Radiol* 2010;39:323–35 CrossRef Medline
22. Nomura Y, Watanabe H, Honda E, et al. **Reliability of voxel values from cone-beam computed tomography for dental use in evaluating bone mineral density.** *Clin Oral Implants Res* 2010;21:558–62 CrossRef Medline
23. Pauwels R, Stamatakis H, Manousaridis G, et al. **SEDENTEXCT Project Consortium. Development and applicability of a quality control phantom for dental cone-beam CT.** *J Appl Clin Med Phys* 2011;12:3478 CrossRef Medline
24. Parsa A, Ibrahim N, Hassan B, et al. **Reliability of voxel gray values in cone beam computed tomography for preoperative implant planning assessment.** *Int J Oral Maxillofac Implants* 2012;27:1438–42 Medline
25. Valiyaparambil JV, Yamany I, Ortiz D, et al. **Bone quality evaluation: comparison of cone beam computed tomography and subjective surgical assessment.** *Int J Oral Maxillofac Implants* 2012;27:1271–77 Medline
26. Oliveira ML, Tosoni GM, Lindsey DH, et al. **Influence of anatomical location on CT numbers in cone beam computed tomography.** *Oral Surg Oral Med Oral Pathol Oral Radiol* 2013;115:558–64 CrossRef Medline
27. Oliveira ML, Tosoni GM, Lindsey DH, et al. **Assessment of CT numbers in limited and medium field-of-view scans taken using Accutomo 170 and Veraviewepocs 3De cone-beam computed tomography scanners.** *Imaging Sci Dent* 2014;44:279–85 CrossRef Medline
28. Lee TC, Aviv RL, Chen JM, et al. **CT grading of otosclerosis.** *AJNR Am J Neuroradiol* 2009;30:1435–39 CrossRef Medline

Can Assessment of the Tongue on Brain MRI Aid Differentiation of Seizure from Alternative Causes of Transient Loss of Consciousness?

J.A. Erickson, M.D. Benayoun, C.M. Lack, J.R. Sachs, and P.M. Bunch

ABSTRACT

BACKGROUND AND PURPOSE: Transient loss of consciousness is commonly evaluated in the emergency department. Although typically caused by epileptic seizure, syncope, or psychogenic nonepileptic seizure, the underlying etiology is frequently misdiagnosed. Lateral tongue bites are reportedly a specific clinical finding of seizure. We have observed tongue signal abnormality suggesting bite injury on brain MR imaging after seizures. We hypothesized an association between tongue signal abnormality and seizure diagnosis among patients in the emergency department imaged for transient loss of consciousness. Our purposes were to determine the prevalence of tongue signal abnormality among this population and the predictive performance for seizure diagnosis.

MATERIALS AND METHODS: For this retrospective study including 82 brain MR imaging examinations, 2 readers independently assessed tongue signal abnormality on T2-weighted and T2-weighted FLAIR images. Discrepancies were resolved by consensus, and interrater reliability (Cohen κ) was calculated. The final diagnosis was recorded. Proportions were compared using the Fisher exact test.

RESULTS: Tongue signal abnormality was present on 19/82 (23%) MR imaging examinations. Interrater reliability was “substantial” ($\kappa = 0.77$). Seizure was diagnosed among 18/19 (95%) patients with tongue signal abnormality and 29/63 (46%) patients without it ($P < .001$). In our cohort, tongue signal abnormality conveyed 97% specificity, 95% positive predictive value, and 63% accuracy for seizure diagnosis.

CONCLUSIONS: Tongue signal abnormality was observed in 23% of the study cohort and conveyed 97% specificity and 95% positive predictive value for seizure diagnosis. By assessing and reporting tongue signal abnormality, radiologists may facilitate a timely and accurate diagnosis of seizure among patients imaged for transient loss of consciousness.

ABBREVIATIONS: ED = emergency department; ES = epileptic seizure; PNES = psychogenic nonepileptic seizure; TLoC = transient loss of consciousness; TSA = tongue signal abnormality

Transient loss of consciousness (TLoC) is defined as a spontaneous, temporary loss of consciousness with complete recovery.¹ TLoC is estimated to affect up to 50% of individuals at some point in their lives¹ and to account for up to 3% of emergency department (ED) visits.² Although >90% of cases of TLoC are known to be caused by epileptic seizure (ES), syncope, or psychogenic nonepileptic seizure (PNES),³ confident determination of the underlying etiology in any given patient remains difficult. In

fact, it is estimated that the underlying cause of TLoC is misdiagnosed in 20%–30% of cases.^{4–7} A timely and accurate diagnosis of seizure identifies patients with TLoC who may benefit from anti-epileptic therapy, whereas an incorrect diagnosis may result in inaccurate, inefficient, and delayed care.

The terminology associated with 2 of the most common causes of TLoC (ES, PNES) is potentially confusing. Thus, clarification is offered on the use of ES and PNES throughout this article. The International League Against Epilepsy defines ES as “a transient occurrence of signs and/or symptoms due to abnormal excessive or synchronous neuronal activity in the brain.”⁸ Most important, the term ES—commonly shortened to seizure—does not imply that the seizure is caused by or the patient has an epilepsy syndrome. Rather, the intent is to differentiate ES from other physical or psychological sudden events that may resemble ES in some ways but which have causes other than abnormal excessive or synchronous neuronal activity in the brain,⁸ for

Received January 14, 2021; accepted after revision April 4.

From the Department of Radiology, Wake Forest School of Medicine, Winston Salem, North Carolina.

Paper previously presented as an electronic scientific poster at: Annual Meeting of the American Society of Neuroradiology, May 20 to June 4, 2020; Virtual. The current submission includes additional data and analyses that were not part of the previous electronic poster.

Please address correspondence to Paul M. Bunch, MD, Department of Radiology, Wake Forest School of Medicine, Medical Center Boulevard, Winston Salem, NC 27157; e-mail: paul.m.bunch@gmail.com; @pbunchmd
<http://dx.doi.org/10.3174/ajnr.A7188>

example PNES, “an event resembling ES but caused by psychological processes”⁹ and historically also referred to as “pseudoseizure.”

Lateral tongue bites have been described as a specific clinical finding of ES.¹⁰⁻¹⁴ Some data suggest that bite injuries limited to the tip of the tongue are specific for syncope;^{10,15,16} however, this pattern of injury has also been observed in ES¹¹ and PNES.¹⁴ On brain MR imaging, we have observed tongue signal abnormality (TSA), which was subsequently proved to correspond to tongue bite injury and was used to support a clinical diagnosis of unrecognized seizure. Neuroimaging is commonly performed in the evaluation of TLoC,¹⁷ and the presence of TSA may implicate ES as the underlying etiology. We hypothesized a positive association between TSA and the clinical diagnosis of ES. The purposes of this study were the following: 1) to determine the prevalence of TSA among patients in the ED undergoing brain MR imaging for TLoC, and 2) to assess associations between TSA and a final clinical diagnosis of seizure.

MATERIALS AND METHODS

Subjects

For this retrospective, Health Insurance Portability and Accountability Act-compliant, institutional review board-approved study, a local institutional radiology database (mPower; Nuance Healthcare) was queried for patients satisfying the following inclusion criteria: 1) 18 years of age or older, 2) evaluated in our institution’s ED between May 2016 and May 2020, and 3) brain MR imaging obtained during ED evaluation including the terms “seizure,” “syncope,” “loss of consciousness,” or “fainting” in the study indication. Examinations were excluded if neither the T2-weighted nor T2-weighted FLAIR images included the tongue or the diagnostic assessment of the tongue was precluded by severe motion, dental, or other imaging artifacts.

Medical Record Review

Patient age and sex, stated indication for imaging, the presence or absence of clinical documentation of tongue bite injury, and the final clinical diagnosis (eg, seizure, syncope, other) were recorded.

Image Acquisition

Given the retrospective nature of this study, there was variability with respect to the MR imaging scanners used to acquire images and the specific T2-weighted and T2-weighted FLAIR sequence acquisition parameters. Most included MR imaging examinations were performed on 1 of three 1.5T MR imaging scanners: Magnetom Avanto ($n = 45$) (Siemens), Magnetom Aera ($n = 17$) (Siemens), and Signa HDxt ($n = 5$) (GE Healthcare). The remaining 15 included MR imaging examinations were performed on 1 of two 3T Magnetom Skyra (Siemens) MR imaging scanners. Representative T2-weighted acquisition parameters for the most commonly used 1.5T MR imaging scanner were the following: 5-mm section thickness, 5-mm spacing, FOV = 230×230 mm, matrix = 320×320 , NEX = 1, TR = 4200 ms, TE = 105 ms, echo-train length = 35. Representative T2-weighted FLAIR acquisition parameters applied to the most commonly used 1.5T MR imaging scanners were the following: 5-mm section

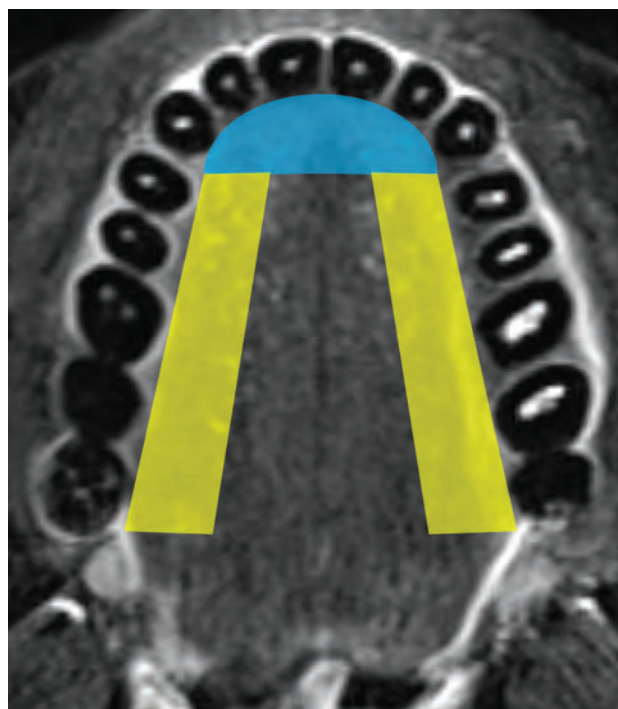


FIG 1. Axial, T2-weighted, fat-suppressed image with color overlay demonstrates the visual standard used to classify the sites of tongue signal abnormality as involving the tip of tongue (*blue shading*), lateral tongue (*yellow shading*), or both.

thickness, 7-mm spacing, FOV = 230×230 mm, matrix = 256×223 , NEX = 1, TR = 8000 ms, TE = 120 ms, TI = 2370 ms, echo-train length = 16.

Reader Assessment

One radiology resident and 1 fellowship-trained attending neuro-radiologist (4 years’ subspecialty experience), both blinded to the clinical information, independently reviewed the T2-weighted and T2-weighted FLAIR images from all included brain MR imaging examinations using our institution’s PACS. Each reviewer recorded the presence or absence of TSA in all patients, defined as abnormally increased fluid signal involving the tongue. For TSA identified on non-fat-suppressed T2-weighted FLAIR images, correlation with corresponding T1-weighted images of the tongue was performed to confirm that the TSA was consistent with fluid signal rather than fat. The recorded results were compared, and discrepancies were resolved by consensus review. Consensus review was performed unblinded to the clinical documentation of the presence or absence of tongue bite injury on physical examination. When a TSA was present, the radiology report was reviewed to determine whether the finding was described. Additionally, both reviewers in consensus characterized the site of TSA as “lateral tongue,” “tip of tongue,” or “both” using a visual standard (Fig 1) modeled after the visual depiction of the bite location by Benbadis et al.¹⁰

Statistical Analysis

Absolute and relative frequencies are reported for categorical variables. The Fisher exact test was used to compare proportions, the Student *t* test was used to compare continuous variables, and the Cohen κ coefficient was calculated to assess interrater reliability.

These analyses were performed with JMP, Version 14 (SAS Institute), and $P < .05$ indicated a statistically significant difference. Measures of diagnostic performance (eg, sensitivity, specificity, positive predictive value) for TSA and clinically documented tongue bite injury were also calculated.

RESULTS

Subjects

A total of 144 brain MR imaging examinations were reviewed, with 55 examinations excluded because the tongue was not included in the scan range of either the T2-weighted or the T2-weighted FLAIR sequences and 7 excluded for artifacts (eg, motion, dental) precluding assessment of the tongue. This process yielded a total of 82 brain MR imaging examinations in the cohort. Characteristics of the study group are summarized in Table 1.

Table 1: Characteristics of the study group

	Total	TSA		P Value
		Yes	No	
Sex (No.)				
Male	42	9	33	.80 ^a
Female	40	10	30	
Age (yr)				
Mean	53.3 (19.1)	48.6 (18.5)	54.7 (19.2)	.22 ^b
Range	20–92	20–92	20–85	
Stated brain MRI indication (No.)				
Seizure	49	16	33	.016 ^a
No seizure	33	3	30	
Syncope	26	2	24	
Loss of consciousness	5	1	4	
Fainting	2	0	2	
Clinically documented tongue bite injury				
Yes	15	12	3	<.001 ^a
No	67	7	60	
Final clinical diagnosis				
Epileptic seizure	47	18	29	<.001 ^a
No epileptic seizure	35	1	34	
Syncope	21	0	21	
Psychogenic nonepileptic seizure	2	0	2	
Other	12	1 ^c	11	

^a Fisher exact test.

^b Student *t* test.

^c Spells of altered attention, likely cognitive fluctuations in the setting of dementia.

Reader Assessment

Following consensus review, TSA was determined to be present on 19 (23%) MR imaging examinations (Fig 2), more commonly unilateral (11/19; 58%) than bilateral (8/19; 42%). The site of the TSA was classified as the lateral tongue only in 12 (63%) patients, tip of tongue only in none (0%), and both the lateral tongue and tip of tongue in 7 (37%) patients. There were no significant differences between the presence of TSA and age ($P = .22$) or sex ($P = .80$). Interrater reliability was substantial ($\kappa = 0.77$). The T2-weighted and T2-FLAIR weighted sequences on which the tongue was evaluable are summarized in Table 2.

TSA was observed in 12/15 (80%) patients with documented tongue bite injuries on physical examination and in 7/67 (10%) patients with no documented tongue bite injury on physical examination ($P < .001$). Among the 15 patients with TSA and documented tongue bite injuries, the sites of the TSA corresponded with the sites of documented tongue bite injuries in all (3/3) patients for whom specific site information (eg, right, left, bilateral) was documented; in the other 12 patients, physical examination documented only “tongue bite injury” or “tongue laceration” with no specification as to sites of injury. The final clinical diagnosis was ES among 18/19 (95%) patients with TSA (11 classified as involving the lateral tongue only and 7 classified as involving both the lateral tongue and tip of tongue) and 29/63 (46%) patients without TSA ($P < .001$). One patient with TSA and a clinically documented tongue bite injury (classified as involving the lateral tongue only) was given a final clinical diagnosis of “spells of altered attention, likely cognitive fluctuations in the setting of dementia.” The final clinical diagnosis was ES for all 7 patients with TSA but no documented tongue bite injury on physical examination.

In our cohort, TSA conveyed 38% sensitivity (95% CI, 25%–54%), 97% specificity (95% CI, 85%–100%), 95% positive predictive value (95% CI, 72%–99%), 54% negative predictive value (95% CI, 48%–60%), and 63% accuracy (95% CI,

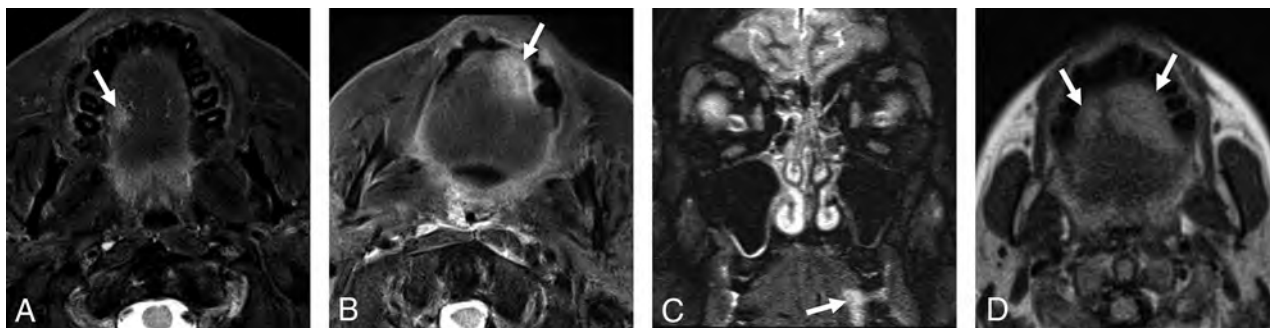


FIG 2. Representative examples of the spectrum of TSA (arrows, A–D) observed in this study from 4 different patients in the ED. All patients were given a final clinical diagnosis of epileptic seizure. Tongue bite injuries were documented on physical examination for the patients depicted in B and D. No tongue bite injury was documented on physical examination for the patients depicted in A and C. TSA was classified as lateral only for A and C and as both lateral and tip of tongue for B and D.

Table 2: Summary of T2-weighted and T2-weighted FLAIR sequences on which the tongue was evaluable within the study cohort and visibility of TSA by sequence

	Tongue Evaluable	TSA Present (%)	TSA Absent (%)	P Value ^a
Axial T2 FS	39	6 (15%)	33 (85%)	.73
Axial FLAIR	26	3 (12%)	23 (88%)	
FS	24	2 (8%)	22 (92%)	.22
Not FS	2	1 (50%)	1 (50%)	
Coronal T2 FS	8	1 (13%)	7 (87%)	.43
Coronal FLAIR	55	16 (29%)	39 (71%)	
FS	44	12 (27%)	32 (73%)	.71
Not FS	11	4 (36%)	7 (64%)	

Note:—FS indicates fat-suppressed.

^a Fisher exact test.

52%–74%) for a final clinical diagnosis of ES. TSA was described in 0/19 radiology reports.

For comparison, the final clinical diagnosis was ES among 14/15 (93%) patients with documented tongue bite injury on physical examination compared with 33/67 (49%) patients without documented tongue bite injury ($P = .001$). In our cohort, documented tongue bite injury conveyed 30% sensitivity (95% CI, 17%–45%), 97% specificity (95% CI, 85%–100%), 93% positive predictive value (95% CI, 66%–99%), 51% negative predictive value (95% CI, 46%–56%), and 59% accuracy (95% CI, 47%–69%) for a final clinical diagnosis of ES.

DISCUSSION

Among patients in the ED undergoing brain MR imaging for TLoC, the overall prevalence of TSA suggesting bite injury was 23%, and the underlying etiology for TLoC was determined to be ES in 95% of patients with TSA. Notably, the final clinical diagnosis was seizure in 100% of patients with TSA but no documented tongue bite injury on physical examination, suggesting that either the physical examination in the ED overlooked a tongue bite injury in these patients or the injury was not apparent at the time of mucosal inspection. Moreover, no interpreting radiologist described the presence of TSA in any of this cohort's brain MR imaging reports, suggesting that radiologists are not habitually assessing the tongue for possible bite injury on brain MR imaging performed for TLoC.

These findings support our hypothesis that TSA—presumed to represent the MR imaging correlate to tongue bite injury—is positively associated with the clinical diagnosis of seizure. Both TSA and clinically documented tongue bite injuries conveyed high specificity (97% for both) and high positive predictive values (95% for TSA, 93% for tongue bite) for a final clinical diagnosis of ES. Most important, the absence of TSA does not preclude seizure as the underlying etiology for TLoC because the sensitivity of TSA for clinical seizure diagnosis was only 38%. Diagnostic performance of TSA for seizure diagnosis was comparable with that of tongue bite injuries both in our cohort and in the published literature, including a meta-analysis reporting a pooled sensitivity of 33% and pooled specificity of 96% for tongue bite injury.¹³

TSA location (lateral, tip of tongue, both) was also assessed, given a previous pooled analysis of data from Benbadis et al¹⁰ and Akor et al¹⁵ reporting 99.8% specificity of a tip of the tongue bite for syncope.¹⁶ There were no patients in our cohort with TSA limited to just the tip of tongue. However, TSA involved both the tip of tongue and the lateral tongue in 7 patients, all of whom were diagnosed with ES. Given reports of tip of the tongue bites in both ES¹¹ and PNES¹⁴ as well as the pooled analysis from Brigo et al¹⁶ including only 2 patients with syncope with tip of tongue bites, we advise caution in drawing conclusions about the underlying cause of TLoC on the basis of tip of tongue bite location alone.

TLoC accounts for up to 3%² of all ED visits, and the underlying cause of TLoC is misdiagnosed in 20%–30% of cases,^{4–7} potentially resulting in inaccurate, inefficient, or delayed care. When interpreting neuroimaging in patients with TLoC, the radiologist should be primarily concerned with evaluating for mass, hemorrhage, infarction, encephalitis, or other structural causes for TLoC. However, radiologists' awareness of, assessment for, and reporting of TSA as a high-specificity finding for ES could facilitate timely identification of patients who may benefit from antiepileptic therapy, particularly given that some tongue bite injuries may be unrecognized on physical examination in the ED setting and that some patients may undergo imaging before comprehensive oral cavity examination. Thus, assessment of the tongue on brain MR imaging may complement clinical history, physical examination, witness accounts,¹⁸ electroencephalography, electrocardiography, heart rhythm monitoring, tilt-table testing, and laboratory evaluation^{19–21} to ascertain underlying TLoC etiology and, in some cases, potentially obviate the need for more involved additional tests. We do not advocate obtaining brain MR imaging in all patients with TLoC to enable TSA assessment. However, in the subset of patients with TLoC whose clinical circumstances warrant brain MR imaging, radiologists have an opportunity to facilitate an accurate diagnosis of seizure by noticing TSA, reporting its presence, and recommending correlation with direct inspection to confirm that the finding indeed represents a tongue bite injury rather than mucosal neoplasm or other potential mimics.

Some radiology practices might consider routinely including the tongue within the scan range of brain MR imaging performed for TLoC (if not always included already) to enable assessment for TSA; however, such a protocol change would likely need to be considered in the context of local practice patterns, radiologists' and referring providers' preferences, and other factors beyond the scope of this study. Although there were no statistically significant differences between the frequencies with which TSA was observed on fat-suppressed-versus-non-fat-suppressed images (Table 2), in our subjective experience, TSA was more easily and more confidently identifiable on the fat-suppressed images. We found both axial and coronal fat-suppressed T2-weighted and T2-weighted FLAIR images equally valuable for TSA identification. Thus, if considering protocol modifications to maximize the potential usefulness of TSA in the imaging of TLoC, we suggest including the tongue in the scan range of at least 1 fat-suppressed T2-weighted or T2-weighted FLAIR sequence. Alternatively, if one is assessing non-fat-suppressed T2-weighted or T2-weighted

FLAIR images for TSA, we emphasize the importance of correlating any findings on the T2-weighted sequences with T1-weighted images to avoid misdiagnosing focal fat (T1 and T2 hyperintense) as TSA (T1 hypointense, T2 hyperintense).

There are limitations to this study. The retrospective design precludes definitive confirmation that TSA represented tongue bite injury in all patients; however, the statistically significant association between the presence of TSA and a documented tongue bite injury, the parallel between the site of TSA and the site of documented bite injury in all patients for whom this level of clinical detail was available, as well as the comparable diagnostic performance of both findings for clinical seizure diagnosis provide evidence that the TSA observed in our study is indeed the MR imaging correlate to tongue bite injury. A substantial proportion of brain MR imaging examinations in the ED performed for TLoC did not include images of the tongue and were, therefore, excluded. Furthermore, the criterion standard of final clinical diagnosis used in this study is known to be imperfect. The real-world clinical impact of radiologists' identification of TSA is uncertain and would likely depend on a number of factors not controlled for in this study, including the following: 1) whether an oral cavity examination was performed before MR imaging, 2) the training and skill level of the oral cavity examiner, 3) whether a tongue bite injury was already identified before imaging, and 4) clinical decision-making related to which patients with TLoC are selected for brain MR imaging. Finally, only 2 patients in the cohort had a final diagnosis of PNES, so any potential relationship between TSA and PNES remains uncertain.

CONCLUSIONS

The prevalence of TSA among patients in the ED undergoing brain MR imaging for TLoC was 23%, and the presence of TSA conveyed 97% specificity and 95% positive predictive value for a final clinical diagnosis of ES.

Radiologists have an opportunity to add value in the MR imaging evaluation of TLoC through awareness of, assessment for, and reporting of TSA as a high-specificity finding for ES, particularly given that some tongue bite injuries may be unrecognized on physical examination in the ED setting.

REFERENCES

1. Cooper PN, Westby M, Pitcher DW, et al. **Synopsis of the National Institute for Health and Clinical Excellence Guideline for Management of Transient Loss of Consciousness.** *Ann Intern Med* 2011;155:543 CrossRef Medline
2. Petkar S, Cooper P, Fitzpatrick AP. **How to avoid a misdiagnosis in patients presenting with transient loss of consciousness.** *Postgrad Med J* 2006;82:630–41 CrossRef Medline
3. Reuber M, Chen M, Jamnadas-Khoda J, et al. **Value of patient-reported symptoms in the diagnosis of transient loss of consciousness.** *Neurology* 2016;87:625–33 CrossRef Medline
4. Zaidi A, Clough P, Cooper P, et al. **Misdiagnosis of epilepsy: many seizure-like attacks have a cardiovascular cause.** *J Am Coll Cardiol* 2000;36:181–84 CrossRef Medline
5. Chadwick D, Smith D. **The misdiagnosis of epilepsy.** *BMJ* 2002;324:495–96 CrossRef Medline
6. Leach JP, Lauder R, Nicolson A, et al. **Epilepsy in the UK: misdiagnosis, mistreatment, and undertreatment?** *Seizure* 2005;14:514–20 CrossRef Medline
7. Fitzpatrick AP, Cooper P. **Diagnosis and management of patients with blackouts.** *Heart* 2005;92:559–68 CrossRef Medline
8. Fisher RS, van Emde Boas W, Blume W, et al. **Epileptic seizures and epilepsy: definitions proposed by the International League Against Epilepsy (ILAE) and the International Bureau for Epilepsy (IBE).** *Epilepsia* 2005;46:470–72 CrossRef Medline
9. Kanemoto K, LaFrance WC, Duncan R, et al. **PNES around the world: Where we are now and how we can close the diagnosis and treatment gaps—an ILAE PNES Task Force report.** *Epilepsia Open* 2017;2:307–16 CrossRef Medline
10. Benbadis SR, Wolgamuth BR, Goren H, et al. **Value of tongue biting in the diagnosis of seizures.** *Arch Intern Med* 1995;155:2346–49 Medline
11. Oliva M, Pattison C, Carino J, et al. **The diagnostic value of oral lacerations and incontinence during convulsive “seizures.”** *Epilepsia* 2008;49:962–67 CrossRef Medline
12. Brigo F, Storti M, Lochner P, et al. **Tongue biting in epileptic seizures and psychogenic events: an evidence-based perspective.** *Epilepsy Behav* 2012;25:251–55 CrossRef Medline
13. Brigo F, Nardone R, Bongiovanni LG. **Value of tongue biting in the differential diagnosis between epileptic seizures and syncope.** *Seizure* 2012;21:568–72 CrossRef Medline
14. Dufresne D, Dubovec K, So NK, et al. **Ictal biting injuries in the epilepsy monitoring unit, a cohort study of incidence and semiological significance.** *Seizure* 2019;66:39–41 CrossRef Medline
15. Akor F, Liu NM, Besag FM, et al. **Value of tongue biting in differentiating between epileptic seizures and syncope.** *Seizure* 2013;22:328 CrossRef Medline
16. Brigo F, Bongiovanni LG, Nardone R. **Lateral tongue biting versus biting at the tip of the tongue in differentiating between epileptic seizures and syncope.** *Seizure* 2013;22:801 CrossRef Medline
17. Huff JS, Melnick ER, Tomaszewski CA, et al; American College of Emergency Physicians. **Clinical policy: critical issues in the evaluation and management of adult patients presenting to the emergency department with seizures.** *Ann Emerg Med* 2004;43:605–25 CrossRef Medline
18. Chen M, Jamnadas-Khoda J, Broadhurst M, et al. **Value of witness observations in the differential diagnosis of transient loss of consciousness.** *Neurology* 2019;92:e895–904 CrossRef Medline
19. Goksu E, Oktay C, Kilicaslan I, et al. **Seizure or syncope: the diagnostic value of serum creatine kinase and myoglobin levels.** *Eur J Emerg Med* 2009;16:84–86 CrossRef Medline
20. Matz O, Zdebek C, Zechbauer S, et al. **Lactate as a diagnostic marker in transient loss of consciousness.** *Seizure* 2016;40:71–75 CrossRef Medline
21. Jiang M, Yan L, Yan X, et al. **The value of serum uric acid levels to differentiate causes of transient loss of consciousness.** *Epilepsy Behav* 2019;99:106489 CrossRef Medline

Recommendations in Second Opinion Reports of Neurologic Head and Neck Imaging: Frequency, Referring Clinicians' Compliance, and Diagnostic Yield

S.A. Heinz, D. Yakar, R.A.J.O. Dierckx, M.J. Lamers, and T.C. Kwee



ABSTRACT

BACKGROUND AND PURPOSE: Second opinion reports of neurologic head and neck imaging are requested with increased regularity, and they may contain a recommendation to the clinician. Our aim was to investigate the frequency and determinants of the presence of a recommendation and the adherence by the referring physician to the recommendation in a second opinion neurologic head and neck imaging report and the diagnostic yield of these recommendations.

MATERIALS AND METHODS: This retrospective study included 994 consecutive second opinion reports of neurology head and neck imaging examinations performed at a tertiary care center.

RESULTS: Of the 994 second opinion reports, 12.2% (121/994) contained a recommendation. An oncologic imaging indication was significantly ($P = .030$) associated with a lower chance of a recommendation in the second opinion report (OR = .67; 95% CI, 0.46–0.96). Clinicians followed 65.7% (88/134) of the recommendations. None of the investigated variables (patient age, sex, hospitalization status, indication for the second opinion report, experience of the radiologist who signed the second opinion report, strength of the recommendation, and whether the recommendation was made due to apparent quality issues of the original examination) were significantly associated with the compliance of the referring physician to this recommendation. The 134 individual recommendations eventually led to the establishment of 52 (38.2%) benign diagnoses and 28 (20.6%) malignant diagnoses, while no definitive diagnosis could be established in 56 (41.2%) cases.

CONCLUSIONS: Recommendations are relatively common in second opinion reports of neurology head and neck imaging examinations, though less for oncologic indications. They are mostly followed by requesting physicians, thus affecting patient management. In most cases, they also lead to the establishment of a diagnosis, hence adding value to patient care.

ABBREVIATION: NHN = neurology head and neck

Tertiary care radiology departments frequently review imaging examinations that have been performed and interpreted elsewhere.^{1,2} Neurology head and neck (NHN) imaging examinations comprise a large proportion of second opinion reports that are generated at tertiary care centers.²

At present, there is an increase in the overall number of second opinion readings.¹ This also applies to second opinion re-evaluations of NHN imaging examinations, with reported growth rates of 245% in the United States from 2011 to 2015.³ Many hospitals also require an official record in the form of a second opinion report to be provided for all outside studies, which may also take extra time. This policy is followed by 37.4%–60.0% of the radiology

departments in the United States.⁴ Altogether, the workload of radiologists due to second opinion interpretations is increasing.

Second opinion interpretations may potentially be beneficial to patient care by avoiding unnecessary additional imaging examinations, improving disease detection, and establishing a more accurate differential diagnosis.^{2,5–9} Tertiary care radiologists may also give a recommendation in the second opinion report to provide guidance on patient management to the clinician. These recommendations may include advice to perform additional imaging, perform a biopsy, refer the patient to another specialty, or compare an examination with previous imaging examinations, among others.

Currently, it is unclear how many second opinion reports of NHN imaging examinations contain a recommendation to the clinician, which factors are associated with the presence of a recommendation in the second opinion report, how frequently the recommendation is followed by the clinician, and which factors affect the adherence of the clinician to the recommendation. Such information would be valuable to determine whether the

Received December 16, 2020; accepted after revision April 5, 2021.

From the Medical Imaging Center, Department of Radiology, University Medical Center Groningen, University of Groningen, Groningen, the Netherlands.

Please address correspondence to Sabine A. Heinz, MD, University Medical Center Groningen, Medical Imaging Center, Department of Radiology, Hanzeplein 1, PO Box 30.001, 9700 RB Groningen, the Netherlands; e-mail: s.a.heinz@gmx.net

<http://dx.doi.org/10.3174/ajnr.A7197>

practice of second opinion reporting with the provision of a recommendation to the clinician affects patient management in the field of NHN imaging. In addition, it is unknown how many of these recommendations eventually allow the establishment of a diagnosis. This information is important to understand their contribution to value-based patient care.

The purpose of this study was, therefore, to investigate the frequency and determinants of the presence of a recommendation and the adherence by the referring physician to the recommendation in a second opinion NHN imaging report and the diagnostic yield of these recommendations.

MATERIALS AND METHODS

Study Design

The local institutional review board of the University Medical Center Groningen approved this retrospective single-center study, and informed consent was waived. All consecutive second opinion reports of NHN imaging examinations that were compiled in our tertiary care center in the Netherlands within a 1-year time period (November 2016 to November 2017) were potentially eligible for inclusion in this study. A second opinion report was included if the original imaging examination was performed and reported in another hospital before referral to our center. A second opinion report was excluded if its content mentioned that no re-evaluation was performed because the second opinion reading became clinically irrelevant due to the availability of more recent imaging examinations, if either the report or the imaging examination was not available in the hospital's PACS, if the re-evaluated imaging examination did not primarily concern NHN imaging (eg, CT of neck, chest, and abdomen in a patient with lymphoma), or if it concerned a re-evaluation of an in-house imaging examination.

Local Practice of Second Opinion Readings

In our department, an outside imaging examination is only reviewed if the treating clinician contacts one of the radiologists and obtains his or her approval for the second opinion reading. The decision to accept or reject the second opinion request is based on the conversation between the clinician and radiologist, and not by a review of the images beforehand. The radiologist accepts all second opinion readings of patients who will be discussed in a multidisciplinary meeting. If patients will not be discussed in a multidisciplinary meeting and the tertiary care radiologist does not see any advantage to re-evaluate a scan that was already interpreted by another radiologist elsewhere (eg, if a case concerns common pathology that is also frequently seen by radiologists who work in nonacademic hospitals), the second opinion request is rejected. The imaging examination and the primary report that was composed in the hospital from which the patient was referred need to be uploaded to our PACS. After review of the relevant imaging examinations, an official written second opinion report is then compiled and made available to the referring physician in the hospital's electronic patient file system. Radiologists (regardless of years of experience) are authorized to report and sign second opinion reports. There is a rule in our department to refrain from any curbside consultations to maintain quality. Note that at the time that our study was performed,

the Dutch Healthcare Authority had a rule in place that it was not possible to submit second opinion readings for billing when patients were referred from one hospital to a treating physician in another hospital.

Data Extraction

For each second opinion report, we collected the following variables: patient age, sex, hospitalization status (in- or outpatient) at the time of the second opinion reporting, imaging indication (developmental, infectious, inflammatory, neurodegenerative, oncologic, benign sellar/parasellar tumors, trauma, vascular, miscellaneous), imaging technique (CT, MR imaging, ultrasonography, or x-ray), years of experience of the radiologist who signed the second opinion report (calculated from the end of residency), whether this radiologist was subspecialized in NHN imaging, and the presence of a recommendation in the second opinion report. Recommendations made in the second opinion report were evaluated as follows: type of recommendation (recommendation for additional imaging, biopsy, referral to another specialty, comparison with previous imaging examinations, or other), strength of the recommendation (hard [eg, wording such as "it is advised to" or "it is indicated to"] or soft [eg, "it can be considered to" or "suggest"]) based on a predefined categorization scheme applied by 2 independent raters (S.A.H. and T.C.K., who were blinded to each other's ratings), whether the recommendation was made due to apparent quality issues of the original imaging examination (ie, insufficient diagnostic quality, including missing sequences for MR imaging), compliance of the referring clinician to the recommendation, and the diagnostic outcome related to the recommendation.

For second opinion reports with a recommendation, the diagnosis in the primary report was compared with the diagnosis in the second opinion report. Referring clinicians' compliance to the recommendation in the second opinion report was determined on the basis of the records in the hospital's electronic patient file system—ie, if the recommended procedure was performed after the second opinion report had been authorized and if there was a clear connection to the recommendation, it was considered to have been followed. The diagnostic outcome of a recommendation was determined on the basis of all available follow-up data during a minimum 2-year follow-up, using 3 categories: A benign diagnosis was established, a malignant diagnosis was established, or no diagnosis could be established even though additional diagnostic procedures may have been performed. Note that our country has a well-developed infrastructure to exchange patient data among hospitals, which allowed tracing follow-up studies outside our hospital if they were performed.

Statistical Analysis

The frequency of second opinion reports with a recommendation as a proportion of the total number of second opinion reports was calculated. The Cohen κ was run to determine the interrater agreement regarding the strength of the recommendations. Logistic regression analyses were performed to determine the association of the presence of a recommendation in the second opinion report with the following variables: patient age, sex, hospitalization status, indication for the second opinion report, and

experience and NHN subspecialization of the radiologist who signed the second opinion report.

The frequency of the referring clinicians' compliance to the recommendations in the second opinion reports was also calculated. Logistic regression analyses were performed to determine the association of the referring clinicians' adherence to the recommendation in the second opinion report with the following variables: patient age, sex, hospitalization status, indication for the second opinion report, experience and NHN subspecialization of the radiologist who signed the second opinion report, the strength of the recommendation, and whether the recommendation was made due to apparent quality issues of the original examination.

Table 1: Patient and NHN examination characteristics for which a second opinion report was requested (n = 994)

Variable	No. (%)
Sex	
Female	541 (54.4)
Male	453 (45.6)
Hospital status	
Inpatient	76 (7.6)
Outpatient	918 (92.4)
No. of imaging examinations evaluated for the second opinion report ^a	
1	864 (86.9)
2	121 (12.2)
3	8 (0.8)
4	1 (0.1)
Imaging modalities for the second opinion report ^b	
CT	224 (19.8)
MR imaging	901 (79.5)
Ultrasonography	7 (0.6)
X-ray	2 (0.2)

^a A second opinion report is not necessarily based on 1 sole imaging examination —eg, both MR imaging and CT can be re-evaluated for the second opinion report.

^b Because some second opinion reports involved an evaluation of multiple imaging modalities, the numbers of imaging modalities used for second opinion reports (n = 1134) are higher than the number of reports included in this study.

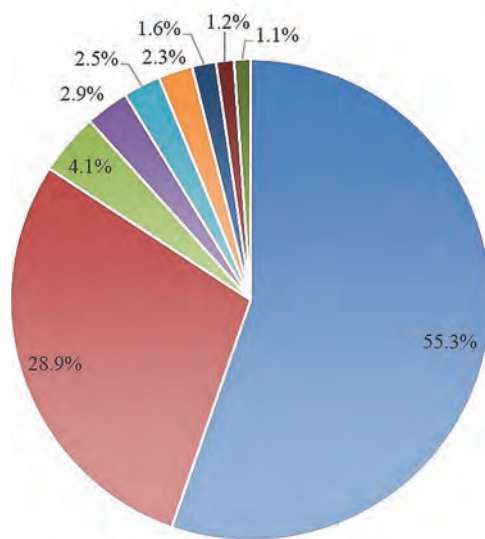


FIGURE. Frequencies of the different imaging indications for the 994 second opinion reports included in this study.

P values < .05 were deemed statistically significant. All statistical analyses were performed using the Statistical Package for the Social Sciences (SPSS, Version 23; IBM).

RESULTS

Second Opinion Reports

A total of 1038 second opinion reports of NHN imaging examinations were made at our tertiary care center between November 2016 and November 2017. Of these 1038 second opinion reports, 22 were excluded because no re-evaluation was performed because the second opinion reading became clinically irrelevant due to the availability of more recent imaging examinations, 11 were excluded because the report or the imaging examination was not available in the hospital's PACS, 10 were excluded because they did not primarily concern NHN imaging, and 1 was excluded because it concerned a re-evaluation of an in-house imaging examination. Eventually, 994 second opinion NHN imaging examinations were included, of which 115 (11.6%) involved comparisons with previous second opinion readings. These 994 second opinion reports concerned 453 male and 541 female patients, with a mean age of 50 (SD, 24) years (range, 0–96 years). Most patients were outpatients (92.4%), most imaging examinations were performed for oncologic reasons (55.3%), almost all imaging examinations concerned MR imaging (79.5%) or CT (19.8%), and most of the second opinion reports comprised 1 imaging examination (86.9%) (Table 1 and Figure). The second opinion reports were authorized by 20 radiologists, of whom 8 were subspecialized NHN radiologists. The mean number of second opinion reports per radiologist was 49.7 (SD, 65.1) (range, 1–197). The mean experience of the radiologists was 12 (SD, 9) years after completion of residency (range, 0–29 years).

Recommendations in Second Opinion Reports and Determinants

Of the 994 second opinion reports, 12.2% (121/994) contained a recommendation. The number of individual recommendations

Indication for the Second Opinion Report

■ Oncologic	n = 550
■ Miscellaneous	n = 287
■ Vascular	n = 41
■ Benign sellar/parasellar tumors	n = 29
■ Developmental	n = 25
■ Trauma	n = 23
■ Infectious	n = 16
■ Neurodegenerative	n = 12
■ Inflammatory	n = 11

totaled 134, because there were 112 reports with a single recommendation, 8 with 2 recommendations, and 2 reports with 3 recommendations. Apparent quality issues of the original imaging examination were responsible for 14.2% (19/134) of recommendations (Table 2). Recommendations involved additional imaging in 82.8% (111/134) and nonimaging procedures in 17.2% (23/134) (Table 3). The same examination (same technique, same body region) as the original study was recommended in 50 cases, of which 8 issues were due to the quality of the original imaging examination. Interrater reliability regarding the strength of the recommendation was almost perfect with $\kappa = 0.954$ (95% CI, 0.924–0.984). Most recommendations (48.5%) were issued by radiologists with 6–15 years of experience after residency (Table 4). Univariate logistic regression showed that an oncologic

imaging indication was significantly ($P = .030$) associated with a lower chance of a recommendation in the second opinion report (OR = 0.67; 95% CI, 0.46–0.96). There were no significant associations between the presence of a recommendation in the second opinion report and any other of the variables that were investigated. Therefore, no further multivariate analysis was performed.

Clinicians' Compliance to Recommendations in Second Opinion Reports and Determinants

Clinicians followed 65.7% (88/134) of the recommendations (Table 3). Medical follow-up records of at least 2 years confirmed that we did not miss any diagnostic test or other action performed at an outside/remote facility that was related to the recommendation in the second opinion report (ie, the treating physician in our academic hospital kept track of these patients and updated their medical documentation for a minimum of 2 years, as evidenced by our review of the medical records). Most interesting, 50% (44/88) of the recommendations that were followed were issued by radiologists with 6–15 years of experience after residency (Table 4). Note that for 4 recommendations, it remained unclear whether they were followed. Because 127 of the remaining 130 recommendations were issued by NHN radiologists, no meaningful statistical analysis could be made on the association between the referring clinicians' compliance with a recommendation in the second opinion report and the subspecialty of the radiologist (NHN versus other) who signed the second opinion report. Otherwise, there were no significant associations between the referring clinicians' compliance with the recommendation in the second opinion report and any of the variables that were investigated.

Table 2: Specifications of the 134 recommendations made in 121 of 994 NHN second opinion reports^a

Variable	No. (%)
Strength of the recommendation	
Hard	78 (58.2)
Soft	56 (41.8)
Recommendation made due to apparent quality issues of the original imaging examination	
Yes	19 (14.2)
No	115 (85.8)
Referring clinicians' compliance to the recommendation	
Followed	88 (65.7)
Not followed	42 (31.3)
Unknown	4 (3.0)

^a The total number of recommendations made is higher than the number of reports because 1 report may contain several recommendations at once.

Table 3: Distribution of recommendations according to 5 groups for recommendations that were followed, that were not followed, and for which it remained unclear whether the recommendation was followed (n = 134)

	Followed (%)	Not Followed (%)	Unknown (%)	Total (%)
RAI	75 (67.6)	36 (32.4)	0 (0.0)	111 (100.0)
Biopsy ^a	6 (75.0)	2 (25.0)	0 (0.0)	8 (100.0)
Referral to another specialty	4 (80.0)	1 (20.0)	0 (0.0)	5 (100.0)
Recommendation to compare with other previous imaging examination	2 (33.3)	3 (50.0)	1 (16.7)	6 (100.0)
Other ^b	1 (25.0)	0 (0.0)	3 (75.0)	4 (100.0)

Note:—RAI indicates recommendation for additional imaging.

^a Recommendations for tissue sampling, either imaging-guided or not.

^b Recommendations for all other procedures—eg, present the case in a multidisciplinary meeting.

Table 4: Distribution of categorized experience of the radiologist for recommendations that were followed, that were not followed, and for which it remained unclear whether the recommendation was followed (n = 134)

	Followed (%)	Not Followed (%)	Unknown (%)	Total (%)
Experience of the radiologist who signed the second opinion report ^a				
0–5 years	18 (64.3)	8 (28.6)	2 (7.1)	28 (100.0)
6–15 years	44 (67.7)	19 (29.2)	2 (3.1)	65 (100.0)
>16 years	26 (63.4)	0 (0.0)	15 (36.6)	41 (100.0)

^a Calculated from the end of residency.

Diagnostic Outcome Related to Recommendations in Second Opinion Reports

For second opinion reports with a recommendation, the diagnosis in the primary report was different from that in the second opinion report in 43 (35.5%) of 121 cases. No diagnostic change was found in 68 (56.2%) cases, whereas in the remaining 10 (8.3%) cases, the primary report was either unavailable or the second opinion report referred to only the poor quality of the imaging examination without mentioning a diagnosis. A definitive diagnosis could be established for 80 (59.7%) recommendations. This was based on additional procedures and test results in 69 (86.3%) cases and in 11 (13.8%) cases on the imaging examination for which the second opinion reading was requested. In total, the 134 individual recommendations in the second opinion reports eventually led to the establishment of 52 (38.2%) benign diagnoses and 28 (20.6%)

Table 5: Distribution of diagnostic outcome for recommendations that were followed, that were not followed, and for which it remained unclear whether the recommendation was followed (n = 136)^a

	Followed (%)	Not Followed (%)	Unknown (%)	Total (%)
Benign	44 (84.6)	6 (11.5)	2 (3.8)	52 (100.0)
Malignant	21 (75.0)	5 (17.9)	2 (7.1)	28 (100.0)
Unknown	24 (42.9)	31 (55.4)	1 (1.8)	56 (100.0)

^a Because some reports contained 1 recommendation asking to check on 2 different structures, the total number is higher than the total count of recommendations (eg, 1 MR imaging focused on the orbits and 1 MR imaging focused on the cerebellopontine angle). The diagnostic outcome was defined as having established either a benign or a malignant diagnosis for a perceived lesion based on the results of the recommended additional diagnostic tests, which clarified perceived lesion nature, or on the second opinion report itself if it already provided a definitive diagnosis.

Table 6: Reference standards of the established benign and malignant diagnoses in the study sample (n = 80)

	Benign (%)	Malignant (%)
Imaging examination	31 (59.6)	7 (25.0)
Biopsy	9 (17.3)	15 (53.6)
Operation	5 (9.6)	6 (21.4)
Follow-up diagnostic tests ^a	4 (7.7)	0 (0.0)
Application of the MDS-PSP criteria	2 (3.8)	0 (0.0)
Clinical evaluation	1 (1.9)	0 (0.0)

Note:—MDS-PSP indicates Movement Disorder Society progressive supranuclear palsy criteria.

^a Either performed by a clinical specialist or lab results or imaging examinations.

malignant diagnoses, while no definitive diagnosis could be established in 56 (41.2%) cases (Table 5). Most benign diagnoses were established on the basis of imaging examinations (n = 31, 59.6%); most malignant diagnoses were based on biopsies (n = 15, 53.6%) (Table 6). Note that 2 second opinion reports, each with a single recommendation, both led to 2 different diagnoses, as a result of which the total number of established and unestablished diagnoses was 136.

DISCUSSION

The results of this study show that 12.2% of second opinion reports of NHN imaging examinations contain a recommendation and that this recommendation was followed by the referring physician in 65.7% of cases. In addition, the recommendations that were made in the second opinion report led to a definitive diagnosis (either benign or malignant) in most cases. Also of interest is that for second opinion reports with a recommendation, the diagnosis of the primary report had already changed with the second opinion reading itself in about one-third of cases. These data indicate that the practice of second opinion reporting in NHN imaging, with a provision of a recommendation to the clinician when appropriate, adds clinical value. They also support that the increasing workload of academic radiologists due to the continuing increase in requests for second opinion reports of NHN imaging examinations^{1,3} should be acknowledged by health care systems, insurance companies, and policy makers. Of note, at present, neither our department nor our hospital receives any reimbursement for the second opinion readings that are performed.

Our results also show that second opinion reports of imaging examinations with an oncologic indication had an approximately one-third lower chance of containing a recommendation than those with other imaging indications. This is probably because

for many common NHN cancers (eg, cerebral glioma or head and neck squamous cell carcinoma), differential diagnostic dilemmas are less common and the subsequent diagnostic work-up is protocolized and well-known among both radiologists and referring physicians.^{10–13} The finding that radiologists relatively less frequently add a recommendation to their second opinion report in these circumstances may be potentially useful when weighing the expected benefits against the labor

spent on a second opinion report when clinicians submit a second opinion request.

On the other hand, none of the patient and second opinion variables that were investigated were significantly associated with the referring physician's adherence to the recommendation in the second opinion report. Of interest, a previous study by our research group showed that 16.4% (191/1,163) of second opinion NHN imaging reports in our patient population in 2018 were actually never read at all by a clinician.¹⁴ In that same study that included second opinion reports from all different radiologic subspecialties, it was also reported that second opinion reports with neurology as the requesting specialty were significantly ($P < .001$) more prone to remaining unread compared with other requesting specialties (including otorhinolaryngologists) (OR = 2.82; 95% CI, 1.78–4.47).¹⁴ Why neurologists more frequently refrain from reading the second opinion report they request remains unclear, but it explains why some recommendations were not followed. Of note, the present study was performed between November 2016 and November 2017, when it was not yet possible to verify whether second opinion reports were read due to technical limitations. However, because the clinical scenario in our previous study¹⁴ is the same as in the present study, the “nonreading” percentage of 16.4% is probably also applicable to the current data set. Further research is necessary to identify other sources of noncompliance to the recommendation in the second opinion report.

There is ample literature on the frequency of recommendations for additional imaging and the adherence by clinicians to these recommendations when it comes to primary imaging readings. For example, a study by Sistrom et al¹⁵ analyzed 5,948,342 radiology reports of different modalities performed between 1995 and 2008 and reported that recommendations for additional imaging increased during the 13 years of the study, with the unadjusted rate rising from roughly 6% to 12%. In another more recent study by Mabotuwana et al¹⁶ that analyzed 2,972,164 radiology examinations performed between 2010 and 2017, there was at least 1 recommendation for follow-up imaging in 10.6% of radiology reports, while the overall follow-up imaging adherence rate was 58.1%. However, the studies by Sistrom et al¹⁵ and Mabotuwana et al¹⁶ did not concern second opinion reports, did not focus on NHN imaging, and did not consider recommendations for nonimaging procedures. Nevertheless, the frequencies of recommendations and compliance rates are quite similar between the present study and those reported by Sistrom et al¹⁵ and Mabotuwana et al.¹⁶

Literature on the topic of second opinion readings is scarce. A previous study by Heinz et al¹⁷ analyzed 2225 second opinion reports of abdominal imaging examinations performed at outside institutions. They reported that 10.4% of secondary abdominal imaging interpretations contained a recommendation for additional imaging and that patient age and the experience of the radiologist who performed the secondary interpretation were independently significantly associated with the presence of a recommendation for additional imaging.¹⁷ Heinz et al¹⁸ also reported an adherence rate of 53.1% to recommendations in second opinion radiology reports of abdominal imaging examinations, while no determinants of the referring physician's compliance could be identified. Finally, the recommendations that were made in the second opinion reports in the study by Heinz et al¹⁸ led to a definitive diagnosis in 41.1%. Although this previous work by Heinz et al^{17,18} was performed in the setting of abdominal imaging, their results on the frequency of recommendations, compliance rate, and diagnostic yield largely resonate with the findings of the present study. A study by Torok et al¹⁹ included 11,753 reports of their Neuroradiology Second Opinion Consultation Services to analyze requests for repeat imaging. In their study, repeat imaging studies were recommended in 1.5% of cases.¹⁹ In addition, in 0.3% of all cases, a subsequent repeat examination was documented in the electronic medical records.¹⁹ However, the study of Torok et al¹⁹ was focused only on recommendations for repeat imaging, used a search strategy based on keywords, and may have underestimated the rate of followed recommendations due to missing clinical information.

The present study had several limitations. First, this study was performed at a tertiary care center where all medical specialists receive a fixed salary, regardless of the number of procedures performed. Therefore, there were no financial incentives for radiologists to add a recommendation to the second opinion report or for referring physicians to follow a recommendation. However, it is unclear whether the results of our study are also applicable to institutions in which the remuneration of medical specialists is, in part, dependent on production numbers.^{16,20,21} Second, most second opinion reports concerned oncologic patients. It is unclear whether the results of this study are generalizable to institutions that provide health care services to a different spectrum of patients undergoing NHN imaging. Third, most recommendations were made by NHN radiologists. Therefore, no logistic regression analysis could be made to compare the compliance of referring physicians with the recommendations made by NHN radiologists versus other radiologists, and no subgroup analyses could be performed to compare these 2 groups in terms of diagnostic yield related to the recommendations made. Thus, it remains unclear if recommendations in second opinion NHN imaging reports made by radiologists without NHN subspecialization also affect patient care. Fourth, there was no analysis on whether the recommendations in the second opinion reports actually improved patient outcome. Fifth, the diagnostic outcome was not always established on the basis of additional procedures and diagnostic tests, but on the imaging examination for which a second opinion reading was requested. This issue may limit the reliability of the established diagnoses. Sixth, because virtually all conversations between clinicians and radiologists about second

opinion requests take place on nonrecorded phone calls, it remains unclear how many second opinion requests were rejected.

CONCLUSIONS

Recommendations are relatively common in second opinion reports of NHN imaging examinations, though this is less the case for oncologic indications. They are mostly followed by requesting physicians, thus affecting patient management. In most cases, they also lead to the establishment of a diagnosis, hence adding value to patient care.

REFERENCES

- Rosenkrantz AB, Glover M, Kang SK, et al. **Volume and coverage of secondary imaging interpretation under Medicare, 2003 to 2016.** *J Am Coll Radiol* 2018;15:1394–1400 CrossRef Medline
- Eakins C, Ellis WD, Pruthi S, et al. **Second opinion interpretations by specialty radiologists at a pediatric hospital: rate of disagreement and clinical implications.** *AJR Am J Roentgenol* 2012;199:916–20 CrossRef Medline
- Hatzoglou V, Omuro AM, Haque S, et al. **Second-opinion interpretations of neuroimaging studies by oncologic neuroradiologists can help reduce errors in cancer care.** *Cancer* 2016;122:2708–14 CrossRef Medline
- Khoshpouri P, Khoshpouri P, Yousem KP, et al. **How do American radiology institutions deal with second opinion consultations on outside studies?** *AJR Am J Roentgenol* 2020;214:144–48 CrossRef Medline
- Briggs GM, Flynn PA, Worthington M, et al. **The role of specialist neuroradiology second opinion reporting: is there added value?** *Clin Radiol* 2008;63:791–95 CrossRef Medline
- Khalilzadeh O, Rahimian M, Batchu V, et al. **Effectiveness of second-opinion radiology consultations to reassess the cervical spine CT scans: a study on trauma patients referred to a tertiary-care hospital.** *Diagn Interv Radiol* 2015;21:423–27 CrossRef Medline
- Lysack JT, Hoy M, Hudon ME, et al. **Impact of neuroradiologist second opinion on staging and management of head and neck cancer.** *J Otolaryngol Head Neck Surg* 2013;42:39–45 CrossRef Medline
- Zan E, Yousem DM, Carone M, et al. **Second-opinion consultations in neuroradiology.** *Radiology* 2010;255:135–41 CrossRef Medline
- Loevner LA, Sonners AI, Schulman BJ, et al. **Reinterpretation of cross-sectional images in patients with head and neck cancer in the setting of a multidisciplinary cancer center.** *AJNR Am J Neuroradiol* 2002;23:1622–26 Medline
- Weller M, van den Bent M, Tonn JC, et al. European Association for Neuro-Oncology (EANO) Task Force on Gliomas. **European Association for Neuro-Oncology (EANO) guideline on the diagnosis and treatment of adult astrocytic and oligodendroglial gliomas.** *Lancet Oncol* 2017;18:e315–29 CrossRef Medline
- Jiang T, Nam DH, Ram Z, et al. Chinese Glioma Cooperative Group (CGCG); Society for Neuro-Oncology of China (SNO-China); Chinese Brain Cancer Association (CBCA); Chinese Glioma Genome Atlas (CGGA); Asian Glioma Genome Atlas (AGGA) network. **Clinical practice guidelines for the management of adult diffuse gliomas.** *Cancer Lett* 2020;6:S0304–35 CrossRef Medline
- Machiels JP, René Leemans C, Golusinski W, et al. EHNS Executive Board, ESMO Guidelines Committee, ESTRO Executive Board. **Squamous cell carcinoma of the oral cavity, larynx, oropharynx and hypopharynx: EHNS-ESMO-ESTRO Clinical Practice Guidelines for diagnosis, treatment and follow-up.** *Ann Oncol* 2020;31:1462–75 CrossRef Medline
- Maghami E, Ismaila N, Alvarez A, et al. **Diagnosis and management of squamous cell carcinoma of unknown primary in the head and neck: ASCO guideline.** *J Clin Oncol* 2020;38:2570–96 CrossRef Medline

14. Heinz SA, Kwee TC, Yakar D. **Unread second-opinion radiology reports: a potential waste of health care resources.** *AJR Am J Roentgenol* 2020;215:934–39 CrossRef Medline
15. Siström CL, Dreyer KJ, Dang PP, et al. **Recommendations for additional imaging in radiology reports: multifactorial analysis of 5.9 million examinations.** *Radiology* 2009;253:453–61 CrossRef Medline
16. Mabotuwana T, Hombal V, Dalal S, et al. **Determining adherence to follow-up imaging recommendations.** *J Am Coll Radiol* 2018;15:422–28 CrossRef Medline
17. Heinz SA, Kwee TC, Yakar D. **Recommendations for additional imaging of abdominal imaging examinations: frequency, benefit, and cost.** *Eur Radiol* 2020;30:1137–44 CrossRef Medline
18. Heinz SA, Yakar D, Kwee TC. **Recommendations in second opinion radiology reports of abdominal imaging examinations: referring clinicians' compliance and diagnostic outcome.** *AJR Am J Roentgenol* 2020;214:400–05 CrossRef Medline
19. Torok CM, Lee C, Nagy P, et al. **Neuroradiology second opinion consultation service: assessment of duplicative imaging.** *AJR Am J Roentgenol* 2013;201:1096–1100 CrossRef Medline
20. Dalal S, Hombal V, Weng WH, et al. **Determining follow-up imaging study using radiology reports.** *J Digit Imaging* 2020;33:121–30 CrossRef
21. Bretas ES, Guimarães RM, Aihara AY, et al. **Estimating the productivity of radiologists in Brazil: the search for a benchmark.** *Radiol Bras* 2020;53:73–80 CrossRef Medline

Dual-Layer Spectral CT Imaging of Upper Aerodigestive Tract Cancer: Analysis of Spectral Imaging Parameters and Impact on Tumor Staging

C.C.-T. Hsu, C. Jeavon, I. Fomin, L. Du, C. Buchan, T.W. Watkins, Y. Nae, N.M. Parry, and R.I. Aviv



ABSTRACT

BACKGROUND AND PURPOSE: Dual-layer spectral CT is a novel technology that utilized conventional single-tube CT acquisition with a dual-layer detector for the separation of high and low-energy photons to create spectral data for material decomposition. We evaluated the spectral parameters of iodine density and Z-effective values in primary head and neck squamous cell carcinoma and determined its impact on local tumor staging.

MATERIALS AND METHODS: Twenty-one patients with primary head and neck squamous cell carcinoma and 15 healthy controls were retrospectively evaluated. Iodine density (milligram/milliliter) and Z-effective values were compared quantitatively between head and neck squamous cell carcinoma and normal neck mucosa. The receiver operating characteristic area under the curve determined the diagnostic performance of the spectral data for local staging. We compared conventional CT images without and with iodine density and Z-effective images to determine its impact on local tumor staging.

RESULTS: Primary head and neck squamous cell carcinoma showed higher mean iodine density (2.01 [SD, 0.26] mg/mL, $P < .001$) and Z-effective values (8.21 [SD, 0.36], $P < .001$). A high interobserver correlation was demonstrated for ROI measurements for both the control group (iodine density, $\kappa = 0.71$, and Z-effective values, $\kappa = 0.78$) and head and neck squamous cell carcinoma (iodine density, $\kappa = 0.84$, and Z-effective values, $\kappa = 0.75$) group. The area under the curve for iodine density and Z-effective values was 0.98 and 0.93, respectively. Optimal thresholds were identified as 1.58 mg/mL (95% CI, 1.45–1.71 mg/mL; $P < .001$; sensitivity = 1.0; specificity = .093) for iodine density and 8.08 (95% CI, 7.96–8.19; $P < .001$; sensitivity = 0.86; specificity = 0.93) for Z-effective values. Conventional CT with the addition of dual-layer spectral data (iodine density and Z-effective values) improved the accuracy of local tumor staging in 3 of 21 patients (14%) with head and neck squamous cell carcinoma compared with the criterion standard surgical staging/histopathology.

CONCLUSIONS: Dual-layer spectral iodine density and Z-effective values provided increased quantitative and qualitative differentiation between upper aerodigestive head and neck squamous cell carcinoma and normal mucosa. Increased tissue differentiation improved the local tumor staging accuracy.

ABBREVIATIONS: DLSCCT = dual-layer spectral CT; HPV = human papillomavirus; HNSCC = head and neck squamous cell carcinoma; ROC = receiver operating characteristic

Head and neck squamous cell carcinoma (HNSCC) is one of the most common malignant cancers of the upper aerodigestive tract. CT and MRI are used for diagnosis and local

staging. Recent advances in CT technologies include dual-energy CT scanners. A variety of dual-energy CT systems are available from multiple vendors including dual-source, single-source (rapid kilovolt switching or twin-beam), and dual-layer detector-based technologies.^{1–5} Postprocessed images from dual-energy CT scanners improve tissue contrast on the basis of the attenuation profile and chemical composition. The dual-layer spectral

Received August 3, 2020; accepted after revision April 20, 2021.

From the Division of Neuroradiology (C.C.-T.H., C.J., I.F., C.B., N.M.P.), Department of Medical Imaging and Division of Nuclear Medicine (L.D.), and Department of Medical Imaging, Gold Coast University Hospital, Queensland, Australia; Department of Medical Imaging (T.W.W.), Princess Alexandra Hospital, Queensland, Australia; Philips Healthcare (Y.N.), Haifa, Israel; and Division of Neuroradiology (R.I.A.), Department of Medical Imaging, The Ottawa Hospital, University of Ottawa, Ontario, Canada.

This study was awarded the Gabriel H. Wilson Award at the Western Neuroradiology Society Annual Meeting, September 26–29, 2019; Coeur d'Alene, Idaho, and was represented at the Annual Meeting of the American Society of Neuroradiology, May 30 to June 4, 2020; Virtual.

Please address correspondence to Dr. Charlie Chia-Tsong Hsu, MBBS, FRANZCR, Division of Neuroradiology, Department of Medical Imaging, Gold Coast University Hospital, 1 Hospital Blvd, Southport, Queensland 4215, Australia; e-mail: charlie.ct.hsu@gmail.com

Indicates article with online supplemental data.

<http://dx.doi.org/10.3174/ajnr.A7239>

CT system (DLSCCT) (IQon Spectral CT; Philips Healthcare) uses a conventional single x-ray tube acquisition with a dual-layer detector.^{5,6} The dual-layer detector distinguishes between low- and high-photon energies. High- and low-energy raw data from the dual-layer detectors are used for the extraction of 2 base models: Compton scattering-like and photoelectric-like effects. DLSCCT parameters derived from the 2 base models are used to reconstruct the iodine density and Z-effective spectral images.⁶ The use of a dual-layer detector enables the acquisition of spectral data being always on despite the conventional (single-tube) CT acquisition, which is different from other commercially available dual-energy CT technologies that use either dual-source (2-tube) or kilovolt switching.

A recent study by van Ommen et al⁷ concluded that dual-layer detector CT enables the acquisition of dual-energy information over a broad range of clinical indications without increasing the radiation exposure compared with a conventional single-layer-detector CT. Quantitative analysis of tissue using these spectral parameters has been made more accessible through the integration of the IntelliSpace Portal software (Philips Healthcare) into the PACS system allowing on-demand analysis of the DLSCCT data (iodine density and Z-effective values) for the radiologist's assessment. Lohöfer et al⁵ are the only group to have previously assessed DLSCCT parameters in patients with HNSCC. They found that tumor tissue had a higher iodine density content compared with the surrounding soft tissue. This study was limited to only iodine density parameter assessment and did not assess diagnostic accuracy or the clinical impact of this single spectral parameter on local tumor staging. The utility of the Z-effective spectral parameter has not been previously reported in HNSCC. The purpose of this study was 3-fold: to define normal mucosal iodine density and Z-effective values, to quantitatively assess iodine density and Z-effective values of HNSCC, and to determine the diagnostic accuracy of Z-effective values and iodine density enhancements of conventional CT on tumor detection. We also, descriptively, looked at the effect on local tumor staging when these spectral parameters were used.

MATERIALS AND METHODS

Patients

This study was approved by the institutional ethics review board at the Gold Coast University Hospital, Queensland, Australia. Fifteen consecutive controls and 26 patients with upper aerodigestive HNSCC scanned with the DLSCCT between June 2019 and March 2020 were identified. Scans of healthy controls comprised normal or near-normal scan results with minor incidental findings (dental periapical lucencies, benign reactive lymph nodes or tonsillar enlargement, and incidental cutaneous lesions such as sebaceous cysts) and no known local or distant malignancy. Inclusion criteria for the patient cohort with HNSCC were patients with histopathologically proved upper aerodigestive tract HNSCC. Participants with confirmed human papillomavirus (HPV)-associated HNSCC were included. Exclusion criteria were suspected HNSCC without histopathologic confirmation and any tumor too small for sampling by the minimum preset ROI. The final study cohort comprised 21 patients with upper aerodigestive HNSCC.

CT Scanning Technique

All patients underwent a head and neck protocol using the same DLSCCT scanner (IQon Spectral CT). Images were acquired after injection of 50 mL of Optiray 350 (Mallinckrodt; 74.0 g/100 mL) at a rate of 1.5 mL/s, followed by a further 50 mL of Optiray 350 injected at a rate of 2 mL/s after a delay of 100 seconds. Patients were scanned 160 seconds after the start of the first contrast bolus. The scanned volume extended from the aortic arch to the top of the ear with a reconstructed FOV of 250 mm, 64 × 0.625 mm beam collimation, 0.27-second rotation time, and 1.234:1 helical pitch. IQon Spectral CT uses conventional CT acquisitions with a dual-layered scintillation detector, comprising an upper layer of an yttrium-based garnet low-density scintillator for detection of lower energy photons and a lower layer of a gadolinium oxysulphide high-density scintillator for detection of higher energy photons. The design of the thickness of the 2 scintillators is optimized for energy separation and an optimal SNR. While all photons are represented superficially, lower energy photons are filtered out with increased depth. The difference in detected photon energy is secondary to augmentation by tissues of different densities. Combining the raw data from each detector layer, IntelliSpace Portal software (Philips Healthcare) reconstructs CT images as conventional CT and additional spectral data overlay maps for each parameter.

Specifically, 2 spectral parameters, iodine density with and without color overlay and Z-effective color overlay, were analyzed in this study. The Z-effective value is the effective atomic number of the tissue, representing the combination of atomic numbers of the elements that comprise the tissue.⁶ The Z-effective value is measured by the ratio between 2 monoenergetic density coefficients, according to the Joshi Method, and is calibrated on the DLSCCT system by fitting measured data to expected values from the National Institute of Standards and Technology data base.^{6,8} The Z-effective value is dimensionless and has no unit of measure. The calculation of the ratio between density coefficients at 2 energies eliminates the dependency on material density. Non-iodine-enhanced soft tissue is expected to have an effective atomic number of about 7.5, whereas with the presence of iodine, the effective atomic number is increased, accounting for the iodine molecules within the soft tissue. The iodine density result is derived by projecting each voxel from the Compton scattering/photoelectric base to the water/iodine base and quantifying the magnitude of the iodine projection.⁶ The water/iodine base is defined using the National Institute of Standards and Technology data base, in which water and iodine densities are projected to the Compton scattering and photoelectric base functions. Non-iodine-enhanced soft tissue is expected to have zero or close to zero iodine content in contrast to iodine-enhanced tissue. Iodine density is measured by milligram/milliliter.

Postprocessing and Image Analysis

For each patient, qualitative assessment and quantitative spectral analysis were performed using the IntelliSpace Portal software (Philips advanced visualization platform, Version 9.0) for the iodine density, iodine density color overlay, and Z-effective images. Each study was initially read independently by 2 readers, C.C.-T.H. (a fellowship-trained neuroradiologist with 5 years of experience)

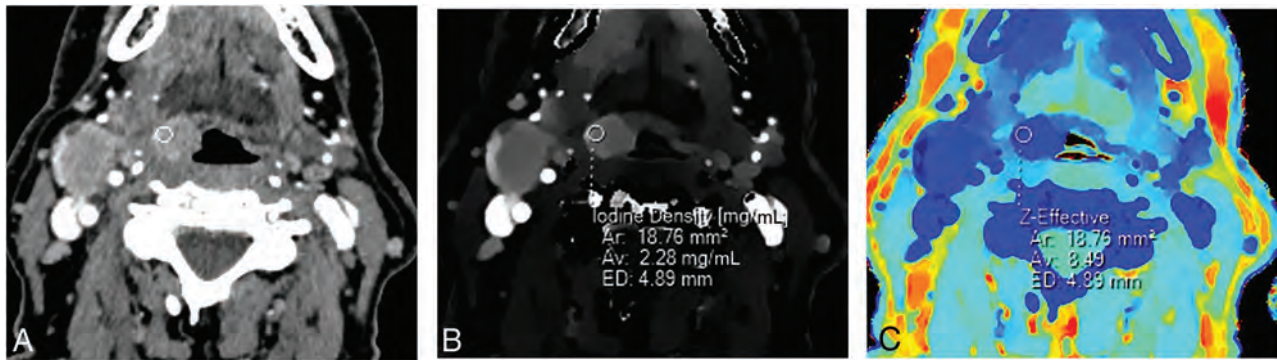


FIG 1. Conventional (A), iodine density (B), and Z-effective (C) images illustrating an ROI placed over a right tongue base squamous cell carcinoma. ROI size is 4.89 mm in diameter (ED), with an average area (Av) of 18.76 mm². ROI measurements were obtained over 3 image slices (not shown), with the average iodine and Z-effective values calculated. A right level IIa cystic nodal metastasis is also present (not labeled).

Summary of iodine density and Z-effective values for normal tissue subsites

Normal Tissue	Iodine Density (mg/mL) (Mean) (SD)	Z-Effective Value (Mean) (SD)
Mucosal subsites		
Floor of mouth	(1.43) (0.26)	(7.95) (0.31)
Buccal mucosa	(0.83) (0.13)	(7.41) (0.24)
Oral tongue	(0.92) (0.17)	(7.67) (0.24)
Soft palate	(1.25) (0.35)	(7.96) (0.26)
Palatine tonsils	(1.32) (0.39)	(8.01) (0.26)
Tongue base	(1.22) (0.48)	(7.89) (0.30)
Aryepiglottic fold	(1.12) (0.38)	(7.79) (0.28)
Vocal fold	(1.13) (0.32)	(7.87) (0.29)
Post-cricoid hypopharynx	(1.02) (0.55)	(7.75) (0.39)
Cervical esophagus	(1.23) (0.60)	(7.91) (0.39)
All mucosa	(1.15) (0.23)	(7.82) (0.34)
Muscle subsites		
SCM	(0.77) (0.20)	(7.84) (0.57)
Longus coli	(0.89) (0.21)	(7.76) (0.16)
Genioglossus	(0.73) (0.22)	(7.67) (0.17)
All muscle	(0.80) (0.22)	(7.76) (0.35)

Note:—SCM indicates sternocleidomastoid muscle.

and L.D. (a fellowship-trained radiologist and nuclear medicine specialist with 10 years of experience), with final placement of ROIs performed together through a consensus reading session. Normal structures were evaluated with 3 nonoverlapping circular ROIs. A total of 10 mucosa and 3 muscle subsites were evaluated, each with 3 ROIs, corresponding to a total of 39 ROIs per control subject. The average ROI area evaluated per structure was 53.2 mm² (range, 25.4–67.8 mm²). For HNSCC, each tumor was evaluated, with a total of 9 ROIs placed on at least 3 separate sections. The tumor ROIs were placed in the homogeneous-appearing enhancing part of the lesion, avoiding areas of cystic change/necrosis or visible artifacts. The minimum individual ROI diameter used was 3 mm (sampled ROI of 7.1 mm²), and the maximum diameter used was 5 mm (sampled ROI of 19.6 mm²) (Fig 1). Mean (SD) iodine density (milligrams/milliliter) and Z-effective values were measured within the ROIs. The average value of the 3 ROIs per area was recorded. Normative data for mucosa and muscles were obtained at 6 different levels in the head and neck on the axial

plane to enable sampling of the mucosa subsites, including the floor of the mouth, buccal mucosa, oral tongue, palatine tonsil, soft palate, tongue base, aryepiglottic fold, vocal fold, post-cricoid hypopharynx, and cervical esophagus. Measured neck muscles from cranial to caudal included the following: longus coli, genioglossus, and the sternocleidomastoid muscle. For consistency, the right side of the neck was evaluated, except for the genioglossus muscles, for which because of their relatively small size, the largest available structure of both sides was evaluated. The time taken to interpret and perform the spectral analysis in healthy controls and subjects with HNSCC was recorded in minutes.

Local Tumor Staging

Two readers (C.C.-T.H. and L.D.) blinded to the clinical history reviewed the DLSCT studies independently; if any discrepancy occurred, the final staging was decided by consensus. Two reading sessions occurred a week apart. In the first reading session, only the conventional CT images (120 kV[peak]) were available. In the second reading session, the conventional CT images with the addition of the iodine density, color overlay iodine density, and Z-effective spectral images were available. The local tumor staging data were compared with the surgical tumor stage determined from the multidisciplinary team meeting after histopathologic confirmation. The outcome of radiologic assessment compared with surgical staging was recorded as no change in T-staging, upstaging, or downstaging.

Statistical Analysis

All statistical analyses were computed using STATA (Version 12.1; StataCorp). Mucosa, muscle, and tumor tissue iodine density and Z-effective values were reported as mean and SD. Comparison of iodine density and Z-effective values between HNSCC and healthy muscle and mucosa was performed using an unpaired 2-tailed Student *t* test. The absolute contrast difference between HNSCC and healthy mucosa iodine and Z-effective images was calculated because both the iodine density and Z-effective images are noiseless with the SD approaching 0. Receiver operating Characteristic (ROC) curves quantified the performance of iodine density and Z-effective values to discriminate tumor from normal mucosal tissue. ROC areas under the curve were presented as an overall assessment of the diagnostic value of each technique and were compared. An

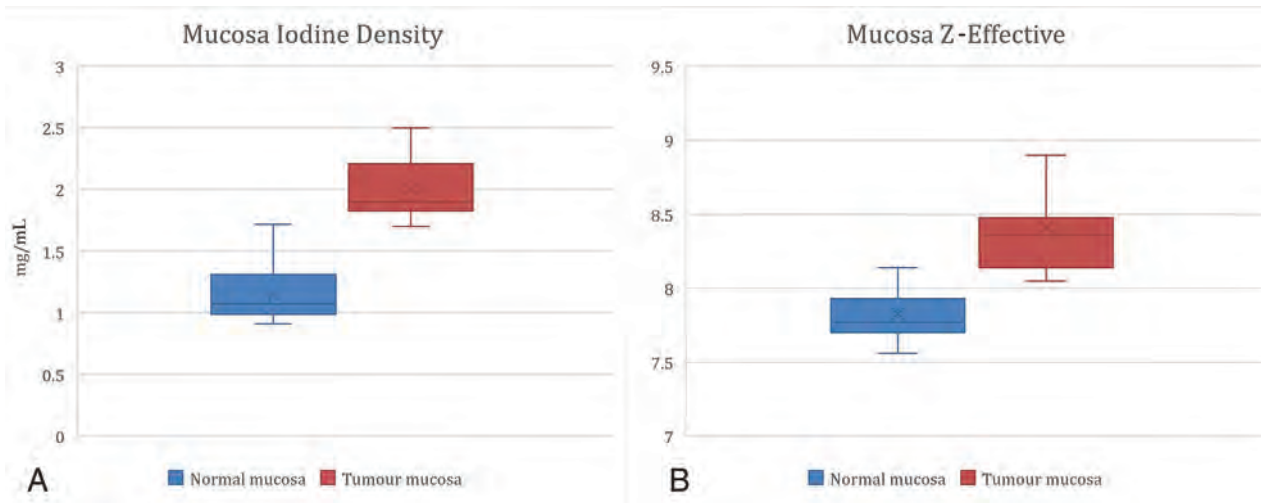


FIG 2. Head and neck squamous cell carcinomas demonstrate a higher mean iodine density = 2.01 (SD 0.26) mg/mL (95% CI, 1.70–2.51 mg/mL) and mean Z-effective value = 8.21 (SD, 0.360) (95% CI, 8.05–8.91) compared with normal tissue ($P < .001$).

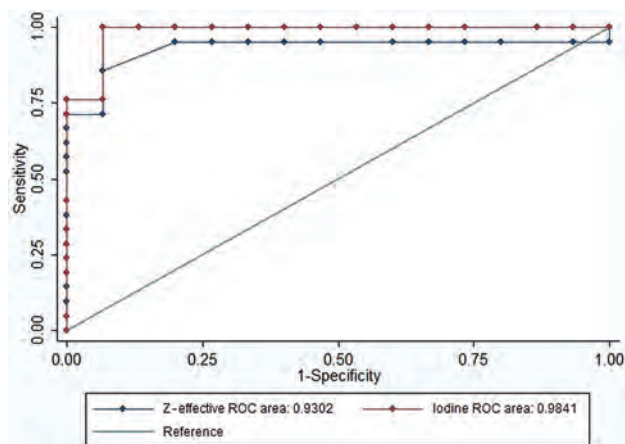


FIG 3. ROC plot of the iodine density and Z-effective values for differentiation of upper aerodigestive HNSCC from normal mucosa tissue. The optimal iodine density cutoff is 1.58 (95% CI, 1.45–1.71; $P < .001$) with a sensitivity of 1 and a specificity of 0.93. The optimal Z-effective cutoff is 8.08 (95% CI, 7.96–8.19; $P < .001$) with a sensitivity of 0.86 and a specificity of 0.93, respectively.

optimal cut-point for each was determined (Youden Index: maximum sensitivity + specificity–1) that maximized both sensitivity and specificity. Using these cut-points for the Z-effective score and iodine density, we compared tumor identification with the predefined histopathologic tumor status. The κ statistic was used to assess the level of agreement between each spectral technique and known tumor status. The number and details of nonagreement were also noted. Finally, descriptive statistical analysis of the local tumor staging of conventional CT images only versus conventional CT with the addition of each spectral data technique was compared with the criterion standard surgical staging/histopathology. Time taken to interpret and perform the spectral analysis was recorded. Mean (SD) and range taken for each reader to interpret the spectral data were calculated.

RESULTS

Quantitative Data

The control group comprised 15 patients (7 women and 8 men; age range, 21–84 years; mean age, 55.3 [SD, 18.9] years). Iodine density and Z-effective values for normal tissue subsites are summarized in the Table. Iodine density and Z-effective values showed slight variation among the mucosa subsites, with the floor of mouth and palatine tonsil having the highest values and buccal mucosa being the lowest.

The HNSCC group consisted of 21 patients (5 women and 16 men; age range, 35–80 years; mean age, 62.0 [SD 10.2] years). Patient demographics and tumor subsite distributions are shown in the Online Supplemental Data. Four participants had histologically confirmed HPV-positive HNSCC. The HPV-associated HNSCC was not statistically analyzed as a separate entity due to the small sample size, in order to produce meaningful statistical results.

The mean iodine density value of tumor was 2.01 (SD 0.26) mg/mL (95% CI, 1.70–2.51 mg/mL), and the Z-effective value was 8.21 (SD, 0.36) (95% CI, 8.05–8.91). HNSCC demonstrated a higher mean iodine density ($P < .001$) and Z-effective values ($P < .001$) (Fig 2) compared with normal tissue. The absolute contrast difference between healthy mucosa and HNSCC for iodine density and Z-effective values was 0.87 mg/mL and 0.38, respectively. A high interobserver correlation was demonstrated for placement of the ROI for both normal mucosa of the control group (iodine density, $\kappa = 0.71$, and Z-effective values, $\kappa = 0.78$) and the HNSCC group (iodine density, $\kappa = 0.84$, and Z-effective values, $\kappa = 0.75$). The ROC area under the curve was slightly greater for iodine density, 0.98, in comparison with the Z-effective value, 0.93 ($P = .27$) (Fig 3). The optimal iodine density threshold of 1.58 showed a sensitivity of 1 and specificity of 0.93, while the optimal Z-effective threshold of 8.08 showed a sensitivity of 0.86 and specificity of 0.93, respectively.

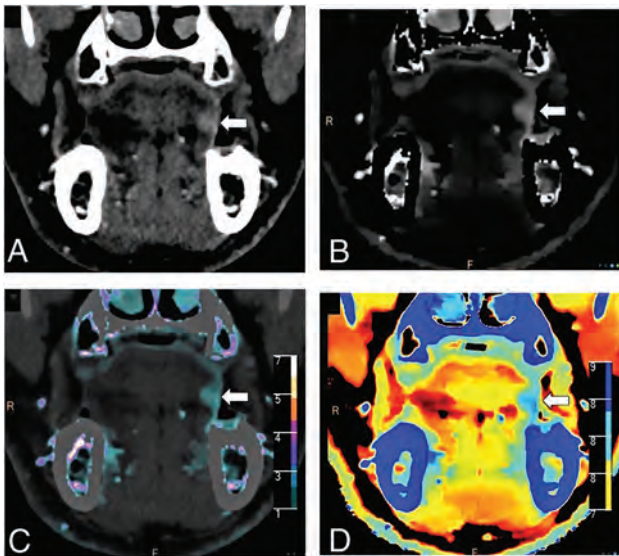


FIG 4. A 61-year-old man with left oral tongue squamous cell carcinoma (arrow) seen on a conventional CT image (A). Iodine density (B), color iodine density overlay (C), and Z-effective (D) images show markedly improved contrast resolution of the tumor from the surrounding normal oral tongue mucosa. The left oral tongue tumor has an iodine density = 2 mg/mL and a Z-effective value = 8.33. Normative oral tongue mucosa values from the healthy control cohort are iodine density = 0.92 mg/mL and Z-effective value = 7.67.

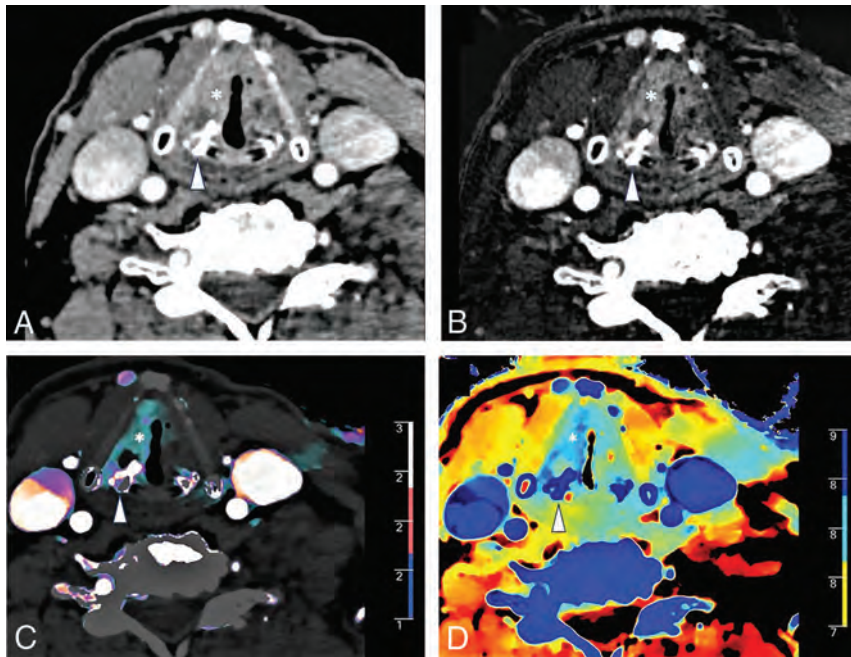


FIG 5. A 70-year-old man with left vocal cord squamous cell carcinoma (asterisk) and asymmetric sclerosis of the right arytenoid cartilage (arrowhead) seen on a conventional CT image (A). Iodine density (B), color iodine density overlay (C), and Z-effective (D) images reveal right paraglottic fat involvement with increased iodine density. The patient was upstaged from T2 to T3.

Qualitative Results: Impact on Staging

The addition of iodine density and Z-effective images improved local tumor staging compared with the conventional CT images (120 kVp) alone. Visually, the iodine density and Z-effective

images provided better delineation of the tumor margin (Fig 4). Upstaging occurred in 3 patients, which included detection of paraglottic involvement in vocal cord squamous cell carcinoma (T2 to T3) (Fig 5), cartilage invasion in post-cricoid hypopharyngeal squamous cell carcinoma (T3 to T4a), and mandible bone invasion from buccal/alveolar mucosa squamous cell carcinoma (T3 to T4a) (Fig 6). No false-positive cases were encountered.

Time Taken for the Interpretation of the Spectral Images

The time taken to interpret and perform the spectral analysis was recorded. Reader 1 took 13.53 (SD, 1.77) minutes (range, 12–18 minutes) to analyze the spectral CT data for healthy subjects and 15.25 (SD 1.68) minutes (range, 13–19 minutes) to analyze the spectral CT data for subjects with HNSCC. Reader 2 took 13.60 (SD, 1.90) minutes (range, 11–18 minutes) to analyze the spectral CT data for healthy subjects and 15.55 (SD, 1.7) minutes (range, 12–20 minutes) to analyze the spectral CT data for subjects with HNSCC.

DISCUSSION

The results demonstrate that quantitative analysis of spectral CT data can improve diagnostic confidence in local staging of upper aerodigestive HNSCC. Our patient cohort with upper aerodigestive HNSCC showed higher iodine density and Z-effective values compared with those of normal upper aerodigestive mucosal tissue.

ROI measurements of the normal mucosa and tumor also showed a high interobserver correlation. On the basis of the ROC curve analysis, the optimal thresholds of iodine density and Z-effective values showed high sensitivity and specificity for differentiation between tumor and normal mucosal tissue. DLSCCT is a relatively new technology with only 1 prior published study analyzing DLSCCT spectral parameters in head and neck cancer. This study also found increased iodine density in tumor tissue compared with surrounding healthy tissue, as well as improved tissue contrast at monoenergetic 40 keV-equivalent reconstructions compared with conventional CT reconstructions.⁵ The results from this study extend on these prior quantitative findings by also demonstrating that the qualitative assessment of tumor staging is enhanced using iodine density and Z-effective overlay images by increasing tumor boundary distinction and therefore assisting in local tumor staging. Although Z-effective images did show inherently poorer spatial resolution and lacked detailed anatomic resolution

seen on the iodine density and conventional CT images, Z-effective images were particularly useful at distinguishing the margin where 2 adjacent tissues had significantly different inherent atomic

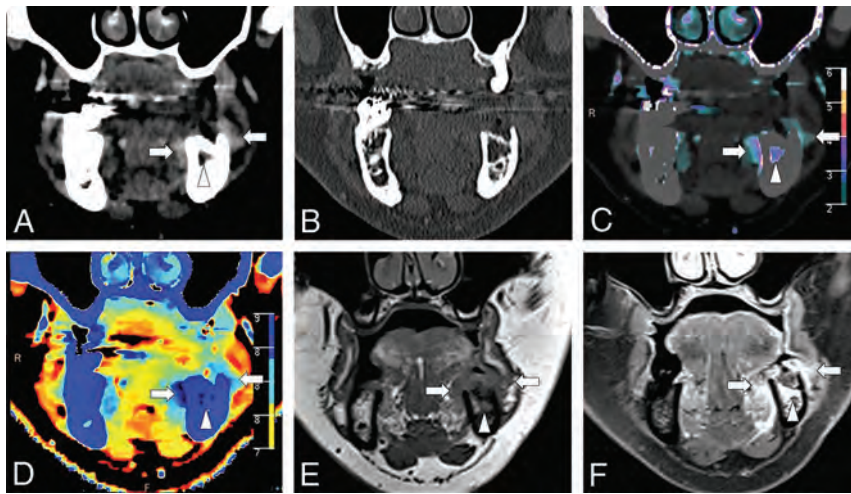


FIG 6. A 63-year-old man with left buccal and alveolar mucosa squamous cell carcinoma (arrows) seen on the conventional images in soft-tissue (A) and bone (B) window settings. Iodine density (C), color iodine density overlay (D), and Z-effective (E) images reveal right mandibular bone invasion with increased iodine density in the medullary cavity of the left hemimandible (arrowhead). T1-weighted MR imaging (E) and post-gadolinium-enhanced T1 fat-saturated (F) image confirm bone marrow infiltration. The patient was upstaged from T3 to T4a.

numbers. For example, Z-effective overlay maps increased the distinction of tumor adjacent or invasion into tissue planes such as paraglottic fat, cartilage, or bone, which is clinically relevant in determining local tumor staging.

Earlier studies have shown the benefits of the dual-energy spectral Hounsfield unit curve and the effective atomic numbers in differentiating benign and malignant neck pathologies.⁹ Currently, the more widely used postprocessed dual-energy CT image to enhance tumor–soft tissue contrast resolution has been achieved using virtual monochromatic image reconstructions with optimal contrast resolution and delineation of the head and neck tumor margin at 40 keV.^{5,10,11} Dual-source CT data can also be used to better depict residual and recurrent tumor, which shows statistically higher spectral Hounsfield units at 40 keV and higher iodine concentration, enabling differentiation from benign posttreatment changes.¹¹ This application is yet to be validated on the DLCT scanner.

This study is the first to propose a healthy control group reference range of normal iodine density and Z-effective values across mucosal and selective neck muscle subsites. There are minimal physiologic variation of iodine density and Z-effective values across the mucosa subsites, with the floor of mouth and palatine tonsil showing consistently higher values across the healthy patient cohort. Head and neck histopathologic studies have previously identified a greater abundance of lymphovascular networks at mucosal subsites with minor salivary and/or intrinsic lymphoid tissue, and this finding is hypothesized to be the cause for consistently increased iodine density and Z-effective values at these 2 mucosal subsites in healthy patients.^{12,13}

Performing and interpreting of spectral data analysis required training and can be time-consuming. In our study, it took both trained readers, on average, 13–15 minutes to perform and interpret the spectral data for research purposes, but we

anticipate that incorporation of spectral analysis into clinical practice would be longer because the radiologists need to incorporate the spectral results into a meaningful report.

There were several limitations to this study. First, the study has a small sample size of patients with HNSCC and healthy controls; however, despite the small cohort, significant differences between iodine density and Z-effective values in the tumor and control groups were demonstrated. Future studies with larger patient cohorts would be helpful to further consolidate these initial findings and increase the statistical accuracy of healthy and disease thresholds. The interobserver agreement in local tumor staging and final ROIs for both Z-effective values and iodine density was not undertaken; however, there were no discrepancies in local tumor staging and complete consensus on final ROIs between 2

expert radiologists. This study did not analyze DLCT parameters in normal or metastatic lymph nodes. This domain has previously been evaluated on dual-source CT by groups such as Foust et al¹⁴ and Tawfik et al,¹⁵ who have shown that metastatic HNSCC lymph nodes, predominately HPV-positive nodes, have statistically lower iodine density compared with normal nodes. Quantitative CT analysis opens the possibility of radiogenomics, which can exploit potential differences in DLCT parameters between HPV-positive and HPV-negative HNSCC. This concept has already been applied to distinguishing esophageal squamous cell carcinoma and adenocarcinoma on the basis of the iodine concentration at 40–70 keV.¹⁶

CONCLUSIONS

This study demonstrates that DLCT-derived iodine density and Z-effective images provide both valuable quantitative data and improved contrast resolution for qualitative assessment of upper aerodigestive HNSCC. DLCT parameters with conventional CT images were found to enhance local tumor staging accuracy compared with surgical histopathology.

ACKNOWLEDGMENT

The authors thank Dr. Michael Lousick and Dr. Matthew Devine for assisting with ethics proposal and editing of the manuscript.

Disclosures: Yael Nae—UNRELATED: Employment: Philips Healthcare, Comments: I am an employee in the Philips Healthcare CT/Advanced Molecular Imaging business.

REFERENCES

1. Forghani R. An update on advanced dual-energy CT for head and neck cancer imaging. *Expert Rev Anticancer Ther* 2019;19: 633–44 CrossRef Medline

2. Forghani R, Kelly HR. **Dual-energy computed tomography in neuro-radiology and head and neck imaging: state-of-the-art.** *Neuroimaging Clin N Am* 2017;27:xvii–xviii CrossRef Medline
3. Forghani R, Kelly HR, Curtin HD. **Applications of dual-energy computed tomography for the evaluation of head and neck squamous cell carcinoma.** *Neuroimaging Clin N Am* 2017;27: 445–59 CrossRef Medline
4. Johnson TR. **Dual-energy CT: general principles.** *AJR Am J Roentgenol* 2012;199: S3–8 CrossRef Medline
5. Lohöfer FK, Kaissis GA, Köster FL, et al. **Improved detection rates and treatment planning of head and neck cancer using dual-layer spectral CT.** *Eur Radiol* 2018;28: 4925–31 CrossRef Medline
6. Hua CH, Shapira N, Merchant TE, et al. **Accuracy of electron density, effective atomic number, and iodine concentration determination with a dual-layer dual-energy computed tomography system.** *Med Phys* 2018;45: 2486–97 CrossRef Medline
7. van Ommen F, de Jong HW, Dankbaar JW, et al. **Dose of CT protocols acquired in clinical routine using a dual-layer detector CT scanner: a preliminary report.** *Eur J Radiol* 2019;112:65–71 CrossRef Medline
8. Joshi M, Langan DA, Sahani DS, et al. **Effective atomic number accuracy for kidney stone characterization using spectral CT.** In: *Proceedings 7622. Medical Imaging 2010: Physics of Medical Imaging.* SPIE; 2010 CrossRef
9. Srinivasan A, Parker RA, Manjunathan A, et al. **Differentiation of benign and malignant neck pathologies: preliminary experience using spectral computed tomography.** *J Comput Assist Tomogr* 2013;37: 666–72 CrossRef Medline
10. Lam S, Gupta R, Levental M, et al. **Optimal virtual monochromatic images for evaluation of normal tissues and head and neck cancer using dual-energy CT.** *AJNR Am J Neuroradiol* 2015;36:1518–24 CrossRef Medline
11. Yamauchi H, Buehler M, Goodsitt MM, et al. **Dual-energy CT-based differentiation of benign posttreatment changes from primary or recurrent malignancy of the head and neck: comparison of spectral Hounsfield units at 40 and 70 keV and iodine concentration.** *AJR Am J Roentgenol* 2016;206:580–87 CrossRef Medline
12. Fossum CC, Chintakuntlawar AV, Price DL, et al. **Characterization of the oropharynx: anatomy, histology, immunology, squamous cell carcinoma and surgical resection.** *Histopathology* 2017;70:1021–29 CrossRef Medline
13. Werner JA, Dunne AA, Myers JN. **Functional anatomy of the lymphatic drainage system of the upper aerodigestive tract and its role in metastasis of squamous cell carcinoma.** *Head Neck* 2003;25:322–32 CrossRef Medline
14. Foust AM, Ali RM, Nguyen XV, et al. **Dual-energy CT-derived iodine content and spectral attenuation analysis of metastatic versus nonmetastatic lymph nodes in squamous cell carcinoma of the oropharynx.** *Tomography* 2018;4:66–71 CrossRef Medline
15. Tawfik AM, Razeq AA, Kerl JM, et al. **Comparison of dual-energy CT-derived iodine content and iodine overlay of normal, inflammatory and metastatic squamous cell carcinoma cervical lymph nodes.** *Eur Radiol* 2014;24: 574–80 CrossRef Medline
16. Zhou Y, Hou P, Zha K, et al. **Spectral computed tomography for the quantitative assessment of patients with carcinoma of the gastroesophageal junction: initial differentiation between a diagnosis of squamous cell carcinoma and adenocarcinoma.** *J Comput Assist Tomogr* 2019;43:187–93 CrossRef Medline

Preoperative MRI Evaluation of Thyroid Cartilage Invasion in Patients with Laryngohypopharyngeal Cancer: Comparison of Contrast-Enhanced 2D Spin-Echo and 3D T1-Weighted Radial Gradient Recalled-Echo Techniques

C.J. Park, J.-H. Kim, S.S. Ahn, S.-K. Lee, Y.W. Koh, and J. Kim



ABSTRACT

BACKGROUND AND PURPOSE: Accurate assessment of thyroid cartilage invasion on preoperative imaging influences management in patients with laryngeal and hypopharyngeal cancers. We evaluated the clinical usefulness of contrast-enhanced 3D T1-weighted radial gradient recalled-echo for preoperative assessment of thyroid cartilage invasion in patients with laryngohypopharyngeal squamous cell carcinoma, compared with 2D spin-echo T1WI.

MATERIALS AND METHODS: Preoperative MR images of 52 consecutive patients who were diagnosed with laryngeal or hypopharyngeal cancer and underwent partial or total laryngectomy were analyzed. Pathologic specimens served as reference standards. Two independent head and neck radiologists evaluated the presence of thyroid cartilage invasion in both contrast-enhanced 2D spin-echo T1WI and 3D gradient recalled-echo sequences. The sensitivity, specificity, and accuracy of the 2 modalities were compared. The area under the curve was a measure of diagnostic performance.

RESULTS: Pathologic neoplastic thyroid cartilage invasion was identified in 24 (46.2%) of the 52 patients. The sensitivity (75.0%), specificity (96.4%), and accuracy (86.5%) of contrast-enhanced 3D gradient recalled-echo were significantly higher than those of 2D spin-echo T1WI (58.3%, 89.3%, and 75.0%; $P = .017$, $.003$, and $.002$, respectively). 3D gradient recalled-echo had significantly better diagnostic performance (area under the curve = 0.963) than 2D spin-echo T1WI (area under the curve = 0.862; $P = .010$).

CONCLUSIONS: Contrast-enhanced 3D gradient recalled-echo was diagnostically superior in identifying neoplastic thyroid cartilage invasion compared with 2D spin-echo T1WI in patients with laryngohypopharyngeal cancer, and therefore, may provide more accurate preoperative staging.

ABBREVIATIONS: AUC = area under the curve; GRE = gradient recalled-echo; SE = spin-echo; THRIVE = T1-weighted high-resolution isotropic volume examination

Accurate preoperative staging is crucial for deciding appropriate treatment strategies and predicting prognosis in patients with head and neck cancers. Specifically, in laryngeal and hypopharyngeal cancers, treatment strategies vary with the presence of thyroid cartilage invasion.¹ If the tumor is localized without extension to the thyroid cartilage, larynx-preserving treatment can be performed. On the contrary, if the tumor extends through the thyroid cartilage, more invasive treatment such as total

laryngectomy is considered.²⁻⁷ Thus, accurate assessment of thyroid cartilage invasion preoperatively is highly desirable in patients with laryngeal and hypopharyngeal cancers.

MR imaging has been shown to be superior to CT in the assessment of cartilage invasion because of its excellent soft-tissue contrast.⁸⁻¹⁰ Becker et al⁹ proposed new diagnostic criteria based on MR imaging to improve the distinction between tumor tissue and peritumoral inflammation involving the laryngeal cartilage in patients with laryngeal and hypopharyngeal cancers. Although MR imaging in head and neck cancer is most widely performed with a conventional 2D spin-echo (SE) sequence, 3D volumetric imaging has emerged as an alternative because it allows isotropic data acquisition with multiplanar image reconstruction, within an acceptable acquisition time. In addition, T1-weighted high-resolution isotropic volume examination (THRIVE), a 3D ultra-fast spoiled gradient MR imaging sequence that incorporates a frequency-selective fat-saturation pulse, was recently shown to be

Received December 5, 2020; accepted after revision April 20, 2021.

From the Department of Radiology (C.J.P., J.-H.K.), Yongin Severance Hospital, Yonsei University College of Medicine, Yongin, Korea; and Departments of Radiology (S.S.A., S.-K.L., J.K.) and Otorhinolaryngology (Y.W.K.), Severance Hospital, Yonsei University College of Medicine, Seoul, Korea.

Please address correspondence to Jinna Kim, MD, PhD, Department of Radiology, Severance Hospital, Yonsei University College of Medicine, 50-1 Yonsei-ro, Seodaemun-gu, Seoul 03722, Korea; e-mail: jinna@yuhs.ac



Indicates article with online supplemental data.

<http://dx.doi.org/10.3174/ajnr.A7213>

clinically superior for preoperative evaluation of head and neck cancer, providing more accurate measurement of tumor size and higher sensitivity to detect the primary tumor in patients with cervical lymph node metastases of unknown primary tumors, compared with 2D SE T1WI.^{11,12}

We hypothesized that contrast-enhanced 3D gradient recalled-echo (GRE) might allow more accurate identification of neoplastic thyroid cartilage invasion compared with 2D SE T1WI in patients with laryngohypopharyngeal cancer. The aim of the present study was to investigate the potential of GRE for the preoperative assessment of thyroid cartilage invasion in patients with laryngohypopharyngeal cancer by comparing it with 2D SE T1WI.

MATERIALS AND METHODS

Study Population

This retrospective study was approved by the institutional review board of our institution, Severance hospital, and the requirement for informed consent was waived on the basis of its retrospective nature. Between July 2012 and June 2019, one hundred twenty-four consecutive patients with laryngeal and hypopharyngeal squamous cell carcinoma who underwent partial or total laryngectomy for curative intent at our institution were initially included. Exclusion criteria were as follows: no preoperative MR imaging ($n = 8$), unavailability of either 2D SE T1WI or 3D GRE scans ($n = 20$), and patients who underwent neoadjuvant chemotherapy or radiation therapy ($n = 44$). Therefore, after accounting for the exclusion criteria, a total of 52 patients (48 men and 4 women; mean age, 66.4 years; range, 33–79 years) were included in this study.

MR Imaging Acquisition

All patients underwent MR imaging with a 3T system (Intera Achieva or Achieva TX; Philips Healthcare) and a head and neck coil. Conventional MR imaging consisting of axial SE T1-weighted (TR = 560 ms, TE = 10 ms, matrix = 256×256 , 4-mm section thickness, 1-mm intersection gap, and 2 signal averages) and fat-saturated axial fast SE T2-weighted imaging (TR = 6480 ms, TE = 70 ms, matrix = 256×256 , 4-mm section thickness, 1-mm intersection gap, and 2 signal averages) were performed according to the routine protocol for the head and neck, respectively, before injecting the contrast material. All images were obtained with a 22- to 25-cm FOV, which was adjusted for each patient. Subsequently, gadopentetate dimeglumine (Magnevist; Bayer HealthCare Pharmaceuticals) was administered intravenously at a dose of 0.2 mL/kg body weight at a rate of 2 mL/s. Forty seconds after administering the contrast material, fat-saturated axial GRE scans were acquired, followed by fat-saturated axial and coronal 2D SE T1WI scans sequentially. The axial GRE images were then reformatted into the coronal and sagittal planes.

The sequence parameters for the contrast-enhanced 2D SE T1WI were as follows: TR = 400–550 ms, TE = 10 ms, flip angle = 90° , bandwidth = 75.3 Hz/pixel, matrix = 256×256 , 4-mm section thickness, 1-mm intersection gap, 2 signal averages, and acquisition time = 303 seconds for axial images and 175 seconds for coronal images. The parameters for the contrast-enhanced 3D GRE were as follows: TR = 4.5 ms, TE = 2.2 ms, flip angle = 10° , bandwidth = 434 Hz/pixel, matrix = 256×256 , 1-mm section thickness, 2 signal averages, and acquisition time = 223 seconds.

Image Analysis

Two experienced head and neck radiologists (with 17 and 3 years of experience, respectively, in head and neck radiology) who were blinded to preoperative clinical findings, patient history, and final pathologic results retrospectively reviewed the MR images of enrolled patients independently. The contrast-enhanced 2D SE T1WI and 3D GRE images were presented to the 2 radiologists in a random fashion, with at least a 2-week interval between the 2 sequences. Each reviewer assessed the presence of thyroid cartilage invasion on the contrast-enhanced 2D SE T1WI and 3D GRE images, using the precontrast SE T1-weighted and fat-saturated fast SE T2-weighted images as references. The presence of thyroid cartilage invasion was determined by comparing the signal intensity of cartilage with that of the adjacent tumor mass visually on fat-saturated SE T2-weighted and contrast-enhanced images, according to MR imaging criteria proposed in 2008.⁹ If the cartilage presented a signal intensity or enhancement degree similar to that of the adjacent tumor, neoplastic thyroid cartilage invasion was suspected. On the contrary, if the cartilage had a higher signal intensity or stronger enhancement than the adjacent tumor, the cartilage was regarded as having peritumoral inflammation. Subsequently, each reviewer determined the invasion of the thyroid cartilage using the following 4-point scoring system: 1, definitely negative; 2, tumor abutting the thyroid cartilage without invasion (probably negative); 3, tumor invading the inner cortex of the thyroid cartilage and confined to the thyroid cartilage (probably positive); and 4, transmural extralaryngeal spread through the cartilage (definitely positive). Disagreements between the 2 radiologists were resolved by consensus for the final evaluation.

A pathologist with 12 years of experience who was blind to the preoperative imaging findings evaluated the surgical specimens. The final histopathologic results after surgery were used as the reference standard.

Statistical Analysis

The contrast-enhanced 2D SE T1WI and 3D GRE image interpretation results were compared with the histopathologic results. Tumors with scores of ≥ 3 were considered to have neoplastic thyroid cartilage invasion, to facilitate calculation of the diagnostic performance. The sensitivity, specificity, accuracy, positive predictive value, and negative predictive value of 2D SE and 3D GRE for detecting pathologic thyroid cartilage invasion were calculated with 95% CIs. The McNemar test was performed to compare the sensitivity, specificity, and accuracy between the 2 sequences. Receiver operating characteristic curves were generated to compare the diagnostic performance of the 2 sequences, and the area under the curve (AUC) was calculated. Pair-wise comparisons of the AUCs were performed using the DeLong method. All statistical analyses were performed using R statistical software, Version 3.4.2 (<http://www.r-project.org/>). P values $< .05$ indicated a statistically significant difference.

RESULTS

Of the 52 patients, 36 had laryngeal cancer and 16 had hypopharyngeal cancer. Primary tumors were found in the glottis ($n = 24$), pyriform sinus ($n = 12$), supraglottis ($n = 11$), posterior pharyngeal

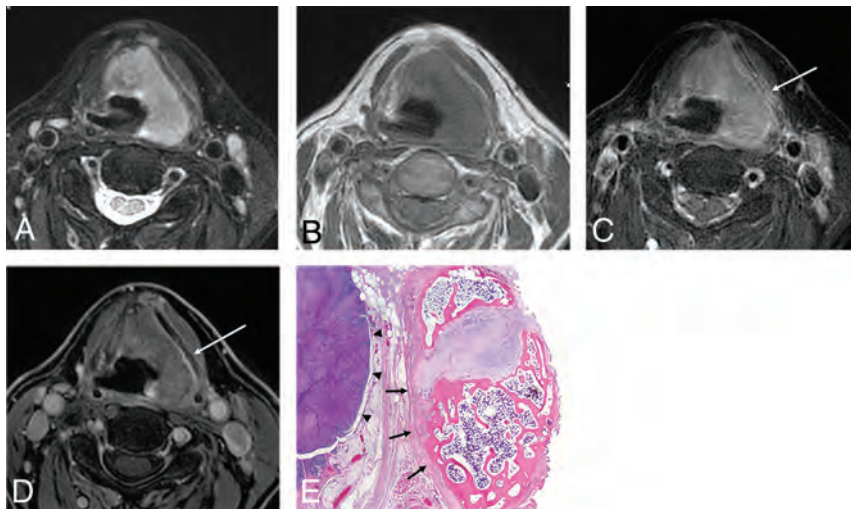


FIG 1. False-positive findings on a 2D SE T1WI and true-negative findings on a 3D GRE image in a 68-year-old man with supraglottic cancer. Axial fat-saturated fast SE T2WI (A) shows a left-sided laryngeal tumor occupying the paraglottic space and iso-signal intensity of the adjacent left thyroid lamina. Axial precontrast (B) and contrast-enhanced 2D SE T1WIs (C) show similar enhancement of the left thyroid lamina (arrow) compared with the adjacent tumor, regarded as tumor invasion of the thyroid cartilage. Axial contrast-enhanced 3D GRE image (D) shows no definite enhancement of the adjacent left thyroid lamina (arrow), suggesting that the tumor was confined to the paraglottic space without thyroid cartilage invasion. Photomicrograph (E) confirms that tumor cells (arrowheads) do not invade thyroid cartilage (arrows) (hematoxylin-eosin stain; original magnification, $\times 1.25$).

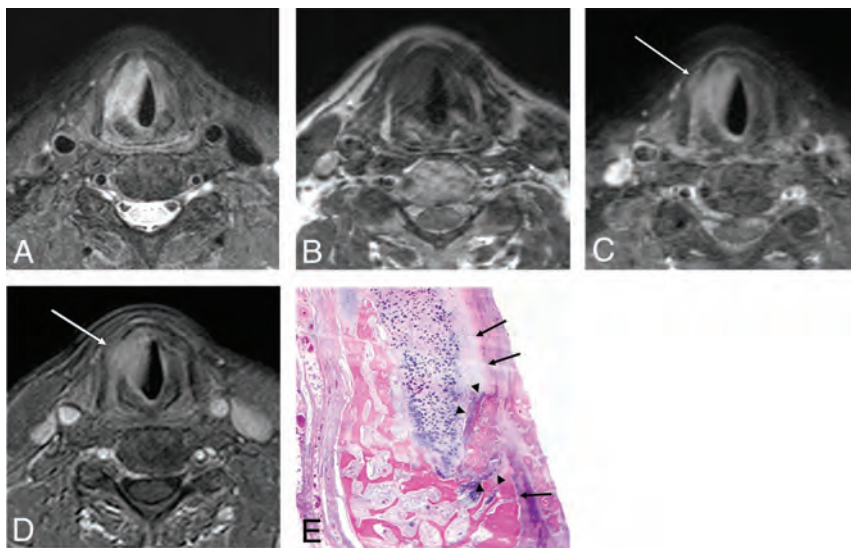


FIG 2. False-negative findings on a 2D SE T1WI and true-positive findings on a 3D GRE image in a 61-year-old man with glottic cancer. Axial fat-saturated fast SE T2WI (A) shows a tumor arising from the right glottis and higher signal intensity of the right thyroid lamina than of the adjacent tumor. Axial precontrast (B) and contrast-enhanced 2D SE T1WIs (C) show strong enhancement of the right thyroid lamina (arrow), regarded as inflammatory changes rather than neoplastic cartilage invasion. Axial contrast-enhanced 3D GRE image (D) shows contrast enhancement of the right thyroid lamina (arrow), similar to that of the adjacent tumor, suggesting neoplastic thyroid cartilage invasion. Photomicrograph (E) confirms that the inner cortex of thyroid cartilage (arrows) is invaded by tumor (arrowheads) (hematoxylin-eosin stain; original magnification, $\times 1.25$).

wall ($n = 3$), subglottis ($n = 1$), and postcricoid region ($n = 1$). The final histopathologic examinations after the operation revealed that thyroid cartilage invasion was present in 24 (46.2%) of the

52 patients. Tumor invasion occurred through the outer cortex of thyroid cartilage in 13 patients (54.2%), whereas the tumor invaded only the inner cortex of the thyroid cartilage in the remaining 11 patients (45.8%).

The Online Supplemental Data summarize the diagnostic performances of contrast-enhanced 2D SE T1WI and 3D GRE in assessing the presence of neoplastic thyroid cartilage invasion. In 24 patients with neoplastic thyroid cartilage diagnosed histopathologically, 3D GRE enabled us to identify thyroid cartilage invasion accurately in 18 patients (75.0%), while 2D SE T1WI enabled us to identify the same in 14 patients (58.3%). The sensitivity of 3D GRE was significantly superior to that of 2D SE T1WI (75.0%; 95% CI, 53.3%–90.2%) versus 58.3% (95% CI, 36.6%–77.9%) ($P = .017$). In 28 patients without neoplastic thyroid cartilage invasion, 3D GRE and 2D SE T1WI enabled us to report the absence of thyroid cartilage invasion accurately in 27 (96.4%) and 25 (89.3%) patients, respectively. The specificity of 3D GRE was significantly superior to that of 2D SE T1WI (96.4%; 95% CI, 81.7%–99.9% versus 89.3%; 95% CI, 71.8%–97.7%) ($P = .003$). The diagnostic accuracy of 3D GRE (86.5%) was significantly higher than that of 2D SE T1WI (75.0%; $P = .002$). False-positive and false-negative results were observed in 10 and 3 patients, respectively, on 2D SE T1WI. In contrast, false-positive and false-negative results were observed in 6 and 1 patient, respectively, on 3D GRE. Representative cases for comparison of contrast-enhanced 3D GRE and 2D SE T1WI are shown in Figs 1 and 2.

The receiver operating characteristic curve analysis revealed that the diagnostic performance of 3D GRE (AUC = 0.963; 95% CI, 0.921–1.000) was significantly better than that of 2D SE T1WI (AUC = 0.862; 95% CI, 0.771–0.952) ($P = .010$, Fig 3).

The clinical and pathologic T-stages of the tumors are summarized in the Table. The 36 laryngeal tumors were classified as pT2 ($n = 3$), pT3 ($n = 20$), and pT4a ($n = 13$), and the 16 hypopharyngeal tumors were classified as pT2 ($n = 3$), pT3 ($n = 6$), and pT4 ($n = 7$). Among the 26 patients with pT3, 22 and 25 patients were assessed accurately with

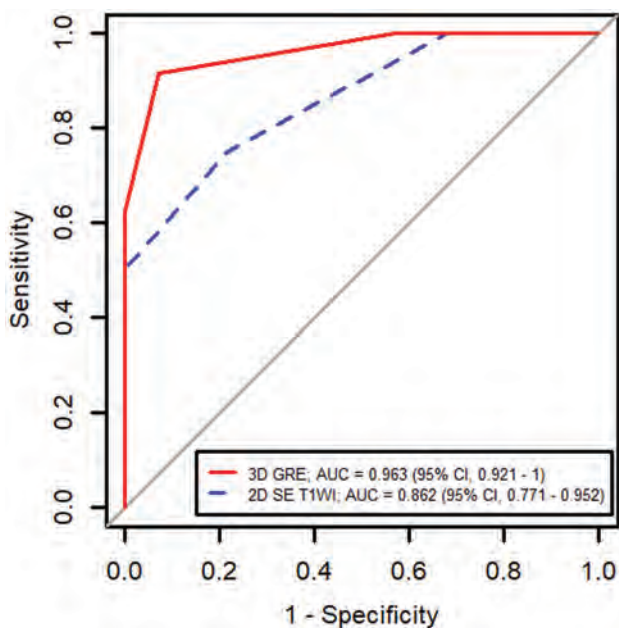


FIG 3. Receiver operating characteristic curve analysis shows the diagnostic performance of 3D GRE and 2D SE T1WI. The AUC was significantly higher with 3D GRE (0.963) than with 2D SE T1WI (0.862, $P = .010$).

The clinical and pathologic T-stages of the tumor

	2D SE T1WI			3D GRE		
	cT3	cT4		cT2	cT3	cT4
pT2	5	1	0	5	1	0
pT3	0	22	4	0	25	1
pT4	0	4	16	0	3	17

cT3 based on 2D SE T1WI and 3D GRE, respectively. Among the 20 patients with pT4, sixteen and 17 patients were assessed accurately with cT4 based on 2D SE T1WI and 3D GRE, respectively.

DISCUSSION

In this study, contrast-enhanced 3D GRE showed superior sensitivity, specificity, and accuracy than contrast-enhanced 2D SE T1WI in detecting thyroid cartilage invasion in patients with laryngohypopharyngeal cancer. In addition, 3D GRE had better diagnostic performance compared with 2D SE T1WI, suggesting that 3D GRE is an acceptable alternative for 2D SE T1WI for accurate preoperative staging in patients with laryngohypopharyngeal cancer.

Accurate preoperative staging is important to determine an adequate surgical resection margin and appropriate treatment options, which may result in improved prognosis and reduced treatment-associated morbidity in patients with head and neck cancer. Specifically, in patients with laryngohypopharyngeal cancer, the presence of thyroid cartilage invasion by the tumor is one of the key factors that determine treatment strategies, ie, total laryngectomy versus larynx-preserving surgery.^{13,14} Therefore, several previous studies evaluated the diagnostic performance of various imaging modalities for the detection of neoplastic cartilage invasion. CT is a well-established method, and a few studies

have reported that dual-energy CT can provide high specificity and acceptable sensitivity for assessing neoplastic thyroid cartilage invasion in patients with laryngohypopharyngeal cancer.^{15,16} However, CT cannot distinguish between nonossified cartilage and tumor because they show similar CT values.^{13,17} In contrast, MR imaging has been regarded as providing higher soft-tissue contrast resolution and superior sensitivity and negative predictive values compared with CT in detecting neoplastic cartilage invasion.^{9,18} However, MR imaging still has limited value with regard to differentiation of neoplastic cartilage invasion and inflammatory changes because edema or inflammatory changes frequently mimic tumor invasion. In addition, motion artifacts with a relatively long scan time are one of the important issues of MR imaging because patients with head and neck cancer often have breathing and swallowing difficulties.¹⁶ Therefore, we attempted to find an optimal contrast-enhanced MR imaging sequence for the assessment of neoplastic thyroid cartilage invasion.

The major advantage of 3D imaging with isotropic data acquisition is that it does not show partial volume averaging artifacts, which are frequently observed on 2D imaging, providing more detailed anatomic information. In addition, there is the potential to reformat images in any plane without compromising image resolution, simplifying imaging protocols and reducing acquisition time when multiplanar imaging is required.¹⁹⁻²¹ Furthermore, the shorter scan time makes 3D imaging less sensitive to motion artifacts.

Among the 3D volumetric sequences, 3D gradient-echo MR images with isotropic data acquisition, such as a volumetric interpolated breath-hold examination and THRIVE, may serve as feasible alternatives to 2D SE for the head and neck as well as other parts of the body. A few previous studies have revealed that 3D GRE could provide more accurate tumor size measurement in head and neck cancer and higher sensitivity for detecting primary tumors in patients with cervical lymph node metastasis of unknown primary tumors, compared with 2D SE T1WI.^{11,12} In particular, because 3D GRE can provide more accurate information of small complex areas (such as the larynx and hypopharynx) and fewer flow-related artifacts, we hypothesized that 3D GRE might perform better diagnostically than 2D SE T1WI in patients with laryngohypopharyngeal cancer.

A previous study devised a new criterion that enabled improved differentiation of neoplastic cartilage invasion from peritumoral inflammation by MR imaging.⁹ However, it is still challenging to distinguish peritumoral inflammation from neoplastic invasion of thyroid cartilage on MR imaging, and doing so may lead to unsatisfactory specificity and false-positive results.^{15,22} Furthermore, minimal cortical invasion of tumor on ossified cartilage is also not easily detectable on MR images, resulting in false-negatives.^{9,15} In our study, we observed 10 false-positive and 3 false-negative cases on 2D SE T1WI, while the number decreased to 6 false-positive and 1 false-negative case on 3D GRE. Therefore, despite the possible disadvantage of a lower signal-to-noise ratio on the 3D sequence, we would expect that 3D GRE with a lesser partial volume averaging effect and higher spatial resolution might enable more accurate differentiation between the inflammatory change and neoplastic invasion of thyroid cartilage as a feasible alternative to ordinary 2D SE T1WI with regard to minimizing false-positive and false-negative cases.

There are several limitations to be addressed. First, radiologists determined the presence of neoplastic thyroid cartilage invasion by visual inspection without measuring the signal intensity of the tissue because these measurements are not usually performed in the clinical setting. Second, during the MR imaging acquisition, 3D GRE was performed first, followed by 2D SE T1WI after contrast injection, without randomizing the order. Nevertheless, scan time delay may not necessarily have affected our study results because the total acquisition time for GRE was approximately 4 minutes. Third, completely blinded interpretations of MR images were not possible because contrast-enhanced 2D SE T1WI and 3D GRE are easily distinguishable by experienced reviewers. Finally, we evaluated the neoplastic invasion of thyroid cartilage only, not the cricoid or arytenoid cartilage in our study. Assessment of tumor extension into the thyroid cartilage was more clinically relevant, and future studies are necessary to validate our study results in the evaluation of cricoid or arytenoid cartilage.

CONCLUSIONS

Contrast-enhanced 3D GRE with 1-mm section thickness and reconstruction had a superior diagnostic performance compared with contrast-enhanced 2D SE T1WI with a 4-mm section thickness in detecting thyroid cartilage invasion in patients with laryngohypopharyngeal cancer. 3D GRE is a clinically relevant and feasible alternative to 2D SE T1WI.

REFERENCES

- Amin MB, Edge SB, Greene FL. *AJCC Cancer Staging Manual*. Springer-Verlag; 2017
- Wolf GT, Fisher SG, Hong WK, et al. Department of Veterans Affairs Laryngeal Cancer Study Group. **Induction chemotherapy plus radiation compared with surgery plus radiation in patients with advanced laryngeal cancer.** *N Engl J Med* 1991;324:1685–90 CrossRef Medline
- Forastiere AA, Goepfert H, Maor M, et al. **Concurrent chemotherapy and radiotherapy for organ preservation in advanced laryngeal cancer.** *N Engl J Med* 2003;349:2091–98 CrossRef Medline
- Christiansen H, Wolff HA, Hess CF, et al. **Larynx preservation clinical trial design: key issues and recommendations—a consensus panel summary: in regard to Lefebvre, et al. for the larynx preservation consensus panel (Int J Radiat Oncol Biol Phys 2009;73:1293-1303).** *Int J Radiat Oncol Biol Phys* 2009;75:633 CrossRef Medline
- Lefebvre JL, Ang KK; Larynx Preservation Consensus Panel. **Larynx preservation clinical trial design: key issues and recommendations—a consensus panel summary (Int J Radiat Oncol Biol Phys 2009;73:1293-1303).** *Head Neck* 2009;31:429–41 CrossRef Medline
- Colevas AD, Yom SS, Pfister DG, et al. **NCCN guidelines insights: head and neck cancers, version 1.2018.** *J Natl Compr Canc Netw* 2018;16:479–90 CrossRef Medline
- Pfister DG, Laurie SA, Weinstein GS, et al. American Society of Clinical Oncology. **American Society of Clinical Oncology clinical practice guideline for the use of larynx-preservation strategies in the treatment of laryngeal cancer.** *J Clin Oncol* 2006;24:3693–704 CrossRef Medline
- Becker M, Zaidi H. **Imaging in head and neck squamous cell carcinoma: the potential role of PET/MRI.** *Br J Radiol* 2014;87:20130677 CrossRef Medline
- Becker M, Zbaren P, Casselman JW, et al. **Neoplastic invasion of laryngeal cartilage: reassessment of criteria for diagnosis at MR imaging.** *Radiology* 2008;249:551–59 CrossRef Medline
- Becker M, Burkhardt K, Dulguerov P, et al. **Imaging of the larynx and hypopharynx.** *Eur J Radiol* 2008;66:460–79 CrossRef Medline
- Ahn SS, Kim J, An C, et al. **Preoperative imaging evaluation of head and neck cancer: comparison of 2D spin-echo and 3D THRIVE MRI techniques with resected tumours.** *Clin Radiol* 2012;67:e98–104 CrossRef Medline
- Yoo MG, Kim J, Bae S, et al. **Detection of clinically occult primary tumours in patients with cervical metastases of unknown primary tumours: comparison of three-dimensional THRIVE MRI, two-dimensional spin-echo MRI, and contrast-enhanced CT.** *Clin Radiol* 2018;73:410.e9–15 CrossRef Medline
- Hermans R. **Staging of laryngeal and hypopharyngeal cancer: value of imaging studies.** *Eur Radiol* 2006;16:2386–400 CrossRef Medline
- Castelijns JA, Becker M, Hermans R. **Impact of cartilage invasion on treatment and prognosis of laryngeal cancer.** *Eur Radiol* 1996;6:156–69 CrossRef Medline
- Kuno H, Sakamaki K, Fujii S, et al. **Comparison of MR imaging and dual-energy CT for the evaluation of cartilage invasion by laryngeal and hypopharyngeal squamous cell carcinoma.** *AJNR Am J Neuroradiol* 2018;39:524–31 CrossRef Medline
- Kuno H, Onaya H, Fujii S, et al. **Primary staging of laryngeal and hypopharyngeal cancer: CT, MR imaging and dual-energy CT.** *Eur J Radiol* 2014;83:e23–35 CrossRef Medline
- Becker M, Zbaren P, Delavelle J, et al. **Neoplastic invasion of the laryngeal cartilage: reassessment of criteria for diagnosis at CT.** *Radiology* 1997;203:521–32 CrossRef Medline
- Becker M, Zbaren P, Laeng H, et al. **Neoplastic invasion of the laryngeal cartilage: comparison of MR imaging and CT with histopathologic correlation.** *Radiology* 1995;194:661–69 CrossRef Medline
- Park HJ, Lee SY, Rho MH, et al. **The usefulness of the three-dimensional enhanced T1 high-resolution isotropic volume excitation MR in the evaluation of shoulder pathology: comparison with two-dimensional enhanced T1 fat saturation MR.** *Br J Radiol* 2015;88:20140830 CrossRef Medline
- Torkzad MR, Ahlström H, Karlbom U. **Comparison of different magnetic resonance imaging sequences for assessment of fistula-in-ano.** *World J Radiol* 2014;6:203–09 CrossRef Medline
- Kim KA, Herigault G, Kim MJ, et al. **Three-dimensional contrast-enhanced hepatic MR imaging: comparison between a centric technique and a linear approach with partial Fourier along both slice and phase directions.** *J Magn Reson Imaging* 2011;33:160–66 CrossRef Medline
- Kuno H, Onaya H, Iwata R, et al. **Evaluation of cartilage invasion by laryngeal and hypopharyngeal squamous cell carcinoma with dual-energy CT.** *Radiology* 2012;265:488–96 CrossRef Medline

When Should a Brain MRI Be Performed in Children with New-Onset Seizures? Results of a Large Prospective Trial

R. Hourani, W. Nasreddine, M. Dirani, G. Hmameess, S. Sabbagh, O. El Tourjuman, J. Wazne, H. Toufaily, N. AlArab, M. El Dassouki, and A. Beydoun



ABSTRACT

BACKGROUND AND PURPOSE: There is a paucity of data regarding the incidence of structural brain lesions in children with new-onset unprovoked seizures. Our aim was to determine the frequencies and types of epileptogenic lesions detected on a dedicated epilepsy protocol MR imaging according to age group, the presence of developmental delay, and the number and types of seizures.

MATERIALS AND METHODS: Consecutive children between 6 months and 18 years of age with new-onset unprovoked seizures were included. The frequencies and types of epileptogenic lesions were determined and then stratified according to sex, age groups, the presence of developmental delay, and the number and types of seizures at presentation. Multivariate analysis was used to identify variables significantly associated with the presence of epileptogenic lesions.

RESULTS: One thousand children were included. An epileptogenic lesion was identified in 26%, with malformations of cortical development being the most common lesion (32%), followed by hypoxic-ischemic injury (20%) and vascular etiologies (16%). Univariate analysis showed a significant increase in the frequency of epileptogenic lesions with decreasing age, the presence of developmental delay, and the number and types of seizures at presentation. The presence of developmental delay and seizure type at presentation remained significant in a multivariate analysis.

CONCLUSIONS: We documented a relatively high rate of epileptogenic lesions in children with new-onset seizures, with the presence of developmental delay and specific seizure types being associated with a higher likelihood of detecting an epileptogenic lesion on neuroimaging. This study fulfills the requirements of the study design recommended by the Practice Committee of the American Academy of Neurology, and we hope that our results will assist the relevant societies and committees in formulating neuroimaging guidelines for children with new-onset seizures.

ABBREVIATIONS: DD = developmental delay; MCD = malformations of cortical development; MTS = mesial temporal sclerosis; NCS = neurocutaneous syndromes; PVL = periventricular leukomalacia

Brain MR imaging is useful in the work-up of patients with new-onset seizures because it can help define the electroclinical syndrome, identify surgically remediable lesions, and assist in predicting medical refractoriness.^{1,2} In addition, according to the new proposed definition of epilepsy, a brain MR imaging may

establish the diagnosis of epilepsy in patients presenting with a single unprovoked seizure.³

There is a paucity of data regarding the frequency of structural brain lesions in children presenting with new-onset unprovoked seizures. Etiologically related neuroimaging abnormalities were identified in 13%–18% of such children, but those studies have several methodologic drawbacks, including the acquisition of head CTs, non-epilepsy protocol brain MRIs, and selection biases.⁴⁻⁶

The practice parameter issued in 2010 and reaffirmed in 2017 by the American Academy of Neurology⁷ determined that there was insufficient evidence to support a recommendation for routine neuroimaging of children with a first afebrile seizure. To overcome the shortcomings of prior studies and to generate definitive evidence regarding the value of neuroimaging studies in the pediatric population with new-onset seizures, a call was made for prospective data to be collected in sufficiently large samples, allowing adequate statistical power to provide precise estimates

Received December 21, 2020; accepted after revision April 5, 2021.

From the Departments of Radiology (R.H., N.A.) and Neurology (W.N., M.D., A.B.), American University of Beirut Medical Center, Beirut, Lebanon; Department of Pediatrics (G.H.), St. George Hospital Medical University Center, University of Balamand, Beirut, Lebanon; Department of Pediatrics (S.S.), Hotel Dieu de France Hospital, Beirut, Lebanon; Department of Neurology (O.E.T., J.W., M.E.D.), Rafic Hariri University Hospital, Beirut, Lebanon; and Department of Neurology (H.T.), Labib Medical Center, Beirut, Lebanon.

R. Hourani and W. Nasreddine contributed equally to this work.

Data are available on reasonable scientific request.

Please address correspondence to Ahmad Beydoun, MD, Professor of Neurology, American University of Beirut Medical Center, PO Box 11-0236, Riad El-Solh 1107 2020, Beirut, Lebanon; e-mail: ab29@aub.edu.lb

<http://dx.doi.org/10.3174/ajnr.A7193>

with narrow confidence intervals.⁷ In addition, the American Academy of Neurology practice parameter stressed the importance of stratifying patients by age groups and including consecutive children for the results to be accurate and generalizable.⁷

The primary aim of this study was to follow the recommendations of the American Academy of Neurology by prospectively assessing the frequencies and types of epileptogenic lesions in a large cohort of consecutive children with new-onset seizures evaluated with a dedicated epilepsy protocol brain MR imaging. The secondary aims were to determine the yields and types of lesions according to sex, the presence and severity of development delay (DD), as well as the number and types of seizure at presentation.

MATERIALS AND METHODS

Study Design and Patient Characteristics

Consecutive children between 6 months and 18 years of age diagnosed with ≥ 1 unprovoked seizure between November 2010 and April 2017 were included in this study. Those children participated in an ongoing centralized prospective study evaluating patients with new-onset seizures. The details of this study were previously reported.⁸

Brain MRI and Classification of Neuroimaging Findings

Brain MRIs were obtained from a 1.5 or 3T scanner (Ingenia; Phillips Healthcare) using an imaging-acquisition protocol that included 3D T1 (1 mm slice thickness) and 3D fast fluid-attenuated inversion recovery (FLAIR; 0.9 or 1 mm slice thickness) of the whole brain with multiplanar reconstruction, axial and coronal inversion recovery (2 mm slice thickness), axial T2 TSE and T2 FFE (4 mm slice thickness) and axial diffusion weighted images (4–5 mm slice thickness). The 3D images were obtained with no interslice gap. This protocol satisfies all the recommendations of the recently published Harmonized Neuroimaging of Epilepsy Structural Sequences (HARNESS-MRI)⁹ except for the lack of acquisition of high in-plane resolution 2D coronal T2-weighted sequences using submillimetric voxel resolution.

The MRIs were interpreted by a neuroradiologist blinded to the clinical data with vast experience in the neuroimaging of patients with epilepsy.

MR imaging findings were classified as epileptogenic on the basis of previously published criteria.^{10–12} Epileptogenic lesions were classified into the following categories: malformations of cortical development (MCD), mesial temporal sclerosis (MTS), hypoxic-ischemic injury (moderate or severe periventricular leukomalacia [PVL] or hypoxic brain injury), vascular lesions, tumoral, neurocutaneous syndromes (NCS), metabolic disorder, and others (eg, postinfectious or posttraumatic encephalomalacia with gliosis, leukodystrophy, and large arachnoid cysts exerting mass effect).

The cases of PVL were graded according to the following scoring system:¹³ severe PVL, diffuse white matter signal abnormality with cystic changes; moderate PVL, diffuse white matter abnormality without cystic changes; and mild PVL, isolated white matter abnormality. We considered only moderate or severe PVL as epileptogenic.¹⁴

MR imaging abnormalities consisting of isolated subcortical lesions or abnormal signal, nonspecific white matter hyperintensities, mild PVL, hydrocephalus, and brain atrophy were considered incidental findings.

Assessment of Intellectual or Global Developmental Delay

All children were evaluated for the presence and severity of DD. Children younger than 6 years of age were assessed with the Denver Development Screening Test.¹⁵ Older children were evaluated according to the *Diagnostic and Statistical Manual of Mental Disorders* criteria that stratify intellectual disability into mild, moderate, severe, and profound on the basis of deficits in intellectual functioning as well as difficulties in conceptual, social, and practical areas of living.¹⁶ For our analysis, we included only 3 groups of DD (mild, moderate, or severe) by combining children with severe and profound delays into a single category.

Classification of Seizure Types

The seizures were classified according to the recent International League Against Epilepsy operational classification.^{17,18} Children were stratified into the following groups based on a detailed description of the seizure semiologies experienced at the time of initial evaluation:

Group 1: Children with epileptic spasms in clusters or frequent tonic or atonic seizures

Group 2: Children with focal-onset seizures (focal aware or focal impaired awareness) with or without focal-to-bilateral tonic-clonic seizures

Group 3: Children with unknown-onset tonic-clonic seizures

Group 4: Children with frequent absence seizures and/or myoclonic seizures with or without generalized-onset tonic-clonic seizures

Group 5: Children with unclassified seizure types. This category included children who experienced what used to be labeled “dialeptic seizures” semiologically characterized by a loss of awareness and motionlessness that did not allow a definite distinction based on the semiologic description alone between absence seizures and focal impaired-awareness seizures.

Ethics Approval

This study was approved by the American University of Beirut Medical Center institutional review board, and all parents signed an informed consent form. Additionally, children between 7 and 17 years of age signed an assent form.

Statistical Analyses

We calculated the percentage of children with an epileptogenic lesion and compared the frequencies and types of lesions according to age groups (0–2 years, 2–5 years, 5–10 years, 10–15 years, 15–18 years), DD, and types and number of seizures at baseline.

For continuous variables, descriptive statistics, including mean, median, range, percentage, and 95% confidence interval were calculated. Statistical analyses were performed using the χ^2 test or Fisher exact test for categorical variables. Significant *P* values were set at $<.05$. Variables that showed a significant association with the presence of an epileptogenic lesion in univariate analyses were entered into a multivariate model.

In addition, a recursive partition analysis was performed to identify variables associated with higher or lower probabilities of detecting epileptogenic lesions. For this analysis, we used the χ^2 Automatic Interaction Detector with cross-validation. At each step, the χ^2 Automatic Interaction Detector algorithm chooses

Table 1: Demographic variables of the 1000 children included in the study

Demographics	
Age	
Mean	7.8 yr
Range	6 mo to 17.9 yr
Sex	
Male/female	581/419
No. of seizures (%)	
1 seizure	315 (31.5%)
Multiple seizures	685 (68.5%)
Seizure type (No.) (%)	
Focal-onset seizures	484 (48.4%)
Unknown-onset tonic-clonic seizures	260 (26.0%)
Absence and/or myoclonus with or without generalized tonic-clonic seizures	130 (13.0%)
Spasms, tonic or atonic seizures	93 (9.3%)
Unclassified	33 (3.3%)
Psychomotor development (No.) (%)	
Normal	777 (77.7%)
Delay	223 (22.3%)
Mild DD	70 (7.0%)
Moderate DD	63 (6.3%)
Severe/profound DD	90 (9.0%)

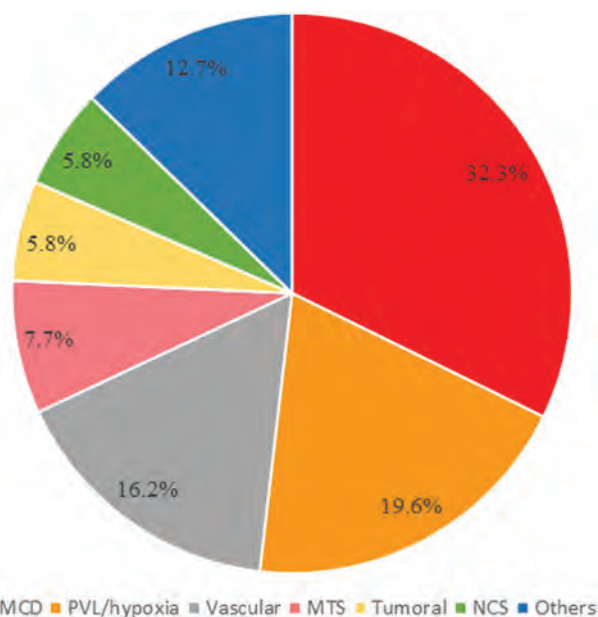


FIG 1. Frequencies of epileptogenic lesions stratified by etiologic categories.

the independent variable that has the strongest interaction with the dependent variable using *P* values with a Bonferroni correction as splitting criteria. The final result is a decision tree with various nodes that can be used to predict the probability of detecting an epileptogenic lesion in each subgroup.

RESULTS

Patient Demographics

Of the 1160 consecutive children enrolled in this study, 160 were excluded for the following reasons: 94 because a brain MR imaging was not yet performed for financial or other reasons, 63 who

underwent a non-epilepsy protocol brain MR imaging, and 3 children in whom a brain MR imaging was contraindicated. Therefore, a total of 1000 children (boys = 58.1%, girls = 41.9%) with a mean age of 7.8 years (range, 6 months to 17.9 years) were included. The number of seizures at initial evaluation, seizure types, and psychomotor development are shown in Table 1.

MR Imaging Findings

Epileptogenic lesions were detected on the brain MR imaging of 260 children (26%; 95% CI, 23.4%–28.8%). The frequencies of epileptogenic lesions stratified by etiologic categories are shown in Fig 1. The most common type of epileptogenic lesion was MCD detected in 84 children. The most frequent abnormalities in this group consisted of focal cortical dysplasia (47.6%), followed by polymicrogyria (22.6%), heterotopia (9.5%), multiple congenital malformations (8.3%), lissencephaly (7.1%), holoprosencephaly (2.4%), and septo-optic dysplasia (2.4%). Evidence of a hypoxic-ischemic injury was detected in 19.6% of children with etiologically relevant lesions on neuroimaging. Epileptogenic lesions associated with a vascular etiology were detected in 16.2% of children. Most (81%) had evidence of a prior ischemic infarction involving the cortex, 14% had a cavernoma, and 5% had an arteriovenous malformation. The next most common type of epileptogenic lesion was MTS, accounting for 7.7% of cases, followed by tumoral etiologies and NCS, each diagnosed in 5.8% of children. The tumors consisted of 8 neuroglial tumors, 4 infiltrative astrocytomas, 2 hypothalamic hamartomas, and 1 epidermoid cyst. Twelve of the 15 children with NCS were diagnosed with tuberous sclerosis, with the remaining 3 diagnosed with neurofibromatosis. The rest of the identified epileptogenic lesions consisted of posttraumatic or postinfectious encephalomalacia with cortical gliosis (*n* = 14), metabolic disorder (*n* = 9), leukodystrophy (*n* = 6), and large arachnoid cysts exerting mass effect (*n* = 4).

Frequencies of Epileptogenic Lesions According to Sex

The frequencies of epileptogenic lesions were not statistically significant between boys (26%) and girls (26%).

Frequencies of Epileptogenic Lesions According to the Number of Seizures at Presentation

At the initial evaluation, 315 children (31.5%) presented with a single seizure. Those who presented with ≥ 2 seizures were significantly more likely to have an epileptogenic lesion (193/685, 28.2%; 95% CI, 24.9%–31.7%) compared with those with a single seizure (67/315, 21.3%; 95% CI, 17.1%–26.1%; *P* = .021). There was, however, no significant difference in the types of identified epileptogenic lesions between those 2 groups.

Frequencies of Epileptogenic Lesions According to Age Groups

There was a gradual and significant reduction in the frequencies of epileptogenic lesions with ascending age groups (Table 2) (*P* < .001). In addition, the predominant subtype of epileptogenic lesions varied according to age groups. For instance, hypoxic-ischemic lesion, which was the most common substrate in children younger than 2 years of age and accounting for 31.7% of epileptogenic lesions in that age group, gradually declined to account for 15.0% of lesions in the 5–10 year age group and 0%

Table 2: Frequencies of epileptogenic lesion subtypes stratified by age groups^a

	0–2 Years (n = 169)	2–5 Years (n = 189)	5–10 Years (n = 281)	10–15 Years (n = 257)	15–18 Years (n = 104)
Epileptogenic lesions	82 (48.5%)	57 (30.2%)	60 (21.4%)	47 (18.3%)	14 (13.5%)
MCD	22 (26.8%)	20 (35.1%)	24 (40.0%)	18 (38.3%)	0 (0.0%)
Hypoxic-ischemic	26 (31.7%)	14 (24.6%)	9 (15.0%)	2 (4.3%)	0 (0.0%)
Vascular	14 (17.1%)	10 (17.5%)	6 (10.0%)	9 (19.1%)	3 (21.4%)
MTS	2 (2.4%)	1 (1.8%)	5 (8.3%)	9 (19.1%)	3 (21.4%)
NCS	8 (9.8%)	1 (1.8%)	4 (6.7%)	1 (2.1%)	1 (7.1%)
Tumoral	0 (0.0%)	3 (5.3%)	4 (6.7%)	4 (8.5%)	4 (28.6%)
Other	10 (12.2%)	8 (14.0%)	8 (13.3%)	4 (8.5%)	3 (21.4%)

^a 95% CI for the percentages of epileptogenic lesions in the 0–2 year, 2–5 year, 5–10 year, 10–15 year, and 15–18 year age groups were 41.1%–56.0%, 24.1%–37%, 17.0%–26.5%, 14.0%–23.5%, and 8.2%–21.3%, respectively.

Table 3: Frequencies of epileptogenic lesions stratified by seizure type at presentation

Seizure Types	Epileptogenic Lesions
Absence and/or myoclonus with or without generalized tonic-clonic seizures (n = 130)	8 (6.2%)
Unknown-onset tonic-clonic seizures (n = 260)	38 (14.6%)
Unclassified (n = 33)	5 (15.2%)
Focal-onset seizures (n = 484)	148 (30.6%)
Spasms, tonic or atonic seizures (n = 93)	61 (65.6%)

in the 15–18 year age group (Table 2). On the other hand, there was a gradual increase in the frequencies of MTS and tumoral etiologies with ascending age groups, peaking in the 15–18 year age group (Table 2). Other types of epileptogenic lesions did not show an apparent age-related pattern. However, children with MCD presented with seizures before 15 years of age.

Frequencies of Epileptogenic Lesions According to the Presence of DD

Two hundred twenty-three children had evidence of DD at the initial evaluation, with a significant difference in frequency across the age groups ($P < .001$). DD was highest in the 0–2 year group (60.9%), followed by the 2–5 year group (29.1%), the 5–10 year group (12.8%), the 10–15 year group (8.9%), and finally the 15–18 year group (5.8%).

The frequency of epileptogenic lesions was significantly higher in children with DD (127/223, 57.0%; 95% CI, 50.4%–63.3%) compared with those with normal development (133/777, 17.1%; 95% CI, 14.6%–19.9%; $P < .001$). There was also a significant increase in the frequencies of epileptogenic lesions as the severity of DD worsened ($P < .001$).

Frequencies of Epileptogenic Lesions According to the Type of Seizures Groups

There was a significant difference in the frequencies of identified epileptogenic lesions according to the seizure types at presentation ($P < .001$, Table 3). The lowest yield of detecting a lesion was in the group of patients with absences and/or myoclonus with or without generalized tonic-clonic seizures (6.2%), and the highest yield was in children who presented with epileptic spasms in clusters or frequent tonic or atonic seizures (65.6%). The frequency of epileptogenic lesions in children with focal-onset seizures was 30.6% (Table 3).

Multivariate Analysis

A logistic regression analysis with an epileptogenic lesion as the dependent variable and all significant variables in the univariate

analyses (≥ 1 seizure on presentation, age groups, presence of DD, and seizure types) as independent variables showed that only the presence of DD (odds ratio = 4.3, $P < .001$) and seizure types on presentation (odds ratio = 2.3, $P < .001$) remained significant. The frequencies of epileptogenic lesions stratified by seizure types and the presence or absence of DD are shown in Fig 2.

The recursive analysis identified the same 2 variables (the presence or absence of DD and seizure type) that partitioned the patients into a decision tree with 4 groups (Fig 3). The highest yield of detecting epileptogenic lesions (63.0%) was in the group of children with DD who presented with focal-onset seizures or with epileptic spasms or tonic or atonic seizures. The frequency of epileptogenic lesions in children without DD who presented with the same seizure types was 24.8%. The corresponding yields for children with and without DD who presented with other seizure types were 36% and 8.8%, respectively.

DISCUSSION

This is the largest study that prospectively evaluated brain MR imaging findings in consecutive children with new-onset unprovoked seizures using a dedicated imaging protocol. We documented that the yield of identifying epileptogenic lesions in that patient population is 26% (95% CI, 23.4%–28.8%).

Three previous studies identified etiologically related neuroimaging abnormalities in 13%–18% of children with new-onset seizures.^{4–6} Those studies had several methodologic shortcomings, including evaluating children with a mixture of head CT and non-epilepsy protocol brain MRIs,^{4,5} selection bias because neuroimaging studies were not systematically performed but only as clinically indicated,^{4,5} and exclusion of children with DD.⁶ For instance, epileptogenic lesions were detected in 18% of 411 children who presented with a first afebrile seizure.⁴ In that study, neuroimaging was only performed in 53% of children, with most studies consisting of head CTs. In a community-based study of 613 children with newly diagnosed epilepsy, neuroimaging studies (approximately two-thirds had a standard brain MR imaging, and one-third underwent a head CT) were obtained in 80%, with etiologically relevant abnormalities detected in 13%.⁵ A subsequent prospective study performed brain MR imaging in 281/349 children with a first-recognized seizure.⁶ Significant abnormalities or those potentially related to seizures were identified in 14% of those children. The relatively low yield of epileptogenic lesions in that study can be explained by the fact that children younger than 6 years of age and those with moderate or severe DD were excluded.⁶

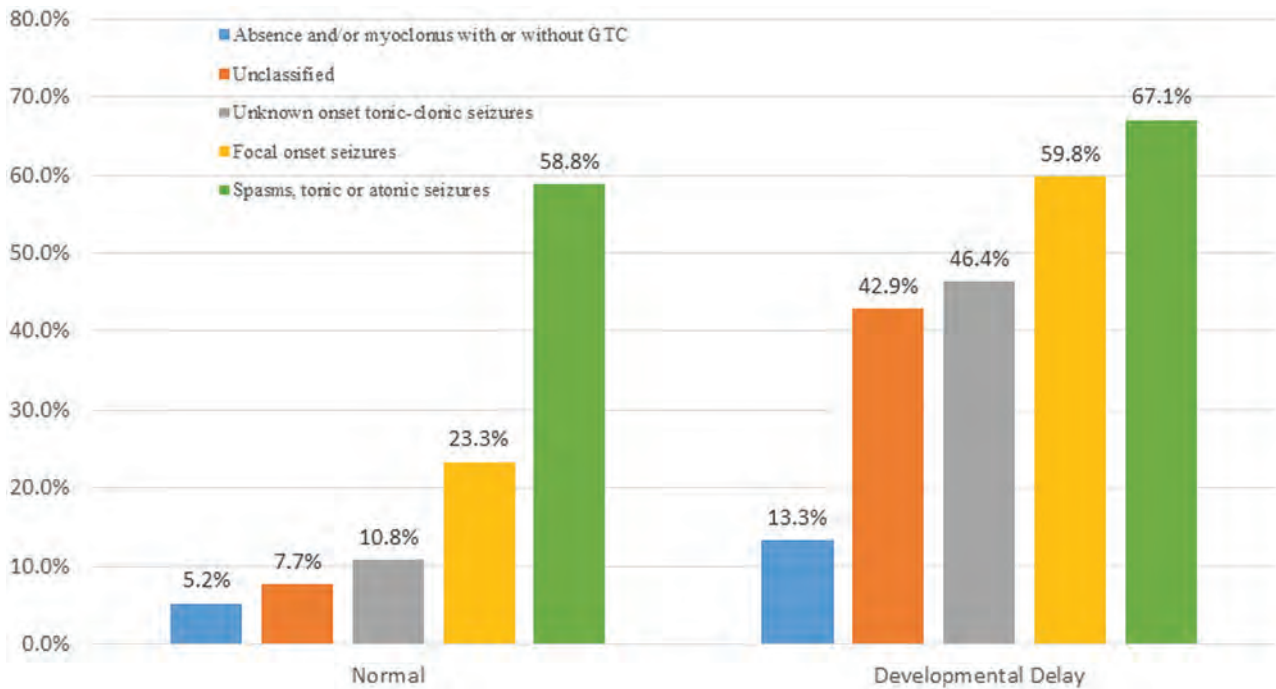


FIG 2. Percentages of children with epileptogenic lesions stratified according to seizure types and the presence or absence of developmental delay. GTC indicates generalized tonic-clonic seizures.

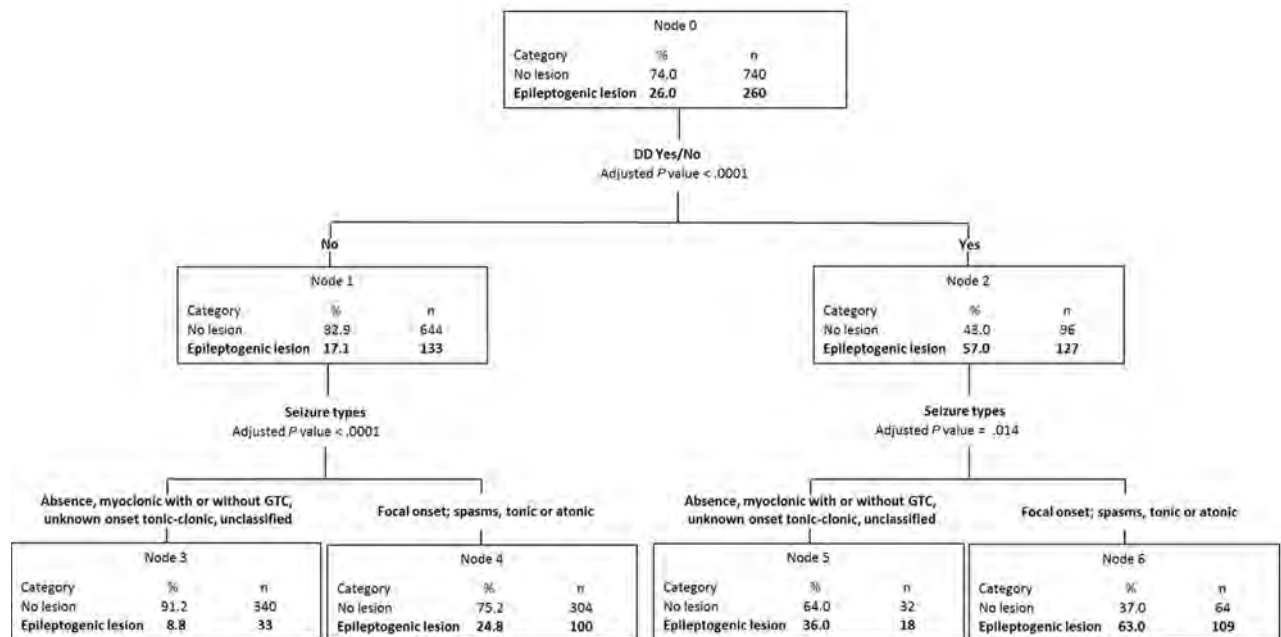


FIG 3. Recursive partition analysis stratified children into 4 groups based only on the presence of DD and seizure types. GTC indicates generalized tonic-clonic seizures.

The most common epileptogenic lesion in our study was MCD, followed by hypoxic-ischemic injuries and vascular lesions. Because of the large number of children enrolled, our study is the first to stratify the pathologic substrate on brain MR imaging according to age groups. We found that in children 2 years of age and younger, the most common underlying etiology was hypoxic-ischemic injury and MCD. Those results are

concordant with those of a smaller study conducted in children younger than 2 years of age with newly diagnosed epilepsy in whom the most common pathologic substrate was developmental brain malformations.¹⁹ We also found that MCD was one of the most common epileptogenic lesions in the 2–15 year age group, while MTS was most frequent in the 10–18 year age group presenting with new-onset seizures.

This is also the first study that documented a gradual increase in the frequency of epileptogenic lesions with decreasing age as well as with the presence and severity of DD. For young children, our results are overall similar to those recently reported in a study that evaluated the frequency of etiologically relevant neuroimaging abnormalities in children with early-life epilepsy, most of whom were evaluated with an epilepsy protocol brain MR imaging.²⁰ In that study, 40% of children 3 years of age and younger were found to have epileptogenic lesions, with a frequency of 61% in those with DD compared with 24% in children with normal development.²⁰ These results are very similar to ours, because in the group of children younger than 2 years of age, we identified an epileptogenic lesion in 48.5%, with a 65% frequency in children with DD compared with 23% in developmentally healthy children. Two other studies that evaluated the yield of neuroimaging in children younger than 2 years of age with new-onset seizures showed similar results, with etiologically relevant abnormalities detected in 42%²¹ and in 51%¹⁹ of children. In our study, the highest frequency of DD was in children younger than 2 years of age, with 61% of children with new-onset seizures having concomitant DD. This finding is consistent with those in previous studies that showed that a substantial proportion of children presenting with seizures in early life have associated DD.^{22,23}

Our data showed that there was a significant difference in the frequencies of epileptogenic lesions according to the seizure types experienced by the child at the time of evaluation. We stratified the seizure types into various groups based on the fact that certain seizure types are known to occur in generalized genetic epilepsy, and others, in focal epilepsy and epileptic encephalopathies. As would be expected, the frequency of detecting an epileptogenic lesion was lowest in children who presented with absence and/or myoclonic seizures with or without generalized tonic-clonic seizures and highest in those who experienced epileptic spasms in clusters or frequent tonic or atonic seizures.

Using logistic regression, we found that only the presence of DD (odds ratio = 4.3), as well as the seizures types (odds ratio = 2.3), remained significantly associated with the presence of an epileptogenic lesion. Because the highest frequency of children with DD was in those younger than 2 years of age, it is not surprising that the age group did not achieve statistical significance in the multivariate model. The results of the recursive partitioning analysis were concordant with those of the logistic regression and provided a tree with 6 nodes based on the seizure types and the presence or absence of DD. The expected yield of detecting an epileptogenic lesion in each of the various nodes could be used as a decision tree to determine when brain MR imaging should be performed.

We purposefully avoided including the electroencephalography results in our analyses because our aim was to establish the yield of neuroimaging based on the clinical presentation alone. Furthermore, because a presumed electroclinical syndrome could be modified by the presence of an epileptogenic lesion on the MR imaging, including the electroencephalography results as a variable can lead to circular reasoning. For example, a developmentally healthy child presenting with an opercular seizure (focal-aware seizure) and found to have rolandic maturational epileptiform discharges on the electroencephalography would be

initially diagnosed as a case of self-limited epilepsy with centro-temporal spikes. The diagnosis on that same child would be changed to structural focal epilepsy if the MR imaging were to reveal a cavernoma in the inferior frontal rolandic cortex.

The strength of our study is that it evaluated a large cohort of consecutive children referred for new-onset unprovoked seizures and who underwent a HARNESSE brain MR imaging protocol.⁹ The acquisition of MRIs was centralized, the neuroimaging studies were obtained shortly after the seizure onset, and the studies were interpreted by an experienced neuroradiologist who was blinded to the clinical data. In addition, we were very conservative in defining epileptogenic lesions and stratified the types and frequencies of lesions according to the seizure types experienced by the child at the time of the initial evaluation. We elected not to include children who underwent a non-epilepsy protocol MR imaging to have a set of uniform data, especially because it was previously shown that up to 65% of studies interpreted as having normal findings would reveal a relevant lesion when a high-quality study was performed.^{24,25}

CONCLUSIONS

Ideally, we believe that brain MR imaging should be performed in every child with new-onset unprovoked seizures, especially when sedation is not required, for several reasons: First, it would be in keeping with the new International League Against Epilepsy classification of the epilepsies, which emphasizes the need to consider the etiology at each step of diagnosis, including a structural etiology, which should preferably be evaluated with brain MR imaging and that will help with the syndromic classification.^{9,18} In addition, for children who present with a single, unprovoked seizure, the presence of specific structural brain lesions could satisfy the diagnosis of epilepsy^{9,17} and will also guide the need for treatment. Furthermore, the pathologic substrate identified on neuroimaging can assist with the prognosis and accelerate referral to a specialized epilepsy center.⁹ When brain MR imaging is not readily available, as in developing nations where the resources might be scarce or in case of financial constraints, it would be useful to have guidelines to recommend when brain MR imaging should be performed in children with new-onset, unprovoked seizures. The practice parameter issued in 2000 and reaffirmed in 2017 by the American Academy of Neurology, the Child Neurology Society, and the American Epilepsy Society for the evaluation of a first nonfebrile seizure in children asserts that brain MR imaging is the preferred technique and that it should be seriously considered in any child with psychomotor delay, focal-onset seizure, and younger than 1 year of age.⁷ The League Against Epilepsy Guidelines recommend imaging (MR imaging is preferred over CT when available) for infants and children with recent-onset epilepsy whenever localization-related epilepsy is known or suspected, when the epilepsy classification is in doubt, or when an epilepsy syndrome with a remote symptomatic cause is suspected.²⁶ However, the authors of the practice parameter stressed that there is insufficient evidence available from the published studies for issuing evidence-based guidelines pertaining to neuroimaging in children with new-onset seizures. They also stressed the need for a large prospective study that enrolls consecutive children using a standardized MR imaging

acquisition protocol and that stratifies the findings according to age groups. Our study fulfills those requirements, and we hope that our results will assist the relevant societies and committees in formulating neuroimaging guidelines for children with new-onset seizures.

REFERENCES

1. Semah F, Picot MC, Adam C, et al. **Is the underlying cause of epilepsy a major prognostic factor for recurrence?** *Neurology* 1998;51:1256–62 CrossRef Medline
2. Stephen LJ, Kwan P, Brodie MJ. **Does the cause of localisation-related epilepsy influence the response to antiepileptic drug treatment?** *Epilepsia* 2002;42:357–62 CrossRef Medline
3. Fisher RS, Acevedo C, Arzimanoglou A, et al. **ILAE official report: a practical clinical definition of epilepsy.** *Epilepsia* 2014;55:475–82 CrossRef Medline
4. Shinnar S, O'Dell C, Mitnick R, et al. **Neuroimaging abnormalities in children with an apparent first unprovoked seizure.** *Epilepsy Res* 2001;43:261–69 CrossRef Medline
5. Berg AT, Testa FM, Levy SR, et al. **Neuroimaging in children with newly diagnosed epilepsy: a community-based study.** *Pediatrics* 2000;106:527–32 CrossRef Medline
6. Kalnin AJ, Fastenau PS, Degrauw TJ, et al. **Magnetic resonance imaging findings in children with a first recognized seizure.** *Pediatr Neurol* 2008;39:404–14 CrossRef Medline
7. Hirtz D, Ashwal S, Berg A, et al. **Practice parameter: evaluating a first nonfebrile seizure in children: report of the quality standards subcommittee of the American Academy of Neurology, the Child Neurology Society, and the American Epilepsy Society.** *Neurology* 2000;55:616–23 CrossRef Medline
8. Arabi M, Dirani M, Hourani R, et al. **Frequency and stratification of epileptogenic lesions in elderly with new onset seizures.** *Front Neurol* 2018;9:995 CrossRef Medline
9. Bernasconi A, Cendes F, Theodore WH, et al. **Recommendations for the use of structural magnetic resonance imaging in the care of patients with epilepsy: a consensus report from the International League Against Epilepsy Neuroimaging Task Force.** *Epilepsia* 2019;60:1054–68 CrossRef Medline
10. Chuang NA, Otsubo H, Chuang SH. **Magnetic resonance imaging in pediatric epilepsy.** *Top Magn Reson Imaging* 2002;13:39–60 CrossRef Medline
11. Urbach H. **Imaging of the epilepsies.** *Eur Radiol* 2005;15:494–500 CrossRef Medline
12. Moosa AN, Wyllie E. **Focal epileptogenic lesions** *Handb Clin Neurol* 2013;111:493–510 CrossRef Medline
13. Volpe JJ. **Confusions in nomenclature: “periventricular leukomalacia” and “white matter injury”: identical, distinct, or overlapping?** *Pediatr Neurol* 2017;73:3–6 CrossRef Medline
14. Humphreys P, Deonandan R, Whiting S, et al. **Factors associated with epilepsy in children with periventricular leukomalacia.** *J Child Neurol* 2007;22:598–605 CrossRef Medline
15. Frankenburg WK, Dodds J, Archer P, et al. *Denver II Training Manual.* Denver Developmental Materials; 1992
16. American Psychiatric Association. *DSM-5 Task Force. Diagnostic and Statistical Manual of Mental Disorders (DSM-5).* American Psychiatric Association; 2013
17. Fisher RS, Cross JH, French JA, et al. **Operational classification of seizure types by the International League Against Epilepsy: Position Paper of the ILAE Commission for Classification and Terminology.** *Epilepsia* 2017;58:522–30 CrossRef Medline
18. Scheffer IE, Berkovic S, Capovilla G, et al. **ILAE classification of the epilepsies: position paper of the ILAE Commission for Classification and Terminology.** *Epilepsia* 2017;58:512–21 CrossRef Medline
19. Eltze CM, Chong WK, Cox T, et al. **A population-based study of newly diagnosed epilepsy in infants.** *Epilepsia* 2013;54:437–45 CrossRef Medline
20. Coryell J, Gaillard WD, Shellhaas RA, et al. **Neuroimaging of early life epilepsy.** *Pediatrics* 2018;142:e20180672 CrossRef Medline
21. Hsieh D, Chang T, Tsuchida T, et al. **New-onset afebrile seizures in infants: role of neuroimaging.** *Neurology* 2010;74:150–56 CrossRef Medline
22. Battaglia D, Rando T, Deodato F, et al. **Epileptic disorders with onset in the first year of life: neurological and cognitive outcome.** *Eur J Paediatr Neurol* 1999;3:95–103 CrossRef Medline
23. Altunbaşak Ş, Incecik F, Hergüner Ö, et al. **Prognosis of patients with seizures occurring in the first 2 years.** *J Child Neurol* 2007;22:307–13 CrossRef Medline
24. Knake S, Triantafyllou C, Wald L, et al. **3T phased array MRI improves the presurgical evaluation in focal epilepsies: a prospective study.** *Neurology* 2005;65:1026–31 CrossRef Medline
25. Kokkinos V, Kallifatidis A, Kapsalaki EZ, et al. **Thin isotropic FLAIR MR images at 1.5 T increase the yield of focal cortical dysplasia transmantle sign detection in frontal lobe epilepsy.** *Epilepsy Res* 2017;132:1–7 CrossRef Medline
26. Gaillard WD, Chiron C, Cross JH, et al. **ILAE, Committee for Neuroimaging, Subcommittee for Pediatric. Guidelines for imaging infants and children with recent-onset epilepsy.** *Epilepsia* 2009;50:2147–53 CrossRef Medline

Radiomic Phenotypes Distinguish Atypical Teratoid/ Rhabdoid Tumors from Medulloblastoma

M. Zhang, S.W. Wong, S. Lummus, M. Han, A. Radmanesh, S.S. Ahmadian, L.M. Prolo, H. Lai, A. Eghbal, O. Oztekin, S.H. Cheshier, P.G. Fisher, C.Y. Ho, H. Vogel, N.A. Vitanza, R.M. Lober, G.A. Grant, A. Jaju, and K.W. Yeom



ABSTRACT

BACKGROUND AND PURPOSE: Atypical teratoid/rhabdoid tumors and medulloblastomas have similar imaging and histologic features but distinctly different outcomes. We hypothesized that they could be distinguished by MR imaging–based radiomic phenotypes.

MATERIALS AND METHODS: We retrospectively assembled T2-weighted and gadolinium-enhanced T1-weighted images of 48 posterior fossa atypical teratoid/rhabdoid tumors and 96 match-paired medulloblastomas from 7 institutions. Using a holdout test set, we measured the performance of 6 candidate classifier models using 6 imaging features derived by sparse regression of 900 T2WI and 900 T1WI Imaging Biomarker Standardization Initiative–based radiomics features.

RESULTS: From the originally extracted 1800 total Imaging Biomarker Standardization Initiative–based features, sparse regression consistently reduced the feature set to 1 from T1WI and 5 from T2WI. Among classifier models, logistic regression performed with the highest AUC of 0.86, with sensitivity, specificity, accuracy, and F1 scores of 0.80, 0.82, 0.81, and 0.85, respectively. The top 3 important Imaging Biomarker Standardization Initiative features, by decreasing order of relative contribution, included voxel intensity at the 90th percentile, inverse difference moment normalized, and kurtosis—all from T2WI.

CONCLUSIONS: Six quantitative signatures of image intensity, texture, and morphology distinguish atypical teratoid/rhabdoid tumors from medulloblastomas with high prediction performance across different machine learning strategies. Use of this technique for preoperative diagnosis of atypical teratoid/rhabdoid tumors could significantly inform therapeutic strategies and patient care discussions.

ABBREVIATIONS: ATRT = atypical teratoid/rhabdoid tumor; AUC = area under the curve; GLCM = gray level co-occurrence matrix; MB = medulloblastoma

Atypical teratoid/rhabdoid tumors (ATRTs) are rare-but-aggressive neoplasms that often affect very young children.^{1,2} They are classically characterized by rhabdoid cells and

divergent differentiation along neuroectodermal, mesenchymal, and epithelial lines. However, many ATRTs often lack rhabdoid cells and are simply dense, small, round, blue cell-rich lesions that mimic medulloblastomas (MBs, Online Supplemental Data).^{3,4} Whereas most ATRTs may be distinguished from MBs by immunohistochemical confirmation of *SMARCB1* (INI1/BAF47/hSNF5) loss (Online Supplemental Data),⁴⁻⁷ up to 22% of ATRTs retain the protein marker.^{5,8,9}

Presurgical distinction of ATRT from MB is not possible by human interpretation of MR imaging; both primarily occupy the posterior fossa, share low T1- and T2-weighted intensities and variable enhancement, and have a reduced diffusion characteristic of

Received February 13, 2021; accepted after revision April 5.

From the Departments of Neurosurgery (M.Z.) and Pathology (S.S.A., H.V.), Stanford Medical Center, Stanford University, Stanford, California; Department of Statistics (S.W.W.), Stanford University, Stanford, California; Department of Physiology and Nutrition (S.L.), University of Colorado, Colorado Springs, Colorado; Department of Pediatrics (M.H.), Children's Hospital of Philadelphia, University of Pennsylvania, Philadelphia, Pennsylvania; Department of Radiology (A.R.), New York University Grossman School of Medicine, New York, New York; Departments of Neurosurgery (L.M.P., G.A.G.), Neurology (P.G.F.), and Radiology (K.W.Y.), Lucile Packard Children's Hospital, Stanford University, Palo Alto, California; Department of Radiology (H.L., A.E.), Children's Hospital of Orange County, Orange, California and University of California, Irvine, Irvine, California; Department of Neuroradiology (O.O.), Cigli Education and Research Hospital, Bakircay University, Izmir, Turkey; Department of Neuroradiology (O.O.), Tepecik Education and Research Hospital, Health Science University, Izmir, Turkey; Division of Pediatric Neurosurgery (S.H.C.), Department of Neurosurgery, Huntsman Cancer Institute, Intermountain Healthcare Primary Children's Hospital, University of Utah School of Medicine, Salt Lake City, Utah; Departments of Clinical Radiology & Imaging Sciences (C.Y.H.), Riley Children's Hospital, Indiana University, Indianapolis, Indiana; Division of Pediatric Hematology/Oncology (N.A.V.), Department of Pediatrics, Seattle Children's Hospital, Seattle, Washington; Division of Neurosurgery (R.M.L.), Department of Pediatrics, Wright State University Boonshoft School of Medicine, Dayton Children's Hospital, Dayton, Ohio; and Department of Medical Imaging (A.J.), Ann and Robert H. Lurie Children's Hospital of Chicago, Northwestern University Feinberg School of Medicine, Chicago, Illinois.

M. Zhang is funded by the National Institutes of Health (5T32CA009695-27). K.W. Yeom is funded by the M. Zhang is funded by the American Brain Tumor Association (DG1800019).

Please address correspondence to Kristen W. Yeom, MD, Department of Radiology, Lucile Salter Packard Children's Hospital, 725 Welch Rd G516, Palo Alto, CA 94304; e-mail: kyeom@stanford.edu

Indicates article with online supplemental data.

<http://dx.doi.org/10.3174/ajnr.A7200>

densely packed cellular tumors (Online Supplemental Data).¹⁰⁻¹³ However, if it were possible, this distinction could add value because their different behaviors demand different treatment strategies. Median survival for patients with ATRTs is approximately 1 year, while the 5-year survival rate for pediatric MB is approximately 70%.¹⁴⁻¹⁸ Thus, an anticipated diagnosis of ATRT may prompt discussion of maximal surgical resection and aggressive adjuvant therapy.^{19,20}

Recent advances in machine learning and computer vision in medicine offer new potentials for precision in oncology, whether it is for tumor subgroup classification or prognosis. For example, feature extraction, such as in radiomics, enables mining of high-dimensional, quantitative image features that facilitate data-driven, predictive modeling. The resulting computational algorithm assigns probabilities for diagnoses and outcomes on the basis of its quantitative analysis of tumor voxels on imaging.²¹⁻²³ While studies have reported various machine learning approaches to MR imaging-based evaluation of pediatric brain tumors, no study has examined quantitative MR imaging features that distinguish ATRT from MB, in part, due to the rarity of ATRT.^{13,19, 24-27}

Radiomics has the potential to not only uncover quantitative image features that may otherwise be imperceptible to the human eye but also offers interpretability of computational features that drive model prediction—a potential advantage over deep learning, in which learned features remain opaque. In this multicenter study, we applied machine learning to uncover MR imaging-based radiomic phenotypes that distinguish ATRT from MB.

MATERIALS AND METHODS

Study Population

We conducted a retrospective study after obtaining institutional review board approval (No. 51059) and data-sharing agreements with 7 participating institutions (Online Supplemental Data): Stanford Children's (ST-Palo Alto, California), Lurie Children's Hospital of Chicago (CG-Chicago, Illinois), Primary Children's Hospital (UT-Salt Lake City, Utah), New York University Langone Medical Center (NY-New York, New York), Children's Hospital Orange County (CH-Irvine, California), Indiana University Riley Hospital for Children (IN-Indianapolis, Indiana), and Tepecik Health Sciences (TK-Izmir, Turkey). We performed a chart review to identify patients with ATRTs and MBs. Inclusion criteria were the following: 1) Patients underwent preoperative MR imaging with gadolinium-enhanced T1WI and T2WI; and 2) surgical specimens of the tumor served as ground truth for pathology, including loss of INI-1 staining to confirm ATRT. Patients were excluded if MR imaging was degraded by motion or other artifacts or was considered nondiagnostic. When available, tumor molecular subgroup information was recorded. To increase the available training information and given the availability of additional MB data, we included twice the number of patients with MB relative to ATRT in the study. The initial MB cohort was randomly match-paired by institution, sex, and age with the ATRT cohort. To avoid overfitting from class imbalance, the ATRT cohort was oversampled to match the number of MBs in the training cohort.

MR Imaging Acquisition

MR imaging brain scans were acquired at either 1.5 and 3T using the following vendors: GE Healthcare (Signa Artist, Discovery 750, Optima 360, Signa Excite, Signa HDxt, Signa Explorer, Optima 450w), Siemens (Aera, Skyra, Avantofit, Espree, Symphony, Symphony Vision, Trio), Philips Healthcare (Ingenia, Intera, Achieva), and Toshiba Canon Medical Systems USA. The T2WI scans were the following: T2 TSE constant level appearance/sensitivity encoding, T2 fast-spin-echo, T2 PROPELLER, T2 BLADE (Siemens), T2 drive sense (TR/TE = 2475.6–9622.24/80–146.048; section thickness = 1–5 mm with a 0.5- or 1-mm skip; matrix ranges = 224–1024 × 256–1024). T1WI postgadolinium MR imaging scans included T1 MPRAGE, T1 BRAVO (GE Healthcare), T1 fast-spoiled gradient recalled, T1 spoiled gradient recalled, and T1 spin-echo (section thickness = 0.8–1.2 mm, matrix ranges = 256–512 × 256–512). All image data were obtained in DICOM format.

Image Preprocessing and Feature Extraction

The volumetric whole-tumor boundary, inclusive of solid and cystic components, was delineated (K.W.Y.) and confirmed (A.J.) by board-certified attending neuroradiologists with Certificates of Added Qualification (K.W.Y., A.J., with >10 years' experience) using OsiriX Imaging Software (<http://www.osirix-viewer.com>). We used PyRadiomics software (Version 2.2.0. post7+gac7458e; <https://github.com/AIM-Harvard/pyradiomics>) for feature extraction with implementation in the Quantitative Image Feature Pipeline (<http://qifp.stanford.edu>).^{28,29} The configuration files for radiomic feature extraction are included in the Online Supplemental Data.

A total of 1800 features (900 each from T2WI and T1WI) was automatically extracted on tumor volume including the following: first order statistics, 2D/3D shape, gray level co-occurrence matrix (GLCM), gray level run length matrix, gray level size zone matrix, neighboring gray-tone difference matrix, and gray level dependence matrix, as defined by the Imaging Biomarker Standardization Initiative.^{29,30} MR imaging studies were normalized for voxel size (1 × 1 × 1 mm) and intensity (scale factor of 100). A fixed bin width (10) was used for gray-value discretization. Preprocessing filters included wavelet (8 coefficients) and Laplacian of Gaussian (3 σ). Feature extraction was calculated for classes including first order statistics, shape descriptors, and gray level derivatives.³¹

Feature Reduction

Training and test sets were randomly allocated from the total cohort in a 70:30 ratio. Feature selection for the allocated training set was performed using sparse regression analysis by a Least Absolute Shrinkage and Selection Operator, performed with 10-fold cross-validation and repeated for 1000 cycles. The mean squared error was calculated for 100 lambdas in each cycle or until a minimum was achieved. The optimal λ was identified as the lowest mean squared error value and used for feature reduction and coefficient calculations. Both radiologic and clinical variables were incorporated at this stage into the primary model. Selected features represented in $\geq 80\%$ of the cycles were retained for subsequent classifier optimization.

Feature reduction was performed using R Studio, Version 1.2.5033 (<http://rstudio.org/download/desktop>).

Classifier Model Building and Analysis

The retained features were submitted to 6 training models, including support vector machine, logistic regression, k-nearest neighbors, random forest, eXtreme Gradient Boosting, and neural net. The cohort underwent resampling to correct for sample imbalance. Training and test sets were randomly allocated from the total cohort in a 75:25 ratio. MB tumor was designated the positive class. Optimal classifier parameters were performed by grid search (Online Supplemental Data). The optimal radiomics classifier was selected by maximizing the area under the curve (AUC). Confidence intervals for each metric were obtained by bootstrapping of the test sets for 2000 random samples. Relative influence of the radiologic features was calculated for logistic regression and tree-based models, random forest, and eXtreme Gradient Boosting. Model training was performed using Python, Version 3.8.5.

Qualitative Evaluation by Human Reader

Two human experts (K.W.Y., A.J.) performed consensus review of T1WI and T2WI on the ATRT and MB cohorts, blinded to pathologic diagnosis or any clinical variables. The readers scored the degree of enhancement (0, no enhancement; 1, < 50% tumor volume with enhancement; 2, \geq 50% tumor volume with enhancement) and the presence or absence of a cyst. Categorical variables were compared using the Fisher exact test, as appropriate. A *P* value < .05 was considered statistically significant for all analyses.

RESULTS

Demographics and Clinical Information

A total of 48 ATRTs (28 males [58.3%]; median age, 13.7 months; range, 1.0–114.6 months at diagnosis) and 96 patients with MB (61 males [63.5%]; median age, 83.0 months; range, 3.0–231.9 months at diagnosis) met the study criteria (Online Supplemental Data). MB molecular subgroup distribution is shown in the Online Supplemental Data. Molecular subgroup information was not available for ATRT.

Feature Reduction and Model Performance

Following feature reduction with sparse regression, 6 textural features were consistently selected in >80% of regression cycles, including 3 shape features, 2 first order features, and 1 GLCM feature (Online Supplemental Data), with 1 feature derived from T1WI, and 5, from T2WI. The single T1WI feature, elongation, was also represented among the T2WI features.

The performances of 6 models were evaluated on the holdout test, with logistic regression demonstrating the highest AUC of 0.8582 (Online Supplemental Data). Sensitivity, specificity, positive predictive value, negative predictive value, accuracy, and F1 score were 0.80, 0.82, 0.91, 0.64, 0.81, and 0.85, respectively. The least effective classifier was neural net with an AUC of 0.73, closely followed by eXtreme Gradient Boosting with an AUC of 0.74. Among other models, k-nearest neighbors was notable, with the highest metrics other than AUC (0.84). Sensitivity, specificity, positive predictive value, negative predictive value, accuracy, and F1 score were 0.80, 0.91, 0.95, 0.67, 0.83, and 0.87, respectively.

Relative Influence of Variables

Relative influence was assessed by logistic regression, random forest, and eXtreme Gradient Boosting (Fig 1, Fig 2 and Online Supplemental Data). In all classifiers, the voxel intensity at the 90th percentile was the most contributory, ranging from 24% to 40%. In the logistic regression, voxel intensity at the 90th percentile was also the only parameter that positively predicted ATRT. This was consistently followed by 2 other textural features, GLCM inverse difference moment normalized and kurtosis. The last 3 features (by relative importance) included T1WI and T2WI measurements for elongation and flatness within the segmented ROI. T1WI elongation was consistently the lowest contributing feature, ranging from 5.2% to 7.8% of classifiers.

Human Evaluation

Based on qualitative assessment by human experts (Online Supplemental Data), the frequencies of 0%, <50%, and \geq 50% enhancement for ATRT were 4.1%, 51.0%, and 44.9%. For MB, the corresponding frequencies were 0%, 35.5%, and 64.5% (*P* < .001). Meanwhile, the frequency of cysts was not different between groups (*P* = .26).

DISCUSSION

In this multi-institutional study, we constructed machine learning classifiers to identify MR imaging-based radiomic phenotypes to distinguish ATRT from MB. This is the largest imaging dataset and first radiomics study of ATRT, a rare-but-aggressive neoplasm.^{32,33}

While loss of INI-1 immunohistochemical staining can confirm the diagnosis in most ATRTs, up to 22% of ATRTs may show no alteration.⁴⁻⁷ Other CNS tumors, such as oligodendroglioma or anaplastic oligoastrocytoma, may also have INI-1 inactivation.⁶ Complex immunophenotypes as well as overlapping histologic features can confound the pathologic diagnosis, particularly with extensive embryonal morphologic components. Thus, reports of pathologic misdiagnoses have included MB, various embryonal tumors, glioblastoma, and, occasionally, choroid plexus carcinoma, in which inactivation of INI-1 may be present.^{6, 33-35}

Here, we identify 6 radiomic features, 1 derived from T1WI and 5 from T2WI, that together distinguish ATRT from MB by logistic regression with AUC = 0.86. Of these radiomic features, 3 describe T2WI-based voxel intensities and texture, and 3 describe tumor morphology.

On the basis of blinded human expert review, we found overlap in visually determined, qualitative image features such as the presence of cysts, suggesting morphologic heterogeneity (eg, cysts/cavities) inherent in both ATRT and MB, as previously described.^{15,19,26,36,37} Most interesting, despite variable MB enhancement, human experts scored MB as enhancing over a larger tumor volume (\geq 50%) in contrast to ATRT, regardless of how brightly or faintly a tumor enhanced (Online Supplemental Data).^{38,39} However, at a quantitative level, tumor brightness that is calculated by first order radiomics features (eg, average intensity/brightness) on T1WI was not selected by our model; suggesting how brightly (or faintly) a tumor enhanced was not a distinguishing feature. Radiomic features of tumor volume and

diameter were also not selected, indicating that tumor size did not contribute.

Overall, T2WI-based voxel intensities were most relevant. For example, 90th percentile voxel intensity emerged as the most important variable, with a higher value associated with ATRT. More heterogeneous texture, as described by the GLCM-based feature inverse difference moment normalized, calculated by larger gradient changes in intensity between neighboring voxels, also

predicted ATRT. Lower kurtosis or a wider distribution of voxel intensities was more characteristic of ATRT and similarly suggested a wider range in tissue composition.

The more heterogeneous texture of ATRT might reflect multiple histologic components of rhabdoid cells juxtaposed to embryonal cells and, sometimes, glial, mesenchymal, and/or epithelial differentiation, compared with more homogeneous and, classically, dense cellular sheet growth of MB.^{19,40,41} In combination, the myxoid background of gelatinous mucopolysaccharide-rich water content that ATRT is known to produce likely contributes to the high T2-voxel intensity value of ATRT.^{40,41}

Prior studies have suggested that ATRT and MB both qualitatively display nondiscriminating, T2-heterogeneous signal.^{11,12,37,42-44} Applying a filter to an image before calculating radiomic features can capture patterns or highlight additional details within the image that might otherwise be imperceptible to the human eye. Here, we show that features derived from wavelet-filtered images (GLCM in-verse difference moment normalized and kurtosis) can uncover textural differences that reside within tumor voxels. Furthermore, radiomics interrogates the

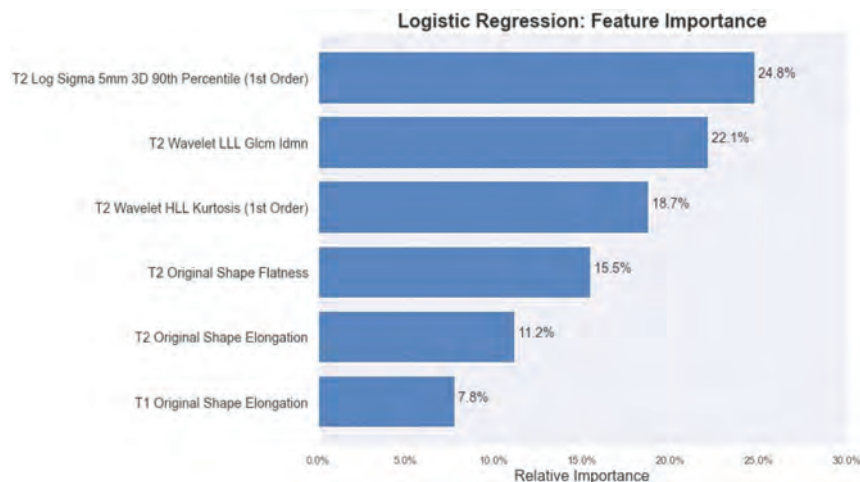


FIG 1. Barplot of the reduced feature set and its relative influence as calculated by logistic regression, trained to distinguish ATRT and medulloblastoma. IDMN indicates inverse difference moment normalized; HLL, High/Low/Low; LLL, Low/Low/Low.

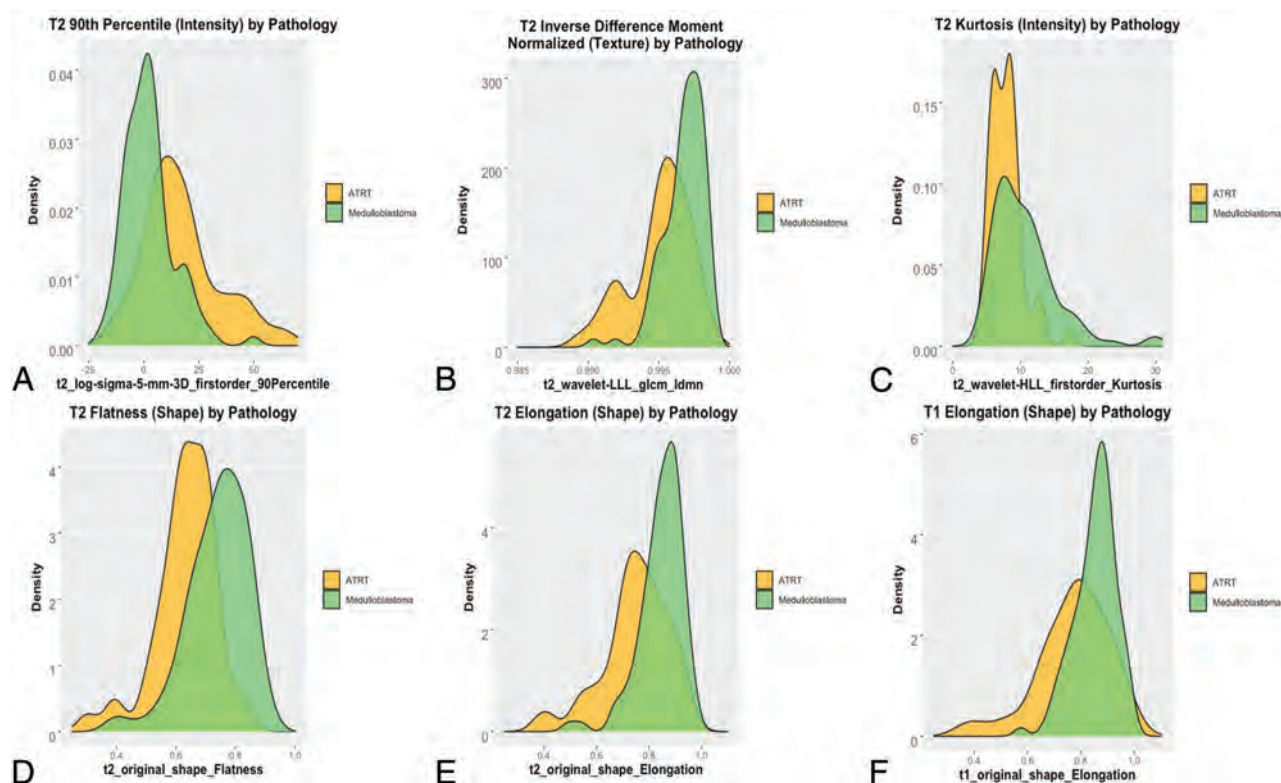


FIG 2. Density plots. A, T2-weighted 90th percentile voxel intensity. B, T2-weighted inverse difference moment normalized. C, T2-weighted kurtosis. D, T2-weighted flatness. E, T2-weighted elongation. F, T1-weighted elongation among patients with ATRT and medulloblastoma. LLL indicates Low/Low/Low.

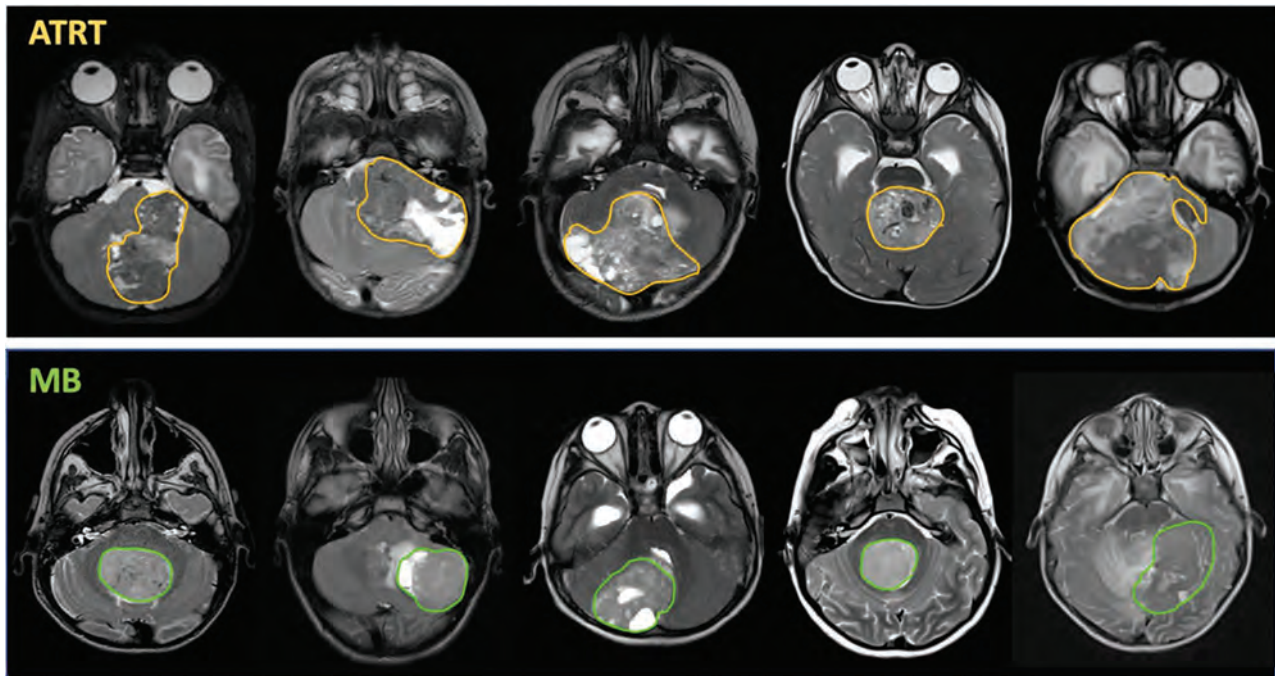


FIG 3. MR imaging correlates of radiomics phenotypes. Despite overlap in gross image features of MB and ATRT, unique quantitative radiomics features associated with shape and texture emerged as predictive features of ATRT and MB. For example, more heterogeneous features derived from GLCM-based texture or kurtosis-based wider distribution of voxel intensities were indicative of ATRT. Furthermore, more spheric morphology characterized MBs, compared with the more elongated or planar configuration of ATRT. Gross examples of the heterogeneous texture of ATRT are shown, including areas of mixed low and high T2-signal that might be seen with blood products, variations in tissue components, as well as cystic areas. While some ATRT tumors were round, many were quantitatively more elongated compared with the more spheric contour of many MB tumors. Despite the presence of cysts or T2-dark foci that might stem from blood products or vascularity, quantitatively, MB showed more even distribution of voxel intensities.

entire tumor phenotype before surgical disturbance, a distinct advantage over histology that probes tumor slices. Thus, heterogeneous texture might also reflect focal cysts, necrosis, and CSF clefts/spaces interspersed between tumor clusters unique to ATRT macro- or microenvironment, which may be difficult to identify either by histology or, qualitatively, on gross visual inspection (Fig 3).^{13,26,36,44}

Most interesting, linear and planar morphology suggested ATRT, whereas more circular and spheric morphology suggested MB (Fig 3). The distribution of the elongation feature showed that low values, ie, those that were more linear, were very specific for ATRT. Conversely, the distribution of the flatness feature showed that the most extreme values, ie, those that were more spheric, were specific to MB. Both elongation and flatness derive from the ellipsoid axes underlying the ROI but mathematically differ on the basis of which secondary axis is used in its calculation ($\sqrt{\frac{\lambda_{minor}}{\lambda_{major}}}$ versus $\sqrt{\frac{\lambda_{least}}{\lambda_{major}}}$, respectively). While there may be some redundancy among these 3 features, their selection internally validates the use of ellipsoid dimensions as predictive features. These morphology features may reflect anatomic origins. Both tumors can occupy the cerebellum and vermis with involvement of the fourth ventricle.^{26,36,45} However, from a histogenic perspective, MBs are derived from the roof of the external granular layer of the fourth ventricle and expand radially in a spheric manner.^{10,41} Meanwhile, ATRTs are thought to have choroid plexus derivation, commonly lateralizing to the cerebellopontine

angle, and may, thus, deform and flatten along its growth trajectory.^{35,46}

The radiomics signatures had consistent performance across different machine learning models, with substantial overlaps in the AUC-confidence intervals of the support vector machine, logistic regression, and k-nearest neighbors models. The k-nearest neighbors, in particular, had high sensitivity and specificity scores, albeit a slightly lower AUC than logistic regression. This feature likely relates to the intrinsic model design of k-nearest neighbors, in which extreme scores are penalized when the parameter for number of neighbors is small. The tree-based classifiers (random forest, eXtreme Gradient Boosting, and neural net) had higher false-negative rates, implying misclassification of a number of MBs. We suspect overfitting during the training phase with these tree-based approaches, given the smaller difference between training error and testing error for the nontree models. A larger ATRT sample size could augment the training pool for better tree-based models.

We note several limitations, including the small cohort size of ATRT due to its rarity. Nevertheless, this is the largest ATRT imaging study to date, with data pooled from multiple institutions. While we describe features derived from T2WI and gadolinium-enhanced T1WI, it is possible that the use of additional MR imaging sequences, such as FLAIR, T2*, or DWI could further optimize the classifier and add new insight into significant radiomic signatures. Although desirable, we did not conduct

radiogenomics analysis of ATRTs because the molecular subgroup information was not available. Our radiomics analysis is contingent on a voxel-based analysis of tumor segmentations. Therefore, it does not identify other potentially useful semantic images features such as anatomic location, perilesional edema, or other features of the brain environment external to the tumor.^{11,13,47} Finally, our model was trained on infratentorial ATRTs and may not infer features of the supratentorial ATRT.

CONCLUSIONS

In this multi-institutional study, we constructed discovery-driven approaches to uncover distinctive MR imaging-based radiomic phenotypes of ATRT and MB. Image intensity, texture, and morphology had high predictive performance across different machine learning strategies. Despite several limitations, including lack of radiogenomics analysis of ATRT tumors, our results suggest potential future roles for machine-enabled classifiers to refine preoperative planning and patient family counseling. Future iterations may additionally incorporate tumor genomics to uncover the biologic significance of quantitative image phenotypes.

ACKNOWLEDGMENTS

We would like to thank Sara Norris of the Intermountain Health Care Imaging Department (Salt Lake City, Utah) for archival image acquisition.

Disclosures: Michael Zhang—UNRELATED: Grant: National Institutes of Health, Comments: Michael Zhang is funded by the National Institutes of Health (5T32CA009695-27). Saman Seyed Ahmadian—UNRELATED: Employment: Stanford, Comments: I am a neuropathology fellow at Stanford. Paul G. Fisher—OTHER RELATIONSHIPS: I am on the Editorial Board of *Journal of Clinical Oncology* (unpaid). Alok Jaju—UNRELATED: Grants/Grants Pending: Incyte Corporation, Comments: research grant; Stock/Stock Options: Gilead Sciences, Comments: stock ownership. Kristen Yeom—RELATED: Grant: American Brain Tumor Association, Comments: Kristen W. Yeom and this study in part are funded by the American Brain Tumor Association (DG1800019).

REFERENCES

- Hilden JM, Meerbaum S, Burger P, et al. **Central nervous system atypical teratoid/rhabdoid tumor: results of therapy in children enrolled in a registry.** *J Clin Oncol* 2004;22:2877–84 CrossRef Medline
- Morgenstern DA, Gibson S, Brown T, et al. **Clinical and pathological features of paediatric malignant rhabdoid tumours.** *Pediatr Blood Cancer* 2010;54:29–34 CrossRef Medline
- Burger PC, Yu IT, Tihan T, et al. **Atypical teratoid/rhabdoid tumor of the central nervous system: a highly malignant tumor of infancy and childhood frequently mistaken for medulloblastoma.** *Am J Surg Pathol* 1998;22:1083–92 CrossRef Medline
- Haberler C, Laggner U, Slavc I, et al. **Immunohistochemical analysis of INI1 protein in malignant pediatric CNS tumors: lack of INI1 in atypical teratoid/rhabdoid tumors and in a fraction of primitive neuroectodermal tumors without rhabdoid phenotype.** *Am J Surg Pathol* 2006;30:1462–68 CrossRef Medline
- Biegel JA, Tan L, Zhang F, et al. **Alterations of the hSNF5/INI1 gene in central nervous system atypical teratoid/rhabdoid tumors and renal and extrarenal rhabdoid tumors.** *Clin Cancer Res* 2002;8:3461–67 Medline

- Judkins AR, Mauger J, Ht A, et al. **Immunohistochemical analysis of hSNF5/INI1 in pediatric CNS neoplasms.** *Am J Surg Pathol* 2004;28:644–50 Medline
- Pfister SM, Korshunov A, Kool M, et al. **Molecular diagnostics of CNS embryonal tumors.** *Acta Neuropathol* 2010;120:553–66 CrossRef Medline
- Hasselblatt M, Gesk S, Oyen F, et al. **Nonsense mutation and inactivation of SMARCA4 (BRG1) in an atypical teratoid/rhabdoid tumor showing retained SMARCB1 (INI1) expression.** *Am J Surg Pathol* 2011;35:933–35 CrossRef Medline
- Schneppenheim R, Frühwald MC, Gesk S, et al. **Germline nonsense mutation and somatic inactivation of SMARCA4/BRG1 in a family with rhabdoid tumor predisposition syndrome.** *Am J Hum Genet* 2010;86:279–84 CrossRef Medline
- Kerleroux B, Cottier JP, Janot K, et al. **Posterior fossa tumors in children: radiological tips and tricks in the age of genomic tumor classification and advance MR technology.** *J Neuroradiol* 2020;47:46–53 CrossRef Medline
- Raybaud C, Ramaswamy V, Taylor MD, et al. **Posterior fossa tumors in children: developmental anatomy and diagnostic imaging.** *Childs Nerv Syst* 2015;31:1661–76 CrossRef Medline
- Rumboldt Z, Camacho DL, Lake D, et al. **Apparent diffusion coefficients for differentiation of cerebellar tumors in children.** *AJNR Am J Neuroradiol* 2006;27:1362–69 Medline
- Sathyakumar K, Mani S, Pathak GH, et al. **Neuroimaging of pediatric infratentorial tumors and the value of diffusion-weighted imaging (DWI) in determining tumor grade.** *Acta Radiol* 2021;62:533–40 CrossRef Medline
- Dufour C, Beaugrand A, Le Deley MC, et al. **Clinicopathologic prognostic factors in childhood atypical teratoid and rhabdoid tumor of the central nervous system: a multicenter study.** *Cancer* 2012;118:3812–21 CrossRef Medline
- von Hoff K, Hinkes B, Dannenmann-Stern E, et al. **Frequency, risk-factors and survival of children with atypical teratoid rhabdoid tumors (AT/RT) of the CNS diagnosed between 1988 and 2004, and registered to the German HIT database.** *Pediatr Blood Cancer* 2011;57:978–85 CrossRef Medline
- Gajjar A, Chintagumpala M, Ashley D, et al. **Risk-adapted craniospinal radiotherapy followed by high-dose chemotherapy and stem-cell rescue in children with newly diagnosed medulloblastoma (St Jude Medulloblastoma-96): long-term results from a prospective, multicentre trial.** *Lancet Oncol* 2006;7:813–20 CrossRef Medline
- Gandola L, Massimino M, Cefalo G, et al. **Hyperfractionated accelerated radiotherapy in the Milan strategy for metastatic medulloblastoma.** *J Clin Oncol* 2009;27:566–71 CrossRef Medline
- Jakacki RI, Burger PC, Zhou T, et al. **Outcome of children with metastatic medulloblastoma treated with carboplatin during craniospinal radiotherapy: a Children's Oncology Group Phase I/II study.** *J Clin Oncol* 2012;30:2648–53 CrossRef Medline
- Biswas A, Kashyap L, Kakkar A, et al. **Atypical teratoid/rhabdoid tumors: challenges and search for solutions.** *Cancer Manag Res* 2016;8:115–25 CrossRef Medline
- Northcott PA, Robinson GW, Kratz CP, et al. **Medulloblastoma.** *Nat Rev Dis Primers* 2019;5:11 CrossRef Medline
- Lambin P, Leijenaar RT, Deist TM, et al. **Radiomics: the bridge between medical imaging and personalized medicine.** *Nat Rev Clin Oncol* 2017;14:749–62 CrossRef Medline
- Napel S, Mu W, Jardim-Perassi BV, et al. **Quantitative imaging of cancer in the postgenomic era: radio(geno)mics, deep learning, and habitats.** *Cancer* 2018;124:4633–49 CrossRef Medline
- Li R, Xing L, Napel S, et al. **Radiomics and Radiogenomics: Technical Basis and Clinical Applications.** Chapman & Hall/CRC; 2021
- Dong J, Li L, Liang S, et al. **Differentiation between ependymoma and medulloblastoma in children with radiomics approach.** *Acad Radiol* 2021;28:318–27 CrossRef Medline
- Zhou H, Hu R, Tang O, et al. **Automatic machine learning to differentiate pediatric posterior fossa tumors on routine MR imaging.** *AJNR Am J Neuroradiol* 2020;41:1279–85 CrossRef Medline

26. Payabvash S, Aboian M, Tihan T, et al. **Machine learning decision tree models for differentiation of posterior fossa tumors using diffusion histogram analysis and structural MRI findings.** *Front Oncol* 2020;10:71 CrossRef Medline
27. Ho DM, Hsu CY, Wong TT, et al. **Atypical teratoid/rhabdoid tumor of the central nervous system: a comparative study with primitive neuroectodermal tumor/medulloblastoma.** *Acta Neuropathol* 2000;99:482–88 CrossRef Medline
28. Mattonen SA, Gude D, Echegaray S, et al. **Quantitative imaging feature pipeline: a web-based tool for utilizing, sharing, and building image-processing pipelines.** *J Med Imaging (Bellingham)* 2020;7:042803 CrossRef Medline
29. van Griethuysen JJ, Fedorov A, Parmar C, et al. **Computational radiomics system to decode the radiographic phenotype.** *Cancer Res* 2017;77:e104–07 CrossRef Medline
30. Zwanenburg A, Vallières M, Abdalah MA, et al. **The Image Biomarker Standardization Initiative: standardized quantitative radiomics for high-throughput image-based phenotyping.** *Radiology* 2020;295:328–38 CrossRef Medline
31. Echegaray S, Bakr S, Rubin DL, et al. **Quantitative Image Feature Engine (QIFE): an open-source, modular engine for 3D quantitative feature extraction from volumetric medical images.** *J Digit Imaging* 2018;31:403–14 CrossRef Medline
32. Lefkowitz IB. **Atypical teratoid tumor of infancy: definition of an entity.** *Ann Neurol* 1987;22:448–44 Medline
33. Rorke LB, Packer RJ, Biegel JA. **Central nervous system atypical teratoid/rhabdoid tumors of infancy and childhood: definition of an entity.** *J Neurosurg* 1996;85:56–65 CrossRef Medline
34. Biegel JA, Fogelgren B, Zhou JY, et al. **Mutations of the INI1 rhabdoid tumor suppressor gene in medulloblastomas and primitive neuroectodermal tumors of the central nervous system.** *Clin Cancer Res* 2000;6:2759–63 Medline
35. Gessi M, Giangaspero F, Pietsch T. **Atypical teratoid/rhabdoid tumors and choroid plexus tumors: when genetics “surprise” pathology.** *Brain Pathol* 2003;13:409–14 CrossRef Medline
36. Warmuth-Metz M, Bison B, Dannemann-Stern E, et al. **CT and MR imaging in atypical teratoid/rhabdoid tumors of the central nervous system.** *Neuroradiology* 2008;50:447–52 CrossRef Medline
37. Jin B, Feng XY. **MRI features of atypical teratoid/rhabdoid tumors in children.** *Pediatr Radiology* 2013;43:1001–08 CrossRef Medline
38. Perreault S, Ramaswamy V, Achrol AS, et al. **MRI surrogates for molecular subgroups of medulloblastoma.** *AJNR Am J Neuroradiol* 2014;35:1263–69 CrossRef Medline
39. Yeom KW, Mobley BC, Lober RM, et al. **Distinctive MRI features of pediatric medulloblastoma subtypes.** *AJR Am J Roentgenol* 2013;200:895–903 CrossRef Medline
40. Graadt van Roggen JF, Hogendoorn PC, Fletcher CD. **Myxoid tumours of soft tissue.** *Histopathology* 1999;35:291–12 CrossRef Medline
41. Koeller KK, Rushing EJ. **From the archives of the AFIP: medulloblastoma: a comprehensive review with radiologic-pathologic correlation.** *Radiographics* 2003;23:1613–37 CrossRef Medline
42. Cheng YC, Lirng JF, Chang FC, et al. **Neuroradiological findings in atypical teratoid/rhabdoid tumor of the central nervous system.** *Acta Radiol* 2005;46:89–96 CrossRef Medline
43. Meyers SP, Khademian ZP, Biegel JA, et al. **Primary intracranial atypical teratoid/rhabdoid tumors of infancy and childhood: MRI features and patient outcomes.** *AJNR Am J Neuroradiol* 2006;27:962–71 Medline
44. Bruggers CS, Moore K. **Magnetic resonance imaging spectroscopy in pediatric atypical teratoid rhabdoid tumors of the brain.** *J Pediatr Hematol Oncol* 2014;36:e341–45 CrossRef Medline
45. Parmar H, Hawkins C, Bouffet E, et al. **Imaging findings in primary intracranial atypical teratoid/rhabdoid tumors.** *Pediatr Radiol* 2006;36:126–32 CrossRef Medline
46. Schittenhelm J, Nagel C, Meyermann R, et al. **Atypical teratoid/rhabdoid tumors may show morphological and immunohistochemical features seen in choroid plexus tumors.** *Neuropathology* 2011;31:461–67 CrossRef Medline
47. Brandão LA, Poussaint TY. **Pediatric brain tumors.** *Neuroimaging Clin N Am* 2013;23:499–525 CrossRef Medline

Synthetic MRI in Neurofibromatosis Type 1

 G. Coban,  S. Parlak,  E. Gumeler,  H. Altunbuker,  B. Konoşkan,  J. Karakaya,  B. Anlar, and  K.K. Oguz



ABSTRACT

BACKGROUND AND PURPOSE: Synthetic MRI enables the generation of various contrast-weighted images and quantitative data in a reasonable scanning time. We aimed to use synthetic MRI to assess the detection and underlying tissue characteristics of focal areas of signal intensity and normal-appearing brain parenchyma and morphometric alterations in the brains of patients with neurofibromatosis type 1.

MATERIALS AND METHODS: Conventional MR imaging and synthetic MRI were prospectively obtained from 19 patients with neurofibromatosis type 1 and 18 healthy controls. Two neuroradiologists independently evaluated focal areas of signal intensity on both conventional MR imaging and synthetic MRI. Additionally, automatically segmented volume calculations of the brain in both groups and quantitative analysis of myelin, including the focal areas of signal intensity and normal-appearing brain parenchyma, of patients with neurofibromatosis type 1 were performed using synthetic MRI.

RESULTS: The comparison of conventional MR imaging and synthetic MRI showed good correlation in the supratentorial region of the brain ($\kappa = 0.82$ –1). Automatically segmented brain parenchymal volume, intracranial volume, and GM volumes were significantly increased in the patients with neurofibromatosis type 1 ($P < .05$). The myelin-correlated compound, myelin fraction volume, WM fraction volume, transverse relaxation rate, and longitudinal relaxation rate values were significantly decreased in focal areas of signal intensity on myelin and WM maps ($P < .001$); however, GM, GM fraction volume, and proton density values were significantly increased on the GM map ($P < .001$).

CONCLUSIONS: Synthetic MRI is a potential tool for the assessment of morphometric and tissue alterations as well as the detection of focal areas of signal intensity in patients with neurofibromatosis type 1 in a reasonable scan time.

ABBREVIATIONS: BPF = brain parenchymal fraction; BPV = brain parenchymal volume; cMRI = conventional MRI; FASI = focal areas of signal intensity; GMFvol = mean amount of GM within a single voxel; HC = healthy control; ICV = intracranial volume; MY = myelin; MyCvol = myelin correlated fraction volume; MyF = myelin fraction; MyV = myelin correlated volume; NABP = normal-appearing brain parenchyma; NF-1 = neurofibromatosis type 1; NoN, non-GM/WM/CSF; PD = proton density; QRAPMASTER = quantification of relaxation times and proton density by multiecho acquisition of a saturation-recovery using turbo spin-echo readout; R1 = longitudinal relaxation rate; R2 = transverse relaxation rate; SyMRI = synthetic MRI; WMFvol = the mean amount of WM within a single voxel

Neuroimaging plays an important role in the diagnosis and follow-up of neurofibromatosis type 1 (NF-1). The most common parenchymal abnormality of the brain in NF-1 is oval or round focal areas of abnormal signal intensity (FASI), mainly in the basal ganglia, cerebellum, and brain stem on T2WI. These

lesions do not show enhancement with gadolinium or mass effects.¹ Additionally, studies in *Drosophila* species and mice with *NF1* gene mutations have shown progressive myelin (MY) defects and behavioral abnormalities in a *neurofibromin 1* dose-dependent fashion.^{2–4} Although evidence is inconclusive, vacuolar changes in myelin, defined as fluid-containing spaces ranging from 5 to 100 nm, have been suggested to explain the FASI.^{5,6}

The synthetic MRI (SyMRI) sequence, called quantification of relaxation times and proton density by multiecho acquisition of a saturation-recovery (QRAPMASTER) using turbo spin-echo readout,⁷ enables automatic segmentation of brain tissue and measurement of myelin-based quantitative values with good accuracy and reproducibility in approximately 6 minutes with full head coverage.⁸ This sequence has had encouraging results for brain metastasis,

Received January 9, 2021; accepted after revision April 19.

From the Departments of Radiology (G.C., S.P., E.G., K.K.O.), Biostatistics (J.K.), and Pediatric Neurology (B.A.), Hacettepe University School of Medicine, Ankara, Turkey; Istanbul İl Ambulans Servisi Başhekimliği, (H.A.), Istanbul, Turkey; and Department of Pediatric Neurology (B.K.), Mardin State Hospital, Mardin, Turkey.

Please address correspondence to Gokcen Coban, MD, Hacettepe Universitesi Tıp Fakültesi Hastanesi 06100 Sıhhiye, Department of Radiology, Ankara, Turkey; e-mail: drgokcencoban@gmail.com

 Indicates article with online supplemental data.

<http://dx.doi.org/10.3174/ajnr.A7214>

multiple sclerosis, meningitis, idiopathic normal pressure hydrocephalus, and Sturge-Weber syndrome in several studies and has been approved by the FDA.⁸⁻¹²

In this study, we aimed to detect and evaluate FASI and examine morphometric changes in the brain in patients with NF-1 using SyMRI. We also sought myelin abnormalities in FASI and normal-appearing brain parenchyma (NABP) in patients with NF-1. Because FASI tends to resolve by early adulthood, we intentionally performed this study with pediatric patients.¹³ Our hypothesis was that SyMRI could detect FASI and quantify morphologic and tissue changes in pediatric patients with NF-1.

MATERIALS AND METHODS

The institutional review board of Hacettepe University School of Medicine approved this prospective study (no = KA-180135). Patients' parents signed an informed consent form.

Ethics Approval

All procedures performed in the studies involving human participants were in accordance with the ethical standards of the institutional and/or the national research committee and with the 1964 Declaration of Helsinki and its later amendments or comparable ethical standards.

Participants and Image Acquisition

Between August 2019 and March 2020, pediatric patients fulfilling the NF-1 diagnostic criteria of the National Institutes of Health participated in this study at Hacettepe University School of Medicine. These patients were diagnosed and followed up by the Pediatric Neurology Department in our hospital, which has served as a reference center for patients with NF-1 in the past decade. Twenty-four patients with NF-1 fulfilling the diagnostic criteria were referred from the Pediatric Neurology Department and scanned in the Radiology Department. Twenty two healthy controls (HCs) without neurologic and systemic abnormalities volunteered to serve as the control group of the study. The exclusion criteria were the presence of optic glioma and brain tumors, hydrocephalus, increased head circumference, and chronic epilepsy in the NF-1 group and any incidental abnormality of the brain parenchyma in HCs. Individuals with reduced image quality on SyMRI or conventional MR imaging (cMRI) were eliminated from the study. One patient with NF-1 with a parenchymal tumor, 3 patients with NF-1 with optic gliomas, and 1 patient with NF-1 and 1 healthy control with reduced image quality were excluded from the study. Thus, of 24 patients with NF-1 and 22 HCs, 19 patients with NF-1 and 18 HCs were included in the study. None of the 37 participants received sedation or contrast media.

All scans were obtained on a 1.5T MR imaging scanner (Aera; Siemens) using a 20-channel phased array head coil. Conventional MR imaging protocol included axial FLAIR (TE/TR/TI, 78/7000/2220 ms; FOV, 230 × 185 mm; section thickness/gaps, 5/2 mm; acquisition time, 4 minutes 6 seconds); axial 3D T1-weighted MPRAGE (TE/TR, 3/1680 ms; FOV, 240 × 195 mm; section thickness/gaps, 1.5/0.75 mm; acquisition time, 5 minutes 8 seconds); and axial T2-weighted turbo spin-echo (TE/TR, 199/3240 ms; FOV, 230 × 185 mm; section

thickness/gaps, 5/2 mm; acquisition time, 3 minutes 42 seconds).

The quantitative sequence QRAPMASTER⁷ is a multi-spin-echo saturation-recovery sequence with multisaturation delays and multislices. The SyMRI technique was performed with the following parameters: axial plane; FOV, 230 × 183 mm; voxel size, 1.5 × 1.5 mm; TE, 14, 28, 42, 56, 70 ms; TR, 4.244 seconds; TI, 0.0974, 0.5846, 1.8511, 4.0919 seconds; saturation flip angle, 120°; and acquisition time, 6 minutes 5 seconds. The full brain was covered with 30 slices with 4-mm thickness and a 1-mm gap.

The SyMRI technique was performed after cMRI. The total scanning time was 12 minutes 56 seconds for cMRI and 6:05 min for SyMRI in our study protocol.

Image Analysis

SyMRI diagnostic software, Version 11.2 (SyntheticMR) was used to create synthetic images and quantify intracranial volume (ICV), brain parenchymal volume (BPV), brain parenchymal fraction (BPF = BPV/ICV), GM, WM, CSF, non-GM/WM/CSF, MY, and myelin fraction (MyF = MY/BPV).¹⁴ Additionally, SyMRI enabled the creation of variable contrast-weighting images while quantifying the longitudinal relaxation rate (R1), transverse relaxation rate (R2), and proton density (PD). The MR imaging acquisition voxel is composed of 4 partial volume compartments: the myelin partial volume, free water partial volume, cellular partial volume, and excess parenchymal water partial volume. The sum of the 4 compartments is 100%, and each partial volume compartment content can range from 0% to 100%.¹⁵ Each partial volume compartment has its own relaxation properties and can be described by its R1, R2, and PD values. By using this approach, SyMRI can estimate the myelin volume in a voxel. The total volume of WM, GM, CSF, non-GM/WM/CSF, and myelin can be calculated by multiplying the summed volume fractions for each tissue type based on predefined tissue characteristics.¹⁵ Additionally, the non-GM/WM/CSF represents the tissue not classified as GM, WM, and CSF and contains flow voids in larger blood vessels.

Qualitative Evaluation

Two blinded neuroradiologists (G.C. and S.P.) independently evaluated the cMRI and SyMRI sets on a standard imaging workstation. The presence and location of FASI on T2WI of cMRI and SyMRI were noted with a 2-week gap. The largest FASI was chosen in consensus for the quantitative analysis. To search for any relationship between FASI and brain morphometry, we grouped the patients by the number of FASI into 4 groups: group 1 (from 1 to 5), group 2 (from 6 to 10), group 3 (from 11 to 15), and group 4 (>15).

Quantitative Evaluation

The raw image dataset was transferred to an imaging workstation (syngo.via; Siemens). SyMRI produced quantification and colored maps of WM, GM, CSF, and myelin correlated volume (MyV). To avoid misalignment, we copied ROIs drawn on an image set to the contralateral side with the mirror copy option available in the SyMRI diagnostic software, Version 11.2.

Table 1: cMRI versus SyMRI and interobserver agreement for FASI detection^a

	cMRI vs SyMRI (Ob1)	cMRI vs SyMRI (Ob2)	interobserver Agreement on SyMRI	interobserver Agreement on cMRI
Thalami	0.9	0.86	0.82	0.94
WM (centrum semiovale)	1	1	1	1
BG	1	1	1	1
Pons	1	0.94	0.9	0.98
Mesencephalon	1	0.92	0.9	0.94
Cerebellum and MCP	0.85	0.84	0.80	0.90
Peridentate area	0.56	0.72	0.65	0.82

Note:—Ob indicates observer; BG, basal ganglia; MCP, middle cerebellar peduncle.

^aWeighted κ analysis.

First, MY colored maps were overlaid on the T2WI of the SyMRI technique, and the ROIs ranging from 0.2 to 0.6 mL were drawn from the globus pallidum, caudate nucleus, internal capsule, putamen, thalamus in the right and left hemispheres and from the center of the pons and midbrain on the colored myelin maps in patients and HCs (Online Supplemental Data). For NABP, ROIs were placed on a nonlesioned region of each centrum semiovale.

In addition, for the quantitative comparison of the FASI and the side, MY colored maps were overlaid on the T2WI from the SyMRI technique, and the ROI (0.2 mL) was drawn on the FASI. The ROI on the FASI was copied to the contralateral NABP. Then, the same measurements were made on the colored WM and GM maps. Measurements were excluded if bilateral FASI were present in the relevant structures. The amounts of MyV, WM, GM, PD, R2, and R1 within the ROIs were noted. Then, these ROIs also yielded myelin correlate fraction volume (MyCvol), the mean amount of WM within a single voxel (WMFvol), and mean amount of GM within a single voxel (GMFvol), which represented the mean amount of MyV, WM, and GM within a single voxel, respectively.

Statistical Analysis

Quantitative variables were evaluated with the Kolmogorov-Smirnov test to reveal the presence of normal distribution. Descriptive statistics were expressed as mean (SD) if variables were normally distributed or median (minimum-maximum) if variables did not show normal distribution. An independent-samples *t* test was used for variables (BPV, ICV, WM, GM, MY, %MY/BPV, %GM/ICV, %MY/ICV, R2) with normal distribution, and the Mann-Whitney *U* test was used for non-normally distributed variables. Comparison of the FASI and NABP (MyCvol, MyV, GMFvol, GM, WMFvol, WM and PD, and R2 and R1 of the MY, GM, and WM) was made with the Wilcoxon test.

For comparisons of continuous variables (BPV, ICV, WM, GM, MY, %MY/BPV, %GM/ICV, %MY/ICV, R2), the adjusted *P* value was obtained using the Benjamini-Hochberg method.¹⁶

Among categoric variables, groups were compared using the χ^2 test. The relationship of continuous and ordinal variables with each other was examined with the Spearman ρ correlation coefficient.

Interobserver agreement for MR imaging features was assessed with weighted κ analysis. In terms of agreement, the κ value was interpreted as poor (< 0.20), fair (0.21–0.40),

moderate (0.41–0.60), good (0.61–0.80), or very good (0.81–1.00). Confidence intervals of the κ values were used to find possible nonoverlapping intervals.

All analyses were performed using SPSS Statistics 23.0 software (IBM) and the R 3.6.3 program (<http://www.r-project.org/>). A *P* value < .05 was considered statistically significant.

RESULTS

There were no statistically significant differences in terms of sex (*P* = .159) or age (*P* = .221) between the patients with NF-1 (female/male: 9:10; mean age, 10.5 [SD, 3.7] years; range, 5–17 years) and HCs (female/male: 12:6; mean age, 11 [SD, 3] years; range, 5–16 years). The demographic characteristics of the patients with NF-1 are given in the Online Supplemental Data.

Qualitative Evaluation

Interobserver agreement for the detection of FASI on SyMRI is provided in Table 1. Raters' detection of FASI on SyMRI was highly correlated in the supratentorial part of the brain (ie, the centrum semiovale, thalamus, and basal ganglia) (κ = 0.82–1) (Fig 1), while it was lower in the infratentorial part (especially in the cerebellum and middle cerebral peduncle and peri-dentate area, Online Supplemental Data) (κ = 0.65–0.85). The interobserver correlation was lowest in the peri-dentate area (κ = 0.65) (Fig 1E, -F). Additionally, the raters noticed that small FASI were not detectable on SyMRI, though they were readily seen on cMRI. Although the raters did not measure the size of the FASI individually, they noticed that those lesions undetected on non-GM/WM/CSF colored maps were <5 mm in diameter. In total, there were 33 FASI of <5 mm in 18 patients with NF-1.

The FASI in patients with NF-1 were in the basal ganglia (*n* = 27), thalamus (*n* = 28), cerebellum and middle cerebellar peduncle (*n* = 17), peri-dentate area (*n* = 23), pons (*n* = 19), mesencephalon (*n* = 17), and cerebral white matter (*n* = 2) on cMRI. By categorization of the number of FASI, there were 6 patients in group 1, nine patients in group 2, three patients in group 3, and 1 patient in group 4. There was no significant correlation between the number of FASI and total brain MY, MyF, BPV, ICV, BPF, WM, GM, and non-WM/GM/CSF volumes.

Quantitative Evaluation

Total brain MY, MyF, BPV, ICV, BPF, WM, GM, and non-WM/GM/CSF volumes and MyV, MyCvol, PD, and R2 and R1 values of the centrum semiovale, globus pallidum, caudate nucleus,

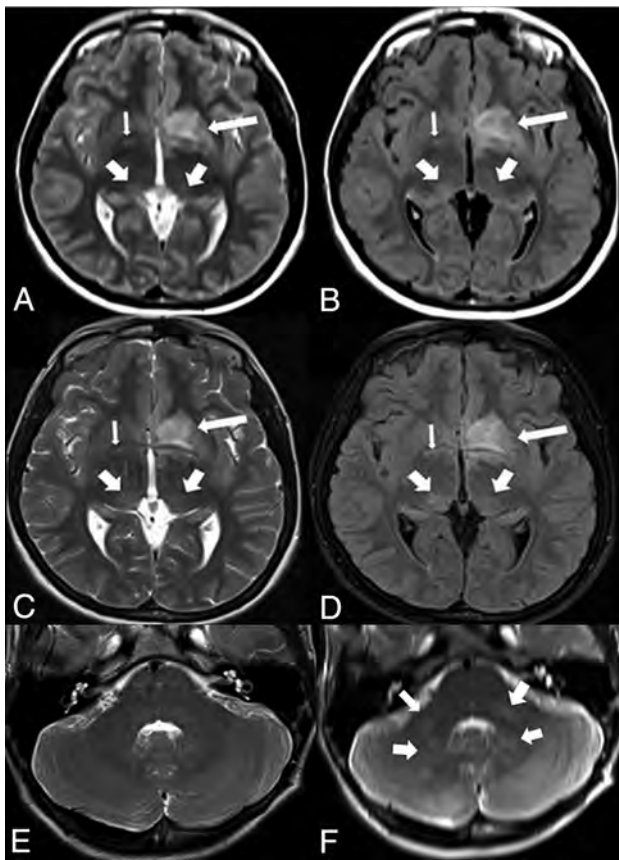


FIG 1. Synthetic T2-weighted (A) and FLAIR (B) images show FASI in the left lentiform nucleus, right globus pallidus, and bilateral thalami, accurately, as shown on the conventional T2-weighted (C) and FLAIR (D) images. T2-weighted image (E) in an HC shows no lesion in the peri-dentate area. However, a hyperintensity is seen in the corresponding area on synthetic T2-weighted image (F, arrows), an artifact probably due to CSF flow.

Table 2: Comparison of SyMRI parameters of patients with NF-1 and healthy controls

Variables	Healthy Controls		NF-1		P Value ^a
	Mean	SD	Mean	SD	
BPV (mL)	1279	109.64	1390	131.23	.035 ^b
ICV (mL)	1401	120.16	1510	138.67	.035 ^b
WM (mL)	396.20	66.78	419.88	48.83	.286
GM (mL)	862.93	82.29	949.16	89.15	.028 ^b
MY (mL)	107.96	14.37	129.27	17.25	.067
%MY/BPV	8.53	0.85	8.51	0.80	.933
%GM/ICV	61.72	4.65	62.26	2.02	.763
%MY/ICV	7.80	0.82	7.87	0.82	.832
R GP R2 ^c	14.49	1.02	13.66	1.31	.062
R CN R2	12.15	0.38	11.82	0.52	.058
L CN R2	12.12	0.37	11.74	0.56	.042 ^b
R thalamus R2	12.74	0.39	12.34	0.52	.035 ^b
L thalamus R2	12.69	0.38	12.28	0.51	.035 ^b
Pons MyV (mL)	21.96	3.01	18.54	3.73	.028 ^b

Note:—GP indicates globus pallidum; CN, caudate nucleus; R, right; L, left.

^aIndependent-samples *t* test; adjusted *P* value was obtained using the Benjamini-Hochberg method.

^bSignificance is <.05.

^cR2 unit is s-1.

putamen, thalamus, and internal capsule from the right and left hemispheres and the centrum of the pons and midbrain of HCs and the NF-1 patient group are provided in the Online Supplemental Data.

Brain parenchymal volume, ICV, and GM volumes (Table 2) were significantly increased in patients with NF-1 ($P < .05$) compared with HCs (Table 2). However, measurements from the aforementioned predetermined regions detected no differences between HCs and patients.

Conversely, MyV, MyCvol, WM, WMFvol, and R2, and R1 values were significantly decreased in the FASI compared with the NABP (Table 3, $P < .001$) (Fig 2). GM, GMFvol, and PD values were significantly increased on GM maps in FASI (Table 3, $P < .001$). FASI were automatically labeled only on the colored GM map, similar to the cortex, and not labeled and calculated on WM and MY maps (Fig 2). There was no significant difference in terms of MyV, MyCvol, PD, and R2 and R1 values of NABP (centrum semiovale) between patients and HCs ($P > .05$).

DISCUSSION

This study presents the first quantitative and qualitative analyses with SyMRI in patients with NF-1. Similar to findings of authors of recent studies testing lesion detection in multiple sclerosis with SyMRI,^{12,17} we found that FASI were more easily detected on conventional T2- and FLAIR-weighted imaging. This finding could be related to lower image contrast, higher noise level, and hence lower contrast/noise ratio of synthetic FLAIR images compared with conventional images.^{12,17} Nevertheless, previous studies showed that the diagnostic ability of SyMRI was comparable with that of cMRI, and they have suggested its clinical use in various diseases.^{8,12} We also found a good correlation between cMRI and SyMRI in the detection of FASI in patients with NF-1, supporting the use of SyMRI in routine practice. Posterior fossa structures, especially the peridentate area, had the lowest interobserver correlation. The major reason for this low correlation was the prominent artifacts due to phase-encoding and fluid-pulsation artifacts in the infratentorial compartment, also mentioned in the literature.^{18,19} Kerleroux et al¹⁹ showed that phase-encoding and fluid-pulsation artifacts were more common in synthetic T2WI than in T2WI on cMRI. However, they noted that the phase-encoding artifacts were easily recognizable and should not be confounded with pathologic conditions. However, fluid-pulsation artifacts might disturb the evaluation of lower brain areas, such as the brain stem or peduncles, in both patients and HCs. Given this limitation of SyMRI, we believe that cMRI is necessary for initial imaging to avoid misinterpretation. On SyMRI, non-GM/WM/CSF maps could not assign FASI that were <5 mm in diameter in our patients, though the raters were able to detect them easily.

The Pediatric Neurology Department of our hospital serves as a reference center for patients with NF-1. During the annual checkups of patients with NF-1, follow-up imaging is required; therefore, brain MR imaging examinations are performed in our neuroradiology department. Most patients cannot tolerate the long imaging time due to accompanying cognitive and neuropsychiatric disorders. With SyMRI, annual checkups can be performed in a shorter time after the baseline cMRI examination,

Table 3: ROI analysis of FASI and normal-appearing WM on MYC, GM, and WM maps, testing MyV, PD, R2, R1, GM, WM, and MyC/WM/GM fractional volumes^a

Variables	Normal-Appearing White Matter		FASI		P Value ^b
	Median	Min-Max	Median	Min-Max	
MyCvol (mL)	0.03	0.01–0.05	0.000	0.00–0.002	.001
MyV (mL)	14.1	6.9–29.9	2.5	0–18.7	.001
MY PD	76.4	66–81.1	83.3	73.2–89	.001
MY R2	12.6	11.19–15.2	10.36	7.08–13.85	.001
MY R1	1.22	1.05–1.76	0.96	0.73–1.27	.001
WMFvol (mL)	0.13	0.05–0.17	0.02	0.00–0.13	.001
WM	64.3	26.7–100	2.7	0.00–73.5	.001
WM PD	76.4	66–80	83.3	51.1–87.8	.001
WM R2	12.6	11.19–15.22	10.36	1.99–76.1	.001
WM R1	1.21	1.05–1.76	0.96	0.73–12.31	.001
GMFvol (mL)	0.06	0.00–0.13	0.11	0.05–0.21	.001
GM	29.2	0.00–70.1	75.2	14.8–86.1	.001
GM PD	76.4	66–81.9	83.3	73.2–90.51	.001
GM R2	12.6	11.19–15.22	10.36	0.9–13.85	.001
GM R1	1.2	1.05–1.76	0.96	0.73–1.27	.001

Note:—Min indicates minimum; Max, maximum; MyC, myelin correlated fraction volume.

^a Units are PD (PU), R1 and R2 (s⁻¹), WM (mL), GM (mL).

^b Wilcoxon test.

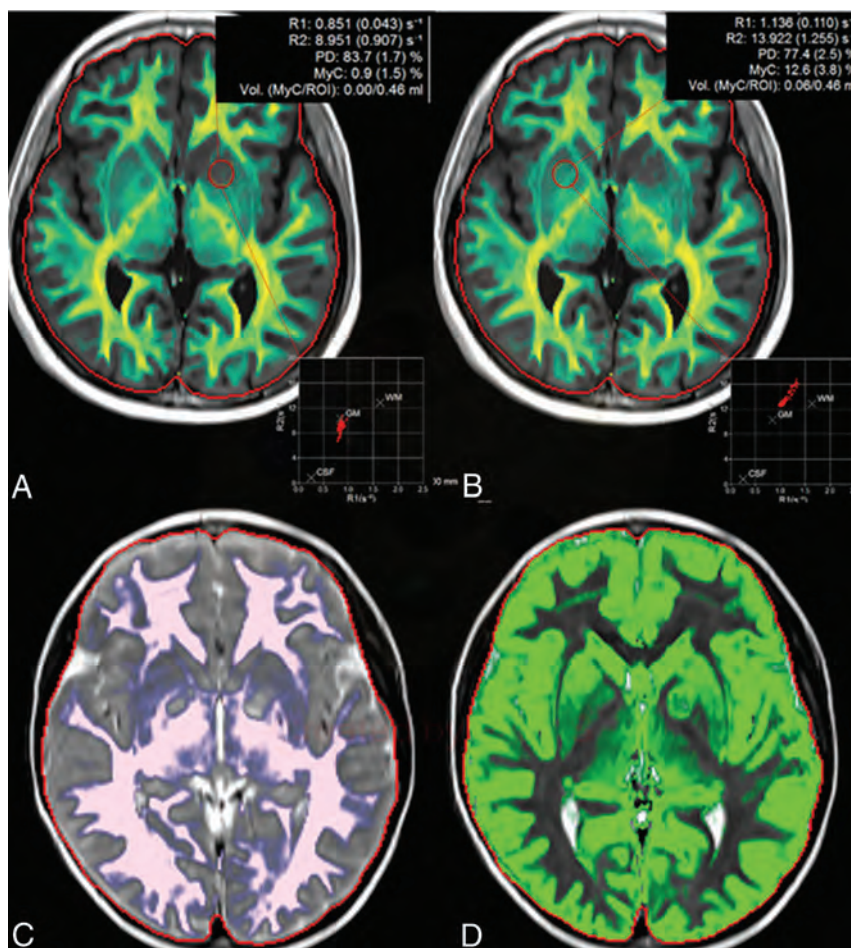


FIG 2. Myelin (A and B), WM (C), and GM (D) maps of a patient with NF-1. FASI in the left lenticular nucleus (A, red ROI) show prominently decreased R1, R2, PD, MyC, and MyCvol values compared with the normal right side (B, red ROI). The WM map (C) does not assign as the FASI; however, GM map (D) signs the FASI as GM.

which would have already been performed at the time of diagnosis. In addition, with the help of the obtained quantitative data on SyMRI, comparing the morphometric data annually during the shrinking or disappearing of the FASI may reduce the need for frequent follow-ups in these patients. However, in some situations requiring intermittent checkups, SyMRI could be very promising, giving additional quantitative information that can be useful in follow-up comparisons.

In our study, patients with NF-1 had a significantly higher ICV than HCs, similar to findings in several previous studies.^{1,3,20} In the literature, BPV and WM volumes were higher and GM volumes were lower than our findings in patients with NF-1.³ However, FASI were labeled and quantified as GM, which might have resulted in higher GM values in our patients with NF-1. Some studies^{3,20} showed that the presence of an optic glioma might influence the mean brain volume in patients with NF-1, but patients with optic and/or brain gliomas were excluded from our study. Therefore, we believe that morphometric alterations in this study may reflect histopathologic abnormalities more accurately than in previous reports.

Morphometric MR imaging studies in NF-1 were limited to BPV, GM, and WM volumes.^{3,20} Although the differences were not statistically significant, MY, MyF, and the non-GM/WM/CSF volumes tended to be higher in patients with NF-1 than in HCs. The MyV of the pons and R2 values of the caudate nucleus and thalami were significantly lower than those in HCs. Additionally, all values except PD were significantly decreased in FASI on myelin maps. These novel findings may point to underlying myelin and/or axonal structural changes, in line with the studies conducted in patients with multiple sclerosis.^{21,22}

Diffusion tensor imaging has also been widely used to understand tissue changes in diseases.^{23–26} Elevated ADC and reduced fractional anisotropy throughout the WM tracts in NF-1 suggest a compromise in the integrity of WM.^{24,26,27} MR spectroscopy studies

suggest an underlying structural abnormality in NF-1, revealing metabolic alterations in both the NABP and FASI.^{28,29} Furthermore, after the disappearance of FASI, fractional anisotropy was reduced in the thalamus, suggesting that a microstructural abnormality may remain.^{30,31} Experimental and clinical imaging studies showed increased radial diffusivity with or without alterations in axial diffusivity in the NABP of patients with NF-1.^{25,26} We did not observe significant abnormalities in the NABP group compared with HCs. However, the younger age of our patients compared with those in previous studies in the literature may explain this finding.

We found significantly decreased MyV, MyCvol, WM, WMFvol, R2, and R1 values in the FASI in myelin maps in the NF-1 group. These findings may also correspond with reported histologic abnormalities, including an increased amount of space in axonal packing (sparse packing), myelin decompaction, and increased myelin thickness²⁶ in patients with NF-1. Further investigations, including the correlation of histologic and molecular changes in myelin with SyMRI, are necessary.

Our study has several limitations. First, our patient population with NF-1 was small as a result of the inclusion criteria of our study. We included only pediatric patients to focus on changes in FASI, which are more prominent early in life. Patients with gliomas were excluded to eliminate the effect of the tumor on increased volume. A larger patient population may yield more significant results. Additionally, because SyMRI was performed on a limited number of pediatric patients, we could not evaluate possible volume changes across age groups, a finding that was shown previously.³ However, considering the age range of the participants and our exclusion criteria, a noticeable sequential change in intracranial volume is not expected. In the GM map, assigning the FASI as part of the GM might have created a false increase in the total GM volume. Additionally, correlations between volume measures and neuropsychological performance, which were not available in this study, would enhance our understanding of morphologic alterations from a clinical perspective.

CONCLUSIONS

SyMRI provides quantitative information in patients with NF-1 in terms of altered morphometry and tissue metrics, providing insights into the disease effects on the brain. A major advantage of this technique is that it reveals multicontrast sequences in a single acquisition, offering a reasonable scan time for clinical use, especially in young children.

ACKNOWLEDGMENT

The authors would like to thank all the MR technicians, Synthetic MRI team, and Ali Avci from Siemens Healthineers, Turkey, for their contribution in performing this study.

Disclosures: Banu Anlar—UNRELATED: Consultancy: Novartis.

REFERENCES

1. Van Es S, North KN, McHugh K, et al. **MRI findings in children with neurofibromatosis type 1: a prospective study.** *Pediatr Radiol* 1996;26:478–87 CrossRef Medline

2. The I, Hannigan GE, Cowley GS, et al. **Rescue of a Drosophila NF1 mutant phenotype by protein kinase A.** *Science* 1997;276:791–94 CrossRef Medline
3. Moore BD 3rd, Slopis JM, Jackson EF, et al. **Brain volume in children with neurofibromatosis type 1: relation to neuropsychological status.** *Neurology* 2000;54:914–20 CrossRef Medline
4. López-Juárez A, Titus HE, Silbak SH, et al. **Oligodendrocyte Nfi controls aberrant notch activation and regulates myelin structure and behavior.** *Cell Rep* 2017;19:545–57 CrossRef Medline
5. DiPaolo DP, Zimmerman RA, Rorke LB, et al. **Neurofibromatosis type 1: pathologic substrate of high-signal-intensity foci in the brain.** *Radiology* 1995;195:721–24 CrossRef
6. Menor F, Marti-Bonmati L, Arana E, et al. **Neurofibromatosis type 1 in children: MR imaging and follow-up studies of central nervous system findings.** *Eur J Radiol* 1998;26:121–31 CrossRef Medline
7. Warntjes JB, Leinhard OD, West J, et al. **Rapid magnetic resonance quantification on the brain: optimization for clinical usage.** *Magn Reson Med* 2008;60:320–29 CrossRef Medline
8. Krauss W, Gunnarsson M, Andersson T, et al. **Accuracy and reproducibility of a quantitative magnetic resonance imaging method for concurrent measurements of tissue relaxation times and proton density.** *Magn Reson Imaging* 2015;33:584–91 CrossRef Medline
9. Hagiwara A, Hori M, Yokoyama K, et al. **Utility of a multiparametric quantitative MRI model that assesses myelin and edema for evaluating plaques, periplaque white matter, and normal-appearing white matter in patients with multiple sclerosis: a feasibility study.** *AJNR Am J Neuroradiol* 2017;38:237–42 CrossRef Medline
10. Andica C, Hagiwara A, Nakazawa M, et al. **The advantage of synthetic MRI for the visualization of early white matter change in an infant with Sturge-Weber syndrome.** *Magn Reson Med Sci* 2016;15:347–48 CrossRef Medline
11. Virhammar J, Warntjes M, Laurell K, et al. **Quantitative MRI for rapid and user-independent monitoring of intracranial CSF volume in hydrocephalus.** *AJNR Am J Neuroradiol* 2016;37:797–801 CrossRef Medline
12. Krauss W, Gunnarsson M, Nilsson M, et al. **Conventional and synthetic MRI in multiple sclerosis: a comparative study.** *Eur Radiol* 2018;28:1692–700 CrossRef Medline
13. Sevcik RJ, Barkovich AJ, Edwards MS, et al. **Evolution of white matter lesions in neurofibromatosis type 1: MR findings.** *AJR Am J Roentgenol* 1992;159:171–75 CrossRef Medline
14. Andica C, Hagiwara A, Hori M, et al. **Automated brain tissue and myelin volumetry based on quantitative MR imaging with various in-plane resolutions.** *J Neuroradiol* 2018;45:164–68 CrossRef Medline
15. Warntjes M, Engström M, Tisell A, et al. **Modeling the presence of myelin and edema in the brain based on multi-parametric quantitative MRI.** *Front Neurol* 2016;7:16 CrossRef Medline
16. Benjamini Y, Hochberg Y. **Controlling the false discovery rate: a practical and powerful approach to multiple testing.** *Journal of the Royal Statistical Society Series B* 1995;57:289–300
17. Blystad I, Warntjes JB, Smedby O, et al. **Synthetic MRI of the brain in a clinical setting.** *Acta Radiol* 2012;53:1158–63 CrossRef Medline
18. Tanenbaum LN, Tsiouris AJ, Johnson AN, et al. **Synthetic MRI for clinical neuroimaging: results of the Magnetic Resonance Image Compilation (MAGiC) prospective, multicenter, multireader trial.** *AJNR Am J Neuroradiol* 2017;38:1103–10 CrossRef Medline
19. Kerleroux B, Kober T, Hilbert T, et al. **Clinical equivalence assessment of T2 synthesized pediatric brain magnetic resonance imaging.** *J Neuroradiol* 2019;46:130–35 CrossRef Medline
20. Said SM, Yeh TL, Greenwood RS, et al. **MRI morphometric analysis and neuropsychological function in patients with neurofibromatosis.** *Neuroreport* 1996;7:1941–44 CrossRef Medline
21. West J, Aalto A, Tisell A, et al. **Normal appearing and diffusely abnormal white matter in patients with multiple sclerosis assessed with quantitative MR.** *PLoS One* 2014;9:e95161 CrossRef Medline
22. Saccenti L, Hagiwara A, Andica C, et al. **Myelin measurement using quantitative magnetic resonance imaging: a correlation study**

- comparing various imaging techniques in patients with multiple sclerosis. *Cells* 2020;9:393 CrossRef Medline
23. Tognini G, Ferrozzi F, Garlaschi G, et al. **Brain apparent diffusion coefficient evaluation in pediatric patients with neurofibromatosis type 1.** *J Comput Assist Tomogr* 2005;29:298–304 CrossRef Medline
 24. Zamboni SL, Loenneker T, Boltshauser E, et al. **Contribution of diffusion tensor MR imaging in detecting cerebral microstructural changes in adults with neurofibromatosis type 1.** *AJNR Am J Neuroradiol* 2007;1:773 Medline
 25. Wang L, Goldstein FC, Veledar E, et al. **Alterations in cortical thickness and white matter integrity in mild cognitive impairment measured by whole-brain cortical thickness mapping and diffusion tensor imaging.** *AJNR Am J Neuroradiol* 2009;30:893–99 CrossRef Medline
 26. Karlsgodt KH, Rosser T, Lutkenhoff ES, et al. **Alterations in white matter microstructure in neurofibromatosis-1.** *PLoS One* 2012;7:e47854 CrossRef Medline
 27. Song SK, Sun SW, Ramsbottom MJ, et al. **Dysmyelination revealed through MRI as increased radial (but unchanged axial) diffusion of water.** *Neuroimage* 2002;17:1429–36 CrossRef Medline
 28. Wilkinson ID, Griffiths PD, Wales JK. **Proton magnetic resonance spectroscopy of brain lesions in children with neurofibromatosis type 1.** *Magn Reson Imaging* 2001;19:1081–89 CrossRef Medline
 29. Jones AP, Gunawardena WJ, Coutinho CM. **1H MR spectroscopy evidence for the varied nature of asymptomatic focal brain lesions in neurofibromatosis type 1.** *Neuroradiology* 2001;43:62–67 CrossRef Medline
 30. Ferraz-Filho JR, da Rocha AJ, Muniz MP, et al. **Diffusion tensor MR imaging in neurofibromatosis type 1: expanding the knowledge of microstructural brain abnormalities.** *Pediatr Radiol* 2012;42:449–54 CrossRef Medline
 31. van Engelen SJ, Krab LC, Moll HA, et al. **Quantitative differentiation between healthy and disordered brain matter in patients with neurofibromatosis type I using diffusion tensor imaging.** *AJNR Am J Neuroradiol* 2008;29:816–22 CrossRef Medline

Evaluation of Posterior Fossa Biometric Measurements on Fetal MRI in the Evaluation of Dandy-Walker Continuum

U.D. Nagaraj, B.M. Kline-Fath, P.S. Horn, and C. Venkatesan



ABSTRACT

BACKGROUND AND PURPOSE: Dandy-Walker malformation, vermian hypoplasia, and Blake pouch remnant represent a continuum of anomalies and are common reasons for referral for fetal MR imaging. This study aimed to determine biometric measurements that quantitatively delineate these 3 posterior fossa phenotypes.

MATERIALS AND METHODS: Our single-center institutional review board approved a retrospective analysis of all fetal MRIs for posterior fossa malformations, including Dandy-Walker malformation, vermian hypoplasia, and Blake pouch remnant. Measurements included the anterior-to-posterior pons, craniocaudal and anterior-to-posterior vermis, lateral ventricle size, and tegmentovermian and posterior fossa angles. Measurements were compared with normal biometry and also between each subgroup.

RESULTS: Thirty-three fetuses met the criteria and were included in the study. Seven were designated as having Dandy-Walker malformation; 16, vermian hypoplasia; and 10, Blake pouch remnant. No significant group interactions with adjusted mean gestational age for tegmentovermian and posterior fossa angles were observed. The tegmentovermian angle was significantly higher in Dandy-Walker malformation (109.5° [SD, 20.2°]) compared with vermian hypoplasia (52.13° [SD, 18.8°]) and Blake pouch remnant (32.1° [SD, 17.9°]), regardless of gestational age. Lateral ventricle sizes were significantly higher in Dandy-Walker malformation at a mean of ≥ 23.1 weeks' gestational age compared with vermian hypoplasia and Blake pouch remnant. The anterior-to-posterior and craniocaudal vermes were significantly smaller in Dandy-Walker malformation compared with vermian hypoplasia and Blake pouch remnant at mean of ≥ 23.1 weeks' gestational age.

CONCLUSIONS: Dandy-Walker malformation can be described in relation to vermian hypoplasia and Blake pouch remnant by an increased tegmentovermian angle; however, other potential qualifying biometric measurements are more helpful at ≥ 23.1 weeks' gestational age. Because they fall along the same spectrum of abnormalities, the difficulty in distinguishing these entities from one another makes precise morphologic and biometric descriptions important.

ABBREVIATIONS: AP = anterior-to-posterior; BP = Blake pouch remnant; CC = craniocaudal; DWM = Dandy-Walker malformation; GA = gestational age; TCD = transverse cerebellar diameter; TVA = tegmentovermian angle; VH = vermian hypoplasia

When Walter E. Dandy and A. Earl Walker first described cases of hydrocephalus secondary to congenital obstruction of the foramina of Luschka and Magendie nearly a century ago, they were not referring to a wide spectrum of abnormalities of the posterior fossa ranging from normal vermian size and morphology with no intervention required and

normal neurodevelopmental outcomes to in utero obstructive hydrocephalus requiring shunting in the neonatal period, lasting profound neurologic deficits, and underlying genetic disorders. Despite the ongoing inconsistency of this terminology in the literature, the so-called “Dandy-Walker Malformation” (DWM) term persists in clinical practice and is one of the most common reasons for referral for fetal MR imaging.¹⁻³

In the past 20 years, there is greater recognition that Blake pouch remnant (BP), vermian hypoplasia (VH), and classic DWM exist along a continuum of abnormalities resulting from abnormal development of the posterior membranous area during fourth ventricle development.^{4,5} There is now increased knowledge of normal posterior fossa development and the appearance of the vermis on fetal MR imaging. Thus, evaluation of posterior fossa structures on fetal MR imaging by categorizing these

Received January 22, 2021; accepted after revision April 19.

From the Departments of Radiology and Medical Imaging (U.D.N., B.M.K.-F.) and Neurology (P.S.H., C.V.), Cincinnati Children's Hospital Medical Center, Cincinnati, Ohio; and University of Cincinnati College of Medicine (U.D.N., B.M.K.-F., P.S.H., C.V.), Cincinnati, Ohio.

Please address correspondence to Usha D. Nagaraj, MD, Department of Radiology and Medical Imaging, Cincinnati Children's Hospital Medical Center, 3333 Burnet Ave, Cincinnati, OH 45229-3026; e-mail: usha.nagaraj@cchmc.org; @CincyKidsRad

Indicates article with online supplemental data.

<http://dx.doi.org/10.3174/ajnr.A7215>

posterior fossa malformations into potentially clinically meaningful groups, including routine measurements, can greatly assist routine clinical practice.^{6,7} However, there is still a relative paucity of literature describing fetal MR imaging biometric measurements in patients with posterior fossa anomalies along the Dandy-Walker continuum.

In this article, the authors aimed to determine whether posterior fossa biometric measurements on fetal MR imaging can be used to qualify these 3 posterior fossa abnormalities in clinical practice.

MATERIALS AND METHODS

Study Design

This study was a single-center, retrospective review. A list of fetal MRIs performed at Cincinnati Children's Hospital Medical Center from January 1, 2000, through March 22, 2018, was compiled using Illuminate Insight software (Softtek Illuminate, Overland Park, KS) with key words "Dandy-Walker," "vermian hypoplasia," and "Blake." These MRIs were retrospectively reviewed by the study radiologists, and patients who did not clearly have a posterior fossa abnormality along the Dandy-Walker continuum were excluded. Only fetuses with adequate available postnatal clinical follow-up by a neurologist within the institution, with or without postnatal neuroimaging, were included. Determination of diagnostic-quality imaging was made at the neuroradiologists' discretion. A chart review was performed to obtain relevant clinical data. This study was compliant with the Health Insurance Portability and Accountability Act and approved by the institutional review board. The requirement for informed consent was waived.

Scanning Parameters

All fetuses included in our study were scanned prenatally on a 1.5T magnet at the Cincinnati Children's Hospital Medical Center using an Ingenia 1.5T (Philips Healthcare) or a Signa HDxt 1.5T (GE Healthcare) system. T2 single-shot FSE images of the brain were obtained in 3 planes: axial, sagittal, and coronal. Three-millimeter section thickness, no-gap interleaved images at 24 weeks' gestational age (GA) and 4-mm, no-gap interleaved images at 24 weeks were used. Although this imaging protocol did not change during the study period, the TRs and TEs varied between each scanner and were changed at times of scanner upgrades to optimize image quality. At least 2 stacks in each plane were obtained to the radiologist's satisfaction, including the midline sagittal image required for the biometric measurements in this study. The smallest FOV possible was used. Axial DWI, T1 spoiled gradient recalled, and echo-planar images of the fetal brain were inconsistently implemented at the radiologist's discretion at the time of imaging before 2016, at which point they became a part of the routine fetal brain malformation protocol.

Image Interpretation

All images were reviewed by 2 board-certified radiologists (U.D.N., B.M.K.-F.), both with added qualifications in pediatric radiology and fellowship training in pediatric neuroradiology, one (B.M.K.-F.) with >15 years of postfellowship attending experience in pediatric neuroradiology in a large academic center, the other (U.D.N.) with

>5 years of experience. The images were viewed on a PACS workstation. Only diagnostic-quality MRIs for the assessment of the fetal and postnatal brain were included in our study; image quality was a subjective assessment made by the neuroradiologists.

The radiologists assigned each patient into 1 of 3 categories: classic DWM, VH, or BP. DWM was assigned to fetuses that met 3 imaging criteria: partial or complete absence of the vermis, cystic enlargement of the fourth ventricle, and an enlarged posterior fossa marked by upward displacement of the tentorium and torcular.⁸ VH was defined as a vermis that was small for GA with an elevated tegmentovermian angle (TVA) (>18°) without posterior fossa enlargement. BP was defined as a vermis that was normal in size for GA; however, the TVA was elevated >18°.⁷ Differences were resolved by consensus.

Multiple measurements of the posterior fossa were acquired and recorded by the radiologists. These measurements included transverse cerebellar diameter (TCD), vermis craniocaudal (CC) height, anterior-to-posterior (AP) vermis, AP pons, and lateral ventricle size of the largest lateral ventricle. Measurements were acquired using PACS measuring tools and recorded in millimeters, rounding to the nearest millimeter. Methods used to acquire these measurements have been described by Tilea et al.^{9,10} The TVA and superior posterior fossa angle were measured with values rounded to the nearest degree; the methods are described by Chapman et al.¹¹ The cisterna magna was described as normal or enlarged; this was a subjective assessment by the radiologist because reproducible measurements were not possible, given vermian rotation and distortion. Vermian foliation was described as normal or abnormal. Postnatal brain MRIs, when available, were reviewed in each patient for confirmation of the prenatal diagnosis.

Statistical Analysis

Measurements were compared with normal values published by Kline-Fath et al.¹² These data were based on a total of 325 normal fetal brain MRIs 94 of which were between 18 and 22 weeks' GA. The reference curves for the healthy group were estimated using the methods described by Wan et al,¹³ with GA as the predictor. The 10th, 50th, and 90th smoothed curves were derived and graphed along with points representing the diagnostic groups. In addition, ANCOVA models were conducted in which a measurement was modeled as a function of the diagnostic group, GA, and their interaction term. To look at diagnostic group differences across time, we compared adjusted means (least square means) to the means at selected GAs for the diagnostic groups being compared. Thus, the mean GA and ages chosen for comparison at the median and lower and upper quartiles examined will depend on whether the healthy cohort is included in that particular model.

All statistical analyses were conducted using SAS statistical software, Version 9.4 (SAS Institute). Comparisons were considered statistically significant with $P < .05$. No adjustments were made for multiple comparisons.

RESULTS

Description of Cohort

A total of 240 fetal MRIs (108 VH, 90 DWM, and 42 BP) were identified by keyword search. Those without documented postnatal

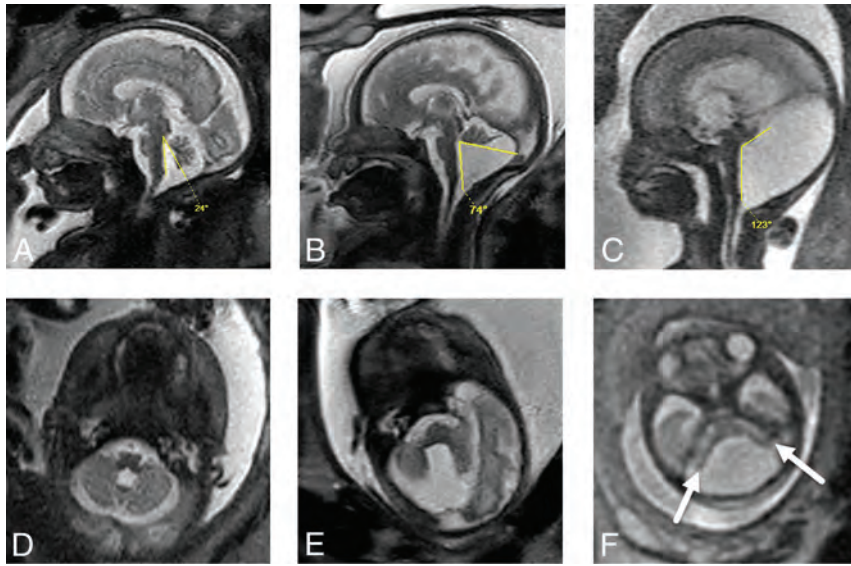


FIG 1. Examples from cohort of Dandy-Walker continuum with TVAs. Sagittal (A) and axial (D) T2 single-shot FSE images from fetal MR imaging at 30 weeks' GA demonstrate a BP with elevated TVA at 24°; however, the vermis is normal in size and morphology. Sagittal (B) and axial (E) T2 single-shot FSE images from fetal MR imaging at 32 weeks' GA with VH. There is a coexisting BP marked by an elevated TVA; however, the tentorium is not considered elevated. Sagittal (C) and axial (F) T2 single-shot FSE images from fetal MR imaging at 24 weeks' GA with classic DWM. The vermis is very small and rotated, and the tentorium is elevated with upward displacement. There is also separation and flattening of the cerebellar hemispheres (F, arrows).

Average measurements in each category

	DWM (n = 7)	VH (n = 16)	BP (n = 10)
TCD (mm)	24.71 (SD, 4.46)	24.88 (SD, 7.63)	31.8 (SD, 11.41)
Vermis height (mm)	7.67 (SD, 3.08) (n = 6)	10.69 (SD, 2.82)	13.7 (SD, 5.44)
AP vermis (mm)	2.83 (SD, 1.33) (n = 6)	5.56 (SD, 2.45)	8.0 (SD, 3.5)
TVA	109.5° (SD, 20.21°) (n = 6)	52.13° (SD, 18.88°)	32.1° (SD, 17.9°)
Cisterna magna enlarged	7 (100%)	11 (68.75%)	5 (50%)
AP pons (mm)	5.4 (2–7)	7.25 (SD, 1.77)	9.4 (SD, 2.8)
Posterior fossa angle	130.86° (SD, 21.27°)	108.75° (SD, 22.83°)	91.1° (SD, 12.5°)
Lateral ventricle size (mm)	20.86 (SD, 8.88)	8.63 (SD, 3.34)	11.7 (SD, 8.1)
Abnormal vermian foliation	7 (100%) (n = 6)	13 (81.25%)	3 (30%)

clinical follow-up in the Cincinnati Children's Hospital medical records were excluded, leaving a total of 48 patients. Images were reviewed by the study radiologists, and 4 additional patients were excluded on the basis of imaging characteristics (prenatal or postnatal) that were consistent with other congenital brain abnormalities (2 Chiari II, 1 Joubert syndrome and related disorders, and 1 aqueductal stenosis). An additional 11 patients with a small vermis and a normal TVA (<18°) were also excluded before analysis, leaving a total of 33 patients. Average maternal age at fetal MR imaging was 29.15 (SD, 6.6) years. Average GA at fetal MR imaging was 24.66 (SD, 4.8) weeks, with 1 patient having a second fetal MR imaging at 32 weeks 3 days' GA. Ninety-seven percent (32/33) of patients had postnatal brain MR imaging available for review, all confirming the prenatal evaluation of the posterior fossa malformation described. The average age at postnatal brain MR imaging was 49.06 (SD, 93.45) days.

Posterior Fossa Measurements

Of the 33 patients included, 7 were considered to have DWM; 16, VH; and 10, BP (Fig 1). The average measurements in each category, regardless of GA, are summarized in the Table. The vermis could not be seen in 1 patient with DWM so that the vermis height, AP vermis, TVA, and vermian foliation could not be assessed. The cisterna magna was considered enlarged in 100% (7/7) of patients with DWM, which was greater than in the other 2 groups (68.75% [11/16] in VH, 50% [5/10] in BP), though it was not statistically significant ($P = .08$). Abnormal vermian foliation was observed in a significantly larger portion of the patients with DWM and VH than in those with BP ($P = .004$).

After adjusting for GA, we made group comparisons from the measurements. The AP vermis, AP pons, and TCD were all significantly affected by the adjusted mean GA ($P < .05$). The AP vermis, CC vermis, and AP pons were significantly smaller in the DWM group compared with the BP and VH groups at ≥ 23.1 weeks' mean GA. No significant differences in the TCD were seen among groups when adjusted for GA. No significant group differences were seen with the AP vermis, CC vermis, AP pons, and TCD at ≤ 21.1 weeks' mean GA. The TVA and posterior fossa angles were not significantly affected by the adjusted mean GA. The TVA was significantly higher in patients with DWM than in those with VH and BP, regardless of GA. Lateral ventricle size was significantly affected by the adjusted mean GA ($P = .045$) and also significantly larger in the DWM group than in the BP and VH groups at ≥ 23.1 weeks' mean GA. No significant differences in ventricle size were observed between BP and VH regardless of GA. *P* values from the ANCOVA by adjusted mean GA are summarized in the Online Supplemental Data. *P* values from the ANCOVA by GA quartiles are summarized in the Online Supplemental Data.

After adjusting for GA, we made comparisons with normal values. AP vermis, CC vermis, AP pons, and TCD all were significantly affected by the adjusted GA ($P < .05$). The AP vermis was significantly smaller than normal values for BP, DWM, and VH regardless of the GA. The CC vermis was significantly smaller than normal values in patients with DWM and VH at ≥ 25 weeks' mean GA. No significant differences among the CC vermis, AP pons, or TCD were noted when BP was compared with normal

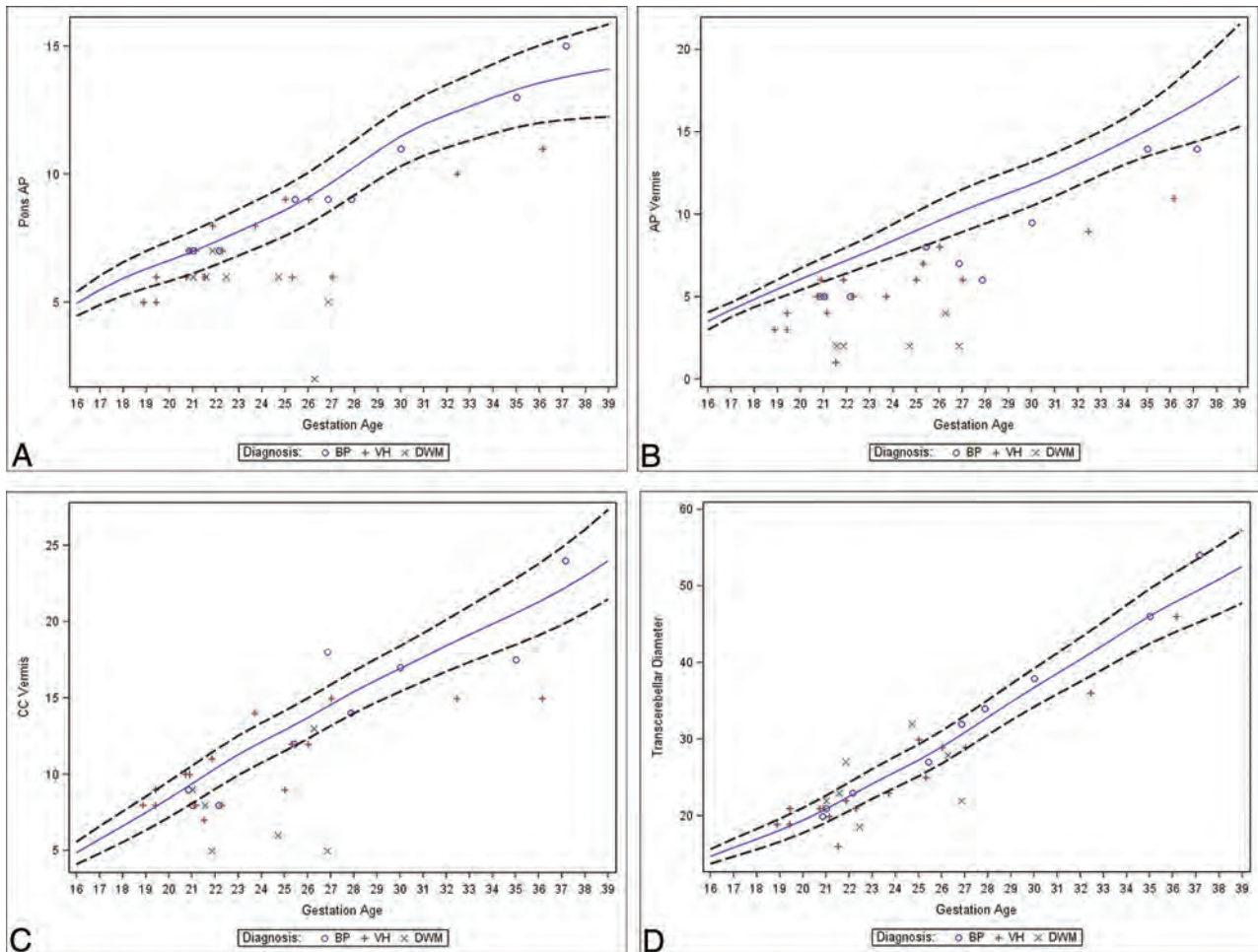


FIG 2. Measurements of the patients included in this cohort for AP pons (A), AP vermis (B), CC vermis (C), and TCD (D) plotted in relation to the normal growth curves by GA.

values, regardless of the GA. Graphs illustrating values compared with normative data are shown in Fig 2. *P* values from the ANCOVA by adjusted mean GA are summarized in the Online Supplemental Data. *P* values from the ANCOVA by GA quartiles are summarized in the Online Supplemental Data.

DISCUSSION

We examined fetal MR imaging findings along the Dandy-Walker continuum to include classic DWM, VH, and BP. We used commonly used metrics in fetal imaging and compared values with normative data. We observed that the AP vermis, CC vermis, AP pons, and TCD were not significantly different among the diagnostic groups at ≤ 21.1 weeks' mean GA. We also found that the TVA was significantly larger in DWM than the VH and BP groups regardless of GA, and in our series, it ranged from 79° to 130° . Finally, we observed a decreased AP vermis in all 3 groups compared with data of healthy fetuses regardless of GA and a decreased CC vermis in those with DWM and VH compared with values of normal fetal brains at ≥ 25 weeks' mean GA.

The initial descriptions of Dandy-Walker malformation were based on observations made before cross-sectional neuroimaging

were widely available and were largely based on intraoperative findings, pathologic specimens, and pneumocephalography.¹⁻³ These observations resulted in the selection of the most severe cases in the pathologic spectrum, and torcular-lambdoid inversion was a description based on the anatomic landmarks that could be reliably identified radiographically. Once CT and MR imaging were routinely used in clinical practice, abnormalities ranging from classic DWM to mega cisterna magna, a normal variant, were described along the same pathologic spectrum, believed to all originate from defects in development of the posterior membranous area.^{4,5,14}

During the past decade, fetal MR imaging has become a crucial part of the evaluation of the brain prenatally and often plays a key role in counseling patients and postnatal management.¹⁵⁻¹⁷ Prenatal identification of a posterior fossa anomaly along the Dandy-Walker continuum does not have the same clinical implications as postnatally diagnosed classic DWM, making counseling and perinatal management challenging. Prenatally diagnosed isolated BP, in which the vermis is normal in size with an elevated TVA, generally portends a good prognosis; however, close follow-up is suggested because postnatal obstructive hydrocephalus can develop.¹⁸⁻²¹ Isolated vermian hypoplasia also can portend a good prognosis.²² However, prenatally diagnosed classic DWM

can portend a worse prognosis, with an increased incidence of chromosomal and associated structural anomalies described.²³⁻²⁵

Our study adds to the existing literature by providing posterior fossa biometric measurements on fetal MR imaging in patients with posterior fossa malformations along the Dandy-Walker continuum in a relatively large group of patients with postnatal imaging confirmation of diagnoses and clinical follow-up. While 1 recent large series examined quantitative data of vermian lobulation and brain stem areas in healthy patients and those with Dandy-Walker continuum on fetal MR imaging, a very important area of work, these metrics can be challenging to use in routine clinical practice, depending on the available PACS measuring tools, and may require postprocessing in a separate software package.²⁶ This study, along with other studies describing advanced imaging analysis of volumetric data of the posterior fossa structures, will likely prove valuable in future studies.²⁷ Our study also observed that the TVA can be a helpful descriptive tool in differentiating classic DWM from the other posterior fossa abnormalities along the spectrum of a TVA of $\geq 80^\circ$ (range, 79° – 130° in our study), regardless of GA. This is valuable information, particularly in the context of descriptions of the clinical outcomes in this patient population based on their grouping. Finally, our study illustrates the limitations of other fetal biometric measures (posterior fossa angle, AP vermian, CC vermian, AP Pons, and TCD) in differentiating these entities along the spectrum at ≤ 21.1 weeks' mean GA. Understanding the limitations of fetal brain biometric measurements early in the second trimester is important in counseling and can help guide the appropriate timing of fetal MR imaging in a given patient with a suspected posterior fossa malformation. These limitations may change with continued advances in MR imaging technology, improving spatial resolution in fetal MR imaging along with more detailed robust reference data for clinical use in the future.

Our study has several limitations. First, the retrospective nature of this study limits its internal validity. Second, given that this is a single-institution study performed within a certain timeframe, the external validity may be limited as well. The use of the diagnostic categories in this study may come under scrutiny, given the overlap in imaging findings and the inconsistent use of terminology in the literature. We chose to use an 18° TVA cutoff for BP based on fetal sonography literature by Volpe et al,¹⁸ though more recent literature in healthy fetuses on MR imaging described the average TVA as 2.5° (SD, 2.3°).¹¹ This was the case for our review based on the interpretations of fetal MRIs during the study period, though it is possible that patients with smaller BPs may have been inadvertently excluded, particularly given the variation in the existing sonography literature.²⁸⁻³⁰ Also, because patients included in our VH group had coexisting BP, which explains vermian rotation in VH, there may be some unintended overlap in patients with mild VH and BP, which can be explained, at least in part, by the inherent limitations in the reproducibility in PACS measuring tools.⁵

We excluded patients with VH in the context of a clear pathologic diagnosis outside the Dandy Walker continuum (Joubert syndrome and related disorders, Chiari II). In addition, we excluded patients with a small vermian that did not have an elevated TVA because these patients may not fall within the same pathologic spectrum of posterior fossa malformations and may be derived from another cause such as an encephaloclastic etiology; however,

we realize that there are inherent limitations to this approach as well.³¹ Also of note, patients with BP have classically been described as having a normal vermian size and morphology; however, 30% (3/10) of patients with BP in our series were described as having abnormal vermian foliation.⁷ We attribute this to mass effect on the vermian related to the BP rather than a true intrinsic abnormality of the vermian, and because the vermian was normal in size, we kept the current categorization. However, BP can be mistaken for mild VH due to the associated mass effect.^{6,32}

Finally, given the heterogeneity of the terminology used in relation to the Dandy-Walker continuum, the applicability to general clinical practice outside our institution is uncertain at this point. Given the relatively good outcomes reported in BP and isolated VH, some fetal imagers discourage the term “Dandy-Walker variant” because it may give the false impression of a worse prognosis than expected.³³ One group of authors described the “tail sign” as a method of differentiating DWM from other posterior fossa malformations; however, this finding has also been seen in other posterior fossa anomalies.^{34,35} Others advocate that all patients with a small and rotated vermian be considered as having DWM, which serves as an imaging phenotype rather than a primary diagnosis, particularly in the setting of genetic abnormalities. In 1 relatively large study examining large-exome sequencing results, genetic mutations involving 27 different genes were identified and were more frequently encountered in patients with cerebellar hypoplasia (51%) than in those who were classified as having DWM by the authors (16%). This study also reported that many DWMs may be the result of in utero vascular insult, and the severity of imaging findings in the posterior fossa alone has not been reliably shown to correlate with the severity of clinical phenotype.³⁶ Our focus in describing the presence of VH with coexisting BP (elevated TVA) and describing those with a “large” BP as having DWM is a way of approaching this patient population in a systematic fashion. Because the terminology of DWM and Dandy Walker continuum is confusing, it may be more worthwhile to describe this pathology along the spectrum of abnormality related to the enlargement of the Blake pouch, the severity of which is illustrated by the TVA. Severe enlargement would coincide with a TVA of $>80^\circ$, and milder forms, to $>18^\circ$. In addition, vermian abnormalities may be best described on the basis of imaging findings of foliation and size.

Despite being one of the largest fetal MR imaging programs in the country, the relatively small number of patients in our cohort, particularly when analyzing subgroups, limits its generalizability. We also chose not to include patients without postnatal follow-up, to help elucidate the clinical implications of the prenatal imaging findings, the value of which will be more evident in future work. In addition, imaging descriptions alone do have inherent limitations, and evaluation of the postnatal clinical outcomes in this patient population, and ultimately large multicenter data collection and analysis, will be necessary to understand the true value of prenatal imaging in this patient population.

CONCLUSIONS

We describe fetal MR imaging findings in patients with posterior fossa anomalies focused on the presence or absence of VH with coexisting BP, also known as the Dandy-Walker continuum. We observed that the TVA can be helpful in the description of classic

DWM when distinguishing it from VH and BP, with a TVA $\geq 80^\circ$. We also observed that other posterior fossa measurements, including posterior fossa angles, AP vermis, CC vermis, AP pons, and TCD are not significantly different among fetuses at ≤ 21.1 weeks' mean GA in our cohort, which may affect the timing of fetal MR imaging scheduling in this patient population. Given the challenges and inherent limitations in assigning a particular category to these patients and considering the heterogeneity of terminology in the current literature, precise morphologic descriptions and biometric measurements have become increasingly important in prenatal evaluation and, ultimately with future studies, counseling and perinatal management of this patient population.

Disclosures: Usha D. Nagaraj—UNRELATED: Royalties: Elsevier, Comments: I write book chapters on topics in pediatric neuroradiology for Elsevier.

REFERENCES

- Dandy W. **The diagnosis and treatment of hydrocephalus due to occlusions of the foramina of Magendie and Luschka.** *Surgery, Gynecology, and Obstetrics* 1921;32:112–24
- Taggart JK, Walker AE. **Congenital atresia of the foramina of Luschka and Magendie.** *Archives of Neurology And Psychiatry* 1942;48:583–612 CrossRef
- Benda C. **The Dandy-Walker syndrome or the so-called atresia of the foramen Magendie.** *J Neuropathol Exp Neurol* 1954;13:14–29 CrossRef Medline
- Barkovich AJ, Kjos BO, Norman D, et al. **Revised classification of posterior fossa cysts and cystlike malformations based on the results of multiplanar MR imaging.** *AJNR Am J Neuroradiol* 1989;10:977–88 Medline
- Tortori-Donati P, Fondelli MP, Rossi A, et al. **Cystic malformations of the posterior cranial fossa originating from a defect of the posterior membranous area.** *Child's Nerv Syst* 1996;12:303–08 CrossRef Medline
- Robinson AJ. **Inferior vermian hypoplasia: preconception, misconception.** *Ultrasound Obstet Gynecol* 2014;43:123–36 CrossRef Medline
- Robinson AJ, Ederies MA. **Diagnostic imaging of posterior fossa anomalies in the fetus.** *Semin Fetal Neonatal Med* 2016;21:312–20 CrossRef Medline
- Kollias SS, Ball WS, Prenger EC. **Cystic malformations of the posterior fossa: differential diagnosis clarified through embryologic analysis.** *Radiographics* 1993;13:1211–31 CrossRef Medline
- Garel C. **Fetal cerebral biometry: normal parenchymal findings and ventricular size.** *Eur Radiol* 2005;15:809–13 CrossRef Medline
- Tilea B, Alberti C, Adamsbaum C, et al. **Cerebral biometry in fetal magnetic resonance imaging.** *Ultrasound Obstet Gynecol* 2009;33:173–81 CrossRef Medline
- Chapman T, Menashe SJ, Zare M, et al. **Establishment of normative values for the fetal posterior fossa by magnetic resonance imaging.** *Prenat Diagn* 2018;38:1035–41 CrossRef Medline
- Kline-Fath B, Bulas DI, Lee W. *Fundamental and Advanced Fetal Imaging*. 2nd ed. Wolters Kluwer Health; 2020
- Wan X, Qu Y, Huang Y, et al. **Nonparametric estimation of age-specific reference percentile curves with radial smoothing.** *Contemp Clin Trials* 2012;33:13–22 CrossRef Medline
- Calabrò Arcuri JR, Jinkins FT, Ospedali Galliera EO, et al. **Blake's pouch cyst: an entity within the Dandy-Walker continuum.** *Neuroradiology* 2000;42:290–95 CrossRef Medline
- Griffiths PD, Bradburn M, Campbell MJ, et al. **MERIDIAN collaborative group. Use of MRI in the diagnosis of fetal brain abnormalities in utero (MERIDIAN): a multicentre, prospective cohort study.** *Lancet* 2017;389:538–46 CrossRef Medline
- Griffiths PD, Brackley K, Bradburn M, et al. **Anatomical subgroup analysis of the MERIDIAN cohort: posterior fossa abnormalities.** *Ultrasound Obstet Gynecol* 2017;50:745–52 CrossRef Medline
- Arroyo MS, Hopkin RJ, Nagaraj UD, et al. **Fetal brain MRI findings and neonatal outcome of common diagnosis at a tertiary care center.** *J Perinatol* 2019;39:1072–77 CrossRef Medline
- Volpe P, Contro E, De Musso F, et al. **Brainstem-vermis and brainstem-tentorium angles allow accurate categorization of fetal upward rotation of cerebellar vermis.** *Ultrasound Obstet Gynecol* 2012;39:632–35 CrossRef Medline
- Gandolfi Colleoni G, Contro E, Carletti A, et al. **Prenatal diagnosis and outcome of fetal posterior fossa fluid collections.** *Ultrasound Obstet Gynecol* 2012;39:625–31 CrossRef Medline
- Cornips EM, Overvliet GM, Weber JW, et al. **The clinical spectrum of Blake's pouch cyst: report of six illustrative cases.** *Childs Nerv Syst* 2010;26:1057–64 CrossRef Medline
- Nagaraj UD, Kline-Fath BM, Calvo-Garcia MA, et al. **Fetal and postnatal MRI findings of Blake pouch remnant causing obstructive hydrocephalus.** *Radiol Case Rep* 2020;15:2535–39 CrossRef Medline
- Tarui T, Limperopoulos C, Sullivan NR, et al. **Long-term developmental outcome of children with a fetal diagnosis of isolated inferior vermian hypoplasia.** *Arch Dis Child Fetal Neonatal Ed* 2014;99:F54–58 CrossRef Medline
- Klein O, Pierre-Kahn A, Boddaert N, et al. **Dandy-Walker malformation: prenatal diagnosis and prognosis.** *Child's Nerv Syst* 2003;19:484–89 CrossRef Medline
- Patek KJ, Kline-Fath BM, Hopkin RJ, et al. **Posterior fossa anomalies diagnosed with fetal MRI: associated anomalies and neurodevelopmental outcomes.** *Prenat Diagn* 2012;32:75–82 CrossRef Medline
- D'Antonio F, Khalil A, Garel C, et al. **Systematic review and meta-analysis of isolated posterior fossa malformations on prenatal ultrasound imaging (Part 1): nomenclature, diagnostic accuracy and associated anomalies.** *Ultrasound Obstet Gynecol* 2016;47:690–97 CrossRef Medline
- Dovjak GO, Diogo MC, Brugger PC, et al. **Quantitative fetal magnetic resonance imaging assessment of cystic posterior fossa malformations.** *Ultrasound Obstet Gynecol* 2020;56:78–85 CrossRef Medline
- Ber R, Bar-Yosef O, Hoffmann C, et al. **Normal fetal posterior fossa in MR imaging: new biometric data and possible clinical significance.** *AJNR Am J Neuroradiol* 2015;36:795–802 CrossRef Medline
- Paladini D, Volpe P. **Posterior fossa and vermian morphometry in the characterization of fetal cerebellar abnormalities: a prospective three-dimensional ultrasound study.** *Ultrasound Obstet Gynecol* 2006;27:482–89 CrossRef Medline
- Ghi T, Contro E, De Musso F, et al. **Normal morphometry of fetal posterior fossa at midtrimester: brainstem-tentorium angle and brainstem-vermis angle.** *Prenat Diagn* 2012;32:440–43 CrossRef Medline
- Contro E, Volpe P, De Musso F, et al. **Open fourth ventricle prior to 20 weeks' gestation: a benign finding?** *Ultrasound Obstet Gynecol* 2014;43:154–58 CrossRef Medline
- Le Strange E, Saeed N, Cowan FM, et al. **MR imaging quantification of cerebellar growth following hypoxic-ischemic injury to the neonatal brain.** *AJNR Am J Neuroradiol* 2004;25:463–68 Medline
- Robinson AJ, Goldstein R. **The cisterna magna septa.** *J Ultrasound Med* 2007;26:83–95 CrossRef Medline
- Wüest A, Surbek D, Wiest R, et al. **Enlarged posterior fossa on prenatal imaging: differential diagnosis, associated anomalies and postnatal outcome.** *Acta Obstet Gynecol Scand* 2017;96:837–43 CrossRef Medline
- Bernardo S, Vinci V, Saldari M, et al. **Dandy-Walker malformation: is the "tail sign" the key sign?** *Prenat Diagn* 2015;35:1358–64 CrossRef Medline
- Chapman T, Kapur RP. **Cerebellar vermian dysplasia: the tale of the tail.** *J Pediatr Neurol Neurosci* 2018;2:17–22 CrossRef
- Aldinger KA, Timms AE, Thomson Z, et al. **Redefining the etiologic landscape of cerebellar malformations.** *Am J Hum Genet* 2019;105:606–15 CrossRef Medline

Enlargement of the Optic Chiasm: A Novel Imaging Finding in Glutaric Aciduria Type 1

 A.A. Ntorkou,  J. Daire,  F. Renaldo,  D. Doummar,  M. Alison,  M. Schiff, and  M. Elmaleh-Bergès

ABSTRACT

SUMMARY: Patients with glutaric aciduria type 1, without early diagnosis and initiation of preventive treatment, often develop movement disorders and various degrees of motor disability due to striatal area-specific damage induced by an acute episode of metabolic decompensation. The neuroimaging phenotype of patients with glutaric aciduria type 1 includes characteristic cyst-like bilateral enlargement of the Sylvian fissures and anterior subarachnoid spaces and signal abnormalities including supratentorial white matter and deep gray matter structure T2 hyperintensities, frequently associated with restricted diffusion. In this retrospective study, we add to the neuroimaging spectrum of glutaric aciduria type 1, a novel imaging finding present regardless of a previous metabolic crisis: the enlargement of the optic chiasm associated with signal abnormalities in the anterior intracranial visual structures observed in 6 of 10 patients. These optic pathway abnormalities are suggested as useful diagnostic clues for glutaric aciduria type 1, and possible pathophysiologic mechanisms are discussed.

ABBREVIATION: GA-1 = glutaric aciduria type 1

Glutaric aciduria type 1 (GA-1) is a rare autosomal recessive neurometabolic disorder caused by a deficiency of the mitochondrial enzyme glutaryl-CoA dehydrogenase, which is involved in the catabolic pathway of the amino acids lysine and tryptophan.^{1,2} Enzyme deficiency results in accumulation of glutaric and glutaconic acids, responsible for a brain cytotoxic effect, particularly in the basal ganglia.^{1,2} The clinical course of the disease varies from asymptomatic, for a minority of patients, to a severe disabling movement disorder that usually occurs early in life following an acute encephalopathic crisis in the setting of catabolic situations such as childhood febrile infections.^{1,2}

Despite phenotypic heterogeneity, typical brain imaging findings have been described, including widening of the Sylvian fissures and subarachnoid frontotemporal spaces and signal abnormalities within the corpus striatum and white matter.³⁻⁵

In this study, we aimed to broaden the neuroimaging phenotype of GA-1 in children and describe novel MR imaging findings.

Case Series

We retrospectively reviewed 10 brain MR imaging studies from 10 children (3 girls and 7 boys from 5 months to 8 years of age with a median age of 1.5 years) with GA-1 to describe the brain morphologic and signal abnormalities. MR imaging examinations were performed in different medical centers with different sequence parameters and were collected in our institution as patients were referred for further investigations and treatment.

Inclusion criteria were a definite diagnosis of GA-1 confirmed on the basis of biochemical (urine organic acids and plasma acylcarnitines) and molecular diagnoses and the availability of a brain MR imaging study of diagnostic quality, including at least axial or coronal T2WI and T1WI and a diffusion-weighted sequence ($b = 0$ and 1000). For symptomatic children having >1 brain MR imaging, the first examination performed after the diagnosis of GA-1 was analyzed for the study. Clinical reports were available for all patients, and specifically, data on visual disturbances were retrieved from clinical charts.

Six children were symptomatic, having already experienced an encephalopathic crisis, and presented with various degrees of dystonia and motor disability at the time of brain MR imaging. Four children of 6 had macrocephaly, and 5 children of 6 presented with mild or moderate intellectual disability. The mean time interval between the encephalopathic crisis, further referred to as a “metabolic crisis,” and the brain MR imaging was 9 months (range, 1–42 months).

Received February 5, 2021; accepted after revision April 19.

From the Departments of Pediatric Radiology (A.A.N., M.A., M.E.-B.), and Pediatric Neurology (J.D., F.R., M.S.), Robert Debré University Hospital, Assistance Publique–Hôpitaux de Paris, Paris, France; Department of Pediatric Neurology (D.D.), Trousseau University Hospital, Assistance Publique–Hôpitaux de Paris, Paris, France.

Please address correspondence to Alexandra A. Ntorkou, MD, Department of Pediatric Radiology, Robert Debré University Hospital, APHP, 48 bdSérurier, 75019 Paris, France; e-mail: alexdorkou@hotmail.com

<http://dx.doi.org/10.3174/ajnr.A7199>

MR imaging features and frequency of regional abnormalities observed in patients with and without previous metabolic crises

MR Imaging Features	Patients (n = 10)	Patients with Previous MC (n = 6)	Patients without Previous MC (n = 4)
Enlargement of the Sylvian fissures	10	6	4
Enlargement of anterior temporal SS	7	4	3
Enlargement of frontal SS	5	4	1
Signal abnormalities in deep gray matter	10	6	4
Corpus striatum	6/0 RD	6/0 RD	0
Globus pallidum	9/5 RD	6/3 RD	3/2 RD
Thalamus	4/2 RD	3/1 RD	1/1 RD
Dentate nucleus	8/0 RD	4/0 RD	4/0 RD
Substantia nigra	5/0 RD	4/0 RD	1/0 RD
Central tegmental tract	6/3 RD	3/1 RD	3/2 RD
Signal abnormalities in AVP	6/5 RD	4/3 RD	2/2 RD
Signal abnormalities in white matter	10/7 RD	6/4 RD	4/3 RD
Signal abnormalities in the medial surface of 3rd ventricle	6/5 RD	4/3 RD	2/2 RD

Note:—MC indicates metabolic crisis; SS, subarachnoid space; RD, restricted diffusion; AVP, anterior visual pathway.

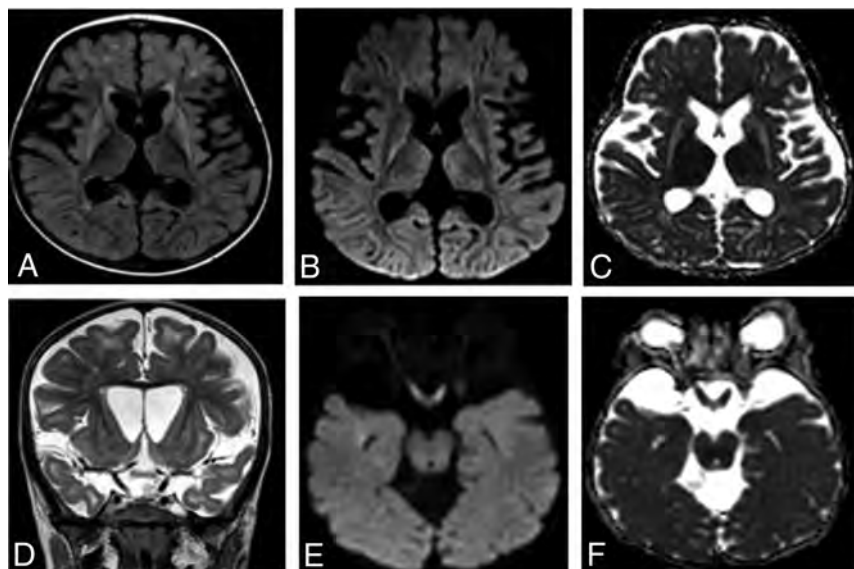


FIG 1. A 16-month-old patient with GA-1, having experienced a metabolic crisis. A and D, Axial FLAIR and coronal T2-weighted images. B and E, Axial diffusion sequences. C and F, Axial ADC maps. Characteristic bat wing widening of the Sylvian fissures and enlargement of subarachnoid temporal spaces are shown. Lateral ventricular moderate dilation is also shown. Bilateral symmetric atrophy and abnormal T2-FLAIR hyperintense signal in striatal area show increased diffusion on ADC maps, suggesting striatal necrosis related to the history of metabolic decompensation. The globus pallidi and thalami also demonstrate bilateral abnormal hyperintensity associated with restricted diffusion away from the acute metabolic crisis. Patchy areas of hyperintense T2-FLAIR signal abnormalities without restricted diffusion are found in the superficial bilateral white matter, persisting on the follow-up for up to 6 years. The optic chiasm is thickened, displaying abnormal hyperintense T2 signal and restricted diffusion also involving the intracranial optic nerves.

At the time of brain MR imaging, 4 children did not present with episodes of metabolic decompensation. Two of them were siblings with macrocephaly and were diagnosed by family screening, 1 child was diagnosed during routine evaluation of macrocephaly, and the last one was evaluated for moderate intellectual disability.

MR images were reviewed in consensus for quality and were interpreted by 2 pediatric radiologists (M.E.-B. and A.A.N.) with experience in neuroradiology.

The lack of a standardized 3D acquisition for all brain MRI in our cohort did not allow us to make reproducible optic chiasm measurements; thus, the observation of optic chiasm enlargement was subjective.

Gray matter and white matter signal abnormalities were defined as areas of hyperintensity on T2WI. White matter signal intensity was considered abnormal if the T2 hyperintensity did not correspond to the normal pattern of myelination according to the age.

Interpretation of DWI was performed qualitatively by visual assessment. When abnormal signal was depicted on conventional sequences, the b-value images and ADC maps were analyzed and compared with normal brain area, to assess restricted diffusion. The calculation of ADC values and a comparative study with an age-matched control group were avoided, taking into account the ongoing process of white matter myelination in the first years of life and the wide age range of children included in the study.

MR Imaging Interpretation

The results are summarized in detail in the Table.

All patients (n = 10) presented with a bilateral cyst-like dilation of the Sylvian fissures, the so-called “bat wing appearance” associated with enlargement of the anterior temporal and frontal subarachnoid spaces (Figs 1 and 2).

All children with previous metabolic crises (n = 6) demonstrated striatal atrophy with bilateral, symmetric T2 hyperintensity and increased diffusion in the putamen, and in 4 children, in the caudate nuclei (Fig 1). Bilateral globus pallidus T2 hyperintensity was observed in all patients who had experienced a metabolic crisis (n = 6), showing restricted diffusion in half of

the patients (n = 3) as well as in 3 of 4 patients free from any history of metabolic crisis.

Signal abnormalities were also observed in deep gray matter structures apart from the basal ganglia, affecting children irrespective of the presence of a previous metabolic crisis. Abnormal

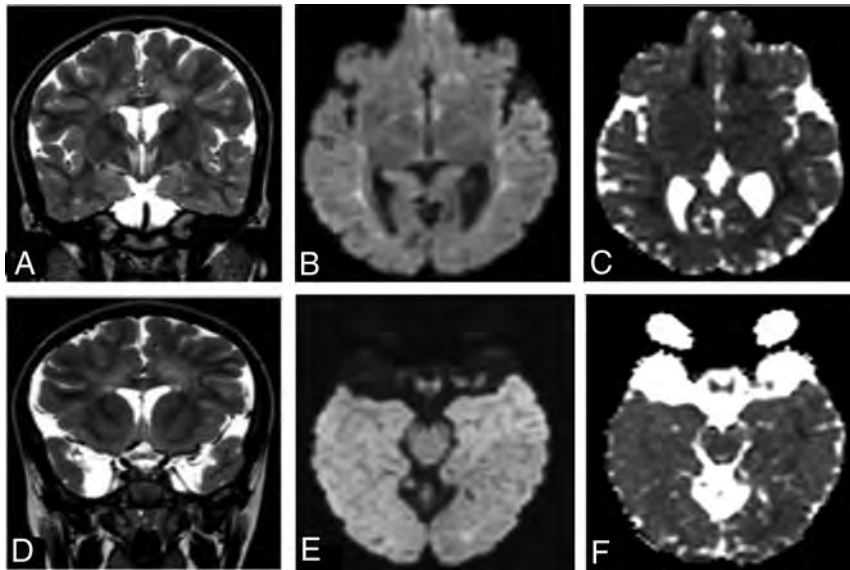


FIG 2. A 7-year 10-month-old patient with GA-1, free from a history of previous metabolic crisis. A and D, Coronal T2-weighted images. B and E, Axial diffusion sequences. C and F, Axial ADC maps. Characteristic Sylvian fissure enlargement and anterior arachnoid temporal cysts are shown. Note the absence of signal abnormalities in the deep gray matter structures, especially in the striatum; however, abnormal hyperintense T2 signal is observed bilaterally in the periventricular white matter displaying restricted diffusion. Abnormal areas of T2 signal with restricted diffusion are also demonstrated in the bilateral medial wall of the hypothalamus and in the markedly enlarged optic chiasm.

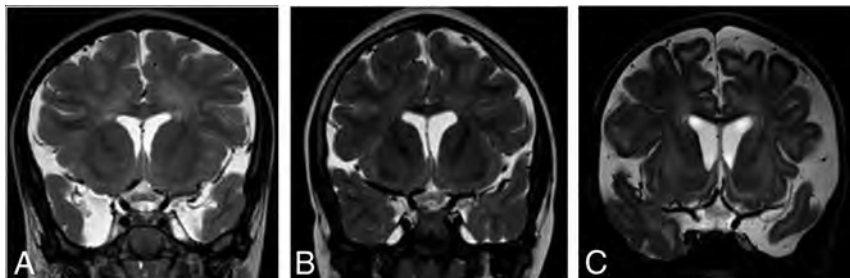


FIG 3. Coronal T2-weighted images showing enlargement of the optic chiasm and displaying an abnormal T2 hyperintensity in 3 different patients. A, A 7-year 10-month-old patient without a history of a previous metabolic crisis. B, An 8-year-old patient not having experienced a metabolic decompensation. C, A 10-month-old patient with a history of encephalopathic crisis at 8 months of age.

T2 hyperintensity with or without restricted diffusion was occasionally demonstrated in the bilateral posteromedial aspect of thalami, in the brainstem nuclei including the substantia nigra the central tegmental tracts, and, finally, in bilateral dentate nucleus.

Supratentorial white matter diffuse hyperintensity on T2WI was invariably observed, with a predominant pattern of periventricular distribution in 9 of 10 patients. White matter hyperintensities displayed restricted diffusion on DWI in 7 children, 4 of them with previous episodes of metabolic crisis (Figs 1 and 2). A single child with only subcortical white matter affected was noticed.

In 6 of 10 children, including 2 patients without previous metabolic crisis, we noticed enlargement of the optic chiasm displaying an abnormal T2 hyperintensity with restricted diffusion in all

except 1 child (Figs 3 and 4). In 4 of 10 patients, including 2 without a previous encephalopathic crisis, the signal abnormalities extended bilaterally in the prechiasmatic intracranial segment of the optic nerves and posteriorly along the optic tracts (Figs 1E, -F and 2E, -F), despite visual disturbances not being noticed according to the available clinical data.

Additionally, in the same patients, abnormal hyperintense T2 signal with restricted diffusion was found in the lower medial surface of the third ventricle, corresponding to the area of the anterior hypothalamic component (Fig 2A, -B).

DISCUSSION

Neuroradiologic findings of GA-1 with emphasis on brain MR imaging have been adequately described in the literature. Despite the variability in the clinical phenotype, patients with GA-1 share some similar characteristic brain imaging findings that should facilitate the diagnosis in the absence of neonate screening.³⁻⁵ The data presented herein show novel GA-1 neuroimaging findings, including enlargement of the optic chiasm and intracranial visual pathway signal abnormalities.

Six of 10 patients in our cohort had abnormalities in the anterior intracranial visual pathway and the lower medial surface of the third ventricle. Enlargement of the optic chiasm and abnormal hyperintensity on T2WI, extending in the intracranial segment of the optic nerves and along the optic tracts, was observed. In 5 of 6 children, restricted diffusion was also noticed. None of the affected patients had known visual disturbances at the time of brain MR imaging; however, full ophthalmologic evaluation was not available.

Eye abnormalities including cataract, strabismus, pigmentary retinopathy, and intraretinal hemorrhages have rarely been reported in patients with GA-1.⁶ A single case of bilateral optic atrophy has also been reported in a child diagnosed with GA-1 by neonate screening.⁷

Optic neuropathy is a well-known complication in the course of several organic acidurias. Several neuroimaging reports have described atrophy and signal abnormalities in the optic nerves and chiasm in individual subjects with propionic and methylmalonic acidurias.^{8,9} Although the exact pathophysiology of optic neuropathy in organic acidurias has not been adequately elucidated, it is believed that it is due to the neurotoxic effect of the

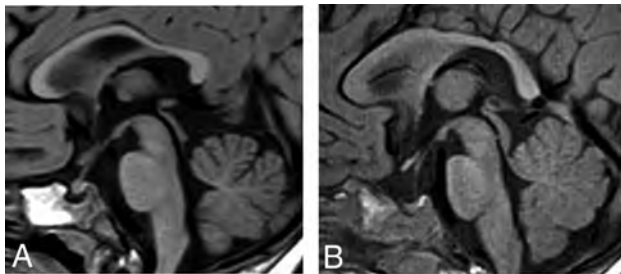


FIG 4. Midline sagittal T1-weighted images showing enlargement of the optic chiasm. A, A 10-month-old patient with GA-1 and a history of encephalopathic crisis, compared with B, a healthy child of a similar age.

accumulated organic acids, with subsequent impairment of mitochondrial energy metabolism.^{8,9}

Atrophy of the optic nerves or chiasm was not observed in our patients. Conversely, the optic chiasm was found enlarged, and signal abnormalities were found even in asymptomatic patients without striatal lesions, suggesting a pathophysiologic mechanism not related to a previous episode of metabolic crisis. As a possible explanation, we suggest that lesions of the optic nerves and chiasm might be related to the same pathophysiologic mechanism proposed for the white matter abnormalities. Neurotoxic spongiform myelinopathy might affect the myelinated nerve fibers in the visual pathway, resulting in cytotoxic edema and restricted diffusion on MR imaging. This suggestion is supported by a postmortem report in a child with GA-1 having experienced acute encephalopathy in which the neuropathology demonstrated spongiform myelinopathy in the white matter and the optic nerves.¹⁰

Patients with lesions of the optic chiasm also demonstrated signal abnormalities around the lower medial surface of the third ventricle, corresponding to the anatomic region of the anterior hypothalamic nuclei. The hypothalamic portion of the third ventricle is composed of a number of nuclei and fiber tracts and represents a region of increased energy demands, with increased susceptibility to energy imbalance.¹¹

Based on imaging findings, in the pediatric population, the differential diagnosis of optic nerve and chiasm enlargement should invariably include optic nerve glioma, frequently seen in the context of neurofibromatosis type 1. Leukemia, histiocytic or granulomatous infiltration, and inflammatory and postviral optic neuritis are also possible differential diagnoses to consider. In a clinical context suggestive of metabolic disorder, the enlargement of the optic chiasm should raise the suspicion of a lysosomal storage disorder. Optic chiasm hypertrophy and enhancement have been described in Krabbe disease, thought to be due to accumulation of the globoid cells that are diagnostic for the disease.¹² Recently, the presence of optic nerve hypertrophy in a patient with early metachromatic leukodystrophy has been reported, and the authors have postulated that it might represent the early stage of optic involvement in metachromatic leukodystrophy, which is expected to lead to optic atrophy.¹³ Finally, a tumorlike enlargement of the optic chiasm has also been described in a child with infantile Alexander disease.¹⁴

In accordance with the literature, all our patients had neuro-radiologic findings previously described in GA-1.

The particular morphology of enlarged bat wing Sylvian fissures was invariably found in our cohort and has been widely described as an almost constant imaging finding, highly suggestive of GA-1 when associated with macrocephaly.³⁻⁵

Furthermore, bilateral and symmetric striatal lesions have been described as the most peculiar imaging finding related to the occurrence of the metabolic crisis in patients with GA.³⁻⁵ Although the exact pathophysiology of these region-specific abnormalities is not fully understood, they are believed to represent cytotoxic edema induced by the brain accumulation and trapping of GA-1 metabolites.^{15,16} There is increasing evidence that glutaric acid and 3-hydroxyglutaric acid induce neurotoxicity, mainly by disturbing the intracellular mitochondrial energy metabolism and impairing the balance in the GABAergic brain neurotransmission process.^{15,16} In our cohort, all striatal lesions observed in patients with previous metabolic crisis had increased diffusion on the ADC maps representing rather the chronic stage of the disease, related to the long time interval between the episode of acute encephalopathy and the MR imaging examination.

Extrastriatal deep gray matter lesions, including mainly the globus pallidus and the thalamus, were observed in our study coexisting with striatal lesions in patients with a previous history of metabolic crisis but also as isolated lesions in children free from metabolic crisis. Previous reports have mentioned the presence of extrastriatal deep gray matter abnormalities in patients with GA-1 without encephalopathy, and a correlation with the presence of prominent white matter lesions has been described, reflecting the fact that globus pallidus, thalamus, and brainstem gray matter nuclei are rich white matter structures and thus are affected by changes in white matter microstructure.^{16,17}

It has been proposed that white matter abnormalities in GA-1 represent spongiform myelinopathy, independent of the acute encephalopathic brain injury, probably attributed to intramyelinic edema caused by the toxic effects of accumulating metabolic substances.¹⁵ Intramyelinic edema with myelin vacuolation decreases the extracellular space, resulting in restricted diffusion. White matter signal abnormalities were invariably described in patients included in our study, displaying restricted diffusion in 8 children. Periventricular white matter distribution was the predominant pattern observed.

This study has limitations that should be addressed. It is retrospective, including a relatively small sample size; however, in rare diseases such as GA-1, the small number of patients enrolled is a limitation difficult to overcome. Another limitation is the lack of a clinico-radiologic association for MR imaging abnormalities observed in the anterior visual pathway.

CONCLUSIONS

We report, for the first time, 6 children with GA-1 presenting with enlargement of the optic chiasm and signal abnormalities in the anterior intracranial visual pathway and the medial surface of the third ventricle, regardless of a previous metabolic crisis. The pathophysiologic mechanism for these lesions is unknown, and correlation with clinical symptoms should be further investigated.

ACKNOWLEDGMENTS

The authors thank Dr Hélène Ogier de Baulny for providing her great clinical expertise in the management of most of the patients.

REFERENCES

1. Boy N, Mühlhausen C, Maier EM, et al. **Proposed recommendations for diagnosing and managing individuals with glutaric aciduria type I: second revision.** *J Inherit Metab Dis* 2017;40:75–101 CrossRef Medline
2. Boy N, Mengler K, Thimm E, et al. **Newborn screening: a disease-changing intervention for glutaric aciduria type I.** *Ann Neurol* 2018;83:970–79 CrossRef Medline
3. Boy N, Garbade SF, Heringer J, et al. **Patterns, evolution, and severity of striatal injury in insidious- vs acute-onset glutaric aciduria type I.** *J Inherit Metab Dis* 2019;42:117–27 CrossRef Medline
4. Boy N, Heringer J, Brackmann R, et al. **Extrastriatal changes in patients with late-onset glutaric aciduria type I highlight the risk of long-term neurotoxicity.** *Orphanet J Rare Dis* 2017;12:77 CrossRef Medline
5. Harting I, Neumaier-Probst E, Seitz A, et al. **Dynamic changes of striatal and extrastriatal abnormalities in glutaric aciduria type I.** *Brain* 2009;132:1764–82 CrossRef Medline
6. Kafil-Hussain NA, Monavari A, Bowell R, et al. **Ocular findings in glutaric aciduria type I.** *J Pediatr Ophthalmol Strabismus* 2000;37:289–93 Medline
7. Tsai FC, Lee HJ, Wang AG, et al. **Experiences during newborn screening for glutaric aciduria type I: diagnosis, treatment, genotype, phenotype, and outcomes.** *J Chin Med Assoc* 2017;80:253–61 CrossRef Medline
8. Kölker S, Valayannopoulos V, Burlina AB, et al. **The phenotypic spectrum of organic acidurias and urea cycle disorders, Part 2: the evolving clinical phenotype.** *J Inherit Metab Dis* 2015;38:1059–74 CrossRef Medline
9. Martinez Alvarez L, Jameson E, Parry NR, et al. **Optic neuropathy in methylmalonic acidemia and propionic acidemia.** *Br J Ophthalmol* 2016;100:98–104 CrossRef Medline
10. Soffer D, Amir N, Elpeleg ON, et al. **Striatal degeneration and spongy myelinopathy in glutaric acidemia.** *J Neurol Sci* 1992;107:199–204 CrossRef Medline
11. Jin S, Diano S. **Mitochondrial dynamics and hypothalamic regulation of metabolism.** *Endocrinology* 2018;159:3596–3604 CrossRef Medline
12. Jones BV, Barron TF, Towfighi J. **Optic nerve enlargement in Krabbe's disease.** *AJNR Am J Neuroradiol* 1999;20:1228–31 Medline
13. Roi D, Mankad K, Kaliakatsos M, et al. **Thickening of the optic nerves in metachromatic leucodystrophy: a new MRI finding.** *Neuroradiol J* 2016;29:134–36 CrossRef Medline
14. Mignot C, Desguerre I, Burglen L, et al. **Tumor-like enlargement of the optic chiasm in an infant with Alexander disease.** *Brain Dev* 2009;31:244–47 CrossRef Medline
15. Klker S, Hoffmann GF, Schor DS, et al. **Glutaryl-CoA dehydrogenase deficiency: region-specific analysis of organic acids and acylcarnitines in post mortem brain predicts vulnerability of the putamen.** *Neuropediatrics* 2003;34:253–60 Medline
16. Strauss KA, Morton DH. **Type I glutaric aciduria, part 2: a model of acute striatal necrosis.** *Am J Med Genet C Semin Med Genet* 2003;121C:53–70.CrossRef Medline
17. Twomey EL, Naughten ER, Donoghue VB, et al. **Neuroimaging findings in glutaric aciduria type I.** *Pediatr Radiol* 2003;33:823–30 CrossRef Medline

Atlas-Based Quantification of DTI Measures in a Typically Developing Pediatric Spinal Cord

 S. Shahrampour,  B. De Leener,  M. Alizadeh,  D. Middleton,  L. Kriza,  A.E. Flanders,  S.H. Faro,  J. Cohen-Adad, and  F.B. Mohamed



ABSTRACT

BACKGROUND AND PURPOSE: Multi-parametric MRI, provides a variety of biomarkers sensitive to white matter integrity. However, spinal cord MRI data in pediatrics is rare compared to adults. The purpose of this work was 3-fold: 1) to develop a processing pipeline for atlas-based generation of the typically developing pediatric spinal cord WM tracts, 2) to derive atlas-based normative values of the DTI indices for various WM pathways, and 3) to investigate age-related changes in the obtained normative DTI indices along the extracted tracts.

MATERIALS AND METHODS: DTI scans of 30 typically developing subjects (age range, 6–16 years) were acquired on a 3T MR imaging scanner. The data were registered to the PAM50 template in the Spinal Cord Toolbox. Next, the DTI indices for various WM regions were extracted at a single section centered at the C3 vertebral body in all the 30 subjects. Finally, an ANOVA test was performed to examine the effects of the following: 1) laterality, 2) functionality, and 3) age, with DTI-derived indices in 34 extracted WM regions.

RESULTS: A postprocessing pipeline was developed and validated to delineate pediatric spinal cord WM tracts. The results of ANOVA on fractional anisotropy values showed no effect for laterality ($P = .72$) but an effect for functionality ($P < .001$) when comparing the 30 primary WM labels. There was a significant ($P < .05$) effect of age and maturity of the left spinothalamic tract on mean diffusivity, radial diffusivity, and axial diffusivity values.

CONCLUSIONS: The proposed automated pipeline in this study incorporates unique postprocessing steps followed by template registration and quantification of DTI metrics using atlas-based regions. This method eliminates the need for manual ROI analysis of WM tracts and, therefore, increases the accuracy and speed of the measurements.

ABBREVIATIONS: AD = axial diffusivity; CV = coefficient of variation; DF = dorsal funiculi; FA = fractional anisotropy; LF = lateral funiculi; MD = mean diffusivity; RD = radial diffusivity; VF = ventral funiculi

In recent years, DTI has shown promise as a noninvasive imaging biomarker for evaluating the tissue microstructure,¹ which is sensitive to the integrity of the spinal cord WM. Recently, numerous studies have demonstrated the utility of DTI as a noninvasive tool to assess adult spinal cord WM microstructure.^{2,3} However, studies

related to the pediatric spinal cord have been limited so far.^{4,5} This issue highlights the importance of studying the pediatric spinal cord at a microstructural level and establishing normative values for various diffusion-derived indices obtained from the WM structures. A limited number of studies in pediatric subjects have demonstrated DTI indices differences between age and cord regions.^{4,5} However, all of these studies, so far, have used manual delineation of the WM structures in the pediatric spinal cord.⁵ Recently, methods have been developed that use automated extraction of the WM structures in the adult spinal cord.⁶ This approach alleviates any subjectivity in identification of WM structures. In this work, we have extended these methods to the pediatric spinal cord.

In summary, the aim of this work was 3-fold: 1) to develop a processing pipeline for atlas-based generation of pediatric spinal cord WM tracts. This provides a faster and more accurate method of tract delineation and eliminates the need for manual WM tract extraction. 2) to derive atlas-based normative values of the DTI parameters for various WM pathways at the C3 level of a typically developing pediatric spinal cord, and 3) to examine age-related changes in the derived normative DTI parameters along the extracted tracts.

Received February 9, 2021; accepted after revision April 19.

From the Departments of Radiology (S.S., M.A., D.M., F.B.M.), Occupational Therapy (L.K.), and Radiology (A.E.F., S.H.F.), Thomas Jefferson University, Philadelphia, Pennsylvania; Department of Computer Engineering and Software Engineering (B.D.L.) and NeuroPoly Lab (J.C.-A.), Institute of Biomedical Engineering, Polytechnique Montreal, Montreal, Quebec, Canada; and Functional Neuroimaging Unit (J.C.-A.), Centre de Recherche de l'Institut Universitaire de Gériatrie de Montréal, Université de Montréal, Montreal, Quebec, Canada.

This work was supported by the National Institute of Neurological Disorders of the National Institutes of Health under award Nos. R01NS079635 and R01NS111113.

Please address correspondence to Feroze Mohamed, PhD, Jefferson Integrated MRI Center, Department of Radiology, Thomas Jefferson University, 901 Walnut St, Philadelphia, PA 19107; e-mail: feroze.mohamed@jefferson.edu

 Indicates open access to non-subscribers at www.ajnr.org

 Indicates article with online supplemental data.

<http://dx.doi.org/10.3174/ajnr.A7221>

MATERIALS AND METHODS

Study Design and Population

All subjects provided written informed consent obtained under a protocol approved by the institutional review board at Thomas Jefferson University. The study used 30 typically developing pediatric subjects (age range, 6–16 years; mean age, 12.38 [SD, 2.81] years). Following the recruitment, all subjects went through a brief assessment, and those with any abnormality of the nervous system were excluded.

MR Imaging Protocol

The scans were obtained using a 3T Verio MR imaging scanner (Siemens) with a 4-channel neck and an 8-channel spine matrix coil. All the subjects underwent the scan protocol, consisting of an initial T2-weighted gradient-echo scout sagittal acquisition of the cervical and thoracic spinal cord. The sagittal scans were used to prescribe axial sections of both the cervical and thoracic spine. Imaging was then followed by obtaining an axial T2-weighted gradient-recalled-echo sequence, a sagittal T2-weighted 3D sampling perfection with application-optimized contrasts by using different flip angle evolution (3D-SPACE; Siemens) sequence, a sagittal TSE T1-weighted sequence, a sagittal TSE T2-weighted sequence, and axial diffusion-weighted scans. We used the 3D-SPACE and diffusion-weighted data in this study. Diffusion-weighted images were acquired axially using 2 overlapping slabs to cover the entire cervical and thoracic spinal cord using an inner FOV spin-echo-based EPI pulse sequence with a tilted excitation plane. The inner FOV diffusion-weighted sequence consists of a spatially selective 2D radiofrequency excitation profile.⁷ This sequence has the advantage of reducing distortion artifacts in diffusion-weighted scans by enabling faster k-space encoding via a reduction of phase-encoding steps. Manual shim and fat-saturation volume adjustments were also performed.

The imaging parameters of the diffusion-weighted acquisition for each slab are as follows: FOV = 164 mm, phase FOV = 28.4% (47 mm), 3 averages of 20 diffusion directions, 6 $b = 0$ acquisitions, $b = 800$ s/mm², voxel size = $0.8 \times 0.8 \times 6$ mm³, number of slices = 40, TR = 7900 ms, TE = 110 ms, acquisition time = 8 minutes and 49 seconds per slab. The T2-weighted SPACE imaging parameters used were: voxel size = $1 \times 1 \times 1$ mm³, TR = 1500 ms, TE = 122 ms, flip angle = 140°, number of averages = 2, and acquisition time = 3 minutes and 17 seconds (for each overlapping slab).

Image Preprocessing

The diffusion-weighted data from all the individual subjects were motion-corrected and later registered to the template (PAM50) in the Spinal Cord Toolbox (SCT; <https://spinalcordtoolbox.com/en/latest/>) for performing atlas-based analysis of WM tracts.⁶ Registration is best done using the high-resolution anatomic image. In this study, all the pre- and postprocessing of the data was performed entirely within the framework of the SCT.⁸ These processes are described in detail below and illustrated in Fig 1.

Procedure for Motion Correction

All diffusion-weighted data were motion-corrected using a slice-wise motion-correction method.⁸ Specifically, using the *sct_dmri_moco* module from SCT, slice-by-slice planar translations within the diffusion-weighted data were estimated, while

the regularization was constrained along the z-direction (*SliceReg* algorithm).

Procedure for Data Registration to the Template

After applying motion correction on the diffusion-weighted data, we registered the data with the PAM50⁶ template available in the SCT. The registration procedure was done following a 2-step multimodal registration process within the SCT. The first step involved registration between the PAM50 template and an anatomical image of all the individual subjects. This was followed by a second registration between the template (in anatomical space) and the diffusion-weighted data of the same subjects. At the end of this process, the PAM50 atlas, which contains the various WM tracts, was registered to our own subject-specific diffusion-weighted data. The following steps describe the registration process in detail:

1. Segmentation of spinal cord: The structural image and diffusion-weighted data of the cervical spine of all subjects were initially segmented using the *sct_propseg*⁹ module. The goal of this step was to extract a binary mask of the segmented spinal cord. Manual corrections were made on the images if the segmentation at certain locations was not satisfactory.
2. Labeling the anatomical image: In this step, the segmented structural images obtained from the previous step were labeled using the *sct_label_vertebrae*¹⁰ module. This step generated segmented cord labeled with vertebral levels.
3. Identifying vertebral levels along the cervical cord: Two vertebral levels (C3 and T1) were identified on the anatomical image using the *sct_label_utils* module. The main purpose of this step was to enable more accurate registration between the pediatric anatomical image and the PAM50 template by providing 2 reference voxels, one at the C3 level and a second one at the T1 level (orange arrows pointing to the corresponding intervertebral discs shown in Fig 1).
4. Next, each subject's individual T2-weighted image was registered to the PAM50 template using the *sct_register_to_template* module. This process includes straightening of the spinal cord and application of local deformations using a multistep nonlinear registration constrained in the axial plane and regularized in the z-direction. A T2 template in the anatomic space (*template2anat*) and the corresponding warping field (*warp_template2anat*) were generated as the output of this step.
5. A second registration was then performed to register (*template2anat*); the image from the previous step to each subject's diffusion data using the *sct_register_multimodal* module. A template image in each individual's diffusion native space (*template2diff*) as well as the corresponding warping field (*warp_anat2diff*) were generated as the output of this step.
6. Concatenation of deformation fields: The warping fields from the last 2 steps of registrations were concatenated to create a single global transformation between the template and diffusion data (*warp_template2diff*).
7. Obtaining the WM atlas: Finally, the global warping field was used to warp the PAM50 template objects (ie, WM atlas) to the diffusion data.

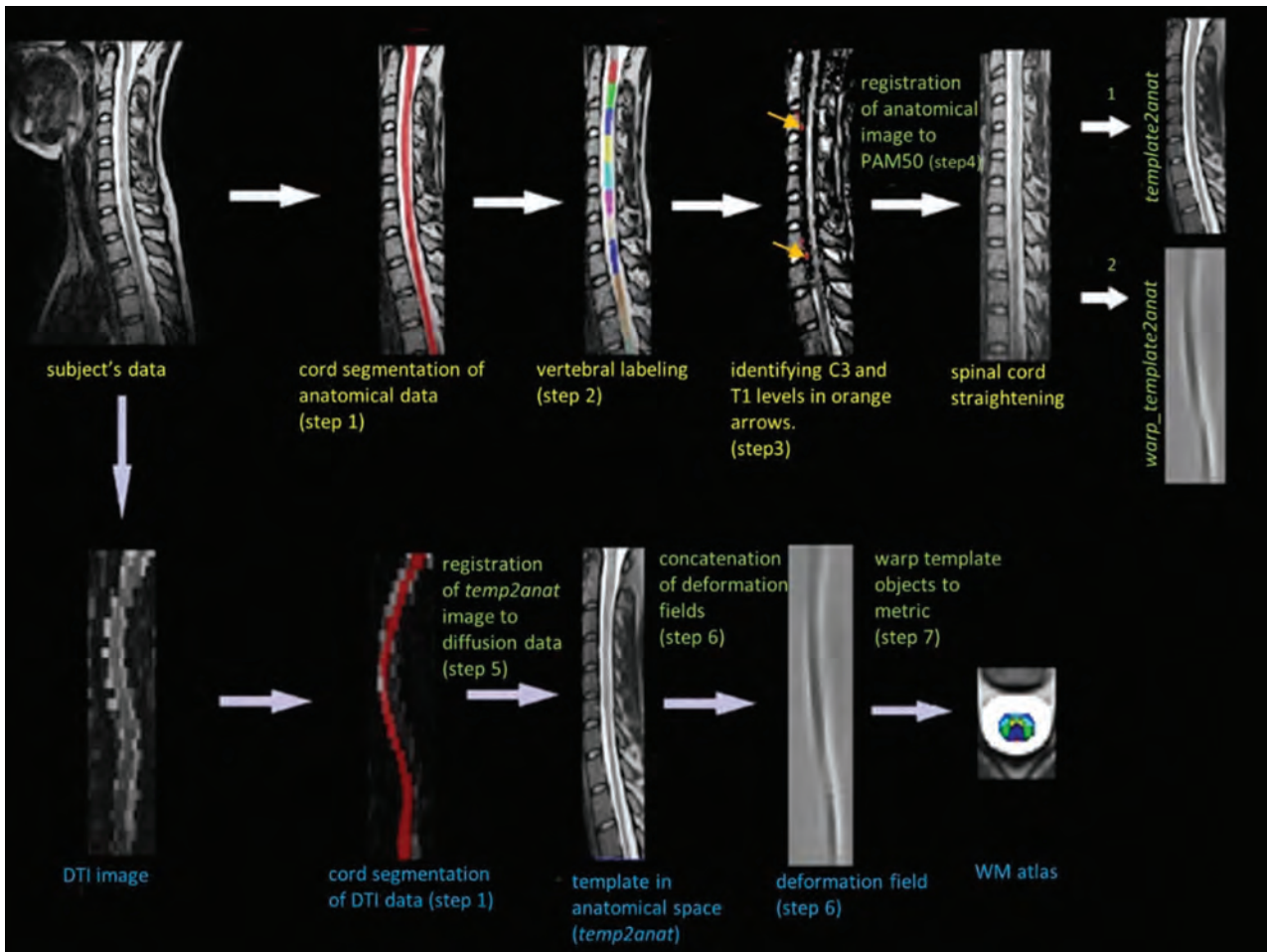


FIG 1. Overview of the template registration pipeline. Initially, T2-weighted scans are registered to the template (*upper row*). Diffusion-weighted data acquired during the same scan session are then registered to the anatomic data, and PAM50 objects are warped to diffusion data (*lower row*) to generate the pediatric WM spinal cord atlas.

Quantifying DTI Metrics Using the Atlas

After successful registration was verified visually for each individual subject, DTI metrics were extracted (*sct_extract_metric*) for each subject at the C3 level using a weighted-average method.¹¹ This step resulted in quantifying DTI metrics of fractional anisotropy (FA), mean diffusivity (MD), axial diffusivity (AD), and radial diffusivity (RD) for 34 extracted WM labels from the PAM50 template. Of the 34 labels, 30 represent individual sensory and motor WM tracts, 3 represent combined labels of the dorsal funiculi (DF), lateral funiculi (LF), and ventral funiculi (VF), and 1 label was assigned to represent the entire WM itself. The normative values were obtained by averaging all these measurements across all 30 subjects. The full names of labels are provided in the Online Supplemental Data.

Statistical Analysis

GraphPad Prism software 8.0 (GraphPad Software), a DOS-based scientific graphing application, was used for statistical analysis of the data. For ease of visualization, DTI normative measurements of all the 34 labels were plotted using violin plots. One-way ANOVA was used to study the laterality (left/right), functionality

(motor/sensory), and age-related changes among all the tracts. Linear regression analysis was used to compare age-related changes of DF, LF, and VF labels using DTI metrics. For the age-related analysis, the subject population was divided into 2 age groups: one group of younger children from 7–11 years of age and the older group from 12–16 years of age. The age groups were defined on the basis of a previous pediatric study.⁵ Throughout the study, a *P* value of .05 was used to determine the statistical significance.

RESULTS

Delineated WM Tracts

Figure 2A depicts a WM atlas of the human spinal cord. Figure 2B illustrates a subset of tracts overlaid on a *b=0* image at the C3 level in a representative subject from this study. The labeled WM tracts in this figure are explained in the figure legend. Figure 2C shows a sagittal T2-weighted cross-section of the spinal cord marked at the C3 level.

Normative Values

The developed automated WM pipeline was successful in extracting DTI values from all the various tracts across all 30 subjects

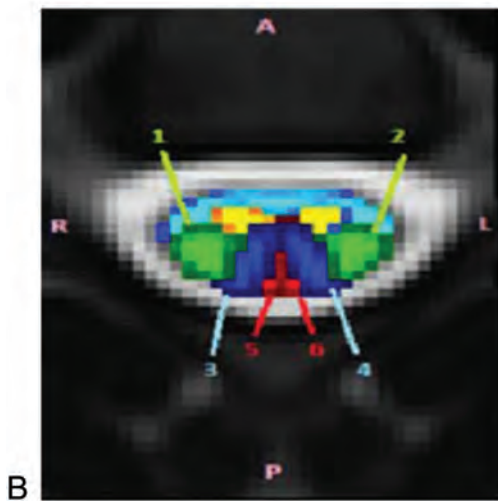
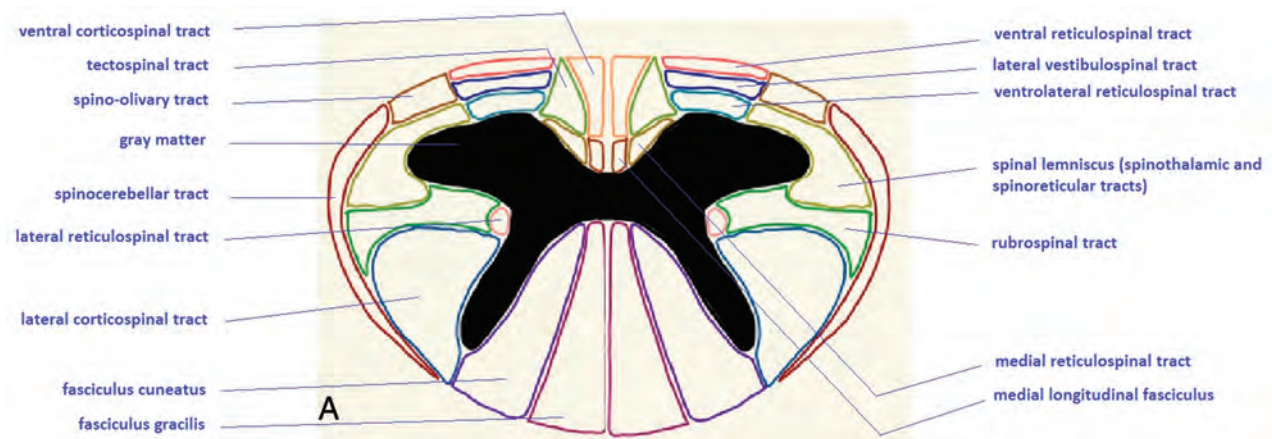


FIG 2. Spinal cord WM atlas. *A*, An atlas of spinal white matter tracts. *B*, Generated white matter atlas of the pediatric spinal cord overlaid on a b_0 image. The selected tracts are labeled with multiple colors: 1) right lateral corticospinal tract, 2) left lateral corticospinal tract, 3) right fasciculus cuneatus, 4) left fasciculus cuneatus, 5) right fasciculus gracilis, 6) left fasciculus gracilis, yellow: gray matter, light blue; unlabeled white matter. *C*, The C3 level is marked green on the sagittal T2-weighted scan.

(Fig 3). The violin plots were subdivided into the dorsal, lateral, and ventral funiculi as well as combined tracts (WM, DF, LF, and VF). The FA in the dorsal column tracts ranged from 0.61 to 0.62 with the mean 0.62 (SD, 0.09). The corresponding values for lateral and ventral columns were 0.47 (SD, 0.12) and 0.28 (SD, 0.12), respectively.

FA, MD, and RD showed a higher level of dispersion in all the tracts, including dorsal, lateral, and ventral tracts compared with AD. The coefficient of variation (CV) of the measurements in FA ranged from 14.62% in the dorsal column to 45.74% in ventral tracts. Similar measurements in MD were observed (23.75% to 34.06% from the dorsal-to-ventral tracts and in RD from 33.43% to 40.90%, respectively). AD showed less variability across all the tracts, with a CV of 22% in the dorsal columns to 26% in the ventral tracts. As observed, ventral funiculi regions present larger variations compared with other WM regions. WM measurements from “combined tracts” had the lowest variation in FA, with a CV of 18.6%, followed by the second lowest in AD (CV = 20.11%). The VF had higher variation in all the metrics, with the average CV of 33% compared with its counterparts DF and LF (CV_(DF) = 22%, CV_(LF) = 25%).

The Table compares the diffusion indices obtained for 6 selected tracts shown in Fig 2B. From all the tracts in the Table, the left fasciculus gracilis shows the highest FA of 0.66 averaged among all 30 subjects with the lowest variation (CV = 14.02%). FA was the lowest in the right lateral corticospinal tract with a higher CV of 18.26%.

Effects of Laterality, Functionality, and Age

Results of ANOVA using FA, MD, RD, and AD showed no significant difference ($P > .05$) between a total of 15 left and 15 right tracts. However, when tested for functionality (i.e., whether a tract is sensory or motor), FA and MD showed a significant difference ($P_{FA} = 3.7E^{-5}$, $P_{MD} = .043$), but AD and RD showed no effect.

Examining the effect of age with each single individual tract as well as combined tracts revealed significant differences among the maturation of some tracts and age. Among all 34 selected tracts studied, only the left spinal lemniscus (spinothalamic and spinoreticular tracts) showed an effect with age using MD, RD, and AD ($P < .05$). Additionally, linear regression analysis showed a positive correlation between FA and age as shown in Fig 4A, while MD, RD, and AD (Fig 4B–D) showed a negative correlation

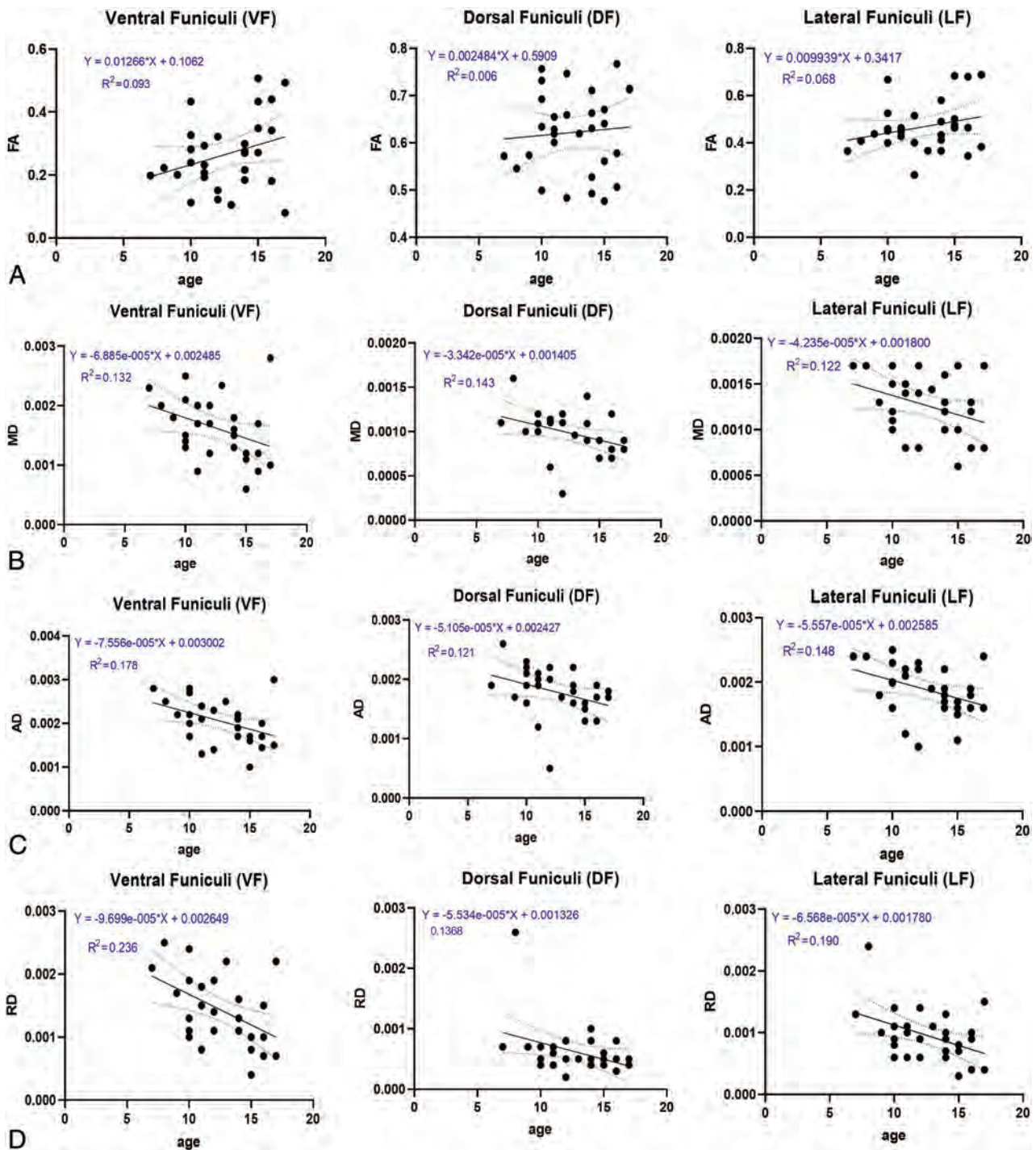


FIG 4. Linear regression plots showing the relationship between age and FA (A), MD (B), AD (C), and RD (D) in the ventral, lateral, and dorsal funiculi. *Solid lines* indicate the age-related trend, and *dashed lines* indicate 95% confidence intervals.

DTI Metrics Quantification of the Spinal Cord

In this work, we obtained normative values of diffusion data at the C3 vertebral level for ventral, dorsal, and lateral spinal cord funiculi as well as a specific subset of WM tracts in the healthy pediatric population. We believe that these values could be useful when comparing healthy and patient populations.¹⁶

Considering the various known spinal cord complications, study of spinal cord WM and characterizing its microstructure

noninvasively will help in accurate understanding and diagnosis of disease and pathologies.

Injury to the spinal cord due to traumatic or nontraumatic events and subsequently to white matter tracts in general leads to specific dysfunction and various clinical disabilities. Therefore, identifying the various specialized types of the WM pathways in the cord that may have been damaged is crucial in helping the prognosis of functional recovery and disease management.

Note that our analysis focused only on a single spinal cord level (C3 vertebral level) due to the better performance of proposed segmentation and registration algorithms with lower inter-rater variability reported by Prados et al.¹⁷ Also, as shown by Losseff et al,¹⁸ C2/C3 level results are the most reproducible values when studying spinal cord atrophy. In addition, the work of Stevenson et al¹⁹ suggests that the measurement variability that occurs using other spinal levels could be eliminated by focusing the analysis on the C2/C3 intervertebral disc. This possibility is due to the excellent contrast of the cord and CSF at the C3 level (i.e., a capacious CSF pool).

When we investigated the function of age and DTI indices, our observed age-related trend of DTI indices matches that of other spinal cord studies.⁵ However, the lack of a statistical significance effect with a decrease in AD observed in the dorsal columns suggests that the proportion of larger-sized axons increases with the child's growth.⁴

In comparing the DTI metrics of the funiculi with age, we found no significant difference between FA values of the LF, DF, and VF. However, MD, RD, and AD values of the VF showed a significant effect with age-related changes. These differences could reflect the variability of the axon diameter among these funiculi²⁰ containing different kinds of tracts. Despite the lack of a significant effect observed between the FA and age, the correlation of age with FA specifically and other DTI-derived indices generally was consistent with that in former studies.^{5,21}

While examining the effect of age on each individual tract in this study, we observed that there is a relationship of diffusivity metrics and maturation of some tracts (i.e., the spinothalamic tract). This could be because of the myelination process in different tracts. Myelination constitutes the last stage in the development of WM, which begins in utero in the second trimester of pregnancy and continues up to the end of adolescence.²² There are several factors that affect the rate of myelination, including the type of fiber, where faster rates are observed in sensory compared with motor tracts.²³ We believe that this could justify the significant effect of spinothalamic tract (a somatosensory tract) maturation in DTI indices in our study.

We also showed that there is no significant difference in the laterality (left/right) of the tracts. These findings suggest structural similarity between the left- and right-sided tracts. In a study by Duval et al,²⁴ the authors have shown similar average axon diameters in identical tracts from the left and right sides of the spinal cord. Although there was no significant difference in the laterality of the tracts, ANOVA showed a significant difference between sensory (i.e., fasciculus gracilis, fasciculus cuneatus) and motor (i.e., corticospinal tract) pathways. We believe that this finding is related to the microstructural organization of the sensory and motor WM tracts. The anatomic variation of axon diameter is noticeable; whereas the dorsal column fasciculus gracilis contains mainly small-diameter axons, the corticospinal tract in the lateral and ventral columns contains a combination of large- and small-diameter axons.²⁵ Another anatomic variation to consider is the fiber density variation along the entire length of the spinal cord, especially at the exit points of the brachial and lumbosacral plexuses.¹² In a study by Ohnishi et al,²⁶ the authors reported a decrease in the number of myelinated fibers of the

fasciculus gracilis in humans between C3 and T5. Terao et al²⁷ also reported an association of axonal diameter variation at the vertebral level in the human lateral corticospinal tract. These observations are in accordance with previous histology work²⁸ in humans, emphasizing the importance of broader studies of histologic validation in the ex vivo human spinal cord.

Limitations

Due to the diffusion data, SNR limitations, lack of anatomical landmarks, and the smaller size of the cord in children, there could be higher intrasubject variability resulting from spatial misalignment during registration of diffusion data to structural scans. This limitation emphasizes the need for tools that provide robust preprocessing, normalization, and motion correction for spinal cord diffusion data. Another limitation stems from the intrinsic variability of spinal cord diffusion imaging, which induces inaccuracies in metrics quantification. This issue, along with the selected registration algorithms method of metric extraction and partial volume effects, contributes to intersubject variability, particularly with a smaller cord size. An additional limitation is the small number of subjects as well as the narrow age range of our population as opposed to other pediatric diffusion studies.⁴ All of the aforementioned limitations could be contributing factors to observed discrepancies in our results compared with other similar studies.

CONCLUSIONS

We demonstrated the feasibility of a fully automated WM tract extraction in the pediatric spinal cord. We also established normative values for DTI-derived indices, looking at specific WM regions of the cord. These results show that the presented values are microstructure-sensitive and evolve in the pediatric spinal cord during development. This finding warrants future work with spinal cord patients (i.e., spinal cord injury) as well as an examination of DTI-derived metrics in the entire cord compared with a single C3 section.

Disclosures: Laura Krisa—RELATED: Grant: National Institutes of Health.*
*Money paid to the institution.

REFERENCES

1. Basser PJ. **Inferring microstructural features and the physiological state of tissues from diffusion-weighted images.** *NMR Biomed* 1995;8:333–44 CrossRef Medline
2. Rossi C, Boss A, Steidle G, et al. **Water diffusion anisotropy in white and gray matter of the human spinal cord.** *J Magn Reson Imaging* 2008;27:476–82 CrossRef Medline
3. Wheeler-Kingshott CA, Hickman SJ, Parker GJ, et al. **Investigating cervical spinal cord structure using axial diffusion tensor imaging.** *Neuroimage* 2002;16:93–102 CrossRef Medline
4. Reynolds BB, By S, Weinberg QR, et al. **Quantification of DTI in the pediatric spinal cord: application to clinical evaluation in a healthy patient population.** *AJNR Am J Neuroradiol* 2019;40:1236–41 CrossRef Medline
5. Saksena S, Middleton DM, Krisa L, et al. **Diffusion tensor imaging of the normal cervical and thoracic pediatric spinal cord.** *AJNR Am J Neuroradiol* 2016;37:2150–57 CrossRef Medline
6. De Leener B, Fonov VS, Collins DL, et al. **PAM50: unbiased multimodal template of the brainstem and spinal cord aligned with the ICBM152 space.** *Neuroimage* 2018;165:170–79 CrossRef Medline

7. Finsterbusch J. **Improving the performance of diffusion-weighted inner field-of-view echo-planar imaging based on 2D-selective radiofrequency excitations by tilting the excitation plane.** *J Magn Reson Imaging* 2012;35:984–92 CrossRef Medline
8. De Leener B, Lévy S, Dupont SM, et al. **SCT: Spinal Cord Toolbox, an open-source software for processing spinal cord MRI data.** *Neuroimage* 2017;145:24–43 CrossRef Medline
9. De Leener B, Kadoury S, Cohen-Adad J. **Robust, accurate and fast automatic segmentation of the spinal cord.** *Neuroimage* 2014;98:528–36 CrossRef Medline
10. Ullmann E, Pelletier Paquette JF, Thong WE, et al. **Automatic labeling of vertebral levels using a robust template-based approach.** *Int J Biomed Imaging* 2014;2014:719520 CrossRef Medline
11. Lévy S, Benhamou M, Naaman C, et al. **White matter atlas of the human spinal cord with estimation of partial volume effect.** *Neuroimage* 2015;119:262–71 CrossRef Medline
12. Standring S. *Gray's Anatomy: The Anatomical Basis of Clinical Practice.* 40th ed. Elsevier Churchill Livingstone; 2008
13. Fradet L, Arnoux PJ, Ranjeva JP, et al. **Morphometrics of the entire human spinal cord and spinal canal measured from in vivo high-resolution anatomical magnetic resonance imaging.** *Spine (Phila Pa 1976)* 2014;39:E262–69 CrossRef Medline
14. Tustison NJ, Avants BB. **Explicit B-spline regularization in diffeomorphic image registration.** *Front Neuroinform* 2013;7:39 CrossRef Medline
15. Cohen-Adad J, Descoteaux M, Rossignol S, et al. **Detection of multiple pathways in the spinal cord using q-ball imaging.** *Neuroimage* 2008;42:739–49 CrossRef Medline
16. By S, Xu J, Box BA, et al. **Application and evaluation of NODDI in the cervical spinal cord of multiple sclerosis patients.** *Neuroimage Clin* 2017;15:333–42 CrossRef Medline
17. Prados F, Cardoso MJ, Yiannakas MC, et al. **Fully automated grey and white matter spinal cord segmentation.** *Sci Rep* 2016;6:36151 CrossRef Medline
18. Losseff NA, Webb SL, O'Riordan JI, et al. **Spinal cord atrophy and disability in multiple sclerosis. a new reproducible and sensitive MRI method with potential to monitor disease progression.** *Brain* 1996;119(Pt 3):701–08 CrossRef Medline
19. Stevenson VL, Leary SM, Losseff NA, et al. **Spinal cord atrophy and disability in MS: a longitudinal study.** *Neurology* 1998;51:234–38 CrossRef Medline
20. Assaf Y, Blumenfeld-Katzir T, Yovel Y, et al. **AxCaliber: a method for measuring axon diameter distribution from diffusion MRI.** *Magn Reson Med* 2008;59:1347–54 CrossRef Medline
21. Alizadeh M, Fisher J, Saksena S, et al. **Age-related diffusion and tractography changes in typically developing pediatric cervical and thoracic spinal cord.** *Neuroimage Clin* 2018;18:784–92 CrossRef Medline
22. Brody BA, Kinney HC, Kloman AS, et al. **Sequence of central nervous system myelination in human infancy, I: an autopsy study of myelination.** *J Neuropathol Exp Neurol* 1987;46:283–301 CrossRef Medline
23. Coll G, de Schlichting E, Sakka L, et al. **Assessment of maturational changes in white matter anisotropy and volume in children: a DTI study.** *AJNR Am J Neuroradiol* 2020;41:1726–32 CrossRef Medline
24. Duval T, McNab JA, Setsompop K, et al. **In vivo mapping of human spinal cord microstructure at 300mT/m.** *Neuroimage* 2015;118:494–507 CrossRef Medline
25. Saliani A, Perraud B, Duval T, et al. **Axon and myelin morphology in animal and human spinal cord.** *Front Neuroanat* 2017;11:129 CrossRef Medline
26. Ohnishi A, O'Brien PC, Okazaki H, et al. **Morphometry of myelinated fibers of fasciculus gracilis of man.** *J Neurol Sci* 1976;27:163–72 CrossRef Medline
27. Terao S, Sobue G, Hashizume Y, et al. **Age-related changes of the myelinated fibers in the human corticospinal tract: a quantitative analysis.** *Acta Neuropathol* 1994;88:137–42 CrossRef Medline
28. Nieuwenhuys R, Voogd J, van Huijzen C. *The Human Central Nervous System: A Synopsis and Atlas.* 4th ed. Springer; 2007

Cervical Spinal Cord Degeneration in Spinocerebellar Ataxia Type 7

C.R. Hernandez-Castillo, R. Diaz, T.J.R. Rezende, I. Adanyeguh, I.H. Harding, F. Mochel, and J. Fernandez-Ruiz



ABSTRACT

BACKGROUND AND PURPOSE: Spinocerebellar ataxia type 7 is an autosomal dominant neurodegenerative disease caused by a cytosine-adenine-guanine (CAG) repeat expansion. Clinically, spinocerebellar ataxia type 7 is characterized by progressive cerebellar ataxia, pyramidal signs, and macular degeneration. In vivo MR imaging studies have shown extensive gray matter degeneration in the cerebellum and, to a lesser extent, in a range of cortical cerebral areas. The purpose of this study was to evaluate the impact of the disease in the spinal cord and its relationship with the patient's impairment.

MATERIALS AND METHODS: Using a semiautomated procedure applied to MR imaging data, we analyzed spinal cord area and eccentricity in a cohort of 48 patients with spinocerebellar ataxia type 7 and compared them with matched healthy controls. The motor impairment in the patient group was evaluated using the Scale for Assessment and Rating of Ataxia.

RESULTS: Our analysis showed a significantly smaller cord area ($t = 9.04$, $P < .001$, $d = 1.31$) and greater eccentricity ($t = -2.25$, $P = .02$, $d = 0.32$) in the patient group. Similarly, smaller cord area was significantly correlated with a greater Scale for Assessment and Rating of Ataxia score ($r = -0.44$, $P = .001$). A multiple regression model showed that the spinal cord area was strongly associated with longer CAG repetition expansions ($P = .002$) and greater disease duration ($P = .020$).

CONCLUSIONS: Our findings indicate that cervical spinal cord changes are progressive and clinically relevant features of spinocerebellar ataxia type 7, and future investigation of these measures as candidate biomarkers is warranted.

ABBREVIATIONS: CAG = cytosine-adenine-guanine; SARA = Scale for Assessment and Rating of Ataxia; SCA7 = spinocerebellar ataxia type 7

Spinocerebellar ataxia type 7 (SCA7) is a neurodegenerative disease characterized by cerebellar ataxia, pyramidal signs, and retinal dystrophy.¹ SCA7 is caused by the expansion of a cytosine-adenine-guanine (CAG) repeat that lies in the coding region of in the *ATXN7* gene on chromosome 3p12-13.² Patients

with SCA7 may eventually develop other neurologic deficits, including loss of manual dexterity, dysarthria, dysphagia, and eye-movement abnormalities.¹

Olivopontocerebellar atrophy associated with SCA7 has been documented in different neuropathologic studies using both postmortem and in vivo imaging techniques. These techniques have identified severe gray matter degeneration in a broad range of cerebellar and cerebral regions, including the cerebellar cortex, the inferior olivary complex tracts, the subthalamic nucleus, the pallidum, and the substantia nigra.³ Similarly, MR imaging studies in SCA7 reported extensive cerebellar degeneration and, to a lesser extent, in cortical cerebral regions such as the pre-/post-central gyri, cuneus, precuneus, inferior occipital gyrus, insula, and inferior frontal gyrus.⁴⁻⁶ However, studies of the central nervous system to date in SCA7 have focused primarily on brain changes, overlooking the possible involvement of spinal cord degeneration on the motor deficits caused by the disease. A number of reports in other ataxias have shown a strong association between spinal cord and the motor deficits that the patients develop, including Friedreich ataxia,⁷ SCA1,⁸ and SCA3.⁹

Received February 5, 2021; accepted after revision April 12.

From the Faculty of Computer Science (C.R.H.-C.), Dalhousie University, Halifax, Nova Scotia, Canada; Physiology Department, Faculty of Medicine (R.D., J.F.-R.), Universidad Nacional Autónoma de México, Ciudad de México, Mexico; Department of Neurology and Neuroimaging Laboratory (T.J.R.R.), School of Medical Sciences, University of Campinas, São Paulo, Brazil; Institut national de la santé et de la recherche médicale, Centre national de la recherche scientifique, Sorbonne Universités, Paris Brain Institute, Paris, France; Department of Neuroscience (I.H.), Central Clinical School, Monash University, Melbourne, Australia; and Department of Genetics (F.M.), Assistance Publique-Hôpitaux de Paris, Pitié-Salpêtrière University Hospital, Paris, France.

This work was supported by Consejo Nacional de Ciencia y Tecnología grant No. A1-S-10669 and Programa de Apoyo a Proyectos de Investigación e Innovación Tecnológica - Universidad Nacional Autónoma de México grant No. IN220019 to Juan Fernandez-Ruiz.

Please address correspondence to Juan Fernandez-Ruiz, MD, PhD, Departamento de Fisiología, Facultad de Medicina, Universidad Nacional Autónoma de México, Av. Universidad 3000, A.P. 70-250, C.P. 04510, CDMX, Mexico; e-mail: jfr@unam.mx



Indicates article with online supplemental data.

<http://dx.doi.org/10.3174/ajnr.A7202>

Table 1: Demographics and descriptive statistics

	SCA7 (n = 48)	Healthy Controls (n = 48)	P Value
Age (mean) (yr)	40.02 (SD, 14.1)	42.31 (SD, 13.61)	.452
Sex (M/F)	26:22	26:22	1.000
Disease duration (mean) (yr)	9.52 (SD, 6.3)	NA	NA
Spinal cord area (mean) (mm ²)	49.45 (SD, 7.7)	63.39 (SD, 7.2)	<.001
Spinal cord eccentricity (mean)	0.75 (SD, 0.07)	0.72 (SD, 0.05)	.026
CAG (mean)	46.72 (SD, 6.1)	NA	NA
SARA (mean)	14.79 (SD, 8.6)	NA	NA

Note:—NA indicates not applicable.

Here, using structural MR images that cover the brain and upper spinal cord, collected using standard clinical protocols, we systematically measured in vivo spinal cord degeneration in a large cohort of patients with SCA7 and matched healthy controls from Mexico and France. We aimed to investigate the hypothesis that SCA7 is associated with decreased cervical spinal cord area and increased spinal cord eccentricity (flattening) and that these measures are associated with ataxia severity. Our results will show the potential use of spinal cord morphology as an MR imaging biomarker for SCA7 progression.

MATERIALS AND METHODS

Subjects

The data set used in this study was previously reported in separate studies for both the Universidad Nacional Autonoma de Mexico and the Pitié-Salpêtrière University Hospital.^{6,10,11} The final sample (48 patients) included 38 patients from Mexico and 10 patients from France. For each site, age- and sex-matched healthy volunteers were invited to participate as a control group. General demographics can be found in Table 1. All participants gave their informed consent before entering the study, and all the procedures in this study were conducted in accordance with the international standards dictated by the Helsinki Declaration of 1964. Additionally, all the procedures were performed in accordance with the ethical standards of the committees on human experimentation of the Universidad Nacional Autonoma de Mexico and by the Comité de Protection des Personnes-Ile de France Paris VI, respectively.

Clinical Assessment

We used the Scale for the Assessment and Rating of Ataxia (SARA) to measure the motor impairment in the patient group. The clinical evaluation was performed either the day of the scanning or within a week from the scanning session. The SARA score comprises 8 items, including tests of gait, stance, sitting, and speech, as well as the finger-chase test, finger-to-nose test, rapid alternating movements, and heel-to-shin test.¹² The score ranges from 0 to 40, with a higher score indicating a greater impairment.

Image Acquisition

Images from the Mexican subset were acquired using a 3T Achieva MR imaging scanner (Phillips Healthcare) and a 32-

channel head coil. The anatomic sequence consisted of a 3D T1 fast-field echo sequence, with a TR/TE = 8/3.7 ms, FOV = 256 × 256 mm, and reconstruction matrix = 256 × 256, resulting in an isometric resolution of 1 mm. The images from the French subset were acquired using a 3T Magnetom Trio scanner (Siemens) and a standard transmit body coil (Siemens) and a 32-channel receive head coil array. The anatomic sequence consisted of a 3D MPRAGE volumetric image with TR = 2530 ms, TE = 3.65 ms, TI = 900 ms, flip angle = 9°, and FOV = 256 × 256 mm, resulting in an isometric resolution of 1 mm.

Spinal Cord Measurement

All the image analyses were implemented in Matlab R2020b (MathWorks). To minimize any systematic differences between scanners, we created a model using an independent set of MR imaging data of healthy subjects from both the Mexican (n = 20) and French (n = 20) sites. In this model, we assigned a different regressor per site. Then, we regressed out the respective site coefficients from the data used in this study before any processing. The spinal cord segmentation was then performed using the Spinal Cord Toolbox, Version 5.0.1 (SCT; www.spinalcordtoolbox.com)¹³ and the ENIGMA-Ataxia pipeline (<http://enigma.ini.usc.edu/ongoing/enigma-ataxia/>) for spinal cord analysis. In brief, the SCT provides a preprocessing platform to segment and normalize automatically the spinal cord into a template, correcting for variations in imaging angle and neck position. Then morphologic metrics of the normalized cross-sections of the spinal cord were obtained for statistical analysis.

On the basis of previous reports,^{8,9} we selected the base (lower limit) of the second and third cervical vertebrae, defined by the location of the relevant intravertebral discs, for further analysis. The selection of the cervical vertebrae in the normalized images required manual intervention. This step was performed by an expert using a graphic interface in which the base of the vertebra of interest was identified in the sagittal plane of the T1 image for each subject. We estimated the mean values of the cross-sectional area and eccentricity of the spinal cord from the analysis of 3 consecutive slices for each vertebra following a validated procedure.¹⁴ These 2 metrics provide different morphologic information—eg, the cross-sectional area can be used to evaluate the overall degeneration, while the eccentricity provides an approximation of the flattening of the cord section.

Statistical Analysis

Statistical tests were performed in Matlab R2020b. Normal distribution of the metrics was evaluated using the Kolmogorov-Smirnov test. We used a Student *t* test to identify significant group differences in the spinal cord area and eccentricity of each vertebra, and we report effect size using the Cohen *D*. Then to test the association between the SARA score and the morphologic metrics in the SCA7 group, we used the Pearson correlation. To control for the variable rate of decline in disease progression as

predicted by the CAG repeat length, we used a multiple regression model to evaluate the effects of CAG repetition expansion and disease duration on the morphology of the spinal cord. Finally, to further explore the association of the spinal cord area and the disease progression, we calculated the Pearson correlation between disease burden and the spinal cord area. The disease burden was calculated as the interaction between the CAG expansion and age. Then we split the patient group into early (<5 years from onset), middle (>5 and <10 years from onset), and late (>10 years from onset) stages, based on the distribution of our sample and to try to get similar group sizes for visualization.

RESULTS

Descriptive statistics of the patients and healthy volunteers can be found in Table 1. The spinal cord area in patients with SCA7 was significantly smaller than in the healthy volunteers (Fig 1) in both C2 ($t=9.04$, $P<.001$, $d=1.31$) and C3 ($t=8.96$, $P<.001$, $d=1.25$). The spinal cord eccentricity was only significantly different in C2 ($t=-2.25$, $P=.02$, $d=0.32$). Spinal cord segmentation of an exemplary subject of each group can be found in the Online Supplemental Data. We found a strong association between the cord area and the SARA score (Fig 2) in both C2

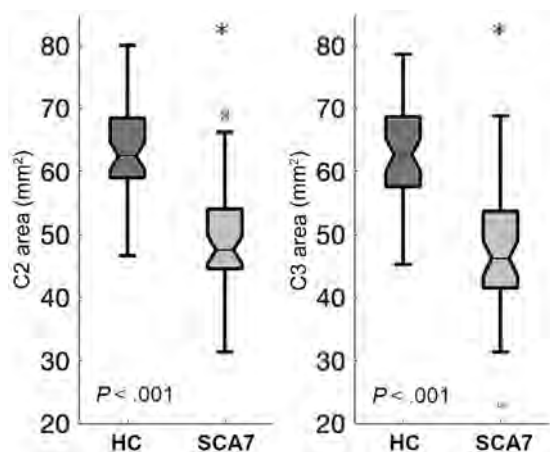


FIG 1. Spinal cord cross-sectional area in patients with SCA7 and healthy controls (HC). The asterisks indicate significant difference.

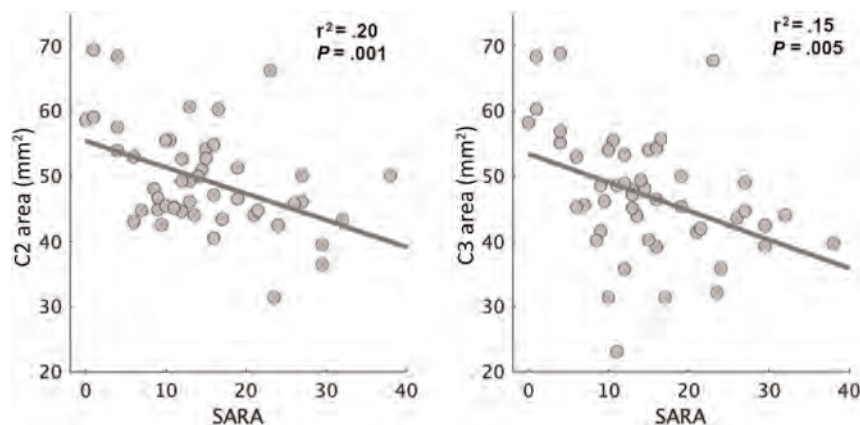


FIG 2. Association between the spinal cord cross-sectional area and the SARA score. Each dot represents 1 patient with SCA7

($r = -0.44$, $P = .001$) and C3 ($r = -0.39$, $P = .005$). We found no association between the cord eccentricity and the SARA score ($P = .896$). Finally, our multiple variable regression showed that the cord area was associated with CAG repetition expansion (coefficient = -1.09 , $P = .002$) and disease duration (coefficient = -3.72 , $P = .02$), while the cord eccentricity was not significantly associated with either of the 2 independent variables (Table 2). We found a strong negative correlation between disease burden and spinal cord area ($r = -0.41$, $P = .003$), suggesting that the spinal cord area is reduced during disease progression. This was more evident when we grouped the patients on the basis of the disease duration. Figure 3 shows that patients in the early stage have a significantly smaller area than the control group ($t = 2.88$, $P = .005$, $d = 0.66$) but a larger area than those in the middle and late stages ($t = 2.39$, $P = .02$, $d = 0.86$).

DISCUSSION

In this study, we report that cervical spinal cord degeneration is a robust feature of the manifestation of SCA7 and is significantly associated with disease severity and duration. These findings support the potential for readily quantifiable MR imaging measures of the spinal cord area to provide biomarkers that allow tracking of the degenerative process in SCA7. The methods used herein enable accurate measurement of the spinal cord using clinically standard brain MR imaging acquisitions. Our results provide the first in vivo corroboration of postmortem neuropathologic reports of spinal atrophy in SCA7¹⁵ and additionally reveal associations between spinal morphology and disease severity. Bang et al,⁴ in 2004, suggested that the degenerative process in SCA7 starts in the brainstem, even before the patients develop ataxia. Only when the cerebellar degeneration becomes prominent do patients develop motor impairment. Given the association between spinal cord atrophy and cerebellar dysfunction in our patient group, it is possible that spinal cord degeneration occurs parallel to cerebellar degeneration, affecting the communication between the cerebellum and motor neurons in the peripheral nervous system. Further investigation using other image modalities, such as diffusion MR imaging, and longitudinal data sets could provide evidence regarding the degenerative mechanism in SCA7 and other ataxias.

Our analysis also revealed differences with previous reports in other SCAs. For example, a strong association between the cord area and the CAG expansion was found in SCA1⁸ and SCA7, but not in SCA3.⁹ Similarly, different amounts of spinal cord flattening (assessed by the cord eccentricity) have been reported in those 3 subtypes.⁷⁻⁹ Flattening of the spinal cord generally reflects the targeted atrophy of ≥ 1 spinal tract (eg, ascending dorsal sensory tracts versus descending ventral motor tracts). The finding of robust reductions in total spinal cord area, along with more modest changes in eccentricity,

Table 2: Results of the multiple variable regression

Dependent Variable	r ² Model	Independent Variable	Regression Coefficient	P Value
Spinal cord area	0.27	CAG	-1.09	.002
		Disease duration	-3.72	.020
		CAG*DD	2.24	.029
Spinal cord eccentricity	0.07	CAG	1.64	.107
		Disease duration	1.24	.218
		CAG*DD	-1.36	.178

Note:—CAG*DD indicates CAG multiplied by disease duration.

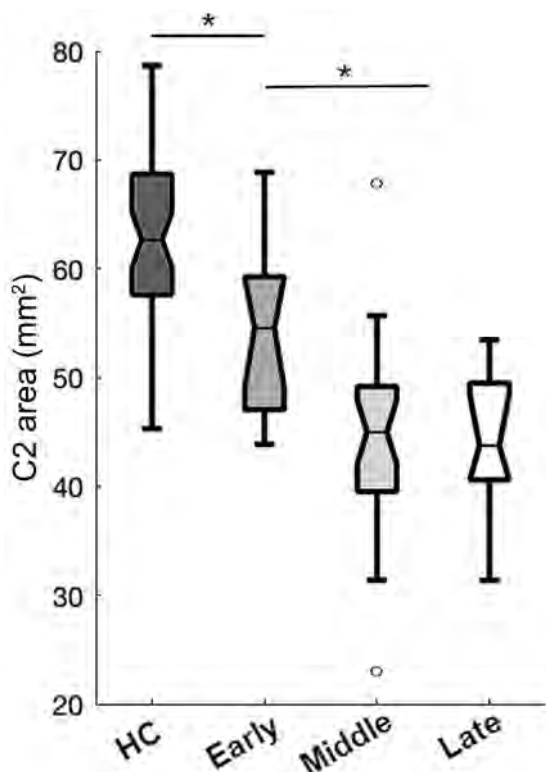


FIG 3. Spinal cord cross-sectional area for healthy controls (HC) and patients with SCA7 subdivided by disease burden (see Materials and Methods). The asterisks indicate significant difference.

may reflect a more generalized pattern of spinal atrophy. Such differences between different SCAs should be further explored on a larger scale to identify whether different areas of the spinal cord are susceptible to specific mutations, an effect that has been reported in the cerebellar cortex.¹⁰

A limitation of this study is that our current analysis is limited to a specific cross-sectional area (see Materials and Methods). For example, in our cohort, we found flattening in the cervical region around the second vertebra but no significant difference around the third vertebra, suggesting different degrees of morphologic changes across levels in the spinal cord. New analytic techniques that analyze the spinal cord in a voxelwise fashion could provide a more detailed mapping of spinal cord degeneration caused by

SCA7. Similarly, the use of other MR imaging modalities such as diffusion-weighted imaging can provide relevant information regarding the integrity of the fibers, a metric that could be more sensitive to the degenerative process. Although our data indicate a clear progressive degeneration, we cannot assess or rule out the potential contribution of developmental hypoplasia to the overall between-group differences. Furthermore, we correlated spine atrophy with the SARA score, which is widely used to assess disease severity in patients with spinocerebellar ataxia. However, the SARA score was not specifically designed to assess pyramidal dysfunction; hence, future studies of spinal degeneration can benefit from using clinical measures of pyramidal tract alterations and sensory deficits.

CONCLUSIONS

SCA7 is characterized by extensive spinal cord degeneration that is associated with the disease severity. The cervical cross-sectional area in the patients is highly related to CAG repetition expansion and disease duration. Hence, spinal cord morphometry provides a compelling candidate for use as a potential MR imaging biomarker of SCA7 progression.

Disclosures: Ian Harding—UNRELATED: Employment: Monash University, Comments: my employer as an academic scientist. Fanny Mochel—RELATED: Grant: Programme hospitalier de recherche clinique BIOSCA-ID RCB: 2010-A01324-35, AOM10094, NCT01470729.* Jaun Fernanex-Ruiz—RELATED: Grant: Consejo Nacional de Ciencia y Tecnología grant No. AI-5-10669 and Programa de Apoyo a Proyectos de Investigación e Innovación Tecnológica - Universidad Nacional Autónoma de México grant No. IN220019.* *Money paid to the institution.

REFERENCES

- Hugosson T, Gränse L, Ponjavic V, et al. **Macular dysfunction and morphology in spinocerebellar ataxia type 7 (SCA 7).** *Ophthalmic Genet* 2009;30:1–6 CrossRef Medline
- Garden GA, La Spada AR. **Molecular pathogenesis and cellular pathology of spinocerebellar ataxia type 7 neurodegeneration.** *Cerebellum* 2008;7:138–49 CrossRef Medline
- Martin JJ. Spinocerebellar ataxia type 7. In: Subramony SL, Dürr A, eds. *Handbook of Clinical Neurology*. Vol 103. Elsevier; 2012:475–91
- Bang OY, Lee PH, Kim SY, et al. **Pontine atrophy precedes cerebellar degeneration in spinocerebellar ataxia 7: MRI-based volumetric analysis.** *J Neurol Neurosurg Psychiatry* 2004;75:1452–56 CrossRef Medline
- Döhlinger S, Hauser TK, Borkert J, et al. **Magnetic resonance imaging in spinocerebellar ataxias.** *Cerebellum* 2008;7:204–14 CrossRef Medline
- Hernandez-Castillo CR, Galvez V, Diaz R, et al. **Specific cerebellar and cortical degeneration correlates with ataxia severity in spinocerebellar ataxia type 7.** *Brain Imaging Behav* 2016;10:252–57 CrossRef Medline
- Chevis CF, Da Silva CB, D’Abreu A, et al. **Spinal cord atrophy correlates with disability in Friedreich’s ataxia.** *Cerebellum* 2013;12:43–47 CrossRef Medline
- Martins CR, Martinez AR, de Rezende TJ, et al. **Spinal cord damage in spinocerebellar ataxia type 1.** *Cerebellum* 2017;16:792–96 CrossRef Medline
- Fahl CN, Branco LM, Bergo FP, et al. **Spinal cord damage in Machado-Joseph disease.** *Cerebellum* 2015;14:128–32 CrossRef Medline
- Hernandez-Castillo CR, King M, Diedrichsen J, et al. **Unique degeneration signatures in the cerebellar cortex for spinocerebellar ataxias 2, 3, and 7.** *Neuroimage Clin* 2018;20:931–38 CrossRef Medline

11. Adanyeguh IM, Perlberg V, Henry P-G, et al. **Autosomal dominant cerebellar ataxias: imaging biomarkers with high effect sizes.** *Neuroimage Clin* 2018;19:858–67 CrossRef Medline
12. Schmitz-Hübsch T, Du Montcel ST, Baliko L, et al. **Scale for the assessment and rating of ataxia: development of a new clinical scale.** *Neurology* 2006;66:1717–20 CrossRef Medline
13. De Leener B, Lévy S, Dupont SM, et al. **SCT: Spinal Cord Toolbox, an open-source software for processing spinal cord MRI data.** *Neuroimage* 2017;145:24–43 CrossRef Medline
14. Bergo FPG, França MC, Chevis CF, et al. **SpineSeg: a segmentation and measurement tool for evaluation of spinal cord atrophy.** In: *7th Iberian Conference on Information Systems and Technologies (CISTI 2012)*, Madrid, Spain, June 20-23, 2012:1–4
15. Martin JJ, Krols L, Ceuterick C, et al. **On an autosomal dominant form of retinal-cerebellar degeneration: an autopsy study of five patients in one family.** *Acta Neuropathol* 1994;88:277–86 CrossRef Medline

Celebrating 35 Years of the AJNR

September 1986 edition

MR of Hemorrhage: A New Approach

Robert R. Edelman¹
Keith Johnson²
Richard Buxton³
Gregory Shoukimas⁴
Bruce R. Rosen⁵
Kenneth R. Davis⁶
Thomas J. Brady^{1,4}

Using a modification of the partial saturation (PS) pulse sequence, we developed an MR method that permits the acquisition of highly T1- and T2-weighted images of the head and body in as little as 10 sec. The PS images, which were acquired at 0.6 T in a series of six patients with acute and subacute hemorrhage, showed a striking reduction in the signal intensity of hemorrhagic lesions. This effect, which is related to bulk magnetic susceptibility variations, was either minimal or absent on conventional T1- and T2-weighted spin-echo (SE) images. Our results suggest that high-field systems are not needed in order to image acute and subacute hemorrhage.

It has recently been proposed that hemorrhage can be uniquely characterized on high-field images on the basis of magnetic susceptibility variations within the lesion [1]. These effects were not identified on low-field images [2-3]. If hemorrhage could be accurately identified only with high-field systems, this would of course provide a significant clinical advantage to these systems. We have recently developed and implemented techniques for the rapid acquisition of T1- and T2-weighted images (Edelman RR, Radiology, submitted; Buxton R, J Comput Assist Tomogr, submitted). Using modifications of the partial saturation sequence, one can obtain these images in as little as 10 sec. It will be shown that, not only can one demonstrate magnetic susceptibility effects on intermediate field images, but that these images can be obtained in an order of magnitude faster than has previously been shown with high-field systems using conventional spin-echo techniques.

Subjects and Methods

Sixteen subjects were studied, including six patients with hemorrhagic lesions and 10 patients with nonhemorrhagic lesions by CT criteria. There were five patients with subacute hemorrhage: one patient with an angiographically occult arteriovenous malformation in the left zone; one patient with postpartum pituitary apoplexy imaged approximately 1 week postpartum; one patient with a 4-week-old right parietal hemorrhage, presumed secondary to an underlying tumor; one patient with a 4-week-old left occipital hemorrhage, also presumed secondary to underlying neoplasm; and one patient whose post-hypertensive cerebellum with an intraparenchymal hematoma resulting from a biopsy 4 weeks before the MRI study. There was one acute right parietal hematoma, imaged 15 hr from the ictus.

The 10 patients with nonhemorrhagic lesions included three patients with intraparenchymal metastases (colon and breast primaries); two patients with intraparenchymal cavernous hemangiomas; two patients with nonhemorrhagic intracranial aneurysms (brainstem, left middle cerebral artery territory); and three patients with nonhemorrhagic intracranial gliomas.

MR was performed on a Technicare 0.6 T superconducting system. Patients were imaged with a variety of T1- and T2-weighted spin-echo (SE) or composite inversion-recovery spin-echo (IR) pulse sequences. T1-weighted sequences included SE 300/14, SE 500/20, and IR 1500/450/20. T2-weighted sequences included multiecho SE 2000/60, 120, and SE 400/60, 120. Acquisition time for the SE and IR images ranged from 5-15 min.

Received May 1, 1986; accepted after revision May 13, 1986.

This work was supported in part by a grant from Technicare Corp., St. Louis, MO, and by NIH grants 1R01 CA 00645-04 and 1R01 CA 40363-01.

¹ Department of Radiology, Massachusetts General Hospital, 30 Fruit St., Boston, MA 02114. Address reprint requests to R. R. Edelman.

² Department of Neurology, Massachusetts General Hospital, Boston, MA 02114.

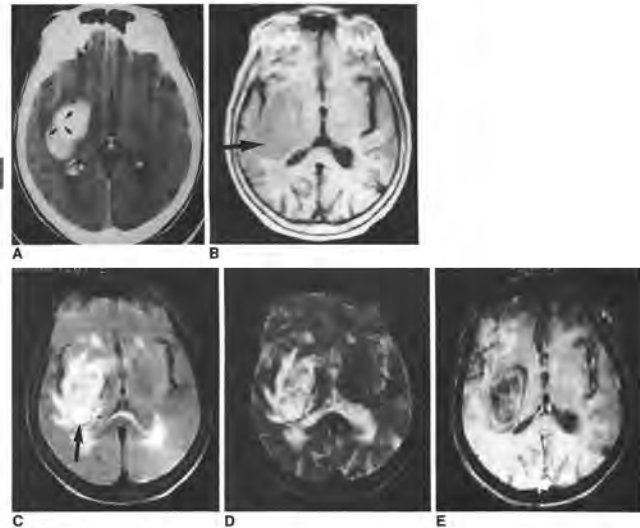
³ Department of Radiology, Physics, Massachusetts General Hospital, Boston, MA 02114.

⁴ Department of Radiology, Massachusetts General Hospital, Boston, MA 02114.

⁵ Department of Medicine, Massachusetts General Hospital, Boston, MA 02114.

Address reprint requests to R. R. Edelman.

© American Society of Neuroradiology



Gd-DTPA in Clinical MR of the Brain: 1. Intraaxial Lesions

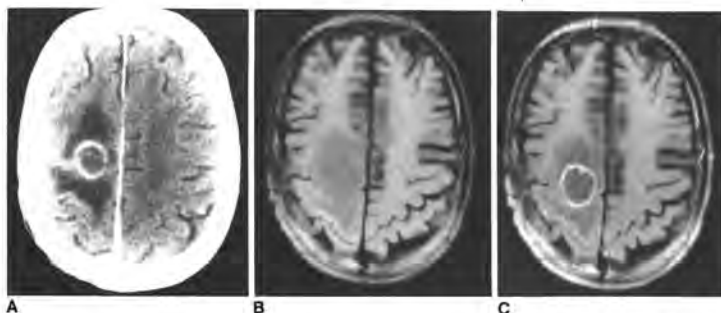
Michael Brant-Zawadzki¹
Isabelle Berry²
Lucy Ozolski³
Robert Brasschi³
Judith Murovic³
David Norman³

Over 35 intraaxial lesions in 15 patients suspected of having intracranial tumors were studied with MR before and after injection of Gadolinium-DTPA (Gd-DTPA). Diseases included primary and metastatic brain tumors, plaques of multiple sclerosis, scott arteriovenous malformations, lymphomas, toxoplasmosis, and pituitary adenomas. The precontrast T2-weighted sequence (SE 2000/30, 60) was found to be most sensitive in detecting intraaxial lesions, showing 17 lesions that were not seen on the post-Gd-DTPA T1-weighted sequence (SE 500/20). In one case of multiple sclerosis, several lesions seen on the pre-Gd-DTPA study on T2-weighted images faded after injection of Gd-DTPA (due to T2 shortening). In two patients with large metastatic foci, other small metastatic lesions were seen better after Gd-DTPA on both T1- and T2-weighted sequences. Four other patients with only one focal-enhancing lesion and one patient with multiple lesions on T1-weighted images actually had a much larger single glioma depicted on pre-Gd-DTPA T2-weighted images. In a patient with AIDS, a ring-enhancing lesion thought to be an abscess proved to be lymphoma. The cystic arteriovenous malformations enhanced but showed more characteristic findings, such as hemorrhage, on pre-Gd-DTPA studies. Our experience suggests that Gd-DTPA may not improve sensitivity of MR in the detection of intraaxial lesions. However, functional aspects of brain disease, such as the presence of perfusion of a lesion and active breach of the blood-brain barrier, are depicted well with Gd-DTPA and are vital for proper diagnosis in many instances.

Early limitations of MR included relatively long study times, suboptimal characterization of disease and its chronicity, perceived inability to separate tumor from edema, and, on occasion, suboptimal sensitivity. CT had similar problems in its early stages, with suboptimal sensitivity being the most unacceptable problem but the one most easily remedied through the use of preexisting iodinated contrast agents. The impact of such contrast agents on CT provided a historical precedent for the development of paramagnetic contrast agents. Gadolinium-DTPA (Gd-DTPA) was the first such substance to be tested for human use in European trials, with the brain and spinal cord as early targets [1-3]. Enthusiasm for this agent's utility is evident in these early trials. The first American clinical trials of Gd-DTPA have been completed and the initial results of tolerance, toxicity, and efficacy from the phase II multicenter trial have been reported [4]. This and the following article [5] elucidate the clinical experience with Gd-DTPA from a referral center for neurologic disease where MR had been used routinely by neurobiologists for 4 years prior to the introduction of this agent.

Subjects and Methods

Thirty patients at the University of California, San Francisco (UCSF), were involved in a multicenter clinical trial of Gd-DTPA under the guidelines of the Food and Drug Administration, the Human Research Committee at UCSF, and the commercial developer of the product (Boehringer Laboratories, New Jersey). Fully informed consent was obtained from every patient.



¹ Department of Neurosurgery, Hôpital Purpan, Toulouse, France.
² Department of Neurosurgery, University of California, San Francisco, CA 94143.
AJNR 7:781-788, September/October 1986
0195-6108/86/07781-07\$1.00
© American Society of Neuroradiology

CT-Guided Caudal Epidural Infiltrations: A Technical Note

Low back pain is a global health problem, and image-guided spinal injections are a major workload for interventional radiologists and neuroradiologists. Epidural injections are frequently performed for sciatica caused by disc herniations and spinal stenosis. There are 3 major access routes for epidural administration of medication: transforaminal, interlaminar, and caudal. In a study comparing these 3 techniques, similar efficacy was observed from each method.¹ This observation makes sense from an anatomic point of view, because the epidural space is a continuous space with an observable free spread of injected medication.² We usually prefer the intralaminar access for epidural injections in our department; however, there are cases when the intralaminar approach is not feasible, such as in patients who have had extensive spinal surgery, patients who have massive osteophytic changes, or when caudal sacral nerve roots should be infiltrated. In these cases, caudal epidural infiltrations are a possible alternative.

Because the previously described landmarked-based, blind technique in adults results in a high number of incorrect needle placements (more than 25% of cases), image guidance with fluoroscopy or sonography has been advocated.³ Interestingly, to the best of our knowledge, guidance with CT has not been described in the literature. CT guidance for caudal epidural infiltrations is easy to perform and offers the best anatomic overview of needle placement, as well as epidural contrast spread. It may be of value if fluoroscopy or sonography are either unavailable or the performing physician is unfamiliar with these imaging modalities. As with other spinal interventions, the usual precautions regarding anticoagulant treatment should be regarded. For a CT-guided caudal epidural infiltration, the patient is in the prone position. A short scan of the caudal sacral bone is performed. The access to the epidural space is at the sacral hiatus, which is formed by the sacral cornua. At this height, the sacral canal consists of epidural space only,

and the thecal sac ends more cranially.³ After sterile draping and subcutaneous local anesthesia, the puncture needle is placed under the sacrococcygeal ligament into the opening of the sacral channel. A small amount of contrast media is administered to ensure the right needle placement (Figure). After confirmation of the correct spread of the contrast media, the medication (usually a mixture of local anesthetics and a glucocorticoid) is injected. We use a mixture of 8 mL of mepivacaine and 2 mL of dexamethasone. After removal of the needle, the patient is observed for at least 45 minutes and should be discharged with intact motor function only.

Thus, caudal epidural infiltrations can be performed easily with CT guidance and offer an alternative access to the epidural space for the interventional radiologist performing spinal pain management.

REFERENCES

1. Manchikanti L, Singh V, Pampati V, et al. **Comparison of the efficacy of caudal, interlaminar, and transforaminal epidural injections in managing lumbar disc herniation: is one method superior to the other?** *Korean J Pain* 2015;28:11–21 CrossRef Medline
2. Paisley K, Jeffries J, Monroe M, et al. **Dispersal patterns of injectate after lumbar interlaminar epidural spinal injections evaluated with computerized tomography.** *Global Spine J* 2012;2:27–32 CrossRef Medline
3. Kao SC, Lin CS. **Caudal epidural blocks: an updated review of anatomy and techniques.** *Biomed Res Int* 2017;2017:1–5 CrossRef Medline

© J. Gossner

Department of Diagnostic and Interventional Radiology
Evangelisches Krankenhaus Göttingen-Weende
Göttingen, Germany

<http://dx.doi.org/10.3174/ajnr.A7178>

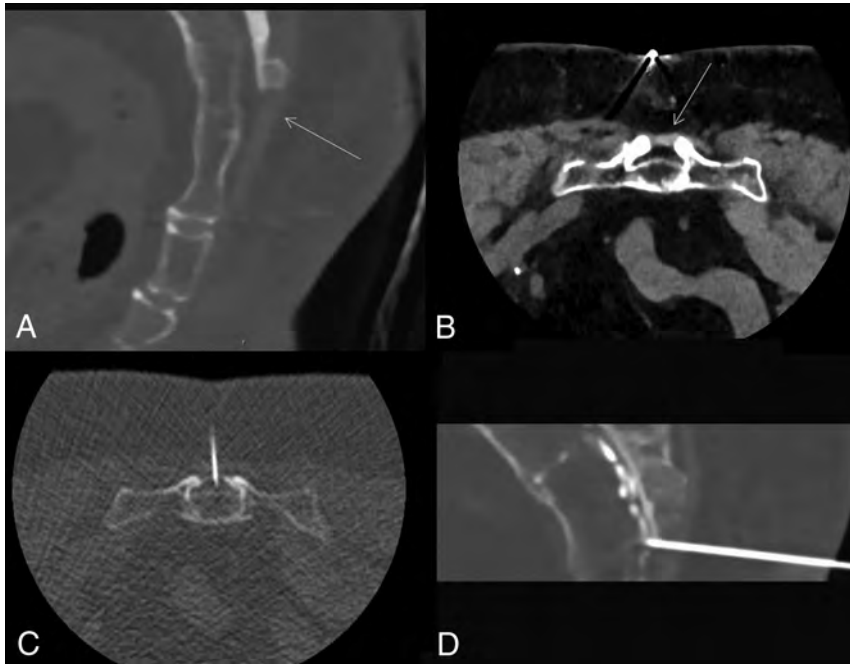


FIGURE. Images of a CT-guided caudal epidural infiltration. The anatomic landmarks of sacral hiatus are shown on sagittal (A) and axial (B) CT images. The needle is placed epidurally at the sacral hiatus (C). After the application of contrast media, the correct epidural spread can be observed (D).

More on Exploiting the T1 Shinethrough and T2* Effects Using Multiecho Susceptibility-Weighted Imaging

We appreciated the response by Fonseca et al¹ to our article “Tumefactive Primary Central Nervous System Vasculitis: Imaging Findings of a Rare and Underrecognized Neuroinflammatory Disease”² on the importance of the “T1 shinethrough effect” on gadolinium-enhanced SWI (Gd-SWI).³ Gd-SWI has been adopted in neuroimaging protocols for imaging of various CNS pathologies, such as primary brain tumor, brain metastasis, and demyelination.³ Although SWI is extremely sensitive to paramagnetic substances such as venous blood, microbleeds, and brain iron, its signal intensity is not only dependent on the T2* susceptibility effect but also the T1-relaxivity effect. When this predominates through the T2* and phase effects, the “T1 shinethrough” phenomenon occurs.³ Fonseca et al¹ emphasized acquiring Gd-SWI to exploit the T1-shinethrough effect, producing comparable imaging quality to post-gadolinium-enhanced T1WI (Gd-T1WI), which can show small enhancing intraparenchymal vessels in tumefactive primary CNS vasculitis.

We have been adopting the use of multiecho SWI sequences at our institution (Gold Coast University Hospital, Queensland, Australia) to further enhance the “T1 shinethrough” phenomenon by altering the scanning parameters. SWI data can be acquired as multiecho sequences.^{4,5} Fine-tuning the TE can modify the image contrast weighting. Recently, multiecho SWI has been studied to provide multiple contrasts for imaging of both arteries and veins from the first and second echoes, respectively.^{4,5} The first echo provides a time-of-flight inflow effect and some mild T1 weighting, even for intermediate flip angles near the Ernst angle of gray and white matter.^{4,5} Therefore, a shorter TE of 10 ms can favor T1 shinethrough while a longer TE of 20 ms produces a stronger T2* effect, as used in a conventional single-echo SWI (Figure). Dual-echo SWI does not require an increase in scan time as both echoes are acquired simultaneously, which eliminates motion artifacts or misregistration between different TE images.^{4,5} Multiple articles have promoted the use of fully flow-compensated dual-echo SWI in a rapid, multicontrast approach that can also be used to quantify spin density and T1, which also has the potential to evaluate local changes in T1 as the source of contrast.^{4,5}

<http://dx.doi.org/10.3174/ajnr.A7175>

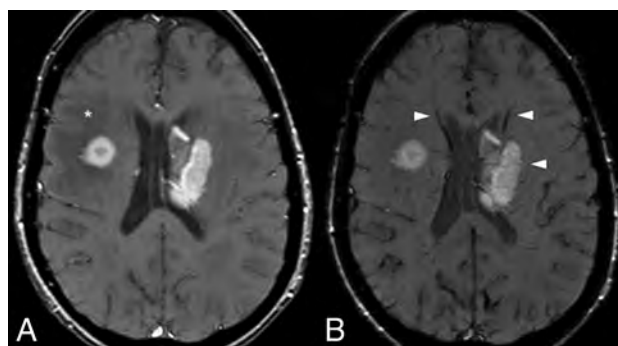


FIGURE. Dual-echo Gd-SWI of a 71-year-old man with primary CNS lymphoma showing periventricular enhancing masses. The shorter echo Gd-SWI (A) produced an image with greater T1-weighting demonstrating homogenous enhancement of the periventricular masses. The enhancing area has a signal-to-noise ratio of 108:1. Perilesional brain edema in the right centrum semiovale is also clearly depicted (*asterisks*). Conversely, the longer echo Gd-SWI (B) also highlights the periventricular enhancing masses, but with a lower signal-to-noise ratio of 53:1, compared with the shorter echo SWI. However, the longer echo Gd-SWI (B) has greater T2* weighting and reveals the draining medullary veins (*arrowheads*). Note that the area of brain vasogenic edema (*asterisks*) seen on shorter echo Gd-SWI (A) is not visible in the longer echo Gd-SWI (B) because the background brain tissue loses the signal faster than the tissue with edema, so it appears isointense. Dual-echo Gd-SWI parameters were: TE 1=10 ms and TE 2=22 ms, TR=29 ms, flip angle=15°, in-plane resolution=0.9×0.9 mm, and a section thickness of 2.5 mm. The data were collected from a 3T MR imaging scanner (Siemens 3.0T Skyra, Erlangen, Germany).

In summary, multiecho Gd-SWI can produce images with different contrast weighting through a single image sequence acquisition, which can be advantageous in the characterization of various CNS pathologies.

REFERENCES

1. Fonseca AP, do Carmo RL, Pacheco FT, et al. **Primary angiitis of the CNS with unremarkable vessel wall MR imaging: how the “T1 shinethrough” effect on SWI adds to the detection of gadolinium enhancement of small intraparenchymal brain vessels.** *AJNR Am J Neuroradiol* 2021;42:E24–26 CrossRef Medline

2. Suthiphosuwana S, Bharatha A, Hsu CC, et al. **Tumefactive primary central nervous system vasculitis: imaging findings of a rare and under-recognized neuroinflammatory disease.** *AJNR Am J Neuroradiol* 2020;41:2075–81 CrossRef Medline
3. Hsu CC, Haacke EM, Heyn CC, et al. **The T1 shine through effect on susceptibility weighted imaging: an under recognized phenomenon.** *Neuroradiology* 2018;60:235–37 CrossRef Medline
4. Wu D, Liu S, Buch S, et al. **A fully flow-compensated multiecho susceptibility-weighted imaging sequence: The effects of acceleration and background field on flow compensation.** *Magn Reson Med* 2016;76:478–89 CrossRef Medline
5. Chen Y, Liu S, Wang Y, et al. **Strategically acquired gradient echo (STAGE) imaging, Part I: creating enhanced T1 contrast and standardized susceptibility weighted imaging and quantitative susceptibility mapping.** *Magn Reson Imaging* 2018;46:130–39 CrossRef Medline

 **C.C.-T. Hsu**

 **L. Du**

 **D. Luong**

Division of Neuroradiology, Department of Medical Imaging
Gold Coast University Hospital
Southport, Queensland, Australia

 **S. Suthiphosuwana**

Division of Neuroradiology, Department of Medical Imaging
St Michael's Hospital
Toronto, Ontario, Canada

 **A. Bharatha**

Division of Neuroradiology, Department of Medical Imaging and Division
Neurosurgery, Department of Surgery
St. Michael's Hospital
Toronto, Ontario, Canada

 **T. Krings**

Division of Neuroradiology, Department of Medical Imaging
Toronto Western Hospital
Toronto, Ontario, Canada

 **E.M Haacke**

Department of Radiology
Wayne State University
Detroit, Michigan

 **A.G Osborn**

Departments of Pathology and Radiology and Imaging Sciences
University of Utah
Salt Lake City, Utah

Susceptibility Artifacts in the Anterior Cranial Fossa Mimicking Hemorrhage in Patients with Anosmia

There has been a steady stream of requests for MR imaging studies of the brain for investigating anosmia in patients with coronavirus disease 2019 (COVID-19) at our institution in Miami, which was briefly the American center of the pandemic. We read with great interest the report of Aragão et al¹ in the September 2020 issue of *AJNR*, titled “Anosmia in COVID-19 Associated with Injury to the Olfactory Bulbs Evident on MRI,” and we have occasionally encountered similar findings in patients with anosmia. In interpreting these examinations, we have assumed (given the limited history available to us) that these patients are either known or presumed to have been infected with COVID-19. As the novelty of these findings has lessened, members of our group have begun to realize similar findings are present in many patients who were referred for unrelated indications. Furthermore, we have ascribed the striking symmetry of the high signal to the presence of methemoglobin. The lack of morphologic (ie, swelling) changes in the areas of high signal and the lack of involvement of the olfactory bulb have led us to question the validity of these findings.

The letter by Dr Mamourian² published in the February 2021 issue of *AJNR* closely echoes the suspicion of members of our group that the observed areas of high signal were artifactual, likely secondary to magnetic susceptibility artifacts from the air-bone interfaces present in the anterior cranial fossa.

In March 2020, a patient underwent 3T MR imaging of her brain at our public hospital for investigation of anosmia. Areas of high T1 signal were present in the anterior cranial fossa bilaterally, localizing symmetrically to the olfactory sulcus and medial orbital gyrus. No abnormality was observed in the olfactory bulb itself (Fig 1). Upon review of the patient’s medical records, it was discovered the patient’s anosmia greatly predated (by many years) the COVID-19 pandemic and that the patient had antibody

negative for COVID-19. This information heightened our suspicion that the T1 shortening observed in this patient and others with similar findings represented magnetic susceptibility artifacts. It was hypothesized that these findings would be absent or less prominent on a repeat examination with a lower strength magnet, as this is a characteristic of magnetic susceptibility artifacts. After a discussion with the referring physician, the patient returned a week later for a repeat examination on a 1.5T scanner, and the previously observed findings were absent. This strongly indicates an artifactual origin of these findings (Fig 2).

While COVID-19 has surely become the most prominent and is an increasingly important cause of anosmia in the American population, other causes of anosmia exist. Learning of purported MR imaging findings in the brain correlating with their symptoms might cause patients distress or a worsening of symptoms. It is incumbent upon neuroradiologists to exercise caution in the description of novel findings in novel diseases.

REFERENCES

1. Aragão MD, Leal MC, Cartaxo FO, et al. **Anosmia in COVID-19 associated with injury to the olfactory bulbs evident on MRI.** *AJNR Am J Neuroradiol* 2020;41:1703–06 CrossRef Medline
2. Mamourian A. **Seeing what we expect to see in COVID-19.** *AJNR Am J Neuroradiol* 2021;42:E1 CrossRef Medline

© J.J. Manov

© M. Alfonso

© G. Saigal

Department of Radiology
University of Miami Miller School of Medicine
Miami, Florida

<http://dx.doi.org/10.3174/ajnr.A7184>

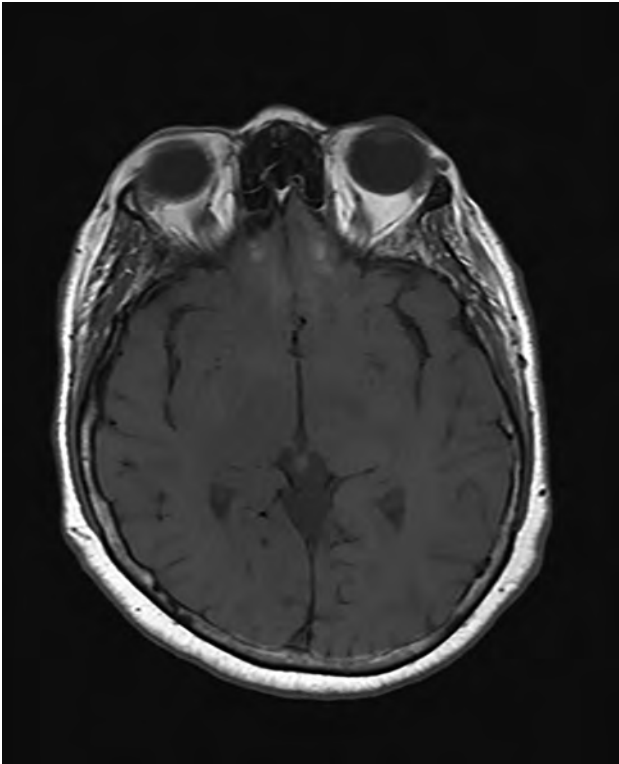


FIG 1. T1-weighted spin-echo sequence obtained on a 3T magnet demonstrating shortening in the olfactory sulcus and medial orbital gyrus.

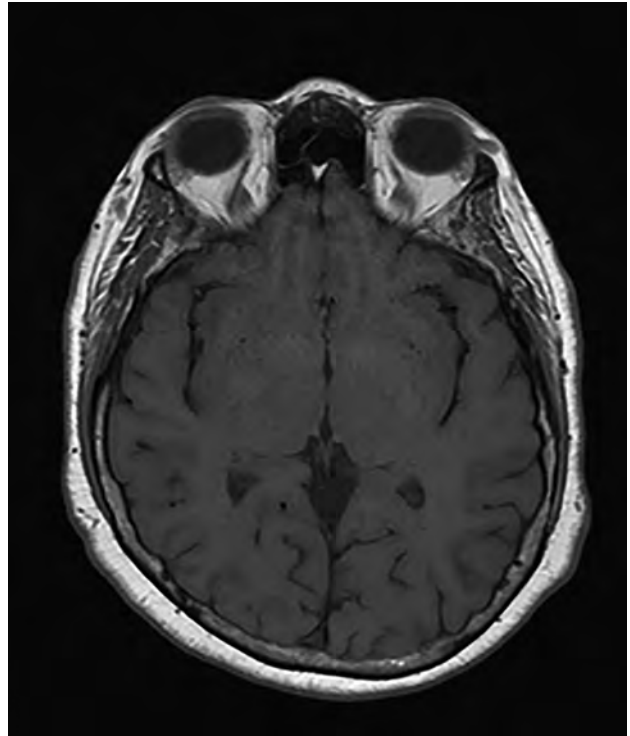


FIG 2. T1-weighted spin-echo sequence obtained on a 1.5T magnet with an absence of the previously observed signal.

REPLY:

First, we would like to thank authors of the new commentary,¹ which gave us the chance to reply to critics of our first publication² entitled “Anosmia in COVID-19 Associated with Injury to the Olfactory Bulbs Evident on MRI” written before the existence of anatomopathologic studies.

Our research group had the opportunity to study and publish 3 other recent articles³⁻⁵ about the same subject. In these articles,³⁻⁵ we explained why we have interpreted² the alterations on brain imaging of patients with coronavirus disease 2019 (COVID-19) detected on thin slices of the coronal fat-suppressed T1WI, pre- and/or postcontrast, as olfactory bulb injuries (blood-brain barrier and/or methemoglobin) and not artifacts. However, we will present these explanations again and also comment about some aspects of your Letter,¹ as follows:

1. We understand the reason for your concern about susceptibility artifacts and confess that initially, we also had the same doubts as you expressed in your Letter when for the first time, we were faced with the images of these olfactory bulb injuries in patients with COVID-19.
2. To make sure that the findings we were identifying in the olfactory bulbs were real and represented an abnormality, we also reviewed the pre- and/or postcontrast fat-suppressed T1WI and STIR MR imaging from our data base of the orbits of healthy subjects obtained before the COVID-19 pandemic, and we explained these findings^{2,3} in our first publication.² We used this precaution because we did not find any article in the literature describing the normal aspect of the olfactory bulbs in pre- and postcontrast fat-suppressed T1WI or STIR.
3. Our research group performed another retrospective study not yet published (performed on 1.5T MR imaging) that show that the normal olfactory bulbs have signal intensity similar to that of the cortical gray matter in the sequence using thin-sliced coronal fat-suppressed T1WI (Fig 1A, arrows) with no contrast enhancement (Fig 1B, and Fig 2A, long arrows). On coronal thin-sliced FSE T2WI, in 90% of olfactory bulbs, the central area has hyperintensity similar to that in the cortical gray matter (Fig 1C and Fig 2B, superior extremity of lines) and the periphery has hypointensity of the white matter (Fig 1C and Fig 2B, horizontal short arrows). This aspect resembles the cell layers observed on histology of normal olfactory bulbs.

Susceptibility artifacts due to the interface between the bone and air were found in 81% of images in our study. All of these susceptibility artifacts were bilateral and symmetric, mainly at the topography of the cribriform plate outside and below the olfactory bulbs (Fig 1B, arrowhead and Fig 2A, short arrow) or the parasagittal region adjacent to the crista galli and more frequently on postcontrast sequences. Forty-five percent of patients also presented with a kind of susceptibility artifact at the sphenoidal level that projected inside the base of the frontal lobe, being easily recognized as an artifact as you also showed in your axial T1WI¹ performed at 3T. These sus-

ceptibility artifacts should not hinder the analyses of olfactory bulbs because they can be recognized.

4. So, as you seemingly know and in fact show in your figures¹ on axial T1WI, artifacts can be easily recognized by radiologists and should not be confounded with enhancement or methemoglobin. The susceptibility artifacts usually have ill-defined margins that eventually vanish and are often bilateral as you have shown in your axial Fig 1.

Anyone reviewing our figures (in the first publication,² in our first reply,³ in our Letter,⁴ and also in our original study recently published⁵) will realize that they show true lesions and not artifacts.

5. In your Letter,¹ you wrote about susceptibility artifacts being worse on 3T brain MRI, and they are reduced and disappear in a minor magnetic field MRI machine such as 1.5T.

All of our patients' brain MRIs were performed on a 1.5T machine,²⁻⁵ and this was clearly described in the Materials and Methods² of our article on which you are commenting. Therefore, the brain MRIs of our cases may have fewer artifacts than yours because we used a 1.5T machine and you used a 3T machine. Perhaps this is the reason you have had difficulty with artifacts.

6. In the figures of your commentary and Letter,¹ we were surprised because you showed figures using axial slices on T1WI, which are not adequate to analyze the olfactory bulbs. It would be better if you had shown this artifact in the coronal plane of your figures.

I would kindly ask you to look again at the figures in our publications²⁻⁵ because we included and analyzed only cases in which there was a sequence with thin slices on the coronal plane.

If the indication for brain MR imaging is to evaluate the olfactory bulbs, it is much better to analyze them in a coronal plane or use 3D acquisitions of the brain with reconstructions in the coronal and sagittal planes.

7. Our MRI findings, as well as other research findings, documented *in vivo*^{2,6-8} the hypothesis of Severe Acute Respiratory Syndrome coronavirus 2 in the olfactory bulbs as a cause of anosmia, even before the first anatomopathologic studies were allowed to be performed and published.^{9,10} And now, recently, the first histopathologic postmortem studies have confirmed our findings.^{9,10}

Lee et al⁹ demonstrated, in an extremely elegant postmortem histopathologic study using much more sophisticated tools (eg, an 11.7T scanner), what we had suggested *in vivo* previously on the 1.5T MR imaging.² This postmortem histopathologic study showed microvascular injury with areas of fibrinogen leakage, thinned basal lamina, and hemorrhagic lesions in the brain and olfactory bulbs,⁹ which can explain our radiologic findings (olfactory bulb enhancement [breakdown of the blood-brain barrier] and/or probable hemorrhagic lesions [methemoglobin]).²⁻⁵

In summary, we explained again, point by point, why our findings are not artifacts.²⁻⁵ We show new data with the features of a normal olfactory bulb on coronal T2WI which frequently has a hyperintense central area (similar to the cortex) surrounded by a hypointense layer (similar to white matter) and susceptibility artifacts at the cribriform plate on coronal fat suppressed T1WI.

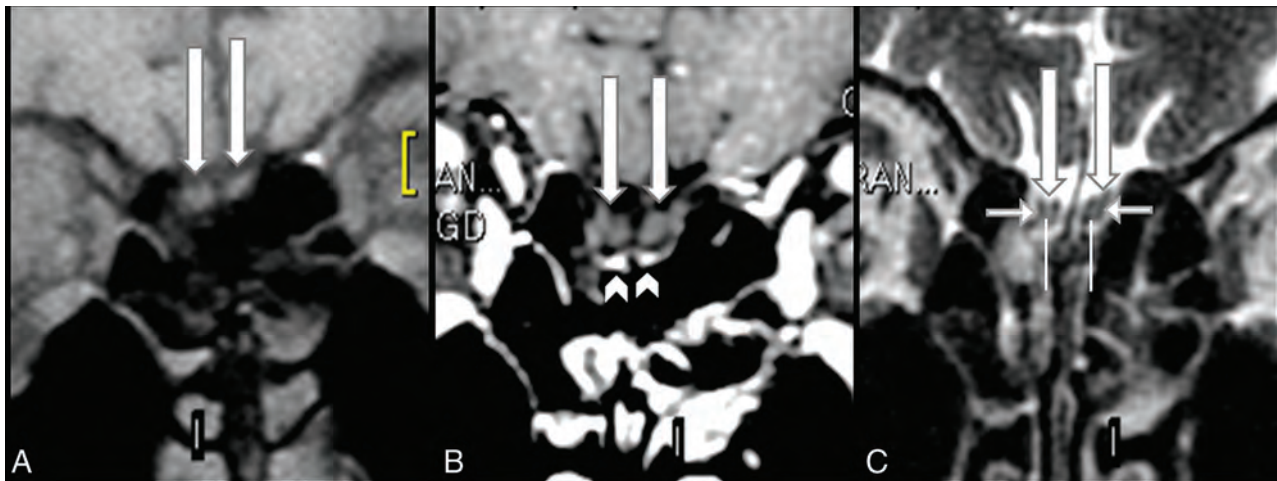


FIG 1. Normal olfactory bulbs and susceptibility artifacts seen on 1.5T MR imaging before the COVID-19 pandemic. The coronal precontrast fat-suppressed TIWI (A) and the postcontrast (B) and coronal FSE T2WI (C) demonstrate normal olfactory bulbs (*long arrows*). The olfactory bulbs are isointense to the cerebral cortex and normally hypointense on pre- (A) and postgadolinium sequences (B) and do not enhance. Susceptibility artifacts on the cribriform plate (B, *arrowheads*) are bilateral and symmetric below the olfactory bulbs and do not hinder the analysis. On thin-sliced coronal FSE T2WI, the normal olfactory bulbs show a “sandwich-like pattern,” which consists of a hyperintense central area (C, *superior extremity of the vertical lines*), similar to the cortical gray matter, and a hypointense periphery (C, *short horizontal arrows*), similar to the white matter that looks like the laminar layers of olfactory bulbs on histology.

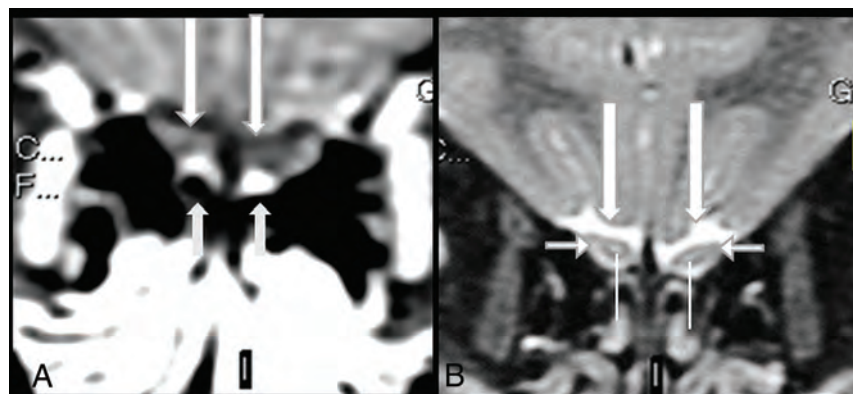


FIG 2. Normal olfactory bulbs and susceptibility artifacts seen on 1.5T MR imaging before the COVID-19 pandemic. The olfactory bulbs are normal, being hypointense, and do not enhance on thin-sliced coronal fat-suppressed postcontrast TIWI (A, *long arrows*). Susceptibility artifacts are bilateral and symmetric and can be recognized as hyperintensity located outside and adjacent to the inferior periphery of the normal olfactory bulbs, mainly at cribriform plate (A, *short arrows*). On coronal T2WI, the normal sandwich-like pattern is observed as the central portion of olfactory bulbs showing hyperintensity (B, *superior extremity of the line*), similar to that of gray matter, and the peripheral portion showing hypointensity, similar to that of white matter (B, *short horizontal arrows*).

We also commented on the Letter¹ from our colleagues in Miami. Therefore, in closing, we would like to state that despite sometimes finding artifacts on MR imaging, an experienced radiologist would recognize the artifacts and have the obligation to communicate if find any other important information about the MR images (such as olfactory bulb injury seen in a retrospective study on MR imaging of patients with COVID-19 not investigated for anosmia but investigated for other neurologic complications in the beginning of this terrible pandemic) in an impartial manner. It is our obligation to present our findings to the scientific community without any preconceptions, recognizing MR imaging artifacts and differentiating them from what seemed true COVID-related lesions in the olfactory bulbs. Increasingly, the scientific community is accumulating proof that there is clinical,

radiologic²⁻⁸ (MR imaging in vivo²⁻⁸ and in postmortem⁹), and anatomopathologic^{9,10} evidence for the presence of injury to the olfactory bulbs in patients with COVID-19.

REFERENCES

1. Manov JJ, Saigal G, Alfonso M. **Susceptibility artifacts in the anterior cranial fossa mimicking hemorrhage in anosmic patients.** *AJNR Am J Neuroradiol* 2021 July [Epub ahead of print] CrossRef
2. Aragão MF, Leal MC, Cartaxo Filho OQ, et al. **Anosmia in COVID-19 associated with injury to the olfactory bulbs evident on MRI.** *AJNR Am J Neuroradiol* 2020;41:1703–16 CrossRef Medline
3. Aragão MF, Leal MC, Fonseca TM, et al. **Reply.** *AJNR Am J Neuroradiol* 2020;2:E2–E3 CrossRef Medline
4. Aragao MF, Oliveira AD, Lima AR, et al. **Virtual biopsy: a reality thanks to advances in radiology.** *AJNR Am J Neuroradiol* 2021 Mar 25. [Epub ahead of print] CrossRef Medline

5. Aragao M, Leal MC, Andrade PH, et al. **Clinical and radiological profiles of COVID-19 patients with neurological symptomatology: a comparative study.** *Viruses* 2021;13:845 CrossRef Medline
6. Lauredon T, Radulesco T, Mugnier J, et al. **Bilateral transient olfactory bulb edema during COVID-19-related anosmia.** *Neurology* 2020;95:224–25 CrossRef Medline
7. Chetrit A, Lechien JR, Ammar A, et al. **Magnetic resonance imaging of COVID-19 anosmic patients reveals abnormalities of the olfactory bulb: preliminary prospective study.** *J Infect* 2020;81:816–46 CrossRef Medline
8. Strauss SB, Lantos JE, Heier LA, et al. **Olfactory bulb signal abnormality in patients with COVID-19 who present with neurologic symptoms.** *AJNR Am J Neuroradiol* 2020;41:1882–87 CrossRef Medline
9. Lee MH, Perl DP, Nair G, et al. **Microvascular injury in the brains of patients with Covid-19.** *N Engl J Med* 2021;384:481–83 CrossRef Medline
10. Matschke J, Lütgehetmann M, Hagel C, et al. **Neuropathology of patients with COVID-19 in Germany: a post-mortem case series.** *Lancet Neurol* 2020;19:919–29 CrossRef

 **M.F.V.V. Aragao**
Universidade Federal de Pernambuco
Recife, Brazil

Multimagem Centro Diagnóstico
Recife, Brazil

 **P.H.P. deAndrade**

 **V.S. da Nobrega Segundo**

 **M.M. Marques**

Universidade Federal de Pernambuco
Recife, Brazil

 **H.J.G. de Azevedo**

Hospital das Clinicas da Universidade Federal de Pernambuco
Recife, Brazil

 **R.J.V. de Mello**

 **M. de Carvalho Leal**

Universidade Federal de Pernambuco
Recife, Brazil

 **M.L. Soares**

Universidade Federal de Alagoas
Maceio, Brazil

Centro Universitario Cesmac
Maceio, Brazil

 **M.M. Valenca**

Universidade Federal de Pernambuco
Recife, Brazil

The Possible Difference of Underlying Pathophysiologies between “Ivy Sign” on Contrast-Enhanced MRI and FLAIR

We read with interest the article by Wang et al¹ titled “Ivy Sign in Moyamoya Disease: A Comparative Study of the FLAIR Vascular Hyperintensity Sign Against Contrast-Enhanced MR Imaging.” The results of the study carried out by Wang et al are agreeable, which show that the ivy sign score on contrast-enhanced MR imaging was statistically significantly correlated with the amount of leptomeningeal collateral from the posterior cerebral artery on digital subtraction angiography, while the ivy sign score on FLAIR was not. A previous report also speculated that the ivy sign score on contrast-enhanced MR imaging may correspond to angiographic cortical microvascularization via leptomeningeal collaterals.²

Although the authors did not clearly mention it, their results revealed different underlying pathophysiologies between the ivy sign on contrast-enhanced MR imaging and FLAIR. Moreover, the ivy sign on contrast-enhanced MR imaging may not be an alternative to that on FLAIR, based on the following opinions derived from their results. First, the ivy sign score on contrast-enhanced MR imaging before surgery was significantly correlated with the postoperative revascularization grade. The study speculated that the more leptomeningeal collaterals present before surgery, the better the outcome of the revascularization operation would be. The ivy sign on contrast-enhanced MR imaging may be angiographic cortical microvascularization via leptomeningeal collaterals. However, the ivy sign on FLAIR before surgery was not significantly correlated with the postoperative revascularization grade. This result indicates that the ivy sign on FLAIR may not reflect leptomeningeal collaterals, but the slow flow of maximally dilated pial vasculature (microscopic cortical microvascularization) compensates for the decreased perfusion.³

The ivy sign may be observed in the posterior MCA region on FLAIR if the ivy sign on FLAIR reflects leptomeningeal collaterals from the posterior cerebral artery similar to the ivy sign on contrast-enhanced MR imaging. However, it was more frequently observed in the anterior MCA region than in the posterior MCA region on FLAIR in our previous study.³ Did the distribution of ivy signs in the study population of Wang et al¹ differ between contrast-enhanced MR imaging and FLAIR? The ivy sign on FLAIR was significantly correlated with the cerebrovascular reserve on SPECT, suggesting that it may reflect the slow flow of maximally dilated pial vasculature.³ The postoperative decrease in ivy signs on

FLAIR in the operative side with an increase in cerebrovascular reserve on SPECT supports the current hypothesis.⁴

Second, they showed that the ivy sign score on contrast-enhanced MR imaging was negatively correlated with CBF in the MCA region in the late Suzuki stage. Their speculation was that it was because of the imbalance between leptomeningeal collaterals and abnormal ICA and Moyamoya vessels; however, posterior circulation (posterior cerebral artery stenosis or occlusion) was often involved in this phase, and various amounts of leptomeningeal collaterals may be present on a case-by-case basis. Therefore, the ivy sign on contrast-enhanced MR imaging in the late Suzuki stage may be attributable to maximally dilated pial vasculature, as well as leptomeningeal collaterals. Further study with the ivy sign distribution and cerebrovascular reserve assessment will be needed to confirm the different underlying pathophysiologies between the ivy sign on contrast-enhanced MR imaging and FLAIR.

REFERENCES

1. Wang LX, Wang H, Hao FB, et al. **Ivy sign in Moyamoya disease: a comparative study of the FLAIR vascular hyperintensity sign against contrast-enhanced MRI.** *AJNR Am J Neuroradiol* 2021;42:694–700 CrossRef Medline
2. Mugikura S, Fujimura M, Takahashi S. **Cortical microvascularization and leptomeningeal collaterals in Moyamoya disease.** *Eur Neurol* 2015;73:351–52 CrossRef Medline
3. Mori N, Mugikura S, Higano S, et al. **The leptomeningeal “Ivy Sign” on fluid-attenuated inversion recovery MR imaging in Moyamoya disease: a sign of decreased cerebral vascular reserve?** *AJNR Am J Neuroradiol* 2009;30:930–35 CrossRef Medline
4. Kawashima M, Noguchi T, Takase Y, et al. **Decrease in leptomeningeal ivy sign on fluid-attenuated inversion recovery images after cerebral revascularization in patients with Moyamoya disease.** *AJNR Am J Neuroradiol* 2010;31:1713–18 CrossRef Medline

© N. Mori

Department of Diagnostic Radiology
Tohoku University Graduate School of Medicine
Sendai, Japan

© S. Mugikura

Department of Diagnostic Radiology
Tohoku University Graduate School of Medicine
Sendai, Japan

Department of Image Statistics
Tohoku Medical Megabank Organization, Tohoku University
Sendai, Japan

REPLY:

We appreciate the comments by Drs Mori and Mugikura and thank the editor for the opportunity to reply to those comments.

As suggested by Drs Mori and Mugikura, our results may “revealed different underlying pathophysiologies” between the two imaging modalities. Until today, most studies support the hypothesis that FLAIR vascular hyperintensity (FVH) represents slow or turbulent flow through the engorged leptomeningeal collaterals (LMCs).¹ As to contrast-enhanced MR imaging (CEMR), a previous study suggested that the pial vascular enhancement in Moyamoya disease could be attributed to a decrease of flow velocity–related signal losses and spin-dephasing effects, which consequently induce high intensity of the vessel from the mixture of blood and contrast medium.² The underlying pathophysiology of the ivy sign on CEMR and FLAIR still needs future validation to explore the association of visible imaging findings and physical mechanisms.

The main objective of our study was to develop a quantitative method on both CEMR and FLAIR and to compare the ability of these two imaging modalities in reference to DSA. As mentioned by Drs Mori and Mugikura in the letter, they found that the distribution of FVH was more frequently seen in the anterior MCA region. Furthermore, they found that LMCs in the anterior and posterior regions could also change along with the Suzuki stages in Moyamoya disease.³ ASPECTS is a widely accepted approach for brain region segmentation in cerebrovascular diseases. In this study, we used this approach and designed a total ivy sign score. As a result, no statistical comparison concerning the distribution of the ivy sign was performed. Nevertheless, in the process of scoring, no obvious visible difference in the distribution of the ivy sign between CEMR and FLAIR was found.

To our knowledge, the relationship between FVH and hemodynamic indicators, cerebrovascular reserve (CVR) and CBF for example, showed different results in previous literature.^{4,5} One possible explanation is the result of our study. Because the presence of FVH seems to be associated with the clinical phase of the ischemic lesion in Moyamoya disease, patients with different clinical phases enrolled in the previous studies may affect the consistency. Another possible reason is the different hemodynamic indicators used. Compared with CBF, which was used in our study, CVR

may be more sensitive for reflecting hemodynamic changes. Physically, the CBF value will decrease when the cerebral vessels reach the maximum of vasodilatory ability.

Another comment was about the correlation between the ivy sign score on CEMR and CBF in the late Suzuki stage. Drs Mori and Mugikura mentioned that posterior circulation involvement is often seen in this phase. In our study, we used posterior cerebral artery involvement as a covariant to address the impact of this confounding factor. We completely agree that the ivy sign on CEMR may be attributed to the maximally dilated pial vasculature, which includes both arterioles and venules. Although we assume that the imbalance between LMCs and abnormal ICA and Moyamoya vessels may be one possible explanation, the underlying mechanism of the negative relationship between the ivy sign score on CEMR and CBF in the late Suzuki stage is still to be determined. Future studies with larger sample sizes, sensitive hemodynamic indicators and advanced imaging processing approach are needed to confirm the current results.

REFERENCES

1. Jiang L, Chen YC, Zhang H, et al. **FLAIR vascular hyperintensity in acute stroke is associated with collateralization and functional outcome.** *Eur Radiol* 2019;29:4879–88 CrossRef Medline
2. Komiyama M, Nakajima H, Nishikawa M, et al. **Leptomeningeal contrast enhancement in Moyamoya: its potential role in postoperative assessment of circulation through the bypass.** *Neuroradiology* 2001;43:17–23 CrossRef Medline
3. Mugikura S, Fujimura M, Takahashi S. **Cortical microvascularization and leptomeningeal collaterals in Moyamoya disease.** *Eur Neurol* 2015;73:351–52 CrossRef Medline
4. Mori N, Mugikura S, Higano S, et al. **The leptomeningeal “ivy sign” on fluid-attenuated inversion recovery MR imaging in Moyamoya disease: a sign of decreased cerebral vascular reserve?** *AJNR Am J Neuroradiol* 2009;30:930–05 CrossRef Medline
5. Noguchi T, Kawashima M, Nishihara M, et al. **Arterial spin-labeling MR imaging in Moyamoya disease compared with clinical assessments and other MR imaging findings.** *Eur J Radiol* 2013;82:e840–47 CrossRef Medline

✉ **L.X. Wang**

Department of Radiology
First Medical Center, Chinese People's Liberation Army General Hospital
Beijing, China
Medical School of Chinese People's Liberation Army
Beijing, China

✉ **L. Ma**

✉ **X. Lou**

Department of Radiology
First Medical Center, Chinese People's Liberation Army General Hospital
Beijing, China

<http://dx.doi.org/10.3174/ajnr.A7233>

Regarding “CTA Evaluation of Basilar Septations: An Entity Better Characterized as Aberrant Basilar Fenestrations”

We read with great interest the recent article by Small et al,¹ “CTA Evaluation of Basilar Septations: An Entity Better Characterized as Aberrant Basilar Fenestrations,” a retrospective review describing luminal abnormalities of the basilar artery. We wish to highlight a recent case at our institution that we believe constitutes an interesting example of a further variation in the luminal morphology of the basilar artery.

A 71-year-old male patient presented with transient sensory disturbance of the right upper limb, clinically considered to be suggestive of a transient ischemic attack. The patient underwent noncontrast CT of the head, CT angiography of the head and neck, and subsequently MR imaging of the brain. Imaging did not demonstrate an acute infarct or vascular occlusion; however, note was made of abnormal morphology of the vertebrobasilar system with what was interpreted as a small communicating vessel joining the distal V4 segments of the vertebral arteries (Fig 1). It is possible, however, that this, in fact, represents a further transversely orientated variant of basilar fenestration morphology, not conforming directly to the classification described by Small et al. We have been unable to identify additional previously described examples of this in the literature.²⁻⁴ Incidentally, the patient’s imaging also demonstrated a right-sided persistent trigeminal artery (Fig 2).

<http://dx.doi.org/10.3174/ajnr.A7206>

REFERENCES

1. Small JE, Macey MB, Wakhloo AK, et al. **CTA evaluation of basilar septations: an entity better characterized as aberrant basilar fenestrations.** *AJNR Am J Neuroradiol* 2021 Feb 18. [Epub ahead of print] CrossRef Medline
2. Pérez-Carrillo GJ, Hogg JP. **Intracranial vascular lesions and anatomical variants all residents should know.** *Curr Probl Diagn Radiol* 2010;39:91–109 CrossRef Medline
3. Case D, Kumpe D, Roark C, et al. **Neuroangiography: review of anatomy, periprocedural management, technique, and tips.** *Semin Intervent Radiol* 2020;37:166–74 CrossRef Medline
4. Thurlow PC, Andrus JM, Wholey MH. **Common cervical and cerebral vascular variants.** *Interv Cardiol Clin* 2014;3:123–34 CrossRef Medline

© J. Hynes

Department of Radiology
Mater Misericordiae University Hospital
Dublin, Ireland

© E. Kavanagh

Department of Radiology
Mater Misericordiae University Hospital
Dublin, Ireland

Department of Radiology
Cappagh National Orthopaedic Hospital
Dublin, Ireland

University College Dublin
Belfield, Ireland



FIG 1. MIP TOF-MRA image demonstrates a small vascular communication (*arrow*) between the distal vertebral arteries.

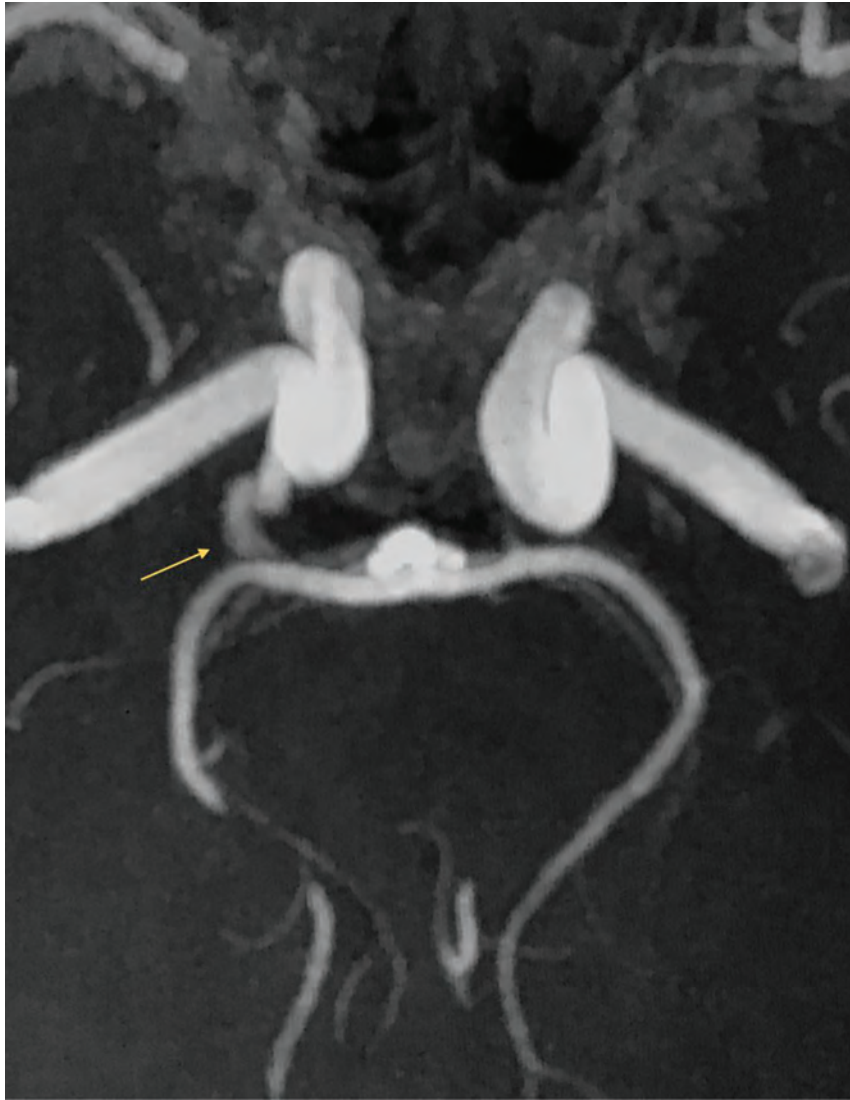


FIG 2. MIP TOF-MRA image demonstrates a right-sided persistent trigeminal artery (*arrow*).